Application de l'interférométrie à l'étude des Céphéides et des étoiles naines

Pierre Kervella

Université Paris VII - Denis Diderot Observatoire de Paris

Habilitation à Diriger des Recherches
Spécialité : Astronomie & Astrophysique

Application de l'interférométrie à l'étude des Céphéides et des étoiles naines

par

Pierre Kervella

Soutenue le 11 juillet 2007 devant le Jury composé de :

M. Gérard Rousset	Président
M. Aurélien Barrau	Rapporteur
M. Alain Chelli	Rapporteur
M. Pierre Léna	Rapporteur
M. David Bersier	Examinateur
M. Pascal Fouqué	Examinateur
M. Denis Mourard	Examinateur
M. Frédéric Thévenin	Examinateur

A Judith et à mes Parents

Sommaire

1 Introduction **1**

1.1 Les débuts de l'interférométrie stellaire 1
1.2 L'interféromètre d'intensité et l'hétérodyne 3
1.3 I2T, premier interféromètre à deux télescopes 4
1.4 Mark III, PTI, IOTA, SUSI, NPOI, CHARA,... 5
1.5 Les premiers géants : Keck, VLTI et OHANA 6
1.6 VINCI, le premier instrument du VLTI 7
1.6.1 **Article SPIE** : "VINCI, the VLTI Commissioning Instrument : status after one year of operations at Paranal" (2002) 9
1.6.2 **Article A&A** : "Data reduction methods for single-mode optical interferometry - Application to the VLTI two-telescopes beam combiner VINCI" (2004) 23
1.7 Résultats astrophysiques avec VINCI 41
1.7.1 Céphéides 41
1.7.2 Etoiles naines 41
1.7.3 Rotateurs rapides 42

2 Les Céphéides **43**

2.1 La méthode Baade-Wesselink 45
2.1.1 **Article A&A** : "Cepheid distances from infrared long-baseline interferometry – I. VINCI/VLTI observations of seven Galactic Cepheids" (2004) 47
2.1.2 **Article A&A** : "II. Calibration of the period-radius and period–luminosity relations" (2004) 65
2.1.3 **Article A&A** : "III. Calibration of the surface brightness-color relations" (2004) 73
2.1.4 **Lettre ApJ** : "The angular size of the Cepheid ℓ Car : a comparison of the interferometric and surface brightness techniques" (2004) 85
2.2 Le facteur de projection : un point clef 91
2.2.1 **Lettre A&A** : "The projection factor of δ Cephei – A calibration of the Baade-Wesselink method using the CHARA Array" (2005) 93
2.2.2 **Article A&A** : "Self consistent modelling of the projection factor for interferometric distance determination" (2004) 99
2.2.3 **Article A&A** : "High resolution spectroscopy for Cepheids distance determination – I. Line asymmetry" (2006) 107
2.3 L'environnement circumstellaire des Céphéides 123
2.3.1 Des indices convergents... 123

2.3.2 **Article A&A** : "Extended envelopes around Galactic Cepheids. I. ℓ Carinae from near and mid-infrared interferometry with the VLTI" (2006) 125
2.3.3 **Article A&A** : "II. Polaris and δ Cep from near-infrared interferometry with CHARA/FLUOR" (2006) 135
2.4 Projets de recherche 145
2.4.1 Etalonnage de l'échelle de distance des Céphéides 145
2.4.2 Spectro-interférométrie avec MIDI et AMBER 145

3 La séquence principale **147**
3.1 Les étoiles de très faible masse 147
3.1.1 **Lettre A&A** : "First radius measurements of very low mass stars with the VLTI" (2003) 149
3.2 Interférométrie et astérosismologie 155
3.2.1 **Article A&A** : "The diameters of α Centauri A and B. A comparison of the asteroseismic and VINCI/VLTI views" (2003) 157
3.2.2 **Article A&A** : "The diameter and evolutionary state of Procyon A. Multi-technique modeling using asteroseismic and interferometric constraints" (2003) 169
3.2.3 **Article A&A** : "VLTI/VINCI diameter constraints on the evolutionary status of δ Eri, ξ Hya, η Boo" (2005) 177
3.3 Assombrissement centre-bord 189
3.3.1 **Article A&A** : "The limb darkening of α Cen B. Matching 3D hydrodynamical models with interferometric measurements" (2006) 191
3.4 La brillance de surface des étoiles naines 199
3.4.1 **Article A&A** : "The angular sizes of dwarf stars and subgiants. Surface brightness relations calibrated by interferometry" (2004) 201
3.5 Projets de recherche 215

4 Les étoiles en rotation rapide **217**
4.1 La rotation des masses fluides 217
4.1.1 Une question ancienne 217
4.1.2 L'équilibre d'une étoile en rotation 219
4.1.3 Deux exemples de rotateurs rapides proches de nous : Saturne et Jupiter . 220
4.2 Altaïr (α Aql) 221
4.2.1 Observations interférométriques et modélisation 221
4.2.2 **Article A&A** : "Gravitational darkening of Altair from interferometry" (2005) 223
4.3 Achernar (α Eri) 237
4.3.1 Observations avec le VLTI 237
4.3.2 La nécessité de la rotation différentielle 237
4.3.3 **Lettre A&A** : "The spinning-top Be star Achernar from VLTI-VINCI" (2003) 239
4.3.4 **Article A&A** : "The polar wind of the fast rotating Be star Achernar. VINCI/VLTI interferometric observations of an elongated polar envelope" (2006) 245
4.3.5 **Article Pour La Science** "Les étoiles, déformées par leur rotation" (2005) 255
4.4 Véga (α Lyr) 264
4.4.1 Une géométrie particulière 264

4.4.2 Observations récentes avec CHARA 264
4.4.3 **Article ApJ** : "First results from the CHARA array. VII. Long-baseline interferometric measurements of Vega consistent with a pole-on, rapidly rotating star" (2006) 267
4.5 Projets de recherche 281

5 Perspectives scientifiques **283**
5.1 Une technique de spécialistes ? 283
5.2 Un nouvel outil pour la physique stellaire 283
5.3 Combien d'étoiles mesurables ? 284
5.4 La fiabilité, clef des grands réseaux 285
5.5 Vers le VLTI de seconde génération 286
5.6 L'interférométrie dans l'espace 288
5.7 Un interféromètre sur la Lune ? 290

A Encadrement de jeunes chercheurs **293**
A.1 Stage de Melle Jessica GALLY (2006) 293
A.2 Stage de Melle Lucile PUPIER (2006) 293

B Résumé sur l'originalité des recherches **295**

Bibliographie **297**

Chapitre 1

Introduction

1.1 Les débuts de l'interférométrie stellaire

La première application astronomique de l'interférométrie a été réalisée sur des étoiles brillantes par Edouard Stéphan à l'Observatoire de Marseille vers 1873, suivant une idée énoncée par Armand Hippolyte Louis Fizeau (Fig. 1.1) en 1867. Mais l'instrument utilisé étant de trop petite taille (base de 65 cm), aucune étoile n'a pu être résolue. Fixant une limlite supérieure de 0,158" au diamètre angulaire des étoiles observées, Stéphan a conclu très justement que "ce diamètre est une très faible fraction du nombre précédent". Le lecteur intéressé pourra consulter l'important recueil d'articles historiques sur l'interférométrie stellaire réuni par Peter Lawson (Lawson 1997) pour plus de détails sur ces observations.

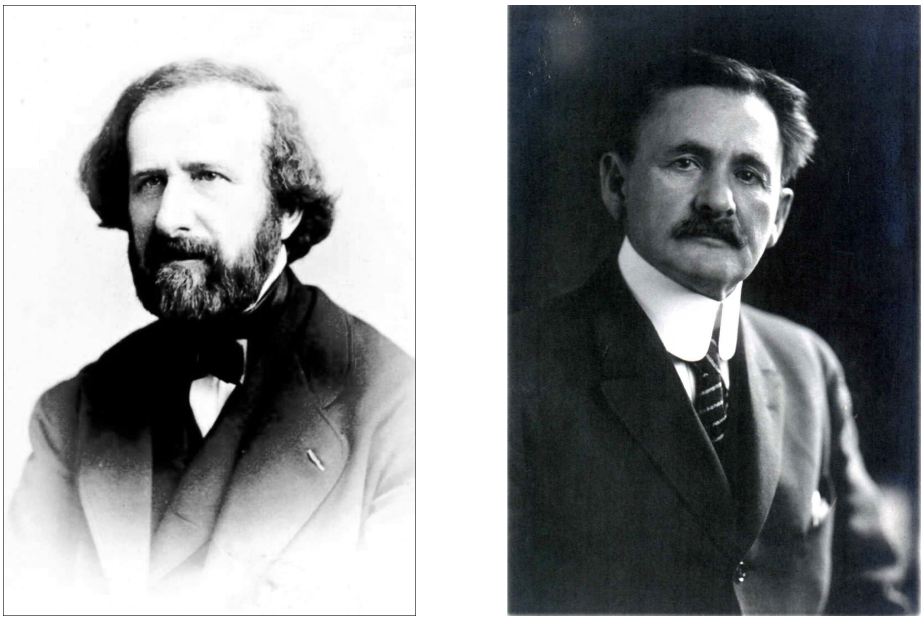

Fig. 1.1 – Armand H. L. Fizeau (1819-1896) et Albert A. Michelson (1852-1931).

Utilisant un instrument beaucoup plus important installé sur le télescope de 100 pouces du Mont Wilson (Californie), le physicien Albert Abraham Michelson (Fig. 1.1) et l'astronome Francis G. Pease ont pu mesurer pour la première fois en 1920 le diamètre angulaire d'une étoile autre que le Soleil, la supergéante rouge Bételgeuse (Michelson & Pease 1921). Cette étoile a pu

être résolue par la base de 20 pieds (6,1 m) du montage périscopique utilisé (Fig. 1.2 et 1.3), car elle présente la plus grande taille apparente de toutes les étoiles, avec un diamètre angulaire de l'ordre de 47 millisecondes d'angle (mas) dans le domaine visible. Cette observation, réalisée à l'œil le 13 décembre 1920, a été immédiatement suivie par une observation de Procyon. L'annulation du constraste observée sur Bételgeuse a ainsi été confirmée par la présence de franges contrastées sur Procyon avec le même réglage de l'instrument. Ceci a permis d'établir le diamètre angulaire de Bételgeuse avec une précision remarquable (environ 10%). Les tailles angulaires de plusieurs autres étoiles brillantes ont été mesurées par la suite avec ce même instrument, parmi lesquelles α Cet, α Boo, α Tau, β Gem, β Peg,... D'intéressantes mesures d'étoiles binaires ont également été obtenues, confirmant en particulier l'orbite spectroscopique de l'étoile Mizar avec une grande précision.

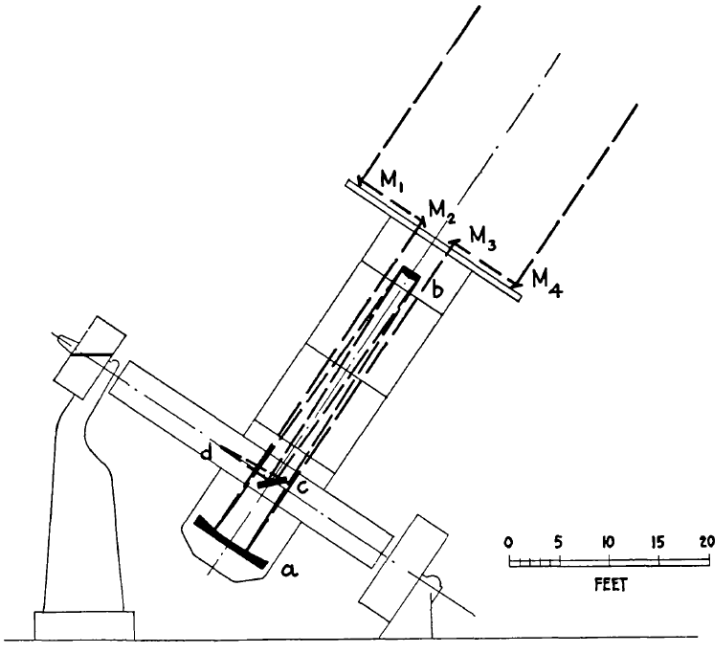

FIG. 1.2 – Montage utilisé par Michelson sur le télescope Hooker de 100 pouces du Mont Wilson pour sa mesure du diamètre angulaire de Betelgeuse (figure tirée de Michelson & Pease 1921).

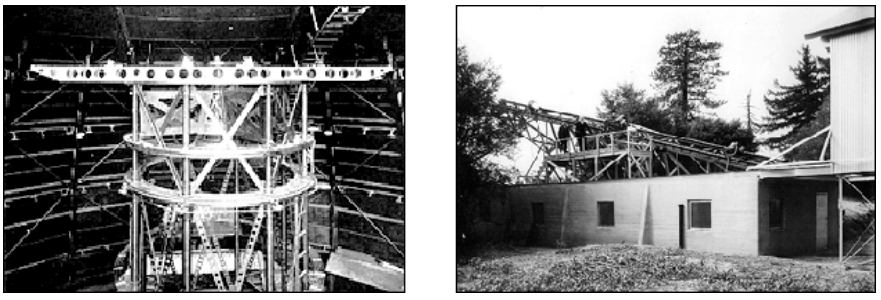

FIG. 1.3 – Instruments de 20 ft et de 50 ft installés par Michelson et Pease sur le Mont Wilson.

Peu après les observations du 20 ft, Pease a entrepris la construction d'un plus grand instrument, cette fois dédié entièrement à l'interférométrie stellaire, d'une base de 50 ft (15,2 m). Avec le soutien de George E. Hale, cet instrument a été construit sur le Mont Wilson (Fig. 1.3), et a

permis de confirmer le résultats obtenus avec le 20 ft. D'une utilisation délicate, il n'a cependant pas permis les progrès augurés par l'augmentation de la longueur de la base interférométrique. Après le succès "facile" du 20 ft, le manque de stabilité de l'instrument a rappelé que les longueurs d'onde optiques imposent des tolérances très serrées sur la conception mécanique des interféromètres.

1.2 L'interféromètre d'intensité et l'hétérodyne

Dans les années 1960, l'interféromètre d'intensité construit par les astronomes britanniques Robert Hanbury Brown (Fig. 1.4) et Richard Q. Twiss (Hanbury Brown & Twiss 1956) a amené un regain d'intérêt pour l'interférométrie optique et la mesure du diamètre angulaire des étoiles. Utilisant un principe novateur pour les longueurs d'onde optiques, l'interféromètre d'intensité mesure la corrélation des temps d'arrivée des photons enregistrés pas deux télescopes séparés. En pratique, les signaux des photomultiplicateurs montés sur chacun des deux télescopes sont multipliés en temps réel, et la valeur moyenne du signal obtenu donne directement une mesure de la cohérence spatiale de la source. Un avantage important de ce type d'instrument est qu'il ne nécessite pas de former une image de bonne qualité de l'étoile. L'interféromètre d'intensité (Fig. 1.4) construit à Narrabri (sud-est de l'Australie) est ainsi constitué de collecteurs de lumière de grande taille mais de faible qualité optique. Grâce à cet instrument fonctionnant aux longueurs d'onde visibles, les diamètres angulaires de 32 étoiles (en particulier des étoiles chaudes) ont pu être mesurés avec une précision remarquable, parfois même encore inégalée à ce jour (Hanbury Brown, Davis & Allen 1974). La faible sensibilité intrinsèque de ce type d'instrument a cependant fait préférer la technique de recombinaison de Michelson pour le développement des interféromètres astronomiques ultérieurs.

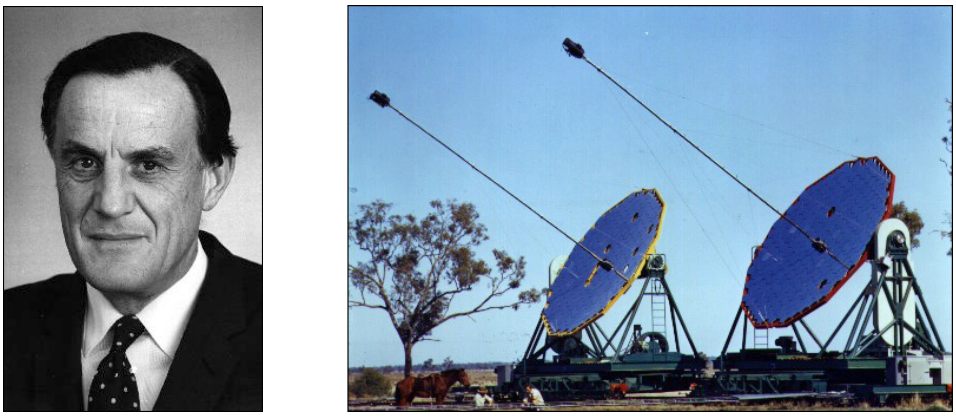

FIG. 1.4 – Robert Hanbury-Brown et l'interféromètre d'intensité de Narrabri (Nouvelles-Galles du Sud, Australie).

En parallèle de l'interférométrie d'intensité, une autre technique dérivée de l'interfrométrie radio (elle-même expérimentée dès 1948) a été mise en œuvre avec succès dès les années 1970 aux longueurs d'ondes infrarouges : l'interférométrie hétérodyne. La corrélation des signaux des deux télescopes est obtenue après un changement de fréquence, ou hétérodynage, de l'onde provenant de l'étoile. Ce changement de fréquence est obtenu par mélange de la lumière stellaire avec un laser utilisé comme oscillateur local, le résultat étant un battement à une fréquence typique de quelques centaines de MHz. L'avantage principal de l'interférométrie hétérodyne sur l'interférométrie de Michelson est qu'elle permet le transport des signaux dans de simples cables

FIG. 1.5 – L'interféromètre hétérodyne ISI (Mont Wilson, Californie).

électriques haute fréquence. Mais comme pour l'interférométrie d'intensité, le défaut principal de l'interférométrie hétérodyne est sa faible sensibilité intrinsèque. La bande spectrale utile est en effet d'une extrême étroitesse, en rapport avec celle du laser utilisé comme oscillateur local. Outre les instruments développés en France à la fin des années 1970 (au CERGA en particulier, voir Assus et al. 1979), l'instrument le plus représentatif de cette technique est l'Infrared Spatial Interferometer installé sur le Mont Wilson (Fig. 1.5). Après avoir obtenu ses premières franges en 1988 sur Bételgeuse (Bester, Danchi & Townes 1990), cet instrument à trois télescopes a produit d'intéressantes observations d'enveloppes circumstellaires d'étoiles évoluées. Une particularité des télescopes utilisés est d'être installés dans des remorques de camion, et donc librement déplaçables.

1.3 I2T, premier interféromètre à deux télescopes

C'est en 1974 que l'astronome français Antoine Labeyrie a réalisé la première recombinaison directe de la lumière de deux télescopes séparés, grâce à l'Interféromètre à 2 Télescopes (I2T, Labeyrie 1974), alors installé à Nice. D'une base maximale de 12 m et utilisant deux sidérostats de 25 cm, cet instrument a permis de démontrer la faisabilité technique du transport, du retardement et de la recombinaison de la lumière collectée par deux télescopes distincts. Même si d'un point de vue physique, le principe de cet instrument est identique à l'interféromètre construit par Michelson 50 ans plus tôt, ce nouveau système permet en principe d'augmenter arbitrairement la longueur de la base et le nombre de collecteurs. Cette flexibilité nouvelle a ouvert la voie à l'équivalent optique du célèbre interféromètre radio Very Large Array (Nouveau-Mexique) et est à l'origine du développement actuel des très grands interféromètres optiques VLTI, Keck, CHARA,...

Le concept de l'I2T a été étendu par la suite à des télescopes de 1,5 m de diamètre installés dans des montures sphériques, sous la forme du Grand Interféromètre à 2 Télescopes (Fig. 1.6, Mourard et al. 1994). I2T et GI2T ont été les premiers interféromètres à disperser spectralement les franges d'interférence. On retrouve aujourd'hui cette dimension conjointe spatiale et spectrale dans l'instrument AMBER du VLTI.

FIG. 1.6 – Un des télescopes de l'I2T d'Antoine Labeyrie (photo : O. von der Lühe) et son successeur le GI2T (photo : P. Lawson).

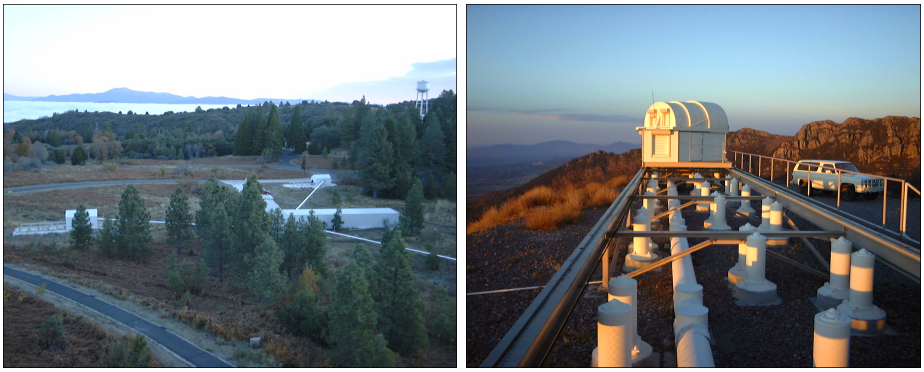

FIG. 1.7 – Vue de l'interféromètre PTI (Mont Palomar, Californie) et un des télescopes de IOTA (Mont Hopkins, Arizona).

1.4 Mark III, PTI, IOTA, SUSI, NPOI, CHARA,...

A la suite des résultats obtenus par Antoine Labeyrie, de nombreux interféromètres stellaires ont été construits dans les années 1980 et 1990, offrant des bases de quelques mètres à quelques centaines de mètres et des ouvertures collectrices de quelques cm à quelques dizaines de cm. Fonctionnant en infrarouge proche (bandes H et K principalement) ou dans le visible (Mark III, SUSI, NPOI), ces instruments ont permis la mesure d'un grand nombre d'étoiles simples ou multiples, ainsi que les premières observations astrométriques par interférométrie. Cette augmentation considérable du nombre d'instruments en activité, et donc du temps total d'observation interférométrique sur le ciel, a apporté la première véritable moisson de résultats scientifiques, avec à ce jour plusieurs centaines d'articles publiés.

En parallèle de la mise en service de ces interféromètres, il est intéressant de noter l'émergence d'un concept particulier d'instrument de recombinaison basé sur des fibres optiques monomodes. L'instrument FLUOR est le premier système de recombinaison utilisant cette technologie à avoir réalisé des observations sur le ciel (Coudé du Foresto et al. 1992). D'abord installé sur le télescope solaire McMath (Kitt Peak, Arizona), il a ensuite été utilisé au foyer de l'interféromètre IOTA (Mont Hopkins, Arizona), avant d'être transporté sur CHARA (Mont Wilson, Californie), où il se trouve actuellement. L'instrument VINCI (Sect. 1.6) a repris le concept de FLUOR dans le cadre du VLTI.

FIG. 1.8 – La coupole d'un des télescopes de 1m de l'interféromètre CHARA (Mont Wilson, Californie) et une vue aérienne du NPOI, installé près de Flagstafff en Arizona (photo : USNO).

FIG. 1.9 – L'interféromètre Keck (photo NASA/JPL) et les quatre télescopes de 8m du VLTI.

1.5 Les premiers géants : Keck, VLTI et OHANA

L'extension des observations interférométriques aux objets faibles, en particulier les noyaux actifs de galaxies et les exoplanètes, réclame simultanément de grandes surfaces collectrices et des longueurs de base hectométriques. Dans ce but, deux très grands interféromètres ont été imaginés dans les années 1980 : le VLTI (mode interférométrique du Very Large Telescope européen) et l'interféromètre Keck. Plus récemment, un concept novateur basé sur l'utilisation de fibres optiques a vu le jour, OHANA.

Le mode interférométrique des deux télescopes Keck (Fig. 1.9 à gauche) permet de combiner la lumière collectée par les deux miroirs segmentés de 10 m de diamètre, séparés de 85 m. L'objectif prioritaire de cet instrument est l'interférométrie à frange noire dans le domaine de l'infrarouge thermique, qui permet d'annuler la lumière d'une étoile en la faisant interférer destructivement. Il est alors possible d'observer le voisinage immédiat de cette étoile, en particulier les exoplanètes et les disques circumstellaires.

Constitué de 4 télescopes principaux de 8 m de diamètre (Fig. 1.9 à droite) et de 4 télescopes mobiles de 1,8 m, le VLTI est le plus grand interféromètre au monde par la surface collectrice. Construit et mis en oeuvre par l'Observatoire Européen Austral (ESO), le VLTI a obtenu ses premières franges le 17 mars 2001 entre deux sidérostats de 35 cm, et le 29 octobre 2001 avec deux télescopes de 8 m, avec l'instrument de recombinaison VINCI (Sect. 1.6). Depuis lors, deux instruments supplémentaires sont entrés en service : MIDI, un recombinateur à deux télescopes

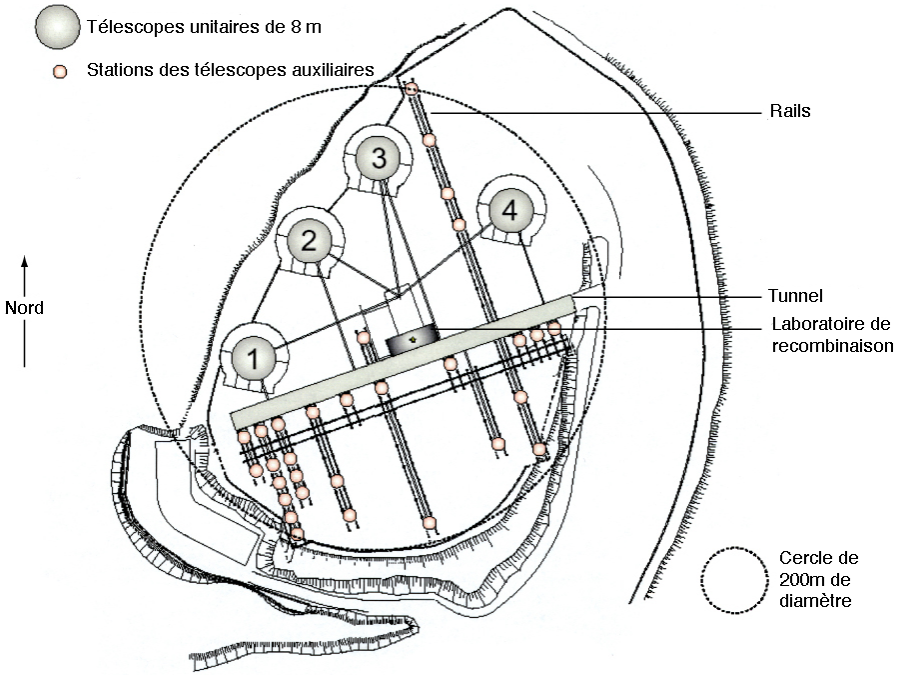

FIG. 1.10 – Elévation de la plate-forme du VLTI montrant les stations utilisables avec les télescopes auxiliaires mobiles de 1,8m et les positions des grands télescopes de 8m (illustration ESO).

en infrarouge thermique (Leinert et al. 2003) et AMBER, un instrument à trois télescopes simultanés fonctionnant en infrarouge proche (Petrov et al. 2000). Une caractéristique essentielle du VLTI est sa flexibilité : il est possible de positionner les télescopes de 1,8 m sur un grand nombre de stations (Fig. 1.10), de manière à obtenir une excellente couverture du plan des fréquences spatiales, couramment appelé "plan (u,v)". Ceci fait du VLTI un interféromètre très bien adapté à l'imagerie interférométrique. Même si actuellement seul AMBER permet d'utiliser trois télescopes à la fois, il est prévu pour la seconde génération d'instruments de pouvoir recombiner simultanément les 8 télescopes de la plate-forme.

OHANA est un concept visant à réunir les plus grands télescopes du Mauna Kea (Hawaii) à l'aide de fibres optiques monomodes. Proposé par Jean-Marie Mariotti en 1996 (Mariotti et al. 1996), les premières franges ont été obtenues tout récemment entre les deux télescopes Keck (Perrin et al. 2006). A terme, cet instrument permettra d'obtenir une combinaison unique de très longues bases (jusqu'à 800 m) et de grandes ouvertures (4 à 10 m), le rendant particulièrement adapté à l'observation des noyaux actifs de galaxies. La Fig. 1.11 montre une vue aérienne du sommet du Mauna Kea, avec les télescopes concernés par le projet OHANA.

1.6 VINCI, le premier instrument du VLTI

Lors de ma thèse et de mon séjour post-doctoral à l'ESO Paranal, j'ai participé à la construction de l'instrument VINCI et j'ai développé le logiciel de traitement des données de cet instrument. Je présente ci-après un article SPIE présentant cet instrument (Sect. 1.6.1), ainsi qu'un article A&A décrivant le système de réduction des données (Sect. 1.6.2). Une description plus détaillée de VINCI, en particulier de son logiciel de contrôle et de ses premières observations, se

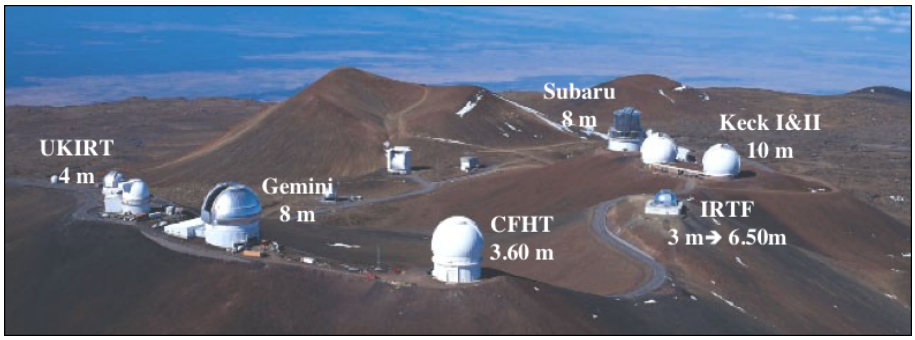

FIG. 1.11 – Vue aérienne des télescopes concernés par le projet d'interféromètre OHANA.

trouve dans ma thèse (Kervella 2001), et n'est pas reprise dans le présent mémoire.

A l'origine conçu pour n'être qu'un simple instrument de test pour le VLTI, VINCI a démontré une grande productivité scientifique. Plus de 30 articles référés ont été publiés, portant sur ses quatre années d'observations régulières (2001-2004), et plusieurs résultats particulièrement significatifs ont fait l'objet de communiqués de presse.

1.6.1 Article SPIE : "VINCI, the VLTI Commissioning Instrument : status after one year of operations at Paranal" (2002)

VINCI a été installé dans le laboratoire interférométrique du VLTI à Paranal à la fin de l'année 2000, et a produit ses premières franges sur le ciel le 17 mars 2001. L'article reproduit ici donne un compte-rendu des résultats obtenus avec cet instrument après une année d'utilisation intensive en laboratoire et sur le ciel. En particulier, je décris un problème important de perte de contraste instrumental qui a affecté le coupleur triple MONA à la mi-2001. Résolu par la suite, ce problème a été causé par la contraction des cables entourant les fibres optiques du fait du changement saisonnier de température (refroidissement de quelques degrés durant l'hiver austral).

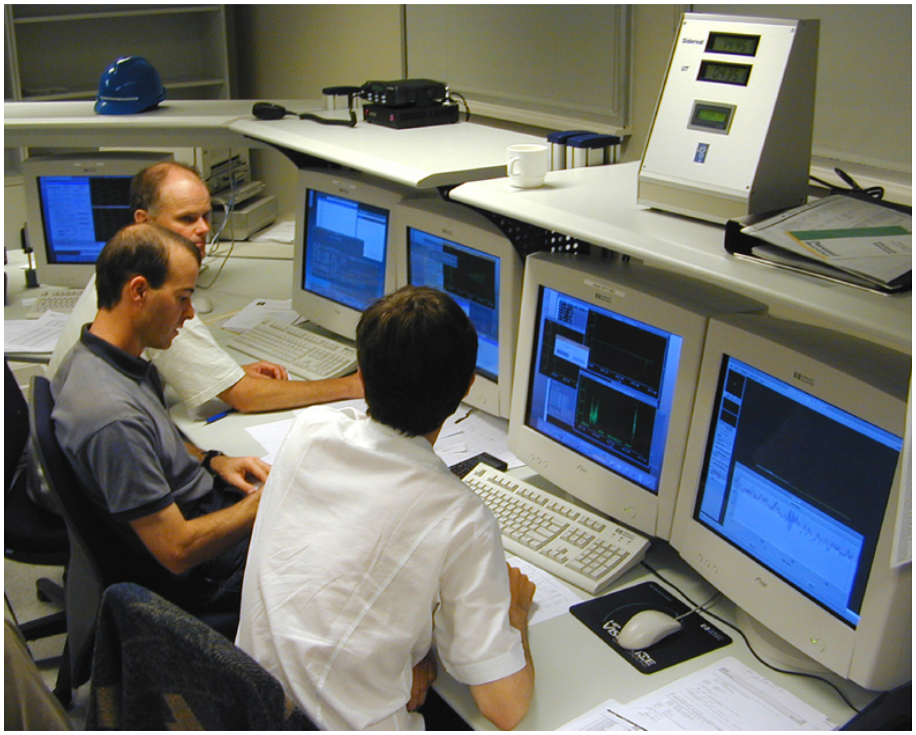

FIG. 1.12 – La console de commande du VLTI à l'Observatoire de Paranal, la nuit des premières franges sur le ciel. (photo ESO)

VINCI, the VLTI Commissioning Instrument: status after one year of operations at Paranal

Pierre Kervella[a*], Philippe Gitton[a], Damien Segransan[c], Emmanuel Di Folco[b], Pierre Kern[d], Mario Kiekebush[a], Thanh Phan Duc[b], Antonio Longinotti[b], Vincent Coudé du Foresto[e], Pascal Ballester[b], Cyrus Sabet[b], William D. Cotton[f], Markus Schöller[a], Rainer Wilhelm[b]
[a] ESO Chile, [b]ESO Germany, [c]Observatoire de Genève, Switzerland, [d]LAOG, Observatoire de Grenoble, France, [e]Observatoire de Paris, France, [f]National Radio Astronomy Observatory, USA

ABSTRACT

Installed at the heart of the Very Large Telescope Interferometer (VLTI), VINCI combines coherently the infrared light coming from two telescopes. The first fringes were obtained in March 2001 with the VLTI test siderostats, and in October of the same year with the 8 meters Unit Telescopes (UTs). After more than one year of operation, it is now possible to evaluate its behavior and performances with a relatively long timescale. During this period, the technical downtime has been kept to a very low level. The most important parameters of the instrument (interferometric efficiency, mechanical stability,...) have been followed regularly, leading to a good understading of its performances and characteristics. In addition to a large number of laboratory measurements, more than 3000 on-sky observations have been recorded, giving a precise knowledge of the behavior of the system under various conditions. We report in this paper the main characteristics of the VINCI instrument hardware and software. The differences between observations with the siderostats and the UTs are also briefly discussed.

Keywords: infrared interferometry, VLTI, optical fibers, integrated optics, wavelets, commissioning.

1. INTRODUCTION

VINCI was the first interferometric instrument to be installed on Paranal. It is the result of a collaboration between the Observatoire de Paris (LESIA) for the design and construction, the Max-Planck Institut für Extraterrestrische Physik (Garching, Germany) for the infrared camera LISA, under the direction of the European Southern Observatory (ESO). As the first interferometric instrument to be installed at ESO, it has been a great source of experience.

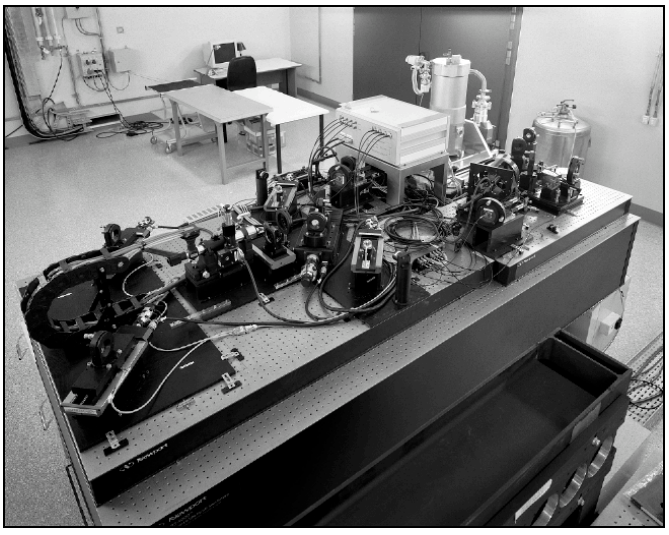

Figure 1. VINCI installed in the VLTI laboratory at Paranal.

* pkervell@eso.org, European Southern Observatory, Alonso de Cordova 3107, Casilla 19001, Vitacura, Santiago 19, Chile, tel. +56 55 435231

2. PRINCIPLE OF VINCI

In its interferometric mode, VINCI operates mostly like FLUOR[4], and produces interferograms modulated in optical path difference from stellar sources. The trajectory of the beams in the stellar interferometer mode is detailed in Figure 2. After the beams have been transported through the VLTI optical trains and delay lines down to the laboratory, they are folded onto the VINCI table, and then injected via fibers into an optical correlator, the MONA box. For a more detailed description of the hardware design of VINCI, the interested reader is referred to Kervella et al.[5].

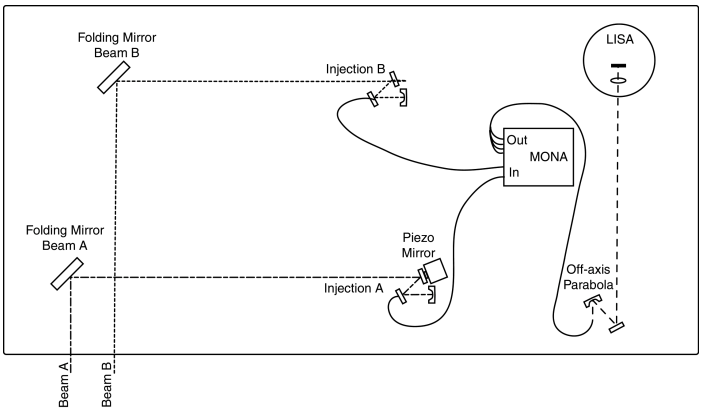

Figure 2. VINCI in stellar interferometer mode.

3. HARDWARE PERFORMANCES IN THE LAB

3.1. Injection optics/mechanics

VINCI relies on an original design of its injection optics to focus the stellar light on the injection fiber heads. It is based on an on-axis parabola, which is much less sensitive to small misalignments than the usual off-axis parabolas (FLUOR). The images produced by this optical setup show little aberration, and the injection efficiency achieved on VINCI is very consistent with the expected one. Using the motorized controls of the injection parabolas of VINCI, the positioning repeatability of the star image on the fiber head has been measured to be better than 0.3 μm, for a fiber core diameter of 6.5 μm. The resulting flux losses are therefore kept to a low level (< 5%).

3.2. Triple coupler

The beam combiner used on VINCI has been designed and built by the Le Verre Fluoré company (France). This device is based on single-mode fluoride glass fibers and couplers, and is operated in the photometric K band (2.0 – 2.4 μm). The waveguides are used to filter out the spatial modes of the atmospheric turbulence. The principle of the MONA box is shown on Figure 3. When used in Autotest mode, i.e. using an artificial light source located in the interferometric laboratory, it produces the type of interferogram presented on Figure 4.

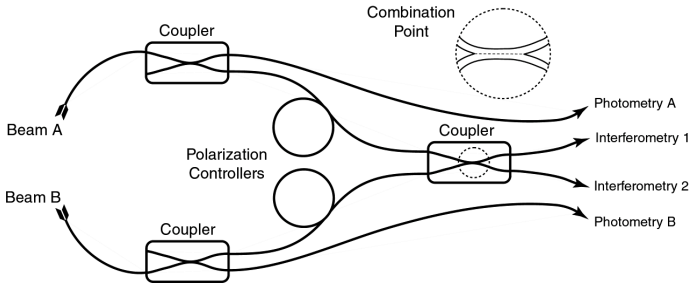

Figure 3. The fiber-based beam combiner of VINCI (MONA)

The fluoride glass fibers used in the MONA beam combiner do not maintain the polarization of the incoming stellar light. Therefore, it is necessary to compensate for the polarization mismatch introduced by the input fibers inside the MONA box, before the combination point. This is achieved using two motorized polarization controllers (Figure 3) that can be individually adjusted. It is then possible to build a map of the instrumental contrast of the beam combiner in two dimensions (Figure 5), and to localize the maximum contrast in Autotest. The procedure is slower when optimizing the fringes contrast on sky, but the principle is the same.

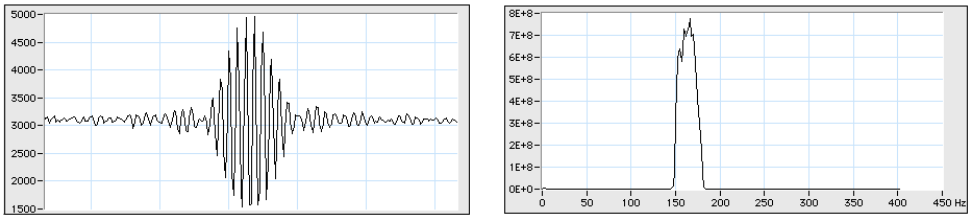

Figure 4. Fringe packet obtained in Autotest and the corresponding power spectral density.

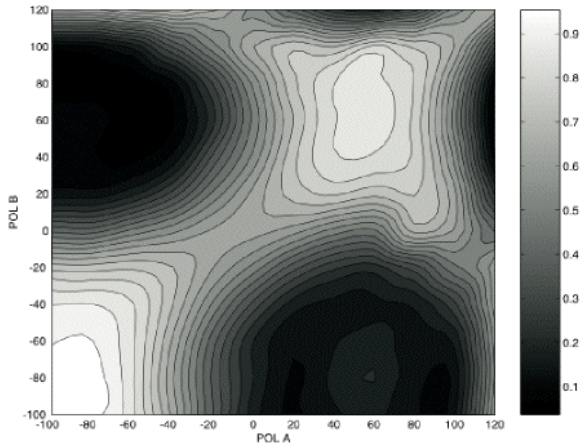

Figure 5. Map of the interferometric efficiency of MONA (in percentage of maximum) as a function of the position of the polarization controllers (arbitrary units).

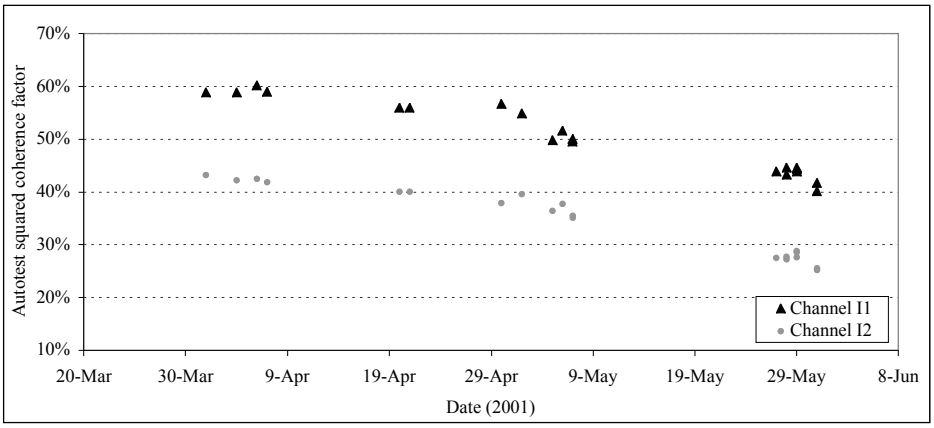

Figure 6. Decrease of the MONA interferometric efficiency in Autotest due to fiber cables contraction.

During the few months that followed first light with the siderostats (when interferometric efficiency was 87% on sky), a loss of interferometric efficiency of the MONA box was observed, both in Autotest and on sky. This loss was difficult to explain, but after some tests, it appeared that the polymer cables that are used to protect the fragile fluoride glass

fibers were to blame. The thermal expansion coefficient of these cables is larger than the one of the fibers themselves. Therefore, when the temperature went down by a few degrees in the laboratory, the fibers suffered a mechanical stress that caused a severe birefringence (Figure 6). The separation of the two polarizations on the final interferograms (Figure 7) produced a very strong loss of contrast, and a strange double-peaked power spectral density (Figure 8) characteristic from the superimposition of the two polarizations fringe packets offset in OPD. This problem was solved by changing the path of the fiber cables, adding curves, therefore giving more space to the fibers inside the cable. After this repair, the contrast of the fringes obtained on sky went back to 70%.

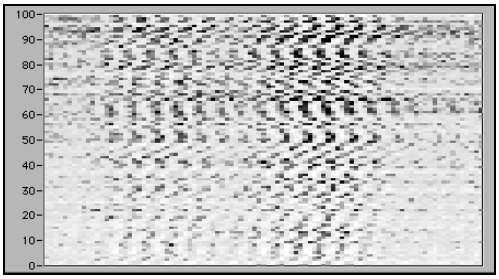

Figure 7. Series of interferograms obtained in Autocollimation mode showing the double peak feature characteristic of birefringence.

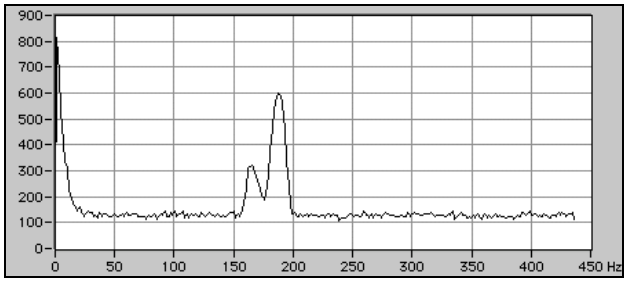

Figure 8. Average power spectral density of the interferograms presented on Figure 7 showing birefringence effect.

3.3. Output stage

The four fiber outputs of VINCI are imaged on four LISA camera photosites. The optics used for this purpose include an off-axis parabola to produce a collimated beam from the MONA fiber bundle, and an achromatic doublet located inside the camera dewar to focus the four images on the detector. The HAWAII detector used in LISA has the particularity to distributes part of the light falling on a single pixel over the four pixels located above, below, left and right of the target pixel. This process of diffusion causes a loss of 42% of the incoming signal from the target pixel[7].

It has been shown experimentally that the percentage of incoming flux that is actually read out of a single pixel of LISA is more than 39% of the total light, for each of the four signals. This yields an optical fiber imaging efficiency of at least 67%. The LISA camera has the possibility to read 2x2 or 3x3 pixels windows, but there is no gain in signal to noise ratio compared to a single pixel, as the gained flux is compensated by the additional readout noise.

3.4. Overall Photometric transmission of VINCI

When used in stellar interferometer mode, VINCI uses a very simple optical configuration (Figure 2), with only four mirror reflections for each arm before the injection in the optical fibers. The output of the four signals from MONA on the LISA camera has more optical elements (off-axis parabola, camera window,...). The main sources of flux loss are listed in Table 1. It is important to emphasize that the atmospheric turbulence is not considered here, and the average efficiency of the light injection is lower than the 78% stated here when observing on sky. The total photometric efficiency of VINCI (6.3%) is defined here as the average number of photons recorded on the four windows of LISA compared to the total number of incoming photons from the two interferometer arms.

Table 1. Photometric transmission of VINCI.

Optical element	**Transmission**
Input mirrors (4)	0.92
Fiber injection (ideal case)	0.78
Transmission of MONA	0.87
LISA window + cold doublet + K filter	0.48
Energy in one LISA pixel	0.39
Quantum efficiency LISA (K)	0.62
TOTAL	**0.063**

3.5. Commissioning tasks

VINCI has performed a number of commissioning measurements on the VLTI infrastructure. The detailed description of the results of these tests is beyond the scope of this paper but for example, one can mention the verification of the performances of the delay lines using a K-band laser, and the measurement of the piston through relatively fast (>30 Hz) tracking of the fringes (Di Folco et al.[6]). Another role played by VINCI during the passed year has been to track the fringes on each new baseline commissioned, in order to constrain the optical path difference model of the VLTI. This was successfully achieved on four baselines up to now (16m, 46m, 66m and 103m long), and will be pursued in the next years with the test siderostats to commission the numerous baselines of the Paranal platform. For further information on the VLTI commissioning, the interested reader is referred to Schöller et al.[10].

4. INFRARED CAMERA

The infrared camera used in VINCI (called LISA) is built around an engineering-grade 1024x1024 pixels HAWAII array (Rockwell) presenting a large number of cosmetic and functional defects (dead quadrant, dead and hot pixels,...). As we are using only four pixels of the array, these defects fortunately do not affect our measurements.

4.1. Readout noise

Controlled by a standard IRACE controller (Meyer et al.[3]), the detector has shown a relatively low readout noise level, especially when using multiple A/D conversion. Figure 9 shows a map of the 64x64 pixels lower left part of the quadrant used in LISA, where grey scale coding corresponds to the readout noise level for single A/D conversion. The scale is linear from 0 to 25 e^-, the white positions corresponding to dead or hot pixels. The readout noises of the four pixels used in VINCI are 12 e^- (PA), 9 e^- (PB), 11 e^- (I1), 16 e^- (I2), in single-conversion mode. By using multiple A/D conversion of the pixel readouts, they are reduced by a factor of two, at the cost of a 20% lower maximum frequency.

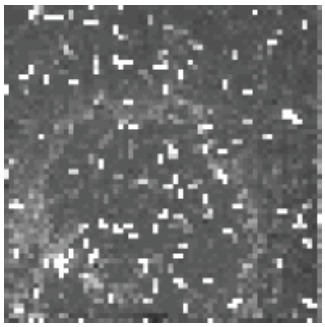

Figure 9. Noise map of LISA.

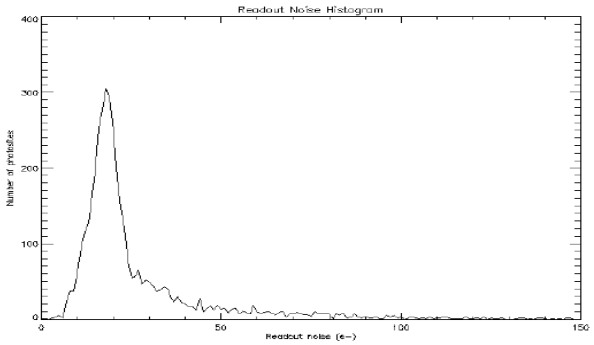

Figure 10. Histogram of LISA readout noises

4.2. Modulation transfer function

When recording a modulated signal, any memory effect on the detector can reduce the measured amplitude. This effect, harmful to the instrumental visibility of the fringes, was studied specifically in VINCI by checking the response of the detector to a chopped signal. Located very close to a single-mode fiber, the chopping wheel produced a shut-off time of 330 μs, shorter than a single frame of the detector, read at a frequency of 2544 Hz. The incoming signal can therefore be considered as a square modulated wave. The frequency response (modulation transfer function) of the camera is then deduced from the ratio of the output signal (Figure 11) to the input wave power spectra. The resulting modulation transfer function is presented on Figure 12 compared to a perfect integrator. The conclusion of these tests were that LISA camera behaves nearly like a perfect integrator (deviation of less than 10% at 1.2 kHz).

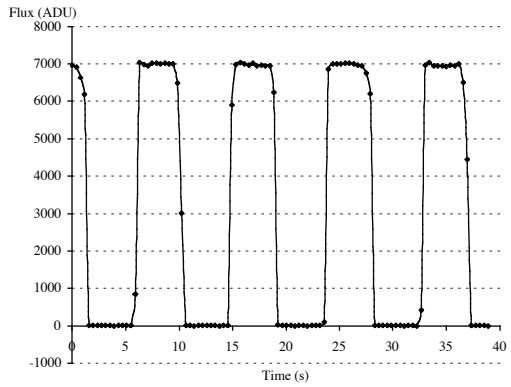

Figure 11. Chopped output signal of LISA.

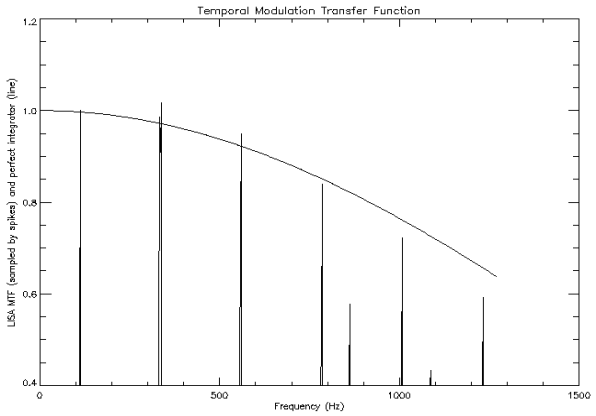

Figure 12. Modulation transfer function of LISA (peaks), compared to a perfect integrator (curve).

5. SOFTWARE STRUCTURE

5.1. Observation preparation

As with the other instruments of the VLT Observatory, the preparation of the observations is based on a several phases. Phase 1 concerns the initial proposal sent to the selection committee. Once the observation program has been accepted, then the astronomers are invited to prepare their observations in details during the Phase 2. This is done using a Java-based program called P2PP (Phase 2 Proposal Preparation tool). This program allows to define precisely the parameters of the observations (number of interferograms to be recorded, exposure time,...). The product of P2PP is a series of Observation Blocks (OBs) that are sent to Paranal, where they are executed by the Observing Software (OS).

The preparation of an interferometric observation is more complex than with a single-dish telescope. The changes in length and orientation of the projected baseline during the night (*supersynthesis*) create particular configurations that can either limit the observability of the object or produce interesting modulations of the actual spatial frequency of the observation. To prepare the observations, a prototype set of observation preparation tools (visibility calculator and exposure time calculator) is available on the ESO web site, at the following internet address:

http://www.eso.org/observing/etc/doc/indexdev.html.

5.2. Fringes detection

The first step for the recording of data is to detect the presence of the fringes in the OPD range scanned by the VINCI piezo mirror (up to 300 μm). Two methods are used in VINCI to detect the fringes: the *quicklook*, and the *peak integral*.

The *quicklook* method is taken directly from the FLUOR instrument. This method allows both to detect and center the fringe packet in the scanned range. During the observations, a simple fringe packet centroid locator algorithm is applied to the data provided by LISA. The principle is to detect the pixels in the photometrically calibrated interferogram that have an intensity above a user-defined number of times the noise level (typically 7). The fringe packet center (in OPD) is measured with a precision of about one fringe (2 μm) after each scan and the resulting error is fed back to the VLTI delay lines as an OPD offset. This capability, called *fringe coherencing*, ensures that the residual OPD is less than a coherence length despite possible instrumental drifts. The correction rate (once per scan, i.e. up to about 50 Hz) is too slow to remove efficiently the differential piston mode of the turbulence.

The *peak integral* is based on the incoherent accumulation of the fringe peak in the power spectral density of several interferograms. Each OPD position is scanned for a number of times (typically 10 to 100), and the detection occurs when the peak goes above a predefined level above the background noise level of the PSD. When the fringes are detected, it is not possible with this method to know their position inside the interferogram. This detection method is used to search for very faint fringes, that escape the classical detection using the *quicklook*. In practice, both detection

methods are used in parallel, to benefit both from the centering capability of the *quicklook* and of the sensitivity of the *peak integral*.

A third fringe detection method is currently being investigated, based on the wavelets transformation. This should make it possible to obtain a better sensitivity to faint fringes, while keeping the coherencing capability (fringe packet centering).

6. DATA PROCESSING

6.1. Fourier transform processing

When the turbulent beams are spatially filtered by the single-mode waveguides, their random phase corrugations are transformed into intensity fluctuations which are monitored by the photometric signals coming out of MONA. It is then possible to correct each interferogram from these fluctuations and produce highly stable fringe visibility measurements that are independent of the spatial modes of the atmospheric turbulence.

Squared coherence factors $|\mu|^2$ (modulus of the complex coherence factor between the two beams) are computed from the normalized energy of the fringe signal in the power spectra of each corrected interferogram, and averaged over a series of a few hundred scans to reduce the statistical noise. The interested reader can find a detailed description of this Fourier transform-based processing algorithm in Coudé du Foresto et al.[1].

6.2. Wavelets transform processing

When dealing with the classical Fourier transform (FT) and especially with a quadratic estimator like $|\mu|^2$ (corresponding to the energy of the spectral density located at the fringe frequency) the debiasing step is critical and may completly spoil the compution of $|\mu|^2$. Among all biases, several are easely removed (white noise), like photon noise and detector noise. Other biases like the ones introduced by photometric fluctuations, differential piston or instrumental spikes are almost impossible to remove using the classical Fourier analysis, therefore requiring a time-frequency approach.

The most direct method for this purpose is the continuous wavelet transform (WT) using the Morlet wavelet (gaussian envelope times plane wave function). The main advantage of this wavelet is that it looks like the VINCI interferograms. It is thus extremely efficient to locate in both time and frequency domains the energy of the fringes. Such an approach, allows to compute the energy of the fringe packet without adding biases that are located outside of the fringe packet in OPD (optical path difference, also time domain) but that are located at the fringes frequency.

Figure 13 illustrates the advantage of the WT compared to the FT. The recorded photometry is very low a few microns from the beginning of the interferogram. The calibration of the interferogram by the photometry (division by $\sqrt{P_A P_B}$) strongly amplifies the noise in the low photometry region (Figure 13b). In the Fourier domain, the effect is spread over all frequencies and recovering the visibility becomes difficult. In wavelets analysis (the WT of the calibrated interferogram is presented on Figure 13c), the amplified noise is not taken into account since the energy is only integrated locally in the OPD and frequency domain as seen on Figure 13d (thick curve).

The wavelets analysis has also the remarkable ability to identify interferograms affected by atmospheric piston, therefore allowing to remove them during the data processing (Segransan[9]). Thanks to the efficient rejection of the noise in the WT, it is also possible to detect fringes in very low signal to noise conditions. It is foreseen in the near future to implement a dedicated WT based algorithm for the real-time detection of the fringes during the observations. A WT module has been added to the VINCI data reduction software based on the work from Segransan[8,9] in addition to the classical FT algorithm.

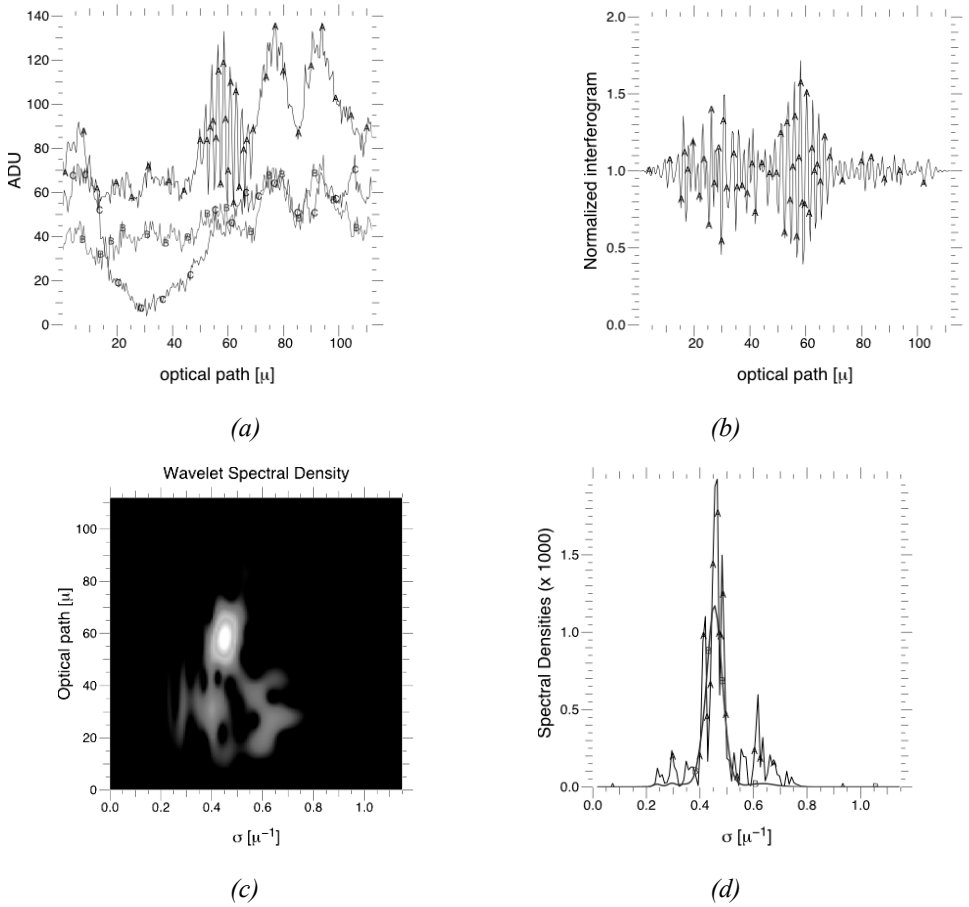

Figure 13. Compared integration of the fringe power between Fourier and Wavelets methods, on VINCI data obtained with UT1-UT3. Figure 13a shows the raw signals I1, PA and PB. Figure 13b is the calibrated interferogram. On Figure 13d, the Fourier power spectral density is the thin line, and the wavelets spectrum (Figure 13c) projected along the frequency axis is the thicker, gaussian shaped curve.

6.3. Calibration and Data analysis

The analysis of the processed fringes data is done using a toolbox programmed in IDL. This interface allows the user to select the interferograms based on a combination of criteria, such as the photometric signal to noise ratio or the strength of the piston effect. From the processed data files, this software outputs calibrated visibility values that can then be compared to an astrophysical model of the observed target or directly used to derive its angular size.

7. ON-SKY OBSERVATIONS

7.1. Siderostats

On-sky interferometric observations with the siderostats have been going on continuously at Paranal since the first fringes obtained on March 19, 2001. The first series of interferograms recorded with the VLTI at this occasion is presented on Figure 14 (time is from bottom to top, one line per interferogram). The fringes were tracked and centered by VINCI, therefore removing part of the atmospheric piston.

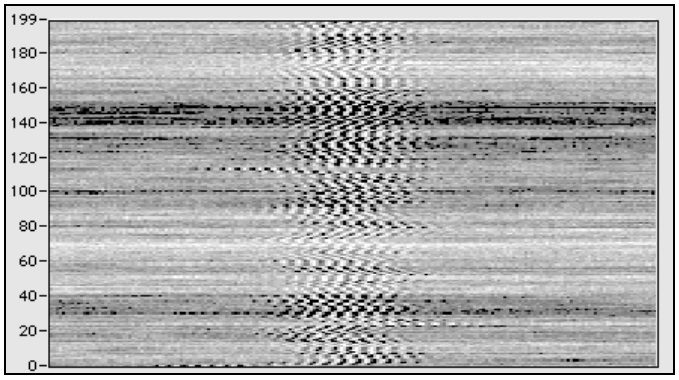

Figure 14. First interference fringes of the VLTI on Hya, X axis is OPD (one fringe equals 2.2 m), Y axis is the scan number in the series (about 90 seconds of data in total)

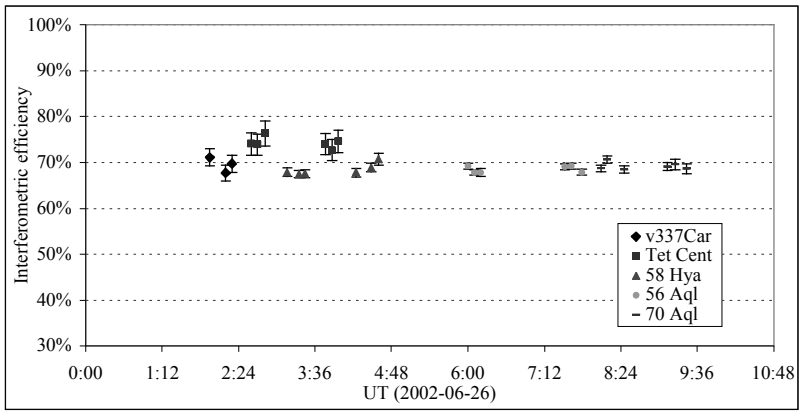

Figure 15. Interferometric efficiency of VINCI and the VLTI test siderostats on sky (66 m baseline, June, 2001)

Over a long timescale, the interferometric efficiency of the MONA beam combiner has evolved substantially, due to the sensitivity of the MONA couplers to temperature (see the discussion in Sec. 3.2). Nethertheless, on a timescale of one night, the interferometric efficiency measured on-sky has been stable, as shown on Figure 15. The excess efficiency visible on the two series of transfer functions computed from the Cen data comes apparently from an overestimation of the a priori angular size of this star taken from a calibrators catalog. The average interferometric efficiency over this night was 69 ± 2 % (Cen data excluded).

7.2. Unit telescopes

After the first fringes with the VLTI test siderostats obtained in March 2001, the first recombination of the light from two 8-meter telescopes of Paranal was achieved in October of the same year. Interference fringes between the star light collected by the telescopes Antu (UT1) and Melipal (UT3), separated by 102.5 meters, were recorded by VINCI. One major surprise of these first observations was that the flux injected in the optical fibers of VINCI was much more stable that initially expected (Figure 16). The common view of the injection of a multi-speckle star image in an optical fiber was initially that a single moving speckle is injected at a time, and that the flux can be completely lost between speckles. In reality, it was observed that light is present on LISA more than 95% of the time.

The interferometric transfer function of the VLTI/VINCI during the first UT1-UT3 commissioning run was measured to be 61%. It should be stressed here that the positions of the polarization controllers of MONA were not optimized, and this value is therefore not optimal and not comparable to the transfer function obtained on the siderostats.

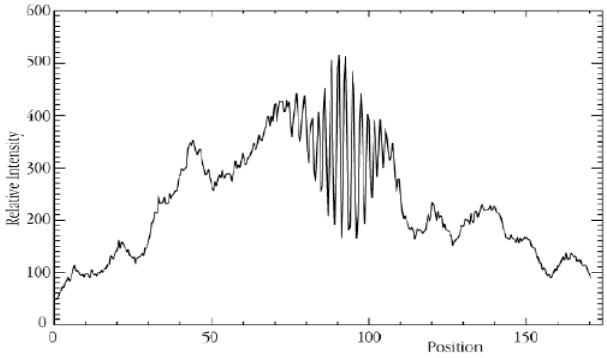

Figure 16. Raw interferogram of Geminorum obtained with UT1-UT3

A number of stars were observed during the four runs of commissioning with the UTs. The faintest object on which fringes were acquired was the main sequence star HD 112282. Observed under Paranal median seeing conditions (0.6 to 0.7" at =0.5 m), it was possible to track the fringes efficiently on this K=7.7 unresolved star, with a signal to noise ratio better than 10 on the interferometric channels, yielding a limiting magnitude better than K=9. A relatively precise value of the transfer function of the interferometer could even be derived from this observation.

7.3. Precision vs. magnitude

The visibility estimators used for the processing of the data of VINCI are quadratic (Coudé du Foresto et al.[1] and Segransan[9]), and therefore the final precision of the measurement is expected to be proportional to the correlated magnitude *CorrK* of the object, defined as the following:

$$CorrK = -2.5\,Log_{10}\left(10^{-\frac{magK}{2.5}} \cdot \mu^2\right)$$

where *magK* is the photometric magnitude of the star and μ^2 is the squared coherence factor. Using the observations obtained on sky with the siderostats, it was possible to quantify the precision achievable with VINCI as a function of the correlated magnitude (Figure 17).

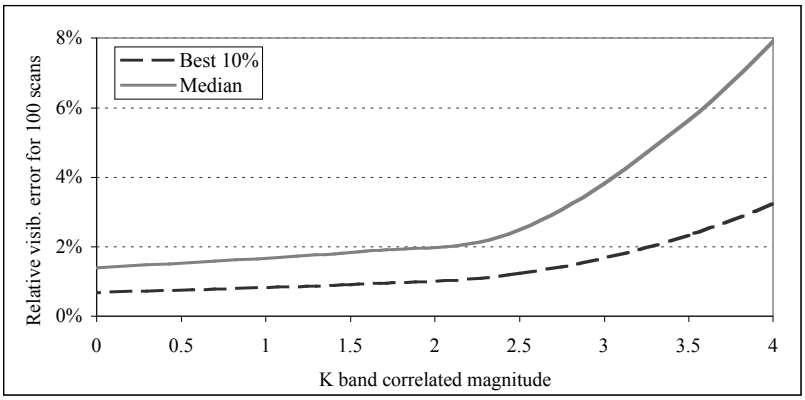

Figure 17. Accuracy of VINCI visibility measurements with the VLTI test siderostats.

The precision does not increase for the brightest sources because of the atmospheric piston effect, not yet corrected on the VLTI by a fringe tracker. Once the FINITO fringe tracker will be installed, the removal of the fringe motion will allow to reach a much better precision. Laboratory measurements at Paranal without piston and in photon shot noise limited regime produced relative precisions (FT estimator) better than 0.05% on the visibility values for 100 interferograms. This value should be the limit of precision achievable with the FT based quadratic visibility estimators.

7.4. Observed stars

During the commissioning of the VLTI, a number of objects have been observed, with the siderostats or with the 8-meter telescopes UT1 and UT3. The list of all observed targets is presented in Table 2. Most of the stars listed have been observed several times, and the number of fringe files is indicated after the name of the object. See also:

http://www.eso.org/projects/vlti/instru/vinci/vinci_data_sets.html

Table 2. Stars observed with VINCI until February 2002.

Star (# Observ.)	alf Sco (19)	del Crv (2)	H Sco (3)	nu Hya (48)	S Ori (23)	V Hya (3)
1 Oph (112)	alf Ser (5)	del Eri (9)	HD 100453 (2)	nu Pav (8)	S Scl (23)	v2111 Oph (6)
1 Pup (5)	alf Tau (4)	del Sgr (9)	HD 10550 (8)	NZ Gem (3)	sig Lib (109)	V3872 Sgr (5)
2 Sex (3)	AR Cet (13)	del02 Gru (4)	HD 112282 (2)	omi Cet (45)	sig Pup (61)	v744 Cen (2)
24 PsA (7)	BD-04 782 (3)	eps Crv (56)	HD 20234 (9)	phi1 Lup (3)	SW Vir (13)	V806 Cen (33)
25 CMa (27)	bet Car (3)	eps Eri (14)	HD 216149 (11)	phi2 Ori (4)	SWR 69 (8)	v919 Cen (2)
39 Eri (22)	bet Cen (13)	eps Lep (137)	HD 787 (6)	pi Eri (15)	T Ari (19)	VY Leo (9)
43 Vir (48)	bet Cet (293)	eps Peg (127)	HD 83443 (4)	pi Hya (8)	T Cet (30)	VZ Pic (9)
6 Pup (10)	bet Cnc (15)	eps Ret (8)	HR 2447 (3)	pi Leo (2)	T Eri (5)	W Cen (7)
AK Hya (4)	bet Cor (6)	eps Sco (177)	HR 4354 (2)	psi Phe (44)	T Lep (39)	W Hya (14)
alf Ant (4)	bet Crv (3)	eta Ara (5)	HR 5152 (3)	Q Car (2)	tau Aqr (6)	W Ori (7)
alf Aql (5)	bet Dor (29)	eta Car (36)	HR 6682 (4)	R Aqr (17)	tau Pup (3)	X Cnc (3)
alf Cen A (38)	bet Gru (254)	eta Cet (8)	kap Lib (4)	R Cnc (29)	tau Pup (3)	X Hya (3)
alf Cen B (6)	bet Ori (13)	eta Gem (6)	KP Pup (2)	R Crt (3)	tau04 Eri (2)	Y Cen (2)
alf Cen C (2)	bet Pic (10)	eta Sgr (147)	KQ Pup (8)	R Hya (3)	tet Cen (227)	YY Psc (6)
alf Cet (42)	C* 284 (13)	FU Ori (12)	l car (9)	R Leo (45)	tet Cma (8)	zet Gem (20)
alf CMa (625)	CE Tau (14)	gam Aql (60)	L02 Pup (28)	R Lep (34)	TW Hor (10)	zet Hya (5)
alf CMi (8)	chi Aqr (13)	gam Cru A (20)	lam Aqr (44)	R Peg (5)	TX Psc (4)	
alf Eri (43)	chi Phe (14)	gam Eri (231)	lam Vel (25)	R Scl (17)	U Ant (4)	
alf Her (8)	CI Ori (10)	gam Sco (4)	mu Gem (3)	R Vel (8)	U Ori (15)	
alf Hya (271)	del CMa (35)	gam Sge (12)	mu Hya (7)	RX Lep (48)	ups Cet (2)	
alf Phe (3)	del Crt (8)	gam02 Vol (22)	NSV 14420 (7)	S Lep (6)	ups Lib (6)	

8. INTEGRATED OPTICS

During a seven nights run on the VLTI (July 17-23, 2002) done in collaboration between ESO and LAOG (Observatoire de Grenoble, France), we tested on VINCI an integrated optics two-telescopes beam combiner, IONIC.

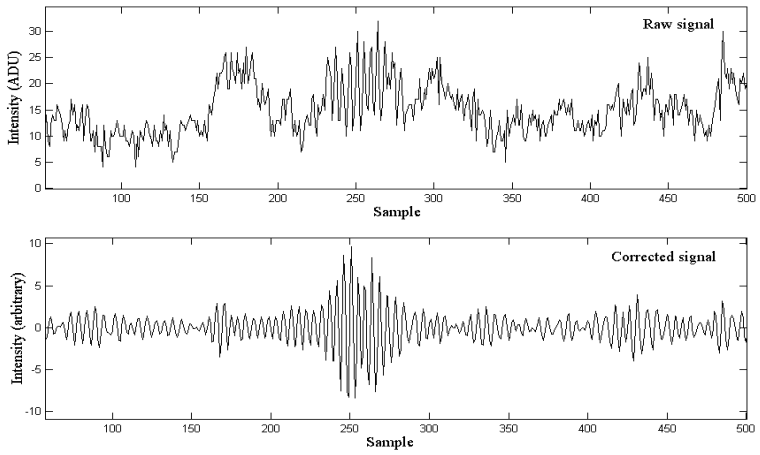

Figure 18. Fringes obtained on Altair (H=0.25) with the IONIC beam combiner installed on VINCI

This type of component had already been tested on sky at the IOTA interferometer in November 2000 (Berger et al.[1]). For this first run at Paranal, the installation of IONIC was realized without any modification of the optical setup of VINCI and only minor software changes were required (due to the single interferometric output of the component while the usual beam combiner MONA has two such outputs). The faintest star observed so far with the siderostats is HD 720 with an H magnitude of 3.1. It is currently difficult to determine the maximum reachable magnitude due to the

mismatch in numerical aperture between the H band optical fibers of IONIC and VINCI feeding optics (optimized for fluoride glass fibers). To obtain the maximum transmission, it would require to change the injection optics of VINCI to adapt them to the numerical aperture of the IONIC fibers (0.12 compared to 0.23 for MONA fibers).

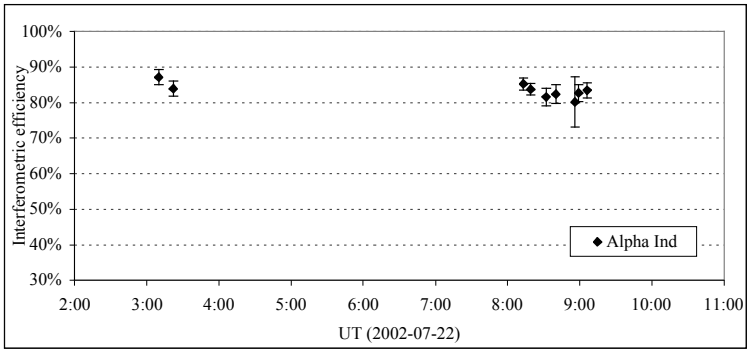

Figure 19. Interferometric efficiency measured on sky with the IONIC component installed on the VLTI.

Fringes were obtained on sky in the H band (1.5-1.8 μm), and their visibility was estimated with a relative accuracy of about 1%. The IONIC component interferometric efficiency previously measured at LAOG is 90% for unpolarized light. As shown on Figure 19, the interferometric efficiency of VLTI+IONIC measured on sky was better than 80% on the star α Ind (uniform disk angular diameter of 3.28 ± 0.04 mas, effective wavelength of 1.58 μm).

9. CONCLUSION

After the first fringes obtained with the VLTI test siderostats and the 8 meters Unit Telescopes, VINCI has demonstrated a high productivity, both in terms of commissioning results and scientific observations of stars. It has recently been opened to proposals from the European astronomical community. While new algorithms are being developed to exploit fully the potential in precision of this instrument (wavelet transform,...), the promising results obtained with the IONIC beam combiner open up exciting new perspectives of multiple telescopes beam combination (Kern et al.[11]), using the technology and experience gained from VINCI.

REFERENCES

1. V. Coudé du Foresto, S. Ridgway and J.-M. Mariotti, *"Deriving object visibilities from interferograms obtained with a fiber stellar interferometer"*, *A&A Suppl. Ser.* **121**, pp. 379-392, 1997
2. J.-P. Berger, P. Haguenauer, P. Kern, K. Perraut, F. Malbet, I. Schanen, M. Severi, R. Millan-Gabet, W. Traub, "*Integrated optics for astronomical interferometers, IV. First measurements of stars"*, *A&A* **376**, p. 31, 2001
3. M. Meyer, G. Finger, H. Mehrgan, G. Nicolini, J. Stegmeier, *"ESO infrared detector high-speed array control and processing electronic IRACE"*, *SPIE* **3354**, p. 134, 1998
4. V. Coudé du Foresto, G. Perrin, C. Ruilier, B. Mennesson, W. A. Traub, M. G. Lacasse, *"FLUOR fibered instrument at the IOTA interferometer"*, *SPIE* **3350**, p. 856, 1998
5. P. Kervella, V. Coudé du Foresto, A. Glindemann, R. Hofmann, *"VINCI: The VLT Interferometer Commissioning Instrument*", *SPIE* **4006**, p. 31 , 2000
6. E. Di Folco, B. Koehler, P. Kervella, V. Coudé du Foresto, et al., *"Atmospheric and internal turbulence measured on the Very Large Telescope Interferometer with VINCI"*, These Proceedings, *SPIE* **4838-35**, 2002
7. G. Finger, *European Southern Observatory*, private communication, 2001
8. D. Segransan, *Ph.D. Thesis*, Université de Grenoble, 2001
9. D. Segransan, *in preparation*, 2002
10. M. Schöller, P. Gitton, et al., *"Commissioning of the VLT Interferometer: from first fringes towards a general user facility"*, These Proceedings, *SPIE* **4838-153**, 2002
11. P. Kern, F. Malbet, J.-Ph. Berger, P. Haguenauer, K. Rousselet-Perraut, C. Perrier-Bellet, *"Increasing the imaging capabilities of the VLTI using integrated optics"*, These Proceedings, *SPIE* **4838-76**, 2002

1.6.2 Article A&A : "Data reduction methods for single-mode optical interferometry - Application to the VLTI two-telescopes beam combiner VINCI" (2004)

Je présente dans cet article le système de réduction des données que j'ai développé pour VINCI. Il reprend le principe décrit par Coudé du Foresto et al. (1997), en améliorant la précision de l'estimation du facteur de cohérence carré μ^2 (aussi appelé "visibilité instrumentale"). Ceci est obtenu grâce à l'utilisation combinée de la transformation en ondelettes (qui permet de mieux localiser dans l'espace et les fréquences l'énergie modulée des franges) et d'un processus de sélection raisonnée des meilleurs interférogrammes. L'algorithme s'est révélé particulièrement efficace pour l'analyse des mesures obtenues à très faible visibilité. Je donne un exemple d'application de ces méthodes à une mesure de visibilité utilisée dans notre étude de l'étoile α Cen (voir aussi la Sect. 3.2.1).

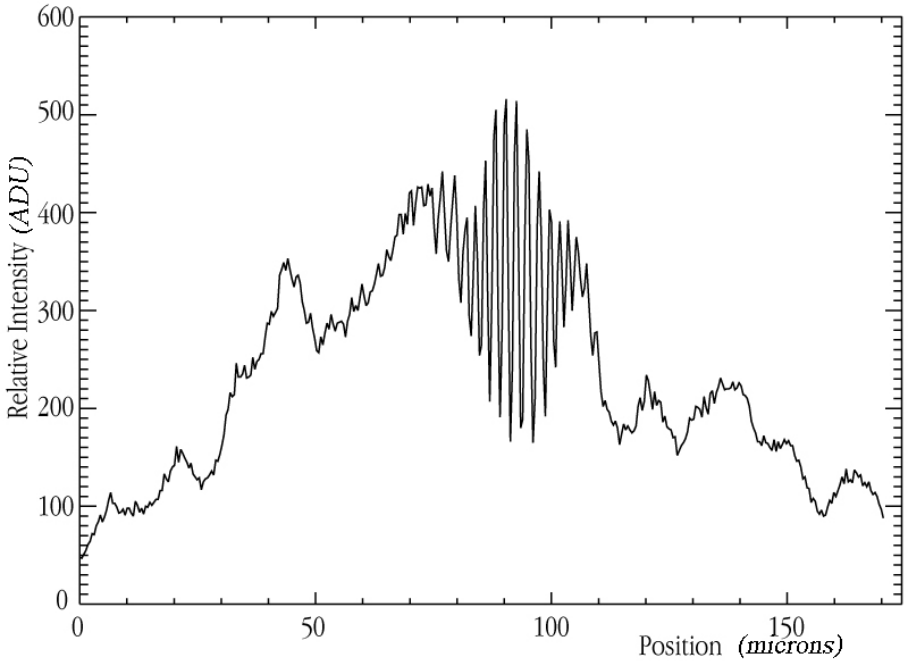

FIG. 1.13 – Premières franges d'interférence obtenues le 29 octobre 2001 entre deux des télescopes de 8 m du VLT, UT1 et UT3, sur une base au sol de 102 m. L'étoile observée est la Céphéide ζ Gem. (illustration ESO)

A&A 425, 1161–1174 (2004)
DOI: 10.1051/0004-6361:20034562

Astronomy & Astrophysics

Data reduction methods for single-mode optical interferometry

Application to the VLTI two-telescopes beam combiner VINCI*

P. Kervella[1,3], D. Ségransan[2], and V. Coudé du Foresto[1]

[1] LESIA, UMR 8109, Observatoire de Paris-Meudon, 5 Pl. Jules Janssen, 92195 Meudon Cedex, France
e-mail: Pierre.Kervella@obspm.fr
[2] Observatoire de Genève, 51 Ch. des Maillettes, 1290 Sauverny, Switzerland
[3] European Southern Observatory, Alonso de Cordova 3107, Casilla 19001, Santiago 19, Chile

Received 22 October 2003 / Accepted 14 June 2004

Abstract. The interferometric data processing methods that we describe in this paper use a number of innovative techniques. In particular, the implementation of the wavelet transform allows us to obtain a good immunity of the fringe processing to false detections and large amplitude perturbations by the atmospheric piston effect, through a careful, automated selection of the interferograms. To demonstrate the data reduction procedure, we describe the processing and calibration of a sample of stellar data from the VINCI beam combiner. Starting from the raw data, we derive the angular diameter of the dwarf star α Cen A. Although these methods have been developed specifically for VINCI, they are easily applicable to other single-mode beam combiners, and to spectrally dispersed fringes.

Key words. techniques: interferometric – methods: data analysis – instrumentation: interferometers

1. Introduction

Although interferometric techniques are now used routinely around the world, the processing of interferometric data is still the subject of active research. In particular, the corruption of the interferometric fringes by the turbulent atmosphere is currently the most critical limitation to the precision of the ground-based interferometric measurements.

Installed at the Very Large Telescope Interferometer (VLTI), the VINCI instrument coherently combines the infrared light coming from two telescopes in the infrared H and K bands. The first fringes were obtained in March 2001 with the VLTI Test Siderostats, and in October 2001 with the 8 m Unit Telescopes (UTs). To reduce the large quantity of data produced by this instrument, we have developed innovative interferometric data analysis methods, using in particular the wavelet transform. We have appplied them successfully to a broad range of interferometric observations obtained with very different configurations of the VLTI (0.35 m siderostats, 8 m Unit Telescopes, 16 m to 140 m baselines, K and H band observations).

Since the first fringes of VINCI, more than 800 nights of observations have been conducted with this instrument. This allowed us to record a large number of individual star observations, under extremely different atmospheric and instrumental conditions. The data processing methods that are described in the present paper were successfully applied to all these configurations, and consistently provided reliable and precise results. This gives us good confidence that they are efficient and robust, and can be generalized to other interferometric instruments.

Our goal in this paper is to give a step by step description of the processing of the VINCI data, from the raw data to the calibrated visibility. To illustrate this processing, we selected from the commissioning data a series of observations of a bright star and its calibrator, α Cen A and θ Cen respectively (Sect. 3). A complete overview of the data analysis work flow is presented in Fig. 1. It can be used as a reference to follow the logical progression of this paper. The photometric calibration of the interferograms is described in Sects. 4 and 5. The criteria for the selection of the interferograms are detailed in Sect. 6, and the computation of the visibility values and associated errors is given in Sect. 7. A number of quality controls is applied to the reduced data; they are described in Sect. 8. The calibration of the visibility is illustrated in Sect. 9. We demonstrate in particular the computation of the statistical and systematic errors on the visibility values.

2. Instrument description

2.1. The VLT Interferometer and VINCI

The Very Large Telescope Interferometer (VLTI, Glindemann et al. 2000, 2003a,b; Schöller et al. 2003) has been operated

* Appendices A, B and C are only available in electronic form at http://www.edpsciences.org

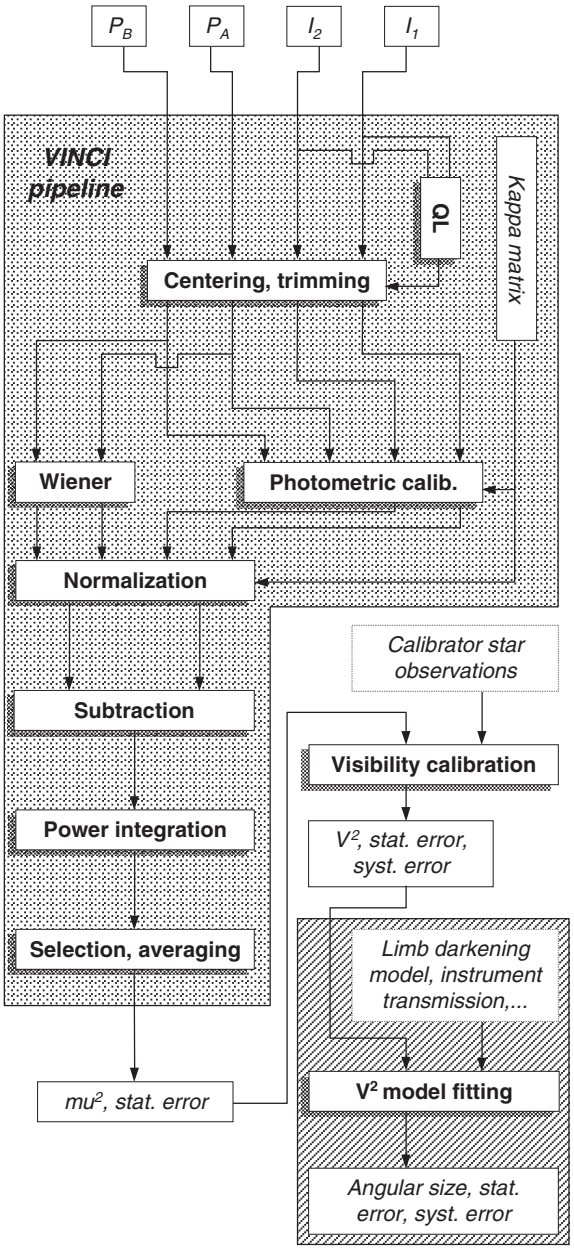

Fig. 1. Overview of the VINCI data analysis work flow. The shaded area delimits the processing executed automatically by the instrument data pipeline. The hatched area (lower right) covers the astrophysical interpretation of the measured visibility, not adressed in the present paper.

by the European Southern Observatory on top of the Cerro Paranal, in Northern Chile since March 2001. In its current state of completion, the light coming from two telescopes can be combined coherently in VINCI, the VLT Interferometer Commissioning Instrument (Fig. 2), or in the MIDI instrument (Leinert et al. 2000). In December 2002, MIDI obtained its first fringes at $\lambda = 8.7\,\mu$m between the two 8 m Unit Telescopes Antu (UT1) and Melipal (UT3). Another instrument, AMBER (Petrov et al. 2000) will soon allow the simultaneous recombination of three telescope beams (its first observations are scheduled for 2004).

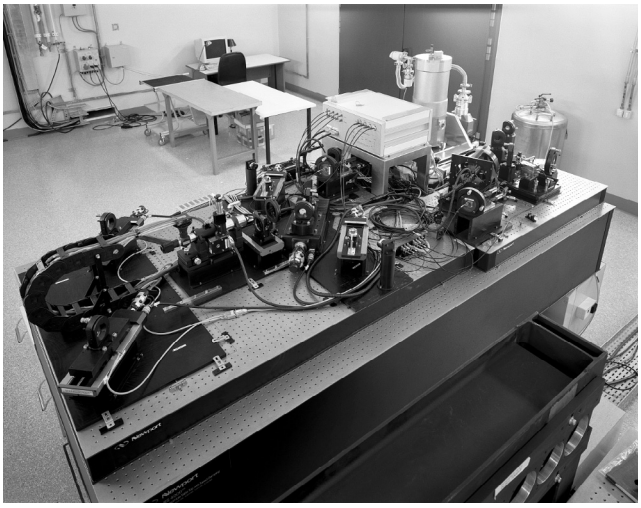

Fig. 2. View of the VINCI instrument installed in the VLTI interferometric laboratory. The MONA beam combiner is the visible above the center of the image (white box), with its optical fiber inputs and outputs. The beams coming from the VLTI Delay Lines enter the optical table from the bottom of the picture.

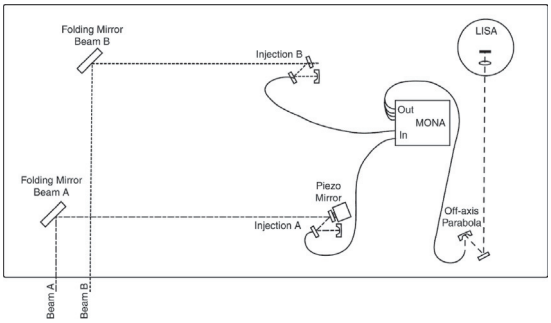

Fig. 3. Principle of the VINCI instrument.

A detailed description of the VINCI instrument, including its hardware and software design, can be found in Kervella et al. (2000). Figure 3 shows the setup of VINCI. The two beams enter the instrument from the bottom of the figure, after having been delayed by two optical delay lines (Derie 2000). Once the stellar light from the two telescopes has been injected into the optical fibers (injections A and B), it is recombined in the MONA triple coupler. VINCI is based on the same principle as the FLUOR instrument (Coudé du Foresto et al. 1998), and recombines the light through single-mode fluoride glass optical fibers that are optimized for K band operation ($\lambda = 2.0$–$2.4\,\mu$m). It uses in general a regular K band filter, but can also observe in the H band ($\lambda = 1.4$–$1.8\,\mu$m) using an integrated optics beam combiner (Berger et al. 2001). The first observations with this new generation coupler installed at the VLTI focus have given promising results (Kervella et al. 2003a; Kern et al. 2003).

2.2. Beam combination

The central element of VINCI is its optical correlator (MONA), based on single-mode fluoride glass fibers and couplers. It was designed and built specifically for VINCI by the

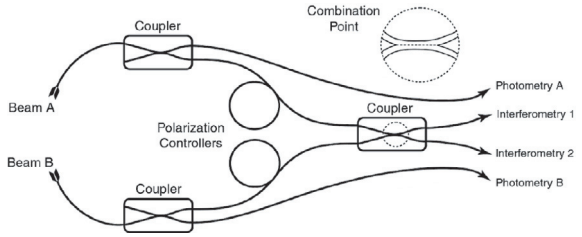

Fig. 4. Principle of the MONA beam combiner.

company Le Verre Fluoré (France). The waveguides are used to filter out the spatial modes of the atmospheric turbulence. In the couplers, the fiber cores are brought very close to each other (a few μm) and the two electric fields interfere directly with each other by evanescent coupling of the electromagnetic waves. Motorized polarization controllers allow the matching of the beam polarizations, in order to obtain the best possible interferometric transfer function.

The general principle of the MONA box is shown in Fig. 4. MONA contains three couplers: two side couplers (that provide two photometric outputs P_A and P_B to monitor the efficiency of the stellar light injection in the optical fibers) and a central coupler that is used for the beam combination. The latter provides two complementary interferometric outputs I_1 and I_2. The four output fibers are eventually arranged on a 125 μm square and imaged onto an infrared camera (LISA), built around a HAWAII detector. Only four small windows, of one pixel each, are read from the detector to increase the frame frequency and reduce the readout noise.

The Optical Path Difference (OPD) between the two beams is modulated by a mirror mounted on a piezo translator. This modulation allows one to sweep through the interference fringes (at zero OPD), that appear as temporal modulations of the I_1 and I_2 intensities on the detector. While the OPD is scanned, the four output signals are sampled at a few kHz. The four resulting time sequence signals (two photometric and two interferometric) are then available for processing. The interferogram acquisition rate can be set between 0.1 Hz (faint objects) and 20 Hz (bright targets).

2.3. Coherencing

During the observations, a simple fringe packet centroiding algorithm is applied in near real-time to the raw data. The fringe packet center is localized with a precision of about one fringe (2 μm) after each scan and the resulting error is fed back to the VLTI delay lines as an OPD offset. This capability, called *fringe coherencing*, ensures that the residual OPD is less than a coherence length despite possible instrumental drifts. Still, the correction rate (once per scan, i.e. a few Hz) is too slow to remove the differential piston mode of the turbulence. A fringe tracking unit is anticipated for the VLTI (FINITO, Gai et al. 2003) that will remove the differential piston and stabilize the interference pattern at the sub-fringe level (fringe cophasing), thus enabling longer integration times for the scientific instrument.

Table 1. Relevant parameters of θ Cen and α Cen A.

	θ Cen	α Cen A
	HD 123139	HD 128620
m_V	2.1	–0.0
m_K	–0.1	–1.5
Spectral type	K0IIIb	G2V
$T_{\rm eff}$ (K)[a]	4980	5790
$\log g$[a]	2.75	4.32
[Fe/H][a]	0.03	0.20
$\theta_{\rm UD}$ (mas)[b]	5.305 ± 0.020	8.314 ± 0.016

[a] $T_{\rm eff}$, $\log g$ and [Fe/H] from Cayrel de Strobel et al. (2001) and Morel et al. (2000), respectively for θ Cen and α Cen A.
[b] Measured diameters from Kervella et al. (2003b).

3. The selected sample data sets

3.1. Targets

To illustrate the processing of the VINCI data on representative files, we have chosen two series of interferograms obtained respectively on a calibrator star, θ Cen, and a target of scientific interest, α Cen A, on the intermediate length E0-G1 baseline (66 m ground length). θ Cen was chosen from the Cohen et al. (1999) catalogue. These authors compiled a grid of calibrator stars whose angular diameter is typically known with a relative precision better than 1%. Bordé et al. (2002) recently revised this catalogue specifically for its application to long baseline interferometry.

The observations of α Cen A and θ Cen discussed here were carried out with the two 0.35 m test siderostats of the VLTI. Both stars are bright, but θ Cen is significantly smaller than α Cen A, therefore its visibility is higher. The relevant properties of θ Cen and α Cen are reported in Table 1. The angular diameter of α Cen A was measured for the first time by Kervella et al. (2003b), based on a series of observations that include the two data sets discussed here.

The file names and characteristics of the two selected data sets are given in Table 2, to allow the interested reader to retrieve them from the ESO Archive (`http://archive.eso.org/`).

3.2. Acquisition parameters and data structure

Following the standard procedure used with VINCI, a series of 500 interferograms was obtained on each object. The two data sets were taken on July 15, 2002, starting at UT times 01:32:32 for θ Cen, and 02:33:09 for α Cen A. The piezo mirror scanning speed was set to 650 μm/s, giving a fringe frequency of 297 Hz. This intermediate speed is used commonly for the operation of VINCI with the VLTI Test Siderostats. The LISA camera frequency was set to 1.5 kHz in order to obtain a sampling of 5 points per fringe. The choice of the scanning speed (hence the sampling rate of the camera) is the result of a compromise between the photometric SNR

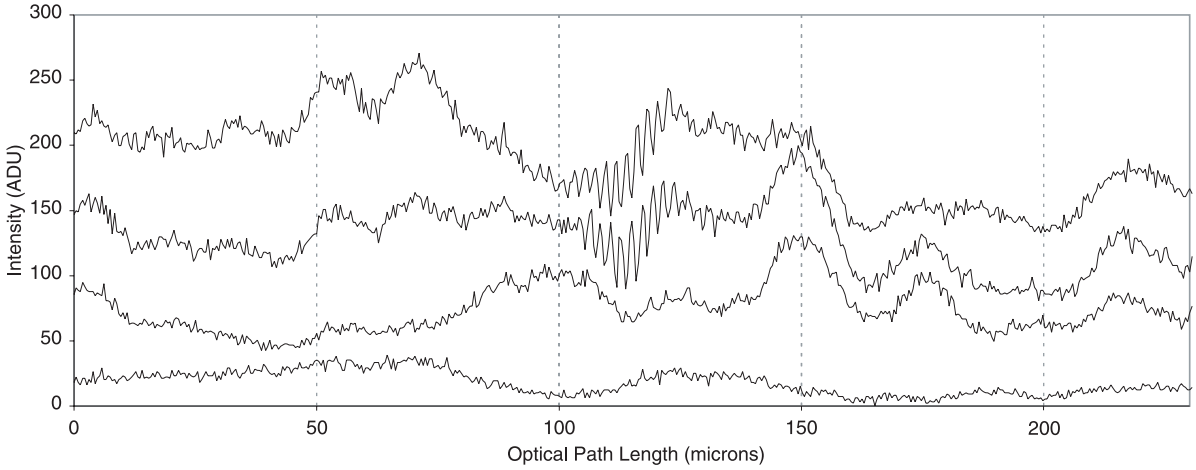

Fig. 5. The raw signals I_1, I_2, P_A and P_B, for one interferogram obtained on θ Cen. The original signals have been translated vertically respectively by +90, +40, +40 and 0 ADUs for clarity.

Table 2. Sample data sets. N is the number of scans.

File name	Target	Type	N
VINCI.2002-07-15T01:30:12.042	θ Cen	Off	100
VINCI.2002-07-15T01:30:53.273	θ Cen	A	100
VINCI.2002-07-15T01:31:36.505	θ Cen	B	100
VINCI.2002-07-15T01:32:31.645	θ Cen	On	500
VINCI.2002-07-15T02:30:49.318	α Cen A	Off	100
VINCI.2002-07-15T02:31:30.046	α Cen A	A	100
VINCI.2002-07-15T02:32:10.840	α Cen A	B	100
VINCI.2002-07-15T02:33:08.661	α Cen A	On	500

and the phase perturbations of the atmosphere (dominant at low scanning speed). The VINCI instrument allows one to scan up to a fringe frequency of 680 Hz (camera frequency of 3.4 kHz). This extreme speed is useful in the case of observations with the 8 m Unit Telescopes to reduce the influence of the photometric fluctuations on the interference fringes (multi-speckle regime). Figure 5 shows the raw signals of one interferogram obtained on θ Cen. This is the second scan in the series of 500, and it is of average quality in terms of injected flux stability. The photometric fluctuations are clearly visible in all four channels, while the interference fringes are located close to the center of the scan. The fringes are naturally in phase opposition between the two channels I_1 and I_2.

Each star observation consists of four files (batches), that each contain a series of acquisitions (scans) of the four signals coming out of MONA, with four different configurations of the instrument. The first three batches are used for the calibration of the camera background and instrument transmission, and usually contain 100 scans. The fourth batch contains the fringes. They are recorded in the following sequence:

1. *Off-source*: the two injection parabolas of VINCI are displaced in order to remove the star image from the single-mode fiber head.
2. *Beam A*: the A injection parabola is brought back to the position where the star light is injected in the optical fiber, while B is still off.
3. *Beam B*: symmetrically, only the beam B is injected in the MONA beam combiner, while A is off. The *Beam A* and *Beam B* sequences are used in the computation of the κ matrix (Sect. 4.1).
4. *On-source*: both beams are injected into MONA, and interference can occur. This last series usually contains 500 scans and is used to compute the squared coherence factor μ^2 (the interferometric observable, defined in Sect. 6.2).

4. Preliminary steps

4.1. Computation of the κ matrix

To properly calibrate the photometric fluctuations of the interferometric signals I_1 and I_2 using the two photometric outputs P_A and P_B, it is necessary to know precisely the coefficients linking the intensities of these four outputs. The relationships between the four channels can be approximated, within a very good precision (Coudé du Foresto et al. 1997), by the following expressions:

$$I_1 = \kappa_{1,A}\, P_A + \kappa_{1,B}\, P_B \quad (1)$$

$$I_2 = \kappa_{2,A}\, P_A + \kappa_{2,B}\, P_B. \quad (2)$$

The κ coefficients correspond to the differential gains between the four channels of VINCI. They include the coupling ratios of the MONA box, the coupling efficiency of each fiber to the physical pixels of the infrared camera, and the differential quantum efficiency between these pixels. Due to the chromatic transmission of the couplers, the color of the observed object plays a role in the κ coefficients, and they also tend to evolve due to the slow motion of the fiber spots on the LISA detector. It is therefore necessary to measure these coefficients (the κ matrix) immediately before each star observation. Each pair of κ coefficients is computed simultaneously using a classical χ^2 minimization algorithm with two variable parameters.

Table 3. κ coefficients measured for θ Cen and α Cen A.

	θ Cen	α Cen A
κ_{1A}	0.7569 ± 0.0061	0.7576 ± 0.0037
κ_{1B}	4.1231 ± 0.0160	4.1877 ± 0.0120
κ_{2A}	1.3089 ± 0.0054	1.2790 ± 0.0044
κ_{2B}	2.4855 ± 0.0143	2.4735 ± 0.0061

The errors on the estimation of the κ coefficients are derived from the residual dispersion of the measurement points around the linear model.

Table 3 gives the κ coefficients derived for the θ Cen and α Cen observations. The small differences between the κ values for the two stars may come from the slightly different colors of these objects, or from a small variation of the alignment of the output spots on the LISA infrared camera pixels between the two observations (they are separated in time by $\Delta t \simeq 1$ h).

Ideally, the κ coefficients should be balanced between the four outputs in order to maximize the efficiency of the interference, and simultaneously to give high SNR photometric signals for the calibration of the interferograms. The observed inbalance (that can reach up to a factor 5 in the selected sample batches) is due to the fact that the unexpectedly fast aging of the three optical couplers in the MONA box has increased significantly their sensitivity to temperature. This effect cannot be corrected on the coupler itself, and causes a slow (timescale of months) but large amplitude evolution of the κ matrix. Due to the very different time scales of these variations (months) and of the scientific observations (hours), this sensitivity is expected to have no significant impact on the observations other than a uniform and moderate reduction of the quality of the LISA signals.

4.2. Fringe localization

The first step of the processing is to trim the long interferogram to restrict it to a shorter segment, where the fringes are centered. The detection of the fringes is then achieved with the *Quicklook* signal *QL*, that is computed using the simple formula:

$$QL = I_1 - a\, I_2 \tag{3}$$

where a is given by

$$a = \frac{\sum_{i=1}^{N} I_1(i)\, I_2(i)}{\sum_{i=1}^{N} I_1^2(i)} \tag{4}$$

where N is the number of samples of the raw signals I_1 and I_2. This operation attenuates the photometric fluctuations and increases the SNR of the fringes. Once the fringes are localized precisely by detecting the maximum of the wavelet power spectral density (WPSD) of the *QL*, the four raw signals are trimmed accordingly. If the fringes have been found too close to the edge of the interferogram, the scan is discarded to avoid any bias of the data. In addition, if a large amplitude jump of the position of the fringe packet is detected between two consecutive scans (more than 20 μm), a strong piston effect is suspected and the scan is rejected (see also Sect. 6).

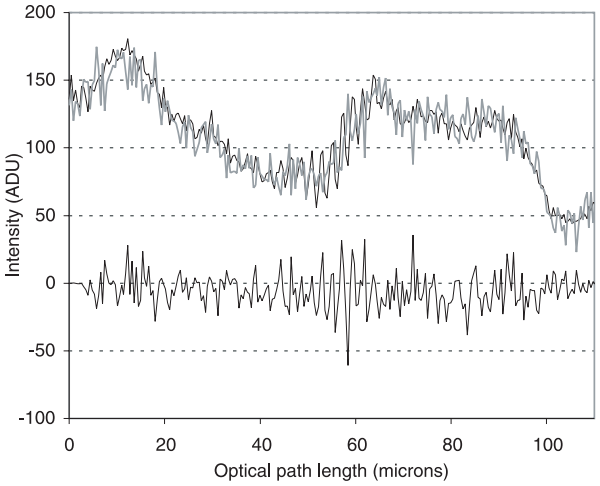

Fig. 6. Photometric calibration of the I_1 signal. The raw I_1 signal is the black line in the upper part of the plot, the photometric calibration signal $\kappa_{1A}P_A - \kappa_{1B}P_B$ is the superimposed grey line, and the result of the subtraction is the lower curve.

5. Photometric calibration

5.1. General principle

The photometric calibration of the interferograms produced by VINCI is achieved using the two photometric control signals P_A and P_B and the κ-matrix. The calibration is computed separately for the I_1 and I_2 channels using the following formulae (see Coudé du Foresto et al. 1997 for their derivation):

$$I_{1\,\mathrm{cal}} = \frac{1}{2\sqrt{\kappa_{1,A}\,\kappa_{1,B}}} \frac{I_1 - \kappa_{1,A}P_A - \kappa_{1,B}P_B}{[\sqrt{P_A\,P_B}]_{\mathrm{Wiener}}} \tag{5}$$

$$I_{2\,\mathrm{cal}} = \frac{1}{2\sqrt{\kappa_{2,A}\,\kappa_{2,B}}} \frac{I_2 - \kappa_{2,A}P_A - \kappa_{2,B}P_B}{[\sqrt{P_A\,P_B}]_{\mathrm{Wiener}}}. \tag{6}$$

The subscript "Wiener" designates optimally filtered signals (Sect. 5.2). This process allows one first to subtract the photometric fluctuations that were introduced in the interferometric channels by the turbulent atmosphere (calibration), and then to normalize the resulting signals to the geometrical mean of the two photometric channels $P = \sqrt{P_A\,P_B}$. As an example of calibration, the subtraction of $\kappa_{1,A}P_A + \kappa_{1,B}P_B$ from the original I_1 is presented in Fig. 6. The Wiener filtering of P, essential to avoid numerical instabilities, is described in the next paragraph (Sect. 5.2). After the normalization, $I_{1\,\mathrm{cal}}$ and $I_{2\,\mathrm{cal}}$ are apodized at their extremities, to prevent any edge effect during the numerical wavelet transform.

5.2. Low pass filtering of photometric signals

The normalization by the P signal is a critical step of the calibration. If P presents too low values ("zero crossing"), the divisions of Eqs. (5) and (6) will amplify the noise of the numerator. This is the reason why the P_A and P_B signals have to be

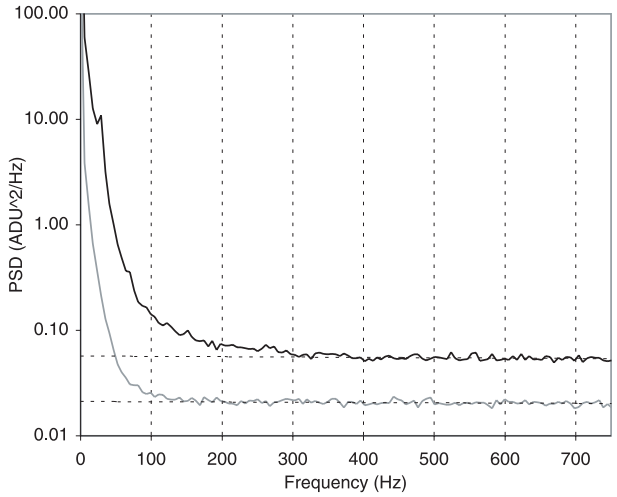

Fig. 7. Average power spectral density of the P_A and P_B signals as measured on θCen. From top to botton: $\widetilde{P_A}^2$, noise model $\widetilde{N_A}^2$ (upper dotted line), $\widetilde{P_B}^2$, noise model $\widetilde{N_B}^2$ (lower dotted line).

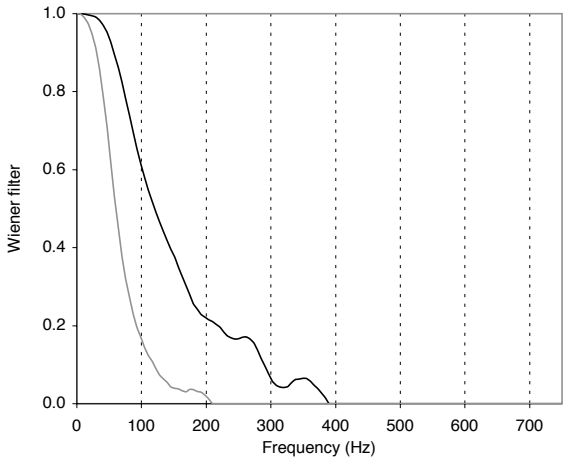

Fig. 8. Wiener filters computed from θCen photometric signals (Fig. 7). W_A is the upper line, and W_B the lower line.

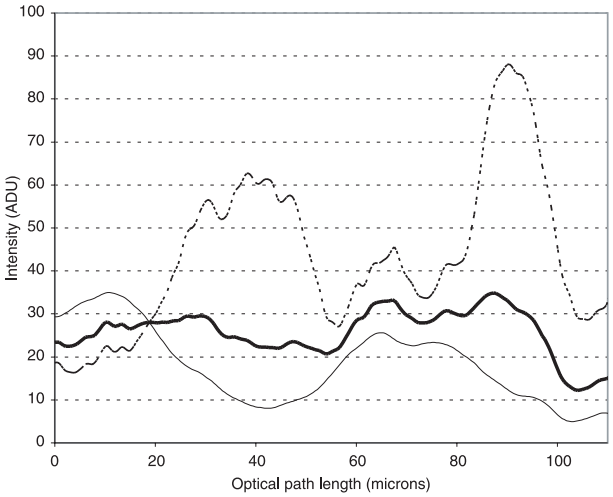

Fig. 9. Photometric normalization signal P (thick line), with the Wiener filtered P_A (dashed line) and P_B channels (thin line). P is the geometric mean of the two filtered photometric channels.

filtered, to improve their SNRs. This is achieved using Wiener filters, that allow one to optimally filter the raw signal and to reject the detector noise. They are computed from the average power spectral density (PSD) of the photometric fluctuations of P_A and P_B using only the on-source spectra. We use the classical definition of the Wiener filter W_x as computed from the signal P_x and the noise N_x (with x = A or B, the Fourier transform being represented by the $\sim$ notation):

$$W_x = \frac{\widetilde{P_x}^2 - \widetilde{N_x}^2}{\widetilde{P_x}^2}. \quad (7)$$

As shown in Fig. 7 (θCen data), we estimate the PSD of the noise directly from the PSD of the signal by assuming that the photon shot noise and detector noise are constant with respect to frequency (white noise). The contribution from the photometric fluctuations is visible at low frequencies. Considering the high frequency part of the spectrum, we extrapolate the level of the PSD background to the lower frequencies. Due to the high SNR of the averaged PSD, the estimation of the background is precise enough to reconstruct W_A and W_B. The first frequency for which the signal becomes smaller than the noise marks the practical limit of the Wiener filter, and the higher frequency values are set to zero. This method is more efficient than estimating the noise PSD from the off-source batch, as it directly takes into account the presence of photon shot noise, that also has to be removed. The resulting Wiener filters are presented in Fig. 8. The filtering of the photometric channels by these filters gives a clean P signal, as shown in Fig. 9.

5.3. Alternative normalization methods

If the SNR of the photometric channels P_A and P_B reaches too low values over the scan length, we choose to normalize the interferograms simply by averaging P over the fringe length, instead of using the Wiener filtered signal. This allows us to significantly reduce the amplification of the noise due to the normalization division. The limit between the two regimes is usually set to 5 times the readout noise. For interferograms that present very low photometric signal over the fringe packet itself, we discard the scan as a significant bias can be expected on the modulated power. Both averaging and Wiener filtering are almost equivalent on the final calibrated interferograms, with a slight advantage to the Wiener filtering when the photometric fluctuations are important (as in the UT observations for example).

5.4. Interferogram subtraction

After their calibration, we subtract the two interferograms $I_{1\,\mathrm{cal}}$ and $I_{2\,\mathrm{cal}}$, in order to cancel the residual photometric fluctuations due to the uncertainty in the estimation of the κ coefficients. This subtraction has proven to significantly enhance the immunity of the interferograms to the contamination coming from the photometric fluctuation background. Figure 10 shows the calibrated and normalized interferometric signal $I_{1\,\mathrm{cal}}$

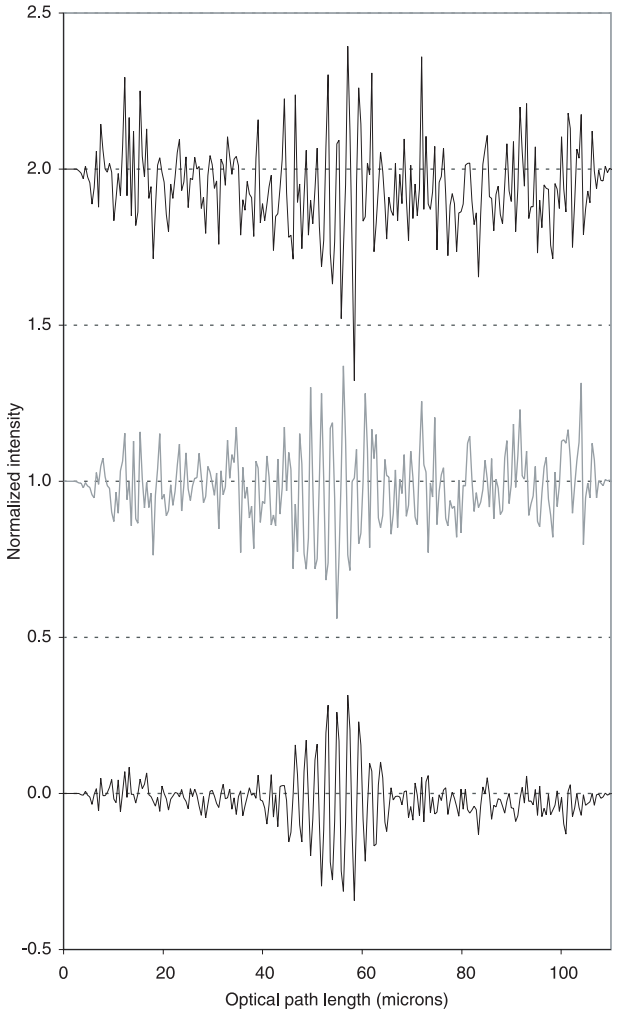

Fig. 10. *From top to bottom*: I_1 normalized interferogram (black), I_2 normalized interferogram (grey), and the result I of the subtraction of these two signals. For clarity, the I_1 and I_2 signals are shifted vertically by +2 and +1, respectively. The correlated noise has disappeared in the combined signal and the fringe packet appears more clearly.

and $I_{2\,\mathrm{cal}}$, together with I the result of the subtraction of these two signals defined as:

$$I = \frac{I_{1\,\mathrm{cal}} - I_{2\,\mathrm{cal}}}{2}. \quad (8)$$

The combined signal I is used for the integration of the fringe power to derive the visibility (Sect. 7). The advantage of using I instead of using separately $I_{1\,\mathrm{cal}}$ and $I_{2\,\mathrm{cal}}$ for the integration of the fringe power is that all the correlated noise between the two signals is eliminated by the subtraction, while the fringes, perfectly opposed in phase, are amplified. This allows us to eliminate the residual photometric fluctuations as well as part of the noise introduced during the photometric calibration.

6. Interferogram selection

6.1. Piston effect

The photometric calibration of the interferograms compensates for the incidence of wavefront corrugation across each subpupil of the interferometer, however it does not help remove the random phase walk (differential piston) *between* the two subapertures.

The differential piston, considered as a time-dependent OPD error $x(t)$, can be locally expressed by a polynomial development around a reference time t_0 (corresponding, for example, to the middle of the acquisition sequence):

$$x(t) = x_0 + \dot{x}\,(t - t_0) + \ddot{x}\,(t - t_0)^2 + ... \quad (9)$$

The effect of the OPD perturbation on the interferogram, and its consequence on the coherence factor measurement, depends on the order:

- **Zeroth order**: The constant term x_0 can be seen as a global offset of the fringe packet. It is detected and corrected by the *QL* algorithm which centers the fringe packet in the middle of the interferogram.
- **First order**: The first order of the piston $\dot{x}$ changes the fringe velocity and induces a simple frequency shift in the PSD. It modifies the fringe peak position, but acts only as a homothetic compression or expansion of the fringe packet along the OPD direction. The first order piston has no immediate effect on the fringe visibility. However, if the shifting speed $\dot{x}$ of the fringe packet is too high, it can result in an undersampling of the fringes that will affect the visibility.
- **Second and higher orders**: Any term of order two (*acceleration*) and beyond breaks the linear relationship in the scan between time and OPD, and consequently the Fourier relationship which is at the basis of the visibility calculation, distorting the shape of the fringe peak. This introduces a non-linear, seeing induced multiplicative noise on the visibility measurements, which is the dominant noise source for strong signals (bright, unresolved objects).

Detailed studies of the properties of atmospheric piston can be found for example in Linfield et al. (2001) and Di Folco et al. (2002). When a dedicated fringe tracking instrument becomes available on the VLTI (e.g. FINITO, Gai et al. 2003), most of the piston will be actively removed by a servo loop. It remains to be checked how the residuals will still limit the final visibility precision.

6.2. Quality control of the interferograms

The goal of the interferometric data processing is to extract the squared visibility V^2 of the fringes. The intermediate step to this end is to measure the squared coherence factor μ^2 of the stellar light. This instrument dependent quantity characterizes the fraction of coherent light present in the total flux of the target. It is calibrated using observations of a known star, as described in Sect. 9. To avoid any bias on μ^2, we have to reject the interferograms that do not contain fringes (false detections), or whose fringes are severely corrupted by the atmospheric turbulence (photometrically or by the piston effect). The selection procedure is in practice similar to a shape recognition process.

For this purpose, we measure in the wavelet power spectral density (WPSD) the properties of the fringe peak both in

the time and frequency domains, and we subsequently compare them with the expected properties of a reference interferogram of visibility unity, derived from the spectral transmission of the instrument. In this paper, we will refer interchangeably to the "time domain" or "optical path difference (OPD) domain" for the WPSD, as they are linearly related through the scanning speed of the VINCI piezo mirror that is used to modulate the OPD. The fringe peak is first localized in frequency by the maximum of the WPSD, and then the full width at half maximum is computed along the two directions: time and frequency. As the fringe packet has been recentered before the calibration, its position in the time domain is zero. Three parameters are then checked for quality:

- peak width in the time domain (typically ±50% around the theoretical value is acceptable);
- peak position in the frequency domain (±30%);
- peak width in the frequency domain (±40%).

In principle, the variation of the fringe contrast over the spectral band should also be taken into account to create the theoretical reference interferogram. But in practice, as long as the visibility of the fringes does not cancel out for a wavelength located inside the spectral band of the observations, the shape of the interferogram remains very close to theoretical fringes of visibility unity. However, when the fringe visibility goes down to zero for a wavelength pertaining to the observation band, the fringe packet appears split in two parts in the time domain. Such a deviation from the "single packet" case can cause misidentifications, and eventually induce a bias on the derived μ^2 value, as some valid interferograms would be rejected. In this case, one should use a dedicated broadband model to predict the reference interferogram, taking into account the expected angular size of the target. The selection criteria should then be adapted to match this reference (increased peak width, presence of two maxima in the WPSD,...). An alternative is to directly adapt the basis functions of the wavelet transform so that they match the predicted interferograms. We have not implemented these methods in our current processing algorithm, whose validity is thus limited to the cases when the visibility is above zero for all wavelengths in the observation band. If this condition is not realized, then the interferogram selection should be disabled, or at least the selection criteria should be made significantly less stringent, in particular regarding the fringe peak width.

Figure 11 shows two examples of interferogram WPSD, one of them being affected by atmospheric piston. The difference in terms of fringe peak shape is clearly noticeable, and leads to the rejection of the corrupted interferogram (bottom figure). This selection process has shown a very low false detection rate, and rejects efficiently the interferograms that are affected by a strong piston effect. However, limited piston of order two (and above) is not identified efficiently. The problem here is that the relevant properties for the estimation of the second order piston are currently difficult to measure with a sufficient SNR from the data, as they are masked by the order 1 piston. We expect that the introduction of the FINITO fringe tracker in 2004 will allow us to derive an efficient metric to reject the interferograms affected by a high order piston effect.

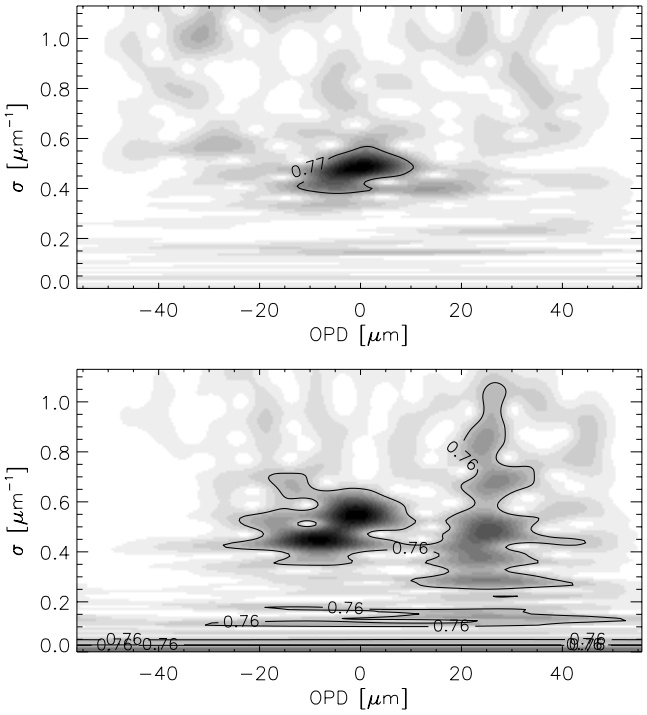

Fig. 11. Wavelet power spectral densities of processed interferograms (σ represents the wave number, i.e. the inverse of the wavelength). The upper figure shows the WPSD of a good quality interferogram: the energy is well confied in the fringe power peak. The bottom WPSD is affected by strong atmospheric piston: a significant part of the fringe power is spread outside of the theoretical fringe peak, both in time and frequency domains. The isocontours delimit 77% and 76% of the total modulated power, respectively.

After the fringe power integration (described in Sect. 7), we filter out the scans which μ^2 deviates by more than $3\,\sigma$ from the median of the full batch of interferograms (usually 500 scans). This step prevents the presence of very strong outliers, which can appear due to the division introduced by the normalization of the interferograms (introduction of Cauchy statistics).

6.3. Immunity to selection biases

An essential aspect of the parameters used for the quality control of the fringe peak properties is that they are largely independent of the visibility of the fringes, and therefore do not create selection biases. In particular, the integral of the fringe peak (directly linked to the visibility) or its height are never considered in the selection. The parameters chosen in Sect. 6.2 clearly depend on the photometric SNR, but are independent of the visibility of the fringes, thanks to the calibration procedure described in Sect. 5.

The upper part of Fig. 12 demonstrates this independence in the difficult case of the batch of interferograms obtained on α Cen A. Despite the very low visibility of the fringes, no systematic deviation is visible for low photometric SNR values, as the dispersion is symmetric around the mean value. The same plot for θ Cen (Fig. 12 bottom) does not show any deviation either. A further discussion of the properties of the histogram of these measurements can be found in Sect. 8.3.

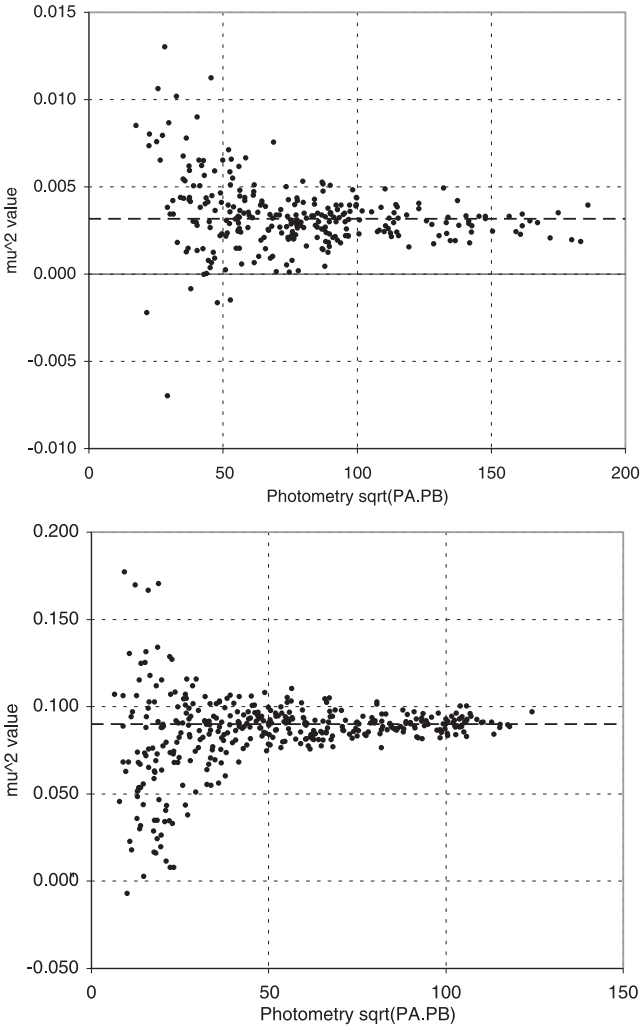

Fig. 12. Squared coherence factor μ^2 as a function of the photometric signal on the fringe packet, for the sample batches obtained on α Cen A (*top*) and θ Cen (*bottom*). The dashed lines show the mean value of the series derived using the bootstrap technique.

This means that the quality control described in this paragraph is not linked to the observable, and thus does not introduce a selection bias. Its effect in the case of the θ Cen and α Cen A observations is discussed in Sect. 8.3.

A critical case is when the visibility is extremely low. In this situation, the fringe peak will tend to blend in with the noise, which tends to make it appear broader and slightly displaced. Therefore, low-visibility data are more likely to be rejected than high-visibility data. This can introduce a bias towards higher μ^2 for low-visibility observations: a scan with a $+1\,\sigma$ deviation is accepted, but a scan with a $-1\,\sigma$ deviation is more likely to be rejected as it fails the selection criteria. However, in this situation, the risk is high to fail to reject the spurious spikes that are created in the calibrated interferograms due to the division by the P signal (Sect. 5). Without the selection procedure, the modulated power of these calibration artefacts will be integrated in the final μ^2 value. As this power is essentially random, but always positive, these misidentifications would then result in a strong positive bias on the final μ^2 value. For this reason, and in spite of the potential rejection of a small part of the valid interferograms, the application of the selection procedure results in a more reliable estimate of μ^2, even for the very low visibility fringes. In any case, the careful examination of the statistical properties of the μ^2 histogram (see Sect. 8), and in particular of its skewness, allows us to detect a possible selection bias.

7. Visibility computation

7.1. Wavelet power spectral density

Once the interferogram has been calibrated and normalized, the squared coherence factor μ^2 is measurable as the average modulated energy of the interference fringes over the batch. It is computed by integrating the power peak of the interferograms in the average WPSD (see also Appendix A and Sect. 7.2.1). The WPSD is a two dimensional matrix, examples of which are shown in Fig. 11. For all wavelet transforms, we use the Morlet wavelet, which is defined as a plane wave multiplied by a Gaussian envelope. It closely matches the shape of the interferometric fringe packet. When computing a classical PSD, the interferogram is projected on a base of sine and cosine functions, which are not localized temporally. This means that the information of the position of the fringe packet is not used, and that the noise of the complete interferogram contributes to the measured power. On the other hand, the wavelet transformation projects the interferogram on a base of wavelets that are localized both in time and frequency, making full use of the localized nature of the modulated energy. As discussed in Appendix A, the modulated energy of the signal is conserved by the wavelet transform in the same way as through the classical Fourier transform.

7.2. Estimation of the squared coherence factor μ^2

7.2.1. Fringe power integration

The average power spectral density of the α Cen A sample batch, computed using the wavelet transform, is shown in Fig. 13. To obtain this 1D spectrum from the original 2D WPSD matrices, we first project the WPSD matrix of each interferogram on the frequency axis, by integrating it over the fringe packet length (time axis). From this we obtain a series of one-dimensional vector PSDs, similar to the Fourier PSD but with a reduced noise. Before the averaging, we recenter each fringe peak using the frequency position information derived from the selection of the interferograms (Sect. 6). This step allows us to confine more tightly the energy of the peak, which is displaced by the first order piston effect. This reduces the influence of piston on the final μ^2 value. The co-added 1D spectrum is the signal used for the final power integration to estimate the μ^2 of the star.

The integration of the fringe power is typically done over 100 pixels in the time domain (20 fringes), and from 2000 to 8000 cm^{-1} in the frequency domain (see also Sect. 8.1).

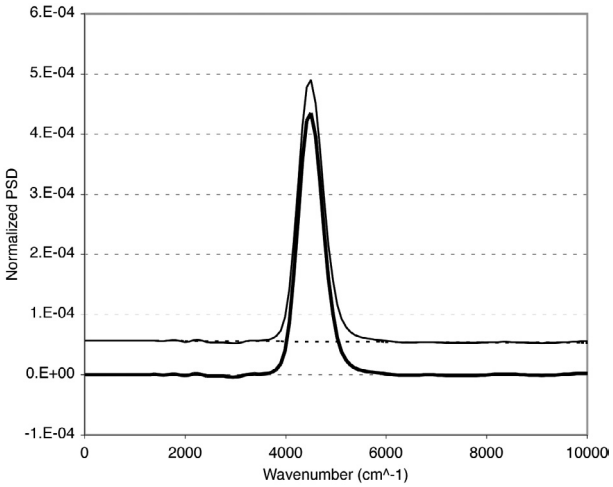

Fig. 13. Average WPSD of the α Cen A observation. The original two-dimensional matrix has been integrated over the fringe packet length in the time domain. The resulting projection on the wave number axis allows one to visualize clearly the noise contribution. The subtracted noise model is shown by the dashed line. The final WPSD (thick line) shows no bias in spite of the large brightness of the star and very low squared coherence factor of the fringes ($\mu^2 \approx 0.3\%$).

7.2.2. Removal of the WPSD background

The power in the fringe peak is contaminated by three additive components:

- the photon shot noise;
- the detector noise;
- the residual photometric fluctuations.

To estimate the modulated power of the fringes, it is essential to precisely remove these contributions from the PSD of the interferograms.

Perrin (2003) has developed an analytical treatment of the photon shot noise based on its particular properties (Poisson statistics). The photon shot noise is perfectly white, as it is created from a purely random process. However, due to the calibration and normalization process of the interferograms, its translation onto the final interferometric signal I could in theory deviate from this property and show a dependence with frequency. Such an effect has not been observed in practice on the VINCI data, and the uniform subtraction of the photon noise background from the PSD of the I signal has proven to be very efficient. A good example of the "whiteness" of the photon shot noise of the processed fringes can be found in Wittkowski et al. (2004), where a very bright star ($m_K = -0.6$) was observed with the two 8 m telescopes UT1 and UT3 (B = 102.5 m). In spite of the extremely large flux on the VINCI detector (100 m^2 collecting optics) and the very low visibility of the fringes ($V^2 \simeq 10^{-2}$), the resulting PSD background is white, therefore validating our photon shot noise removal method under the most demanding conditions.

In order to fully justify our background removal procedure, we still have to verify the "whiteness" of the detector noise, whose statistics and frequency structure depends on the type of detector and readout electronics used. The infrared camera of VINCI (LISA) is based on a HAWAII array, which is read using an IRACE controller (Meyer et al. 2000). As only four pixels of the 1024×1024 array are actually used, an engineering grade detector was chosen for the instrument. It presents a large quantity of dead and hot pixels, and therefore it was necessary to thoroughly check its noise characteristics. This was achieved during extensive laboratory testing, and is also verified automatically for each observation. It appeared that the LISA detector noise is perfectly white, without any significant electronic interference signature.

This satisfactory behavior of the detector and photon shot noises allows us to remove them simultaneously by subtracting to the μ^2 value of each interferogram an average of its WPSD at high frequency, measured outside of the domain of frequency of the interferometric fringes. To correct for potential residuals of the photometric calibration, we fit a linear model of the residual background to the *average* WPSD of the interferograms in the batch. In this procedure, we allow for a limited slope of the background model, in order to correct a possible residual power from photometry. Thanks to the averaging of a large number of scans, the noise on the average WPSD is very low, and the fitting procedure is very precise. Most of the time, and even for the most important fluctuation cases (Unit Telescopes in multispeckle mode), the contribution of the residual photometric noise is totally negligible on the combined interferogram I obtained from the subtraction of the calibrated signals $I_{1\,\mathrm{cal}}$ and $I_{2\,\mathrm{cal}}$ (Eq. (8)).

An illustration of the background quality is presented in Fig. 13. The WPSD background noise appears perfectly white, even at the very enlarged scale used to visualize the very small fringe peak of α Cen A ($\mu^2 \approx 0.3\%$). In particular, no "color" or electronic interference ("pickup") are present.

7.3. Estimation of the statistical error

To compute the statistical error on the μ^2 estimation, we integrate separately the fringe power in each WPSD of the batch, correct the detector and photon shot noise biases individually, and use a weighted bootstrapping technique on this set of measurements. Our sample is made of N pairs (μ_i^2, w_i) where μ_i^2 is the squared coherence factor obtained by integrating the WPSD of the scan of rank i in the series and w_i is its associated weight. It is defined as the average level of the photometric signal P over the fringe packet length (20 fringes in the K band) multiplied by the inbalance between the two photometric channels P_A and P_B:

$$w_i = \frac{\min(\overline{P_{\mathrm{A},i}}, \overline{P_{\mathrm{B},i}})}{\max(\overline{P_{\mathrm{A},i}}, \overline{P_{\mathrm{B},i}})} \overline{\left(\sqrt{P_{\mathrm{A},i} P_{\mathrm{B},i}}\right)}_{\mathrm{Fringes}}. \quad (10)$$

It characterizes well the clarity of the total photometric signal that contributes to the formation of the fringes. The final dispersion of the μ^2 values is reduced by this weighting. The detailed description of the weighted bootstrapping method used for the computation of the error bars is given in Appendix B.

The bootstrapping technique has the important advantage of not making any assumption on the type of statistical distribution that the data points follow. In particular, it is more reliable

than the classical approach that assumes a Gaussian distribution of the measurements. Skewness and other deviations from a Gaussian distribution are automatically included in the error bars, which can be asymmetric.

The statistical dispersion of VINCI measurements shows two regimes: for bright stars the precision is limited by the piston and photon shot noise, while for the fainter objects, the main contributor to the dispersion is the detector noise of the camera, and the precision degrades rapidly. A discussion of the different types of noise intervening in the visibility measurements can be found for instance in Colavita (1999) and Perrin (2003). The μ^2 measurements discussed in this paper have a relative statistical precision of ±3.00% for α Cen A, and ±0.53% for θ Cen. The lowest relative statistical dispersion $\sigma(\mu)/\mu$ reached up to now on the coherence factor with VINCI is in the 2% range. Under good conditions, this translates into a bootstrapped statistical error of less than ±0.1% on μ for 5 min of observations.

8. Post-processing quality control

After a batch of interferograms is processed, several quality controls are performed in order to detect any problem in the resulting visibility values and statistical error bars. This step is essential to ascertain the quality of the interferometric data, as it can vary depending on the atmospheric conditions (e.g. seeing, coherence time) and on the general behavior of the instrument (e.g. injection of the stellar light in the optical fibers, beam combiner properties, polarization mismatch of the two beams).

8.1. Power peak integration boundaries

A potentially damaging effect of the atmospheric piston on the visibility of the fringes is that it tends to move the position of the fringe peak, and to spread it over a wider frequency range. If the frequency boundaries for the integration of the fringe peak are set too tight, the result could be that part of the modulated power is not taken into account, creating a bias. These boundaries are automatically changed as a function of the ground baseline length to account for the increased piston strength on longer baselines. They are not modified as a function of the projected baseline, and are thus identical for scientific targets and calibrators.

To check for the presence of such an effect, we measure the fringe peak shape in the WPSD. More precisely, we estimate its central wave number, full width at half maximum, as well as the limit wave numbers for which the background level is reached. Using these extended limits, we integrate the fringe power and compare this value to the one obtained with the user-specified wave number limits. If a discrepancy is found at a significant level, the batch is considered dubious and can be rejected after further examination.

8.2. Histogram properties

As the noise sources acting on the μ^2 values have normal statistics, it is expected that the distribution of the μ^2 values over the batch is also normal. Although the bootstrapping procedure used to compute the μ^2 error bars is not sensitive to the type of distribution, a large skewness or kurtosis would betray a problem in the calibration of the interferograms that could eventually bias the final μ^2 value. The relevant parameters for this verification are the skewness coefficient s (third moment of the distribution) defined as:

$$s = \sum_{i=1}^{N} \frac{(\mu_i^2 - \overline{\mu^2})^3}{(N-1)\sigma^3} \tag{11}$$

and the kurtosis coefficient k (fourth moment):

$$k = \sum_{i=1}^{N} \frac{(\mu_i^2 - \overline{\mu^2})^4}{(N-1)\sigma^4} - 3 \tag{12}$$

where μ_i^2 are the squared coherence factor values, σ the standard deviation, $\overline{\mu^2}$ the unweighted average, and N the number of scans. The skewness characterizes the presence of a "tail" on the histogram. A large value of s is therefore a symptom of a potential bias problem in the distribution, as a significant number of values are either too large or too small compared to the average value of the sample. A positive kurtosis coefficient means a distribution more peaked than the normal one. However, it should be stressed that the kurtosis is not a very robust parameter to assess if the sample is drawn from a normal distribution. It requires a large number of sample values to be relevant, and it is very sensitive to the presence of outliers. Therefore, it should only be used in conjunction with other statistical tests. A range of ±0.5 can be considered acceptable for k. When random samples are drawn from a normal population, the resulting skewness coefficients will fall into the range ±0.18, with a probability of 90%. We therefore choose this value as an acceptable range.

Table 4. Reasons for the rejection of θ Cen and α Cen A interferograms during the processing. The lower part of this table corresponds to the selection criteria related to the atmospheric piston effect.

Reason	θ Cen	α Cen A
Photometry too low	77	24
Large OPD jump	13	47
Fringes at edge	6	27
Fringe packet width	1	47
Fringe peak position	3	40
Fringe peak width	5	33
Outliers (3σ)	9	5
Total number of rejected scans	114/500	223/500

8.3. Application to θ Cen and α Cen A

Table 4 gives the reasons for the rejection of the interferograms of the θ Cen and α Cen A batches. In the case of α Cen A, a larger number of interferograms are rejected due to the very low visibility of the fringes.

Table 5. Statistical properties of the θ Cen and α Cen A sample batches. The values obtained when disabling the selection of the interferograms based on their piston properties are given in brackets for comparison.

	θ Cen	α Cen A
Reduced scans	386 (395)	277 (391)
Average μ^2 (%)	8.995 (8.999)	0.3180 (0.2949)
Stat. error (1σ)	0.048 (0.050)	0.0095 (0.0142)
Rel. error σ/μ^2	0.53% (0.56%)	3.00% (4.81%)
Skewness s	+0.023 (+0.013)	−0.007 (+0.160)
Kurtosis k	+0.164 (+0.062)	+0.044 (−0.042)

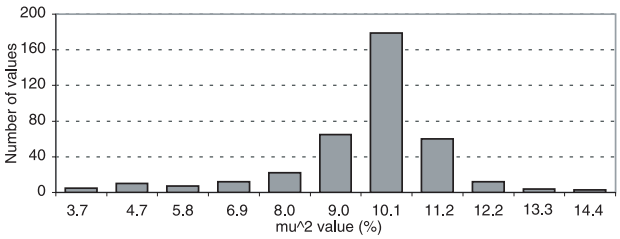

Fig. 14. Histogram of the μ^2 values obtained on θ Cen. No significant skewness is present.

The measured statistical properties of the processed interferograms of θ Cen and α Cen A are given in Table 5. The values in brackets were obtained by disabling the piston selection of the interferograms (based on the fringe packet width, and on the position and width of the fringe peak in the power spectrum of the interferogram). The comparison of the selected vs. non-selected versions of the data processing shows that the piston selection has a positive effect on the dispersion of the measurements. For θ Cen, the difference is minimal between the two kinds of processing. In particular, the total number of processed interferograms is almost identical for the two cases. However, for α Cen A, the difference is clearly noticeable, as the final error bars are 60% larger when the selection is disabled, in spite of a total number of processed scans approximately 40% larger. The skewness of the histogram is also much larger in this case (by a factor of 20). This clearly shows the advantage of the fringe selection procedure, in particular for the rejection of the calibration artefacts (false detections) in the very low visibility case (see also Sect. 6.3).

In the case of θ Cen (Fig. 14) and α Cen A (Fig. 15), no skewness is present. For θ Cen, a small positive kurtosis $k \approx 0.16$ is detected, meaning that the distribution is slightly too peaked (*leptokurtic*, as opposed to a *platykurtic* distribution that is too flat). However, it is easily inside the acceptable range (±0.5), and this property is taken into account in the bootstrapped error bars.

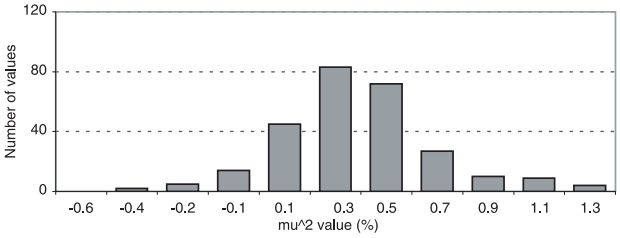

Fig. 15. Histogram of the μ^2 values obtained on α Cen A.

9. Visibility calibration

9.1. Principle

The data reduction software of VINCI yields accurate estimates of the squared modulus of the coherence factor μ^2, which is linked to the squared object visibility V^2 by the relation:

$$V^2 = \frac{\mu^2}{T^2} \tag{13}$$

where T^2 is the response of the system to a point source, also called transfer function (hereafter TF), interferometric efficiency, or system visibility. It is measured by bracketing the science target with observations of calibrator stars whose V^2 is supposed to be known a priori. The accuracy of our knowledge of the calibrator angular diameter, and the precision with which we estimate its μ^2 are therefore decisive for the final quality of the scientific target observation. Typically, the scientific targets are bracketed by calibrator observations, so as to be able to verify the stability of the TF. In this respect, the VLTI has often proved to be stable at a scale of a few percent over several nights. Nevertheless, and to guarantee the quality of the VINCI data, calibrators are regularly observed during the night, before and after each scientific target.

9.2. Interferometric transfer function estimation

9.2.1. Transfer function model

By nature, the interferometric TF is affected by a large number of parameters: atmospheric conditions (seeing, coherence time), polarization (incidence of the stellar beams on the siderostat mirrors), spectrum of the target, etc. These effects combine to make T^2 a stochastic variable, that can evolve over a wide range of timescales. In order to estimate its value and uncertainty on a particular date at which it was not directly measured (e.g. during the observation of a scientific target), it is necessary to use a model of its evolution. Such a model relies necessarily on an hypothesis, for instance that the value of T^2 is constant between two (or more) calibrator observations, that it varies linearly, quadratically, or any higher order model. Let us now evaluate the most suitable type of TF model for the observations with VINCI.

As a practical example, Fig. 16 shows the evolution of T^2 over one night of observations, with a typical sampling rate of one measurement every 15 min. This series of 27 observations was obtained during the night of 29 May 2003 on

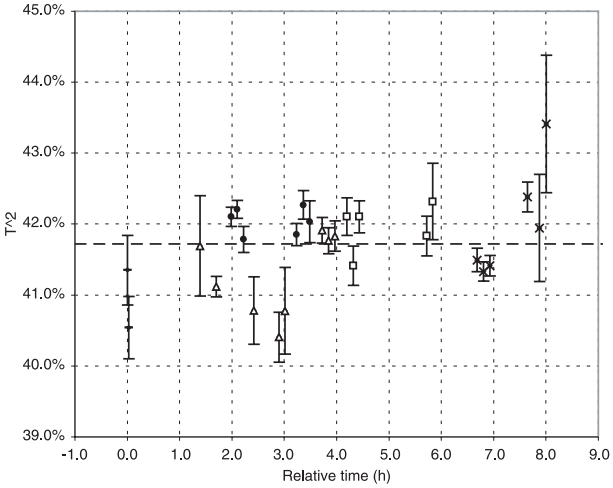

Fig. 16. Evolution of the transfer function T^2 during one night (2002-05-29) on the E0-G0 baseline of the VLTI (16 m in ground length). Each symbol corresponds to a different star.

the E0-G0 baseline (16 m ground length). A number of different stars with known angular diameters were observed, covering spectral types in the G-K range. During these observations, spread over 8 h, the seeing evolved from 1.0 to 2.0 arcsec, the altitude of the observed objects was distributed almost uniformly between 25 and 80 degrees, and the azimuth values covered 15 to 90 degrees (N = 0, E = 90). Due to this broad range of conditions, this series represents a worst case in terms of TF stability. As a reminder, under normal conditions, a calibrator is selected as close as possible to the scientific target, in time, position and spectral type.

Over the whole night, the overall stability is satisfactory, with a dispersion of $\sigma_{\rm tot} = 0.64\%$ around the average value of $\overline{T^2} = 41.75\%$. In order to estimate the external dispersion $\sigma_{\rm ext}$ of the transfer function over the night (due to the atmosphere and instrumental drifts), we can subtract the average of the intrinsic variances σ_i^2 of the T_i^2 values $\sigma_{\rm int}^2$ from the total variance $\sigma_{\rm tot}^2$:

$$\sigma_{\rm ext}^2 = \sigma_{\rm tot}^2 - \sigma_{\rm int}^2. \quad (14)$$

The average precision of each individual T^2 measurement in our sample night is $\sigma_{\rm int} = 0.21\%$. This gives an external dispersion of $\sigma_{\rm ext} = 0.60\%$. In this particular case, the external dispersion is thus dominant over the internal measurement errors, by a factor of almost three.

From this example, we can conclude that the rate of one measurement every 15 min is insufficient to sample the fluctuations of the TF. Due to this, we do not gain in precision by interpolating the TF values using a high order model (quadratic, splines,...). In the current state of the VLTI (siderostat observations), the most adequate model for the estimation of the TF is thus a constant value between the observations of the calibrators. The 1.8 m Auxiliary Telescopes will soon allow us to sample the TF with a much higher rate, of the order of 1 min, and higher order models of the TF variations could become necessary. As we are dominated by the external dispersion $\sigma_{\rm ext}$, the uncertainty on the TF has to be estimated from the dispersion of the individual T^2 measurements obtained before and after the scientific target, without averaging of their associated error bars.

9.2.2. Refinement of the transfer function model

Under good and stable conditions, the random dispersion of T^2 introduced by the atmosphere can be very low between two consecutive observations of a calibrator. In this case, we want to evaluate the true uncertainty on the model T^2 by comparing the hypothesis of stability to the calibrator observations, and subsequently refine the hypothesis used to estimate the error bar on T^2.

The observational strategy chosen with VINCI is to record several series of interferograms consecutively for each calibrator observation (typically three), over a period of about 15 min. To decide if the atmospheric and instrumental conditions are stable over this period, we compute the following χ^2 expression:

$$\chi^2_{\rm tot} = \sum_i \frac{(T_i^2 - \overline{T^2})^2}{\sigma^2_{{\rm stat},i}} \quad (15)$$

where T_i^2 are the consecutive estimates of the TF obtained on the calibrator, $\sigma^2_{{\rm stat},i}$ the statistical error of each measurement, and T^2 the weighted average of the T_i^2 values (using the inverse of the statistical variance as weights). If the resulting χ^2 is small (less than 3), then the hypothesis that the TF is constant is probably true: the T_i^2 values can be averaged and the global statistical error bar reduced accordingly. If not, then this hypothesis cannot be made, and a realistic approach is to consider as the true measurement error of the average TF the standard deviation of the T_i^2 sample.

When several series of interferograms are obtained on the same calibrator and the conditions described above are verified, the resulting estimates of the TF can be averaged in order to reduce the attached statistical error bar. However, the systematic error introduced by the a priori uncertainty on the angular size of one calibrator cannot be reduced by repeatedly observing this star, but only by combining the TF measurements obtained on independent objects.

9.3. Application to the sample observation of α Cen A

In the case of the observations described in this paper, θ Cen was observed one hour before α Cen A. Assuming a UD angular diameter of $\theta_{\rm UD} = 5.305 \pm 0.020$ mas (Kervella et al. 2003b), and taking into account the spectrum of the source and the bandwidth averaging effect (also called bandwidth smearing, see e.g. Davis et al. 2000), we expect a squared visibility of $V^2_{\rm theo} = 0.1796$ and a $1\,\sigma$ systematic uncertainty $\sigma_{\rm syst} = \pm 0.0027$ for the 65.929 m projected baseline (weighted average over the interferogram series). As we observed an instrumental coherence factor of $\mu^2 = 0.08995 \pm 0.00048$, the transfer function T^2 is estimated to be:

$$T^2 = \frac{0.08995\ [\pm 0.00048]_{\rm stat}}{0.1796\ [\pm 0.0027]_{\rm syst}}. \quad (16)$$

Using the relations detailed in Appendix C to compute the error bars of the ratio μ^2/T^2, we obtain

$$T^2 = 0.5010\,[\pm 0.0027]_{\rm stat}\,[\pm 0.0077]_{\rm syst}. \quad (17)$$

As we consider here only one calibrator observation, we cannot estimate the external dispersion of T^2, and we consider only the internal statistical and systematic error bars. As a remark, this T^2 value is not identical to the one computed in Sect. 9.2.1, as it was obtained more than one month later. The VINCI coupler is known to be sensitive to long term temperature variations (over a timescale of weeks), an effect that can explain the observed difference.

The squared visibility value of α Cen A is then:

$$V^2_{\alpha\,\rm Cen} = 0.00635\,[\pm 0.00019]_{\rm stat}\,[\pm 0.00010]_{\rm syst}. \quad (18)$$

The uncertainty on this value is dominated by the statistical error, despite the importance of the systematic error on the value of T^2. The average baseline of this measurement is 61.470 m, and we can now deduce the uniform disk model angular diameter of α Cen A, $\theta_{\rm UD} = 8.305 \pm 0.024$ mas, which is very close to the published value of $\theta_{\rm UD} = 8.314 \pm 0.016$ mas from Kervella et al. (2003b). This computation takes into account the wavelength averaging effect due to the broadband K filter of VINCI as described by Kervella et al. (2003b).

10. Conclusion

We have described the data reduction methods that are used on VINCI, the VLTI Commissioning Instrument. In particular, we detailed the photometric calibration of the interferometric signals, followed by the normalization of the fringes, and the subtraction of the two calibrated interferograms. Due to the efficient spatial filtering provided by the single-mode optical fibers, this procedure provides a clean calibration of the fringes, and allows us to derive the squared coherence factor μ^2 with high accuracy. Combined with observations from a calibrator star, it yields the squared visibility V^2. This value can be interpreted physically through the use of a dedicated model of the observed object. Applying the data reduction methods described in this paper to sample data from α Cen A yields a realistic value of its uniform disk angular diameter. Our procedures can easily be adapted to other single mode interferometric instruments. In particular, they can be generalized to spectrally dispersed fringes and to a multiple beam recombiner using the integrated optics technology (Kern et al. 2003). Such a device could allow the simultaneous recombination of the beams from the four 8 m Unit Telescopes and four Auxiliary Telescope of the VLTI in a compact instrument.

Acknowledgements. D.S. acknowledges the support of the Swiss FNRS. We wish to thank Dr. Guy Perrin for important comments that led to improvements of this paper. The interferometric data presented in this paper have been obtained using the Very Large Telescope Interferometer, operated by the European Southern Observatory at Cerro Paranal, Chile. It has been retrieved from the ESO/ST-ECF Archive Facility (Garching, Germany). Observations with the VLTI are only made possible through the efforts of the VLTI team, to whom we are grateful.

References

Babu, G. J., & Feigelson, E. D. 1996, Astrostatistics (London: Chapman & Hall)
Berger, J.-P., Haguenauer, P., Kern, P., et al. 2001, A&A, 376, 31
Bordé, P., Coudé du Foresto, V., Chagnon, G., & Perrin, G. 2002, A&A, 393, 183
Browne, J. M. 2002, Probabilistic Design Course Notes, available at `http://www.ses.swin.edu.au/homes/browne`
Cayrel de Strobel, G., Soubiran, C., & Ralite, N. 2001, A&A, 373, 159
Cohen, M., Walker, R. G., Carter, B., et al. 1999, AJ, 117, 1864
Colavita, M. M. 1999, PASP, 111, 111
Coudé du Foresto, V., Ridgway, S., & Mariotti, J.-M. 1997, A&AS, 121, 379
Coudé du Foresto, V., Perrin, G., Ruilier, C., et al. 1998, Proc. SPIE, 3350, 856
Daubechies, I. 1992, Ten lectures on wavelets, Proc. CBMS-NSF Conf., June 1990, in Philadelphia: Society for Industrial and Applied Mathematics
Davis, J., Tango, W. J., & Booth, A. J. 2000, MNRAS, 318, 387
Derie, F. 2000, Proc. SPIE, 4006, 25
Di Folco, E., Koehler, B., Kervella, P., et al. 2002, Proc. SPIE, 4838, 1115
Efron, B. 1979, Ann. Statist., 7, 1
Efron, B., & Tibshirani, R. J. 1993, An Introduction to the Bootstrap. Monographs on Statistics and Applied Probability, 57 (New York: Chapman & Hall)
Farge, M. 1992, Annual Review of Fluid Mechanics, 24, 395
Gai, M., Bonino, D., Corcione, L., Delage, L., et al. 2003, MmSAI, 74, 130
Glindemann, A., Abuter, R., Carbognani, F., et al. 2000, Proc. SPIE, 4006, 2
Glindemann, A., Argomedo, J., Amestica, R., et al. 2003a, Proc. SPIE, 4838, 89
Glindemann, A., Argomedo, J., Amestica, R., et al. 2003b, Ap&SS, 286, 1
Goupillaud, P., Grossmann, A., & Morlet, J. 1984, Geoexploration, 23, 85
Kern, P., Malbet, F., Berger, J.-P., et al. 2003, Proc. SPIE, 4838, 312
Kervella, P., Coudé du Foresto, V., Glindemann, A., & Hofmann, R. 2000, Proc. SPIE, 4006, 31
Kervella, P., Gitton, Ph., Ségransan, D., et al. 2003a, Proc. SPIE, 4838, 858
Kervella, P., Thévenin, F., Ségransan, D., et al. 2003b, A&A, 404, 1087
Leinert, C., Graser, U., Waters, L. B. F. M., et al. 2000, Proc. SPIE, 4006, 43
Linfield, R. P., Colavita, M. M., & Lane, B. F. 2001, ApJ, 554, 505
Mallat, S. 1999, A Wavelet Tour of Signal Processing (Academic Press)
Meyer, M., Finger, G., Mehrgan, H., et al. 1998, Proc. SPIE, 3354, 134
Morel, P., Provost, J., Lebreton, Y., et al. 2000, A&A, 363, 675
Perrier, V., Philipovitch, T., & Basdevant, C. 1995, J. Math. Phys., 36, 1506
Perrin, G. 2003, A&A, 398, 385
Petrov, R., Malbet, F., Richichi, A., et al. 2000, Proc. SPIE, 4006, 68
Schöller, M., Gitton, Ph., Argomedo, J., et al. 2003, Proc. SPIE, 4838, 870
Wittkowski, M., Aufdenberg, J., & Kervella, P. 2004, A&A, 413, 711

Appendix A: The wavelet transform

The wavelet transform belongs to the class of time-frequency transforms which are powerful tools to study non-stationary processes such as turbulent flows in fluid mechanics. Wide band coaxial interferograms recorded through a turbulent atmosphere can be strongly distorted due to the differential piston effect and fast photometric fluctuations. In this context, the wavelet transform is an efficient tool to study and analyse the interferograms recorded from the ground.

The continuous wavelet transform (hereafter CWT) is defined by:

$$W(s,\tau) = \frac{1}{\sqrt{s}} \int_{-\infty}^{+\infty} f(t)\, \psi^* \left(\frac{t-\tau}{s} \right) \mathrm{d}t \tag{A.1}$$

where $f(t)$ is the signal defined as a function of time, $\psi(t)$ the chosen wavelet function, ψ^* its complex conjugate, s the scale, and τ the translation.

For the present application of the CWT to interferometry, we have chosen to use the Morlet wavelet, that is defined as a Gaussian envelope multiplied by a plane wave (Goupillaud et al. 1984; Farge 1992):

$$\psi(\eta) = \exp(i 2\pi \nu_0 \eta)\ \exp(-\eta^2/2) \tag{A.2}$$

where η is the non dimensional time parameter and ν_0 is the non dimensional frequency. Initially used for the analysis of seismic signals, the Morlet wavelet is a good approximation of the fringe pattern produced by VINCI. The data processing methods presented here make extensive use of this particular wavelet for the recognition and localization of the fringes (Sect. 4.2) and subsequently for the integration of the modulated power of the interference fringes (Sect. 7). Figure A.1 shows the shape of the imaginary part of the Morlet wavelet assuming typical parameters for the processing of data from the MONA beam combiner (K band).

If we now express the CWT in the Fourier domain (Eq. (A.3)), it appears clearly that the CWT is a filtered version of the signal for different sets of filters:

$$W(s,\tau) = \sqrt{s} \int_{-\infty}^{+\infty} \widehat{f}(\nu)\, \widehat{\psi}^*(s\nu)\, \mathrm{e}^{i\,2\pi\nu\tau}\, \mathrm{d}\nu. \tag{A.3}$$

Since the CWT is simply a convolution between the signal $f(t)$ and expanded/contracted versions of the wavelet function (Eq. (A.1)), the Morlet wavelet is very efficient to analyse wide-band coxial interferograms. The CWT of an interferogram using the Morlet wavelet is a complex quantity and its maximum energy is found for the wavelet that is most similar to the recorded interferogram.

The CWT using the Morlet wavelet is not orthogonal but since it relies on a set of filtered versions of the signal with strong redundancy, the original signal can easily be reconstructed (Farge 1992; Perrier 1995). The energy properties of Wavelets are similar to the ones of the Fourier analysis, with the equivalent of the Parseval theorem (Perrier 1995). We have therefore the equivalence of the two following expressions of the energy E of the signal:

$$E = \frac{1}{2\,C_\psi} \int_0^{+\infty} \int_{-\infty}^{+\infty} |W(s,\tau)|^2\, \frac{\mathrm{d}s}{s^2}\, \mathrm{d}\tau \tag{A.4}$$

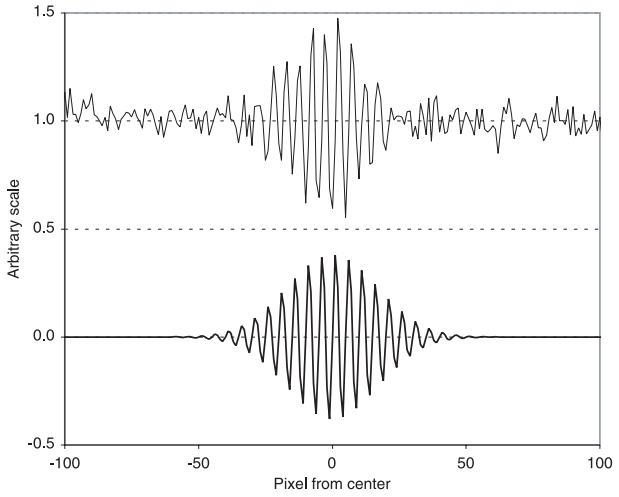

Fig. A.1. VINCI interferometric fringes (upper curve, from a processed interferogram of θ Cen) and the Morlet wavelet function imaginary part (bottom curve).

$$E = \int_{-\infty}^{+\infty} \left| \widehat{f}(\nu) \right|^2 \mathrm{d}\nu \tag{A.5}$$

with the coefficient C_ψ defined as:

$$C_\psi = \int_{-\infty}^{+\infty} \frac{|\psi(s\,\nu)|^2}{\nu}\, \mathrm{d}\nu. \tag{A.6}$$

As a consequence, we are able to recover the modulated energy of the original signal (the interferometric fringes) by integrating its wavelet power spectrum over the time and frequency regions where the interferogram is present.

Compared to the classical Fourier analysis, such an approach allows to minimize the biases due to both the white and colored (frequency dependent) noises. Thanks to its localization both in time and frequency, the Morlet wavelet is better suited to the study of interferometric fringe packets than the classical Fourier base functions (sine and cosine), as the noise present outside of the fringe packet in the scan is excluded from the integrated power. The interested reader will find a more detailed treatment of the wavelet transform in Daubechies (1992), Farge (1992), Perrier (1995) and Mallat (1999).

Appendix B: Computation of weighted bootstrapped error bars

Originally developed by Efron (1979), the bootstrap analysis, also called sampling with replacement, consists of constructing a hypothetical, large population derived from the original measurements and estimate the statistical properties from this population. This technique allows us to recover the original distribution characteristics without any assumption on the properties of the underlying population (e.g. Gaussianity). An introduction to bootstrap analysis can be found in Efron (1993) and Babu (1996).

Our implementation of the bootstrapping technique draws, with repetition, a large number M of samples containing N elements from the original set of measurements (μ_i^2, w_i), also N elements in length. μ_i^2 designates the squared coherence factor

associated with the scan of rank i in the series, and w_i is its associated weight. The result of this drawing is an $N \times M$ matrix of $(\mu^2_{k,j}, w_{k,j})$ pairs ($1 \leq k \leq N$; $1 \leq j \leq M$). The fact that the same element of the original data set can be repeated several times in the drawing is essential, as it allows us to create independent samples. Typically, several thousand samples are obtained from the original data, which contains a few hundred μ^2 values. The weighted average values μ^2_k are computed for each of the N drawings:

$$\mu^2_j = \frac{1}{\left(\sum_{k=1}^{N} w_{k,j}\right)} \sum_{k=1}^{N} w_{k,j}\mu^2_{k,j}. \tag{B.1}$$

The resulting ensemble $[\mu^2_j]$ (M elements) is sorted in ascending order, and reindexed with the percentiles of the rank of each value in the set:

$$\mu^2_{0/M}, ..., \mu^2_{j/M}, ..., \mu^2_{M/M}. \tag{B.2}$$

The 16% lower and upper values are discarded, and the new extremes values of this vector give the limits of the 68% confidence interval:

$$\mu^2_{\rm min} = \mu^2_{0.16}\ ; \quad \mu^2_{\rm max} = \mu^2_{0.84}. \tag{B.3}$$

This is the probabilistic definition of $1\,\sigma$ error bars, and we therefore obtain the σ_+ and σ_- asymmetric error bars through:

$$\sigma_+ = \mu^2_{\rm max} - \overline{\mu^2}\ ; \quad \sigma_- = \overline{\mu^2} - \mu^2_{\rm min} \tag{B.4}$$

where $\overline{\mu^2}$ is the weighted average of the original sample $[\mu^2_i]$ using the weights $[w_i]$. The same process can be applied using 2.5–97.5% percentile limits to obtain the error bars equivalent to $2\,\sigma$, and 0.5–99.5% for $3\,\sigma$.

Alternatively, one can derive the bootstrapped variance $\sigma^2_{\rm BS}$ directly from the μ^2_k ensemble:

$$\sigma^2_{\rm BS} = \frac{1}{M} \sum_{j=1}^{M} \left(\mu^2_j - \overline{\mu^2}\right)^2. \tag{B.5}$$

The internal bias $b_{\rm BS}$ of the population is given by:

$$b_{\rm BS} = \overline{\mu^2_j} - \overline{\mu^2}. \tag{B.6}$$

This bias is naturally taken into account in the computation of the confidence interval limits as described above.

Appendix C: Statistical and systematic errors of the ratio of μ^2 and T^2

In the expression of T^2 of Eq. (16), we have to separate the contributions from the systematic uncertainty on the calibrator knowledge, and the statistical error of the instrumental measurement of μ^2. While these two terms contribute to the global uncertainty on the squared visibility V^2, their nature is fundamentally different. While it is possible to reduce the statistical error by averaging several measurements, the systematic uncertainty originating in the calibrator diameter error bar will not be changed. This last term is therefore a fundamental limitation to the absolute precision of the visibility measurement. This limit can be reduced by using several calibrators, or by selecting very small stars as calibrators. We then benefit from the fact that the visibility function $V^2(B, \theta)$ for a stellar disk is nearly flat when the star is not significantly resolved, and the resulting systematic error on V^2 remains small.

Considering a symmetric error bar on the assumed angular diameter of the calibrator, the resulting error bar on the V^2 estimate is in general not exactly symmetric, due to the non linearity of the visibility function. In practice, asymmetric error bars are easily manageable numerically. However, in order to simplify the notations in the present discussion, we make the assumption that this asymmetry is negligible.

The estimation of the two kinds of error contributions relies on an approximation of the Cauchy statistical law characteristics. When dividing two normal statistical variables x and y of respective means and standard deviations $(\overline{x}, \sigma^2_x)$ and $(\overline{y}, \sigma^2_y)$, the resulting ratio x/y follows a Cauchy statistics that has, strictly speaking, no defined mean value. It is therefore necessary to make an approximation for the case when $\sigma_y \ll \overline{y}$. In this case, a second order approximation of the mean $\overline{z}$ and variance σ^2_z of $z = x/y$ is given by Browne (2002):

$$\overline{z} = \frac{\overline{x}}{\overline{y}}\left(1 + \frac{\sigma^2_y}{\overline{y}^2}\right) \tag{C.1}$$

$$\sigma^2_z = \frac{\overline{x}^2}{\overline{y}^2}\left(\frac{\sigma^2_x}{\overline{x}^2} + \frac{\sigma^2_y}{\overline{y}^2} - \frac{\sigma^4_y}{\overline{y}^4}\right). \tag{C.2}$$

It is not possible to obtain a meaningful average value of the ratio x/y if the standard deviation σ_y of the denominator y is not small compared to its average value. As a remark, the average value of x/y is in general different from $\overline{x}/\overline{y}$.

The average value of the transfer function T^2 and its associated statistical error bars are computed by replacing in formulas (C.1) and (C.2) the values of $(\overline{x}, \sigma^2_x)$ and $(\overline{y}, \sigma^2_y)$ by the following terms:

$$\overline{x} \rightarrow \left[\mu^2\right]_{\theta\,\rm Cen} \qquad \sigma^2_x \rightarrow \left[\sigma_{\rm stat}\right]^2_{\theta\,\rm Cen} \tag{C.3}$$

$$\overline{y} \rightarrow \left[V^2_{\rm theo}\right]^2_{\theta\,\rm Cen} \qquad \sigma^2_y \rightarrow 0. \tag{C.4}$$

Similarly, the systematic error is computed using the replacements:

$$\overline{x} \rightarrow \left[\mu^2\right]_{\theta\,\rm Cen} \qquad \sigma^2_x \rightarrow 0 \tag{C.5}$$

$$\overline{y} \rightarrow \left[V^2_{\rm theo}\right]^2_{\theta\,\rm Cen} \qquad \sigma^2_y \rightarrow \left[\sigma_{\rm theo}\right]^2_{\theta\,\rm Cen}. \tag{C.6}$$

Applying this computation to the numerical values found for $\theta\,$Cen, we find:

$$T^2 = 0.5009\ [\pm 0.0027]_{\rm stat}\ [\pm 0.0077]_{\rm syst}. \tag{C.7}$$

The uncertainty on this value is dominated by the systematic error. The only remaining calibration step is now to divide the μ^2 value obtained on $\alpha\,$Cen A by the T^2 value. Again, we have to separate the two contributions on the error by replacing

in the above formulas the mean values and standard deviations of x and y by the following terms for the statistical error:

$$\overline{x} \rightarrow \left[\mu^2\right]_{\alpha\,\mathrm{Cen}} \qquad \sigma_x^2 \rightarrow [\sigma_{\mathrm{stat}}]^2_{\alpha\,\mathrm{Cen}} \tag{C.8}$$

$$\overline{y} \rightarrow T^2 \qquad \sigma_y^2 \rightarrow [\sigma_{\mathrm{stat}}]^2_{T^2} \tag{C.9}$$

while the systematic error is computed using

$$\overline{x} \rightarrow \left[\mu^2\right]_{\alpha\,\mathrm{Cen}} \qquad \sigma_x^2 \rightarrow 0 \tag{C.10}$$

$$\overline{y} \rightarrow T^2 \qquad \sigma_y^2 \rightarrow \left[\sigma_{\mathrm{syst}}\right]^2_{T^2}\,. \tag{C.11}$$

We obtain the calibrated squared visibility of α Cen A:

$$V^2_{\alpha\,\mathrm{Cen}} = 0.00635\ [\pm 0.00033]_{\mathrm{stat}}\ [\pm 0.00010]_{\mathrm{syst}}. \tag{C.12}$$

1.7 Résultats astrophysiques avec VINCI

Je décris dans ce mémoire l'application de l'interférométrie optique à l'étude de trois types d'étoiles : les Céphéides (Chapitre 2), les étoiles de la séquence principale (Chapitre 3), et les étoiles en rotation rapide (Chapitre 4). Je montre qu'une utilisation judicieuse de mesures interférométriques, spectrographiques et photométriques permet de cerner précisément les propriétés physiques de ces objets. Les informations apportées par l'interférométrie sont précieuses, car inaccessibles aux autres techniques, mais elles sont également parcellaires. Contrairement à la pupille connexe d'un télescope classique, un interféromètre ne peut échantillonner qu'un domaine restreint de fréquences spatiales. Grâce à la mise en oeuvre conjointe de plusieurs méthodes d'observation sur un même objet, il est possible d'obtenir des contraintes physiques beaucoup plus fortes que celles apportées par chaque technique considérée séparément. C'est cette utilisation de l'interférométrie en synergie avec différents moyens d'observation qui constitue l'originalité principale de mon travail.

1.7.1 Céphéides

Il est possible de mesurer la distance des Céphéides les plus brillantes avec une excellente précision, d'une manière quasi-géométrique, en combinant des mesures interférométriques et spectrographiques. De telles mesures de distance sont particulièrement importantes pour cette classe d'étoiles variables, car très peu de Céphéides sont suffisamment proches pour qu'une mesure précise de parallaxe trigonométrique soit possible. Les distances ainsi déterminées permettent d'étalonner la célèbre relation Période-Luminosité (P–L). Cette relation est régulièrement utilisée pour estimer la distance de galaxies lointaines (jusqu'à 100 Mpc), et joue un rôle important dans l'échelle des distances cosmologiques. L'incertitude actuelle sur l'étalonnage du point zéro de la relation P–L est de l'ordre de 10%. Notre programme de mesure de distances par interférométrie nous permettra à terme d'améliorer considérablement cette précision, notre objectif étant d'arriver à mieux que 1%. Au total, ce sont près de 40 étoiles Céphéides que nous prévoyons d'observer à l'aide des interféromètres VLTI (notamment avec l'instrument AMBER) et CHARA (instrument FLUOR). Je présente au Chapitre 2 l'état d'avancement actuel de ce grand programme.

Au cours de nos premières observations avec les instruments VINCI et MIDI du VLTI d'une part, et FLUOR sur CHARA d'autre part, nous avons mis en évidence pour la premire fois l'existence d'enveloppes circumstellaires à l'échelle de quelques rayons stellaires autour des Céphéides δ Cep, Polaris et ℓ Car. Pour l'instant limitées à ces trois étoiles, les enveloppes de Céphéides pourraient en réalité être très répandues. Dans le but de caractériser ces enveloppes, j'ai initié en 2006 avec Antoine Mérand une recherche de la signature de la perte de masse des Céphéides dans la raie à 21 cm de l'hydrogène neutre, à l'aide du grand radiotélescope de Nançay.

1.7.2 Etoiles naines

L'intérêt principal de l'interférométrie pour la physique stellaire est de permettre la mesure directe de deux observables fondamentales : le diamètre angulaire et la répartition de lumière de l'étoile (assombrissement centre-bord, enveloppes circumstellaires, binarité,...). Lorsque ces informations sont combinées avec la parallaxe, il devient possible de contraindre à la fois la structure interne de l'étoile (grâce à son diamètre photosphérique) et sa structure atmosphérique (par l'analyse de l'assombrissement centre-bord). Au delà de ces deux observables, dans le cas de l'observation d'étoiles binaires, l'interférométrie utilisée en combinaison avec la spectroscopie permet

de déterminer l'orbite et d'estimer la distance, la masse, le rayon et le rapport de luminosité des étoiles.

Pour les étoiles naines, la mesure interférométrique du rayon permet de contraindre de manière décisive les modèles numériques, et ainsi de sonder l'intérieur de ces étoiles. Là encore, l'interférométrie n'est pleinement utile que combinée à d'autres techniques d'observations, en particulier les mesures astérosismiques réalisées par spectrographie. J'ai réalisé dès 2003 la première utilisation conjointe de ces deux techniques, appliquée à l'étude de α Cen A et B (article présenté au Chapitre 3). Ce travail a en particulier permis de confirmer les masses déterminées par Thévenin et al. (2002) et de contraindre leur état évolutif (âge, structure interne,...). A titre de remarque, notre confirmation d'une masse de seulement $0.907\,M_{\odot}$ pour α Cen B, plus faible d'environ 30 masses de Jupiter par rapport à la masse astrométrique de Pourbaix et al. (2002) nous a conduit à rechercher par imagerie classique et optique adaptative la présence d'un compagnon substellaire orbitant autour de cette étoile. J'ai présenté le résultat de cette recherche dans un article soumis à A&A (non reproduit dans ce mémoire).

Au delà des étoiles de type solaire, j'ai également contribué à l'étude des naines de très faible masse, avec notamment la première mesure directe de la taille de *Proxima*, qui ne dépasse pas 1,5 fois celle de Jupiter. Nos observations ont également permis l'étalonnage des relations de brillance de surface des étoiles naines, très utiles pour estimer précisément la taille angulaire des étoiles hors de portée de mesures interférométriques directes.

1.7.3 Rotateurs rapides

Les étoiles en rotation rapide présentent des spectres très particuliers, avec un élargissement considérables des raies par effet Doppler. L'effet de la vitesse de rotation, parfois extrêmement rapide, peut aussi être observé directement sur la déformation de la photosphère. Ceci nécessite bien sûr de résoudre spatialement la surface des étoiles, et est donc une application idéale pour l'interférométrie optique à longue base. Dès 2002, alors que les d'observations interférométriques de rotateurs rapides étaient encore rares, j'ai réalisé une série de mesures avec VINCI de l'étoile Achernar (α Eri). Présentant parfois la raie Hα de l'hydrogène en émission, cette étoile de type spectral B3Vpe est connue pour être en rotation très rapide. Nous avons mis en évidence un aplatissement considérable de l'étoile, grâce à l'obtention de son "profil interférométrique". Je présente ces résultats à la Sect. 4.3.

Nous avons également observé deux autres étoiles en rotation rapide : Altaïr et Véga. Pour cette dernière étoile, l'orientation très particulière de l'axe polaire, presque aligné avec la ligne de visée, donne une signature spectrale minime de la rotation, alors que l'étoile tourne pourtant à une vitesse proche de sa limite de dislocation. L'assombrissement centre-bord anormal que nous avons mesuré nous a permis d'estimer à la fois la vitesse de rotation, l'aplatissement réel et la distribution spectrale d'énergie équatoriale et polaire de Véga.

Tout dernièrement, des observations plus poussées avec VINCI ont montré que l'étoile Achernar possède une enveloppe circumstellaire allongée selon son axe polaire. Cette détection confirme la présence de deux phénomènes distincts dans l'environnement proche des étoiles Be : un disque équatorial (épisodes Be) et une enveloppe polaire entretenue par le vent stellaire rapide provenant des pôles surchauffés de l'étoile (effet Von Zeipel).

Chapitre 2

Les Céphéides

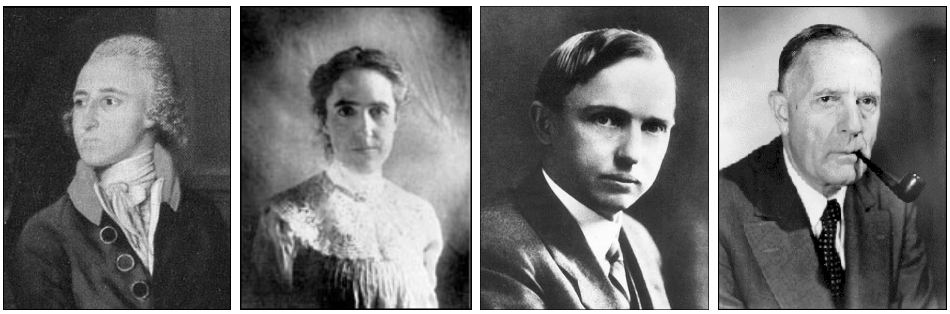

FIG. 2.1 – Portraits de personnalités importantes de l'étude des Céphéides : de gauche à droite John Goodricke (1764-1786), Henrietta Swan Leavitt (1868-1921, photo AAVSO), Harlow Shapley (1885-1972) et Edwin Hubble (1889-1953).

Quelques acteurs importants de l'étude des Céphéides :

- **John Goodricke** (1764-1786) découvre la variabilité photométrique de δ Cephei (en 1784), mais aussi d'Algol et de nombreuses autres étoiles. Il propose d'expliquer la variabilité d'Algol par la présences éclipses mutuelles. Sourt-muet depuis son enfance, membre de la Royal Society, il disparaît à l'âge de 22 ans des suites d'une pneumonie.
- **Henrietta Leavitt** (1868-1921) découvre en 1912 la relation Période-Luminosité des Céphéides (Fig. 2.2), ainsi que plus de 2400 étoiles variables, soit la moitié de toutes celles connues à l'époque.
- **Harlow Shapley** (1885-1972) explique en 1916 la variation des Céphéides par leur pulsation, et étalonne le point zéro de la relation P–L.
- **Edwin Hubble** (1889-1953) mesure en 1926 les distances des galaxies NGC 6822, puis Messier 31 et 33, grâce à l'observations de la variation photométrique de Céphéides de ces galaxies. En 1929, il établit la loi d'expansion de l'Univers qui porte son nom.
- **Arthur Eddington** (1882-1944) décrit en 1941 le mécanisme physique de la pulsation des Céphéides (le κ-mécanisme).
- **Walter Baade** (1893-1960) sépare en 1956 les Céphéides en deux groupes distincts (W Vir, δ Cep), possédant chacun leur propre relation P–L.
- **Allan Sandage** (1926-) introduit la relation Période-Luminosité-Couleur des Céphéides en 1958, et présente, avec G. Tammann, une valeur de H_0 relativement basse d'environ 50 km/s/Mpc.
- **Wendy Freedman** (1957-) conclut en 2001 le *Hubble Key Project* de mesure de H_0, qui

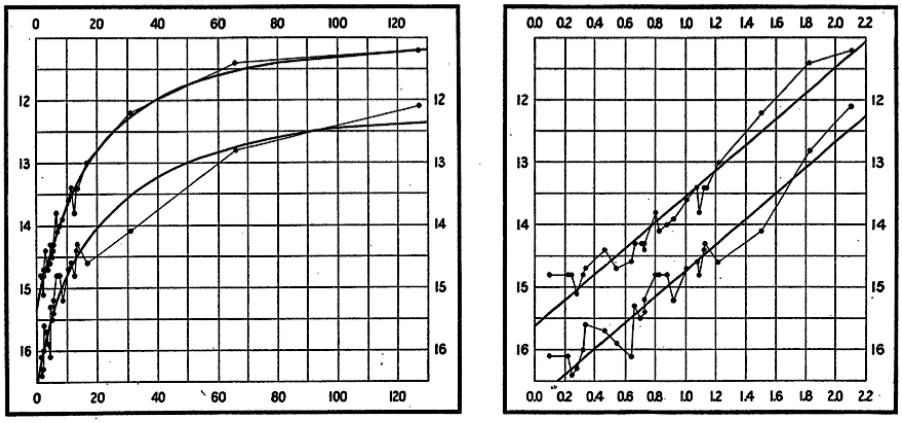

FIG. 2.2 – Découverte de la relation Période–Luminosité des Céphéides par Henrietta Swan Leavitt (figure tirée de Leavitt & Pickering 1912), sur la base de 25 variables observées dans le Petit Nuage de Magellan. La période est en échelle linéaire à gauche et en échelle logarithmique à droite.

s'appuie largement sur les Céphéides jusqu'à des distances supérieures à 100 Mpc.

Cette célèbre classe d'étoiles variables est utilisées depuis près d'un siècle comme "chandelle standard" pour mesurer les distances extragalactiques jusqu'à environ 20 Mpc (Freedman et al. 2001). La propriété particulière de ces étoiles est d'avoir une luminosité intrinsèque directement proportionnelle à leur période (en grandeurs logarithmiques). La relation Période–Luminosité (P–L ci-après) prend classiquement la forme suivante

$$M_\lambda = a_\lambda(\log P - 1) + b_\lambda \tag{2.1}$$

avec M_λ la magnitude absolue de l'étoile, P sa période de pulsation, a_λ la pente de la relation et b_λ son ordonnée à l'origine (on parle aussi de "point zéro"), définies pour une longueur d'onde particulière λ.

L'étalonnage des relation P–L est purement empirique, basé sur l'observation. Le principe de la détermination de la pente a_λ est simple : en observant un ensemble de Céphéides situées à la même distance de l'observateur (par exemple dans les nuages de Magellan), et on l'obtient directement par un ajustement linaire des magnitudes apparentes moyennes mesurées dans la bande photométrique choisie. L'ordonnée à l'origine b_λ est par contre beaucoup plus difficile à déterminer. Physiquement, b_λ correspond à la magnitude absolue d'une Céphéide possédant une période de variation de 10 jours (avec la définition de l'Eq. 2.1). La mesure de b_λ réclame de connaître la magnitude absolue d'un nombre suffisant de Céphéides, c'est-à-dire d'avoir leurs distances, par une méthode indépendante de la relation P–L. Plusieurs méthodes peuvent être employées pour estimer la distance d'une Céphéide, et ainsi étalonner b_λ :

- **Parallaxe trigonométrique** (Hipparcos, HST) : cette méthode purement géométrique est naturellement la plus directe. Cependant, les Céphéides sont des étoiles rares dans la Galaxie, et ces mesures sont trés difficiles du fait de leur grande distance, même pour les plus proches.
- **Céphéides dans les amas ouverts** : dans une association de Céphéides avec des étoiles naines, il est possible d'obtenir la magnitude absolue par ajustement de la position verticale de la séquence principale dans le diagramme Hertzsprung-Russell. Cette méthode relativement imprécise et affectée d'une erreur systématique de l'ordre de 0,2 mag.


FIG. 2.3 – Walter Baade (1893-1960) et Adriaan Wesselink (1909-1995) (photos Mt Wilson Observatory et Smits, respectivement).

– **Méthode Baade-Wesselink** : c'est la méthode la plus généralement employée. Son principe est développé à la section suivante.

2.1 La méthode Baade-Wesselink

Inventée indépendamment par Baade (1926) et Wesselink (1946), la méthode portant aujourd'hui leurs deux noms permet de calculer, à partir d'observations spectroscopiques et photométriques, le rayon d'une étoile pulsante.

D'une part, le flux et les variations de température donnent le rapport du rayon instantané de l'étoile $R(t)$ à son rayon initial $R(0)$ selon la formule suivante, où la température effective est supposée constante pour simplifier :

$$\frac{R(t)}{R(0)} = \frac{L(t)}{L(0)} = 10^{-0,4[m(t)-m(0)]} \tag{2.2}$$

Avec $L(t)$ la luminosité de l'étoile à l'instant t et $L(0)$ sa luminosité initiale.

D'autre part l'intégration de la courbe de vitesse pulsationnelle $v_p(t)$ donne l'amplitude linéaire de la pulsation au cours du temps $R(t)$:

$$R(t) - R(0) = -\int_0^t v_p(t).dt \tag{2.3}$$

Le signe négatif provient de la convention de définition de la vitesse pulsationnelle (et de la vitesse radiale) : elle est positive pour un éloignement de la source (donc une contraction de l'étoile pour une Céphéide). Le rayon initial $R(0)$ est déduit immédiatement en résolvant le système constitué par les équations 2.2 et 2.3.

Pour obtenir la distance de l'étoile, il reste à estimer son diamètre angulaire. Il peut être obtenu essentiellement de deux manières :

– **La brillance de surface** : Il s'agit de la méthode classique. On utilise la couleur de l'étoile et sa magnitude apparente pour en déduire son diamètre angulaire. Ces trois grandeurs sont en effet liées par le fait que l'étoile rayonne pratiquement comme un corps noir. J'ai réalisé un étalonnage des relations de brillance de surface pour les Céphéides, qui est présenté à la Sect. 2.1.3.

– **La mesure directe par interférométrie** : depuis la mise en service des grands interféromètres optiques et infrarouges, il est maintenant possible de mesurer directement le diamètre angulaire des Céphéides proches. Ceci permet une application plus simple et directe de la méthode Baade-Wesselink (BW), qui me passe pas par une estimation de la température effective de l'étoile. Je présente une application pratique de cette méthode utilisant des données de l'instrument VINCI à la Sect. 2.1.1.

D'une manière générale, l'approche cohérente et exhaustive des différents aspects de la méthode BW que j'ai organisée a pour but final de réaliser un étalonnage interférométrique du point zéro de la relation P–L avec une précision de 1%. L'obtention de ce résultat passe par une connaissance approfondie de l'atmosphère des Céphéides.

2.1.1 Article A&A : "Cepheid distances from infrared long-baseline interferometry – I. VINCI/VLTI observations of seven Galactic Cepheids" (2004)

Ce premier article de notre série rapporte les mesures interférométriques de sept Céphéides australes obtenues à l'aide de l'instrument VINCI du VLTI. En utilisant la méthode Baade-Wesselink interférométrique, nous avons pu déduire la distance et le rayon de quatre de ces étoiles, pour lesquelles la variation de diamètre angulaire est clairement détectée. Pour les trois autres étoiles de notre échantillon, nous avons obtenu un rayon moyen, et déduit leur distance à partir d'une relation période-rayon pré-existante.

FIG. 2.4 – Les télescopes UT2 (Kueyen) et UT3 (Melipal) du VLT (Cerro Paranal, Chili).

A&A 416, 941–953 (2004)
DOI: 10.1051/0004-6361:20031743

Astronomy & Astrophysics

Cepheid distances from infrared long-baseline interferometry

I. VINCI/VLTI observations of seven Galactic Cepheids⋆

P. Kervella[1], N. Nardetto[2], D. Bersier[3], D. Mourard[2], and V. Coudé du Foresto[4]

[1] European Southern Observatory, Alonso de Cordova 3107, Casilla 19001, Vitacura, Santiago 19, Chile
[2] Département Fresnel, UMR CNRS 6528, Observatoire de la Côte d'Azur, BP 4229, 06304 Nice Cedex 4, France
[3] Harvard-Smithsonian Center for Astrophysics, 60 Garden St., Cambridge, MA 02138, USA
[4] LESIA, Observatoire de Paris-Meudon, 5 place Jules Janssen, 92195 Meudon Cedex, France

Received 19 June 2003 / Accepted 26 November 2003

Abstract. We report the angular diameter measurements of seven classical Cepheids, X Sgr, η Aql, W Sgr, ζ Gem, β Dor, Y Oph and ℓ Car that we have obtained with the VINCI instrument, installed at ESO's VLT Interferometer (VLTI). We also present reprocessed archive data obtained with the FLUOR/IOTA instrument on ζ Gem, in order to improve the phase coverage of our observations. We obtain average limb darkened angular diameter values of $\overline{\theta_{\rm LD}}$[X Sgr] = 1.471 ± 0.033 mas, $\overline{\theta_{\rm LD}}[\eta\,{\rm Aql}]$ = 1.839 ± 0.028 mas, $\overline{\theta_{\rm LD}}$[W Sgr] = 1.312 ± 0.029 mas, $\overline{\theta_{\rm LD}}[\beta\,{\rm Dor}]$ = 1.891 ± 0.024 mas, $\overline{\theta_{\rm LD}}[\zeta\,{\rm Gem}]$ = 1.747 ± 0.061 mas, $\overline{\theta_{\rm LD}}$[Y Oph] = 1.437 ± 0.040 mas, and $\overline{\theta_{\rm LD}}[\ell\,{\rm Car}]$ = 2.988 ± 0.012 mas. For four of these stars, η Aql, W Sgr, β Dor, and ℓ Car, we detect the pulsational variation of their angular diameter. This enables us to compute directly their distances, using a modified version of the Baade-Wesselink method: $d[\eta\,{\rm Aql}] = 276^{+55}_{-38}$ pc, d[W Sgr] = 379^{+216}_{-130} pc, $d[\beta{\rm Dor}] = 345^{+175}_{-80}$ pc, $d[\ell\,{\rm Car}] = 603^{+24}_{-19}$ pc. The stated error bars are statistical in nature. Applying a hybrid method, that makes use of the Gieren et al. (1998) Period-Radius relation to estimate the linear diameters, we obtain the following distances (statistical and systematic error bars are mentioned): d[X Sgr] = 324 ± 7 ± 17 pc, $d[\eta\,{\rm Aql}]$ = 264 ± 4 ± 14 pc, d[W Sgr] = 386 ± 9 ± 21 pc, $d[\beta{\rm Dor}]$ = 326 ± 4 ± 19 pc, $d[\zeta\,{\rm Gem}]$ = 360 ± 13 ± 22 pc, d[Y Oph] = 648 ± 17 ± 47 pc, $d[\ell\,{\rm Car}]$ = 542 ± 2 ± 49 pc.

Key words. techniques: interferometric – stars: variables: Cepheids – stars: oscillations

1. Introduction

For almost a century, Cepheids have occupied a central role in distance determinations. This is thanks to the existence of the Period–Luminosity (P–L) relation, $M = a \log P + b$, which relates the logarithm of the variability period of a Cepheid to its absolute mean magnitude. These stars became even more important since the *Hubble Space Telescope* Key Project on the extragalactic distance scale (Freedman et al. 2001) has totally relied on Cepheids for the calibration of distance indicators to reach cosmologically significant distances. In other words, if the calibration of the Cepheid P–L relation is wrong, the whole extragalactic distance scale is wrong.

There are various ways to calibrate the P–L relation. The avenue chosen by the *HST* Key-Project was to *assume* a distance to the Large Magellanic Cloud (LMC), thereby adopting a zero point of the distance scale. Freedman et al. (2001) present an extensive discussion of all available LMC distances, and note, with other authors (see e.g. Benedict et al. 2002), that the LMC distance is currently the weak link in the extragalactic distance scale ladder. Another avenue is to determine the zero point of the P–L relation with Galactic Cepheids, using for instance parallax measurements, Cepheids in clusters, or through the Baade-Wesselink (BW) method. We propose in this paper and its sequels (Papers II and III) to improve the calibration of the Cepheid P–R, P–L and surface brightness–color relations through a combination of spectroscopic and interferometric observations of bright Galactic Cepheids.

In the particular case of the P–L relation, the slope a is well known from Magellanic Cloud Cepheids (e.g. Udalski et al. 1999), though Lanoix et al. (1999) have suggested that a Malmquist effect (population incompleteness) could bias this value. On the other hand, the calibration of the zero-point b (the hypothetic absolute magnitude of a 1-day period Cepheid) requires measurement of the distance to a number of nearby Cepheids with high precision. For this purpose, interferometry enables a new version of the Baade-Wesselink method (BW, Baade 1926; Wesselink 1946) for which we do not need to measure the star's temperature, as we have directly access to its angular diameter (Davis 1979; Sasselov & Karovska 1994). Using this method, we derive directly the distances to the four

Send offprint requests to: P. Kervella, e-mail: pkervell@eso.org
⋆ Tables 3 to 10 are only available in electronic form at http://www.edpsciences.org

nearby Cepheids η Aql, W Sgr, β Dor and ℓ Car. For the remaining three objects of our sample, X Sgr, ζ Gem and Y Oph, we apply a hybrid method to derive their distances, based on published values of their linear diameters.

After a short description of the VINCI/VLTI instrument (Sect. 2), we describe the sample Cepheids that we selected (Sect. 3). In Sects. 4 and 5, we report our new observations as well as reprocessed measurements of ζ Gem retrieved from the FLUOR/IOTA instrument archive. Section 6 is dedicated to the computation of the corresponding angular diameter values, taking into account the limb darkening and the bandwidth smearing effects. In Sects. 7 and 8, we investigate the application of the BW method to our data, and we derive the Cepheid distances.

We will discuss the consequences of these results for the calibration of the Period-Radius (P–R), Period-Luminosity (P–L) and Barnes-Evans relations of the Cepheids in forthcoming papers (Papers II and III).

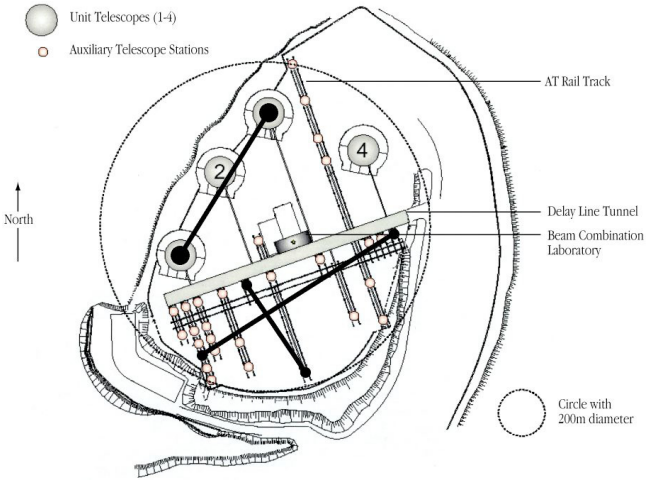

Fig. 1. Layout of the three baselines used for the VINCI/VLTI Cepheids observations, UT1-UT3 (102.5 m), E0-G1 (66 m) and B3-M0 (140 m).

2. Instrumental setup

The European Southern Observatory's Very Large Telescope Interferometer (Glindemann et al. 2000) is in operation on Cerro Paranal, in Northern Chile since March 2001. For the observations reported in this paper, the beams from two Test Siderostats (0.35 m aperture) or two Unit Telescopes (8 m aperture) were recombined coherently in VINCI, the VLT INterferometer Commissioning Instrument (Kervella et al. 2000, 2003a). We used a regular K band filter (λ = 2.0−2.4 μm) that gives an effective observation wavelength of 2.18 μm for the effective temperature of typical Cepheids (see Sect. 6.4 for details). Three VLTI baselines were used for this program: E0-G1, B3-M0 and UT1-UT3 respectively 66, 140 and 102.5 m in ground length. Figure 1 shows their positions on the VLTI platform.

3. Selected sample of Cepheids

Despite their brightness, Cepheids are located at large distances, and the HIPPARCOS satellite (Perryman et al. 1997) could only obtain a limited number of Cepheid distances with a relatively poor precision. If we exclude the peculiar first overtone Cepheid α UMi (Polaris), the closest Cepheid is δ Cep, located at approximately 250 pc (Mourard et al. 1997; Nordgren et al. 2000). As described by Davis (1979) and Sasselov & Karovska (1994), it is possible to derive directly the distance to the Cepheids for which we can measure the amplitude of the angular diameter variation. Even for the nearby Cepheids, this requires an extremely high resolving power, as the largest Cepheid in the sky, ℓ Car, is only 0.003″ in angular diameter. Long baseline interferometry is therefore the only technique that allows us to resolve these objects. As a remark, the medium to long period Cepheids ($D \approx 200\,D_\odot$) in the Large Magellanic Cloud (LMC) ($d \approx 55$ kpc) are so small ($\theta \approx 30\,\mu$as) that they would require a baseline of 20 km to be resolved in the K band (5 km in the visible). However, such a measurement is highly desirable, as it would provide a precise geometrical distance to the LMC, a critical step in the extragalactic distance ladder.

Mourard (1996) has highlighted the capabilities of the VLTI for the observation of nearby Cepheids, as it provides long baselines (up to 202 m) and thus a high resolving power. Though they are supergiant stars, the Cepheids are very small objects in terms of angular size. A consequence of this is that the limit on the number of interferometrically resolvable Cepheids is not set by the size of the light collectors, but by the baseline length. From photometry only, several hundred Cepheids can produce interferometric fringes using the VLTI Auxiliary Telescopes (1.8 m in diameter). However, in order to measure accurately their size, one needs to resolve their disk to a sufficient level. Kervella (2001a) has compiled a list of more than 30 Cepheids that can be measured from Paranal using the VINCI and AMBER (Petrov et al. 2000) instruments. Considering the usual constraints in terms of sky coverage, limiting magnitude and accessible resolution, we have selected seven bright Cepheids observable from Paranal Observatory (latitude λ = −24 deg): X Sgr, η Aql, W Sgr, β Dor, ζ Gem, Y Oph and ℓ Car. The periods of these stars cover a wide range, from 7 to 35.5 days. This coverage is important to properly constrain the P–R and P–L relations. To estimate the feasibility of the observations, the angular diameters of these stars were deduced from the BW studies by Gieren et al. (1993). For ζ Gem and η Aql, previously published direct interferometric measurements by Nordgren et al. (2000), Kervella et al. (2001b) and Lane et al. (2002) already demonstrated the feasibility of the observations. The relevant parameters of the seven Cepheids of our sample, taken from the literature, are listed in Table 1.

4. Interferometric data processing

4.1. Coherence factors

We used a modified version (Kervella et al. 2003c) of the standard VINCI data reduction pipeline, whose general principle is based on the original algorithm of the FLUOR instrument (Coudé du Foresto et al. 1997, 1998a). The VINCI/VLTI commissioning data we used for this study are publicly available

Table 1. Relevant parameters of the observed sample of Cepheids, sorted by increasing period.

	X Sgr HD 161592	η Aql HD 187929	W Sgr HD 164975	β Dor HD 37350	ζ Gem HD 52973	Y Oph HD 162714	ℓ Car HD 84810
m_V[a]	4.581	3.942	4.700	3.731	3.928	6.164	3.771
m_K[b]	2.56	1.966	2.82	1.959	2.11	2.682	1.091
Sp. Type	F5-G2II	F6Ib-G4Ib	F4-G2Ib	F4-G4Ia-II	F7Ib-G3Ib	F8Ib-G3Ib	F6Ib-K0Ib
π (mas)[c]	3.03 ± 0.94	2.78 ± 0.91	1.57 ± 0.93	3.14 ± 0.59	2.79 ± 0.81	1.14 ± 0.80	2.16 ± 0.47
Min $T_{\rm eff}$ (K)	5670	5400	5355	5025	5150		
Mean $T_{\rm eff}$ (K)[d]	6150	5870	5769	5490	5430	*5300*	5090
Max $T_{\rm eff}$ (K)	6820	6540	6324	6090	5750		
Min $\log g$	1.86	1.25	1.72	1.60			
Mean $\log g$[e]	2.14	1.49	1.82	1.83	1.50	*1.50*	1.50
Max $\log g$	2.43	1.73	2.02	2.06			
[M/H][e]	0.04	0.05	−0.01	−0.01	0.04	0.05	0.30
T_0 (JD-2.452 × 10^6)[f]	723.9488	519.2477	726.8098	214.2153	210.7407	715.4809	290.4158
P (days)[g]	7.013059	7.176769	7.594904	9.842425	10.150967	17.126908	35.551341
Intensity profiles[h]							
a_1	+0.7594	+0.8816	+0.8002	+0.7969	+0.8713	+0.8549	+0.8500
a_2	−0.4530	−0.7418	−0.5135	−0.4596	−0.6536	−0.5602	−0.4991
a_3	+0.0347	+0.3984	+0.1583	+0.1341	+0.3283	+0.2565	+0.2113
a_4	+0.0751	−0.0778	+0.0109	+0.0082	−0.0610	−0.0437	−0.0340

[a] m_V from Barnes et al. (1987) for X Sgr, from Barnes et al. (1997) for η Aql, from Moffett & Barnes (1984) for W Sgr and ζ Gem, from Berdnikov & Turner (2001) for β Dor and ℓ Car, and from Coulson & Caldwell (1985) for Y Oph.

[b] m_K from Welch et al. (1984) for X Sgr, and W Sgr, from Laney & Stobie (1992) for β Dor, Y Oph, and ℓ Car, from Ducati et al. (2001) for ζ Gem, from Barnes et al. (1997) for η Aql.

[c] Parallaxes from the HIPPARCOS catalogue (Perryman et al. 1997).

[d] From Kiss & Szatmàry (1998) for ζ Gem and η Aql, Bersier et al. (1997) for W Sgr, and Pel (1978) for X Sgr and β Dor.

[e] From Andrievsky et al. (2002), Cayrel de Strobel et al. (1997, 2001), and Pel (1978), except for $\log g$ of Y Oph.

[f] Reference epoch T_0 values have been computed near the dates of the VINCI observations, from the values published by Szabados (1989a).

[g] P values from Szabados (1989a). The periods of η Aql, ζ Gem and W Sgr are known to evolve. The values above correspond to the T_0 chosen for these stars.

[h] Four-parameters intensity profiles from Claret (2000) in the K band, assuming a microturbulence velocity of 4 km s^{-1} and the average values of $T_{\rm eff}$ and $\log g$.

through the ESO Archive, and result from two proposals of our group, that were accepted for ESO Periods 70 and 71.

The goal of the raw data processing is to extract the value of the modulated power contained in the interferometric fringes. This value is proportional to the squared visibility V^2 of the source on the observation baseline, which is in turn directly linked to the Fourier transform of the light distribution of the source through the Zernike-Van Cittert theorem.

One of the key advantages of VINCI is to use single-mode fibers to filter out the perturbations induced by the turbulent atmosphere. The wavefront that is injected in the fibers is only the mode guided by the fiber (Gaussian in shape, see Ruilier 1999 or Coudé du Foresto 1998b for details). The atmospherically corrupted part of the wavefront is not injected into the fibers and is lost into the cladding. Due to the temporal fluctuations of the turbulence, the injected flux changes considerably during an observation. However, VINCI derives two photometric signals that can be used to subtract the intensity fluctuations from the interferometric fringes and normalize them continuously. The resulting calibrated interferograms are practically free of atmospheric corruption, except the piston mode (differential longitudinal delay of the wavefront between the two apertures) that tends to smear the fringes and affect their visibility. Its effect is largely diminished by using a sufficiently high scanning frequency, as was the case for the VINCI observations.

After the photometric calibration has been achieved, the two interferograms from the two interferometric outputs of the VINCI beam combiner are subtracted to remove the residual photometric fluctuations. As the two fringe patterns are in perfect phase opposition, this subtraction removes a large part of the correlated fluctuations and enhances the interferometric fringes. Instead of the classical Fourier analysis, we implemented a time-frequency analysis (Ségransan et al. 1999) based on the continuous wavelet transform (Farge 1992). In this approach, the projection of the signal is not onto a sine wave (Fourier transform), but onto a function, i.e. the wavelet, that is localised in both time and frequency. We used as a basis the Morlet wavelet, a gaussian envelope multiplied by a sine wave. With the proper choice of the number of oscillations inside the gaussian envelope, this wavelet closely matches a VINCI

interferogram. It is therefore very efficient at localizing the signal in both time and frequency.

The differential piston corrupts the amplitude and the shape of the fringe peak in the wavelet power spectrum. A selection based on the shape of fringe peak in the time-frequency domain is used to remove "pistonned" and false detection interferograms. Squared coherence factors μ^2 are then derived by integrating the wavelet power spectral density (PSD) of the interferograms at the position and frequency of the fringes. The residual photon and detector noise backgrounds are removed by making a least squares fit of the PSD at high and low frequency.

4.2. Calibrators

The calibration of the Cepheids' visibilities was achieved using well-known calibrator stars that have been selected in the Cohen et al. (1999) catalogue, with the exception of ϵ Ind. This dwarf star was measured separately (Ségransan et al. 2004) and used to calibrate one of the η Aql measurements. The angular diameters of 39 Eri A, HR 4050 and HR 4546 (which belong to the Cohen et al. 1999 catalogue) were also measured separately, as these stars appeared to give a slightly inconsistent value of the interferometric efficiency.

For 39 Eri A and HR 4546, the measured angular diameters we find are $\theta_{\rm UD} = 1.74 \pm 0.03$ and 2.41 ± 0.04 mas, respectively. These measured values are only $2\,\sigma$ lower than the Cohen et al. (1999) catalogue values of $\theta_{\rm UD} = 1.81 \pm 0.02$ and 2.53 ± 0.04 mas. A possible reason for this difference could be the presence of faint, main sequence companions in orbit around these two giant stars. The additional contribution of these objects would bias the diameter found by spectrophotometry towards larger values, an effect consistent with what we observe. For HR 4050, we obtained $\theta_{\rm UD} = 5.18 \pm 0.05$ mas, only $+1\,\sigma$ away from the catalogue value of $\theta_{\rm UD} = 5.09 \pm 0.06$ mas. The characteristics of the selected calibrators are listed in Table 2. The limb-darkened disk (LD) angular diameters of these stars were converted into uniform disk values using linear coefficients taken from Claret et al. (1995). As demonstrated by Bordé et al. (2002), the star diameters in the Cohen et al. (1999) list have been measured very homogeneously to a relative precision of approximately 1% and agree well with other angular diameter estimation methods.

The calibrators were observed soon before and after the Cepheids, in order to verify that the interferometric efficiency (IE) has not changed significantly during the Cepheid observation itself. In some cases, and due to the technical nature of commissioning observations, part of the Cepheid observations could not be bracketed, but only immediately preceded or followed by a calibrator. However, the stability of the IE has proved to be generally very good, and we do not expect any significant bias from these single-calibrator observations. Some observations included several calibrators to allow a cross-check of of their angular sizes. The calibrators were chosen as close as possible in the sky to our target Cepheids, in order to be able to observe them with similar airmass. This selection has taken into account the constraints in terms of limiting magnitude and sky coverage imposed by the VLTI siderostats and delay lines. The IE was computed from the coherence factor measurements obtained on the calibrators, taking into account the bandwidth smearing effect (see Sect. 6.4) and a uniform disk angular diameter model. This calibration process yielded the final squared visibilities listed in Tables 3 to 9.

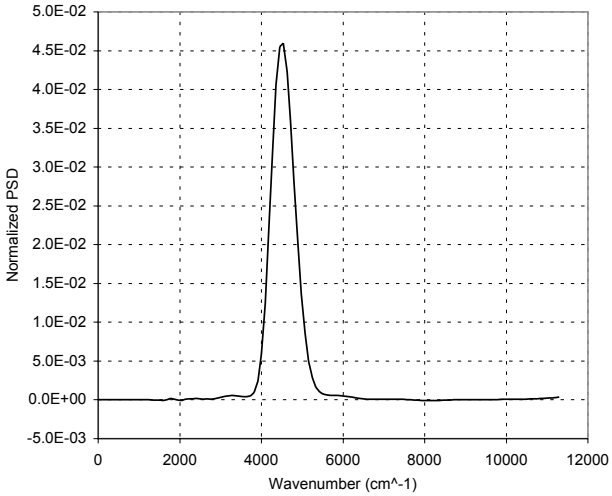

Fig. 2. Average wavelets power spectral density of 302 interferograms obtained on X Sgr on JD = 2 452 768.8462. No background or bias is present. The integration of the fringes modulated power is done between 2000 and 8000 $\rm cm^{-1}$.

5. Data quality

5.1. General remarks

Due to the fact that we used two types of light collectors (siderostats and UTs) and several baselines (from 66 to 140 m in ground length), the intrinsic quality of our data is relatively heterogeneous. In this section, we discuss briefly the characteristics of our observations of each target. One particularity of our measurements is that they have all been obtained during the commissioning period of the VLTI, during which technical tasks were given higher priority. In particular, the long baseline B3-M0 was only available during a few months over the two years of operations of the VLTI with VINCI. The UT1-UT3 observations were executed during two short commissioning runs and it was not possible to obtain more than one or two phases for the observed stars (β Dor and ζ Gem). However, the very large SNR values provided by the large aperture of the UTs, even without high-order adaptive optics, gave high-precision visibility measurements.

The VINCI processing pipeline produces a number of outputs to the user for the data quality control, including in particular the average wavelet power spectral density (WPSD) of the processed interferograms. This is an essential tool to verify that no bias is present in the calibrated and normalized fringe power peak. Figure 2 shows the average WPSD of a series of 302 interferograms obtained on X Sgr. No bias is present, and the residual background is very low. The power integration being

Table 2. Relevant parameters of the calibrators.

Name		m_V	m_K	Sp. Type	$T_{\rm eff}$(K)	$\log g$	π (mas)[a]	$\theta_{\rm LD}$(mas)[b]	$\theta_{\rm UD}$(mas)[c]
χ Phe	HD 12524	5.16	1.52	K5III	3780	1.9	8.76 ± 0.64	2.77 ± 0.032	2.69 ± 0.031
39 Eri A	HD 26846	4.90	2.25	K3III	4210	2.2	15.80 ± 0.95	1.79 ± 0.031*	1.74 ± 0.030*
ϵ Ret	HD 27442	4.44	1.97	K2IVa	4460	2.3	54.84 ± 0.50	1.95 ± 0.049	1.90 ± 0.048
HR 2533	HD 49968	5.69	2.10	K5III	3780	1.9	6.36 ± 0.92	1.93 ± 0.020	1.87 ± 0.019
HR 2549	HD 50235	5.00	1.39	K5III	3780	1.9	3.60 ± 0.56	2.25 ± 0.036	2.18 ± 0.035
γ^2 Vol	HD 55865	3.77	1.52	K0III	4720	2.6	23.02 ± 0.69	2.50 ± 0.060	2.44 ± 0.059
6 Pup	HD 63697	5.18	2.62	K3III	4210	2.2	12.87 ± 0.71	1.88 ± 0.039	1.83 ± 0.038
HR 3046	HD 63744	4.70	2.31	K0III	4720	2.6	14.36 ± 0.48	1.67 ± 0.025	1.63 ± 0.024
HR 4050	HD 89388	3.38	0.60	K3IIa	4335	2.3	4.43 ± 0.49	5.32 ± 0.050*	5.18 ± 0.048*
HR 4080	HD 89998	4.83	2.40	K1III	4580	2.5	16.26 ± 0.56	1.72 ± 0.020	1.68 ± 0.019
HR 4526	HD 102461	5.44	1.77	K5III	3780	1.9	3.97 ± 0.61	3.03 ± 0.034	2.94 ± 0.033
HR 4546	HD 102964	4.47	1.56	K3III	4210	2.2	7.03 ± 0.72	2.48 ± 0.036*	2.41 ± 0.035*
HR 4831	HD 110458	4.67	2.28	K0III	4720	2.6	17.31 ± 0.65	1.70 ± 0.018	1.66 ± 0.018
χ Sco	HD 145897	5.25	1.60	K3III	4210	2.2	7.43 ± 0.91	2.10 ± 0.023	2.04 ± 0.022
70 Aql	HD 196321	4.90	1.21	K5II	3780	1.9	1.48 ± 0.91	3.27 ± 0.037	3.17 ± 0.036
7 Aqr	HD 199345	5.50	2.00	K5III	3780	1.9	5.42 ± 0.99	2.14 ± 0.024	2.08 ± 0.023
ϵ Ind	HD 209100	4.69	2.18	K4.5V	4580	4.5	275.79 ± 0.69	1.89 ± 0.051*	1.84 ± 0.050*
λ Gru	HD 209688	4.48	1.68	K3III	4210	2.2	13.20 ± 0.78	2.71 ± 0.030	2.64 ± 0.029
HR 8685	HD 216149	5.41	1.60	M0III	3660	1.4	2.95 ± 0.69	2.07 ± 0.021	2.01 ± 0.020

[a] Parallaxes from the HIPPARCOS catalogue (Perryman et al. 1997).
[b] Catalogue values from Cohen et al. (1999), except for ϵ Ind, HR 4050, HR 4546 and 39 Eri A.
[c] Linear limb darkening coefficients factors from Claret et al. (1995).
* The angular diameters of ϵ Ind, HR 4050, HR 4546 and 39 Eri A have been measured separately with VINCI.

done between 2000 and 8000 cm^{-1}, the complete modulated power of the fringes is taken into account without bias.

5.2. X Sgr, W Sgr and Y Oph

X Sgr was observed 8 times on the B3-M0 baseline (140 m ground length), using exclusively the two 0.35 m Test Siderostats (TS). The projected baseline length varied between 118.4 and 139.7 m, and the observed squared visibilities were confined between $V^2 = 56.9$ and 71.1%. Thanks to its declination of $\delta = -28$ deg, X Sgr culminates almost at zenith over Paranal (−24 deg), and all the observations were obtained at very low airmasses. It is located on the sky near two other Cepheids of our sample, Y Oph and W Sgr, and these three stars share the same calibrator, χ Sco. The average signal to noise ratio (SNR) was typically 2 to 5 on the photometric outputs of VINCI, and 4 to 6 on the interferometric channels, for a constant fringe frequency of 242 Hz. A total of 4977 interferograms were processed by the pipeline. The same remarks apply to W Sgr and Y Oph, as they have almost the same magnitude and similar angular diameters. The number of processed interferograms for these two stars was 4231 and 2182, respectively, during 9 and 4 observing sessions.

5.3. η Aql

η Aql was observed once on the E0-G1 baseline (66 m) and 10 times on the B3-M0 baseline (140 m ground length). The total number of processed interferograms is 5584. The SNRs were typically 4 and 7 on the photometric and interferometric outputs at a fringe frequency of 242 to 272 Hz. Due to its northern declination ($\delta = +1$ deg) and to the limits of the TS, it was not possible to observe η Aql for more than two hours per night, therefore limiting the number of interferograms and the precision of the measurements.

5.4. β Dor

β Dor is a difficult target for observation with the TS, as it is partially hidden behind the TS periscopes that are used to direct the light into the VLTI tunnels. This causes a partial vignetting of the beams and therefore a loss in SNR. The data from the TS are thus of intermediate quality, considering the brightness of this star. It is located at a declination of −62 deg, relatively close to ℓ Car, and therefore these two stars share some calibrators. In addition to the 5 observations with the TS, four measurements were obtained during three commissioning runs on the UT1-UT3 baseline. A total of 8129 interferograms were processed, of which 5187 were acquired with the 8 m Unit Telescopes (96 min spread over four nights were spent on β Dor using UT1 and UT3).

5.5. ζ Gem

At a declination of +20 deg, ζ Gem is not accessible to the TS due to a mechanical limitation. This is the reason why this star was observed only on two occasions with UT1 and UT3, for a total of 3857 interferograms, obtained during 41 min on the

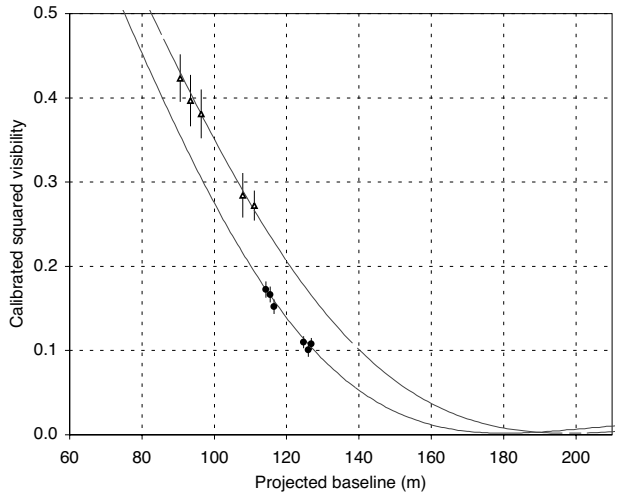

Fig. 3. Squared visibilities obtained on ℓ Car on JD = 2 452 742.712 (dashed line) and 2 452 763.555 (solid line), respectively at pulsation phases 0.722 and 0.308. The two UD visibility models correspond to $\theta_{\rm UD}$ = 2.801 and 3.075 mas, and take the bandwidth smearing effect into account. The first minimum of the visibility function (that never goes down to zero) occurs for baselines of approximately 199 and 181 m, for an effective wavelength of 2.18 μm.

target. The average on-source SNRs were typically 50 for the interferometric channels and 30 for the photometric signals, at a fringe frequency of 694 Hz.

The data obtained using the FLUOR/IOTA instrument are described in Kervella et al. (2001b). They were reprocessed using the latest release of the FLUOR software that includes a better treatment of the photon shot noise than the 2001 version. As the baseline of IOTA is limited to 38 m, the visibility of the fringes is very high, and the precision on the angular diameter is reduced compared to the 102.5 m baseline UT1-UT3.

5.6. ℓ Car

As for β Dor, the observation of ℓ Car ($\delta = -62$ deg) is made particularly difficult by the vignetting of the TS beams. Thanks to its brightness ($K \approx 1$) the SNRs are 15–20 on the interferometric channels, and 10–15 on the photometric signals, using the TS and a fringe frequency of 242 Hz. One observation was obtained on the E0-G1 baseline (66 m ground length), and 19 measurements on the B3-M0 baseline. ℓ Car is the most observed star in our sample, with a total of 22 226 processed interferograms. Its average diameter of approximately 3 mas makes it an ideal target for observations with baselines of 100 to 200 m. On the B3-M0 baseline, we achieved projected baselines of 89.7 to 135.0 m, corresponding to V^2 values of 8 to 42%. This range is ideal to constrain the visibility model and derive precise values of the angular diameter.

Figure 3 shows the squared visibility points obtained at two phases on ℓ Car. The change in angular diameter is clearly visible. Thanks to the variation of the projected baseline on sky, we have sampled a segment of the visibility curve.

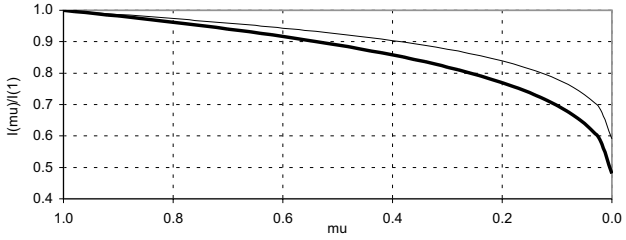

Fig. 4. Average intensity profiles computed from the four-parameter approximations of Claret (2000) for X Sgr (thin line) and ℓ Car (thick line), using the parameters listed in Table 1.

6. Angular diameters

The object of this section is to derive the angular diameters of the Cepheids as a function of their pulsational phase. We discuss the different types of models that can be used to compute the angular diameter from the squared visibility measurements.

6.1. Uniform disk angular diameters

This very simple, rather unphysical model is commonly used for interferometric studies as it is independent of any stellar atmosphere model. The relationship between the visibility V and the uniform disk angular diameter (UD) is:

$$V(B, \theta_{\rm UD}) = \left| \frac{2J_1(x)}{x} \right| \quad (1)$$

where $x = \pi B \theta_{\rm UD}/\lambda$ is the spatial frequency. This function can be inverted numerically to retrieve the uniform disk angular diameter $\theta_{\rm UD}$.

While the true stellar light distributions depart significantly from the UD model, the UD angular diameters $\theta_{\rm UD}$ given in Tables 3 to 9 have the advantage that they can easily be converted to LD values using any stellar atmosphere model. This is achieved by computing a conversion factor $\theta_{\rm LD}/\theta_{\rm UD}$ from the chosen intensity profile (see e.g. Davis et al. 2000 for details).

6.2. Static atmosphere intensity profile

The visibility curve shape before the first minimum is almost impossible to distinguish between a uniform disk (UD) and limb darkened (LD) model. Therefore, it is necessary to use a model of the stellar disk limb darkening to deduce the photospheric angular size of the star, from the observed visibility values. The intensity profiles that we chose were computed by Claret (2000), based on model atmospheres by Kurucz (1992). They consist of four-parameter approximations to the function $I(\mu)/I(1)$, where $\mu = \cos\theta$ is the cosine of the azimuth of a surface element of the star. They are accurate approximations of the numerical results from the ATLAS modeling code. The analytical expression of these approximations is given by:

$$I(\mu)/I(1) = 1 - \sum_{k=1}^{4} a_k \left(1 - \mu^{\frac{k}{2}}\right). \quad (2)$$

The a_k coefficients are tabulated by Claret (2000) for a wide range of stellar parameters ($T_{\rm eff}$, $\log g$,...) and photometric

bands (U to K). The a_k values for each Cepheid are given in Table 1 for the K band, and the intensity profiles $I(\mu)/I(1)$ of X Sgr and ℓ Car are shown in Fig. 4.

The limb darkening is directly measurable by interferometry around the first minimum of the visibility function, as demonstrated by several authors on giant stars (Quirrenbach et al. 1996; Wittkowski et al. 2001). Unfortunately, even for ℓ Car observed in the K band, this requires a baseline of more than 180 m that was not available for the measurements reported here. It is intended in the near future to measure directly the LD of a few nearby Cepheids, using the shorter wavelength bands of AMBER (Petrov et al. 2000) and the longest baselines of the VLTI (up to 202 m).

6.3. Changes of limb darkening with phase

As shown by Marengo et al. (2002), the atmosphere of the Cepheids departs from that of a non-variable giant with identical $T_{\rm eff}$ and $\log g$, due in particular to the presence of energetic shock waves at certain phases of the pulsation.

However, this effect is enhanced at visible wavelengths compared to the infrared, and appears to be negligible in the case of the VINCI observations. Marengo et al. (2003) have derived in the H band a relative variation of the limb darkening coefficient $k = \theta_{\rm UD}/\theta_{\rm LD}$ of only 0.2%. This is below the precision of our measurements and is neglected in the rest of this paper. Furthermore, the VINCI/VLTI measurement wavelength being longer (2.18 μm) than the H band, the LD correction is even smaller, as is its expected variation.

From the results of Marengo et al. (2003) it appears clearly that the interferometers operating at infrared wavelengths are ideally suited for Cepheid measurements that aim at calibrating the P–R and P–L relations. On the other hand, as pointed out by these authors, the visible wavelength interferometers should be favored to study the dynamical evolution of the atmosphere (including the limb darkening) during the pulsation. The geometrical determination of the pulsation parallax is almost independant of the adopted atmosphere model in the K band, while this is not the case at shorter wavelengths.

6.4. Visibility model and limb darkened angular diameters

The VINCI instrument bandpass corresponds to the K band filter, transparent between $\lambda = 2.0$ and 2.4 μm. An important effect of this relatively large spectral bandwidth is that several spatial frequencies are simultaneously observed by the interferometer. This effect is known as *bandwidth smearing* (Kervella et al. 2003b).

To account for the bandwidth smearing, the model visibility is computed for regularly spaced wavenumber spectral bins over the K band, and then integrated to obtain the model visibility. In this paper, we assume that the limb darkening law does not change over the K band. This is reasonable for a hot and compact stellar atmosphere, but is also coherent with the range of visibilities measured on the Cepheids of our sample. If necessary, this computation can easily be extended to a wavenumber dependant $I(\mu, \sigma)$ intensity profile. Following Davis et al. (2000), using a Hankel integral, we can derive the visibility law $V(B, \theta_{\rm LD}, \sigma)$ from the intensity profile:

$$V = \frac{1}{A} \int_0^1 I(\mu) J_0 \left(\pi B \sigma \theta_{\rm LD} \sqrt{1-\mu^2} \right) \mu \, {\rm d}\mu \tag{3}$$

where σ is the wavenumber:

$$\sigma = 1/\lambda \tag{4}$$

and A is a normalization factor:

$$A = \int_0^1 I(\mu) \mu \, {\rm d}\mu. \tag{5}$$

The integral of the binned squared visibilities is computed numerically over the K band and gives the model V^2 for the projected baseline B and the angular diameter $\theta_{\rm LD}$ through the relation:

$$V^2(\theta_{\rm LD}, B) = \int_K \left[V(B, \theta_{\rm LD}, \sigma) \, T(\sigma) \right]^2 \, {\rm d}\sigma \tag{6}$$

where $T(\sigma)$ is the normalized instrumental transmission defined so that

$$\int_K T(\sigma) \, {\rm d}\sigma = 1. \tag{7}$$

We computed a model of $T(\sigma)$ by taking into account the instrumental transmission of VINCI and the VLTI. It was first estimated by considering all known factors (filter, fibers, atmospheric transmission,...) and then calibrated on sky based on several observations of bright stars with the 8 meter UTs (see Kervella et al. 2003b for more details). This gives, for our sample of Cepheids, a measurement wavelength of 2.179 ± 0.003 μm. The variation of effective temperature between the stars of our sample and over the pulsation does not change this value by more than ± 0.001 μm. The uncertainty on the effective wavelength of the measurement translates to a 0.15% uncertainty on the measured angular diameters. Considering the level of the other sources of error (statistical and systematic), the effect on our angular diameter results is negligible.

The $V^2(\theta_{\rm LD}, B)$ model is adjusted numerically to the observed (B, V^2) data using a classical χ^2 minimization process to derive $\theta_{\rm LD}$. A single angular diameter is derived per observation session, the fit being done directly on the set of V^2 values obtained during the session. The systematic and statistical errors are considered separately in the fitting procedure, to estimate the contribution of the uncertainty of the calibrator diameter on the final error bar.

Each observation session was generally executed in less than 3 h, a short time compared to the pulsation periods of the Cepheids of our sample. Therefore, we do not expect any phase induced smearing from this averaging.

6.5. Measured angular diameters

The derived angular diameters are given in Tables 3 to 9 for the seven Cepheids of our sample. Two error bars are given for each angular diameter value:

– one statistical uncertainty, computed from the dispersion of the V^2 values obtained during the observation;

– one systematic uncertainty defined by the error bars on the calibrator stars a priori angular sizes.

While the statistical error can be diminished by repeatedly observing the target, the systematic error is not reduced by averaging measurements obtained using the same calibrator.

The reference epochs T_0 and periods P for each Cepheid are given in Table 1. N is the number of batches (500 interferograms) recorded during the corresponding observing session. For each angular diameter, the statistical and systematic calibration errors are given separately, except for the FLUOR/IOTA measurements of ζ Gem, for which the systematic calibration error is negligible compared to the statistical uncertainty.

7. Linear diameter curves

For each star we used radial velocity data found in the literature. Specifically, we collected data from Bersier (2002) for η Aql, ℓ Car, and β Dor; from Bersier et al. (1994) for ζ Gem; from Babel et al. (1989) for W Sgr. All these data have been obtained with the CORAVEL radial velocity spectrograph (Baranne et al. 1979). We also obtained data from Evans & Lyons (1986) for Y Oph and from Wilson et al. (1989) for X Sgr.

In theory, the linear diameter variation could be determined by direct integration of pulsational velocities (within the assumption that the $\tau = 1$ photosphere is comoving with the atmosphere of the Cepheid during its pulsation). However these velocities are deduced from the measured radial velocities by the use of a projection factor p. The Cepheid's radii determined from the BW method depend directly from a good knowledge of p. Sabbey et al. (1995) and Krockenberger et al. (1997) have studied in detail the way to determine the p-factor. We used a constant projection factor $p = 1.36$ in order to transform the radial velocities into pulsation velocities. Burki et al. (1982) have shown that this value is appropriate for the radial velocity measurements that we used.

8. Cepheids parameters

8.1. Angular diameter model fitting and distance measurement

From our angular diameter measurements, we can derive both the average linear diameter and the distance to the Cepheids. This is done by applying a classical χ^2 minimization algorithm between our angular diameter measurements and a model of the star pulsation. The minimized quantity with respect to the chosen model is

$$\chi^2 = \sum_i \frac{(\theta_{\mathrm{LD\,observ}}(\phi_i) - \theta_{\mathrm{LD\,model}}(\phi_i))^2}{\sigma_{\mathrm{observ}}(\phi_i)^2} \quad (8)$$

where ϕ_i is the phase of measurement i. The expression of $\theta_{\mathrm{LD\,model}}(\phi_i)$ is defined using the following parameters:

– the average LD angular diameter $\overline{\theta_{\mathrm{LD}}}$ (in mas);
– the linear diameter variation $\Delta D(\phi_i)$ (in $D_\odot$);
– the distance d to the star (in pc).

The resulting expression is therefore:

$$\theta_{\mathrm{LD\,model}}(\phi_i) = \overline{\theta_{\mathrm{LD}}} + 9.305 \left(\frac{\Delta D(\phi_i)}{d}\right) [\mathrm{mas}]. \quad (9)$$

As $\Delta D(\phi_i)$ is known from the integration of the radial velocity curve (Sect. 7), the only variable parameters are the average LD angular diameter $\overline{\theta_{\mathrm{LD}}}$ and the distance d. From there, three methods can be used to derive the distance d, depending on the level of completeness and precision of the angular diameter measurements:

– **Constant diameter fit (order 0):** the average linear diameter $\overline{D}$ of the star is supposed known a priori from previously published BW measurements or P–R relations (see Sect. 8.2). We assume here that $\Delta D(\phi) = 0$. The only remaining variable to fit is the distance d. This is the most basic method, and is useful as a reference to assess the level of detection of the pulsational diameter variation with the other methods.
– **Variable diameter (order 1):** we still consider that the average linear diameter $\overline{D}$ of the star is known a priori, but we include in our model the radius variation derived from the integration of the radial velocity curve. This method is well suited when the intrinsic accuracy of the angular diameter measurements is too low to measure precisely the pulsation amplitude (ζ Gem, X Sgr and Y Oph). The distance d is the only free parameter for the fit.
– **Complete fit (order 2):** the average LD angular diameter $\overline{\theta_{\mathrm{LD}}}$ and the distance d are both considered as variables and adjusted simultaneously to the angular diameter measurements. In the fitting process, the radius curve is matched to the observed pulsation amplitude. Apart from direct trigonometric parallax, this implementation of the BW method is the most direct way of measuring the distance and diameter of a Cepheid. It requires a high precision angular diameter curve and a good phase coverage. It can be applied directly to our η Aql, W Sgr, β Dor and ℓ Car measurements.

8.2. Published linear diameter values

In this section, we survey the existing linear diameter determinations for the Cepheids of our sample, in order to apply the order 0 and 1 methods to our observations.

A large number of BW studies have been published, using both visible and infrared wavelength observations. For ζ Gem and η Aql, the pulsation has been resolved using the Palomar Testbed Interferometer (Lane et al. 2000, 2002), thererefore giving a direct estimate of the diameter and distance of these stars. Table 10 gives a list of the existing diameter estimates for the Cepheids of our sample from the application of the classical BW method ("BAADE-WESSELINK" section of the table).

From the many different P–R relations available, we chose the Gieren et al. (1998) version, as it is based on infrared colors for the determination of the temperature of the stars. Compared to visible colors, the infrared colors give a much less dispersed

Table 11. Order 0. Cepheid average angular diameters and distances derived from the VINCI interferometric measurements, assuming a constant diameter model ($\Delta D = 0$), The average diameter $\overline{D}$ is taken from Gieren et al. (1998). Two error bars are given in brackets for the angular diameter: the statistical dispersion and the calibration systematics. The uncertainty mentioned for the distance d is the quadratic sum of the statistical, calibration and P–R a priori diameter errors, the last two being systematic in nature. The three types of errors are also reported separately in brackets. The results for ℓ Car are mentioned only for completeness, but are not meant to be used for further analysis, as our observations are inconsistent with a constant diameter model.

Star	$\overline{\theta_{\rm LD0}}$ (mas)	d_0 (pc)	χ^2_0
X Sgr	$1.471 \pm 0.033_{[0.013\ 0.031]}$	$324 \pm 18_{[3\ 7\ 17]}$	0.38
η Aql	$1.856 \pm 0.028_{[0.009\ 0.026]}$	$261 \pm 14_{[1\ 4\ 14]}$	3.98
W Sgr	$1.348 \pm 0029_{[0.011\ 0.027]}$	$376 \pm 22_{[3\ 8\ 21]}$	0.90
β Dor	$1.926 \pm 0.024_{[0.014\ 0.020]}$	$319 \pm 20_{[3\ 2\ 19]}$	1.31
ζ Gem	$1.747 \pm 0.061_{[0.025\ 0.056]}$	$360 \pm 25_{[5\ 12\ 22]}$	0.51
Y Oph	$1.459 \pm 0.040_{[0.023\ 0.033]}$	$638 \pm 50_{[10\ 14\ 47]}$	0.16
(ℓ Car)	$3.071 \pm 0.012_{[0.004\ 0.011]}$	$524 \pm 49_{[1\ 2\ 49]}$	23.2

Table 12. Order 1. Cepheid angular diameters and distances, assuming the average diameter $\overline{D}$ of Gieren et al. (1998). The diameter variation curve $\Delta D(\phi)$ is integrated from the radial velocity curve. Only the distance is ajusted by the fitting procedure. The error bars on d are given as in Table 11.

Star	$\overline{\theta_{\rm LD1}}$ (mas)	d_1 (pc)	χ^2_1
X Sgr	$1.461 \pm 0.033_{[0.013\ 0.031]}$	$326 \pm 18_{[3\ 7\ 17]}$	1.36
η Aql	$1.839 \pm 0.028_{[0.009\ 0.026]}$	$264 \pm 14_{[1\ 4\ 14]}$	0.40
W Sgr	$1.312 \pm 0029_{[0.011\ 0.027]}$	$386 \pm 22_{[3\ 8\ 21]}$	0.42
β Dor	$1.884 \pm 0.024_{[0.014\ 0.020]}$	$326 \pm 20_{[3\ 2\ 19]}$	0.23
ζ Gem	$1.718 \pm 0.061_{[0.025\ 0.056]}$	$366 \pm 25_{[5\ 12\ 22]}$	0.88
Y Oph	$1.437 \pm 0.040_{[0.023\ 0.033]}$	$648 \pm 51_{[10\ 15\ 47]}$	0.03
ℓ Car	$2.977 \pm 0.012_{[0.004\ 0.011]}$	$542 \pm 49_{[1\ 2\ 49]}$	0.71

P–R relation. Indeed, this relation has a very good intrinsic precision of the order of 5 to 10% for the period range of our sample. Moreover, it is identical to the law determined by Laney & Stobie (1995). The compatibility with the individual BW diameter estimates is also satisfactory. The linear diameters deduced from this P–R law are mentioned in the "EMPIRICAL P–R" section of Table 10. We assume these linear diameter values in the following.

8.3. Angular diameter fitting results

The results of both constant and variable diameter fits for the seven Cepheids of our sample are listed in Tables 11 to 13. η Aql, W Sgr, β Dor and ℓ Car gave results for all fitting methods, while X Sgr, ζ Gem and Y Oph were limited to order 1 models. For X Sgr, the order 1 fit is less adequate than the order 0, considering the quality of our measurements of this star. This is shown by the fact that the χ^2 is significantly higher for the order 1 fit (1.36) than for the order 0 (0.38).

Table 13. Order 2. Cepheid average angular diameters and distances determined through the application of the modified BW method. The only input is the diameter variation curve $\Delta D(\phi)$ derived from the integration of the radial velocity. The distance and average angular diameter are ajusted simultaneously. The statistical and systematic errors on d are listed separately in brackets.

Star	$\overline{\theta_{\rm LD2}}$ (mas)	d_2 (pc)	χ^2_2
η Aql	$1.839 \pm 0.028_{[0.009\ 0.026]}$	$276^{+55}_{-38}\ [^{55\ 6}_{38\ 4}]$	0.43
W Sgr	$1.312 \pm 0.029_{[0.011\ 0.027]}$	$379^{+216}_{-130}\ [^{216\ 11}_{130\ 7}]$	0.48
β Dor	$1.891 \pm 0.024_{[0.014\ 0.020]}$	$345^{+175}_{-80}\ [^{175\ 5}_{80\ 2}]$	0.25
ℓ Car	$2.988 \pm 0.012_{[0.004\ 0.011]}$	$603^{+24}_{-19}\ [^{24\ 3}_{19\ 2}]$	0.49

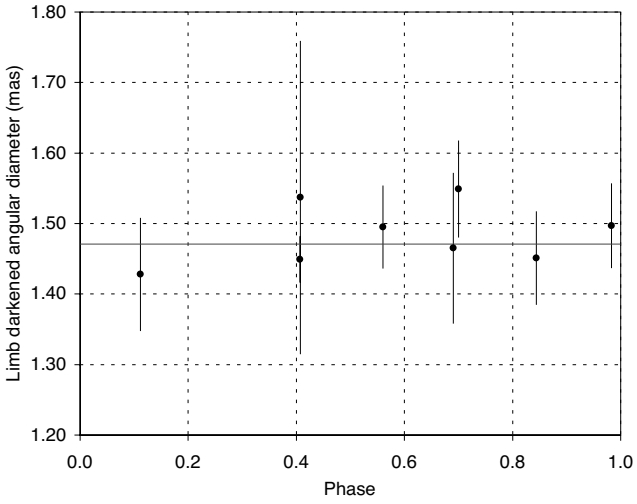

Fig. 5. Order 0 model fit for X Sgr.

In the case of ℓ Car, the fit of a constant diameter results in a very high χ^2 value. This means that the average diameters $\overline{\theta_{\rm UD0}}$ and $\overline{\theta_{\rm LD0}}$ should not be used for further analysis. The pulsation curve of this star is not sampled uniformly by our interferometric observations, with more values around the maximum diameter. This causes the larger diameter values to have more weight in the average diameter computation, and this produces a significant positive bias. This remark does not apply to the orders 1 and 2 fitting methods.

As a remark, no significant phase shift is detected at a level of 2.5×10^{-4} (14 min of time) between the predicted radius curve of ℓ Car and the observed angular diameter curve. The values of P and T_0 used for the fit are given in Table 3.

Figures 5 to 11 show the best models for each star, together with the VINCI/VLTI angular diameter measurements for the seven Cepheids of our sample. Figure 12 gives an enlarged view of the maximum diameter of ℓ Car.

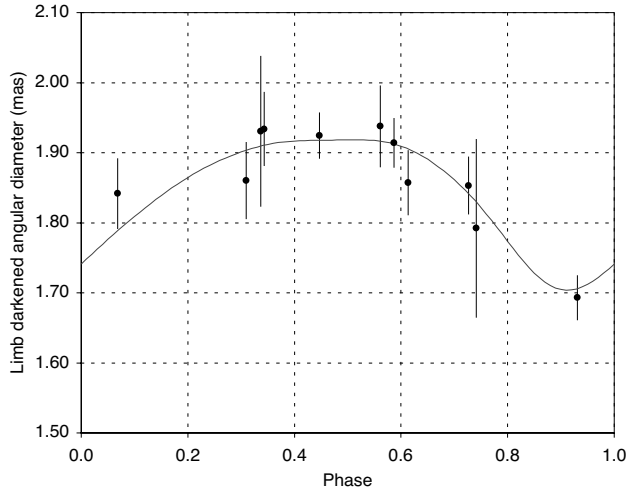

Fig. 6. Order 2 model fit for η Aql. The superimposed angular diameter variation curve (thin line) is derived from the integration of the radial velocity curve.

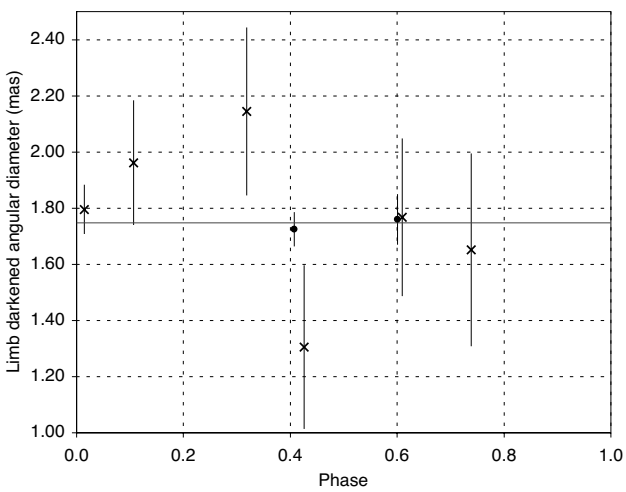

Fig. 9. Order 0 model fit for ζ Gem. The crosses represent the FLUOR/IOTA data, and the two points are UT1-UT3 observations with VINCI.

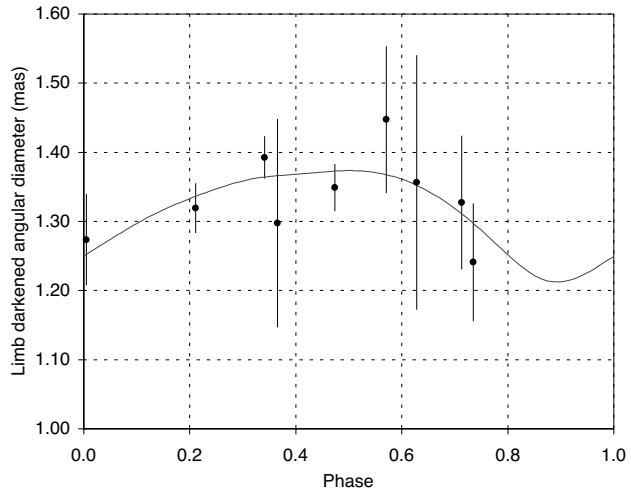

Fig. 7. Order 2 model fit for W Sgr.

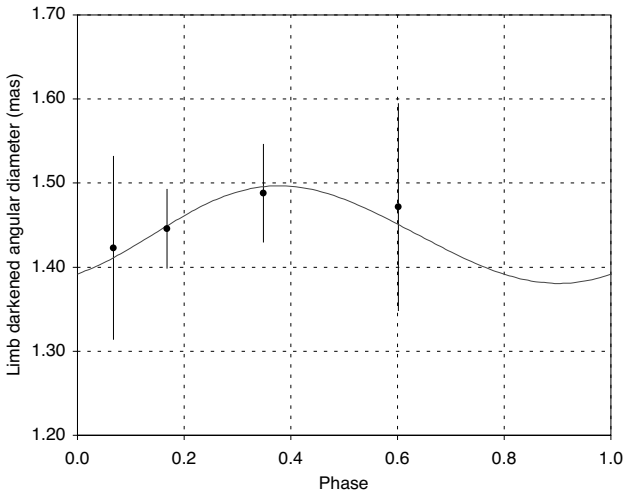

Fig. 10. Order 1 model fit for Y Oph.

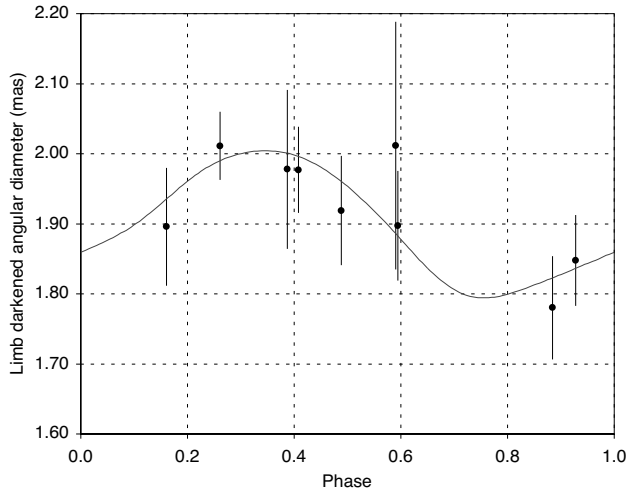

Fig. 8. Order 2 model fit for β Dor.

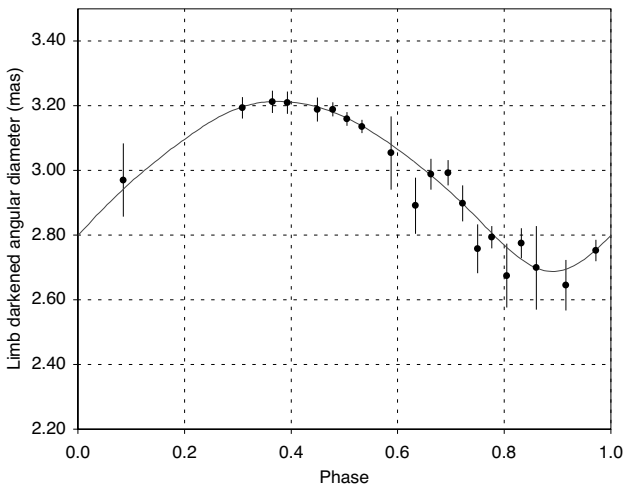

Fig. 11. Order 2 model fit for ℓ Car.

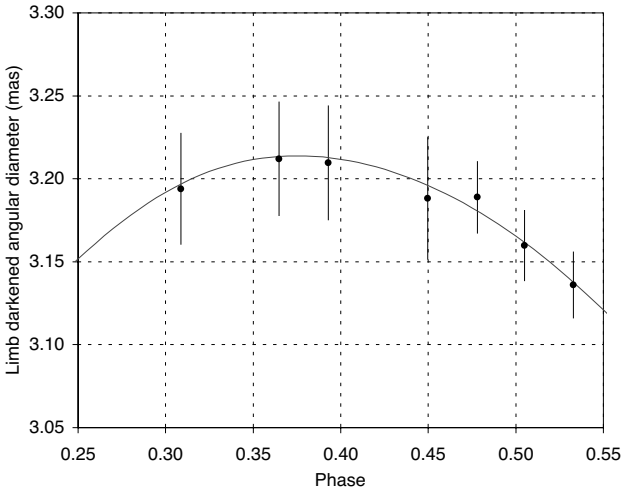

Fig. 12. Detail of Fig. 11 showing the angular diameter curve of ℓ Car around the maximum diameter.

Table 14. Average UD angular diameter of η Aql and ζ Gem from the litterature, and the associated conversion factor $\rho = \theta_{\rm LD}/\theta_{\rm UD}$ from the linear limb darkening coefficients of Claret (2000). References: (1) Armstrong et al. (2001) and Nordgren et al. (2000), (2) Lane et al. (2002), (3) this work.

Ref.	λ (μm)	$\theta_{\rm UD}$ (mas)	ρ	$\theta_{\rm LD}$ (mas)
η Aql				
(1)	0.73	1.65 ± 0.04	1.048	1.73 ± 0.04
(2)	1.65	1.73 ± 0.07	1.024	1.77 ± 0.07
(3)	2.18	1.80 ± 0.03	1.021	1.84 ± 0.03
ζ Gem				
(1)	0.73	1.48 ± 0.08	1.051	1.56 ± 0.08
(2)	1.65	1.61 ± 0.03	1.027	1.65 ± 0.03
(3)	2.18	1.70 ± 0.06	1.023	1.75 ± 0.06

9. Discussion

9.1. Limb darkening of η Aql and ζ Gem

From the NPOI (Armstrong et al. 2001; Nordgren et al. 2000), PTI (Lane et al. 2002) and VINCI/VLTI measurements, we know the average UD angular diameters of η Aql and ζ Gem at several effective wavelengths with high precision. Table 14 gives the angular diameter values and the corresponding wavelengths. Claret's (2000) linear limb darkening parameters u were used to compute the expected conversion factors $\rho = \theta_{\rm LD}/\theta_{\rm UD}$. To read the u table, we have considered the closest parameters to the average values for η Aql and ζ Gem in Table 1, and we computed ρ using the formula from Hanbury Brown et al. (1974):

$$\rho = \sqrt{\frac{1 - u/3}{1 - 7u/15}}. \quad (10)$$

For the NPOI observation ($\lambda_{\rm eff} \approx 0.73\,\mu$m), we have chosen an intermediate value of u between the R and I bands.

We note that the value of $\theta_{\rm LD}$ for η Aql that we derive for the NPOI observation, $\theta_{\rm LD} = 1.73 \pm 0.04$ mas, is not identical to the LD angular diameter originally given by Armstrong et al. (2001), $\theta_{\rm LD} = 1.69 \pm 0.04$ mas. There is a 1σ difference, that may be due to the different source of limb darkening coefficient that these authors used for their modeling (Van Hamme 1993).

The resulting $\theta_{\rm LD}$ values for the three observations are compatible at the $2\,\sigma$ level, but there is a slight trend that points towards an underestimation of the limb darkening effect at shorter wavelengths, or alternatively its overestimation at longer wavelengths. Considering that the limb darkening is already small in the infrared, the first hypothesis seems more plausible. Marengo et al. (2002, 2003) have shown that the Cepheids limb darkening can be significantly different from stable giant stars, particularly at visible wavelengths. This could explain the observed difference between the $0.73\,\mu$m and K band diameters of η Aql and ζ Gem, the latter being probably closer to the true LD diameters, thanks to the lower limb darkening in the infrared.

In the case of η Aql, another explanation could be that the measurement at visible wavelengths is biased by the blue companion of η Aql. However, it is 4.6 mag fainter than the Cepheid in the V band (Böhm-Vitense & Proffitt 1985, see also Sect. 9.2), and therefore should not contribute significantly to the visibility of the fringes.

9.2. Binarity and other effects

As demonstrated by several authors (see Szabados 2003 for a complete database), binarity and multiplicity are common in the Cepheid class. Evans (1992) has observed that 29% of the Cepheids of her sample have detectable companions.

Our sample of Cepheids contains four confirmed binary Cepheids, out of a total of seven stars. As it is biased towards bright and nearby Cepheids, this large fraction is an indication that many Cepheids currently believed to be single could have undetected companions. X Sgr (Szabados 1989b), η Aql (Böhm-Vitense & Proffitt 1985), and W Sgr (Böhm-Vitense & Proffitt 1985; Babel et al. 1989) are confirmed members of binary or multiple systems. ζ Gem is a visual binary star (Proust et al. 1981), but the separated companion does not contribute to our observations. Y Oph was once suspected to be a binary (Pel 1978), but Evans (1992) has not confirmed the companion, and has set an upper limit of A0 on its spectral type.

The physical parameters of the companions of η Aql and W Sgr have been derived by Böhm-Vitense & Proffitt (1985) and Evans (1991), based on ultraviolet spectra. The latter has derived spectral types of B9.8V and A0V, respectively. The orbital parameters of the binary W Sgr were computed by Babel et al. (1989) and Albrow & Cottrell (1996). Based on IUE spectra, Evans (1992) has set an upper limit of A0 on the spectral type of the companion of X Sgr.

The difference in V magnitude between these three Cepheids and their companions is $\Delta M_V \geq 4.5$. The ΔM_K is even larger due to the blue color of these stars, $\Delta M_K \geq 5.7$. Therefore, the effect on our visibility measurements is negligible, with a potential bias of $\Delta V^2 \leq 0.5\%$. For example, this translates into a maximum error of $\pm 11\,\mu$as on the average

angular diameter of η Aql, (a relative error of ±0.6%), that is significantly smaller than our error bars (±1.5%). In the K band, the effect of the companions of the other Cepheids is also negligible at the precision level of our measurements. However, the presence of companions will have to be considered for future measurements with angular diameter precisions of a few μas. In this respect, long-period Cepheids, such as ℓ Car, are more reliable, as their intrinsic brightness is larger than the short-period pulsators, and therefore they dominate their potential companions even more strongly.

Fernie et al. (1995b) have found that the amplitude of the light curve of Y Oph has been decreasing for a few decades. A similar behavior has been observed only on Polaris (e.g. Evans et al. 2002). The uncertainty on our $\theta_{\rm LD}$ measurements has not allowed us to detect unambiguously the pulsation of this star, but it is clearly an important target for future observations using the Auxiliary Telescopes (1.8 m) of the VLTI in order to estimate its parameters with high precision.

Interestingly, Gieren et al. (1993) have studied the impact of binary Cepheids on their determination of the period-luminosity relation using 100 Cepheids, and they conclude that it is negligible. This is due to the very large intrinsic luminosity of the Cepheids that overshine by several orders of magnitude most of the other types of stars.

10. Conclusion and perspectives

We have reported in this paper our long-baseline interferometric observations of seven classical Cepheids using the VINCI/VLTI instrument. For four stars (η Aql, W Sgr, β Dor and ℓ Car), we were able to apply a modified version of the BW method, resulting in an independent estimate of their distance. For all stars, we also derived their distances from lower order fitting methods, that use an a priori estimate of their linear diameter from the P–R relation of Gieren et al. (1998). We would like to emphasize that the order 0/1 and order 2 error bars are different in nature, and they should be treated differently in any further use of these results. While the order 2 error bars can be treated as statistical (i.e. reduced by averaging), the order 0/1 methods errors are dominated by the systematic uncertainty introduced by the a priori estimation of the linear radius. The respective contributions of the statistical and systematic uncertainties are given separately in Tables 11 and 12. These values assume a constant value of the p-factor of 1.36, and can be scaled linearly for other values.

We will use these distances in Paper II, together with previously published measurements, to calibrate the zero points of the Period-Radius and Period-Luminosity relations. In Paper III, we will calibrate the surface brightness–color relation, with a particular emphasis on the evolution of ℓ Car in this diagram over its pulsation. These three empirical relations are of critical importance for the extragalactic distance scale.

The direct measurement of the limb darkening of nearby Cepheids by interferometry is the next step of the interferometric study of these stars. It will allow a refined modeling of the atmosphere of these stars. This observation will be achieved soon using in particular the long baselines of the VLTI equipped with the AMBER instrument, and the CHARA array for the northern Cepheids. Another improvement of the interferometric BW methow will come from radial velocity measurements in the near infrared (see e.g. Butler & Bell 1997). They will avoid any differential limb darkening between the interferometric and radial velocity measurements, and therefore make the resulting distances more immune to limb darkening uncertainties.

Acknowledgements. DB acknowledges support from NSF grant AST-9979812. PK acknowledges support from the European Southern Observatory through a postdoctoral fellowship. Based on observations collected at the European Southern Observatory, Cerro Paranal, Chile, in the framework of ESO shared-risk programme 071.D-0425 and unreferenced commissioning programme in P70. The VINCI/VLTI public commissioning data reported in this paper have been retrieved from the ESO/ST-ECF Archive (Garching, Germany). This work has made use of the wavelet data processing technique, developed by D. Ségransan (Observatoire de Genève), and embedded in the VINCI pipeline. This research has made use of the SIMBAD database at CDS, Strasbourg (France). We are grateful to the ESO VLTI team, without whose efforts no observation would have been possible.

References

Albrow, M. D., & Cottrell, P. L. 1996, MNRAS, 280, 917
Andrievsky, S. M., Kovtyukh, V. V., Luck, R. E., et al. 2002, A&A, 381, 32
Armstrong, J. T., Nordgren, T. E., Germain, M. E., et al. 2001, AJ, 121, 476
Baade, W. 1926, Astron. Nachr., 228, 359
Babel, J., Burki, G., Mayor, M., et al. 1989, A&A, 216, 125
Baranne, A., Mayor, M., & Poncet, J. L. 1979, Vist. Astron., 23, 279
Barnes, T. G., III, Moffett, T. J., & Slovak, M. H. 1987, ApJS, 65, 307
Barnes, T. G., III, Fernley, J. A., Frueh, M. L., et al. 1997, PASP, 109, 645
Benedict, G. F., McArthur, B. E., Fredrick, L. W., et al. 2002, AJ, 123, 473
Berdnikov, L. N., & Turner, D. G. 2001, ApJS, 137, 209
Bersier, D., Burki, G., Mayor, M., et al. 1994, A&AS, 108, 25
Bersier, D., & Burki, G. 1996, A&A, 306, 417
Bersier, D., Burki, G., & Kurucz, R. L. 1997, A&A, 320, 228
Bersier, D. 2002, ApJS, 140, 465
Böhm-Vitense, E., & Proffitt, C. 1985, ApJ, 296, 175
Bordé, P., Coudé du Foresto, V., Chagnon, G. & Perrin, G. 2002, A&A, 393, 183
Burki, G., Mayor, M., & Benz, W. 1982, A&A, 109, 258
Butler, R. P., & Bell, R. A. 1997, ApJ, 480, 767
Cayrel de Strobel, G., Soubiran, C., Friel, E. D., Ralite, N., & Francois, P. 1997, A&AS, 124, 299
Cayrel de Strobel, G., Soubiran, C., & Ralite, N. 2001, A&A, 373, 159
Claret, A., Diaz-Cordovez, J., & Gimenez, A. 1995, A&AS, 114, 247
Claret, A. 2000, A&A, 363, 1081
Cohen, M., Walker, R. G., Carter, B., et al. 1999, AJ, 117, 1864
Coudé du Foresto, V., Ridgway, S., & Mariotti, J.-M. 1997, A&AS, 121, 379
Coudé du Foresto, V., Perrin, G., Ruilier, C., et al. 1998a, SPIE, 3350, 856
Coudé du Foresto, V. 1998b, ASP Conf. Ser., 152, 309
Coulson, I. M., & Caldwell, J. A. R. 1985, South African Astron. Observ. Circ., 9, 5

Davis, J. 1979, Proc. IAU Coll. 50 (Sydney: Davis & Tango), 1
Davis, J., Tango, W. J., & Booth, A. J. 2000, MNRAS, 318, 387
Ducati, J. R., Bevilacqua, C. M., Rembold, S. B., & Ribeiro, D. 2001, ApJ, 558, 309
Evans, N. R., & Lyons, R. 1986, AJ, 92, 436
Evans, N. R. 1991, ApJ, 372, 597
Evans, N. R. 1992, ApJ, 384, 220
Evans, N. R., Sasselov, D. D., & Short, C. I. 2002, ApJ, 567, 1121
Farge, M. 1992, Ann. Rev. Fluid Mech., 24, 395
Fernie, J. D. 1995a, AJ, 110, 3010
Fernie, J. D., Khoshnevissan, M. H., & Seager, S. 1995b, AJ, 110, 1326
Fouqué, P., Storm, J., & Gieren, W. 2003, [astro-ph/0301291], Proc. Standard Candles for the Extragalactic Distance Scale, Concepciòn, Chile, 9-11 Dec. 2002
Freedman, W., Madore, B. F., Gibson, B. K., et al. 2001, ApJ, 553, 47
Gieren, W. P., Barnes, T. G., III, & Moffett, T. J. 1993, ApJ, 418, 135
Gieren, W. P., Fouqué, P., & Gómez, M. 1998, ApJ, 496, 17
Glindemann, A., Abuter, R., Carbognani, F., et al. 2000, SPIE, 4006, 2
Groenewegen, M. A. T. 1999, A&AS, 139, 245
Hanbury Brown, R., Davis, J., Lake, R. J. W., & Thompson, R. J. 1974, MNRAS, 167, 475
Kervella, P., Coudé du Foresto, V., Glindemann, A., & Hofmann, R. 2000, SPIE, 4006, 31
Kervella, P. 2001a, Ph.D. Thesis, Université Paris 7
Kervella, P., Coudé du Foresto, V., Perrin, G., et al. 2001b, A&A, 367, 876
Kervella, P., Gitton, Ph., Ségransan, D., et al. 2003a, SPIE, 4838, 858
Kervella, P., Thévenin, F., Ségransan, D., et al. 2003b, A&A, 404, 1087
Kervella, P., Ségransan, D., & Coudé du Foresto, V. 2003c, A&A, submitted
Kiss, L. L., & Szatmàry, K. 1998, MNRAS, 300, 616
Krockenberger, M., Sasselov, D. D., & Noyes, R. W. 1997, ApJ, 479, 875
Kurucz, R. L. 1992, The Stellar Populations of Galaxies, IAU Symp., 149, 225
Lane, B. F., Kuchner, M. J., Boden, A. F., Creech-Eakman, M., & Kulkarni, S. R. 2000, Nature, 407, 485
Lane, B. F., Creech-Eakman, M., & Nordgren, T. E. 2002, ApJ, 573, 330
Laney, C. D., & Stobie, R. S. 1992, ASP Conf. Ser., 30, 119
Laney, C. D., & Stobie, R. S. 1995, MNRAS, 274, 337
Lanoix, P., Paturel, G., & Garnier, R. 1999, ApJ, 517, 188
Marengo, M., Sasselov, D. D., Karovska, M., & Papaliolios, C. 2002, ApJ, 567, 1131
Marengo, M., Karovska, M., Sasselov, D. D., et al. 2003, ApJ, 589, 968
Moffett, T. J., & Barnes, T. J., III 1984, ApJS, 55, 389
Moffett, T. J., & Barnes, T. J., III 1987, ApJ, 323, 280
Mourard, D. 1996, ESO Workshop Science with the VLTI, ed. F. Paresce (Garching)
Mourard, D., Bonneau, D., Koechlin, L., et al. 1997, A&A, 317, 789
Nordgren, T. E., Armstrong, J. T., Germain, M. E., et al. 2000, ApJ, 543, 972
Pel, J. W. 1978, A&A, 62, 75
Perryman, M. A. C., Lindegren, L., Kovalevsky, J., et al. 1997, The HIPPARCOS Catalogue, A&A, 323, 49
Petrov, R., Malbet, F., Richichi, A., et al. 2000, SPIE, 4006, 68
Proust, D., Ochsenbein, F., & Pettersen, B. R. 1981, A&AS, 44, 179
Quirrenbach, A., Mozurkewitch, D., Busher, D. F., Hummel, C. A., & Armstrong, J. T. 1996, A&A, 312, 160
Ruilier, C. 1999, Ph.D. Thesis, Université Paris 7
Sabbey, C. N., Sasselov, D. D., Fieldus, M. S., et al. 1995, ApJ, 446, 250
Sachkov, M. E., Rastorguev, A. S., Samus, N. N., & Gorynya, N. A. 1998, AstL, 24, 377
Sasselov, D. D., & Lester, J. B. 1990, ApJ, 362, 333
Sasselov, D. D., & Karovska M. 1994, ApJ, 432, 367
Ségransan, D., Forveille, T., Millan-Gabet, C. P. R., & Traub, W. A. 1999, ASP Conf. Ser., 194, 290
Ségransan, D. 2001, Ph.D. Thesis, Grenoble
Ségransan, D., et al. 2004, in preparation
Szabados, L. 1989a, Commmunications of the Konkoly Observatory Hungary, 94, 1
Szabados, L. 1989b, MNRAS, 242, 285
Szabados, L. 2003, IBVS, 5394, 1
see also http://www.konkoly.hu/CEP/intro.html
Taylor, M. M., Albrow, M. D., Booth A. J., & Cottrell, P. L. 1997, MNRAS, 292, 662
Taylor, M. M., & Booth A. J. 1998, MNRAS, 298, 594
Turner, D. G., & Burke, J. F. 2002, AJ, 124, 2931
Udalski, A., Szymański, M., Kubiak, M., Pietrzyński, et al. 1999, Acta Astron., 49, 201
Van Hamme, W. 1993, AJ, 106, 2096
Welch, D. L., Wieland, F., McAlary, C. W., et al. 1984, ApJS, 54, 547
Welch, D. L. 1994, AJ, 108, 1421
Wesselink, A. 1946, Bull. Astron. Inst. Netherlands, 10, 91
Wilson, T. D., Carter, M. W., Barnes, T. G., III, van Citters, G. W., Jr., & Moffett, T. J. 1989, ApJS, 69, 951
Wittkowski, M., Hummel, C. A., Johnston, K. J., et al. 2001, A&A, 377, 981

Table 3. VINCI/VLTI angular diameter measurements of X Sgr.

JD	Stations	Baseline (m)	Phase	θ_{UD} (mas) ± stat. ± syst.	θ_{LD} (mas) ± stat. ± syst.	N	χ^2_{red}	Calibrators
2 452 741.903	B3-M0	138.366	0.560	1.458 ± 0.048 ± 0.032	1.495 ± 0.049 ± 0.033	2	0.66	χ Sco
2 452 742.885	B3-M0	137.432	0.700	1.511 ± 0.058 ± 0.034	1.549 ± 0.059 ± 0.035	3	0.52	χ Sco
2 452 743.897	B3-M0	137.903	0.844	1.415 ± 0.055 ± 0.034	1.451 ± 0.057 ± 0.035	3	0.08	χ Sco
2 452 744.868	B3-M0	139.657	0.983	1.460 ± 0.051 ± 0.029	1.497 ± 0.052 ± 0.030	2	0.09	χ Sco
2 452 747.848	B3-M0	139.530	0.408	1.499 ± 0.213 ± 0.038	1.537 ± 0.219 ± 0.039	1	-	χ Sco
2 452 749.832	B3-M0	139.084	0.691	1.429 ± 0.099 ± 0.034	1.465 ± 0.101 ± 0.034	2	0.35	χ Sco
2 452 766.811	B3-M0	138.853	0.112	1.393 ± 0.070 ± 0.036	1.428 ± 0.071 ± 0.037	4	0.09	χ Sco
2 452 768.877	B3-M0	128.228	0.406	1.413 ± 0.016 ± 0.028	1.449 ± 0.016 ± 0.029	6	0.62	χ Sco

Table 4. Angular diameter measurements of η Aql.

JD	Stations	Baseline (m)	Phase	θ_{UD} (mas) ± stat. ± syst.	θ_{LD} (mas) ± stat. ± syst.	N	χ^2_{red}	Calibrators
2 452 524.564	E0-G1	60.664	0.741	1.746 ± 0.100 ± 0.074	1.792 ± 0.103 ± 0.076	3	0.08	70 Aql
2 452 557.546	B3-M0	137.625	0.336	1.877 ± 0.098 ± 0.037	1.931 ± 0.101 ± 0.038	1	-	ϵ Ind
2 452 559.535	B3-M0	138.353	0.614	1.806 ± 0.037 ± 0.027	1.857 ± 0.038 ± 0.027	1	-	7 Aqr, ϵ Ind
2 452 564.532	B3-M0	136.839	0.310	1.809 ± 0.043 ± 0.031	1.860 ± 0.045 ± 0.032	3	0.42	7 Aqr, ϵ Ind
2 452 565.516	B3-M0	138.495	0.447	1.871 ± 0.017 ± 0.027	1.924 ± 0.017 ± 0.028	3	0.13	7 Aqr
2 452 566.519	B3-M0	137.845	0.587	1.861 ± 0.023 ± 0.026	1.914 ± 0.024 ± 0.026	5	0.23	7 Aqr
2 452 567.523	B3-M0	137.011	0.727	1.802 ± 0.027 ± 0.030	1.853 ± 0.028 ± 0.030	2	0.62	7 Aqr
2 452 573.511	B3-M0	136.303	0.561	1.884 ± 0.053 ± 0.022	1.938 ± 0.054 ± 0.022	1	-	λ Gru, HR 8685
2 452 769.937	B3-M0	139.632	0.931	1.647 ± 0.026 ± 0.018	1.693 ± 0.026 ± 0.018	3	0.06	χ Sco
2 452 770.922	B3-M0	139.400	0.068	1.791 ± 0.041 ± 0.027	1.842 ± 0.042 ± 0.028	3	0.15	χ Sco
2 452 772.899	B3-M0	138.188	0.343	1.880 ± 0.044 ± 0.026	1.934 ± 0.046 ± 0.027	3	0.16	7 Aqr

Table 5. Angular diameter measurements of W Sgr.

JD	Stations	Baseline (m)	Phase	θ_{UD} (mas) ± stat. ± syst.	θ_{LD} (mas) ± stat. ± syst.	N	χ^2_{red}	Calibrators
2 452 743.837	B3-M0	137.574	0.571	1.408 ± 0.096 ± 0.038	1.447 ± 0.099 ± 0.039	1	-	χ Sco
2 452 744.915	B3-M0	137.166	0.713	1.292 ± 0.088 ± 0.034	1.327 ± 0.090 ± 0.035	2	0.04	χ Sco
2 452 749.868	B3-M0	139.632	0.365	1.262 ± 0.141 ± 0.040	1.297 ± 0.145 ± 0.041	1	-	χ Sco
2 452 751.866	B3-M0	139.538	0.628	1.320 ± 0.174 ± 0.041	1.357 ± 0.179 ± 0.042	1	-	χ Sco
2 452 763.888	B3-M0	131.830	0.211	1.284 ± 0.019 ± 0.029	1.319 ± 0.020 ± 0.030	4	0.73	χ Sco
2 452 764.856	B3-M0	135.926	0.339	1.355 ± 0.021 ± 0.021	1.393 ± 0.021 ± 0.022	4	0.76	χ Sco
2 452 765.880	B3-M0	132.679	0.473	1.313 ± 0.022 ± 0.025	1.349 ± 0.023 ± 0.026	4	1.43	χ Sco
2 452 767.867	B3-M0	132.637	0.735	1.208 ± 0.073 ± 0.039	1.241 ± 0.075 ± 0.040	3	0.01	χ Sco
2 452 769.914	B3-M0	120.648	0.005	1.240 ± 0.055 ± 0.034	1.274 ± 0.056 ± 0.035	2	0.33	χ Sco

Table 6. Angular diameter measurements of β Dor.

JD	Stations	Baseline (m)	Phase	θ_{UD} (mas) ± stat. ± syst.	θ_{LD} (mas) ± stat. ± syst.	N	χ^2_{red}	Calibrators
2 452 215.795	U1-U3	89.058	0.161	1.842 ± 0.036 ± 0.074	1.896 ± 0.036 ± 0.074	3	0.03	χ Phe, γ^2 Vol
2 452 216.785	U1-U3	89.651	0.261	1.954 ± 0.026 ± 0.040	2.011 ± 0.026 ± 0.040	7	0.10	γ^2 Vol
2 452 247.761	U1-U3	83.409	0.408	1.921 ± 0.045 ± 0.039	1.977 ± 0.045 ± 0.039	5	0.40	ϵ Ret
2 452 308.645	U1-U3	75.902	0.594	1.844 ± 0.027 ± 0.071	1.897 ± 0.027 ± 0.071	5	1.01	HD 63697
2 452 567.827	B3-M0	134.203	0.927	1.793 ± 0.039 ± 0.049	1.848 ± 0.039 ± 0.049	1	-	HR 2549
2 452 744.564	B3-M0	89.028	0.884	1.730 ± 0.064 ± 0.032	1.780 ± 0.064 ± 0.032	2	0.09	HR 3046, 4831
2 452 749.514	B3-M0	98.176	0.387	1.921 ± 0.106 ± 0.029	1.978 ± 0.106 ± 0.029	3	0.11	HR 3046
2 452 750.511	B3-M0	98.189	0.488	1.864 ± 0.065 ± 0.039	1.919 ± 0.065 ± 0.039	2	0.24	HR 3046
2 452 751.519	B3-M0	95.579	0.591	1.954 ± 0.169 ± 0.030	2.012 ± 0.169 ± 0.030	3	0.03	HR 3046

Table 7. VINCI/VLTI and FLUOR/IOTA angular diameter measurements of ζ Gem. No systematic calibration error is given for FLUOR/IOTA values (negligible compared to the statistical uncertainty). The baseline is given for the VINCI/VLTI observations (in m), while the spatial frequency (in *italic*) is listed for the measurements obtained with FLUOR, expressed in cycles/arcsec.

JD	Stations	B, *SF*	Phase	θ_{UD} (mas) ± stat. ± syst.	θ_{LD} (mas) ± stat. ± syst.	N	χ^2_{red}	Calibrators
2 452 214.879	U1-U3	82.423	0.408	1.677 ± 0.030 ± 0.051	1.725 ± 0.031 ± 0.052	8	0.25	39 Eri
2 452 216.836	U1-U3	72.837	0.600	1.712 ± 0.057 ± 0.067	1.760 ± 0.058 ± 0.069	6	0.28	39 Eri, γ^2 Vol
2 451 527.972	IOTA-38m	*84.870*	0.739	1.606 ± 0.334	1.651 ± 0.343	1	-	HD 49968
2 451 601.828	IOTA-38m	*83.917*	0.014	1.709 ± 0.086	1.795 ± 0.088	3	0.02	HD 49968
2 451 259.779	IOTA-38m	*83.760*	0.318	2.040 ± 0.291	2.144 ± 0.299	1	-	HD 49968
2 451 262.740	IOTA-38m	*84.015*	0.610	1.692 ± 0.273	1.767 ± 0.281	2	0.13	HD 49968
2 451 595.863	IOTA-38m	*83.790*	0.427	1.391 ± 0.284	1.306 ± 0.292	2	1.72	HD 49968
2 451 602.764	IOTA-38m	*85.010*	0.107	1.867 ± 0.216	1.962 ± 0.222	2	0.02	HD 49968

Table 8. Angular diameter measurements of Y Oph.

JD	Stations	Baseline (m)	Phase	θ_{UD} (mas) ± stat. ± syst.	θ_{LD} (mas) ± stat. ± syst.	N	χ^2_{red}	Calibrators
2 452 742.906	B3-M0	139.569	0.601	1.427 ± 0.115 ± 0.034	1.472 ± 0.119 ± 0.035	2	0.10	χ Sco
2 452 750.884	B3-M0	139.057	0.067	1.380 ± 0.100 ± 0.034	1.423 ± 0.103 ± 0.035	2	0.41	χ Sco
2 452 772.831	B3-M0	139.657	0.349	1.443 ± 0.051 ± 0.025	1.488 ± 0.053 ± 0.026	3	0.22	χ Sco
2 452 782.186	B3-M0	129.518	0.168	1.402 ± 0.027 ± 0.037	1.445 ± 0.028 ± 0.038	4	0.30	χ Sco

Table 9. Angular diameter measurements of ℓ Car.

JD	Stations	Baseline (m)	Phase	θ_{UD} (mas) ± stat. ± syst.	θ_{LD} (mas) ± stat. ± syst.	N	χ^2_{red}	Calibrators HR
2 452 453.498	E0-G1	61.069	0.587	2.958 ± 0.039 ± 0.102	3.054 ± 0.041 ± 0.105	4	0.01	4050
2 452 739.564	B3-M0	130.468	0.634	2.786 ± 0.073 ± 0.042	2.891 ± 0.076 ± 0.043	2	0.03	4526
2 452 740.569	B3-M0	128.821	0.662	2.879 ± 0.017 ± 0.042	2.989 ± 0.018 ± 0.044	7	0.77	4526
2 452 741.717	B3-M0	96.477	0.694	2.893 ± 0.025 ± 0.028	2.993 ± 0.026 ± 0.029	5	0.28	4526
2 452 742.712	B3-M0	99.848	0.722	2.801 ± 0.034 ± 0.042	2.899 ± 0.035 ± 0.043	5	0.09	4526
2 452 743.698	B3-M0	99.755	0.750	2.667 ± 0.071 ± 0.015	2.758 ± 0.074 ± 0.016	2	0.08	4831
2 452 744.634	B3-M0	114.981	0.776	2.698 ± 0.031 ± 0.012	2.794 ± 0.032 ± 0.013	6	0.73	4831
2 452 745.629	B3-M0	115.791	0.804	2.584 ± 0.094 ± 0.017	2.675 ± 0.097 ± 0.017	2	0.01	3046, 4546, 4831
2 452 746.620	B3-M0	116.828	0.832	2.679 ± 0.023 ± 0.039	2.775 ± 0.023 ± 0.040	5	0.65	3046, 4546
2 452 747.599	B3-M0	120.812	0.860	2.606 ± 0.122 ± 0.025	2.699 ± 0.127 ± 0.026	3	0.70	4546, 4831
2 452 749.576	B3-M0	124.046	0.915	2.553 ± 0.075 ± 0.011	2.645 ± 0.077 ± 0.012	4	1.18	4546
2 452 751.579	B3-M0	122.555	0.971	2.657 ± 0.027 ± 0.017	2.753 ± 0.028 ± 0.017	4	1.16	3046, 4831
2 452 755.617	B3-M0	112.185	0.085	2.867 ± 0.109 ± 0.013	2.970 ± 0.113 ± 0.013	1	-	4831
2 452 763.555	B3-M0	120.632	0.308	3.077 ± 0.008 ± 0.031	3.194 ± 0.009 ± 0.033	6	1.02	4546
2 452 765.555	B3-M0	119.629	0.365	3.094 ± 0.011 ± 0.031	3.212 ± 0.011 ± 0.033	6	1.19	4546
2 452 766.550	B3-M0	120.005	0.393	3.092 ± 0.011 ± 0.032	3.210 ± 0.011 ± 0.033	7	0.99	4546
2 452 768.566	B3-M0	115.135	0.450	3.075 ± 0.010 ± 0.034	3.188 ± 0.011 ± 0.035	7	0.46	4546
2 452 769.575	B3-M0	113.082	0.478	3.075 ± 0.018 ± 0.011	3.189 ± 0.018 ± 0.012	3	0.03	3046, 4831
2 452 770.535	B3-M0	121.152	0.505	3.044 ± 0.019 ± 0.009	3.160 ± 0.020 ± 0.009	2	0.20	3046, 4831
2 452 771.528	B3-M0	122.014	0.533	3.021 ± 0.017 ± 0.010	3.136 ± 0.017 ± 0.010	3	0.88	4831

Table 10. Published linear diameter estimates, expressed in $D_\odot$.

	X Sgr	η Aql	W Sgr	β Dor	ζ Gem	Y Oph	ℓ Car
INTERFEROMETRY							
Kervella et al. (2001b)*					63^{+35}_{-19}		
Lane et al. (2002)		61.8 ± 7.6			66.7 ± 7.2		
Nordgren et al. (2000)*		69^{+28}_{-15}			60^{+25}_{-14}		
BAADE-WESSELINK							
Bersier et al. (1997)			56.0 ± 2.9		89.5 ± 13.3		
Fouqué et al. (2003)		48.1 ± 1.1					201.7 ± 3.0
Krockenberger et al. (1997)			56.8 ± 2.3		$69.1^{+5.5}_{-4.8}$		
Laney & Stobie (1995)				63.5 ± 1.8		92.2 ± 3.2	180.1 ± 4.5
Moffett & Barnes (1987)[a]	47.8 ± 4.5	52.8 ± 3.8	60.8 ± 7.6		62.6 ± 11.5		
Moffett & Barnes (1987)[b]	49.6 ± 4.6	54.8 ± 3.9	63.1 ± 7.8		64.9 ± 11.9		
Sabbey et al. (1995)[c]	42.2 ± 4.1	62.7 ± 3.1			61.8 ± 3.5		
Sabbey et al. (1995)[d]	66.6 ± 4.9	65.8 ± 3.2			64.4 ± 3.6		
Sachkov et al. (1998)					74 ± 10		
Taylor et al. (1997)							179.2 ± 10.4
Taylor & Booth (1998)				67.8 ± 0.7			
Turner & Burke (2002)		52.6 ± 8.9		53.8 ± 1.9			
Sasselov & Lester (1990)	67 ± 6	62 ± 6					
MEAN B–W (overall σ)	52.5 (11.4)	59.9 (5.7)	57.0 (3.4)	65.8 (7.2)	65.3 (9.8)	92.2 (-)	180 (-)
EMPIRICAL P–R							
Gieren et al. (1998)	51.2 ± 2.6	52.1 ± 2.7	54.4 ± 2.9	66.0 ± 3.9	67.6 ± 4.0	100.1 ± 7.3	173.1 ± 15.8

* ζ Gem values were derived from Kervella et al. (2001b) and Nordgren et al. (2000) using the HIPPARCOS parallaxes. η Aql was taken from Nordgren et al. (2000)

[a] Assuming a constant p–factor.

[b] Assuming a variable p–factor.

[c] Bisector method.

[d] Parabolic fit method.

2.1.2 Article A&A : "II. Calibration of the period-radius and period–luminosity relations" (2004)

L'étalonnage de la relation Période–Luminosité est l'objectif principal de notre grand programme d'observations interférométriques de Céphéides. Il est prévu d'observer à terme 40 Céphéides par interférométrie (instruments VINCI, AMBER et FLUOR/CHARA) pour étalonner le point zéro de la relation P–L avec une précision de 1%. Dans cet article, je présente les premiers résultats obtenus à partir des mesures interférométriques existantes, notamment celles obtenues avec l'instrument VINCI (article reproduit à la Sect. 2.1.1). Je présente également un étalonnage original de la relation Période-Rayon, qui est d'une grande importance pour contraindre les modèles numériques de pulsation.

FIG. 2.5 – Les télescopes UT1, UT2 et UT3 du VLT, vers l'Ouest.

A&A 423, 327–333 (2004)
DOI: 10.1051/0004-6361:20035596

Astronomy & Astrophysics

Cepheid distances from infrared long-baseline interferometry

II. Calibration of the period–radius and period–luminosity relations

P. Kervella[1,2], D. Bersier[3], D. Mourard[4], N. Nardetto[4], and V. Coudé du Foresto[1]

[1] LESIA, UMR 8109, Observatoire de Paris-Meudon, 5 place Jules Janssen, 92195 Meudon Cedex, France
e-mail: pierre.kervella@obspm.fr
[2] European Southern Observatory, Alonso de Cordova 3107, Casilla 19001, Vitacura, Santiago 19, Chile
[3] Space Telescope Science Institute, 3700 San Martin Drive, Baltimore, MD 21218, USA
[4] Observatoire de la Côte d'Azur, Département GEMINI, UMR 6203, BP 4229, 06304 Nice Cedex 4, France

Received 29 October 2003 / Accepted 4 May 2004

Abstract. Using our interferometric angular diameter measurements of seven classical Cepheids reported in Kervella et al. (2004, A&A, 416, 941 – Paper I), complemented by previously existing measurements, we derive new calibrations of the Cepheid period–radius (P–R) and period–luminosity (P–L) relations. We obtain a P–R relation of $\log R = [0.767 \pm 0.009]\ \log P + [1.091 \pm 0.011]$, only 1 σ away from the relation obtained by Gieren et al. (1998, ApJ, 496, 17). We therefore confirm their P–R relation at a level of $\Delta(\log R) = \pm 0.02$. We also derive an original calibration of the P–L relation, assuming the slopes derived by Gieren et al. (1998) from LMC Cepheids, $\alpha_K = -3.267 \pm 0.042$ and $\alpha_V = -2.769 \pm 0.073$. With a P–L relation of the form $M_\lambda = \alpha_\lambda (\log P - 1) + \beta_\lambda$, we obtain $\log P = 1$ reference points of $\beta_K = -5.904 \pm 0.063$ and $\beta_V = -4.209 \pm 0.075$. Our calibration in the V band is statistically identical to the geometrical result of Lanoix et al. (1999, MNRAS, 308, 969).

Key words. stars: variables: Cepheids – cosmology: distance scale – stars: oscillations – techniques: interferometric

1. Introduction

The period–luminosity (P–L) relation of the Cepheids is the basis of the extragalactic distance scale, but its calibration is still uncertain at a $\Delta M = \pm 0.10$ mag level. Moreover, it is not excluded that a significant bias of the same order of magnitude affects our current calibration of this relation. On the other hand, the period–radius relation (P–R) is an important constraint to the Cepheid models (see e.g. Alibert et al. 1999).

Traditionally, there have been two ways to calibrate the P–L relation. For Cepheids in clusters one can use main sequence fitting, assuming that the main sequence is similar to that of the Pleiades. This method has been questioned however, following the release of Hipparcos data (e.g., Pinsonneault et al. 1998; but see also Pan et al. 2004; Robichon et al. 1999). Another route to the P–L relation is the Baade-Wesselink (BW) method where one combines photometry and radial velocity data to obtain the distance and radius of a Cepheid. Recent applications of the BW method to individual stars can be found for instance in Taylor et al. (1997) and Taylor & Booth (1998), while the calibration of the P–R and P–L relations using BW distances and radii is demonstrated in Gieren et al. (1998, hereafter GFG98). A requirement of this method is a very accurate measurement of the Cepheid's effective temperature at all observed phases, in order to determine the angular diameter. Interferometry allows us to bypass this step and its associated uncertainties by measuring *directly* the variation of angular diameter during the pulsation cycle. As shown by Kervella et al. (2004, hereafter Paper I) and Lane et al. (2002), the latest generation of long baseline visible and infrared interferometers have the potential to provide precise distances to Cepheids up to about 1 kpc, using the interferometric BW method (see Sect. 2).

The main goal of the present paper is to explore the application of this technique to the calibration of the P–R and P–L relations, and to verify that no large bias is present in the previously published calibrations of these important relations. Our sample is currently too limited to allow a robust determination of the P–L relation, defined as $M_\lambda = \alpha_\lambda(\log P - 1) + \beta_\lambda$, that would include both the slope α_λ and the $\log P = 1$ reference point β_λ. However, if we suppose that the slope is known a priori from the literature, we can derive a precise calibration of β_λ. In Sect. 3, we present our determination of the P–R relation using new angular diameter values from Paper I, as well as previously published interferometric and trigonometric parallax measurements. Section 4 is dedicated to the calibration of the P–L relation reference points β_λ in the K and V bands. The consequences for the LMC distance are briefly discussed in Sect. 4.5.

2. Cepheid distances by interferometry

We have obtained angular diameter measurements for seven Cepheids with the VLT interferometer (Kervella et al. 2004, Paper I). These K-band measurements were made with the

VINCI instrument (Kervella et al. 2003) fed by two 0.35 m siderostats. Several baselines were used, ranging from 60 m to 140 m. Our measurements, described in detail in Paper I, have a typical precision of 1 to 3%. This is good enough to actually *resolve* the pulsation of several Cepheids; in other words we can follow the change in angular diameter. We have combined these measurements with radial velocity data and derived a radius and distance for four Cepheids of our sample. For the remaining three stars, we were able to derive their mean angular diameters, but the pulsation remained below our detection threshold. This sample was completed by previously published measurements obtained with other instruments.

In the present work, we have retained the limb darkened (LD) angular diameters $\theta_{\rm LD}$ provided by each author. Marengo et al. (2002, 2003) have shown that the LD properties of Cepheids can be different from those of stable stars, in particular at visible wavelengths. For the measurements obtained using the GI2T (Mourard et al. 1997) and NPOI (Nordgren et al. 2000), the LD correction is relatively large ($k = \theta_{\rm LD}/\theta_{\rm UD} \simeq 1.05$), and this could be the source of a bias at a level of a 1 to 2% (Marengo et al. 2004). However, in the infrared, the correction is much smaller ($k \simeq 1.02$), and the error on its absolute value is expected to be significantly below 1%. The majority of the Cepheid interferometric measurements was obtained in the H and K bands (FLUOR/IOTA, PTI, VLTI/VINCI), and we believe that the potential bias introduced on our fits is significantly smaller than their stated error bars. The final answer about the question of the limb darkening of Cepheids will come from direct interferometric observations, that will soon be possible with the AMBER instrument (Petrov et al. 2000) of the VLTI.

The radial velocity data were taken from Bersier (2002). They have been obtained with the CORAVEL spectrograph (Baranne et al. 1979). This instrument performs a cross-correlation of the blue part of a star's spectrum (3600−5200 Å) with the spectrum of a red giant. A Gaussian function is then fitted to the resulting cross-correlation function, yielding the radial velocity.

In Paper I, we have applied three distinct methods (orders 0, 1 and 2) to derive the distances d to seven Galactic Cepheids from interferometric angular diameter measurements. Not all three methods can be used to derive the distance for every star, depending on the level of completeness and precision of the available angular diameter measurements:

- **Order 0:** constant diameter model.
  This is the most basic method, used when the pulsation of the star is not detected. The average linear diameter $\overline{D}$ of the star is supposed to be constant and known a priori, e.g. from a previously published P–R relations (such as the relation derived by GFG98). Knowing the linear and angular radii, the only remaining variable to fit is the distance d.
- **Order 1:** variable diameter model.
  We still consider that the average linear diameter of the star is known a priori, but we include in our angular diameter model the radius variation curve derived from the integration of the radial velocity of the star. This method is well suited when the intrinsic accuracy of the angular diameter measurements is too low to measure precisely the pulsation amplitude. The distance d is the only free parameter for the fit.
- **Order 2:** interferometric BW method.
  The interferometric variant of the BW method (Davis 1979; Sasselov et al. 1994) combines the angular amplitude of the pulsation measured by interferometry and the linear displacement of the stellar photosphere deduced from the integration of the radial velocity curve to retrieve the distance of the star geometrically. This method is also called "parallax of the pulsation". In the fitting process, the radius curve is matched to the observed angular diameter curve, using both the distance and linear diameter as variables. Apart from direct trigonometric parallax, this method is the most direct way of measuring the distance of a Cepheid. It requires a high precision angular diameter curve and a good phase coverage.

The order 0/1 methods, on one hand, and 2 on the other hand, are fundamentally different in their assumptions, and the distance estimates are affected by different kinds of errors. While the order 2 method errors are due to the interferometric measurement uncertainties (mostly statistical), the order 0/1 distances carry the systematic error bars of the assumed P–R relation. As they are fully correlated for all stars in the sample, they cannot be averaged over the sample. In particular, the order 0/1 diameters cannot be used to calibrate the P–R relation, as they assume this relation to be known a priori.

Due to its stringent requirements in terms of precision, the interferometric BW method (order 2) was applied successfully up to now to five Cepheids only: ℓ Car (Paper I), β Dor (Paper I), η Aql (Paper I; Lane et al. 2002), W Sgr (Paper I) and ζ Gem (Lane et al. 2002). However, it is expected that many more stars will be measurable with the required precision in the near future (see Sect. 5).

3. Period–radius relation

3.1. Method

The period–radius relation (P–R) of the Cepheids takes the form of the linear expression:

$$\log R = a \log P + b. \quad (1)$$

In order to calibrate this relation, we need to estimate directly the linear radii of a set of Cepheids. We have applied two methods to determine the radii of the Cepheids of our sample: the interferometric BW method, and a combination of the average angular diameter and trigonometric parallax. While the first provides directly the average linear radius and distance, we need to use trigonometric parallaxes to derive the radii of the Cepheids for which the pulsation is not detected. We applied the Hipparcos parallaxes (Perryman et al. 1997) to all the order 0/1 measurements, except δ Cep, for which we considered the recent measurement by Benedict et al. (2002). Table 1 lists the Cepheid linear radii that we obtain.

Table 1. Weighted averages of the interferometric mean angular diameters $\overline{\theta_{\rm LD}}$ and of the geometric distances d to nearby Cepheids (bold characters). These values were used to compute the linear radii given in the last two columns. The individual measurements used in the averaging process are also given separately for each star. References: (1) Mourard et al. (1997); (2) Nordgren et al. (2000); (3) Lane et al. (2002); (4) Mozurkewich et al. (1991); (5) Paper I; (6) Benedict et al. (2002); (7) Perryman et al. (1997).

Star	P (d)	$\log P$	Ref. $\theta_{\rm LD}$	$\overline{\theta_{\rm LD}}$ (mas)	Ref. d	d (pc)	$R\,(R_\odot)$	$\log R$
δ Cep	5.3663	0.7297		$\mathbf{1.521 \pm 0.010}$		$\mathbf{274^{+12}_{-11}}$	$\mathbf{44.8^{+1.9}_{-1.8}}$	$\mathbf{1.651^{+0.018}_{-0.018}}$
			(1)	1.60 ± 0.12				
			(2)	1.52 ± 0.01				
					(6)	273^{+12}_{-11}		
					(7)	301^{+64}_{-45}		
X Sgr	7.0131	0.8459		$\mathbf{1.471 \pm 0.033}$		$\mathbf{330^{+148}_{-78}}$	$\mathbf{52.2^{+23}_{-12}}$	$\mathbf{1.717^{+0.161}_{-0.118}}$
			(5)	1.471 ± 0.033				
					(7)	330^{+148}_{-78}		
η Aql	7.1768	0.8559		$\mathbf{1.791 \pm 0.022}$		$\mathbf{308^{+27}_{-24}}$	$\mathbf{59.3^{+5.3}_{-4.6}}$	$\mathbf{1.773^{+0.037}_{-0.035}}$
			(2)	1.69 ± 0.04				
			(3)	1.793 ± 0.070	(3)	320^{+32}_{-32}		
			(5)	1.839 ± 0.028	(5)	276^{+55}_{-38}		
					(7)	360^{+175}_{-89}		
W Sgr	7.5949	0.8805		$\mathbf{1.312 \pm 0.029}$		$\mathbf{400^{+210}_{-114}}$	$\mathbf{56.4^{+30}_{-16}}$	$\mathbf{1.751^{+0.184}_{-0.146}}$
			(5)	1.312 ± 0.029	(5)	379^{+216}_{-130}		
					(7)	637^{+926}_{-237}		
β Dor	9.8424	0.9931		$\mathbf{1.884 \pm 0.024}$		$\mathbf{323^{+68}_{-42}}$	$\mathbf{65.4^{+14}_{-8.6}}$	$\mathbf{1.816^{+0.083}_{-0.061}}$
			(5)	1.884 ± 0.024	(5)	345^{+175}_{-80}		
					(7)	318^{+74}_{-50}		
ζ Gem	10.1501	1.0065		$\mathbf{1.688 \pm 0.022}$		$\mathbf{362^{+37}_{-34}}$	$\mathbf{65.6^{+6.7}_{-6.3}}$	$\mathbf{1.817^{+0.042}_{-0.044}}$
			(2)	1.55 ± 0.09				
			(3)	1.675 ± 0.029	(3)	362^{+38}_{-38}		
			(4)	1.73 ± 0.05				
			(5)	1.747 ± 0.061				
					(7)	358^{+147}_{-81}		
Y Oph	17.1269	1.2337		$\mathbf{1.438 \pm 0.051}$		$\mathbf{877^{+2100}_{-360}}$	$\mathbf{136^{+325}_{-56}}$	$\mathbf{2.132^{+0.531}_{-0.231}}$
			(5)	1.438 ± 0.051				
					(7)	877^{+2100}_{-360}		
ℓ Car	35.5513	1.5509		$\mathbf{2.988 \pm 0.012}$		$\mathbf{597^{+24}_{-19}}$	$\mathbf{191.2^{+7.6}_{-6.0}}$	$\mathbf{2.281^{+0.017}_{-0.014}}$
			(5)	2.988 ± 0.012	(5)	603^{+24}_{-19}		
					(7)	463^{+129}_{-83}		

We can use the results from both order 0/1 and 2 methods at the same time, as the obtained linear radii obtained in this way are fully independent on each other. On one hand (BW method), we obtain them considering the *amplitude* of the pulsation and the radial velocity curve, while on the other hand, they are derived from the *average* angular diameter and the trigonometric parallax. As the amplitude of the pulsation and the average diameter values are distinct observables, these two methods can be used simultaneously in the fit.

3.2. Calibration results

Figure 1 shows the distribution of the measured diameters on the P–R diagram, based on the values listed in Table 1. When we choose to consider a constant slope of $a = 0.750 \pm 0.024$, as found by GFG98, we derive a zero point of $b = 1.105 \pm 0.017 \pm 0.023$ (statistical and systematic errors). As a comparison, GFG98 have obtained a value of $b = 1.075 \pm 0.007$, only $-1.6\,\sigma$ away from our result. The relations found by Turner & Burke (2002) and Laney & Stobie (1995) are very similar to GFG98, and are also compatible with our calibration within their error bars.

Fitting simultaneously both the slope and the zero point to our data set, we obtain $a = 0.767 \pm 0.009$ and $b = 1.091 \pm 0.011$. These values are only $\Delta a = +0.7\,\sigma$ and $\Delta b = +1.2\,\sigma$ away from the GFG98 calibration. Considering the limited size of our sample, the agreement is very satisfactory. On the other hand, the slopes derived by Ripepi et al. (1997) and

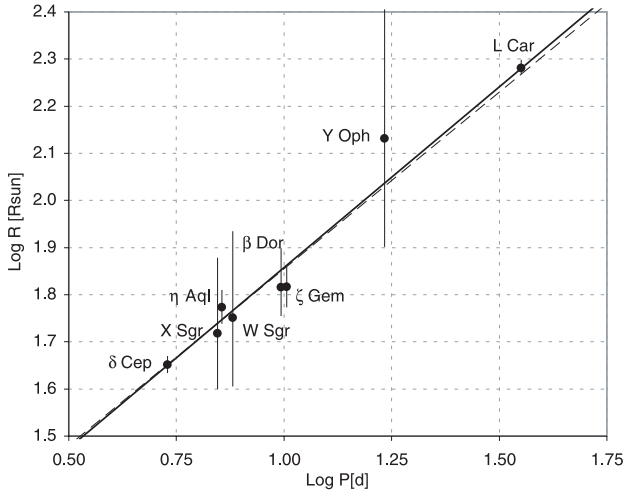

Fig. 1. Period–radius diagram deduced from the interferometric observations of Cepheids listed in Table 1. The thin dashed line represents the best-fit P–R relation assuming the slope of GFG98, $\log R = 0.750$ [±0.024] $\log P + 1.105$ [±0.017 ± 0.023]. The solid line is the best-fit relation allowing both the slope and zero point to vary, $\log R = 0.767$ [±0.009] $\log P + 1.091$ [±0.011].

Table 2. Period–radius relations, assuming an expression of the form $\log R = a \log P + b$. For the fitting of b alone, the slope has been assumed as known a priori from GFG98. In this case, its error bar translates to a systematic uncertainty on the b value derived from the fit (given in brackets). References: (1) GFG98; (2) Turner & Burke (2002); (3) This work.

Ref.	Fit	$a \pm \sigma_{\rm stat}$	$b \pm \sigma_{\rm stat}$ [$\pm\sigma_{\rm syst}$]
(1)		0.750 ± 0.024	1.075 ± 0.007
(2)		0.747 ± 0.028	1.071 ± 0.025
(3)	b only		**1.105 ± 0.017** [±**0.023**]
(3)	a, b	**0.767 ± 0.009**	**1.091 ± 0.011**

Krockenberger et al. (1997), both around 0.60, seem to be significantly too shallow.

4. Period–luminosity relation

4.1. Distance estimates

For the order 0 and 1 methods (Paper I), we used an a priori P–R relation (from GFG98) to predict the true linear diameter of the Cepheids of our sample. This relation relies on the measurement of the photometric flux, effective temperature (classical BW method) and radial velocity. The apparent magnitude also intervenes in the computation of the absolute magnitude, and therefore we cannot use these distance estimates to calibrate the P–L relation without creating a circular reference. For this reason, we have considered only the distances obtained using the interferometric BW method (order 2) for our P–L relation calibration, complemented by the Benedict et al. (2002) trigonometric parallax of δ Cep.

Table 3. Apparent magnitudes and extinctions in the K and V bands for the Cepheid whose distances have been measured directly by interferometry. $(B-V)_0$ is the mean $(B-V)$ index as reported in the online database by Fernie et al. (1995). The E_{B-V} values were taken from Fernie (1990). The extinctions in the K and V bands are given respectively in the "A_K" and "A_V" columns, in magnitudes.

Star	$(B-V)_0$	E_{B-V}	m_K	A_K	m_V	A_V
δ Cep	0.66	0.09	2.31	0.03	3.99	0.30
η Aql	0.79	0.15	1.97	0.04	3.94	0.49
W Sgr	0.75	0.11	2.82	0.03	4.70	0.36
β Dor	0.81	0.04	1.96	0.01	3.73	0.15
ζ Gem	0.80	0.02	2.11	0.01	3.93	0.06
ℓ Car	1.30	0.17	1.09	0.05	3.77	0.58

Table 4. Absolute magnitudes of Cepheids measured exclusively using the interferometric Baade-Wesselink method, except for δ Cep, whose parallax was taken from Benedict et al. (2002). The same error bars apply to the K and V band absolute magnitudes. The Cepheid periods are listed in Table 1. References: (1) Lane et al. (2002); (2) Benedict et al. (2002); (3) Paper I.

Star	Ref.	d	$\pm\sigma$	M_K	M_V	$\pm\sigma$
δ Cep	(2)	273	$^{+12}_{-11}$	–4.90	–3.49	$^{+0.09}_{-0.09}$
η Aql	(1)	320	$^{+32}_{-32}$	–5.60	–4.08	$^{+0.23}_{-0.21}$
η Aql	(3)	276	$^{+55}_{-38}$	–5.28	–3.76	$^{+0.32}_{-0.39}$
W Sgr	(3)	379	$^{+216}_{-130}$	–5.10	–3.56	$^{+0.91}_{-0.98}$
β Dor	(3)	345	$^{+175}_{-80}$	–5.74	–4.10	$^{+0.57}_{-0.89}$
ζ Gem	(1)	362	$^{+38}_{-38}$	–5.69	–3.92	$^{+0.24}_{-0.22}$
ℓ Car	(3)	603	$^{+24}_{-19}$	–7.86	–5.72	$^{+0.07}_{-0.08}$

4.2. Absolute magnitudes

The average apparent magnitudes in V and K of δ Cep were computed via a Fourier series fit of the data from Moffett & Barnes (1984) and Barnes et al. (1997) for the K band and Barnes et al. (1997) for the V band. The sources for the other apparent magnitudes are given in Paper I (Table 1). Following Fouqué et al. (2003), the extinction A_λ has been computed using the relations:

$$A_\lambda = R_\lambda \, E_{B-V} \tag{2}$$

$$R_V = 3.07 + 0.28\,(B-V)_0 + 0.04\,E_{B-V} \tag{3}$$

$$R_K = R_V/11 \simeq 0.279. \tag{4}$$

The resulting extinction values are listed in Table 3, and the final absolute magnitudes M_λ of the Cepheids of our sample are listed in Table 4.

4.3. Calibration of the P–L relation

We have considered for our fit the P–L slope measured on LMC Cepheids. This is a reasonable assumption, as it can be measured precisely on the Magellanic Clouds Cepheids, and in addition our sample is currently too limited to derive both the slope and the $\log P = 1$ reference point simultaneously.

Table 5. Period–luminosity relation intercept β_K for a 10 days period Cepheid ($\log P = 1$), in the K band. We assume an expression of the form $M_K = \alpha_K (\log P - 1) + \beta_K$. The slope value is taken from GFG98 ($\alpha_K = -3.267 \pm 0.042$). The systematic error corresponds to the uncertainty on the GFG98 slope.

Ref.	β_K	$\pm\sigma_{\rm stat}$	$\pm\sigma_{\rm syst}$
GFG98	−5.701	±0.025	
This work, all stars	**−5.904**	**±0.063**	**±0.005**
Without δ Cep and ℓ Car	−5.956	±0.191	±0.006

Table 6. Period–luminosity relation intercept β_V ($\log P = 1$) in the V band, derived using the GFG98 slope ($\alpha_V = -2.769 \pm 0.073$).

	β_V	$\pm\sigma_{\rm stat}$	$\pm\sigma_{\rm syst}$
GFG98	−4.063	±0.034	
LPG99	−4.21	±0.05	
This work, all stars	**−4.209**	**±0.075**	**±0.001**
Without δ Cep and ℓ Car	−4.358	±0.197	±0.010

Recently, Fouqué et al. (2003) have revised the P–L slopes derived from the large OGLE2 survey (Udalski et al. 1999), and obtain values of $\alpha_V = -2.774 \pm 0.042$ and $\alpha_K = -3.215 \pm 0.037$. These values are consistent within their error bars with LPG99 ($\alpha_V = -2.77 \pm 0.08$), GFG98 ($\alpha_V = -2.769 \pm 0.073$, $\alpha_K = -3.267 \pm 0.042$) and Sasselov et al. (1997; $\alpha_V = -2.78 \pm 0.16$). Considering this consensus, we have chosen to use the slope from GFG98 to keep the consistence with the P–R relation assumed in Paper I.

Tables 5 and 6 report the results of our calibrations of the P–L relations, and the positions of the Cepheids on the P–L diagram are shown in Figs. 2 and 3. The final $\log P = 1$ reference points are given in bold characters in Tables 5 and 6. Our calibrations differ from GFG98 by $\Delta b_K = +0.20$ mag in the K band, and $\Delta b_V = +0.14$ mag in V, corresponding to +3.0 and $+1.8\,\sigma$, respectively. The sample is dominated by the high precision ℓ Car and δ Cep measurements. When these two stars are removed from the fit, the difference with GFG98 is slightly increased, up to +0.25 and +0.30 mag, though the distance in σ units is reduced (+1.3 and +1.5). From this agreement, ℓ Car and δ Cep do not appear to be systematically different from the other Cepheids of our sample.

It is difficult about conclude firmly to a significant discrepancy between GFG98 and our results, as our sample is currently too limited to exclude a small-statistics bias. However, if we assume an intrinsic dispersion of the P–L relation $\sigma_{\rm PL} \simeq 0.1$ mag, as suggested by GFG98, then our results point toward a slight underestimation of the absolute magnitudes of Cepheids by these authors. On the other hand, we obtain precisely the same $\log P = 1$ reference point value in V as Lanoix et al. (1999, using parallaxes from Hipparcos). The excellent agreement between these two fully independent, geometrical calibrations of the P–L relation is remarkable.

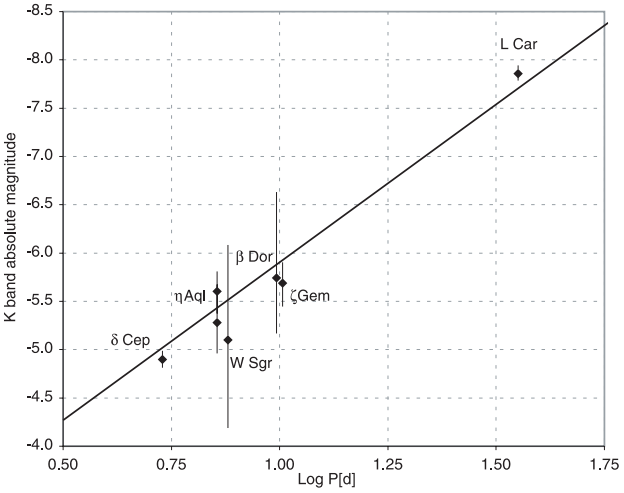

Fig. 2. Period–luminosity diagram in the K band using only interferometric BW distances and the δ Cep parallax listed in Table 4. The solid line represents the best-fit P–L relation using the slope derived by GFG98 (classical least-squares fit: the individual measurements are weighted by the inverse of their variance).

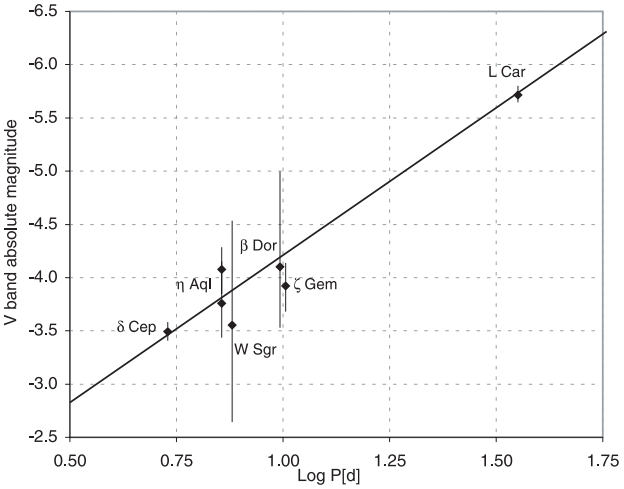

Fig. 3. Period–luminosity diagram in the V band (slope from GFG98).

4.4. P–L relation slopes in the Galaxy and in the LMC

The question of the difference in slope between the Galactic and LMC Cepheid P–L relations has recently been discussed by Fouqué et al. (2003) and Tammann et al. (2003). These authors conclude that the Galactic slopes are significantly steeper than their LMC counterparts. For example, Tamman et al. (2003) obtain α_V[Gal] $= -3.14 \pm 0.10$, while Fouqué et al. (2003) derive α_V[Gal] $= -3.06 \pm 0.11$ and α_V[LMC] $= -2.774 \pm 0.042$.

However, our fit is largely insensitive to the precise value assumed for the P–L relation slope. Considering the steeper Tammann et al. (2003) slope, we obtain a best fit $\log P = 1$ absolute magnitude of $\beta_V = -4.211 \pm 0.075 \pm 0.001$, identical to the calibration obtained using the GFG98 slope. The small systematic error bar that we obtain on β_V (corresponding to the ±0.10 error on α_V) shows the weakness of the correlation between α and β in our fit. However, the reduced χ^2 of the fit

is significantly larger with this steeper slope ($\chi^2_{\rm red} = 1.25$) than with the LMC slope from GFG98 ($\chi^2_{\rm red} = 0.53$).

4.5. The distance to the LMC

The apparent magnitudes in V and K of a 10 day period Cepheid in the Large Magellanic Cloud (LMC) derived by Fouqué et al. (2003) from the OGLE Cepheids are $\mathrm{ZP}_K = 12.806 \pm 0.026$ and $\mathrm{ZP}_V = 14.453 \pm 0.029$. These authors assumed in their computation a constant reddening of $E(B-V) = 0.10$ for all the LMC Cepheids they have used (more than 600). Our calibrations of the Galactic Cepheids P–L relations in K and V thus implies LMC distance moduli of $\mu_K = 18.71 \pm 0.07$ and $\mu_V = 18.66 \pm 0.08$, respectively.

From a large number of photometric measurements of LMC and SMC Cepheids obtained in the framework of the EROS programme, Sasselov et al. (1997) have shown that a $\delta\mu$ correction has to be applied to the LMC distance modulus to account for the difference in metallicity between the LMC and the Galactic Cepheids. They have determined empirically a value of:

$$\delta\mu = \mu_{\rm true} - \mu_{\rm observed} = -0.14 \pm 0.06 \quad (5)$$

this correction has been questioned by Udalski et al. (2001), based on Cepheid observations in a low metallicity galaxy (IC 1613), and its amplitude is still under discussion (Fouqué et al. 2003).

Averaging our K and V band zero point values (without reducing the uncertainty, that is systematic in nature), we obtain a final LMC distance modulus of $\mu_0 = 18.55 \pm 0.10$. This value is only $+0.8\,\sigma$ away from the $\mu_0 = 18.46 \pm 0.06$ value obtained by GFG98, and $-1\,\sigma$ from the $\mu_0 = 18.70 \pm 0.10$ value derived of Feast & Catchpole (1997). It is statistically identical to the LMC distance used by Freedman et al. (2001) for the *HST Key Project*, $\mu_0 = 18.50 \pm 0.10$. Alternatively, if we consider the smaller metallicity correction of $\delta\mu = 0.06 \pm 0.10$.

5. Conclusion and perspectives

We have confirmed in this paper the P–R relation of GFG98 and Turner & Burke (2002), to a precision of $\Delta(\log R) = \pm 0.02$. We also derived an original calibration of the P–L relations in K and V, assuming the slopes from GFG98 that were established using LMC Cepheids. Our P–L relation calibration yields a distance modulus of $\mu_0 = 18.55 \pm 0.10$ for the LMC, that is statistically identical to the value used by Freedman et al. (2001) for the *HST Key Project*. We would like to emphasize that this result, though encouraging, is based on six stars only (seven measurements, dominated by two stars), and our sample needs to be extended in order to exclude a small-number statistical bias. In this sense, the P–L calibration presented here should be considered as an intermediate step toward a final and robust determination of this important relation by interferometry.

While our results are very encouraging, the calibration of the PR and PL relations as described here may still be affected by small systematic errors. In particular the method relies on the fact that the displacements measured through interferometry and through spectroscopy (integration of the radial velocity curve) are in different units (milli-arcseconds and kilometers respectively) but are the same physical quantity. This may not be the case. The regions of a Cepheid's atmosphere where the lines are formed do not necessarily move homologously with the region where the K-band continuum is formed. This means that the two diameter curves may not have exactly the same amplitude; there could even be a phase shift between them. As discussed in Sect. 2, the limb darkening could also play a role at a level of $\simeq$1%. A full exploration of these effects is far beyond the scope of this paper. We can nevertheless put an upper bound on the systematic error that could result from this mismatch. Our PL relation can be compared to that derived from Cepheids in open clusters, whose distances are obtained via main sequence fitting. The two distance scales are in excellent agreement (Gieren & Fouqué 1993; Turner & Burke 2002). These distances are consistent with a Pleiades distance modulus of 5.56; if anything they are slightly larger.

The availability of 1.8 m Auxiliary Telescopes (Koehler et al. 2002) on the VLTI platform in 2004, to replace the current 0.35 m Test Siderostats, will allow to observe many Cepheids with a precision at least as good as the observations of ℓ Car reported in Paper I (angular diameters accurate to 1%). In addition, the AMBER instrument (Petrov et al. 2000) will extend the VLTI capabilities toward shorter wavelengths (J and H bands), thus providing higher spatial resolution than VINCI (K band). The combination of these two improvements will extend significantly the accessible sample of Cepheids, and we expect that the distances to more than 30 Cepheids will be measurable with a precision better than ±5%. This will provide a high precision calibration of both the $\log P = 1$ reference point (down to ±0.01 mag) and the slope of the Galactic Cepheid P–L. As the galaxies hosting the Cepheids used in the *Key Project* are close to solar metallicity on average (Feast 2001), this Galactic calibration will allow us to bypass the LMC step in the extragalactic distance scale. Its attached uncertainty of ±0.06 due to the metallicity correction of the LMC Cepheids will therefore become irrelevant for the measurement of H_0.

Acknowledgements. D.B. acknowledges partial support from NSF grant AST-9979812. P.K. acknowledges support from the European Southern Observatory through a post-doctoral fellowship. Based on observations collected at the VLT Interferometer, Cerro Paranal, Chile, in the framework of the ESO shared-risk programme 071.D-0425 and an unreferenced programme in P70. The VINCI/VLTI public commissioning data reported in this paper have been retrieved from the ESO/ST-ECF Archive (Garching, Germany). This research has made use of the SIMBAD database at CDS, Strasbourg (France). We are grateful to the ESO VLTI team, without whose efforts no observation would have been possible.

References

Alibert, Y., Baraffe, I., Hauschildt, P., & Allard, F. 1999, A&A, 344, 551
Baranne, A., Mayor, M., & Poncet, J. L. 1979, Vist. Astron., 23, 279
Barnes, T. G., III, Fernley, J. A., Frueh, M. L., et al. 1997, PASP, 109, 645
Benedict, G. F., McArthur, B. E., Fredrick, L. W., et al. 2002, AJ, 124, 1695

Bersier, D. 2002, ApJS, 140, 465
Claret, A. 2000, A&A, 363, 1081
Davis, J. 1979, Proc. IAU Coll. 50, ed. J. Davis, & W. J. Tango, 1
Feast, M. W. 2001, Odessa Astron. Pub., 14, 144
Feast, M. W., & Catchpole, R. M. 1997, MNRAS, 286, L1
Fernie, J. D. 1990, ApJS, 72, 153
Fernie, J. D., Beattie, B., Evans, N. R., & Seager, S. 1995, IBVS, No. 4148
Fouqué, P., Storm, J., & Gieren, W. 2003, Proc. Standard Candles for the Extragalactic Distance Scale, Concepción, Chile, 9–11 Dec. 2002, Lect. Notes Phys., 635, 21
Freedman, W., Madore, B. F., Gibson, B. K., et al. 2001, ApJ, 553, 47
Gieren, W. P., & Fouqué, P. 1993, AJ, 106, 734
Gieren, W. P., Fouqué, P., & Gómez, M. 1998, ApJ, 496, 17 (GFG98)
Kervella, P., Gitton, Ph., Ségransan, D., et al. 2003, SPIE, 4838, 858
Kervella, P., Nardetto, N., Bersier, D., Mourard, D., & Coudé du Foresto, V. 2004, A&A, 416, 941 (Paper I)
Koehler, B., Flebus, C., Dierickx, P., et al. 2002, ESO Messenger, 110, 21
Krockenberger, M., Sasselov, D. D., & Noyes, R. W. 1997, ApJ, 479, 875
Lane, B. F., Creech-Eakman, M., & Nordgren, T. E. 2002, ApJ, 573, 330
Laney, C. D., & Stobie, R. S. 1995, MNRAS, 274, 337
Lanoix, P., Paturel, G., & Garnier, R. 1999, MNRAS, 308, 969 (LPG99)
Marengo, M., Sasselov, D. D., Karovska, M., & Papaliolios, C. 2002, ApJ, 567, 1131
Marengo, M., Karovska, M., Sasselov, D. D., et al. 2003, ApJ, 589, 968
Marengo, M., Karovska, M., Sasselov, D. D., & Sanchez, M. 2004, ApJ, 603, 285
Mourard, D., Bonneau, D., Koechlin, L., et al. 1997, A&A, 317, 789
Moffett, T. J., & Barnes, T. J., III 1984, ApJS, 55, 389
Mozurkewich, D., Johnston, K. H., Richard, S. S., et al. 1991, AJ, 101, 2207
Nordgren, T. E., Armstrong, J. T., Germain, M. E., et al. 2000, ApJ, 543, 972
Pan, X., Shao, M., & Kulkarni, S. R. 2004, Nature, 427, 326
Perryman, M. A. C., Lindegren, L., Kovalevsky, J., et al. 1997, The Hipparcos Catalogue, A&A, 323, 49
Petrov, R., Malbet, F., Richichi, A., et al. 2000, SPIE, 4006, 68
Pinsonneault, M., Stauffer, J., Soderblom, D. R., King, J. R., & Hanson, R. B. 1998, ApJ, 504, 170
Ripepi, V., Barone, F., Milano, L., & Russo, G. 1997, A&A, 318, 797
Robichon, N., Arenou, F., Mermilliod, J.-C., & Turon, C. 1999, A&A, 345, 471
Sasselov, D. D., & Karovska, M. 1994, ApJ, 432, 367
Sasselov, D. D., Beaulieu, J.-P., Renault, C., et al. 1997, A&A, 324, 471
Tammann, G. A., Sandage, A., & Reindl, B. 2003, A&A, 404, 423
Taylor, M. M., Albrow, M. D., Booth, A. J., & Cottrell, P. L. 1997, MNRAS, 292, 662
Taylor, M. M., & Booth, A. J. 1998, MNRAS, 298, 594
Turner, D. G., & Burke, J. F. 2002, AJ, 124, 2931
Udalski, A., Szymańnski, M., Kubiak, M., et al. 1999, Acta Astron., 49, 201
Udalski, A., Wyrzykowski, G., Pietrzynńnski, O., et al. 2001, Acta Astron., 51, 221

2.1.3 Article A&A : "III. Calibration of the surface brightness-color relations" (2004)

Les relations reliant la couleur et la brillance de surface des étoiles sont très utiles pour l'application de la version classique de la méthode Baade-Wesselink. Elles permettent d'obtenir une estimation précise du diamètre angulaire à partir de simples mesures photométriques dans deux bandes différentes. Je donne dans cet article un étalonnage empirique de ces relations basé uniquement sur des mesures interférométriques de Céphéides. Les relations basées sur une combinaison des magnitudes visibles (B et V) et infrarouge (bandes H et K) sont les moins dispersées et donnent les meilleures estimations.

FIG. 2.6 – Les télescopes UT1, UT2 et UT3 du VLT, vers le Nord. La partie supérieure du bâtiment de recombinaison interférométrique du VLTI est visible à droite.

A&A 428, 587–593 (2004)
DOI: 10.1051/0004-6361:20041416

Astronomy & Astrophysics

Cepheid distances from infrared long-baseline interferometry*

III. Calibration of the surface brightness-color relations

P. Kervella[1,5], D. Bersier[2], D. Mourard[3], N. Nardetto[3], P. Fouqué[4,5], and V. Coudé du Foresto[1]

[1] LESIA, UMR 8109, Observatoire de Paris-Meudon, 5 place Jules Janssen, 92195 Meudon Cedex, France
e-mail: Pierre.Kervella@obspm.fr
[2] Space Telescope Science Institute, 3700 San Martin Drive, Baltimore, MD 21218, USA
[3] GEMINI, UMR 6203, Observatoire de la Côte d'Azur, Avenue Copernic, 06130 Grasse, France
[4] Observatoire Midi-Pyrénées, UMR 5572, 14, avenue Edouard Belin, 31400 Toulouse, France
[5] European Southern Observatory, Alonso de Cordova 3107, Casilla 19001, Vitacura, Santiago 19, Chile

Received 4 June 2004 / Accepted 15 July 2004

Abstract. The recent VINCI/VLTI observations presented in Paper I have nearly doubled the total number of available angular diameter measurements of Cepheids. Taking advantage of the significantly larger color range covered by these observations, we derive in the present paper high precision calibrations of the surface brightness-color relations using exclusively Cepheid observations. These empirical laws make it possible to determine the distance to Cepheids through a Baade-Wesselink type technique. The least dispersed relations are based on visible-infrared colors, for instance $F_V(V-K) = -0.1336_{\pm 0.0008}\,(V-K) + 3.9530_{\pm 0.0006}$. The convergence of the Cepheid (this work) and dwarf star (Kervella et al. 2004c) visible-infrared surface brightness-color relations is strikingly good. The astrophysical dispersion of these relations appears to be very small, and below the present detection sensitivity.

Key words. stars: variables: Cepheids – cosmology: distance scale – stars: oscillations – techniques: interferometric

1. Introduction

The surface brightness (hereafter SB) relations link the emerging flux per solid angle unit of a light-emitting body to its color, or effective temperature. These relations are of considerable astrophysical interest for Cepheids, as a well-defined relation between a particular color index and the surface brightness can provide accurate predictions of their angular diameters. When combined with the radius curve, integrated from spectroscopic radial velocity measurements, they give access to the distance of the Cepheid (Baade-Wesselink method). This method has been applied recently to Cepheids in the LMC (Gieren et al. 2000) and in the SMC (Storm et al. 2004)

The accuracy that can be achieved in the distance estimate is conditioned for a large part by our knowledge of the SB relations. In our first paper (Kervella et al. 2004a, hereafter Paper I), we presented new interferometric measurements of seven nearby Cepheids. They complement a number of previously published measurements from several optical and infrared interferometers. We used these data in Paper II (Kervella et al. 2004b) to calibrate the Cepheid Period–Radius and Period–Luminosity relations. Nordgren et al. (2002) derived a preliminary calibration of the Cepheid visible-infrared SB relations, based on the three stars available at that time (δ Cep, η Aql and ζ Gem). In the present Paper III, we take advantage of the nine Cepheids now resolved by interferometry to derive refined calibrations of the visible and infrared SB relations of these stars.

2. Definition of the surface brightness relations

By definition, the bolometric surface flux $f \sim L/D^2$ is linearly proportional to $T_{\rm eff}^4$, where L is the bolometric flux of the star, D its bolometric diameter and $T_{\rm eff}$ its effective temperature. In consequence, $F = \log f$ is a linear function of the stellar color indices, expressed in magnitudes (logarithmic scale), and SB relations can be fitted using for example the following expressions:

$$F_B = a_0\,(B-V)_0 + b_0 \quad (1)$$

$$F_V = a_1\,(V-K)_0 + b_1 \quad (2)$$

$$F_H = a_2\,(B-H)_0 + b_2 \quad (3)$$

where F_λ is the surface brightness. When considering a perfect blackbody curve, any color can in principle be used to obtain the SB, but in practice the linearity of the correspondence between $\log T_{\rm eff}$ and color depends on the chosen wavelength

* Table 3 is only available in electronic form at
http://www.edpsciences.org

bands. The index 0 designates the dereddened magnitudes, and will be omitted in the rest of the paper. The a_i and b_i coefficients represent respectively the slopes and zero points of the different versions of the SB relation. Historically, the first calibration of the SB relation based on the $(B - V)$ index was obtained by Wesselink (1969), and the expression $F_V(V - R)$ is also known as the Barnes-Evans (B-E) relation (Barnes & Evans 1976). The relatively large intrinsic dispersion of the visible light B-E relations has led to preferring their infrared counterparts, in particular those based on the K band magnitudes ($\lambda = 2.0$–2.4 μm), as the color-$T_{\rm eff}$ relation is less affected by microturbulence and gravity effects (Laney & Stobie 1995). The surface brightness F_λ is given by the following expression (Fouqué & Gieren 1997):

$$F_\lambda = 4.2207 - 0.1\, m_{\lambda_0} - 0.5\, \log \theta_{\rm LD} \quad (4)$$

where $\theta_{\rm LD}$ is the limb darkened angular diameter, i.e. the angular size of the stellar photosphere.

3. Selected measurement sample

3.1. Interferometric observations

Following the direct measurement of the angular diameter of δ Cep achieved by Mourard et al. (1997) using the Grand Interféromètre à 2 Télescopes (GI2T), Nordgren et al. (2000) obtained the angular diameters of three additional Cepheids (η Aql, ζ Gem and α UMi) with the Navy Prototype Optical Interferometer (NPOI). These last authors also confirmed the angular diameter of δ Cep. Kervella et al. (2001) then determined the average angular size of ζ Gem, in the K band, from measurements obtained with the Fiber Linked Unit for Optical Recombination (FLUOR), installed at the Infrared Optical Telescope Array (IOTA). Simultaneously, the Palomar Testbed Interferometer (PTI) team resolved for the first time the pulsational variation of the angular diameter of ζ Gem (Lane et al. 2000) and η Aql (Lane et al. 2002). In Paper I, we have more than doubled the total number of measured Cepheids with the addition of X Sgr, W Sgr, β Dor, Y Oph and ℓ Car, and new measurements of η Aql and ζ Gem. These observations were obtained using the VLT INterferometer Commissioning Instrument (VINCI), installed at ESO's Very Large Telescope Interferometer (VLTI).

Including the peculiar first overtone Cepheid α UMi (Polaris), the number of Cepheids with measured angular diameters is presently nine. The pulsation has been resolved for five of these stars in the infrared: ζ Gem (Lane et al. 2002), W Sgr (Paper I), η Aql (Lane et al. 2002, Paper I), β Dor and ℓ Car (Paper I). The total number of independent angular diameter measurements taken into account in the present paper is 145, as compared to 59 in the previous calibration by Nordgren et al. (2002). More importantly, we now have a significantly wider range of effective temperatures, an essential factor for deriving precise values of the slopes of the SB-color relations.

To obtain a consistent sample of angular diameters, we have retained only the uniform disk (UD) values from the literature. The conversion of these model-independent measurements to limb darkened (LD) values was achieved using the linear LD coefficients u from Claret (2000), and the conversion formula from Hanbury Brown et al. (1974). These coefficients are broadband approximations of the Kurucz (1992) model atmospheres. They are tabulated for a grid of temperatures, metallicities and surface gravities and we have chosen the models closest to the physical properties of the stars. We have considered a uniform microturbulent velocity of 2 km s^{-1} for all stars. The conversion factors $k = \theta_{\rm LD}/\theta_{\rm UD}$ are given for each star in Table 1. Marengo et al. (2002, 2003) have shown that the LD properties of Cepheids can be different from those of stable stars, in particular at visible wavelengths. For the measurements obtained using the GI2T (Mourard et al. 1997) and NPOI (Nordgren et al. 2000), the LD correction is relatively large ($k = \theta_{\rm LD}/\theta_{\rm UD} \simeq 1.05$), and this could be the source of a bias at a level of 1 to 2% (Marengo et al. 2004). However, in the infrared the correction is much smaller ($k \simeq 1.02$), and the error on its absolute value is expected to be significantly below 1%. Considering the relatively low average precision of the currently available measurements at visible wavelengths, the potential bias due to limb darkening on the SB-color relations fit is considered negligible.

Table 1. Limb darkening corrections $k = \theta_{\rm LD}/\theta_{\rm UD}$ derived from the linear limb darkening coefficients determined by Claret (2000). The k_R coefficients were used for the GI2T measurements, $k_{R/I}$ for the NPOI, k_H for the PTI, and k_K for VINCI/VLTI and FLUOR/IOTA

Star	k_R	$k_{R/I}$	k_H	k_K
α UMi		1.046		
δ Cep	1.051	1.046		
X Sgr				1.020
η Aql		1.048	1.024	1.021
W Sgr				1.021
β Dor				1.023
ζ Gem		1.051	1.027	1.023
Y Oph				1.024
ℓ Car				1.026

3.2. Photometric data and reddening corrections

We compiled data in the *BVRI* and *JHK* filters from different sources. Rather than try to use the largest amount of data from many different sources, we decided to limit ourselves to data sets with high internal precision, giving smooth light curves, as we wanted to fit Fourier series to the photometric data. These Fourier series were interpolated to obtain magnitudes at the phases of our interferometric measurements. The R band magnitudes were only available in sufficient number and quality for three stars: α UMi, β Dor and ℓ Car. Overall, the number of stars and photometry points per band are the following: B and V: 9 stars, 145 points; R: 3 stars, 35 points; I: 8 stars, 119 points; J: 6 stars, 127 points; H: 5 stars, 100 points; K: 8 stars, 128 points. We took the periods from Szabados (1989, 1991) to compute phases.

The *BVRI* band magnitudes are defined in the Cousins system. There is no widely used standard system in the infrared (*JHK*). We used three sources of data: Wisniewski & Johnson (1968) in the Johnson system, Laney & Stobie (1992)

in the SAAO system, and Barnes et al. (1997) in the CIT system. There is a large body of homogeneous and high quality data for Cepheids (Laney & Stobie 1992) in the SAAO system (Carter 1990). Furthermore, many stars in the list of Laney & Stobie are going to be observed with the VLTI in the near future. For convenience, we thus decided to transform all photometry into this system, using transformation relations in Glass (1985) and Carter (1990).

α UMi: For this low amplitude variable ($\Delta m_V \simeq 0.1$), we considered its average photometry, as we have only an average angular diameter measurement by Nordgren et al. (2000). The B and V magnitudes were taken from the HIPPARCOS catalogue (Perryman et al. 1997), the R and I bands are from Morel & Magnenat (1978), and the K band is from Ducati (2002).

δ Cep: We used *BVI* data from Moffett & Barnes (1984) Barnes et al. (1997) and Kiss (1998). The *JHK* data of Barnes et al. (1997) have been transformed to the SAAO system.

X Sgr: Optical data come from Moffett & Barnes (1984), Berdnikov & Turner (2001a), Berdnikov & Turner (1999), Berdnikov & Turner (2000), and Berdnikov & Caldwell (2001).

η Aql: We used *BVI* data from Barnes et al. (1997), Kiss (1998), Berdnikov & Turner (2000), Berdnikov & Turner (2001a), Berdnikov & Caldwell (2001), and Caldwell et al. (2001). The *JHK* data are from Barnes et al. (1997). They have been transformed to the SAAO system using formulae given in Carter (1990).

W Sgr: We used optical data from Moffett & Barnes (1984), Berdnikov & Turner (1999), Berdnikov & Turner (2000), Berdnikov & Turner (2001a), Berdnikov & Turner (2001b), Berdnikov & Caldwell (2001), and Caldwell et al. (2001).

β Dor: We used *BVRI* data from Berdnikov & Turner (2001a), Berdnikov & Turner (2000), Berdnikov & Turner (2001b), and Berdnikov & Caldwell (2001). In the infrared we used the data in Laney & Stobie (1992).

ζ Gem: We used *BVI* data from Moffett & Barnes (1984), Shobbrook (1992), Kiss (1998), Berdnikov & Turner (2001a), Berdnikov & Turner (2001b), and Berdnikov & Caldwell (2001). In the *JK* bands we used data from Johnson, transformed using formulae in Glass (1985).

Y Oph: In the optical we used data from Moffett & Barnes (1984) and Coulson & Caldwell (1985). In the infrared we used the data in Laney & Stobie (1992).

ℓ Car: We used *BVRI* from Berdnikov & Turner (2001a), and Berdnikov & Turner (2000). Infrared data are from Laney & Stobie (1992).

The extinction A_λ (Table 2) was computed for each star and each band using the relations:

$$A_\lambda = R_\lambda\, E(B-V) \tag{5}$$

where we have (Fouqué et al. 2003; Hindsley & Bell 1989 for the R band):

$$R_B = R_V + 1 \tag{6}$$

$$R_V = 3.07 + 0.28\,(B-V) + 0.04\,E(B-V) \tag{7}$$

$$R_R = R_V - 0.97 \tag{8}$$

Table 2. Pulsation parameters (T_0 is the Julian date of the reference epoch, P is the period in days) and color excesses (from Fernie 1990) for the Cepheids discussed in this paper. $(B-V)_0$ is the mean dereddened $(B-V)$ color as reported in the online database by Fernie et al. (1995).

Star	T_0 (JD)	P (days)	$(B-V)_0$	$E(B-V)$
α UMi	2 439 253.230	3.972676	0.598	–0.007
δ Cep	2 436 075.445	5.366341	0.657	0.092
X Sgr	2 452 723.949	7.013059	0.739	0.197
η Aql	2 445 342.479	7.176769	0.789	0.149
W Sgr	2 452 519.248	7.594904	0.746	0.111
β Dor	2 452 214.215	9.842425	0.807	0.044
ζ Gem	2 442 059.774	10.15097	0.798	0.018
Y Oph	2 452 715.481	17.12691	1.377	0.655
ℓ Car	2 452 290.416	35.55134	1.299	0.170

$$R_I = 1.82 + 0.205\,(B-V) + 0.0225\,E(B-V) \tag{9}$$

$$R_J = R_V/4.02 \tag{10}$$

$$R_H = R_V/6.82 \tag{11}$$

$$R_K = R_V/11. \tag{12}$$

4. General surface brightness relations

The data that we used for the SB-color relation fits are presented in Table 3, that is available in electronic form at `http://www.edpsciences.org/`. The limb darkened angular diameters $\theta_{\rm LD}$ were computed from the uniform disk values available in the literature, using the conversion coefficients $k = \theta_{\rm LD}/\theta_{\rm UD}$ listed in Table 1. The *BVRIJHK* magnitudes are interpolated values, corrected for interstellar extinction (see Sect. 3.2).

The resulting SB relation coefficients are presented in Table 4, and Fig. 1 shows the result for the $F_V(V-K)$ relation. The other relations based on the V band surface brightness F_V are plotted in Fig. 2. The smallest residual dispersions are obtained for the infrared-based colors, for instance:

$$F_B = -0.1199_{\pm 0.0006}\,(B-K) + 3.9460_{\pm 0.0007} \tag{13}$$

$$F_V = -0.1336_{\pm 0.0008}\,(V-K) + 3.9530_{\pm 0.0006}. \tag{14}$$

The reduced χ^2 of all the visible-infrared SB relations fits is below 1.0, meaning that the true intrinsic dispersion is undetectable at the current level of precision.

In the present paper, no error bars have been considered in the reddening corrections. This is justified by the low sensitivity of the visible-infrared SB relations to the reddening, but may create biases in the purely visible SB relations (based on the $B-V$ index for instance). However, the maximum amplitude of these biases is expected to be significantly below the residuals of the fits σ_λ listed in Table 4.

In an attempt to refine the reddening coefficients, we tentatively adjusted their values in order to minimize the dispersion of the fitted SB relations. We confirm the results of Fernie (1990) for most stars, but we find higher color excesses for

Table 4. Surface brightness relations using *BVRIJHK* based colors: $F_\lambda(C_\lambda - C_1) = a_\lambda(C_\lambda - C_1) + b_\lambda$. The 1σ errors in each coefficient are given in superscript, *multiplied by 1000* to reduce the length of each line, i.e. $-0.2944^{2.4}$ stands for -0.2944 ± 0.0024. The standard deviation of the residuals σ is listed for each SB relation, together with the reduced χ^2 of the fit and the total number of measurements $N_{\rm meas}$ taken into account (photometric data were unavailable for some stars).

$C_\lambda \downarrow$	$C_1 \rightarrow B$	V	R	I	J	H	K
a_B		$-0.2944^{2.4}$	$-0.1978^{1.6}$	$-0.1800^{0.9}$	$-0.1401^{0.8}$	$-0.1224^{0.7}$	$-0.1199^{0.6}$
b_B		$3.8813^{1.1}$	$3.8719^{0.9}$	$3.9283^{0.6}$	$3.9297^{0.8}$	$3.9423^{0.8}$	$3.9460^{0.7}$
$\sigma_B/\chi^2_{\rm red}$		0.017/1.20	0.008/0.46	0.015/1.41	0.015/0.65	0.014/0.63	0.015/0.75
$N_{\rm meas}$		145	34	119	127	100	128
a_V	$0.1956^{1.8}$		$-0.3789^{10.0}$	$-0.3077^{2.4}$	$-0.1759^{1.4}$	$-0.1379^{1.0}$	$-0.1336^{0.8}$
b_V	$3.8828^{0.9}$		$3.8516^{2.2}$	$3.9617^{0.7}$	$3.9407^{0.7}$	$3.9490^{0.7}$	$3.9530^{0.6}$
$\sigma_V/\chi^2_{\rm red}$	0.017/1.75		0.014/0.75	0.016/0.89	0.015/0.57	0.014/0.58	0.015/0.70
$N_{\rm meas}$	145		34	119	127	100	128
a_R	$0.0994^{1.1}$	$0.2868^{8.0}$		$-1.2894^{26.4}$	$-0.2240^{3.2}$	$-0.1458^{1.6}$	$-0.1386^{1.5}$
b_R	$3.8746^{0.6}$	$3.8554^{1.7}$		$4.3248^{2.9}$	$3.9532^{0.7}$	$3.9426^{0.6}$	$3.9430^{0.6}$
$\sigma_R/\chi^2_{\rm red}$	0.008/0.72	0.015/1.10		0.060/1.19	0.006/0.12	0.005/0.14	0.005/0.18
$N_{\rm meas}$	34	34		34	34	34	34
a_I	$0.0808^{0.6}$	$0.2105^{1.9}$	$1.8067^{38.4}$		$-0.2854^{7.1}$	$-0.1713^{2.6}$	$-0.1630^{2.0}$
b_I	$3.9304^{0.4}$	$3.9642^{0.5}$	$4.6102^{4.3}$		$3.9323^{1.7}$	$3.9491^{0.9}$	$3.9548^{0.8}$
$\sigma_I/\chi^2_{\rm red}$	0.015/2.23	0.016/1.37	0.089/1.35		0.013/0.34	0.010/0.40	0.013/0.50
$N_{\rm meas}$	119	119	34		101	74	102
a_J	$0.0399^{0.6}$	$0.0753^{1.1}$	$0.1243^{2.2}$	$0.1877^{5.3}$		$-0.2988^{10.2}$	$-0.2614^{6.8}$
b_J	$3.9295^{0.6}$	$3.9403^{0.6}$	$3.9536^{0.5}$	$3.9335^{1.2}$		$3.9679^{1.7}$	$3.9722^{1.3}$
$\sigma_J/\chi^2_{\rm red}$	0.015/0.89	0.015/0.86	0.006/0.20	0.013/0.54		0.015/0.21	0.016/0.29
$N_{\rm meas}$	127	127	34	101		100	127
a_H	$0.0223^{0.5}$	$0.0375^{0.8}$	$0.0460^{1.1}$	$0.0700^{1.8}$	$0.2060^{7.2}$		$-2.3858^{309.8}$
b_H	$3.9422^{0.6}$	$3.9487^{0.5}$	$3.9428^{0.4}$	$3.9480^{0.7}$	$3.9710^{1.2}$		$4.0653^{8.4}$
$\sigma_H/\chi^2_{\rm red}$	0.014/0.77	0.014/0.74	0.005/0.22	0.010/0.62	0.015/0.35		0.029/0.03
$N_{\rm meas}$	100	100	34	74	100		100
a_K	$0.0197^{0.5}$	$0.0331^{0.7}$	$0.0389^{1.1}$	$0.0618^{1.4}$	$0.1704^{4.7}$	$2.7121^{354.8}$	
b_K	$3.9458^{0.5}$	$3.9524^{0.5}$	$3.9435^{0.4}$	$3.9539^{0.5}$	$3.9767^{0.9}$	$4.0970^{9.6}$	
$\sigma_K/\chi^2_{\rm red}$	0.015/0.94	0.015/0.92	0.005/0.28	0.012/0.80	0.016/0.51	0.034/0.03	
$N_{\rm meas}$	128	128	34	102	127	100	

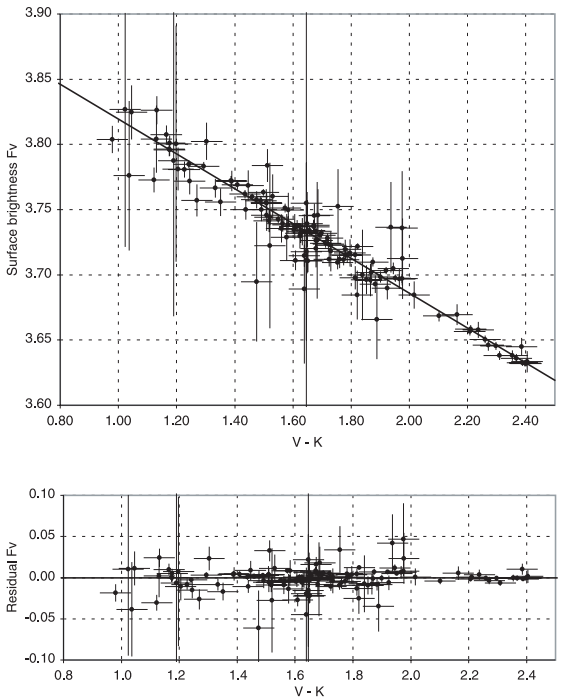

Fig. 1. Linear fit of $F_V(V-K)$ (upper part) and the corresponding residuals (lower part). The fitted coefficients are given in Table 4.

X Sgr ($\simeq$0.38) and W Sgr ($\simeq$0.29), and a slightly lower value for Y Oph ($\simeq$0.54). However, these numbers should be considered with caution, as our method relies on the assumption that all Cepheids follow the same SB relations. Considering that we cannot verify this hypothesis based on our data, we did not use these coefficients for the fits presented in this section.

5. Specific surface brightness relations

For ζ Gem, η Aql and ℓ Car, the pulsation is resolved with a high SNR (Paper I; Lane et al. 2002). Therefore we can derive specific SB relations over their pulsation cycle, and compare them to the global ones derived from our complete sample. In particular, the slope may be different between these Cepheids that cover a relatively broad range in terms of linear diameter and pulsation period. We have limited our comparison to the $F_V(V-K)$ relations, which give small dispersions. The best fit SB relations are the following:

– η Aql ($\sigma = 0.011$):

$$F_V = -0.1395_{\pm 0.0013}\,(V-K) + 3.9634_{\pm 0.0004}. \quad (15)$$

– ζ Gem ($\sigma = 0.016$):

$$F_V = -0.1098_{\pm 0.0011}\,(V-K) + 3.9134_{\pm 0.0002}. \quad (16)$$

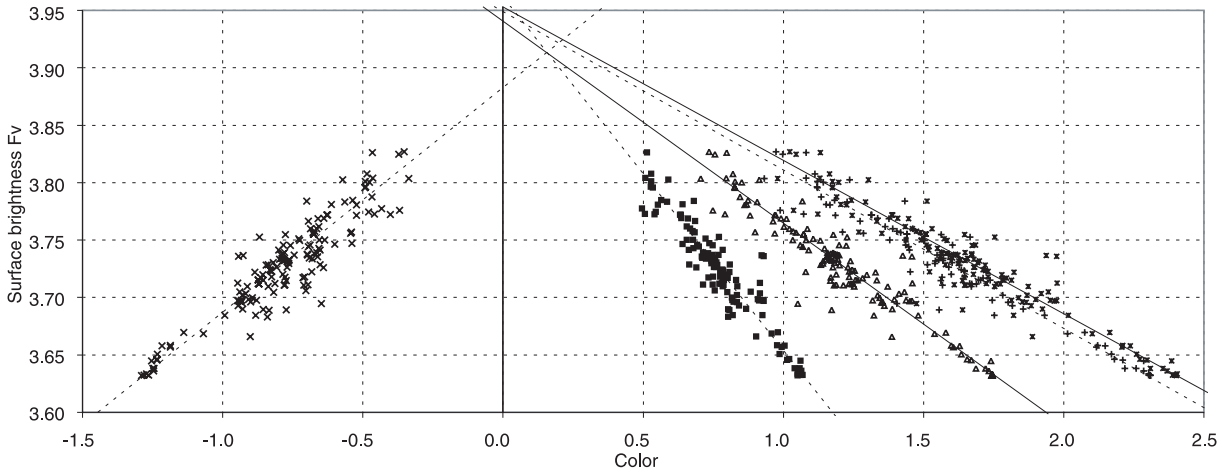

Fig. 2. Surface brightness F_V relations as a function of color. The error bars have been omitted for clarity, and the fitted models are represented alternatively as solid and dashed lines. From left to right, using the colors: $(V-B)$, $(V-I)$, $(V-J)$, $(V-H)$ and $(V-K)$. The zero-axis intersection does not happen at the same point for all relations.

– ℓ Car ($\sigma = 0.004$):

$$F_V = -0.1355_{\pm 0.0010}\,(V-K) + 3.9571_{\pm 0.0004}. \quad (17)$$

– All stars ($\sigma = 0.015$):

$$F_V = -0.1336_{\pm 0.0008}\,(V-K) + 3.9530_{\pm 0.0006}. \quad (18)$$

As shown in Fig. 3, the agreement between the extreme period η Aql ($P = 7$ days), ℓ Car ($P = 35.5$ days) and the average of all stars is good. The difference observed for ζ Gem could come from the relatively large dispersion of the measurements of this star. The poor infrared photometry available for this star could also explain part of this difference.

This result is an indication that SB-color relations for Cepheids do not depend strongly on the pulsation period of the star. Going into finer detail, it appears that the slope of the $F_V(V-K)$ relation of η Aql is slightly steeper than the slope of the same relation for ℓ Car. This could be associated with the larger surface gravity of η Aql, but the difference remains small.

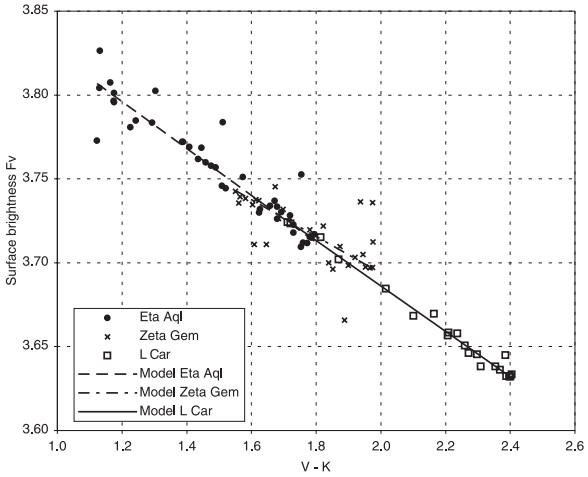

Fig. 3. Specific $F_V(V-K)$ relation fits for η Aql, ζ Gem and ℓ Car. The error bars have been omitted for clarity.

6. Comparison with previous calibrations

Welch (1994) and Fouqué & Gieren (1997, FG97) proposed a calibration of the SB relations of Cepheids based on an extrapolation of the corresponding relations of giants. The latter obtained the following expression for $F_V(V-K)$:

$$F_V(\mathrm{FG97}) = -0.131_{\pm 0.002}\,(V-K) + 3.947_{\pm 0.003} \quad (19)$$

to be compared with the relation we obtained in the present work:

$$F_V(V-K) = -0.1336_{\pm 0.0008}\,(V-K) + 3.9530_{\pm 0.0006}. \quad (20)$$

The agreement between these two independent calibrations is remarkable, with a less than 2σ difference on both the slope and the zero point.

Nordgren et al. (2002, N02) achieved a similar calibration using a larger sample of 57 stars observed with the NPOI, and find consistent results. In addition, they compared these relations with the ones obtained from interferometric measurements of three classical Cepheids (δ Cep, η Aql, ζ Gem). They obtained:

$$F_V(\mathrm{N02}) = -0.134_{\pm 0.005}\,(V-K) + 3.956_{\pm 0.011}. \quad (21)$$

This calibration is statistically identical to our result within less than 1σ, but part of the interferometric and photometric data used for the fits is common with our sample.

Several other calibrations of the SB relations for giants have been proposed in recent years, thanks to the availability of interferometric measurements. Van Belle (1999a, VB99) used a sample of 190 giants and 67 carbon stars and Miras measured with the PTI (Van Belle et al. 1999b), IOTA (e.g. Dyck et al. 1998) and lunar occultation observations (e.g. Ridgway et al. 1982) to calibrate the $F_V(V-K)$ relation of giant and supergiant stars. This author obtained an expression equivalent to:

$$F_V(\mathrm{VB99}) = -0.112_{\pm 0.005}\,(V-K) + 3.886_{\pm 0.026}. \quad (22)$$

Though the slope and zero point are significantly different from our values, the maximum difference in predicted surface brightness F_V over the whole color range of the Cepheids of our sample ($1.0 \leq V-K \leq 2.4$) is less than 0.05, only twice the formal error on the zero point. The agreement is thus reasonably good.

7. Comparison with the surface brightness relations of dwarf stars

From the interferometric measurement of the angular diameters of a number of dwarfs and subgiants, Kervella et al. (2004c) calibrated the SB-color relations of these luminosity classes with high accuracy. The residual dispersion on the zero-magnitude limb darkened angular diameter was found to be below 1% for the best relations (based on visible and infrared bands). This corresponds to a dispersion in the surface brightness F of the order of 0.05% only. The metallicities [Fe/H] of the nearby dwarfs and subgiants used for these fits cover the range −0.5 to +0.5, but no significant trend of the SB with metallicity was detected in the visible-infrared SB relations.

The question of the universality of the SB-color relations can now be adressed by comparing the stable dwarf stars and the Cepheids. The stars of these two luminosity classes represent extremes in terms of physical properties, with for instance linear photospheric radii between 0.15 and 200 $R_\odot$ and effective gravities between $\log g = 1.5$ and 5.2, a range of three orders of magnitudes. Figure 4 shows the positions of dwarfs and Cepheids in the $F_V(B-V)$ diagram. It appears from this plot that stable dwarfs tend to have lower SB than Cepheids above $(B-V) \simeq 0.8$. The difference is particularly strong in the case of ℓ Car, whose surface brightness F_V is significantly larger than that of a dwarf with the same $B-V$ color. A qualitative explanation for this difference is that for the same temperature (spectral type), giants are redder than dwarfs. This can be understood because there is more line blanketing in the supergiant atmospheres, due to their lower surface gravity and lower gas density (more ion species can exist).

Figure 5 shows the same plot for the $F_V(V-K)$ relation. In this case, the SB relations appear very close to linear for both dwarfs and Cepheids. It is almost impossible to distinguish the two populations on a statistical basis. For instance, we have:

$$F_V(\text{Dwarf}) = -0.1376_{\pm 0.0005}\,(V-K) + 3.9618_{\pm 0.0011} \quad (23)$$

$$F_V(\text{Ceph.}) = -0.1336_{\pm 0.0008}\,(V-K) + 3.9530_{\pm 0.0006}. \quad (24)$$

Over the full $(V-K)$ color range of our Cepheid sample, the difference in surface brightness predicted by these relations is always:

$$F_V(\text{Dwarf}) - F_V(\text{Ceph.}) \leq 0.005. \quad (25)$$

From this remarkable convergence we conclude that the $V-K$ dereddened color index is an excellent tracer of the effective temperature. Kervella et al. (2004c) have shown that the visible-L band color indices are even more efficient than those based on the K band, and lead to extremely small intrinsic dispersions of the SB-color relations, down to ±0.002. High precision photometric measurements of Cepheids in the L band are unfortunately not available at present, and we therefore recommend obtaining data in this band, to reach the smallest possible SB relation dispersions.

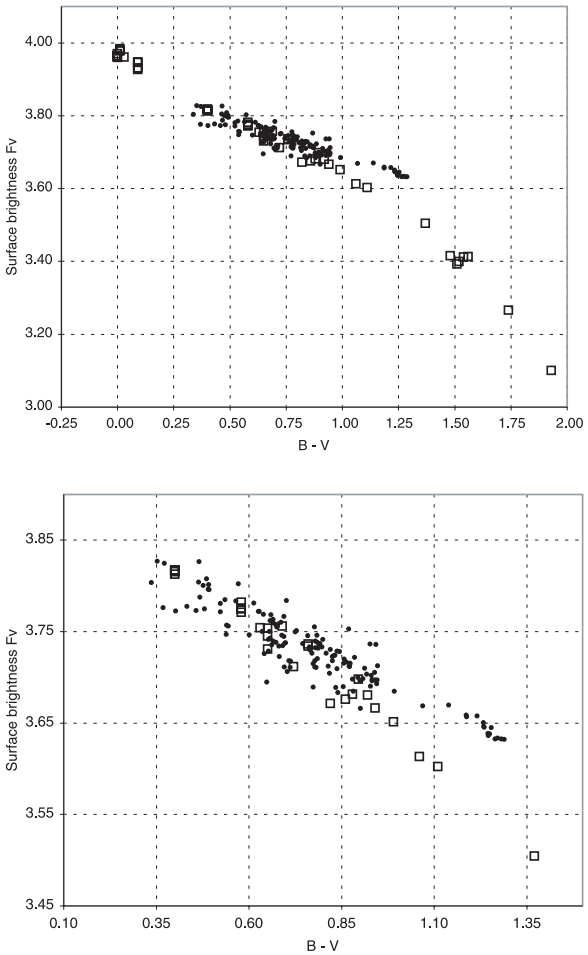

Fig. 4. Comparison of the positions of the Cepheids (solid dots) and dwarfs (open squares) in the $F_V(B-V)$ diagram. The lower part of the figure shows an enlargement of the Cepheid color range.The error bars have been omitted for clarity.

8. Conclusion

Taking advantage of a large sample of interferometric observations, we were able to derive precise calibrations of the SB-color relations of Cepheids. The astrophysical dispersion of the visible-infrared SB relations is undetectable at the present level of accuracy of the measurements, and could be minimal, based on the SB relations obtained for nearby dwarfs by Kervella et al. (2004c). The visible-infrared SB-color relations represent a very powerful tool for estimating the distances of Cepheids. The interferometric version of the Baade-Wesselink method that we applied in Paper I is currently limited to distances of 1–2 kpc, due to the limited length of the available baselines, but the infrared surface brightness technique can reach extragalactic Cepheids, as already demonstrated by Gieren et al. (2000) and Storm et al. (2004) for the Magellanic Clouds. The present calibration increases the level of confidence in the Cepheid distances derived by this method.

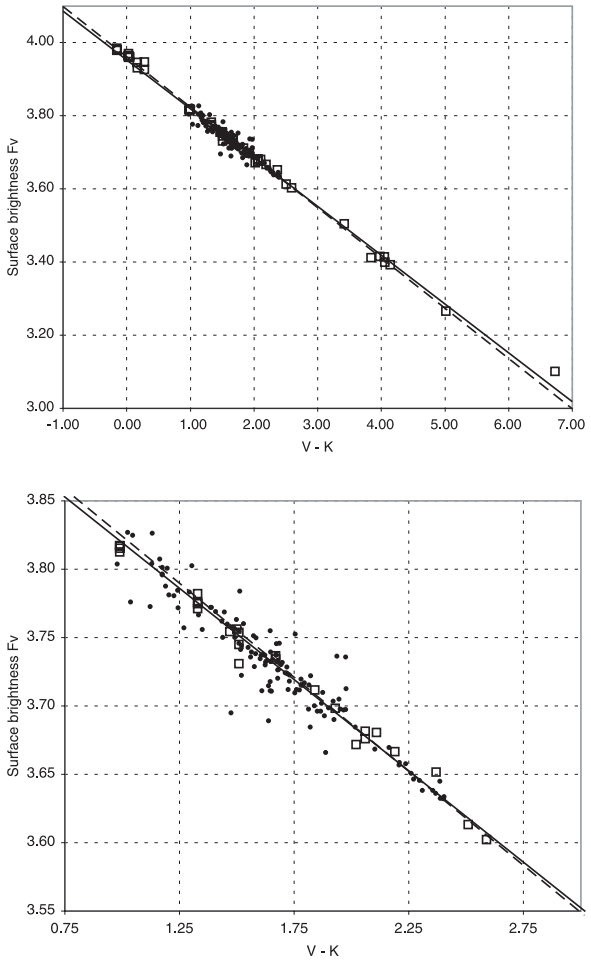

Fig. 5. Comparison of the positions of the Cepheids (solid dots) and dwarfs (open squares) in the $F_V(V-K)$ diagram. The dashed line represents the best fit SB-color relation for dwarf stars and the solid line for Cepheids. The lower part of the figure is an enlargement of the Cepheid color range.

Acknowledgements. We would like to thank Dr. Jason Aufdenberg for fruitful discussions, and we are grateful to the ESO VLTI team, without whose efforts no observation would have been possible. D.B. acknowledges support from NSF grant AST-9979812. P.K. acknowledges partial support from the European Southern Observatory through a post-doctoral fellowship. Based on observations collected at the VLT Interferometer, Cerro Paranal, Chile, in the framework of the ESO shared-risk programme 071.D-0425 and an unreferenced programme in P70. This research has made use of the SIMBAD and VIZIER databases at CDS, Strasbourg (France).

References

Barnes, T. G., & Evans, D. S. 1976, MNRAS, 174, 489
Barnes, T. G., III, Fernley, J. A., Frueh, M. L., et al. 1997, PASP, 109, 645
Berdnikov, L. N., & Caldwell, J. A. R. 2001, J. Astron. Data, 7, 3
Berdnikov, L. N., & Turner, D. G. 1999, A&A Trans., 16, 291
Berdnikov, L. N., & Turner, D. G. 2000, A&A Trans., 18, 679
Berdnikov, L. N., & Turner, D. G. 2001a, ApJS, 137, 209
Berdnikov, L. N., & Turner D. G. 2001b, A&A Trans., 19, 689
Caldwell, J. A. R., Coulson, I. M., Dean, J. F., & Berdnikov, L. N. 2001, J. Astron. Data, 7, 4
Carter, B. S. 1990, MNRAS, 242, 1
Claret, A. 2000, A&A, 363, 1081
Coulson, I. M., & Caldwell, J. A. R. 1985, South African Astron. Observ. Circ., 9, 5
Ducati, J. R. 2002, NASA Ref. Pub., 1294
Dyck, H. M., Van Belle, G. T., & Thompson, R. R. 1998, AJ, 116, 981
Fernie, J. D. 1990, ApJS, 72, 153
Fernie, J. D., Beattie, B., Evans, N. R., & Seager, S. 1995, IBVS, No. 4148
Fouqué, P., & Gieren, W. P. 1997, A&A, 320, 799
Fouqué, P., Storm, J., & Gieren, W. 2003, Proc. Standard Candles for the Extragalactic Distance Scale, Concepción, Chile, 9–11 Dec. 2002 [arXiv:astro-ph/0301291]
Gieren, W. P., Storm, J., Fouqué, P., Mennickent, R. E., & Gómez, M. 2000, ApJ, 533, L107
Glass, I. S. 1985, Ir. Astr. J., 17, 1
Hanbury Brown, R., Davis, J., Lake, J. W., & Thompson, R. J. 1974, MNRAS, 167, 475
Hindsley, R. B., & Bell, R. A. 1989, ApJ, 341, 1004
Kervella, P., Coudé du Foresto, V., Perrin, G., et al. 2001, A&A, 367, 876
Kervella, P., Nardetto, N., Bersier, D., Mourard, D., & Coudé du Foresto, V. 2004a, A&A, 416, 941 (Paper I)
Kervella, P., Bersier, D., Mourard, D., Nardetto, N., & Coudé du Foresto, V. 2004b, A&A, 423, 327 (Paper II)
Kervella, P., Thévenin, F., Di Folco, E., & Ségransan, D. 2004c, A&A, 426, 297
Kiss, L. L. 1998, MNRAS, 297, 825
Kurucz, R. L. 1992, The Stellar Populations of Galaxies, IAU Symp., 149, 225
Lane, B. F., Kuchner, M. J., Boden, A. F., Creech-Eakman, M., & Kulkarni, S. R. 2000, Nature, 407, 485
Lane, B. F., Creech-Eakman, M., & Nordgren, T. E. 2002, ApJ, 573, 330
Laney, C. D., & Stobie, R. S. 1992, A&AS, 93, 93
Laney, C. D., & Stobie, R. S. 1995, MNRAS, 274, 337
Marengo, M., Sasselov, D. D., Karovska, M., & Papaliolios, C. 2002, ApJ, 567, 1131
Marengo, M., Karovska, M., Sasselov, D. D., et al. 2003, ApJ, 589, 968
Marengo, M., Karovska, M., Sasselov, D. D., & Sanchez, M. 2004, ApJ, 603, 285
Mourard, D., Bonneau, D., Koechlin, L., et al. 1997, A&A, 317, 789
Moffett, T. J., & Barnes, T. J., III 1984, ApJS, 55, 389
Morel, M., & Magnenat, P. 1978, A&AS, 34, 477
Nordgren, T. E., Armstrong, J. T., Germain, M. E., et al. 2000, ApJ, 543, 972
Nordgren, T. E., Lane, B. F., Hindsley, R. B., & Kervella, P. 2002, AJ, 123, 3380
Perryman, M. A. C., Lindegren, L., Kovalevsky, J., et al. 1997, The HIPPARCOS Catalogue, A&A, 323, 49
Ridgway, S. T., Jacoby, G. H., Joyce, R. R., & Wells, D. C. 1982, AJ, 87, 1044
Shobbrook, R. R. 1992, MNRAS, 255, 486
Storm, J., Carney, B. W., Gieren, W. P., et al. 2004, A&A, 415, 531
Szabados, L. 1989, Comm. Konkoly Obs., 94, 1
Szabados, L. 1991, Comm. Konkoly Obs., 96, 1
Van Belle, G. T. 1999a, PASP, 11, 1515
Van Belle, G. T., Lane, B. F., Thompson, R. R., et al. 1999b, AJ, 117, 521
Welch, D. L. 1994, AJ, 108, 1421
Wesselink, A. J. 1969, MNRAS, 144, 297
Wisniewski, W. Z., & Johnson, H. L. 1968, Commun. Lunar Planet. Lab., 7, 57

Table 3. Interferometric and photometric data used in the present paper. The references for the interferometric measurements are: Nordgren et al. (2000, N00), Mourard et al. (1997, M97), Nordgren et al. (2002, N02), Lane et al. (2002, L02), and Kervella et al. (2004a, K04). JD is the Julian date of the measurement, λ the interferometric measurement wavelength (in μm), ϕ the phase, $\theta_{\rm UD}$ the uniform disk and $\theta_{\rm LD}$ the limb darkened angular diameters (in mas). The magnitudes are corrected for interstellar extinction (see Sect. 3.2).

Star	Ref.	JD	λ	ϕ	$\theta_{\rm LD}$	B_0	V_0	R_0	I_0	J_0	H_0	K_0
α UMi	N00	avg	0.74	avg	3.284 ± 0.021	2.66	1.99	1.55	1.23	–	–	0.49
δ Cep	M97	2 449 566.6000	0.67	0.032	1.376 ± 0.620	3.60	3.25	–	–	2.51	2.27	2.22
δ Cep	M97	2 449 572.5000	0.67	0.132	1.534 ± 0.767	3.87	3.40	–	–	2.56	2.27	2.21
δ Cep	M97	2 449 642.3000	0.67	0.139	1.440 ± 0.567	3.89	3.41	–	–	2.56	2.27	2.21
δ Cep	M97	2 449 643.3000	0.67	0.325	2.070 ± 0.431	4.33	3.68	–	–	2.63	2.28	2.21
δ Cep	M97	2 449 541.6000	0.67	0.374	1.776 ± 0.504	4.42	3.74	–	–	2.66	2.28	2.22
δ Cep	M97	2 449 569.5000	0.67	0.573	1.660 ± 0.504	4.71	3.93	–	–	2.76	2.36	2.28
δ Cep	M97	2 449 570.5000	0.67	0.759	1.324 ± 0.841	4.83	4.05	–	–	2.87	2.49	2.40
δ Cep	M97	2 449 640.3000	0.67	0.766	1.797 ± 0.462	4.82	4.04	–	–	2.87	2.49	2.40
δ Cep	M97	2 449 571.5000	0.67	0.945	1.671 ± 0.431	3.70	3.33	–	–	2.58	2.34	2.30
δ Cep	N02	2 450 788.6300	0.74	0.754	1.621 ± 0.063	4.83	4.05	–	–	2.87	2.48	2.40
δ Cep	N02	2 450 994.9100	0.74	0.193	1.705 ± 0.094	4.02	3.48	–	–	2.58	2.27	2.21
δ Cep	N02	2 450 995.9300	0.74	0.383	1.485 ± 0.115	4.44	3.75	–	–	2.66	2.29	2.22
δ Cep	N02	2 450 996.9700	0.74	0.577	1.548 ± 0.220	4.71	3.94	–	–	2.76	2.37	2.29
δ Cep	N02	2 450 997.9300	0.74	0.756	1.422 ± 0.115	4.83	4.05	–	–	2.87	2.48	2.40
δ Cep	N02	2 450 998.9300	0.74	0.942	1.328 ± 0.125	3.72	3.35	–	–	2.59	2.35	2.30
δ Cep	N02	2 451 007.9600	0.74	0.625	1.590 ± 0.105	4.78	4.00	–	–	2.81	2.40	2.32
δ Cep	N02	2 451 008.9200	0.74	0.804	1.391 ± 0.084	4.72	3.99	–	–	2.86	2.49	2.41
δ Cep	N02	2 451 009.9600	0.74	0.998	1.548 ± 0.073	3.56	3.22	–	–	2.52	2.29	2.24
δ Cep	N02	2 451 010.9200	0.74	0.177	1.610 ± 0.073	3.98	3.46	–	–	2.57	2.27	2.21
δ Cep	N02	2 451 011.9100	0.74	0.361	1.537 ± 0.073	4.40	3.72	–	–	2.65	2.28	2.21
δ Cep	N02	2 451 012.9000	0.74	0.546	1.569 ± 0.073	4.66	3.90	–	–	2.73	2.34	2.27
δ Cep	N02	2 451 088.8100	0.74	0.691	1.380 ± 0.125	4.83	4.05	–	–	2.85	2.45	2.36
δ Cep	N02	2 451 089.7800	0.74	0.872	1.527 ± 0.073	4.27	3.73	–	–	2.76	2.44	2.38
δ Cep	N02	2 451 093.7600	0.74	0.614	1.475 ± 0.021	4.77	3.98	–	–	2.80	2.39	2.31
δ Cep	N02	2 451 097.7800	0.74	0.363	1.537 ± 0.052	4.40	3.72	–	–	2.65	2.28	2.21
δ Cep	N02	2 451 098.8500	0.74	0.562	1.694 ± 0.063	4.69	3.92	–	–	2.75	2.36	2.28
X Sgr	K04	2 452 741.9033	2.18	0.560	1.487 ± 0.058	4.88	4.17	–	3.44	–	–	–
X Sgr	K04	2 452 742.8848	2.18	0.700	1.541 ± 0.067	4.91	4.21	–	3.45	–	–	–
X Sgr	K04	2 452 743.8965	2.18	0.844	1.443 ± 0.065	4.48	3.94	–	3.20	–	–	–
X Sgr	K04	2 452 744.8676	2.18	0.983	1.489 ± 0.059	4.02	3.62	–	3.08	–	–	–
X Sgr	K04	2 452 747.8477	2.18	0.408	1.528 ± 0.217	4.65	4.00	–	3.34	–	–	–
X Sgr	K04	2 452 749.8324	2.18	0.691	1.457 ± 0.104	4.92	4.21	–	3.46	–	–	–
X Sgr	K04	2 452 766.8110	2.18	0.112	1.420 ± 0.078	4.18	3.70	–	3.15	–	–	–
X Sgr	K04	2 452 768.8768	2.18	0.406	1.441 ± 0.032	4.65	4.00	–	3.34	–	–	–
η Aql	N02	2 450 638.8600	0.74	0.990	1.959 ± 0.084	3.48	3.02	–	2.51	2.23	1.95	1.90
η Aql	N02	2 450 640.8800	0.74	0.271	1.781 ± 0.094	3.93	3.27	–	2.61	2.26	1.89	1.82
η Aql	N02	2 450 641.8600	0.74	0.408	1.938 ± 0.084	4.24	3.47	–	2.73	2.33	1.93	1.85
η Aql	N02	2 450 997.8300	0.74	0.008	1.697 ± 0.199	3.48	3.02	–	2.51	2.22	1.94	1.89
η Aql	N02	2 450 998.8800	0.74	0.154	1.781 ± 0.063	3.86	3.23	–	2.60	2.26	1.92	1.84
η Aql	N02	2 451 007.8800	0.74	0.408	1.917 ± 0.063	4.24	3.47	–	2.73	2.33	1.93	1.85
η Aql	N02	2 451 008.9100	0.74	0.552	1.603 ± 0.210	4.53	3.66	–	2.89	2.43	1.99	1.90
η Aql	N02	2 451 009.8500	0.74	0.683	1.771 ± 0.084	4.66	3.80	–	3.00	2.51	2.08	2.00
η Aql	N02	2 451 010.8400	0.74	0.821	1.456 ± 0.084	4.25	3.55	–	2.87	2.49	2.12	2.04
η Aql	N02	2 451 011.8400	0.74	0.960	1.509 ± 0.073	3.52	3.05	–	2.54	2.25	1.97	1.92
η Aql	N02	2 451 012.8700	0.74	0.104	1.603 ± 0.105	3.73	3.16	–	2.57	2.24	1.92	1.86
η Aql	L02	2 452 065.4200	1.64	0.764	1.694 ± 0.011	4.53	3.73	–	2.98	2.53	2.13	2.05
η Aql	L02	2 452 066.4140	1.64	0.903	1.694 ± 0.017	3.75	3.22	–	2.65	2.34	2.03	1.97
η Aql	L02	2 452 067.4050	1.64	0.041	1.735 ± 0.041	3.54	3.05	–	2.52	2.22	1.93	1.87
η Aql	L02	2 452 075.3830	1.64	0.153	1.783 ± 0.028	3.86	3.23	–	2.60	2.26	1.92	1.85
η Aql	L02	2 452 076.3840	1.64	0.292	1.843 ± 0.014	3.95	3.28	–	2.61	2.26	1.89	1.82
η Aql	L02	2 452 077.3720	1.64	0.430	1.867 ± 0.022	4.30	3.51	–	2.76	2.35	1.94	1.86
η Aql	L02	2 452 089.3500	1.64	0.099	1.757 ± 0.019	3.71	3.15	–	2.56	2.24	1.92	1.86

Table 3. continued.

Star	Ref.	JD	λ	ϕ	$\theta_{\rm LD}$	B_0	V_0	R_0	I_0	J_0	H_0	K_0
η Aql	L02	2 452 090.3540	1.64	0.239	1.842 ± 0.020	3.92	3.26	–	2.61	2.26	1.90	1.83
η Aql	L02	2 452 091.3460	1.64	0.377	1.807 ± 0.023	4.14	3.41	–	2.69	2.30	1.92	1.84
η Aql	L02	2 452 095.3600	1.64	0.936	1.605 ± 0.050	3.59	3.10	–	2.58	2.28	1.99	1.94
η Aql	L02	2 452 099.3370	1.64	0.490	1.844 ± 0.026	4.44	3.60	–	2.83	2.40	1.97	1.88
η Aql	L02	2 452 101.3290	1.64	0.768	1.672 ± 0.038	4.51	3.72	–	2.97	2.53	2.13	2.05
η Aql	L02	2 452 103.2930	1.64	0.042	1.697 ± 0.041	3.54	3.05	–	2.52	2.22	1.93	1.87
η Aql	L02	2 452 105.3000	1.64	0.321	1.842 ± 0.025	3.99	3.31	–	2.63	2.27	1.90	1.82
η Aql	L02	2 452 106.2830	1.64	0.458	1.860 ± 0.016	4.38	3.56	–	2.79	2.37	1.95	1.86
η Aql	L02	2 452 107.3020	1.64	0.600	1.853 ± 0.028	4.59	3.71	–	2.93	2.46	2.02	1.93
η Aql	L02	2 452 108.3080	1.64	0.740	1.744 ± 0.033	4.60	3.77	–	3.00	2.54	2.13	2.04
η Aql	L02	2 452 116.2760	1.64	0.851	1.650 ± 0.024	4.07	3.43	–	2.79	2.44	2.09	2.02
η Aql	K04	2 452 524.5643	2.18	0.741	1.782 ± 0.124	4.60	3.77	–	3.00	2.54	2.13	2.04
η Aql	K04	2 452 557.5462	2.18	0.336	1.916 ± 0.105	4.03	3.34	–	2.64	2.28	1.90	1.83
η Aql	K04	2 452 559.5346	2.18	0.614	1.843 ± 0.045	4.60	3.73	–	2.94	2.46	2.03	1.94
η Aql	K04	2 452 564.5321	2.18	0.310	1.846 ± 0.053	3.97	3.30	–	2.62	2.26	1.89	1.82
η Aql	K04	2 452 565.5155	2.18	0.447	1.910 ± 0.032	4.35	3.54	–	2.78	2.36	1.95	1.86
η Aql	K04	2 452 566.5185	2.18	0.587	1.900 ± 0.034	4.57	3.70	–	2.92	2.45	2.01	1.92
η Aql	K04	2 452 567.5232	2.18	0.727	1.839 ± 0.040	4.63	3.79	–	3.00	2.54	2.12	2.04
η Aql	K04	2 452 573.5114	2.18	0.561	1.923 ± 0.057	4.54	3.67	–	2.90	2.43	2.00	1.91
η Aql	K04	2 452 769.9372	2.18	0.931	1.681 ± 0.031	3.61	3.12	–	2.59	2.29	2.00	1.95
η Aql	K04	2 452 770.9222	2.18	0.068	1.828 ± 0.049	3.61	3.09	–	2.54	2.23	1.92	1.86
η Aql	K04	2 452 772.8988	2.18	0.343	1.919 ± 0.051	4.04	3.35	–	2.65	2.28	1.90	1.83
W Sgr	K04	2 452 743.8373	2.18	0.571	1.438 ± 0.103	5.43	4.59	–	3.78	–	–	–
W Sgr	K04	2 452 744.9149	2.18	0.713	1.319 ± 0.094	5.55	4.72	–	3.91	–	–	–
W Sgr	K04	2 452 749.8676	2.18	0.365	1.289 ± 0.147	5.00	4.32	–	3.59	–	–	–
W Sgr	K04	2 452 751.8659	2.18	0.628	1.348 ± 0.179	5.52	4.66	–	3.86	–	–	–
W Sgr	K04	2 452 763.8884	2.18	0.211	1.311 ± 0.035	4.75	4.15	–	3.51	–	–	–
W Sgr	K04	2 452 764.8766	2.18	0.341	1.383 ± 0.030	4.88	4.24	–	3.55	–	–	–
W Sgr	K04	2 452 765.8802	2.18	0.473	1.341 ± 0.033	5.24	4.46	–	3.71	–	–	–
W Sgr	K04	2 452 767.8671	2.18	0.735	1.234 ± 0.083	5.52	4.71	–	3.91	–	–	–
W Sgr	K04	2 452 769.9137	2.18	0.005	1.266 ± 0.064	4.35	3.92	–	3.42	–	–	–
β Dor	K04	2 452 215.7953	2.18	0.161	1.884 ± 0.082	4.21	3.46	3.13	2.73	2.30	1.91	1.86
β Dor	K04	2 452 216.7852	2.18	0.261	1.999 ± 0.048	4.40	3.58	3.22	2.80	2.34	1.92	1.86
β Dor	K04	2 452 247.7611	2.18	0.408	1.965 ± 0.060	4.76	3.81	3.42	2.97	2.45	1.99	1.93
β Dor	K04	2 452 308.6448	2.18	0.594	1.886 ± 0.076	4.73	3.85	3.46	3.03	2.53	2.11	2.04
β Dor	K04	2 452 567.8272	2.18	0.927	1.834 ± 0.063	4.02	3.39	3.09	2.73	2.35	2.01	1.95
β Dor	K04	2 452 744.5645	2.18	0.884	1.770 ± 0.072	4.12	3.47	3.16	2.79	2.39	2.03	1.98
β Dor	K04	2 452 749.5139	2.18	0.387	1.965 ± 0.110	4.71	3.78	3.39	2.95	2.43	1.98	1.91
β Dor	K04	2 452 750.5111	2.18	0.488	1.907 ± 0.076	4.83	3.91	3.48	3.04	2.52	2.05	1.98
β Dor	K04	2 452 751.5186	2.18	0.591	1.999 ± 0.172	4.74	3.86	3.47	3.04	2.53	2.10	2.04
ζ Gem	N02	2 451 098.9800	0.74	0.477	1.566 ± 0.221	5.06	4.11	–	3.19	2.65	–	2.13
ζ Gem	N02	2 451 229.8300	0.74	0.368	1.461 ± 0.231	4.95	4.02	–	3.10	2.59	–	2.08
ζ Gem	N02	2 451 232.7200	0.74	0.652	1.619 ± 0.053	4.82	3.96	–	3.18	2.67	–	2.18
ζ Gem	N02	2 451 233.7100	0.74	0.750	1.514 ± 0.063	4.61	3.85	–	3.10	2.63	–	2.18
ζ Gem	L02	2 451 605.2260	1.64	0.349	1.720 ± 0.015	4.91	4.00	–	3.08	2.58	–	2.08
ζ Gem	L02	2 451 206.2410	1.64	0.044	1.719 ± 0.048	4.32	3.65	–	2.92	2.48	–	2.07
ζ Gem	L02	2 451 214.1920	1.64	0.827	1.845 ± 0.062	4.46	3.77	–	3.05	2.58	–	2.16
ζ Gem	L02	2 451 615.1800	1.64	0.330	1.783 ± 0.032	4.88	3.97	–	3.06	2.57	–	2.07
ζ Gem	L02	2 451 617.1670	1.64	0.525	1.629 ± 0.029	5.04	4.10	–	3.21	2.67	–	2.15
ζ Gem	L02	2 451 618.1430	1.64	0.622	1.575 ± 0.008	4.89	4.00	–	3.19	2.67	–	2.18
ζ Gem	L02	2 451 619.1680	1.64	0.723	1.590 ± 0.018	4.67	3.88	–	3.12	2.64	–	2.18
ζ Gem	L02	2 451 620.1690	1.64	0.821	1.627 ± 0.029	4.47	3.77	–	3.06	2.58	–	2.16
ζ Gem	L02	2 451 622.1980	1.64	0.021	1.717 ± 0.047	4.30	3.64	–	2.93	2.48	–	2.07
ζ Gem	L02	2 451 643.1610	1.64	0.086	1.707 ± 0.012	4.37	3.68	–	2.91	2.48	–	2.05
ζ Gem	L02	2 451 981.1820	1.64	0.386	1.730 ± 0.014	4.98	4.04	–	3.12	2.60	–	2.09
ζ Gem	L02	2 451 982.1640	1.64	0.482	1.679 ± 0.021	5.06	4.11	–	3.20	2.65	–	2.13

Table 3. continued.

Star	Ref.	JD	λ	ϕ	$\theta_{\rm LD}$	B_0	V_0	R_0	I_0	J_0	H_0	K_0
ζ Gem	L02	2 451 983.2010	1.64	0.584	1.631 ± 0.022	4.96	4.05	–	3.21	2.67	–	2.17
ζ Gem	L02	2 451 894.3870	1.64	0.835	1.662 ± 0.020	4.45	3.76	–	3.05	2.57	–	2.16
ζ Gem	L02	2 451 895.3690	1.64	0.932	1.672 ± 0.014	4.32	3.66	–	2.98	2.52	–	2.11
ζ Gem	K04	2 452 214.8787	2.18	0.408	1.715 ± 0.059	5.01	4.07	–	3.14	2.62	–	2.10
ζ Gem	K04	2 452 216.8357	2.18	0.600	1.751 ± 0.088	4.93	4.03	–	3.21	2.67	–	2.18
ζ Gem	K04	2 451 527.9722	2.12	0.739	1.643 ± 0.334	4.63	3.86	–	3.11	2.63	–	2.18
ζ Gem	K04	2 451 601.8285	2.12	0.014	1.748 ± 0.086	4.30	3.64	–	2.93	2.48	–	2.08
ζ Gem	K04	2 451 259.7790	2.12	0.318	2.087 ± 0.291	4.85	3.95	–	3.05	2.57	–	2.06
ζ Gem	K04	2 451 262.7400	2.12	0.610	1.730 ± 0.273	4.91	4.02	–	3.20	2.67	–	2.18
ζ Gem	K04	2 451 595.8520	2.12	0.426	1.423 ± 0.284	5.03	4.08	–	3.15	2.63	–	2.11
ζ Gem	K04	2 451 602.7640	2.12	0.107	1.910 ± 0.216	4.40	3.69	–	2.91	2.48	–	2.05
Y Oph	K04	2 452 742.9056	2.18	0.601	1.462 ± 0.120	4.93	4.10	3.86	3.29	2.96	2.58	2.52
Y Oph	K04	2 452 750.8842	2.18	0.067	1.414 ± 0.106	4.26	3.64	3.50	3.00	2.77	2.49	2.44
Y Oph	K04	2 452 772.8308	2.18	0.349	1.478 ± 0.057	4.75	3.95	3.72	3.16	2.86	2.50	2.43
Y Oph	K04	2 452 786.8739	2.18	0.168	1.436 ± 0.046	4.45	3.76	3.59	3.07	2.79	2.48	2.42
ℓ Car	K04	2 452 453.4978	2.18	0.587	3.035 ± 0.109	4.73	3.46	2.89	2.41	1.72	1.16	1.06
ℓ Car	K04	2 452 739.5644	2.18	0.634	2.859 ± 0.084	4.73	3.48	2.91	2.42	1.74	1.19	1.09
ℓ Car	K04	2 452 740.5691	2.18	0.662	2.954 ± 0.046	4.72	3.47	2.92	2.42	1.75	1.22	1.12
ℓ Car	K04	2 452 741.7171	2.18	0.694	2.969 ± 0.038	4.71	3.46	2.93	2.42	1.77	1.24	1.15
ℓ Car	K04	2 452 742.7009	2.18	0.722	2.874 ± 0.054	4.69	3.45	2.94	2.43	1.80	1.27	1.18
ℓ Car	K04	2 452 743.6985	2.18	0.750	2.737 ± 0.073	4.66	3.44	2.94	2.44	1.81	1.30	1.21
ℓ Car	K04	2 452 744.6336	2.18	0.776	2.769 ± 0.033	4.62	3.43	2.92	2.43	1.82	1.31	1.22
ℓ Car	K04	2 452 745.6285	2.18	0.804	2.652 ± 0.095	4.53	3.39	2.88	2.41	1.81	1.32	1.23
ℓ Car	K04	2 452 746.6198	2.18	0.832	2.749 ± 0.045	4.40	3.33	2.81	2.37	1.79	1.31	1.23
ℓ Car	K04	2 452 747.5988	2.18	0.860	2.674 ± 0.125	4.22	3.23	2.73	2.30	1.74	1.29	1.21
ℓ Car	K04	2 452 749.5763	2.18	0.915	2.620 ± 0.076	3.82	2.96	2.53	2.13	1.63	1.23	1.15
ℓ Car	K04	2 452 751.5785	2.18	0.972	2.726 ± 0.032	3.62	2.79	2.40	2.01	1.54	1.15	1.08
ℓ Car	K04	2 452 755.6166	2.18	0.085	2.942 ± 0.110	3.78	2.85	2.44	2.01	1.51	1.06	0.98
ℓ Car	K04	2 452 763.5551	2.18	0.309	3.157 ± 0.032	4.31	3.13	2.63	2.15	1.53	1.01	0.92
ℓ Car	K04	2 452 765.5545	2.18	0.365	3.175 ± 0.033	4.43	3.19	2.69	2.21	1.56	1.02	0.93
ℓ Car	K04	2 452 766.5497	2.18	0.393	3.173 ± 0.033	4.48	3.25	2.72	2.23	1.57	1.04	0.95
ℓ Car	K04	2 452 768.5663	2.18	0.450	3.155 ± 0.036	4.60	3.35	2.78	2.29	1.62	1.07	0.98
ℓ Car	K04	2 452 769.5746	2.18	0.478	3.155 ± 0.021	4.65	3.39	2.81	2.32	1.64	1.08	1.00
ℓ Car	K04	2 452 770.5353	2.18	0.505	3.124 ± 0.021	4.69	3.41	2.84	2.35	1.66	1.10	1.01
ℓ Car	K04	2 452 771.5281	2.18	0.533	3.100 ± 0.019	4.72	3.43	2.86	2.38	1.69	1.12	1.03
ℓ Car	K04	2 452 786.6200	2.18	0.957	2.700 ± 0.064	3.64	2.82	2.42	2.03	1.56	1.17	1.09

2.1.4 Lettre ApJ : "The angular size of the Cepheid ℓ Car : a comparison of the interferometric and surface brightness techniques" (2004)

Cette Lettre compare les prédictions de diamètre angulaire obtenues par la technique de la brillance de surface aux mesures interférométriques directes de la Céphéide brillante ℓ Carinae. Les deux méthodes sont en excellent accord l'une avec l'autre sur la plus grande partie du cycle de pulsation, avec cependant une déviation significative près de la phase de diamètre minimum. Cet effet pourrait être dû à la présence d'ondes de choc importantes lors du rebond de l'atmosphère de l'étoile.

FIG. 2.7 – Vue du camp de base de l'Observatoire de Paranal depuis la plate-forme du VLT.

THE ASTROPHYSICAL JOURNAL, 604:L113–L116, 2004 April 1

THE ANGULAR SIZE OF THE CEPHEID ▫ CARINAE: A COMPARISON OF THE INTERFEROMETRIC AND SURFACE BRIGHTNESS TECHNIQUES

PIERRE KERVELLA,[1,2] PASCAL FOUQUÉ,[1,3] JESPER STORM,[4] WOLFGANG P. GIEREN,[5] DAVID BERSIER,[6] DENIS MOURARD,[7] NICOLAS NARDETTO,[7] AND VINCENT COUDÉ DU FORESTO[2]

Received 2004 January 15; accepted 2004 February 12; published 2004 March 5

ABSTRACT

Recent interferometric observations of the brightest and angularly largest classical Cepheid, ▫ Carinae, with ESO's Very Large Telescope Interferometer have resolved with high precision the variation of its angular diameter with phase. We compare the measured angular diameter curve to the one that we derive by an application of the Baade-Wesselink–type infrared surface brightness technique and find a near-perfect agreement between the two curves. The mean angular diameters of ▫ Car from the two techniques agree very well within their total error bars (1.5%), as do the derived distances (4%). This result is an indication that the calibration of the surface brightness relations used in the distance determination of far-away Cepheids is not affected by large biases.

Subject headings: Cepheids — distance scale — stars: distances — stars: fundamental parameters — stars: oscillations — techniques: interferometric

On-line material: color figures

1. INTRODUCTION

Cepheid variables are fundamental objects for the calibration of the extragalactic distance scale. Distances of Cepheids can be derived in at least two different ways: by using their observed mean magnitudes and periods together with a period-luminosity relation, or by applying a Baade-Wesselink (BW) type technique to determine their distances and mean diameters from their observed variations in magnitude, color, and radial velocity. This latter technique has been dramatically improved by the introduction of the (near-)infrared surface brightness (IRSB) method by Welch (1994) and later by Fouqué & Gieren (1997), who calibrated the relation between the *V*-band surface brightness and near-infrared colors of Cepheids. For this purpose, they used the observed interferometric angular diameters of a number of giants and supergiants bracketting the Cepheid color range. This method has been applied to a large number of Galactic Cepheid variables, for instance by Gieren et al. (1997, 1998) and Storm et al. (2004).

Applying the surface brightness relation derived from stable stars to Cepheids implicitly assumes that the relation also applies to pulsating stars. The validity of this assumption can now be addressed by comparing direct interferometric measurements of the angular diameter variation of a Cepheid to the one derived from the IRSB technique. It has recently been shown by Kervella et al. (2004, hereafter K04) that the Very Large Telescope Interferometer (VLTI) on Paranal is now in a condition not only to determine accurate *mean* angular diameters of nearby Cepheid variables, but to follow their angular diameter *variations* with high precision. Using the Palomar Testbed Interferometer, Lane et al. (2000, 2002) resolved the pulsation of the Cepheids ζ Gem and η Aql as early as 2000, but the comparison that we present in this Letter is the first in which error bars on the derived distance and linear diameter are directly comparable at a few percent level between the interferometric and IRSB techniques.

The star that we discuss in this Letter, ▫ Car, is the brightest Cepheid in the sky. Its long period of about 35.5 days implies a large mean diameter, which together with its relatively short distance makes it an ideal target for resolving its angular diameter variations with high accuracy. In this Letter, we compare the interferometrically determined angular diameter curve of ▫ Car with that determined from the IRSB technique, and we demonstrate that the two sets of angular diameters are in excellent agreement. On the basis of the available high-precision angular diameter and radial velocity curves for this star, we also derive a revised value of its distance and mean radius.

Several authors (Sasselov & Karovska 1994; Marengo et al. 2003, 2004) have pointed out potential sources of systematic uncertainties in the determination of Cepheid distances using the interferometric BW method. In particular, imperfections in the numerical modeling of Cepheid atmospheres could lead to biased estimates of the limb darkening and projection factor. We discuss the magnitude of these uncertainties in the case of ▫ Car.

2. INTERFEROMETRIC OBSERVATIONS

The interferometric observations of ▫ Car were obtained with the VLTI (Glindemann et al. 2000), using its commissioning instrument VINCI (Kervella et al. 2000, 2003) and 0.35 m test siderostats. This instrument recombines the light from two telescopes in the infrared *K* band (2.0–2.4 μm), at an effective wavelength of 2.18 μm. A detailed description of the interferometric data recorded on ▫ Car can be found in K04.

The limb-darkening (LD) models used to derive the photospheric diameters from the fringe visibilities were taken from Claret (2000). The correction introduced on the uniform disk (UD) interferometric measurements by the LD is small in the *K* band: for ▫ Car, we determine $k = \theta_{\rm UD}/\theta_{\rm LD} = 0.966$. Con-

[1] European Southern Observatory, Casilla 19001, Santiago 19, Chile; pkervell@eso.org, pfouque@eso.org.
[2] LESIA, Observatoire de Paris-Meudon, 5 place Jules Janssen, F-92195 Meudon Cedex, France; vincent.foresto@obspm.fr.
[3] Observatoire Midi-Pyrénées, UMR 5572, 14 avenue Edouard Belin, F-31400 Toulouse, France.
[4] Astrophysikalisches Institut Potsdam, An der Sternwarte 16, D-14482 Potsdam, Germany; jstorm@aip.de.
[5] Universidad de Concepción, Departamento de Física, Casilla 160-C, Concepción, Chile; wgieren@coma.cfm.udec.cl.
[6] Space Telescope Science Institute, 3700 San Martin Drive, Baltimore, MD 21218; bersier@stsci.edu.
[7] GEMINI, UMR 6203, Observatoire de la Côte d'Azur, Avenue Copernic, F-06130 Grasse, France; denis.mourard@obs-azur.fr, nicolas.nardetto@obs-azur.fr.

sidering the magnitude of this correction, a total systematic uncertainty of $\pm 1\%$ appears reasonable. However, until the LD of a sample of Cepheids has been measured directly by interferometry, this value relies exclusively on numerical models of the atmosphere. This is expected to be achieved in the next years using, for instance, the longest baselines of the VLTI (up to 202 m) and the shorter *J* and *H* infrared bands accessible with the AMBER instrument (Petrov et al. 2000).

The LD correction is changing slightly over the pulsation of the star because of the change in effective temperature, but Marengo et al. (2003) have estimated the amplitude of this variation to less than 0.3% peak to peak in the *H* band (for the 10 day period Cepheid ζ Gem). It is even lower in the *K* band and averages out in terms of rms dispersion. As a consequence, we have neglected this variation in the present study.

The limb-darkened angular diameter measurements are listed in Table 1. Two error bars are given for each point, corresponding, respectively, to the statistical uncertainty (internal error) and to the systematic error introduced by the uncertainties on the assumed angular diameters of the calibrator stars (external error). The phases given in Table 1 are based on the new ephemeris derived in § 4. These measurements were obtained during the commissioning of the VLTI, and part of them is affected by relatively large uncertainties (3%–5%) due to instrumental problems. However, the precision reached by VINCI and the test siderostats on this baseline is of the order of 1% on the angular diameter, as demonstrated around the maximum diameter phase.

TABLE 1

Angular Diameter Measurements of δ Car

Julian Date	Phase	θ_{LD} (mas)	Uncertainties
2452453.498	0.618	3.054 ± 0.113	[0.041, 0.105]
2452739.564	0.665	2.891 ± 0.087	[0.076, 0.043]
2452740.569	0.693	2.989 ± 0.047	[0.018, 0.044]
2452741.717	0.726	2.993 ± 0.039	[0.026, 0.029]
2452742.712	0.754	2.899 ± 0.056	[0.035, 0.043]
2452743.698	0.781	2.758 ± 0.076	[0.074, 0.016]
2452744.634	0.808	2.794 ± 0.035	[0.032, 0.013]
2452745.629	0.836	2.675 ± 0.098	[0.097, 0.017]
2452746.620	0.864	2.775 ± 0.046	[0.023, 0.040]
2452747.599	0.891	2.699 ± 0.129	[0.127, 0.026]
2452749.576	0.947	2.645 ± 0.078	[0.077, 0.012]
2452751.579	0.003	2.753 ± 0.033	[0.028, 0.017]
2452755.617	0.117	2.970 ± 0.113	[0.113, 0.013]
2452763.555	0.340	3.194 ± 0.034	[0.009, 0.033]
2452765.555	0.396	3.212 ± 0.034	[0.011, 0.033]
2452766.550	0.424	3.210 ± 0.035	[0.011, 0.033]
2452768.566	0.481	3.188 ± 0.037	[0.011, 0.035]
2452769.575	0.509	3.189 ± 0.022	[0.018, 0.012]
2452770.535	0.536	3.160 ± 0.022	[0.020, 0.009]
2452771.528	0.564	3.136 ± 0.020	[0.017, 0.010]
2452786.620	0.989	2.727 ± 0.064	[0.012, 0.063]

Note.—The statistical and systematic calibration uncertainties are in brackets.

3. THE IRSB TECHNIQUE

The IRSB technique has been presented and discussed in detail in Fouqué & Gieren (1997, hereafter FG97). In brief, the angular diameter curve of a given Cepheid variable is derived from its *V* light and $V-K$ color curve, appropriately corrected for extinction. It is then combined with its linear displacement curve, which is essentially the integral of the radial velocity curve. A linear regression of pairs of angular diameters and linear displacements, obtained at the same pulsation phases, yields both the distance and the mean radius of the star.

While there are several sources of systematic uncertainty in the method, as discussed in Gieren et al. (1997), one of its great advantages is its strong insensitivity to the adopted reddening corrections and to the metallicity of the Cepheid (Storm et al. 2004). With excellent observational data at hand, individual Cepheid distances and radii can be determined with an accuracy of the order of 5% *if* the adopted *K*-band surface brightness–color relation is correct.

A first calibration of this relation coming directly from interferometrically determined angular diameters of Cepheid variables was presented by Nordgren et al. (2002, hereafter N02). They found a satisfactory agreement with the FG97 calibration, within the combined 1 σ uncertainties of both surface brightness–color calibrations. Considering more closely the results from N02, an even better agreement is found between the $F_V(V-K)$ relations *before* the zero point if forced between the different colors. Before this operation, N02 found the relation

$$F_{V_0} = (3.956 \pm 0.011) - (0.134 \pm 0.005)(V-K)_0 \quad (1)$$

that translates, after forcing the zero point to the average of the three selected colors, to the relation

$$F_{V_0} = (3.941 \pm 0.004) - (0.125 \pm 0.005)(V-K)_0. \quad (2)$$

On the other hand, FG97 obtain

$$F_{V_0} = (3.947 \pm 0.003) - (0.131 \pm 0.003)(V-K)_0. \quad (3)$$

From this comparison, it appears that the slope initially determined by N02 for $F_V(V-K)$ is significantly different both from their final value and from the FG97 relation. This difference could cause a bias because of the averaging of the multicolor zero points. Although small in absolute value, such a bias is of particular importance for δ Car because of its relatively large $V-K$ color.

Another argument in favor of the FG97 surface brightness relation is that it relies on a sample of 11 Cepheids with periods of 4–39 days, while the relations established by N02 were derived from the observations of only three Cepheids with periods of 5–10 days. Such short-period Cepheids are significantly hotter than δ Car ($P = 35.5$ days), and a local difference of the slope of the IRSB relations cannot be excluded. For these two reasons, we choose to retain the FG97 calibration for our analysis of the Cepheid δ Car in the following section.

4. DIAMETER AND DISTANCE

4.1. *Angular Diameter*

We have combined the photometric data from Pel (1976) and Bersier (2002) to construct the *V*-band light curve for δ Car. The two data sets are spanning almost 30 years and allow an improved determination of the period of this variable. We find $P = 35.54804$ days. The time of maximum *V* light has been adopted from Szabados (1989), who give a value of $T_0 = 2440736.230$, which is also in good agreement with the more recent data. The resulting light curve is shown in Figure 1. The *K*-band light curve is based on the data from Laney & Stobie (1992) and is also shown in Figure 1. The $V-K$ color

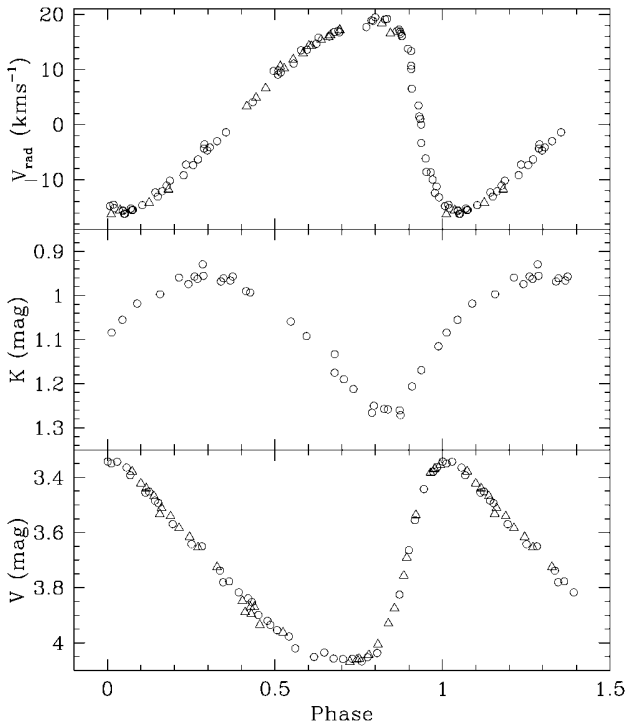

FIG. 1.—Radial velocity curve of ▫ Car (*top panel*) using data from Taylor et al. (1997) shifted by -1.5 km s^{-1} (*circles*) and from Bersier (2002; *triangles*). The *K*-band photometric measurements (*middle panel*) were taken from Laney & Stobie (1992). We have relied on Pel (1976; *circles*) and Bersier (2002; *triangles*) for the *V*-band data.

curve that is needed by the IRSB method has been constructed on the basis of the observed *V*-band data and a Fourier fit to the *K*-band data as described in Storm et al. (2004).

For the radial velocity curve we have used the data from Taylor et al. (1997) and Bersier (2002). Using the new ephemeris from above we detected a slight offset of 1.5 km s^{-1} between the two data sets. We choose to shift the Taylor et al. (1997) data set by -1.5 km s^{-1} to bring all the data on the well-established CORAVEL system of Bersier (2002). We note that the exact radial velocity zero point is irrelevant as the method makes use of *relative* velocities. The combined radial velocity data are displayed in Figure 1.

The application of the IRSB method has followed the procedure described in Storm et al. (2004). We have adopted the same reddening law with $R_V = 3.30$ and $R_K = 0.30$, a reddening of $E(B-V) = 0.17$ (Fernie 1990), and a projection factor, p, from radial to pulsational velocity of $p = 1.39 - 0.03 \log P = 1.343$ (Hindsley & Bell 1986; Gieren et al. 1993). As discussed by Storm et al. (2004), we only consider the points in the phase interval from 0.0 to 0.8 (phase zero is defined by the *V*-band maximum light). We have applied a small phase shift of -0.025 to the radial velocity data to bring the photometric and radial velocity–based angular diameters into agreement. We note that a similar phase shift can be achieved by lowering the systemic velocity by 1.5 km s^{-1} .

The angular diameter curve obtained from the photometry has been plotted in Figure 2, together with the linear displacement curve. The photometric and interferometric diameter curves are directly compared in Figure 3, where they are plotted as a function of phase. With these data we can compute the average angular diameters obtained from each technique. For the IRSB, we find an average limb-darkened angular diameter

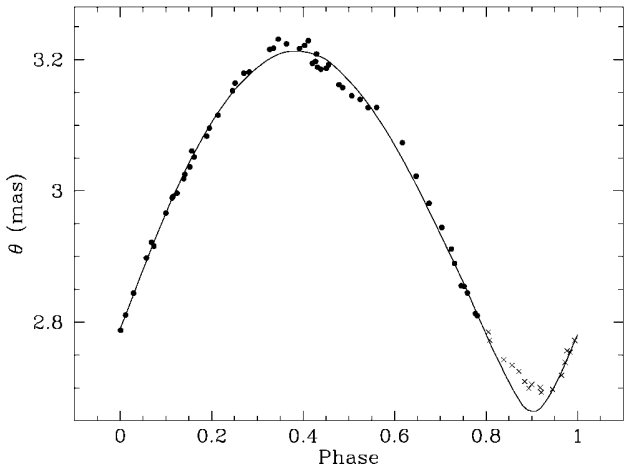

FIG. 2.—Photometric angular diameters plotted against phase for our best-fitting distance. The solid curve represents the integrated radial velocity curve of ▫ Car for the adopted distance. [*See the electronic edition of the Journal for a color version of this figure.*]

$\overline{\theta_{\rm LD}} = 2.974 \pm 0.046$ mas, and for the interferometric measurements we find $\overline{\theta_{\rm LD}} = 2.992 \pm 0.012$ mas. The agreement between these two values is strikingly good. This is a serious indication that the calibration of the surface brightness–color relation (FG97), based on nonpulsating giant stars, does apply to Cepheids.

4.2. *Distance*

The surface brightness method yields a distance of 560 ± 6 pc and a mean radius of $R = 179 \pm 2\,R_\odot$. The corresponding mean absolute *V* magnitude is $M_V = -5.57 \pm 0.02$ mag, and the distance modulus is $(m - M)_0 = 8.74 \pm 0.05$. The error estimates are all intrinsic 1 σ random errors. In addition to these random errors, a systematic error of the order of 4% should be taken into account, as discussed by Gieren et al. (1997). The final IRSB values are thus $d = 560 \pm 23$ pc and $R = 179 \pm 7\,R_\odot$. Compared to Storm et al. (2004), we find a significantly (0.24 mag) shorter distance modulus for ▫ Car. This

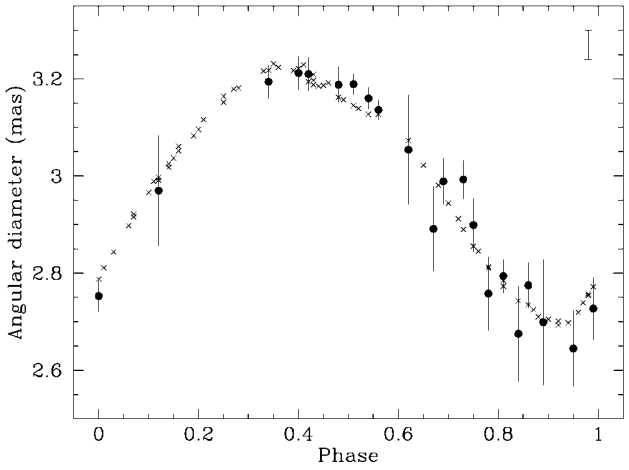

FIG. 3.—Interferometrically determined angular diameters, plotted against phase (*filled circles*) with the angular diameters derived with the IRSB method overplotted (*crosses*). In the top right corner a typical error bar for the surface brightness method data is shown. [*See the electronic edition of the Journal for a color version of this figure.*]

can be explained by the use in the present Letter of the new and superior radial velocity data from Taylor et al. (1997) and Bersier (2002).

K04 found $d = 603^{+24}_{-19}$ pc, using the interferometric angular diameters and a subset of the radial velocity data used here. To make the comparison more relevant, we determined the distance and radius using the same data (interferometric diameters from Table 1 and radial velocity from Taylor et al. 1997 and Bersier 2002; see above), the same ephemeris, and the same projection factor (see § 4.1). Using the method of K04, we find a distance $d = 566^{+24}_{-19}$ and a linear radius $R = 182^{+8}_{-7}\ R_{\odot}$. This is in excellent agreement with the values obtained from the IRSB method.

This 6% difference in the distances based on interferometric diameters (603 pc for K04 vs. 566 pc here) has two major causes. First, the *p*-factor used in the present Letter is ~1.3% smaller than in K04. The choice of the reference used for the *p*-factor has currently an impact of a few percents on its value. This indicates that the average value of the *p*-factor for a given Cepheid is currently uncertain by at least a similar amount, and this systematic error translates linearly to the distance determination.

Second, the use of a different—and superior—data set for the radial velocity makes the radius curve different from K04. In particular the amplitude is smaller here than in K04 by ~3%. This is likely due to the more complete phase coverage that we have here and possibly also to a different choice of spectral lines to estimate the radial velocity. This amplitude difference translates linearly on the distance through the BW method.

5. CONCLUSION

The main point of our Letter is to show that with a consistent treatment of the data, the internal accuracy of both methods (IRSB or interferometry) is extremely good: the angular diameter variation observed using the VLTI agrees very well with that derived from the $F_V(V-K)$ version of the IRSB technique as calibrated by FG97. For all the interferometric measurements, the corresponding IRSB angular diameter at the same phase lies within the combined 1 σ error bars of the two measurements (Fig. 3). Even more importantly, the mean angular diameter of the Cepheid as derived from both independent sets of angular diameter determination are in excellent agreement, within a few percents.

Unfortunately, this is not equivalent to say that the Cepheid distance scale is calibrated to a 1% accuracy. We have drawn attention to remaining sources of systematic errors that can affect Cepheid radii and distances up to several percents. As an illustration of these sources, K04 obtain a distance $d = 603^{+24}_{-19}$ pc for ▫ Car, while we obtain $d = 566^{+24}_{-19}$ pc from the same interferometric data.

We have already shown that most of the 6% difference (equivalent to 1.3 σ) can be explained by the use of different radial velocity data and projection factor. Another thing to consider is the phase interval used. K04 used measurements over the whole pulsation cycle whereas in the IRSB technique, one avoids the phase interval 0.8–1 (Fig. 2). During that phase interval, which corresponds to the rebound of the atmosphere around the minimum radius, energetic shock waves are created. As discussed by Sabbey et al. (1995), they produce asymmetric line profiles in the Cepheid spectrum. Recent modeling using a self-consistent dynamical approach also shows that the $\tau = 1$ photosphere may not be comoving with the atmosphere of the Cepheid during its pulsation, at the 1% level (N. Nardetto et al. 2004, in preparation). Such an effect would impact the *p*-factor, modify the shape of the radial velocity curve, and thus bias the amplitude of the radius variation, possibly up to a level of a few percents. As the BW method (either its classical or its interferometric versions) relies linearly on this amplitude, a bias at this level currently cannot be excluded.

The interferometric BW method is currently limited to distances of 1–2 kpc because of the limited length of the available baselines. The IRSB technique, on the other hand, can reach extragalactic Cepheids as already demonstrated by Gieren et al. (2000) for the Large Magellanic Cloud and by Storm et al. (2004) for the Small Magellanic Cloud. Using high-precision interferometric measurements of ▫ Car and other Cepheids, it will be possible to calibrate the IRSB method down to the level of a few percents. From the present comparison, we already see that this fundamental calibration will be very similar to the calibration found by FG97 and N02.

W. P. G. acknowledges support for this work from the Chilean FONDAP Center for Astrophysics 15010003.

REFERENCES

Bersier, D. 2002, ApJS, 140, 465
Claret, A. 2000, A&A, 363, 1081
Fernie, J. D. 1990, ApJS, 72, 153
Fouqué, P., & Gieren, W. P. 1997, A&A, 320, 799 (FG97)
Gieren, W. P., Barnes, T. G., & Moffett, T. J. 1993, ApJ, 418, 135
Gieren, W. P., Fouqué, P., & Gómez, M. 1997, ApJ, 488, 74
———. 1998, ApJ, 496, 17
Gieren, W. P., Storm, J., Fouqué, P., Mennickent, R. E., & Gómez, M. 2000, ApJ, 533, L107
Glindemann, A., et al. 2000, Proc. SPIE, 4006, 2
Hindsley, R. B., & Bell, R. A. 1986, PASP, 98, 881
Kervella, P., Coudé du Foresto, V., Glindemann, A., & Hofmann, R. 2000, Proc. SPIE, 4006, 31
Kervella, P., et al. 2003, Proc. SPIE, 4838, 858
———. 2004, A&A, in press (astro-ph/0311525) (K04)
Lane, B. F., Creech-Eakman, M. J., & Nordgren, T. E. 2002, ApJ, 573, 330
Lane, B. F., Kuchner, M., Boden, A., Creech-Eakman, M., & Kulkarni, S. 2000, Nature, 407, 485
Laney, C. D., & Stobie, R. S. 1992, A&AS, 93, 93
Marengo, M., Karovska, M., Sasselov, D. D., & Sanchez, M. 2004, ApJ, 603, 286
Marengo, M., et al. 2003, ApJ, 589, 968
Nordgren, T. E., Lane, B. F., Hindsley, R. B., & Kervella, P. 2002, AJ, 123, 3380 (N02)
Pel, J. W. 1976, A&AS, 24, 413
Petrov, R., et al. 2000, Proc. SPIE, 4006, 68
Sabbey, C. N., et al. 1995, ApJ, 446, 250
Sasselov, D. D., & Karovska, M. 1994, ApJ, 432, 367
Storm, J., Carney, B. W., Gieren, W. P., Fouqué, P., Latham, D. W., & Fry, A. M. 2004, A&A, 415, 531
Szabados, L. 1989, Commun. Konkoly Obs., 94, 1
Taylor, M. M., Albrow, M. D., Booth, A. J., & Cottrell, P. L. 1997, MNRAS, 292, 662
Welch, D. L. 1994, AJ, 108, 1421

2.2 Le facteur de projection : un point clef

La méthode BW (classique et interférométrique) a été appliquée avec succès à un grand nombre d'étoiles pulsantes, en particulier des Céphéides. Elle est cependant limitée par la précision des modèles d'atmosphère stellaire utilisés pour dériver la variation ΔR de rayon à partir des variations de vitesse radiale. La conversion de la vitesse radiale observée (intégrée sur le disque) en vitesse pulsante est en effet rendue délicate par la dynamique interne complexe de l'atmosphère, l'assombrissement centre-bord, et les variations de température effective de l'étoile.

Actuellement, l'ensemble de ces inconnues se trouve rassemblé dans un facteur multiplicatif reliant la vitesse radiale (mesurée sur les spectres) à la vitesse pulsationnelle (celle de la photosphère de l'étoile) appelé facteur de projection (ou p-facteur). L'Eq. 2.3 formulée cette fois sur la base de la vitesse radiale mesurée sur le spectre devient la suivante :

$$R(t) - R(0) = -\int_0^t v_r(t)\, p(t)\, dt \tag{2.4}$$

En général, p est supposé constant au cours de la pulsation, mais il est probable que cette approximation n'est plus valable à l'échelle de quelques pourcents. Une conséquence importante est que les distances déterminées par la méthode BW sont linéairement liées au facteur de projection choisi. Par ricochet, toutes les estimations de distances extragalactiques basées sur la relation P–L des Céphéides (qui est étalonnée par la méthode BW) sont donc également liées linéairement au p-facteur.

Jusqu'à présent, le choix du facteur de projection était arbitraire : le plus souvent fixé à 1,36, en référence au travail de modélisation simplifiée de Burki, Mayor & Benz (1982). Ce facteur n'ayant jamais été mesuré directement, un biais potentiellement important ne pouvait pas être exclu. Pour améliorer cette situation, nous avons abordé l'étude de la question du facteur de projection à la fois de manière théorique (modélisation numérique), et de manière observationnelle (interférométrie et spectroscopie). Les premiers résultats dans ces directions sont présentés dans les articles A&A reproduits dans les Sect. 2.2.1, 2.2.2 et 2.2.3. Nous rapportons en particulier la première mesure directe d'un facteur de projection, sur la Céphéide prototype δ Cep.

2.2.1 Lettre A&A : "The projection factor of δ Cephei – A calibration of the Baade-Wesselink method using the CHARA Array" (2005)

Grâce aux très longues bases interférométriques du réseau de télescopes CHARA et à la grande précision de mesure de l'instrument de recombinaison FLUOR, nous avons obtenu la première mesure directe d'un facteur de projection, celui de δ Cep. Nous avons utilisé pour cela l'excellente mesure de parallaxe trigonométrique obtenue par Benedict et al. (2002) à l'aide de l'interféromètre FGS du *Hubble Space Telescope*. La connaissance de la distance de l'étoile nous a permis d'inverser la méthode Baade-Wesselink pour déterminer non plus la distance et le rayon, mais directement le p-facteur.

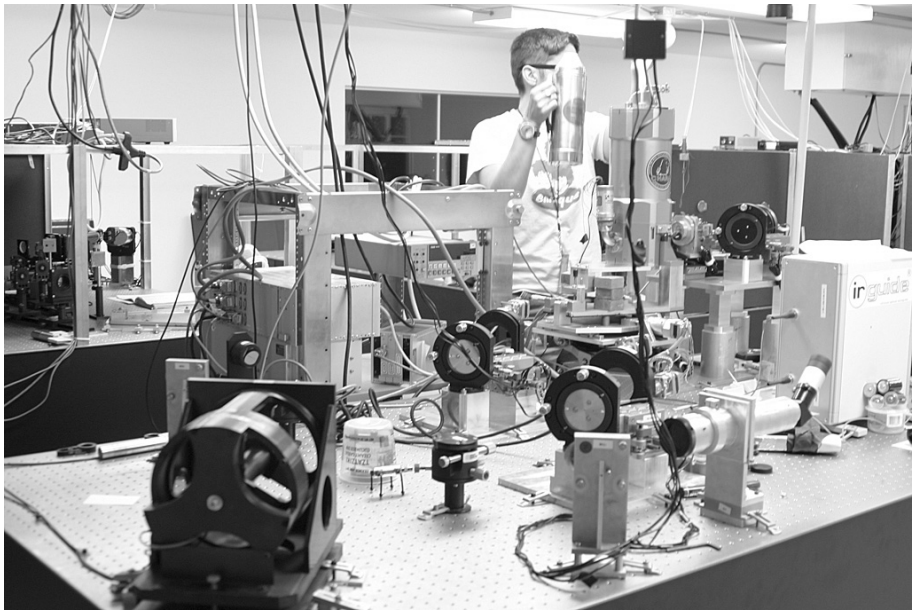

FIG. 2.8 – La table optique de l'instrument FLUOR installé dans le laboratoire de recombinaison de CHARA (Mont Wilson, Californie).

A&A 438, L9–L12 (2005)
DOI: 10.1051/0004-6361:200500139

Astronomy & Astrophysics

The projection factor of δ Cephei

A calibration of the Baade-Wesselink method using the CHARA Array⋆

A. Mérand[1], P. Kervella[1], V. Coudé du Foresto[1], S. T. Ridgway[1,2,3], J. P. Aufdenberg[2], T. A. ten Brummelaar[3], D. H. Berger[3], J. Sturmann[3], L. Sturmann[3], N. H. Turner[3], and H. A. McAlister[3]

[1] LESIA, UMR8109, Observatoire de Paris-Meudon, 5, place Jules Janssen, 92195 Meudon Cedex, France
e-mail: antoine.merand@obspm.fr
[2] National Optical Astronomical Observatory 950 North Cherry Avenue, Tucson, AZ 85719, USA
[3] Center for High Angular Resolution Astronomy, Georgia State University, PO Box 3965, Atlanta, Georgia 30302-3965, USA

Received 6 May 2005 / Accepted 7 June 2005

Abstract. Cepheids play a key role in astronomy as standard candles for measuring intergalactic distances. Their distance is usually inferred from the period–luminosity relationship, calibrated using the semi-empirical Baade-Wesselink method. Using this method, the distance is known to a multiplicative factor, called the projection factor. Presently, this factor is computed using numerical models – it has hitherto never been measured directly. Based on our new interferometric measurements obtained with the CHARA Array and the already published parallax, we present a geometrical measurement of the projection factor of a Cepheid, δ Cep. The value we determined, $p = 1.27 \pm 0.06$, confirms the generally adopted value of $p = 1.36$ within 1.5 sigmas. Our value is in line with recent theoretical predictions of Nardetto et al. (2004, A&A, 428, 131).

Key words. techniques: interferometric – stars: variables: Cepheids – stars: individual: δ Cep – cosmology: distance scale

1. Introduction

Cepheid stars are commonly used as cosmological distance indicators, thanks to their well-established period–luminosity law (P–L). This remarkable property has turned these supergiant stars into primary standard candles for extragalactic distance estimations. With intrinsic brightnesses of up to 100 000 times that of the Sun, Cepheids are easily distinguished in distant galaxies (up to about 30 Mpc distant). As such, they are used to calibrate the secondary distance indicators (supernovae, etc...) that are used to estimate even larger cosmological distances. For instance, the *Hubble Key Project* to measure the Hubble constant H_0 (Freedman et al. 2001) is based on the assumption of a distance to the LMC that was established primarily using Cepheids. Located at the very base of the cosmological distance ladder, a bias on the calibration of the Cepheid P–L relation would impact our whole perception of the scale of the Universe.

1.1. Period–luminosity calibration

The P–L relation takes the form $\log L = \alpha \log P + \beta$, where L is the (absolute) luminosity, P the period, α the slope, and β the zero point. The determination of α is straightforward: one can consider a large number of Cepheids in the LMC, located at a common distance from us. Calibrating the zero-point β is a much more challenging task, as it requires an independent distance measurement to a number of Cepheids. Ideally, one should measure directly their geometrical parallaxes, in order to obtain their absolute luminosity. Knowing their variation period, β would then come out easily. However, Cepheids are rare stars: only a few of them are located in the solar neighborhood, and these nearby stars are generally too far away for precise parallax measurements, with the exception of δ Cep.

1.2. The Baade-Wesselink method

The most commonly used alternative to measure the distance to a pulsating star is the Baade-Wesselink (BW) method. Developed in the first part of the 20th century (Baade 1926; Wesselink 1946), it utilizes the pulsational velocity $V_{\rm puls.}$ of the surface of the star and its angular size. Integrating the pulsational velocity curve provides an estimation of the linear radius variation over the pulsation. Comparing the *linear* and *angular* amplitudes of the Cepheid pulsation gives directly its distance. The most recent implementation (Kervella et al. 2004) of the BW method makes use of long-baseline interferometry to measure directly the angular size of the star.

⋆ Table 3 is only available in electronic form at
http://www.edpsciences.org

Unfortunately, spectroscopy measures the apparent radial velocity $V_{\rm rad.}$, i.e. the Doppler shift of absorption lines in the stellar atmosphere, projected along the line of sight and integrated over the stellar disk. This is where p, a projection factor, has to be introduced, which is defined as $p = V_{\rm puls.}/V_{\rm rad.}$. The general BW method can be summarized in the relation:

$$\theta(T) - \theta(0) = -2\,\frac{p}{d}\int_0^T \left(V_{\rm rad.}(t) - V_\gamma\right)\,{\rm d}t \qquad (1)$$

where d is the distance, p the projection factor, θ the angular diameter and V_γ the systematic radial velocity. There are in fact many contributors to the p-factor. The main ones are the sphericity of the star (purely geometrical) and its limb darkening (due to the stellar atmosphere structure). A careful theoretical calculation of p requires modeling dynamically the formation of the absorption line in the pulsating atmosphere of the Cepheid (Parsons 1972; Sabbey et al. 1995; Nardetto et al. 2004).

Until now, distance measurements to Cepheids used a p-factor value estimated from numerical models. Looking closely at Eq. (1), it is clear that any uncertainty on the value of p will create the same relative uncertainty on the distance estimation, and subsequently to the P−L relation calibration. In other words, the Cepheid distance scale relies implicitly on numerical models of these stars. But how good are the models? To answer this question, one should confront their predictions to measurable quantities. Until now, this comparison was impossible due to the difficulty to constrain the two variables $\theta(T)$ and d from observations, i.e. the angular diameter and the distance.

Among classical Cepheids, δ Cep (HR 8571, HD 213306) is remarkable: it is not only the prototype of its kind, but also the Cepheid with the most precise trigonometric parallax currently available, obtained recently using the FGS instrument aboard the *Hubble Space Telescope* (Benedict et al. 2002). This direct measurement of the distance opens the way to the direct measurement (with the smallest sensitivity to stellar models) of the p factor of δ Cep, provided that high-precision angular diameters can be measured by interferometry.

2. Application of the BW method to δ Cep

To achieve this goal, interferometric observations were undertaken at the CHARA Array (ten Brummelaar et al. 2003; ten Brummelaar et al. 2005), in the infrared K' band ($1.95\ \mu{\rm m} \leq \lambda \leq 2.3\ \mu{\rm m}$) with the Fiber Linked Unit for Optical Recombination (Coudé du Foresto et al. 2003) (FLUOR) using two East-West baselines of the CHARA Array: E1-W1 and E2-W1, with baselines of 313 and 251 m respectively. Observations took place during summer 2004 for E2-W1 (seven nights between JD 2 453 216 and JD 2 453 233) and Fall 2004 for E1-W1 (six consecutive nights, from JD 2 453 280 to JD 2 453 285). The pulsation phase was computed using the following period and reference epoch (Moffett & Barnes 1985): $P = 5.366316$ d, $T_0 = 2\,453\,674.144$ (Julian date), the 0-phase being defined at maximum light in the V band. The resulting phase coverage is very good for the longest baseline (E1-W1), while data lack at minimum diameter for the smaller one (E2-W1)

Table 1. Calibrators with spectral type, uniform disk angular diameter in K band (in milliarcsecond) and baseline (Mérand et al. 2005).

	S. type	UD diam. (mas)	Baseline
HD 2952	K0III	0.938 ± 0.013	W1-E1
HD 138852	K0III-IV	0.952 ± 0.012	W1-E1
HD 139778	K1III:	1.072 ± 0.014	W1-E2
HD 186815	K2III	0.713 ± 0.009	W1-E2
HD 206349	K1II-III	0.869 ± 0.011	W1-E1, W1-E2
HD 206842	K1III	1.214 ± 0.016	W1-E2
HD 214995	K0III:	0.947 ± 0.013	W1-E1
HD 216646	K0III	1.051 ± 0.015	W1-E1, W1-E2
HD 217673	K1.5II	1.411 ± 0.020	W1-E2

The FLUOR Data reduction software (DRS) (Coudé du Foresto et al. 1997), was used to extract the squared modulus of the coherence factor between the two independent apertures. All calibrator stars were chosen in a catalogue computed for this specific purpose (Mérand et al. 2005) (see Table 1). Calibrators chosen for this work are all K giants, whereas δ Cep is a G0 supergiant. The spectral type difference is properly taken into account in the reduction, even though it has no significant influence on the final result. The interferometric transfer function of the instrument was estimated by observing calibrators before and after each δ Cep data point. The efficiency of CHARA/FLUOR was consistent between all calibrators and stable over the night around 85%. Data that share a calibrator are affected by a common systematic error due to the uncertainty of the a priori angular diameter of this calibrator. In order to interpret our data properly, we used a specific formalism (Perrin 2003) tailored to propagate these correlations into the model fitting process. Diameters are derived from the visibility data points using a full model of the FLUOR instrument including the spectral bandwidth effects (Kervella et al. 2003). The stellar center-to-limb darkening is corrected using a model intensity profile taken from tabulated values (Claret 2000) with parameters corresponding to δ Cep ($T_{\rm eff} = 6000$ K, $\log g = 2.0$ and solar metallicity). The limb darkened (LD) angular diameter comes out 3% larger than its uniform disk (UD) counterpart.

The theoretical correction for LD has only a weak influence on the p-factor determination, since that determination is related to a diameter *variation*. For example, based on our data set, a general bias of 5% in the diameters (due to a wrongly estimated limb darkening) leads to a bias smaller than 1% in terms of the p-factor. Differential variations of the LD correction during the pulsation may also influence the projection factor: comparison between hydrodynamic and hydrostatic simulations (Marengo et al. 2003) showed negligible variations. An accuracy of 0.2% on the angular diameters for a given baseline is required to be sensitive to dynamical LD effects. This is close to, but still beyond, the best accuracy that we obtained on the angular diameter with a single visibility measurement: 0.35% (median 0.45%).

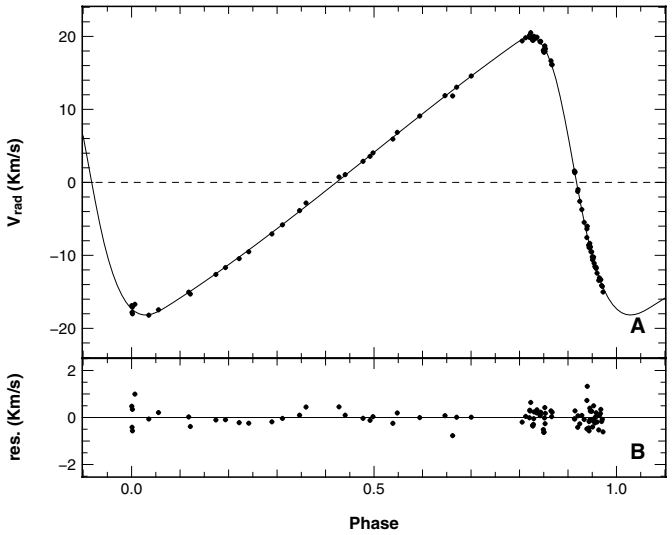

Fig. 1. Radial velocity smoothed using splines. A. Radial velocity data points, as a function of pulsation phase (0-phase defined as the maximum of light). This set was extracted using a cross-correlation technique (Bersier et al. 1994). The solid line is a 4-knot periodic cubic spline fit. B. Residuals of the fit.

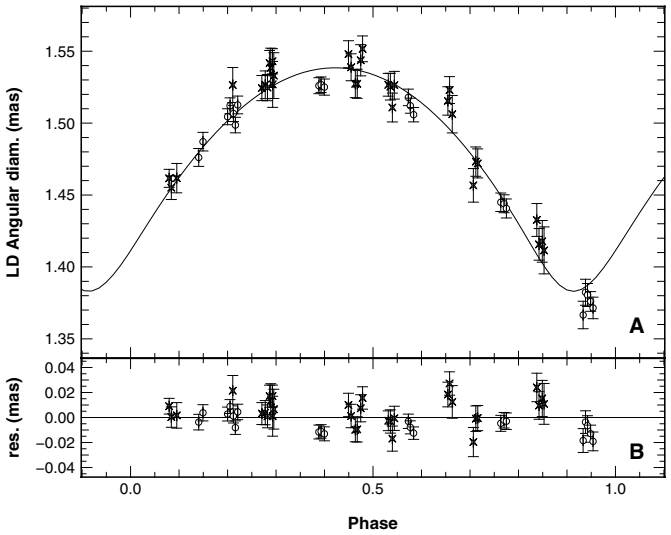

Fig. 2. p-factor determination. A. Our angular diameter measurements (points). Crosses correspond to the medium baseline (E2-W1), while circles correspond to the largest baseline (E1-W1). The continuous line is the integration of the 4-knots periodic cubic spline fitted to the radial velocities (Fig. 1). Integration parameters: $\overline{\theta}$ = 1.475 mas, p = 1.269 and d = 274 pc. B. Residuals of the fit.

Among the various sets of measurements of the radial velocity $V_{\mathrm{rad.}}(t)$ available for δ Cep, we chose measurements from Bersier et al. (1994) and Barnes et al. (2005). These works offer the best phase coverage, especially near the extrema, in order to accurately estimate the associated photospheric amplitude. In order not to introduce any bias due to a possible mismatch in the radial velocity zero-point between the two data sets, we decided to reduce them separately and then combine the resulting p-factor. An integration over time is required to obtain the photospheric displacement (see Eq. (1)). This process is noisy for unequally spaced data points: the radial velocity profile was smoothly interpolated using a periodic cubic spline function.

Fitting the inferred photospheric displacement and observed angular diameter variations, we adjust three parameters: the mean angular diameter $\overline{\theta}$, a free phase shift ϕ_0 and the projection factor p (see Fig. 1). The mean angular diameter is found to be 1.475 ± 0.004 mas (milliarcsecond) for both radial velocity data sets. Assuming a distance of 274 ± 11 pc (Benedict et al. 2002), this leads to a linear radius of 43.3 ± 1.7 solar radii. The fitted phase shift is very small in both cases (of the order of 0.01). We used the same parameters (Moffett & Barnes 1985) to compute the phase from both observation sets and considering that they were obtained more than ten years apart, this phase shift corresponds to an uncertainty in the period of approximately five seconds. We thus consider the phase shift to be reasonably the result of uncertainty in the ephemeris.

The two different radial velocity data sets lead to a consolidated value of p = 1.27 ± 0.06, once again assuming a distance of 274 ± 11 pc. The final reduced χ^2 is 1.5. The error bars account for three independent contributions: uncertainties in the radial velocities, the angular diameters and the distance. The first was estimated using a bootstrap approach, while the others were estimated analytically (taking into account calibration correlation for interferometric errors): for p, the detailed error is $p = 1.273 \pm 0.007_{V\mathrm{rad.}} \pm 0.020_{\mathrm{interf.}} \pm 0.050_{\mathrm{dist.}}$. The error is dominated by the distance contribution (see Table 2).

Table 2. Best fit results for p, with the two different radial velocity sets. The third line is a weighted average of the two individual measurements. Fourth and fith lines are the detailed quadratic contribution to the final error bar. Last line gives the final adopted value with the overall error bar. References are: (1) Bersier et al. (1994); and (2) Barnes et al. (2005).

$p \pm \sigma_{\mathrm{Vrad.}}$	1.269 ± 0.008	ref. (1)
	1.280 ± 0.012	ref. (2)
$p \pm \sigma_{\mathrm{Vrad.}}$	1.273 ± 0.007	consolidated
$\sigma_{\mathrm{interf.}}$	±0.020	
$\sigma_{\mathrm{dist.}}$	±0.050	
p	1.27 ± 0.06	

3. Discussion

Until now, the p-factor has been determined using models: hydrostatic models (Burki et al. 1982) produced the generally adopted value, p = 1.36. First attempts were made by Sabbey et al. (1995) to take into account dynamical effects due to the pulsation. They concluded that the average value of p should be 5% larger than in previous works (1.43 instead of 1.36) and that p is not constant during the pulsation. Because they increased p by 5%, they claimed that distances and diameters have to be larger in the same proportion. More recently Nardetto et al. (2004) computed p specifically for δ Cep using dynamical models. Different values of p were found, whether one measures diameters in the continuum or in the layer where the specific line is formed. In our case, broad band stellar interferometry (angular diameters are measured in the continuum)

these authors suggest $p = 1.27 \pm 0.01$. Concerning the variation of p during the pulsation, they estimate that the error in terms of distance is of the order of 0.2%, smaller than what we would have been able to measure with our interferometric data set. While our estimate, $p = 1.27 \pm 0.06$, is statistically compatible with this recent work, marginally with the widely used $p = 1.36$, and not consistent with the former value $p = 1.43$ at a 2σ level. We note that Gieren et al. (2005) have recently derived an expression of the p-factor as a function of the period that predicts a value of 1.47 ± 0.06 for δ Cep. While this value is in agreement with the modeling by Sabbey et al. (1995), is is slightly larger than the present measurement (by 2.4σ). As a remark, Gieren et al. obtain a distance of 280 ± 4 pc for δ Cep, that is slightly larger than Benedict et al.'s (2002) value 274 ± 11 pc assumed in the present work. Assuming this new distance estimation with our data would result in a p-factor of 1.30 ± 0.06, bringing the agreement to 2σ only.

Our geometrical determination of the p-factor, $p = 1.27 \pm 0.06$, using the IBW method is currently limited by the error bar on the parallax (Benedict et al. 2002). Conversely, assuming a perfectly known p-factor, the uncertainty of the stellar distance determined using the same method would have been only 1.5%, two-times better than the best geometrical parallax currently available. The value we determined for p is statistically compatible with the value generally adopted to calibrate the Cepheid P–L relation in most recent works. It is expected that the distance to approximatively 30 Cepheids will be determined interferometrically in the near future using particularly the CHARA Array and the VLT Interferometer (Glindemann 2005). In order not to limit the final accuracy on the derived distances, theoretical p-factor studies using realistic hydrodynamical codes is necessary. With a better understanding of the detailed dynamics of the Cepheid atmospheres, we will be in a position to exclude a p-factor bias on the calibration of the P–L relation, at a few percent level.

Acknowledgements. We thank P. J. Goldfinger for her assistance during the observations. The CHARA Array was constructed with funding from Georgia State University, the National Science Foundation, the W. M. Keck Foundation, and the David and Lucile Packard Foundation. The CHARA Array is operated by Georgia State University with support from the College of Arts and Sciences, from the Research Program Enhancement Fund administered by the Vice President for Research, and from the National Science Foundation under NSF Grant AST 0307562.

References

Baade, W. 1926, Astron. Nachr., 228, 359
Barnes, J. R., Cameron, A. C., Donati, J.-F., et al. 2005, MNRAS, 357, L1
Benedict, G. F., McArthur, B. E., Fredrick, L. W., et al. 2002, AJ, 124, 1695
Bersier, D., Burki, G., Mayor, M., & Duquennoy, A. 1994, A&A, 108, 25
Burki, G., Mayor, M., & Benz, W. 1982, A&A, 109, 258
Claret, A. 2000, A&A, 363, 1081
Coudé du Foresto, V., Bordé, P. J., Mérand, A., et al. 2003, in Interferometry for Optical Astronomy II, ed. W. A. Traub, Proc. SPIE, 4838, 280
Coudé du Foresto, V., Ridgway, S., & Mariotti, J.-M. 1997, A&A, 121, 379
Freedman, W. L., Madore, B. F., Gibson, B. K., et al. 2001, ApJ, 553, 47
Glindemann, A. 2005, in New Frontiers in Stellar Interferometry, ed. W. A. Traub, Proc. SPIE, 5491, 417
Kervella, P., Nardetto, N., Bersier, D., Mourard, D., & Coudé du Foresto, V. 2004, A&A, 416, 941
Kervella, P., Thévenin, F., Ségransan, D., et al. 2003, A&A, 404, 1087
Marengo, M., Karovska, M., Sasselov, D. D., et al. 2003, ApJ, 589, 968
Mérand, A., Bordé, P., & Coudé du Foresto, V. 2005, 433, 433
Moffett, T. J., & Barnes, T. G. 1985, ApJS, 58, 843
Nardetto, N., Fokin, A., Mourard, D., et al. 2004, A&A, 428, 131
Parsons, S. B. 1972, ApJ, 174, 57
Perrin, G. 2003, A&A, 596, 702
Sabbey, C. N., Sasselov, D. D., Fieldus, M. S., et al. 1995, ApJ, 446, 250
ten Brummelaar, T. A., McAlister, H. A., Ridgway, S. T., et al. 2005, ApJ, accepted
ten Brummelaar, T. A., McAlister, H. A., Ridgway, S. T., et al. 2003, in Interferometry for Optical Astronomy II, ed. W. A. Traub, Proc. SPIE, 4838, 69
Wesselink, A. 1946, Bull. Astron. Inst. Netherlands, 10, 91

Table 3. Individual measurements. Columns are (1) date of observation, JD_0 = 2 453 200.5; (2) phase; (3, 4) $u - v$ coordinate in meter; (5) squared visibility and error; (6) corresponding limb darkened disk diameter in mas; (7, 10) HD number of calibrators, prior and after the given data point respectivaly, 0 means that there was no calibrator; (8, 9, 11, 12) quantities for computing the correlation matrix (Perrin 2003): σ_{V^2} are errors on the estimated visibility of the calibrators.

JD–JD$_0$	ϕ	U(m)	V(m)	V^2 (%)	θ_{LD} (mas)	HD$_a$	α	$\sigma_{V_a^2}$	HD$_b$	β	$\sigma_{V_b^2}$
16.3844	0.289	−246.23	−13.93	12.09 ± 0.58	1.539 ± 0.014	206842	0.232	0.0106	217673	0.313	0.0096
16.4051	0.293	−245.91	−41.24	11.94 ± 0.69	1.526 ± 0.016	217673	0.354	0.0096	217673	0.322	0.0095
17.3801	0.475	−246.08	−11.83	12.79 ± 0.47	1.524 ± 0.011	217673	0.096	0.0102	216646	0.270	0.0114
17.4005	0.478	−246.11	−38.71	11.89 ± 0.37	1.529 ± 0.009	216646	0.154	0.0114	216646	0.152	0.0114
18.3443	0.654	−237.44	31.26	16.33 ± 0.48	1.489 ± 0.010	216646	0.188	0.0111	216646	0.189	0.0112
18.3630	0.658	−243.62	7.08	14.64 ± 0.43	1.499 ± 0.009	216646	0.173	0.0112	216646	0.183	0.0114
18.3935	0.663	−246.44	−33.07	13.63 ± 0.59	1.491 ± 0.013	217673	0.373	0.0096	216646	0.177	0.0114
19.3289	0.838	−231.37	47.22	21.53 ± 0.63	1.407 ± 0.011	0	–	–	216646	0.474	0.0110
19.3536	0.842	−241.79	15.84	20.50 ± 0.61	1.390 ± 0.011	216646	0.209	0.0110	216646	0.262	0.0112
19.3889	0.849	−246.53	−30.66	17.95 ± 0.77	1.403 ± 0.015	217673	0.417	0.0098	216646	0.250	0.0114
19.4093	0.853	−243.71	−57.56	17.59 ± 0.86	1.399 ± 0.016	216646	0.214	0.0114	217673	0.526	0.0095
21.3301	0.211	−234.72	38.94	17.02 ± 0.57	1.484 ± 0.012	216646	0.296	0.0095	0	–	–
28.4176	0.531	−230.78	−99.51	11.94 ± 0.36	1.514 ± 0.008	206349	0.111	0.0089	216646	0.153	0.0114
28.4406	0.536	−215.78	−127.18	12.38 ± 0.41	1.509 ± 0.010	216646	0.272	0.0114	206349	0.030	0.0083
28.4630	0.540	−196.83	−152.03	12.49 ± 0.47	1.517 ± 0.011	216646	0.171	0.0114	206349	0.099	0.0083
28.4848	0.544	−174.70	−173.74	12.24 ± 0.48	1.537 ± 0.011	216646	0.060	0.0114	206349	0.169	0.0083
29.3593	0.707	−246.59	−27.63	15.93 ± 0.57	1.445 ± 0.012	206842	0.318	0.0106	216646	0.186	0.0114
29.3863	0.712	−242.60	−63.16	14.92 ± 0.49	1.451 ± 0.010	216646	0.161	0.0114	216646	0.224	0.0114
29.4074	0.716	−234.58	−90.27	14.80 ± 0.48	1.450 ± 0.010	216646	0.385	0.0114	0	–	–
31.3590	0.080	−246.38	−34.41	15.37 ± 0.38	1.453 ± 0.008	186815	0.099	0.0071	206349	0.165	0.0090
31.3828	0.084	−242.03	−65.75	15.39 ± 0.40	1.441 ± 0.008	206349	0.126	0.0090	216646	0.226	0.0114
31.4433	0.095	−207.08	−139.54	15.96 ± 0.51	1.435 ± 0.010	216646	0.415	0.0114	0	–	–
32.3850	0.271	−240.48	−72.01	12.49 ± 0.38	1.503 ± 0.009	138852	0.050	0.0094	216646	0.260	0.0114
32.4220	0.278	−221.30	−118.17	12.68 ± 0.44	1.500 ± 0.010	216646	0.139	0.0114	216646	0.183	0.0114
32.4470	0.282	−201.55	−146.52	13.09 ± 0.42	1.501 ± 0.009	216646	0.168	0.0114	216646	0.152	0.0112
32.4710	0.287	−177.75	−171.09	12.86 ± 0.42	1.520 ± 0.010	216646	0.173	0.0112	216646	0.125	0.0110
32.5025	0.293	−140.59	−198.07	13.78 ± 0.43	1.523 ± 0.010	216646	0.121	0.0110	216646	0.171	0.0107
33.3435	0.449	−246.55	−21.14	12.40 ± 0.41	1.527 ± 0.010	139778	0.062	0.0102	216646	0.245	0.0114
33.3723	0.455	−243.42	−59.13	11.72 ± 0.47	1.525 ± 0.011	216646	0.183	0.0114	206349	0.084	0.0089
33.4189	0.463	−221.54	−117.75	12.58 ± 0.45	1.502 ± 0.010	216646	0.151	0.0114	216646	0.169	0.0114
33.4404	0.467	−204.89	−142.38	12.56 ± 0.41	1.511 ± 0.009	216646	0.315	0.0114	0	–	–
80.3020	0.200	253.48	183.15	2.41 ± 0.12	1.491 ± 0.005	185395	0.008	0.0139	216646	0.086	0.0112
80.3295	0.205	220.84	218.17	2.46 ± 0.12	1.500 ± 0.006	216646	0.078	0.0112	2952	0.022	0.0112
80.3667	0.212	166.28	257.01	2.85 ± 0.13	1.502 ± 0.006	2952	0.046	0.0112	2952	0.049	0.0112
80.3888	0.216	129.38	274.56	3.20 ± 0.13	1.498 ± 0.006	2952	0.050	0.0112	2952	0.056	0.0112
80.4145	0.221	83.29	289.27	3.19 ± 0.15	1.511 ± 0.006	2952	0.088	0.0112	37128	0.009	0.0409
81.3127	0.388	238.39	200.90	2.12 ± 0.11	1.511 ± 0.006	216646	0.040	0.0110	216646	0.051	0.0112
81.3371	0.393	206.72	230.09	2.28 ± 0.12	1.514 ± 0.006	216646	0.083	0.0112	2952	0.009	0.0112
81.3739	0.400	149.99	265.47	2.61 ± 0.13	1.519 ± 0.006	216646	0.052	0.0112	2952	0.044	0.0112
82.3031	0.573	246.42	191.85	2.32 ± 0.13	1.498 ± 0.006	216646	0.053	0.0110	216646	0.049	0.0112
82.3246	0.577	220.02	218.91	2.45 ± 0.12	1.501 ± 0.006	216646	0.057	0.0112	2952	0.037	0.0112
82.3611	0.584	166.58	256.84	2.78 ± 0.11	1.504 ± 0.005	2952	0.033	0.0112	2952	0.060	0.0112
83.3260	0.764	214.60	223.63	3.73 ± 0.17	1.445 ± 0.006	214995	0.026	0.0097	2952	0.107	0.0112
83.3625	0.770	159.85	260.49	4.29 ± 0.18	1.444 ± 0.006	2952	0.063	0.0112	2952	0.080	0.0112
83.3878	0.775	116.78	279.31	4.75 ± 0.20	1.440 ± 0.007	2952	0.080	0.0112	2952	0.076	0.0112
84.2374	0.933	294.80	103.39	6.53 ± 0.36	1.342 ± 0.010	216646	0.171	0.0109	216646	0.139	0.0109
84.2635	0.938	278.68	143.65	5.77 ± 0.32	1.359 ± 0.009	216646	0.136	0.0109	216646	0.138	0.0110
84.2855	0.942	259.31	175.36	5.64 ± 0.28	1.365 ± 0.008	216646	0.178	0.0110	2952	0.061	0.0112
84.3201	0.949	218.81	219.98	5.68 ± 0.24	1.376 ± 0.007	2952	0.101	0.0112	2952	0.088	0.0112
84.3468	0.954	180.34	248.69	6.29 ± 0.27	1.371 ± 0.008	2952	0.118	0.0112	2952	0.093	0.0112
85.3490	0.140	172.71	253.33	3.36 ± 0.16	1.476 ± 0.006	176598	0.013	0.0105	2952	0.097	0.0112
85.3962	0.149	91.77	287.10	3.70 ± 0.17	1.487 ± 0.006	2952	0.066	0.0112	2952	0.053	0.0112

2.2.2 Article A&A : "Self consistent modelling of the projection factor for interferometric distance determination" (2004)

Cet article présente une approche numérique de la question du facteur de projection des Céphéides. Nous avons utilisé pour cela un modèle autocohérent des oscillations de l'étoile δ Cep, qui nous a permis d'étudier l'évolution d'une raie spectrale parmi les plus significatives de cette étoile au cours de son cycle de pulsation. Notre conclusion principale est que différentes valeurs du p-facteur doivent être utilisées selon la méthode d'extraction de la vitesse radiale (gaussienne, minimum de la raie,...), mais aussi de manière plus inattendue selon la méthode de mesure interférométrique (large bande, monochromatique,...).

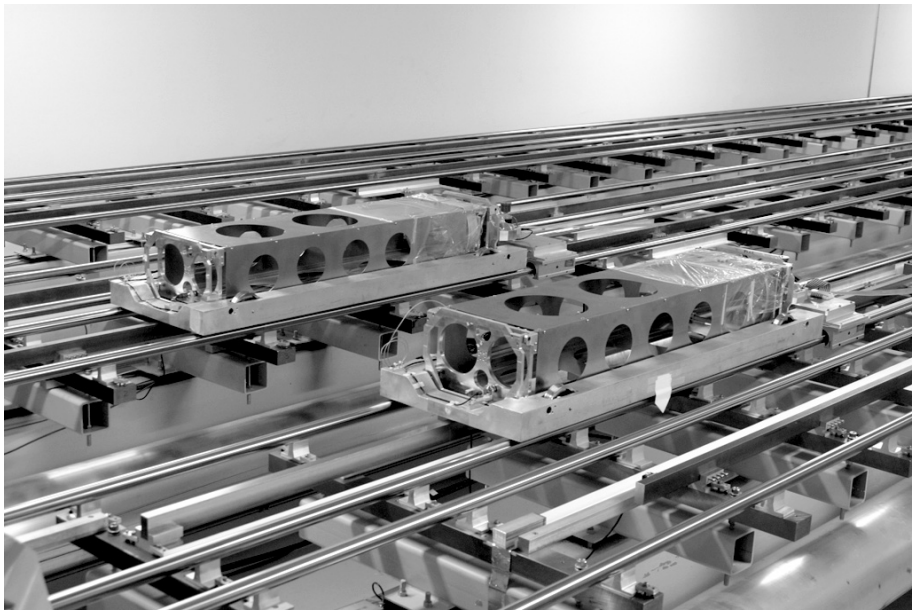

FIG. 2.9 – Deux chariots mobiles des lignes à retard de CHARA.

A&A 428, 131–137 (2004)
DOI: 10.1051/0004-6361:20041419

Astronomy & Astrophysics

Self consistent modelling of the projection factor for interferometric distance determination

N. Nardetto[1], A. Fokin[1,2,5], D. Mourard[1], Ph. Mathias[1], P. Kervella[3], and D. Bersier[4]

[1] Observatoire de la Côte d'Azur, Dpt. Gemini, UMR 6203, 06130 Grasse, France
e-mail: Nicolas.Nardetto@obs-azur.fr
[2] Institute of Astronomy of the Russian Academy of Sciences, 48 Pjatnitskaya Str., Moscow 109017, Russia
[3] Observatoire de Paris-Meudon, LESIA, UMR 8109, 5 place Jules Janssen, 92195 Meudon Cedex, France
[4] Space Telescope Science Institute, 3700 San Martin Drive, Baltimore, MD 21218, USA
[5] Isaak Newton Institute, Moscow Branch

Received 4 June 2004 / Accepted 28 July 2004

Abstract. The distance of galactic Cepheids can be derived through the interferometric Baade-Wesselink method. The interferometric measurements lead to angular diameter estimations over the whole pulsation period, while the stellar radius variations can be deduced from the integration of the pulsation velocity. The latter is linked to the observational velocity deduced from line profiles by the so-called projection factor p. The knowledge of p is currently an important limiting factor for this method of distance determination. A self-consistent and time-dependent model of the star δ Cep is computed in order to study the dynamical structure of its atmosphere together with the induced line profile. Different kinds of radial and pulsation velocities are then derived. In particular, we compile a suitable average value for the projection factor related to different observational techniques, such as spectrometry, and spectral-line or wide-band interferometry. We show that the impact on the average projection factor and consequently on the final distance deduced from this method is of the order of 6%. We also study the impact of a constant or variable p-factor on the Cepheid distance determination. We conclude on this last point that if the average value of the projection factor is correct, then the influence of the time dependence is not significant as the error in the final distance is of the order of 0.2%.

Key words. stars: atmospheres – stars: distances – stars: oscillations – stars: variables: Cepheids

1. Introduction

The period–luminosity (P–L) relation of the Cepheids is the basis of the extragalactic distance scale, but its calibration is still uncertain at a $\Delta M = \pm 0.10$ mag level. In order to calibrate this relation, two procedures have been recently considered, both based on the Baade-Wesselink method (hereafter BW), with distances deduced from the ratio of radius to angular variations.

The first method is the near-infrared surface brightness method introduced by Welch (1994), and later by Fouqué & Gieren (1997). The angular diameter variation is photometrically inferred from calibrations of the V light and $(V-K)$ color curves, and compared to the radius variation obtained spectroscopically. In the second method, called the interferometric version of the Baade-Wesselink method (hereafter IBW), the angular diameter variation is directly measured through the latest generation of long-baseline interferometers in the visible and in the IR, and then again compared to radius variations in order to derive distances (Kervella et al. 2004a; Lane et al. 2002) and then calibrate the P–L relation (Kervella et al. 2004b).

Both methods are in perfect agreement on the angular diameter, with a discrepancy of less than 1.5% (Kervella et al. 2004c). However, a difficulty remains in the derivation of the radius variation. The radius displacement is obtained through the integration of the pulsation velocity curve, hereafter called $v_{\rm puls}$. But when one measures radial velocities from line profiles, hereafter called $v_{\rm rad}$, they include the integration in two directions over the surface, through limb-darkening, and over the radius, through velocity gradients in line forming regions. Moreover, both the limb-darkening and velocity gradients depend on the pulsation phase, as already pointed out by Marengo et al. (2003). Therefore, the knowledge of the projection factor, defined as $v_{\rm puls} = p * v_{\rm rad}$, is of crucial importance for deriving a correct estimate of the radius variation curves from the integration of the pulsation velocity curve.

1.1. Previous work

The problem of the projection factor has been first studied by Eddington (1926), Carroll (1928) and Getting (1935). These authors consider both effects of limb-darkening and

atmospheric expansion at constant velocity on the line profile. These studies led to a p-value of $\frac{24}{17} = 1.41$, which was used for several decades in the Baade-Wesselink method.

Later, Van Hoof & Deurinck (1952) showed that when the natural width of the line is much smaller than the shift induced by the Doppler effect, the resulting profile must be distorted, and the p-factor can be measured from the convolution of the static line profile with this distortion function. Parsons (1972), using a model atmosphere with uniform expansion, numerically determined p-values between 1.31 and 1.34 depending on the width of the line.

Karp (1973, 1975) introduced a velocity gradient within the line forming regions and computed the emerging flux for both weak and strong lines. Weak lines, appear asymmetrical similar to the ones obtained by Van Hoof & Deurinck (1952), while the distortion for the stronger lines is mainly due to the velocity gradient within the atmosphere. Albrow & Cottrell (1994) determine values for p larger by 10% than those obtained by Parsons (1972), a difference interpreted as due to the use of a different limb-darkening law. Indeed, the p-factor depends on many parameters, such as the wavelength (p is larger in the infrared, Sasselov & Lester 1990), or the effective temperature of the star (Hindsley & Bell 1986; Montañés Rodriguez & Jeffery 2001).

From an observational point of view, Burki et al. (1982) determined $p = 1.36$ from the measure of the centroid of the correlation profile, a value which has been widely used in spectroscopy.

Finally, since p is determined both through geometrical effects and atmospheric dynamics, which change during the pulsation cycle, it should itself vary with the pulsation phase. In particular, Sabbey et al. (1995) showed that this effect on p can increase the BW radius by about 6%.

1.2. This work

We apply for δ Cep a nonlinear self-consistent hydrodynamical model (Fokin 1990). In addition, radiative transfer is considered in the outer layers to produce a realistic atmosphere model. The derived quantities have been found to be in good agreement with observations for different classes of pulsators such as RR Lyrae (Fokin & Gillet 1997), RV Tauri (Fokin 2001), post-AGB (Jeannin et al. 1997), BL Herculis (Fokin & Gillet 1994) and more recently β Cephei stars (Fokin et al. 2004). In particular, this model has already been used in the case of δ Cep (Fokin et al. 1996). Our model has some limitations (no convection, no adaptive grid), but is able to reproduce the main observational characteristics such as the presence of shocks or the correct shape and amplitude of the velocity curve. Thus we are confident that our model is valid for our study, and that the results are consistent.

The influence of the projection factor on the distance determination of Cepheids can be safely studied in the context of the IBW method. The main objectives of this paper are, firstly, to have an idea of the best value of the p-factor for interferometric observations, and to compare it with the generally used value of $p = 1.36$, and secondly, to quantify the impact of a constant or time-dependent projection factor on the distance determination of the star.

The paper is organized as follows. In Sect. 2 we describe our model of the prototype of the Cepheids, δ Cep, constrained from observational parameters referenced in the literature. In Sect. 3, we define the radial and pulsation velocities considered in the following. Section 4 deals essentially with the study of the projection factor and Sect. 5 concerns the impact of the choice of a time-varying p-factor on the distance determination. Finally, Sect. 6 presents the conclusions of this work.

2. The model of δ Cep

The model needs only 4 input parameters: the luminosity (L), the effective temperature ($T_{\rm eff}$), the mass (M) and the chemical composition (X and Y). The model is run until it reaches its limit cycle (for δ Cep this is the fundamental mode). Radiative transfer in the line is then solved in the frame of this hydrodynamical model to provide line profiles (Fokin 1991). For the present study, which is a first step, we have arbitrarily considered the metallic line Fe I 6003.012 Å. Therefore, we can compare the velocity in a given mass zone ($v_{\rm puls}$) with the velocity measured from the synthetic line profile ($v_{\rm rad}$). The latter was determined by two methods: measuring the velocity associated with the pixel at the minimum of the line profile (hereafter called profile minimum), and the Gaussian method in which we fit the whole profile with a Gaussian function. Note that theoretical variations follow the usual convention in which the pulsation phase $\phi = 0$ corresponds to maximum luminosity.

Since the main stellar quantities of δ Cep (HD 213306) are still uncertain, we tried several sets of luminosity L, effective temperature $T_{\rm eff}$ and mass M in order to get suitable observational quantities such as the pulsation period, the average radius of the star, bolometric and radial velocity curves, and line profiles. This leads to the following set for the 106-zone model: $M = 4.8\,M_\odot$, $L = 1995\,L_\odot$, $T_{\rm eff} = 5877$ K. This latter is in agreement with the one measured by Fernley et al. (1989). Mass and luminosity are related through the M–L relation of Chiosi et al. (1993):

$$\log \frac{L}{L_\odot} = -0.015 + 3.14Y - 10.0Z + 3.502 \log \frac{M}{M_\odot} + 0.25$$

where $Y = 0.28$ and $Z = 0.02$ correspond to typical Pop. I chemical composition. The inner boundary has been fixed at about $T = 1.0 \times 10^6$ K, corresponding to about 16% of the photospheric radius, so the model envelope with the atmosphere contains about 7% of the stellar mass. The atmosphere itself contains about 1.0×10^{-7} of the total stellar mass. In the hydrodynamical model we used the OPAL92 opacity table. Note that in the following line transfer calculation for each chosen phase we used the snapshots of the pulsating atmosphere given by the nonlinear model. In addition, we used the relevant frequency-dependent atomic opacities both in the continuum and in the line.

We started the hydrodynamical calculations with an initial velocity profile with a value of 25 km s^{-1} at the surface. At the limit cycle the pulsation period is 5.419 days, very close (1%) to the observational value deduced by

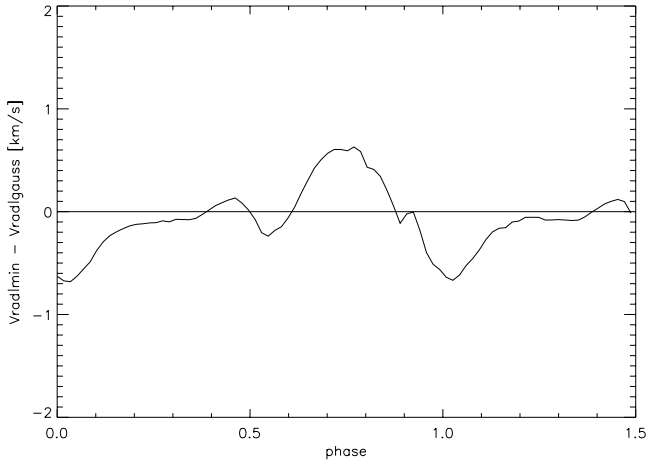

Fig. 1. Difference between the theoretical radial velocity curves measured by the profile minimum method ($v_{\rm rad|min}$) and the Gaussian fitting method ($v_{\rm rad|gauss}$). The small difference induces a bias in the determination of the p-factor. The horizontal line is the zero velocity in the stellar rest frame.

Szabados et al. (1980). Bolometric and radial velocity amplitudes are respectively $\Delta m_{\rm bol} = 0.85$ mag and $\Delta V = 35\,{\rm km\ s^{-1}}$. The relative radius amplitude at the surface is $\Delta R/R = 10\%$. The mean photospheric radius is about $\overline{R} = 43.5\,R_\odot$, in agreement with interferometric and parallax measurements obtained by Mourard et al. (1997), Nordgren et al. (2000) and Benedict et al. (2002).

We then generated a series of snapshots of the atmospheric structure (about 60 per pulsation period) and after the line profile computation we deduced the radial velocity variations. For all phases we assume the same microturbulence velocity of $1\,{\rm km\ s^{-1}}$, and we neglect the rotation ($v \sin i \sim 5\,{\rm km\ s^{-1}}$, Breitfellner & Gillet 1993).

3. Velocities

To study the projection factor, we now define different radial and pulsational velocities.

3.1. The radial velocity

Theoretical line profiles deduced from the δ Cep model are used to determine apparent radial velocities considering either the minimum of the profile or the Gaussian fit. The maximum velocity difference between these two methods reaches about 0.7 km s^{-1} during extrema phases ($\phi = 0.7$–0.8 and $\phi = 0.9$–0.1), see Fig. 1. We will show later that such a difference is not negligible for the projection factor determination.

3.2. The pulsation velocity

The projection factor may have different definitions depending on the pulsating layer considered. From a spectroscopic point of view, one considers the gas velocity associated to the optical barycenter of the line forming region. However, the instruments, spectrograph and interferometer, do not probe the same layers of the star. For instance, with the IBW method, the layers that are seen by the interferometer depend on the spectral resolution. Indeed, a wide spectral band will rather probe the continuum (photospheric) region. Conversely, in a specific line, the visibility function is the Fourier transform of the image of the star in the considered line. Thus different cases, corresponding to each type of observation, have to be considered.

Firstly, for spectroscopic observations the gas velocity is that of the line-forming layers. However this region may represent an appreciable fraction of the height of the atmosphere. Sabbey et al. (1995) determined the layer corresponding to the optical center of gravity of the line from contribution functions. In our case, we consider the standard definition in which the line core is formed at an optical depth of $\tau = 2/3$. Hence, we use the definition:

$$v_{\rm puls_{(s)}} = v\left(\tau_l = \frac{2}{3}\right) \tag{1}$$

where τ_l is the optical depth at the center of the line and "(s)" means "Spectroscopy".

Secondly, for interferometric observations in one particular line, it is better to consider the velocity of optical layers corresponding to an optical depth of $\tau_l = 2/3$. It is not the gas velocity that is considered here but the *velocity of the optical layer* deduced from the pulsation model, defined by:

$$v_{\rm puls_{(il)}} = \frac{\partial R(\tau_l = 2/3)}{\partial \phi} \tag{2}$$

where "(il)" is for "Interferometry in one Line".

Similarly, for interferometric observations in a wide band, the most appropriate pulsation velocity is the one associated to the photospheric layer that corresponds, by definition, to $\tau = 2/3$ in the continuum:

$$v_{\rm puls_{(ic)}} = \frac{\partial R(\tau_{\rm c} = 2/3)}{\partial \phi} \tag{3}$$

where "(ic)" is for "Interferometry in the Continuum".

Note that we consider here the continuum next to the line. Figure 2 represents the different pulsation velocities defined above. These three pulsation velocity curves are different by a maximum of 5% during the extrema phases, because the atmosphere is not co-moving. The asymmetry in the profile is maximum during the phases of extrema of the radial velocity curve, thus there should be a large velocity gradient between the different layers.

4. The projection factor

4.1. Combination of radial and pulsation velocities

It is now possible to combine the radial velocities (two cases) with the pulsation velocities (three cases) to derive the projection factor. Figures 3a–c shows the three pulsation velocities together with the radial velocity using the Gaussian method. Note that the estimators of radial and pulsation velocities, in (s) and (il) cases, are supposed to probe the same part of the star, the line forming region. In other words the two curves should cancel at the same phase respectively in Figs. 3a and 3b, which

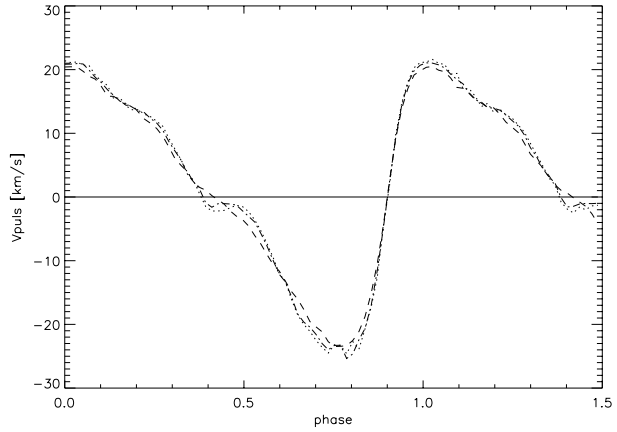

Fig. 2. Pulsation velocities vs. phase. The dashed curve shows the velocity of the photospheric layer ($\tau = 2/3$ in the continuum), the dot-dashed curve the velocity of the layer corresponding to $\tau = 2/3$ in the spectral center of the line and the dotted curve the *gas* velocity corresponding to $\tau = 2/3$ in the line. The horizontal line is the zero velocity in the stellar rest frame.

is actually the case with a good precision ($\phi \sim 0.4$). This is an indication that our estimator of the optical barycenter $\tau = 2/3$ is correct. The result should have been the same considering the profile minimum as the velocity curve cancels at the same phase (see $\phi = 0.4$ in Fig. 1). However, we note in Fig. 3c that the zero point of the photospheric velocity is at a slightly later phase. This is the result of asynchronous motions in the atmosphere.

All these curves, with their amplitude and shape, will have an impact on the projection factor and its variation over the pulsation. In the following section we compute a suitable average value of the projection factor for each case, considering two estimators which are not simply the average of the ratio of pulsation to radial velocities. In Sect. 5, we consider more specifically the time dependence of the projection factor.

4.2. Two estimators of p

To determine a constant projection factor, we cannot simply consider the mean value of the ratio of the pulsation to radial velocities. Due to the non-comoving character of the atmospheric motions, this would lead to a ratio of physical quantities close to zero ($\phi \sim 0.4$) but not *exactly* at the same phase, whatever the case considered in Fig. 3. Consequently, two more suitable tests were used to estimate a constant value of p. The first consists in applying a classical χ^2 minimization algorithm between the quantity $v_{\rm rad}.p_{\rm const}$ and the considered pulsation velocity (hereafter estimator 1):

$$\chi^2 = \sum_i \frac{(v_{\rm rad}(\phi_i).p_{\rm const} - v_{\rm puls}(\phi_i))^2}{\sigma_{\rm puls}(\phi_i)^2} \quad (4)$$

where $\sigma_{\rm puls}(\phi_i)$ is the statistical error in the pulsation velocity, arbitrarily fixed to a reasonable value of 1 km s^{-1}, in order to evaluate the corresponding error on p. The phases ϕ_i, in this case, are sampled following the snapshots of the model. Here,

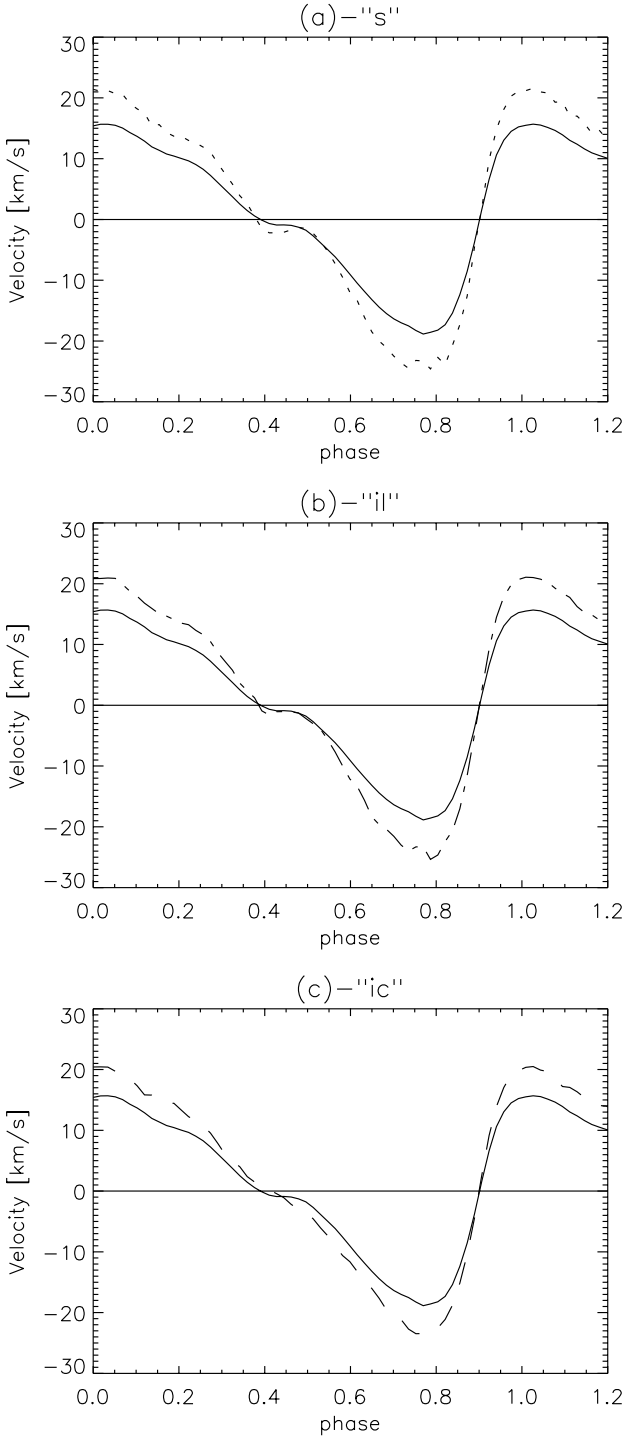

Fig. 3. Radial velocity curve deduced from the theoretical line profiles by the Gaussian method together with **a)** the gas velocity corresponding to $\tau = 2/3$ in the line forming region according to Eq. (1), **b)** the $\tau = 2/3$ "optical layer" velocity according to Eq. (2), **c)** the velocity of the photospheric layer ($\tau = 2/3$ in the continuum, see Eq. (3)).

$v_{\rm rad}$ is the radial velocity deduced from either the profile minimum or the Gaussian fit, and $v_{\rm puls}$ is related to Eqs. (1)–(3).

The second estimator of the p-factor is directly based on the radius variation of the star, obtained either by integration of the radial velocity or directly by the position of the layer as

Table 1. Optimal constant values for the p-factor for different cases of interest. $v_{\rm rad|gauss}$ and $v_{\rm rad|min}$ are the radial velocity deduced from theoretical line profiles using the Gaussian and minimum method respectively. Estimator (1) and (2) of the *constant* projection factor correspond to Eqs. (4) and (5) respectively. In each case the pulsational velocity $v_{\rm puls}$ and radius $\Delta R_{\rm puls}$ used are indicated.

	Estimator 1	Estimator 2
	$v_{\rm puls_{(s)}} = v(\tau_l = 2/3)$	$\Delta R_{\rm puls_{(s)}} = \int v(\tau_l = 2/3)$
$v_{\rm rad\|gauss}$	1.35 ± 0.01	1.32 ± 0.01
$v_{\rm rad\|min}$	1.31 ± 0.01	1.30 ± 0.01
	$v_{\rm puls_{(il)}} = \dfrac{\partial R(\tau_l = 2/3)}{\partial \phi}$	$\Delta R_{\rm puls_{(il)}} = \Delta R(\tau_l = 2/3)$
$v_{\rm rad\|gauss}$	1.33 ± 0.01	1.32 ± 0.01
$v_{\rm rad\|min}$	1.30 ± 0.01	1.29 ± 0.01
	$v_{\rm puls_{(ic)}} = \dfrac{\partial R(\tau_c = 2/3)}{\partial \phi}$	$\Delta R_{\rm puls_{(ic)}} = \Delta R(\tau_c = 2/3)$
$v_{\rm rad\|gauss}$	1.28 ± 0.01	1.27 ± 0.01
$v_{\rm rad\|min}$	1.24 ± 0.01	1.24 ± 0.01

provided by the radius of the mass zone involved. Hence, the quantity defined by $\int v_{\rm rad}.p_{\rm const}$ is compared with the pulsating radius (hereafter estimator 2):

$$\chi^2 = \sum_i \frac{\left(\int v_{\rm rad}(\phi_i).p_{\rm const} - \Delta R_{\rm puls}(\phi_i)\right)^2}{\sigma_{\rm puls}(\phi_i)^2} \quad (5)$$

where $\sigma_{\rm puls}(\phi_i)$ is the statistical error in the pulsation radius, fixed to $0.1\,R_\odot$ to obtain the same uncertainty in the p-factor for both estimators. The quantity $v_{\rm rad}$ is the same as in estimator 1. The radius variation $\Delta R_{\rm puls}$ may be either:

$$\Delta R_{\rm puls_{(s)}} = \int v(\tau_l = 2/3) \quad (6)$$

or

$$\Delta R_{\rm puls_{(il)}} = \Delta R(\tau_l = 2/3) \quad (7)$$

or

$$\Delta R_{\rm puls_{(ic)}} = \Delta R(\tau_c = 2/3), \quad (8)$$

with each case corresponding theoretically to the integration of Eqs. (1)–(3). However, note that for Eqs. (7) and (8) the radius variations are deduced directly from the model. An integration algorithm was used to derive Eq. (6). We also define $R_{\rm puls} = \overline{R_{\rm puls}} + \Delta R_{\rm puls}$ for each case.

4.3. Results and discussion

Table 1 lists the computation results for the twelve cases considered, leading to the following conclusions.

Firstly, the p-factors obtained considering the two estimators differ by 2% in extreme cases. This is expected for two reasons. On the one hand, the two minimized quantities are different, so it is expected that the associated p-factor values will also be different. On the other hand, when the radius is fitted, the estimator may be less sensitive to velocity variation shapes.

Secondly, these results indicate a systematic shift of 0.02–0.04 (or 3%) in p-values between the radial velocities associated with the Gaussian and the profile minimum methods. This is logically linked to the systematic difference in velocity curves, as shown in Fig. 1. Therefore it is important to choose the p-factor value that corresponds to the method that was used to estimate the projected velocity. In addition, it is best to use the method that is least sensitive to velocity gradients and marginal effects, in order to obtain a value for the p-factor that is generally applicable. That is why in the following discussions, we consider only the radial velocity deduced from the Gaussian method.

Thirdly, the difference between the pulsation layers considered should be related to the different observational techniques, as we pointed out in Sect. 3. For spectroscopic measurements of the gas velocity within the line, the recommended value is $p = 1.35$, which is close to the classical value of $p = 1.36$ (Burki et al. 1982). In this case, one should preferably consider the first estimator since one has to deal with the pulsation velocity of the gas to account for the atmosphere dynamics. Conversely, for interferometric observations in a "photospheric" line, the best value is $p = 1.32$, and one should consider the second estimator (this result will be confirmed in the next section). For broadband interferometric observations, one should use a lower value of $p = 1.27$. These results indicate that an error of 6% can be made if one takes the usual value of $p = 1.36$ regardless of the observational method used.

Finally, an initial error of 1 km s^{-1} in the pulsation velocity, or $0.1\,R_\odot$ in the pulsation radius, leads to a final statistical error in the p-factor of about 0.01 for both estimators.

5. The effect of a constant projection factor on distance determination

The IBW method combines interferometric and spectrometric observations to deduce the distance of the star (see Kervella et al. 2004a). In the previous section we have obtained different average values for p, considering different kinds of velocities and estimators. We now study the influence of the time-dependence of p on distance determination. Since the definition of p involves phase-dependent factors, p itself should be time-dependent. This is illustrated in Fig. 4 which shows the quantity $v_{\rm puls} - p_{\rm const} * v_{\rm rad}$. As it has already been pointed out in Sect. 4.2, plotting the p-factor against the phase is misleading as the ratio of pulsation to radial velocities is not representative when these quantities are close to zero ($\phi \sim 0.4$). Moreover, in the framework of the IBW method, the quantity of interest is the pulsation velocity rather than the projection factor itself.

On the one hand, we simulate angular diameters $\theta_{\rm obs}$, fixing arbitrarily the distance of the star ($d = 275$ pc) and using the radius variations provided by the pulsation model:

$$\theta_{\rm obs}(\phi_i) = 9.305 \left(\frac{R_{\rm puls}(\phi_i)}{275}\right) [\rm mas] \quad (9)$$

where $R_{\rm puls}$ (in $R_\odot$) is one of the three quantities:

$$R_{\rm puls_{(s)}} = \int v(\tau_l = 2/3) \quad (10)$$

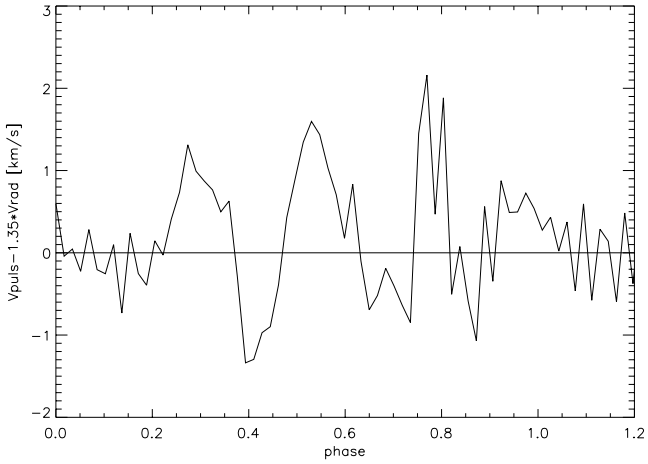

Fig. 4. The quantity $v_{\rm puls} - 1.35 * v_{\rm rad}$ versus the phase in the case of Fig. 3a: $v_{\rm puls}$ is the gas velocity corresponding to $\tau = 2/3$ in the line formation region according to Eq. (1), and $v_{\rm rad}$ is the radial velocity curve deduced from the theoretical line profiles by the Gaussian method. $p = 1.35$ is the optimum value obtained from the estimator 1, as described in Sect. 4.2

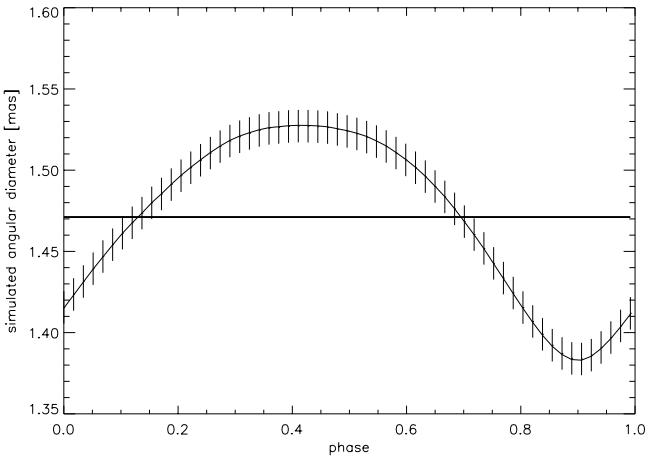

Fig. 5. Simulated angular diameter points deduced from Eq. (9) with $R_{\rm puls_{(ic)}} = R(\tau_{\rm c} = 2/3)$. Each point is shown with its arbitrary theoretical error bar of 0.01 mas. This curve simulates interferometric observations used in the IBW method.

or

$$R_{\rm puls_{(il)}} = R(\tau_l = 2/3) \tag{11}$$

or

$$R_{\rm puls_{(ic)}} = R(\tau_{\rm c} = 2/3), \tag{12}$$

as provided by the integration of Eqs. (1)–(3). The phases ϕ_i are sampled from the snapshots of the model. Figure 5 shows the simulated angular diameter curve considering $R_{\rm puls_{(ic)}} = R(\tau_{\rm c} = 2/3)$.

On the other hand, the IBW method is used as follows. Firstly, a radial velocity curve is derived from the synthetic spectra considering both the Gaussian fit and the minimum profile methods. Then, a constant value for the p-factor is chosen corresponding to one of the twelve cases of Table 1. Finally,

Table 2. Distance results corresponding to the mean p-factor results of Table 1. The different expressions of the radius refer to Eqs. (10)–(12) respectively and correspond to the quantity used in the Eq. (9) of the simulated angular diameters.

	Estimator 1	Estimator 2
	$R_{\rm puls} = \int v(\tau_l = 2/3)$	
$v_{\rm rad\|gauss}$	279.6 ± 7.2	274.6 ± 7.2
$v_{\rm rad\|min}$	278.2 ± 7.2	274.8 ± 7.2
	$R_{\rm puls} = R(\tau_l = 2/3)$	
$v_{\rm rad\|gauss}$	278.2 ± 7.2	274.6 ± 7.2
$v_{\rm rad\|min}$	276.9 ± 7.2	274.7 ± 7.2
	$R_{\rm puls} = R(\tau_{\rm c} = 2/3)$	
$v_{\rm rad\|gauss}$	276.0 ± 7.2	274.9 ± 7.2
$v_{\rm rad\|min}$	274.6 ± 7.2	274.8 ± 7.2

the integration of the pulsation velocity deduced from the radial velocity and the projection factor leads to an estimation of the radius variation of the star. This leads to an angular variation curve:

$$\theta_{\rm model}(\phi_i) = \overline{\theta} + 9.305 \left(\frac{\Delta R(\phi_i)}{d}\right) [\rm mas], \tag{13}$$

where $\Delta R(\phi_i) = \int v_{\rm rad}(\phi_i).p_{\rm const}$. Finally, applying a classical χ^2 minimization algorithm, we fit both the average angular diameter $\overline{\theta}$ and the distance d to the star. The minimized quantity is:

$$\chi^2 = \sum_i \frac{(\theta_{\rm obs}(\phi_i) - \theta_{\rm model}(\phi_i))^2}{\sigma_{\rm obs}(\phi_i)^2}. \tag{14}$$

The values for $\sigma_{\rm obs}(\phi_i)$ are arbitrarily fixed to 0.01 mas which is a realistic value considering the measurement precision achieved recently by long-baseline interferometers (see Fig. 5).

Table 2 gives the computed distances using the p-factors shown in Table 1. The mean angular diameters obtained correspond to the anticipated values of $\overline{\theta_{\rm obs}} = 1.471$ mas for the (ic) case and $\overline{\theta_{\rm obs}} = 1.476$ for (s) and (il) cases. The statistical errors obtained are around 0.001 mas.

Since p is constant, we have $\Delta R \sim \Delta R_{\rm puls}$, and any departure from the predefined distance (275 pc) is the result of the time-dependence of the projection factor or the choice of the estimator: there is no model effect. It appears that the computed and reference distances are closer for estimator 2. Thus, estimator 2 provides projection factors less biased than those provided by estimator 1 in the frame of the IBW method.

An important conclusion is that for the best p-factor value, the systematic error in the derived distance does not exceed 0.2%, independent of the radial and pulsation velocities considered. This important result indicates that a time-dependent p-factor is not required at the moment since the final error of 0.2% is well below our best estimation of recent distance determination.

Finally, note that the initial uncertainty of 0.01 mas in theoretical angular diameters leads to a final statistical error in the distance of 7.2 pc.

6. Conclusion

A self-consistent nonlinear model for δ Cephei was generated reproducing the main observational features of this star.

On the basis of this model we studied the effect of the projection factor which links radial and pulsation velocity on the IBW method for distance determination. Two methods were considered for deriving the radial velocity curve: a Gaussian fit and the profile-minimum method. Similarly, three pulsation velocities were defined corresponding to different regions of the stellar atmosphere: two concern the line forming region, while the third corresponds to the photosphere. These three pulsation velocities are linked to different observational techniques such as spectrometry and wide-band or spectral-line interferometry. An important result of this study is the very weak influence of the time-dependence of the p-factor on distance determination. The choice of a *constant* p-factor instead of one that is time-dependent gives a systematic error in the final distance of the order of 0.2%, which is below the best estimations of current distance determination. More important, the projection factor should be chosen depending on the observational techniques used. For spectroscopic observations, if we use the Gaussian method to derive the radial velocity, we propose $p = 1.35$. For wide-band interferometry, the best value is $p = 1.27$, and for interferometric observations in a specific (metal) line it is $p = 1.32$. Note that this latter value has been determined for a given line: considering lines formed in other atmospheric regions should lead to different values. An extensive study of this dependence, outside the scope of the present paper, is currently in progress.

Note also that these values have been determined for δ Cep. The generalization of our results to other classical Cepheids will require the study of a larger sample of stars. The AMBER instrument (Petrov et al. 2000) will also permit observations in one particular line with a good resolution ("Interferometry in one Line"). Cepheids are bright sources and observations in an absorption line of their atmospheres appears feasible in terms of signal to noise ratio of as long as one can use large telescopes and adaptive optics. It will be then possible to compare the same layer of the star with interferometry and spectrometry.

Acknowledgements. We thank Ph. Berio for having provided the χ^2 minimization algorithm and for useful discussions. A. Fokin acknowledges the Observatoire de la Côte d'Azur for financial support.

References

Albrow, M. D., & Cottrell, P. L. 1994, MNRAS, 267, 584
Benedict, G. F., McArthur, B. E., Fredrick, L. W., et al. 2002, AJ, 124, 1695
Breitfellner, M. G., & Gillet, D. 1993, A&A, 277, 524B
Burki, G., Mayor, M., Benz, W. 1982, A&A, 109, 258
Caroll, M. A. 1928, MNRAS, 88, 548
Chiosi, C., Wood, P. R., & Capitanio, N. 1993, ApJS, 86, 541
Eddington, A. S. 1926, The Internal Constitution of the Stars (Cambridge University Press), 185
Fernley, J. A., Skillen, I., & Jameson, R. F. 1989, MNRAS, 237, 947
Fokin, A. B. 1990, Ap&SS, 164, 95
Fokin, A. B. 1991, MNRAS, 250, 258
Fokin, A. B. 2001, in Stellar pulsation – nonlinear studies ASSL series, ed. M. Takeuti, & D. D. Sasselov, 257, 103
Fokin, A. B., & Gillet, D. 1994, A&A, 290, 875
Fokin, A. B., & Gillet D. 1997, A&A, 325, 1013
Fokin, A. B., Gillet, D., & Breitfellner, M. G. 1996, A&A, 307, 503
Fokin, A. B., Mathias, Ph., Chapellier, E., Gillet, D., & Nardetto, N. 2004, A&A, 426, 687
Fouqué, P., & Gieren, W. P. 1997, A&A, 320, 799
Getting, I. A. 1935, MNRAS, 95, 141
Hindsley, R., & Bell, R. A. 1986, PASP Conf. Ser., 98, 881
Jeannin L., Fokin A. B., Gillet D., & Baraffe I. 1997, A&A, 326, 203
Karp, A. H. 1973, ApJ, 180, 895
Karp, A. H. 1975, ApJ, 201, 641
Kervella, P., Nardetto, N., Bersier, D., et al. 2004a, A&A, 416, 941
Kervella, P., Bersier, D., Mourard D., Nardetto, N., & Coudé Du Foresto, V. 2004b, A&A, 423, 327
Kervella, P., Fouqué, P., Storm, J., et al. 2004, ApJ, 604, L113
Lane, B. F., Creech-Eakman, M., & Nordgren, T. E. 2002, ApJ, 573, 330
Parsons, S. B. 1972, ApJ, 174, 57
Petrov, R., Malbet, F., Richichi, A., et al. 2000, Proc. SPIE, 4006, 68
Marengo, M., Karovska, M., Sasselov, D. D., et al. 2003, ApJ, 589, 975
Montañés Rodriguez, P., & Jeffery, C. S. 2001, A&A, 375, 411
Mourard, D., Bonneau, D., Koechlin, L., et al. 1997, A&A, 317,789
Nordgren, T. E., Armstrong, J. T., Germain, M. E., et al. 2000, ApJ, 543, 972
Sabbey, C. N., Sasselov, D. D., Fieldus, M. S., et al. 1995, ApJ, 446, 250
Sasselov, D. D., & Lester, J. B. 1990, ApJ, 362, 333
Szabados L. 1980, Comm. Konkoly Obs. Hungary., 76, 1
Van Hoof, A., & Deurinck, R. 1952, ApJ, 115, 166
Welch, D. L. 1994, AJ, 108, 1421

2.2.3 Article A&A : "High resolution spectroscopy for Cepheids distance determination – I. Line asymmetry" (2006)

L'analyse des spectres à haute résolution est une des deux composantes de la méthode Baade-Wesselink. Elle permet d'extraire la vitesse radiale, qui est ensuite utilisée, après intégration et correction par le facteur de projection, pour estimer la variation de rayon de l'étoile. Nous présentons dans cet article une première analyse de spectres à très haute résolution ($R = 120\,000$) obtenus avec le spectrographe HARPS (installé sur le télescope de 3,6 m de l'ESO). Dans cet article, nous examinons l'évolution de l'asymmétrie d'une raie spectrale au cours de la pulsation pour neuf Céphéides de périodes variées. Nous mettons en évidence une dépendance de la vitesse de rotation de l'étoile avec la période ainsi qu'un important décalage systématique de l'asymmétrie pour les étoiles à longue période.

FIG. 2.10 – Dôme du télescope de 3,6m de l'ESO à l'Observatoire de La Silla (photo ESO).

A&A 453, 309–319 (2006)
DOI: 10.1051/0004-6361:20054333

Astronomy & Astrophysics

High resolution spectroscopy for Cepheids distance determination

I. Line asymmetry⋆

N. Nardetto[1], D. Mourard[1], P. Kervella[2], Ph. Mathias[1], A. Mérand[2], and D. Bersier[3,4]

[1] Observatoire de la Côte d'Azur, Dept. Gemini, UMR 6203, 06130 Grasse, France
e-mail: Nicolas.Nardetto@obs-azur.fr
[2] Observatoire de Paris-Meudon, LESIA, UMR 8109, 5 place Jules Janssen, 92195 Meudon Cedex, France
[3] Space Telescope Science Institute, 3700 San Martin Drive, Baltimore, MD 21218, USA
[4] Astrophysics Research Institute, Liverpool John Moores University, Twelve Quays House, Egerton Wharf, Birkenhead, CH41 1LD, UK

Received 11 October 2005 / Accepted 11 March 2006

ABSTRACT

Context. The ratio of pulsation to radial velocity (the projection factor) is currently limiting the accuracy of the Baade-Wesselink method, and in particular of its interferometric version recently applied to several nearby Cepheids.
Aims. This work aims at establishing a link between the line asymmetry evolution over the Cepheids' pulsation cycles and their projection factor, with the final objective to improve the accuracy of the Baade-Wesselink method for distance determinations.
Methods. We present HARPS⋆⋆ high spectral resolution observations (R = 120 000) of nine galactic Cepheids: R Tra, S Cru, Y Sgr, β Dor, ζ Gem, Y Oph, RZ Vel, ℓ Car and RS Pup, having a good period sampling (P = 3.39d to P = 41.52d). We fit spectral line profiles by an asymmetric bi-Gaussian to derive radial velocity, Full-Width at Half-Maximum in the line ($FWHM$) and line asymmetry for all stars. We then extract correlations curves between radial velocity and asymmetry. A geometric model providing synthetic spectral lines, including limb-darkening, a constant $FWHM$ (hereafter σ_C) and the rotation velocity is used to interpret these correlations curves.
Results. For all stars, comparison between observations and modelling is satisfactory, and we were able to determine the projected rotation velocities and σ_C for all stars. We also find a correlation between the rotation velocity ($V_{\rm rot}\sin i$) and the period of the star: $V_{\rm rot}\sin i = (-11.5 \pm 0.9)\log(P) + (19.8 \pm 1.0)$ [km s^{-1}]. Moreover, we observe a systematic shift in observational asymmetry curves (noted γ_O), related to the period of the star, which is not explained by our static model: $\gamma_O = (-10.7 \pm 0.1)\log(P) + (9.7 \pm 0.2)$ [in %]. For long-period Cepheids, in which velocity gradients, compression or shock waves seem to be large compared to short- or medium-period Cepheids we observe indeed a greater systematic shift in asymmetry curves.
Conclusions. This new way of studying line asymmetry seems to be very promising for a better understanding of Cepheids atmosphere and to determine, for each star, a dynamic projection factor.

Key words. techniques: spectroscopic – stars: atmospheres – stars: oscillations – stars: variables: Cepheids – stars: distances

1. Introduction

Long-baseline interferometers currently provide a new quasi-geometric way to calibrate the Cepheid Period-Luminosity relation. Indeed, it is now possible to determine the distance of galactic Cepheids up to 1kpc with the Interferometric Baade-Wesselink method, hereafter IBW method (see for e.g. Sasselov & Karovska 1994; and Kervella et al. 2004, hereafter Paper I). Interferometric measurements lead to angular diameter estimations over the whole pulsation period, while the stellar radius variations can be deduced from the integration of the pulsation velocity. The latter is linked to the observational velocity deduced from line profiles by the projection factor p. In this method, angular and linear diameters have to correspond to the same layer in the star to provide a correct estimate of the distance.

The spectral line profile, in particular its asymmetry, is critically affected by the dynamical structure of Cepheids' atmosphere: photospheric pulsation velocity (hereafter $V_{\rm puls}$), velocity gradients, limb-darkening, turbulence and rotation. Thus, radial velocities measured from line profiles, hereafter $V_{\rm rad}$, include the integration in two directions: over the surface, through limb-darkening, and over the radius, through velocity gradients. All these phenomena, except the rotation, are supposed to vary with the pulsation phase. However, they are currently merged in one specific quantity, generally considered as constant with time: the projection factor p, defined as $V_{\rm puls} = pV_{\rm rad}$.

The interferometric definition of the projection factor is of crucial importance in the IBW method, as it can induce a bias of up to 6% on the derived distance (Nardetto et al. 2004; Mérand et al. 2005). Otherwise, the limb-darkening is also required to derive a correct estimation of the angular diameter of the star. With the latest generation of long-baseline interferometers, studying its phase-dependence is of crucial importance (Marengo et al. 2002, 2003; Nardetto et al. 2006).

Line asymmetry was first observed for short-period cepheids by Sasselov et al. (1989). Then, Sasselov et al. (1990) studied

⋆ Tables 3–5 are only available in electronic form at http://www.edpsciences.org
⋆⋆ High Accuracy Radial velocity Planetary Search project developed by the European Southern Observatory.

Table 1. Observed sample of Cepheids sorted by increasing period.

Name	HD	P^a [days]	T_0^a [days]	Nb. of spectra	Nb. of cycles	$m_V{}^b$
R TrA	135592	3.38925	2 451 649.96	14	15	6.66
S Cru	112044	4.68976	2 451 645.64	12	3	6.60
Y Sgr	168608	5.77338	2 451 650.92	17	10	5.74
β Dor	37350	9.84262	2 451 643.54	49	3	3.75
ζ Gem	52973	10.14960	2 451 641.78	50	3	3.90
Y Oph	162714	17.12520	2 451 653.32	7	4	6.17
RZ Vel	73502	20.40020	2 451 633.58	10	3	7.08
ℓ Car	84810	35.551341	2 452 290.4158	118	2	3.74
RS Pup	68860	41.51500	2 451 644.22	15	3	7.03

[a] For ℓ Car, the reference Julian date (T_0) and the pulsation period (P) used to compute the phase are from Szabados (1989). For others stars we used ephemeris from Berdnikov et al. (2001).
[b] The visible magnitude (m_V) is from Berdnikov et al. (2000).

the impact of the asymmetry on radius and distances determinations. The link between line profiles asymmetry and the projection factor has been studied by Albrow et al. (1994). Finally, an error analysis of the IBW method is given in Marengo et al. (2004).

We present here a new original study of the line asymmetry using the very high spectral resolution of HARPS ($R = 120\,000$). We have observed 9 galactic Cepheids with periods ranging from $P = 3.39$ d to $P = 41.52$ d. Radial velocity, full-width at half-maximum (hereafter $FWHM$) and line asymmetry are presented for all stars in Sect. 2.

Section 3 deals with modelling and Sect. 4 with observations interpretation. Through a geometric model different definitions of the projection factor are proposed and compared in order to find the best procedure. Then the model is used to interpret observational radial velocity and asymmetry correlation curves. A set of parameters is thus derived for all stars. Taking into account the whole sample of stars we discuss general properties and in particular the period-dependencies.

2. HARPS observations

2.1. Journal of observations

HARPS is a spectrometer dedicated to the search for extrasolar planets by means of radial velocity measurements. It is installed at the Coudé room of the 3.6 m telescope at La Silla. The resolution is $R = 120\,000$ and the average Signal to Noise Ratio we obtain over all observations in the continuum (292 spectra) is 300 per pixel. The observed sample of Cepheids is presented in Table 1.

We have used the standard ESO/HARPS pipe-line reduction package with a special attention for the normalization process. We have noted on metallic line profiles of all stars a good reproduction from cycle-to-cycle. Therefore, spectra for a given star have been recomposed into an unique cycle.

Using Kurucz models (1992) we have identified about 150 unblended spectral lines. This first study considers only the unblended metallic line Fe I 6056.005 Å.

2.2. A new estimator of the radial velocity, FWHM and asymmetry: the bi-Gaussian

Several methods have been used to measure radial velocities of Cepheids, each having advantages and drawbacks. Among these methods there is the line minimum (usually determined via a parabolic fit to a few pixels near the bottom of the line) a Gaussian fit (obviously not adequate for asymmetric lines), the line centroid, determined from the integration of the line profile (requires high *Signal*/*Noise* ratio), and the line bisector where one measures the width of the line at one or several depths. Our bi-Gaussian approach combines advantages of methods useful for low S/N data while providing information usually associated with high resolution and high S/N data (asymmetry).

Radial velocity, full width at half-maximum ($FWHM$) and asymmetry have been derived simultaneously applying a classical χ^2 minimization algorithm between the observed line profile ($S(\lambda)$) and a modelled spectral line profile ($f(\lambda)$). The corresponding reduced χ^2 is:

$$\chi_{\rm red}{}^2 = \frac{1}{N-\nu}\sum_{i=0}^{N}\frac{(S(\lambda_i)-f(\lambda_i))^2}{\sigma(\lambda_i)^2} \quad (1)$$

with N the number of pixel in the spectral line, ν the number of degrees of freedom and $\sigma(\lambda_i) = SNR * f(\lambda_i)$ is the statistical uncertainty associated to each pixel. SNR is the estimate of the Signal to Noise Ratio in the continuum.

The analytic line profile is defined by:

$$f(\lambda) = 1 - D\exp\left(\frac{4\ln 2(\lambda-\lambda_{\rm m})^2}{(FWHM(1+A))^2}\right) \text{ if } \lambda > \lambda_{\rm m} \quad (2)$$

and

$$f(\lambda) = 1 - D\exp\left(\frac{4\ln 2(\lambda-\lambda_{\rm m})^2}{(FWHM(1-A))^2}\right) \text{ if } \lambda < \lambda_{\rm m} \quad (3)$$

with four free parameters:

- D, the depth of the line. This quantity has no dimension;
- $\lambda_{\rm m}$, the wavelength associated to the minimum of the line (in Å). The corresponding radial velocity is noted $RV_{\rm m}$;
- $FWHM$ is the Full-Width at Half-Maximum in the line, also in Å;
- A is the asymmetry as a percentage of the $FWHM$.

The $4\ln 2$ factor is to obtain a correct definition of the $FWHM$. Forcing asymmetry to zero in this minimization process is equivalent to fitting a Gaussian to the line profile. In this case we can derive another type of radial velocity noted $RV_{\rm g}$.

There are different ways to define the line asymmetry (see e.g. Sasselov et al. 1990; Sabbey et al. 1995). The advantage of the bi-Gaussian method is that it offers the possibility to derive statistical uncertainties directly from the minimization process.

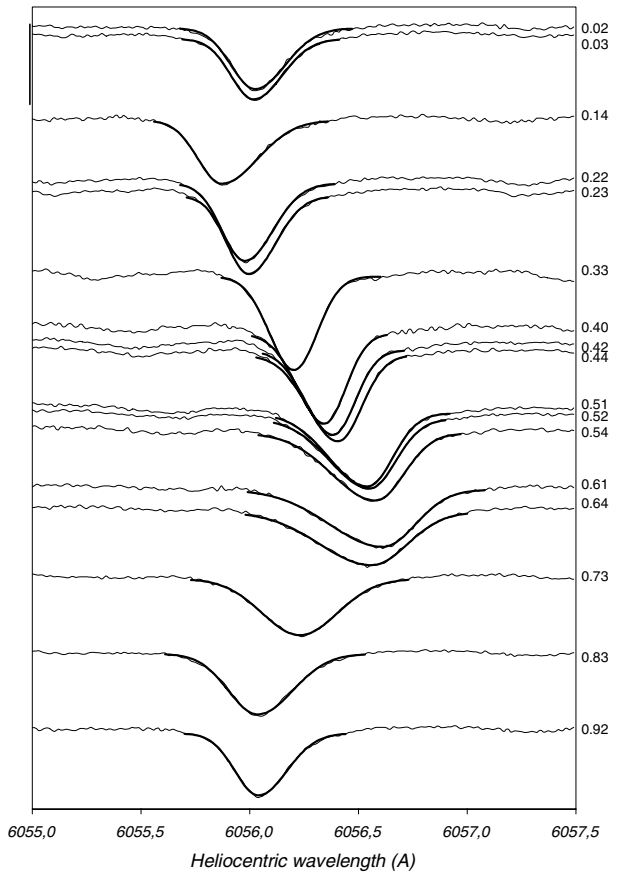

Fig. 1. Spectral line evolution of β Dor together with the modelled bi-Gaussian (bold). Line asymmetry is clear. The vertical line at the top corresponds to a differential flux of 0.3. Pulsation phases are given on the right of each profile.

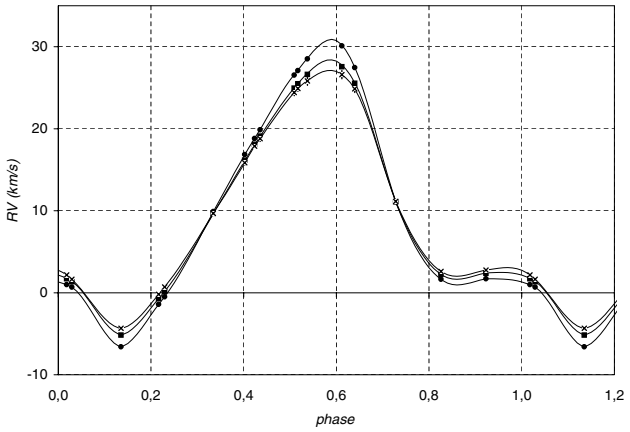

Fig. 2. β Dor radial velocities obtained with different method: $RV_{\rm m}$ (points), $RV_{\rm g}$ (squares), and $RV_{\rm c}$ (crosses). Statistical uncertainties at $\pm 1\sigma$ are indicated but too small to be visualized. We can therefore see the impact of the choice of the method in the case of a very asymmetric line (Fig. 1).

Moreover, all parameters ($RV_{\rm m}$, $FWHM$, D and A) are fitted simultaneously leading to a very consistent set of information. The largest reduced χ^2 we obtain with this method is of about 10 corresponding to a SNR of 438, but in most cases we have a reduced $\chi^2 \simeq 1$ or 2 corresponding to a SNR ranging from 75 to 350. That means that our analytic model is well suited to the data quality. We note also that the reduced χ^2 is not sensitive to the spectral line resolution.

As an example, Fig. 1 presents line profile variation for β Dor together with the analytic spectral line profile. We find that the asymmetry is insensitive to the choice of the continuum. However, this one has to be correctly defined to derive correct values of the $FWHM$ and line depth D.

Another radial velocity definition, the centroid velocity ($RV_{\rm c}$) or, the first moment of the spectral line profile, has been estimated as:

$$RV_{\rm c} = \frac{\int_{\rm line} \lambda S(\lambda) {\rm d}\lambda}{\int_{\rm line} S(\lambda) {\rm d}\lambda}. \quad (4)$$

Tables 3−5 present the resulting values of $RV_{\rm g}$, $RV_{\rm m}$, $RV_{\rm c}$, $FWHM$, D, A, SNR and $\chi^2_{\rm red}$ together with the corresponding uncertainties computed from the fitting method.

2.3. Radial velocity

As indicated in the previous section, we can derive three types of radial velocity: the velocity associated to the Gaussian fit ($RV_{\rm g}$), the line minimum ($RV_{\rm m}$) and the barycenter of the spectral line ($RV_{\rm c}$). Figure 2 shows these radial velocity curves obtained in the case of β Dor. Figure 3 represents for each star of our sample, the $RV_{\rm m}$ variation (arbitrary shifted). The solid lines are the interpolated curves using a periodic cubic spline function. This function is calculated either directly on the observational points (e.g. β Dor) or using arbitrary pivot points (e.g. RZ Vel). In the latter case, a classical minimization process between observations and the interpolated curve is used to optimize the position of the pivot points. All the interpolated curves presented in this study are derived using one of these two methods. The only exception is Y Oph (too few points) for which we performed a linear interpolation.

2.4. The Full-Width at Half-Maximum in the line

Figure 4 presents the $FWHM$ curve as a function of phase for all stars. We note that the largest $FWHM$ values are obtained for the maximum contraction velocities. RS Pup, the longest period Cepheid of our sample, seems to present an important compression or shock wave signature. Figure 5 presents line profile variation for this star. Unfortunately the phase coverage is not very good, but we can clearly see a strong increase of the $FWHM$ at $\phi = 0.83$. Such phenomenon has been already detected in β Cepheids (Fokin et al. 2004).

2.5. Asymmetry

Figure 6 shows the asymmetry variation for all stars. Generally speaking, the shape of the aymmetry curve is similar to the shape of the velocity curve $RV_{\rm m}$.

As already mentioned in Sect. 2.3, the radial velocity according to the choice of the method considered is sensitive to the line asymmetry. Figure 7 shows the correlation between the differences of radial velocity ($\Delta V = RV_{\rm m} - RV_{\rm g}$) and the asymmetry of the line. We have only presented here the case of ℓ Car and RS Pup. Each star presents a similar behavior. A typical difference in velocity of about 4 km s^{-1} can be obtained for an asymmetry of 40% in extreme cases (Y Sgr and R TrA). The relation between the radial velocity difference and the asymmetry is certainly affected by star characteristics (rotation, $FWHM$, velocity gradients) present in the line asymmetry. In particular

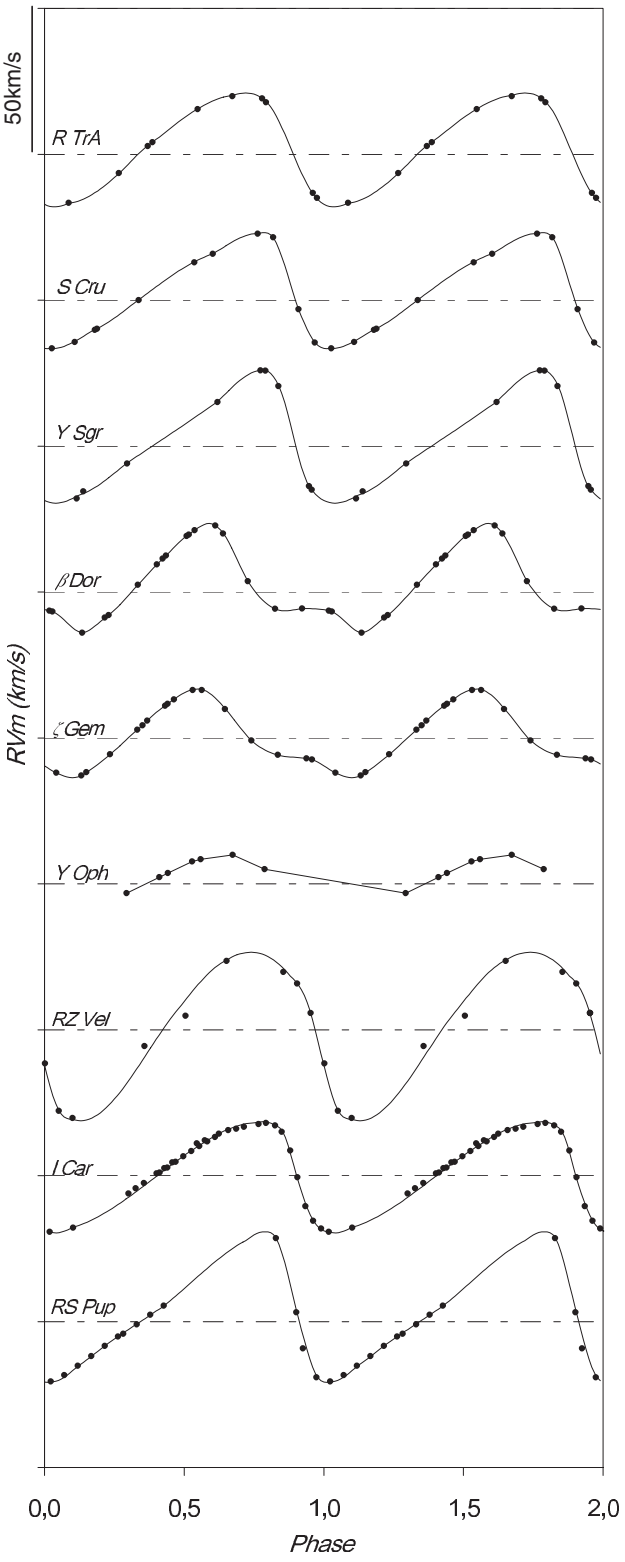

Fig. 3. Radial velocity curves ($RV_{\rm m}$). Curves have been arbitrarily shifted vertically. The horizontal lines are the zero velocity in the stellar rest frame. Largest velocities are for receding motion.

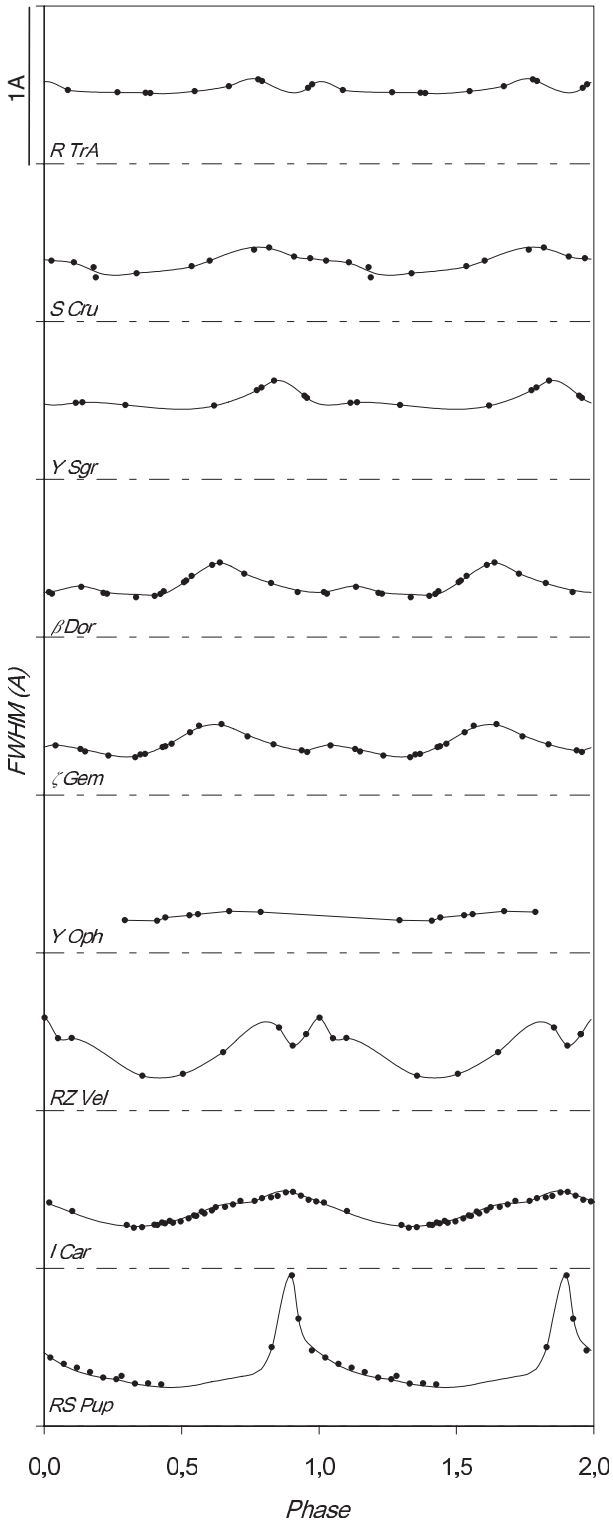

Fig. 4. *FWHM* versus phase for all stars. Curves have been arbitrarily shifted vertically. The horizontal lines correspond to a zero *FWHM*. Note the particular case of RS Pup, which may present the signature of an important compression or shock wave. RS Pup has the longest period of our sample.

RS Pup signature is certainly affected by strong velocity gradient effects. The fact that the $RV_{\rm m}$ and $RV_{\rm g}$ radial velocities present such differences as a function of the pulsation phase is an additional difficulty concerning an average projection factor and its time-dependence determination. With the centroid estimator of the radial velocity ($RV_{\rm g} - RV_{\rm c}$ or $RV_{\rm m} - RV_{\rm c}$) results are quite similar.

In next sections, we summarize all observational results in correlation diagrams between radial velocity and asymmetry. These correlations are interpreted using the geometric model

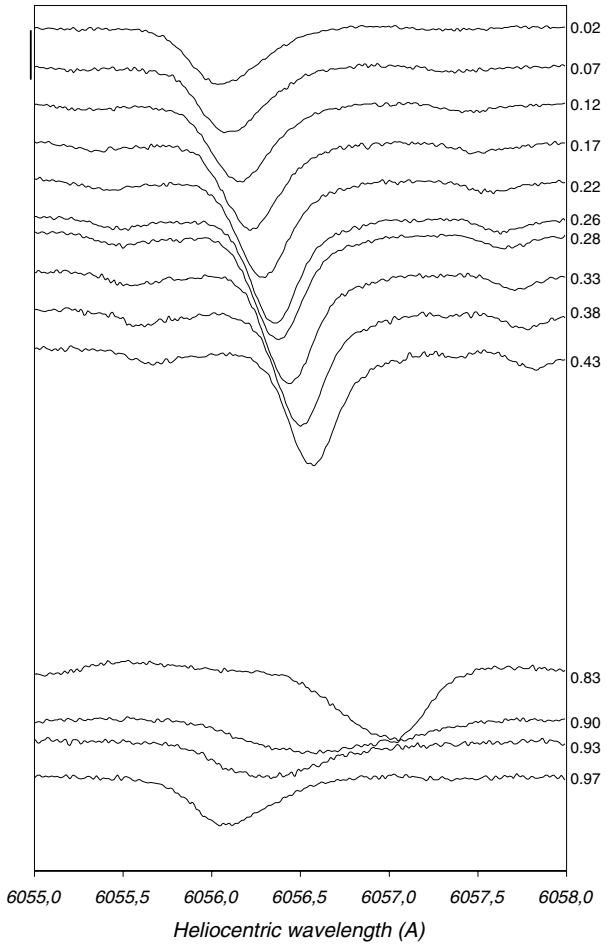

Fig. 5. FeI 6056.005 Å spectral line evolution of RS Pup. The vertical line at the top corresponds to a differential flux of 0.2. We note the broadening of the line at $\phi = 0.83$ which could be the signature of a strong velocity gradient (compression or shock wave).

in order to determine some physical parameters of our stars and to obtain information about dynamical effects in Cepheids atmosphere.

3. A toy model

We consider a limb-darkened pulsating star in rotation with an one-layer atmosphere. Our model has four parameters:

- the limb-darkening of the star: we consider a linear law for the continuum-intensity profile of the star defined by $I(\cos(\theta)) = 1 - u_V + u_V \cos(\theta)$, where u_V is the limb-darkening of the star in V band (Claret et al. 2000). Its value is about 0.7 for Cepheids. θ is the angle between the normal of the star and the line-of-sight;
- the projected rotation velocity $V_{\rm rot} \sin i$, where i is the angle between the line-of-sight and the rotation axis (in km s^{-1});
- the pulsation velocity (in km s^{-1});
- the width of the spectral line (in Å), hereafter named $\sigma_{\rm C}$. It is the $FWHM$ of the line with no pulsation nor rotation velocities. It is supposed to be constant with the pulsation phase.

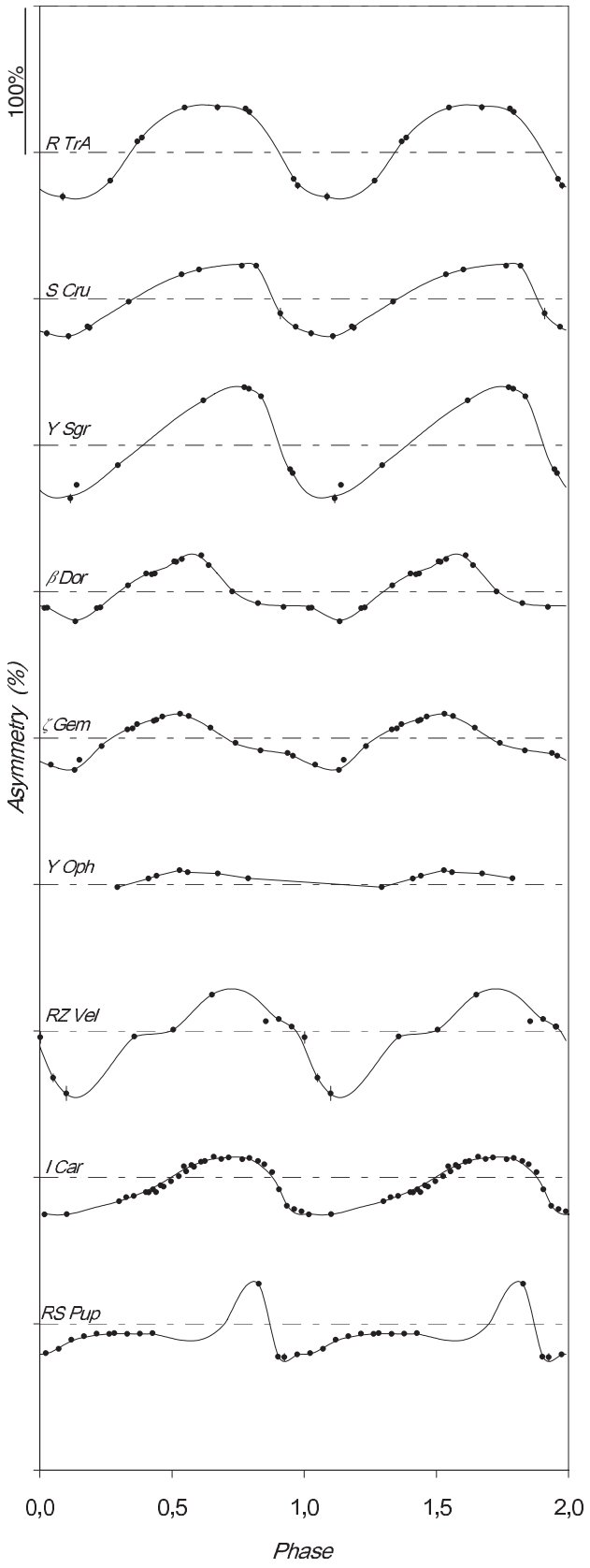

Fig. 6. Asymmetry against phase for all stars. Curves have been arbitrarily shifted vertically. The horizontal lines correspond to an asymmetry of zero.

The velocity field is a combination of pulsation and rotation velocities. Through the Doppler effect, this field can be transposed into wavelengths, and weighted by the surface brightness (limb-darkening) to obtain the weighting of the spectral line. We have

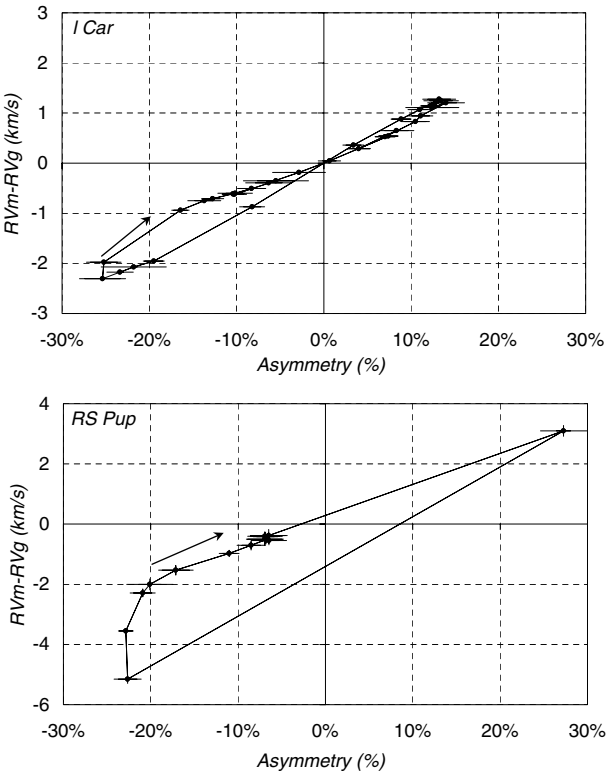

Fig. 7. Difference between the radial velocity obtained with the line minimum and the Gaussian fit methods as a function of the asymmetry in the case of ℓ Car and RS Pup. Statistical uncertainties are provided for each point. Arrows indicate the direction and the origin $\phi = 0$ of the curves. These relations are not linear and certainly affected by star characteristics (rotation, *FWHM*, velocity gradients...).

then to convolve it with the intrinsic profile to obtain the synthetic spectral line profile. The weighting or the synthetic spectral line profile are presented in different cases in Fig. 8.

We now consider a pulsation velocity curve defined by:

$$V_{\rm puls}(\phi_i) = V_{\rm max} \cos(2\pi\phi_i) \quad (5)$$

with a typical value for the maximal pulsation velocity of $V_{\rm max} = 30\ {\rm km\,s^{-1}}$. This relation which is a poor approximation of the pulsation velocity curve is only used for the projection factors determination (see below). It has no incidence on the results (see Sect. 4.1). From the synthetic spectral line profiles, we perform a bi-Gaussian fit to derive the four parameters described in Sect. 2.2: D, $\lambda_{\rm m}$, *FWHM* and A. Then we derive the $RV_{\rm m}$, $RV_{\rm g}$, $RV_{\rm c}$ velocities, and the corresponding radial velocity-asymmetry correlation curves (hereafter RV-A plot). In Fig. 10, the RV-A plots are represented for different values of the $\sigma_{\rm C}$ and rotation parameters. The limb-darkening (considered as constant with the pulsation phase) has a very small effect in the weighting of the line profile and thus practically no impact on the RV-A plot. Applying a classical minimization process between the pulsation and radial velocities, we have also derived for each set of parameters the corresponding constant projection factors: $p_{\rm m} = \frac{V_{\rm puls}}{RV_{\rm m}}$, $p_{\rm g} = \frac{V_{\rm puls}}{RV_{\rm g}}$ and $p_{\rm c} = \frac{V_{\rm puls}}{RV_{\rm c}}$.

Firstly, we note that the $\sigma_{\rm C}$ of the line and the rotation have different effects on the slope and/or shape of the correlation curves.

Secondly, correlation curves are slightly different from one definition of radial velocity to another. But the interesting point is that the $RV_{\rm c}$ velocity does not depend of $\sigma_{\rm C}$ and/or rotation.

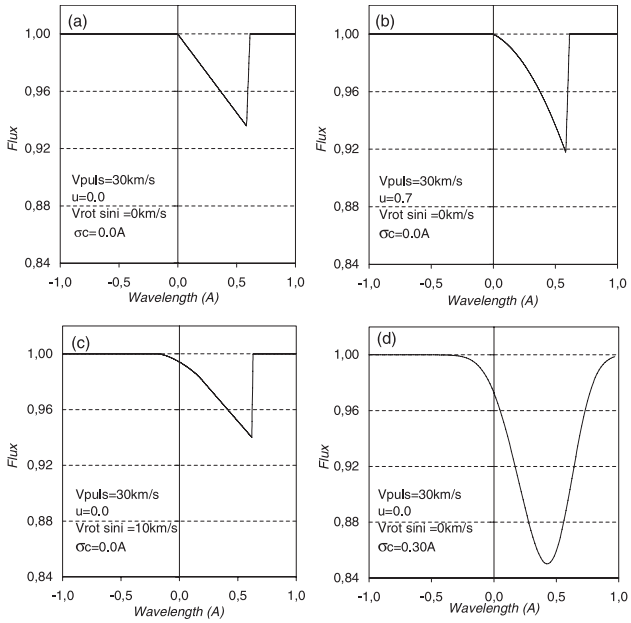

Fig. 8. The weighting or the synthetic spectral line profile in different cases, considering **a)** the pulsation velocity, **b)** the limb-darkening, **c)** the rotation and, **d)** an intrinsic width for the line ($\sigma_{\rm C}$).

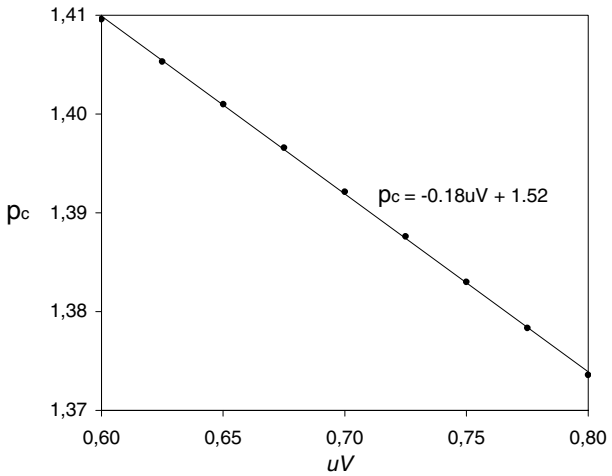

Fig. 9. The projection factor corresponding to the centroid velocity ($p_{\rm c}$) as a function of the limb-darkening parameter (u_V). Dots are the results from the toy model and the solid line corresponds to the linear approximation ($\chi^2 \simeq 10^{-5}$).

This behavior is clearly seen on diagrams 10b and 10d: the centroid projection factor $p_{\rm c}$ is constant with the $\sigma_{\rm C}$ and the rotation while the Gaussian and the minimum projection factors, $p_{\rm g}$ and $p_{\rm m}$, are varying. For the Cepheids of our sample the centroid projection factor ranges from $p_{\rm c} = 1.40$ ($u_V = 0.64$; R TrA) to $p_{\rm c} = 1.38$ ($u_V = 0.75$; ℓ Car), through the following relation:

$$p_{\rm c} = -0.18 u_V + 1.52 \quad (6)$$

This relation is a linear approximation from the geometrical model (see Fig. 9). Note that the geometrical model does not contain the physics of the pulsations, and thus the relation may not hold when instead of u_V a more realistic limb-darkening (taking into account hydrodynamic effects) is used. In particular, hydrodynamic effects can result in a much larger limb-darkening, especially at the wavelengths corresponding to spectral line (see e.g. Marengo et al. 2003).

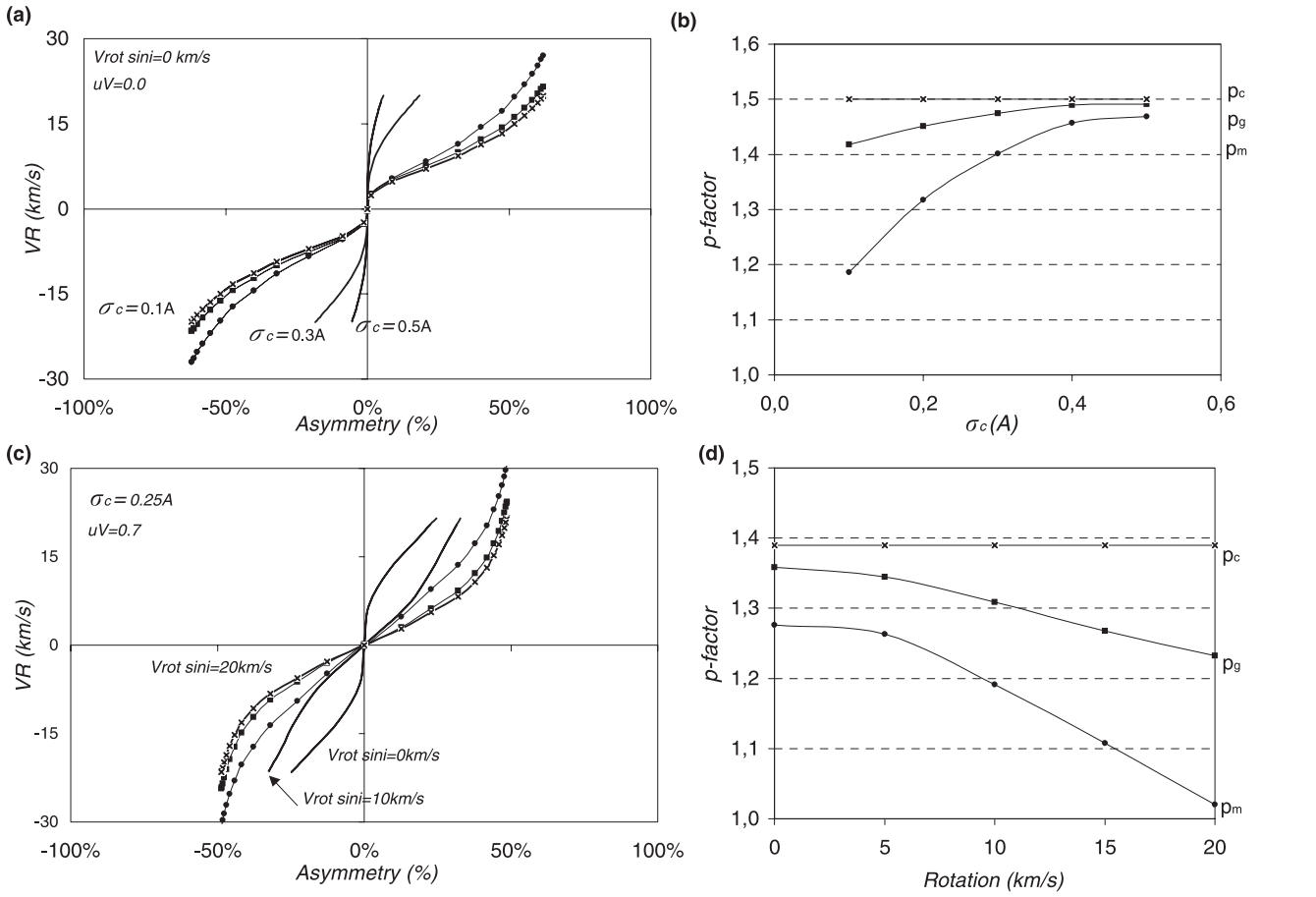

Fig. 10. Results of the geometric model of pulsating star. **a)**, **b)** The radial velocity-asymmetry correlation curves for different σ_C, with no rotation and no limb-darkening (uniform disk). Points, squares and crosses correspond respectively to the RV_m, RV_g and RV_c radial velocities. For clarity RV_g and RV_m are represented only for σ_C = 0.1 Å. The solid lines are the interpolated curves using a cubic spline function. The corresponding projection factors are represented on diagram **b)**. **c)**, **d)** Same plots but for different values of the rotation. The σ_C and the limb-darkening are respectively of 0.25 Å and 0.7. These RV-A plot are used to interpret HARPS observations.

This behavior is of great importance in the context of the IBW method. Indeed, the community has often used the p_c = 1.36 value of the projection factor (Burki et al. 1982) using the Gaussian method instead of the centroid method. As seen here, and already pointed out by Burki et al. (1982), this estimator is biased by the rotation velocity, even if Cepheids are supposed to be slow rotators, and also by the σ_C. We thus recommend the centroid based methods (spectral observable and p-factor) for the analysis of Cepheid radial velocities. For the present work, we have therefore chosen the RV_c definition of the radial velocity. Even though this requires substantial S/N, its advantages outweigh the drawback of spending more telescope time to acquire the data.

4. Interpretation

4.1. Methodology

Modeling results obtained in the previous section are now helpful to elaborate a strategy in a comparison of observations and models.

Firstly, the effective temperature $T_{\rm eff}$ and the surface gravity $\log g$ have been used to derive the intensity profile of stars through linear limb-darkening coefficients u_V of Claret et al. (2000) (see Table 2).

Secondly, we determine the projection factor p_c using Eq. (6). The pulsation velocity is then derived through $V_{\rm puls} = p_c RV_c$, where RV_c is the observational radial velocity corrected from the heliocentric velocity given in Table 2. The pulsation velocity $V_{\rm puls}$ and the projection factor p_c (see Table 2) obtained are not physically realistic, because our model does not include dynamical effects and in particular velocity gradients in the atmosphere, nevertheless this procedure imposes the surimposition of observational and modelled radial velocity curves RV_c. Moreover, as a very good agreement is observed for each phase (better than 1%), it validates the use of a *constant* projection factor (p_c). We find also that the poor description of the pulsation velocity (Eq. (5)) used to derive p_c has no incidence on the resulting modelled RV_c curve. By this procedure, we can thus concentrate only on the asymmetry, making the interpretation easier. Note that Nardetto et al. (2004) already gave an indication of the impact of velocity gradients on the projection factor, and thus on the distance determination, in the case of δ Cep (about −6%). In Table 2, we also indicate for each star the corresponding projection factors p_g and p_m for comparison.

Thirdly, σ_C and $V_{\rm rot} \sin i$ are determined together from the observational RV-A and $FWHM$ curves. We first consider the minimum of the observational $FWHM$ curve to obtain an indication on the value of σ_C. We then find the rotation which gives the best slope and shape for the RV-A curve. But as the rotation has also an impact on the $FWHM$ (about 0.02 Å), we have then

Table 2. Optimized parameters obtained for each sample Cepheid through the confrontation of HARPS observations with our geometric model.

stars	R TrA	S Cru	Y Sgr	β Dor	ζ Gem	Y Oph	RZ Vel	l Car	RS Pup
Period	3.38925	4.68976	5.77338	9.84262	10.14960	17.12520	20.40020	35.551341	41.51500
mean $T_{\rm eff}$[a][K]	6354	5995	5350	5490	5727	5907	5537	5091	5143
mean $\log(g)$[a]	2.0	1.9	1.0	1.8	1.5	1.5	1.5	1.5	0.4
u_V^b	0.6371	0.6541	0.7194	0.6999	0.6721	0.6514	0.6970	0.7541	0.7121
$v_\gamma{}^c$ [km s^{-1}]	−13.2	−7.1	−2.5	7.4	6.9	−6.6	24.1	3.6	22.1
$\sigma_{\rm C}^d$ [Å]	0.29	0.27	0.27	0.23	0.23	0.20	0.23	0.25	0.30
$V_{\rm rot}\sin i^e$ [km s^{-1}]	15	10	16	6	6	4	3	7	<1
$p_{\rm m} = \frac{V_{\rm puls}}{RV_{\rm m}}$	1.13	1.23	1.10	1.23	1.23	1.23	1.26	1.23	1.31
$p_{\rm g} = \frac{V_{\rm puls}}{RV_{\rm g}}$	1.28	1.31	1.26	1.32	1.32	1.33	1.34	1.31	1.36
$p_{\rm c} = \frac{V_{\rm puls}}{RV_{\rm c}}$	1.40	1.40	1.39	1.39	1.40	1.40	1.39	1.38	1.39
$\gamma_{\rm O}^e$ [%]	3.3	0.7	2.0	0.2	−2.4	–	−3.2	−6.9	−6.5
$\gamma_{\rm C}^g$ [%]	3.1	4.3	0.4	2.9	0.5	–	1.4	1.2	0.6
$\gamma_{\rm O-C}^h$ [%]	0.2	−3.6	1.6	−2.7	−2.9	–	−4.6	−8.2	−7.1

[a] $T_{\rm eff}$[K] and $\log(g)$, deduced from Gieren et al. (1998) for R TrA, S Scu, Y Oph and RZ Vel. For Y Sgr, β Dor, ζ Gem, ℓ Car, and RS Pup these quantities have taken from Cayrel de Strobel et al. (1997, 2001).
[b] u_V from Claret et al. (2000).
[c] v_γ from Galactic Cepheid database (online: `http://www.astro.utoronto.ca/DDO/research/cepheids`).
[d] Uncertainty on $\sigma_{\rm C}$ is of about 0.02 Å.
[e] Uncertainty on $V_{\rm rot}\sin i$ is of about 1 km s^{-1}.
[f] $\gamma_{\rm O}$ [%] is the averaged value of the observational asymmetry curves. The associated statistical uncertainties are of the order of 0.3%.
[g] $\gamma_{\rm C}$ [%] is the averaged value of the computed asymmetry curves.
[h] $\gamma_{\rm O-C}$ [%] is the average value of the O−C asymmetry curve.

to slightly readjust $\sigma_{\rm C}$ accordingly. By this process we finally find the best and unique values for $\sigma_{\rm C}$ and $V_{\rm rot}\sin i$.

The uncertainties on $V_{\rm rot}\sin i$ and $\sigma_{\rm C}$, associated to the minimization process, were estimated to be respectively 1 km s^{-1} and 0.02 Å. Similar uncertainties are found if one considers several metallic lines. Note however that our toy model is too simple to provide secure and precise values of the rotation, which is the most interesting parameter. In particular the broadening of the spectral line due to the macro-turbulence can certainly affect our rotation values (Bersier & Burki 1996). Nevertheless our principal and first objective is to probe the dynamical effects by a direct comparison of our static model with observations.

4.2. Observations versus modelisation

We now apply our methodology to each Cepheid of our sample. Results are indicated in Table 2. RV-A plot are represented in Figs. 11 and 12. Note that RV-A plot deduced from the model have been shifted in asymmetry to match the observations (this point is discussed in next section). For R TrA and Y Sgr, we can notice a very small slope for the RV-A plot and a very large value for the observational $FWHM$. It indicates a large rotational velocity $V_{\rm rot}\sin i$ and a properly small value for $\sigma_{\rm C}$ (see Figs. 10a,c). Thus, the corresponding Gaussian and minimum projection factors ($p_{\rm g}$ and $p_{\rm m}$) are lower than for others stars (see Figs. 10b,d). Conversely, for Y Oph and RZ Vel the RV-A plot have relatively large slope while the observational $FWHM$ is typical (about 0.3). This has a direct consequence on the rotation, which is then very small, and on the projection factors ($p_{\rm g}$ and $p_{\rm m}$) which are then relatively large. Comparatively, S Cru, β Dor and ζ Gem can be considered as intermediate cases. For ℓ Car and RS Pup, we obtain an atypical RV-A plot which is greatly shifted in asymmetry. For RS Pup, we obtain a specific RV-A plot characterized by a strong curvature which can be interpreted by our geometric model as a very slow rotation velocity $V_{\rm rot}\sin i < 1$ km s^{-1}. Note that atypical points which are observed at the top of the RV-A plot are certainly due to dynamical effects since they corresponds to phases of outwards acceleration.

4.3. Discussion

As observed in the particular case of ℓ Car and RS Pup, an important systematic shift in asymmetry can be present between observations and models. We define respectively $\gamma_{\rm O}$ and $\gamma_{\rm C}$ the averaged value of the observational and computed asymmetry curves [in %]. Note that the phases are sampled in the same way for data and model. Results are indicated in Table 2. We have also calculated for each star the residuals between the observational and computed asymmetry curves, noted O−C curves (Fig. 13). We define $\gamma_{\rm O-C}$, the average value of these residual curves. These O−C asymmetry curves contain the whole dynamical information present in the observational asymmetry, mainly: the limb-darkening variation in the spectral line and with the pulsation phase, the micro- and macro- turbulence, velocity gradient and temperature effects. For R TrA, S Cru, Y Sgr, RZ Vel and RS Pup, we note a bump in the O−C asymmetry curves which is approximately linked to the cross of the compression wave just after the maximum contraction velocity (see Fig. 3). However β Dor, ζ Gem and ℓ Car do not present such bump, which may be interpreted as the presence of a very small compression wave. In the case of Y Oph the phase sampling seems insufficient to conclude. Consistent hydrodynamical model would be helpful to confirm these results.

$\gamma_{\rm O}$, $\gamma_{\rm C}$ and $\gamma_{\rm O-C}$ are represented as a function of the pulsation period in Fig. 14a. The open squares represent $\gamma_{\rm C}$. We want to emphasize here that our model produces asymmetry curves with *non*-zero average value. Indeed, it is a natural consequence of the shape of the observational radial velocity curve used to derive the pulsation velocity. We find a similar behavior for all stars independently of the period.

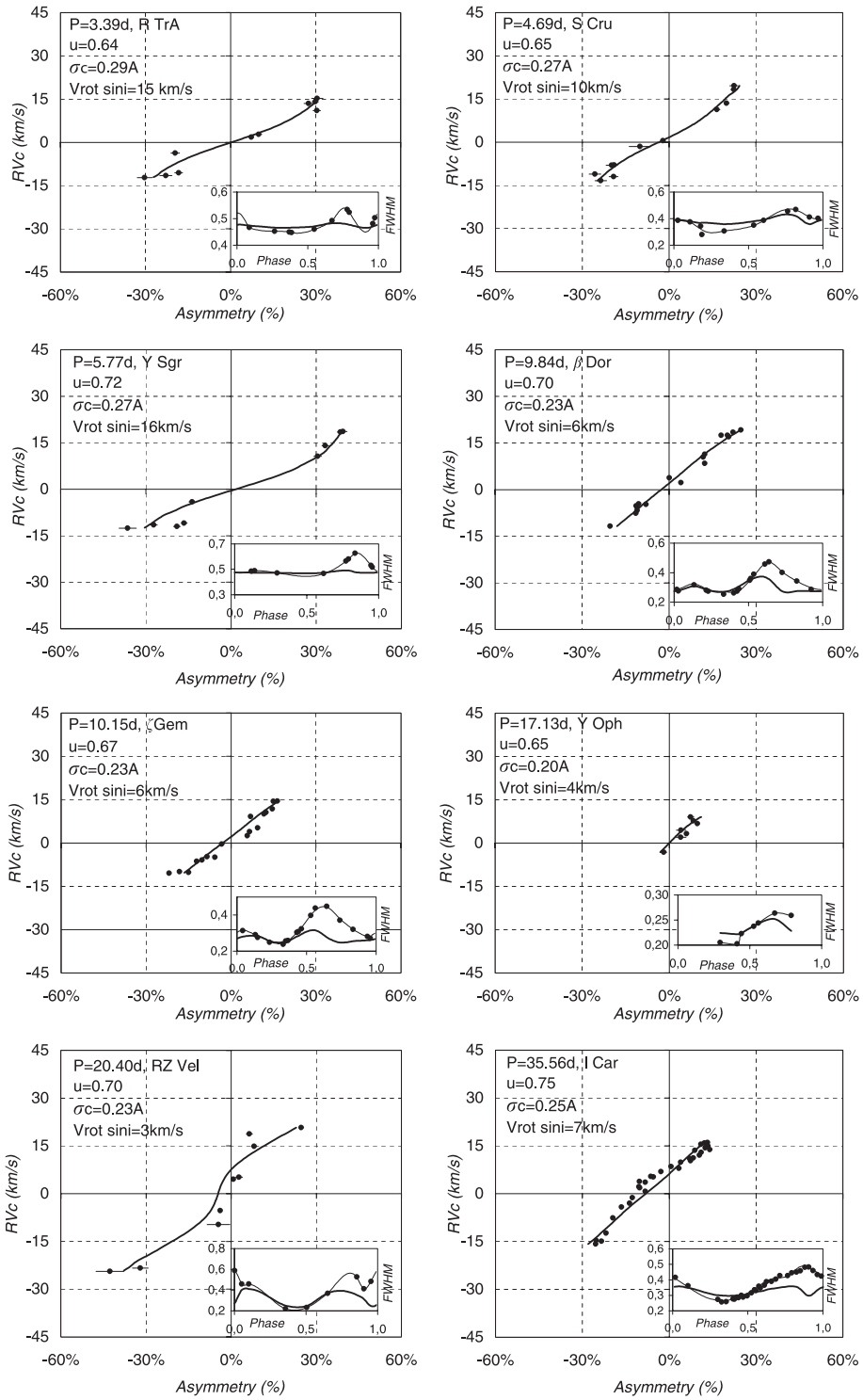

Fig. 11. Radial velocity (RV_c) – asymmetry correlation curves for R TrA, S Cru, Y Sgr, β Dor, ζ Gem, Y Oph, RZ Vel and ℓ Car. Dots and bold curves correspond respectively to observations and models. The statistical uncertainties are indicated. Note that RV-A plot deduced from the model have been shifted in asymmetry. The small plot on each diagram correspond to the comparison of the observational (dots) and model (bold curve) $FWHM$.

The shifts obtained on the observational asymmetry curves (γ_O) show a very interesting linear dependence with the logarithm of the pulsation period:

$$\gamma_O = (-10.7 \pm 0.1)\log(P) + (9.7 \pm 0.2)\ [\text{in \%}]\ . \quad (7)$$

Moreover we note that the dependence of γ_{O-C} with the pulsation period is very similar to the one of γ_O. We can conclude that this behavior is related to the dynamical effects in the atmosphere, which are not taken into account in our toy model. This can be explained by the fact that long-period Cepheids have extended atmosphere and consequently strong velocity gradient (see for example the case of RS Pup mentioned above). Thus, the line forming region can be seriously perturbed leading to a systematic shift in asymmetry (Albrow & Cottrell 1994). However,

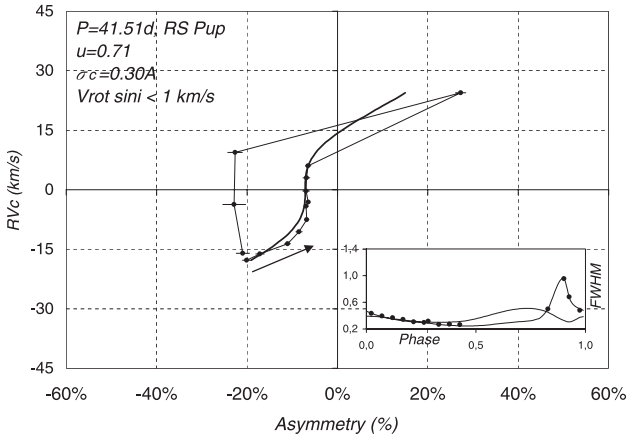

Fig. 12. Same as Fig. 11 but for RS Pup. RS Pup seems to be a non-rotating star as requested by the shape of its RV-A curve. Note also atypical points in observational RV-A plot, which can certainly be interpreted through the presence of a strong compression or shock wave in the stellar atmosphere.

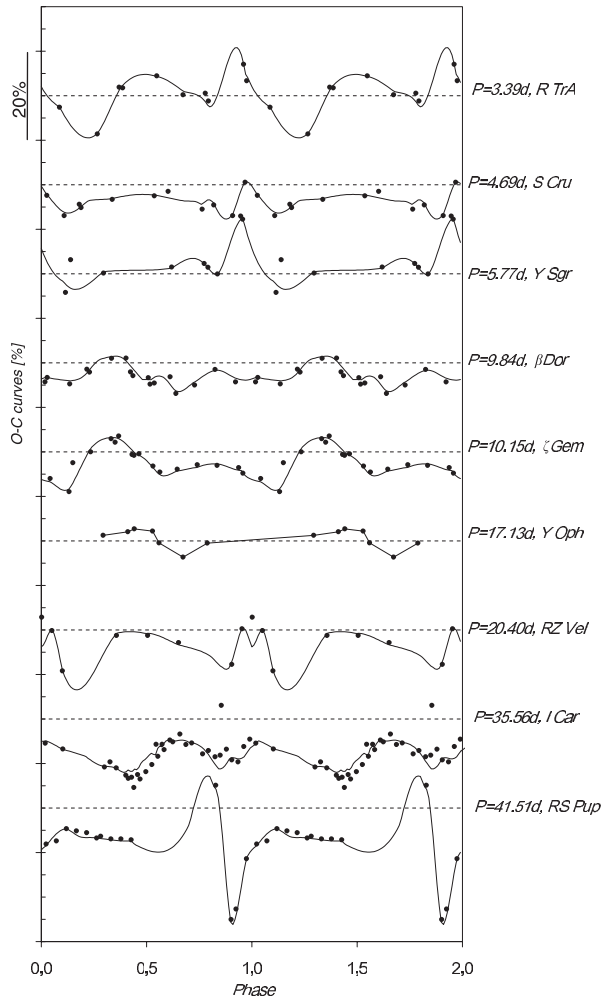

Fig. 13. Difference of the Observational and Computed asymmetry curves (O−C curves) for each stars. Curves are arbitrarily shifted. The horizontal dotted lines corresponds to a zero asymmetry for each star.

such an interpretation remains tricky and needs confirmation. Forthcoming hydrodynamical models are likely to bring out important insight in this field.

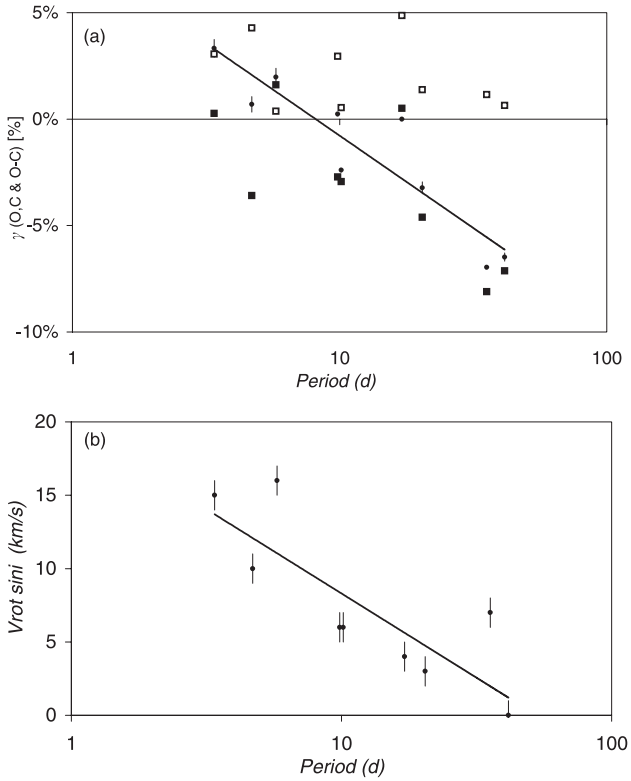

Fig. 14. a) Average values of the observational (black circles) and computed (open squares) asymmetry curves, together with the $\gamma_{\rm O-C}$ (filled squares) average values as a function of the pulsation period. **b)** Dependence of the projected rotation velocity with the pulsation period.

From results of Table 2, it appears also that the projected rotational velocity varies as a function of the pulsation period (Fig. 14b). We obtain the following relationship:

$$V_{\rm rot} \sin i = (-11.5 \pm 0.9) \log(P) + (19.8 \pm 1.0) \; [\text{in km s}^{-1}]. \quad (8)$$

The projected rotation is an important parameter which can be used, for example, to study evolution of Cepheids together with their mass loss. However, note again that our toy model does not include the physics of the pulsations and it is also very difficult to separate the rotation and macroturbulence effects in the resulting broadening of the spectral line. Thus this relation has to be considered very carefully as it is certainly model dependent.

5. Conclusion

We have presented HARPS high spectral resolution (R = 120 000) observations of nine galactic Cepheids having a good period sampling (P = 3.39d to P = 41.52d). We fit spectral line profile with an asymmetric bi-Gaussian to derive radial velocity, *FWHM* and line asymmetry for all stars. The presence of a very important compression or shock wave in the case of RS Pup, the longest period Cepheid of our sample has been identified. We have also translated the measured spectroscopic quantities into meaningful correlation curves between radial velocity and asymmetry.

A simple geometric model providing synthetic spectral lines, including limb-darkening, the $\sigma_{\rm C}$ and the projected rotation velocity is then used to interpret these correlations curves.

Firstly, we find that the centroid projection factor ($p_{\rm c}$) is independent of $\sigma_{\rm C}$ and the rotation velocity. This projection factor

is thus certainly the best one to use in the context of the Baade-Wesselink method.

Secondly, we find for each stars an optimized set of parameters which allows to reproduce observational radial velocity – asymmetry correlation curves. In particular, we find a dependence of the derived projected rotation velocities with the period of the star: $V_{\rm rot} \sin i = (-11.5 \pm 0.9) \log(P) + (19.8 \pm 1.0)$ [in km s^{-1}].

Finally, by comparing the outputs of our static models and the observed quantities, we gain access to dynamical effects. In particular, we found that long-period Cepheids with strong velocity gradient, like RS Pup, have a systematic shift in their asymmetry curve. We thus derived a linear relation between the observational shift in asymmetry and the logarithm of the period: $\gamma_{\rm O} = (-10.7 \pm 0.1) \log(P) + (9.7 \pm 0.2)$ [in %]. A detailed interpretation of these empirical relation is very difficult, but forthcoming hydrodynamical models are likely to bring out important insight in this field.

In conclusion, line asymmetry, which contains most of the physics involved in Cepheid atmosphere, is an important tool. But additional hydrodynamical considerations together with a multi-lines study are now required to have a better understanding of the dynamical processes present in Cepheid atmosphere and in particular to determine realistic projection factors including velocity gradients.

Acknowledgements. Based on observations collected at La Silla observatory, Chile, in the framework of European Southern Observatory's programs 072.D-0419 and 073.D-0136. This research has made use of the SIMBAD and VIZIER databases at CDS, Strasbourg (France). We thank David Chapeau for his helpful collaboration concerning computing aspects, Olivier Chesneau and Philippe Stee for their careful reading of the manuscript, as well as Vincent Coudé du Foresto and Andrei Fokin for useful discussions.

References

Albrow, M. D., & Cottrell, P. L. 1994, MNRAS, 267, 548
Berdnikov, L. N., & Caldwell, J. A. R. 2001, ApJ, 7, 3
Berdnikov, L. N., Dambis, A. K., & Vozyakova, O. V. 2000, A&AS, 143, 211
Bersier, D., & Burki, G. 1996, A&A, 306, 417
Burki, G., Mayor, M., & Benz, W. 1982, A&A, 109, 258
Cayrel de Strobel, G., Soubiran, C., Friel, E. D., et al. 1997, A&A, 124, 299
Cayrel de Strobel, G., Soubiran, C., & Ralite, N. 2001, A&A, 373, 159
Claret, A. 2000, A&A, 363, 1081
Fokin, A., Mathias, Ph., Chapellier, E., et al. 2004, A&A, 426, 687
Gieren, W. P., Fouqué, P., & Gómez, M. 1998, ApJ, 496, 17
Kervella, P., Nardetto, N., Bersier, D., et al. 2004, A&A, 416, 941
Kurucz, R. L. 1992, The Stellar Populations of Galaxies, IAU Symp., 149, 225
Marengo, M., Sasselov, D. D., Karovska, M., et al. 2002, ApJ, 567, 1131
Marengo, M., Karovska, M., Sasselov, D. D., et al. 2003, ApJ, 589, 975
Marengo, M., Karovska, M., Sasselov, D. D., et al. 2004, ApJ, 603, 285
Mérand, A., Kervella, P., Coude du Foresto, V., et al. 2005, A&A, 438, L9
Nardetto, N., Fokin, A., Mourard, D., et al. 2004, A&A, 428, 131
Nardetto, N., Fokin, A., Mourard, D., et al. 2006, A&A, accepted
Sabbey, C. N., Sasselov, D. D., Fieldus, M. S., et al. 1995, ApJ, 446, 250
Sasselov, D. D., & Karovska, M. 1994, ApJ, 432, 367
Sasselov, D. D., Lester, J. B., & Fieldus, M. S. 1989, ApJ, 337, 29
Sasselov, D. D., Lester, J. B., & Fieldus, M. S. 1990, ApJ, 362, 333
Szabados, L. 1989, Communications of the Konkoly Observatory Hungary, 94, 1

Table 3. HARPS observations results for R TrA, S Cru and Y Sgr.

JD_c (a)	phase (b)	Cy. (c)	Sp. (d)	RV_g (e)	RV_m (f)	RV_c (g)	$FWHM$ (h)	D (i)	A (j)	SNR (k)	χ^2_{red} (l)
R TrA											
202.53	0.09	14	1	–26.74 ± 0.07	–29.88 ± 0.17	–25.43 ± 1.16	0.467 ± 0.009	0.14	–30.3 ± 2.7	231	2.0
206.53	0.27	15	1	–17.70 ± 0.05	–19.71 ± 0.13	–16.92 ± 0.91	0.452 ± 0.005	0.17	–19.5 ± 1.5	224	1.6
152.65	0.37	1	2	–11.18 ± 0.03	–10.41 ± 0.08	–11.39 ± 0.56	0.449 ± 0.002	0.19	7.4 ± 0.8	241	1.6
203.55	0.39	14	1	–10.08 ± 0.04	–9.06 ± 0.11	–10.47 ± 0.71	0.447 ± 0.003	0.18	9.9 ± 1.1	257	1.1
156.65	0.55	2	2	–0.98 ± 0.04	2.20 ± 0.09	–2.15 ± 0.52	0.460 ± 0.005	0.19	30.4 ± 1.3	209	1.0
204.52	0.67	14	1	3.29 ± 0.06	6.70 ± 0.15	2.02 ± 0.74	0.492 ± 0.008	0.17	30.6 ± 2.0	207	1.4
150.65	0.78	1	2	2.26 ± 0.04	5.89 ± 0.09	0.89 ± 0.50	0.534 ± 0.005	0.16	29.9 ± 1.1	255	1.3
201.54	0.79	14	1	1.34 ± 0.06	4.64 ± 0.14	0.30 ± 0.74	0.524 ± 0.007	0.16	27.5 ± 1.6	247	1.7
154.65	0.96	2	2	–24.46 ± 0.05	–26.46 ± 0.13	–23.76 ± 0.79	0.481 ± 0.004	0.12	–18.3 ± 1.4	241	1.2
205.54	0.98	15	1	–25.60 ± 0.08	–28.18 ± 0.19	–24.71 ± 1.24	0.503 ± 0.007	0.12	–22.8 ± 2.1	243	1.4
S Cru											
207.46	0.03	3	1	–21.58 ± 0.05	–23.61 ± 0.13	–20.47 ± 1.01	0.386 ± 0.005	0.16	–23.6 ± 2.0	230	1.5
151.56	0.11	1	1	–19.32 ± 0.05	–21.43 ± 0.12	–18.20 ± 0.93	0.375 ± 0.005	0.18	–25.6 ± 2.0	214	1.4
203.49	0.18	3	2	–15.82 ± 0.03	–17.26 ± 0.07	–14.98 ± 0.50	0.344 ± 0.002	0.21	–19.0 ± 1.0	224	1.7
156.63	0.19	1	1	–15.65 ± 0.04	–16.90 ± 0.10	–15.07 ± 0.52	0.281 ± 0.004	0.19	–19.8 ± 1.9	221	2.4
152.63	0.34	1	1	–6.94 ± 0.02	–7.08 ± 0.06	–6.54 ± 0.46	0.306 ± 0.001	0.26	–2.1 ± 0.8	255	1.9
153.57	0.54	1	1	4.61 ± 0.03	5.87 ± 0.08	4.21 ± 0.62	0.351 ± 0.002	0.26	16.5 ± 1.1	209	2.5
205.47	0.60	3	1	7.09 ± 0.03	8.77 ± 0.06	6.44 ± 0.59	0.386 ± 0.002	0.26	19.9 ± 0.9	269	2.5
154.64	0.76	1	1	13.40 ± 0.05	15.66 ± 0.12	12.48 ± 1.06	0.454 ± 0.005	0.23	22.5 ± 1.4	181	1.6
206.48	0.82	3	1	12.07 ± 0.04	14.42 ± 0.09	11.17 ± 0.59	0.469 ± 0.004	0.20	22.4 ± 1.0	285	1.5
150.63	0.91	1	1	–9.32 ± 0.14	–10.19 ± 0.35	–8.58 ± 1.37	0.412 ± 0.008	0.17	–10.1 ± 3.7	87	1.4
202.49	0.97	3	1	–19.91 ± 0.05	–21.62 ± 0.12	–19.05 ± 0.70	0.401 ± 0.004	0.15	–19.2 ± 1.5	287	2.0
Y Sgr											
204.63	0.12	10	2	–16.53 ± 0.06	–20.47 ± 0.15	–15.07 ± 0.86	0.485 ± 0.011	0.15	–36.4 ± 3.0	160	1.1
152.80	0.14	1	2	–15.07 ± 0.04	–18.08 ± 0.09	–14.02 ± 0.56	0.488 ± 0.004	0.16	–27.2 ± 1.3	251	1.4
205.67	0.30	10	1	–6.93 ± 0.05	–8.45 ± 0.12	–6.56 ± 0.65	0.472 ± 0.003	0.19	–13.7 ± 1.1	244	2.6
149.80	0.62	1	2	9.37 ± 0.04	12.58 ± 0.09	8.13 ± 0.62	0.467 ± 0.005	0.21	30.5 ± 1.3	178	1.0
202.65	0.77	10	2	18.50 ± 0.04	23.46 ± 0.09	16.08 ± 0.71	0.565 ± 0.007	0.19	39.5 ± 1.4	231	1.5
150.79	0.79	1	2	18.31 ± 0.03	23.31 ± 0.08	15.98 ± 0.61	0.581 ± 0.006	0.18	38.5 ± 1.1	270	1.8
156.83	0.84	2	2	13.31 ± 0.04	18.07 ± 0.11	11.56 ± 0.63	0.626 ± 0.007	0.16	33.2 ± 1.2	255	1.6
203.65	0.95	10	2	–14.27 ± 0.04	–16.27 ± 0.11	–13.47 ± 0.50	0.530 ± 0.003	0.13	–16.5 ± 1.0	288	1.4
151.75	0.96	1	2	–15.22 ± 0.05	–17.50 ± 0.12	–14.51 ± 0.61	0.517 ± 0.004	0.13	–19.1 ± 1.2	254	1.1

(a) JD_c, average Julian date of observation defined by $JD_c = JD - 2\,453\,000$ [in days].
(b) phase, averaged pulsation phase of observation. For ephemeris see Table 1.
(c) Cy., pulsating cycle of the star corresponding to observation.
(d) Sp., number of spectra associated to observation. Results corresponding to these spectra are averaged.
(e) RV_g, Gaussian fit radial velocity and the associated error barre [in km s^{-1}].
(f) RV_m, minimum radial velocity derived from the bi-Gaussian fit [in km s^{-1}].
(g) RV_c, radial velocity corresponding to the first moment of the spectral line [in km s^{-1}].
(h) $FWHM$, Full-Width at Half-Maximum derived from the bi-Gaussian fit [in Angstroms].
(i) D, line depth derived from the bi-Gaussian fit [no dimension]. Errors bars are not indicated but of the order of 10^{-4}.
(j) A, asymmetry derived from the bi-Gaussian fit [in percentage].
(k) SNR, observational spectral line signal to noise ratio.
(l) χ^2_{red}, reduced χ^2 factor corresponding to the bi-Gaussian fit.

Table 4. HARPS observations results for β Dor, ζ Gem, Y Oph, and RZ Vel. See Table3 for legend.

JD_c (a)	phase (b)	Cy. (c)	Sp. (d)	RV_g (e)	RV_m (f)	RV_c (g)	$FWHM$ (h)	D (i)	A (j)	SNR (k)	χ^2_{red} (l)
						β Dor					
21.68	0.02	1	4	1.70 ± 0.01	0.99 ± 0.02	2.17 ± 0.14	0.286 ± 0.001	0.23	–11.3 ± 0.4	345	3.7
31.64	0.03	2	3	1.35 ± 0.01	0.68 ± 0.02	1.64 ± 0.12	0.275 ± 0.001	0.23	–11.0 ± 0.4	404	2.4
32.68	0.14	2	3	–5.16 ± 0.01	–6.59 ± 0.03	–4.33 ± 0.19	0.318 ± 0.001	0.24	–20.3 ± 0.6	298	2.1
23.64	0.22	1	4	–0.73 ± 0.01	–1.42 ± 0.01	–0.19 ± 0.11	0.280 ± 0.001	0.30	–11.4 ± 0.2	423	4.9
33.61	0.23	2	3	0.15 ± 0.01	–0.49 ± 0.02	0.71 ± 0.12	0.275 ± 0.001	0.31	–11.0 ± 0.3	443	7.9
34.64	0.33	2	2	9.67 ± 0.01	9.90 ± 0.02	9.68 ± 0.22	0.253 ± 0.001	0.36	4.1 ± 0.3	330	2.5
15.62	0.40	1	3	16.16 ± 0.01	16.85 ± 0.02	15.85 ± 0.28	0.261 ± 0.001	0.35	12.3 ± 0.4	262	2.4
25.68	0.42	2	3	18.10 ± 0.01	18.80 ± 0.02	17.86 ± 0.24	0.273 ± 0.001	0.33	11.8 ± 0.3	399	3.3
35.64	0.44	3	2	19.09 ± 0.01	19.87 ± 0.02	18.80 ± 0.35	0.290 ± 0.001	0.33	12.3 ± 0.4	337	2.0
16.67	0.51	1	3	24.95 ± 0.01	26.53 ± 0.02	24.41 ± 0.38	0.347 ± 0.001	0.28	20.5 ± 0.4	352	3.2
26.59	0.52	2	2	25.48 ± 0.01	27.09 ± 0.02	24.91 ± 0.34	0.359 ± 0.001	0.27	20.2 ± 0.3	473	4.9
36.64	0.54	3	2	26.61 ± 0.01	28.52 ± 0.04	25.83 ± 0.54	0.388 ± 0.001	0.26	22.1 ± 0.5	336	2.2
17.69	0.61	1	3	27.57 ± 0.02	30.11 ± 0.04	26.60 ± 0.51	0.457 ± 0.002	0.22	24.8 ± 0.5	303	2.2
37.64	0.64	3	2	25.54 ± 0.02	27.46 ± 0.04	24.86 ± 0.45	0.473 ± 0.001	0.20	18.0 ± 0.5	409	3.1
28.67	0.73	2	3	11.09 ± 0.01	11.09 ± 0.03	11.15 ± 0.20	0.401 ± 0.001	0.21	0.1 ± 0.3	456	2.7
29.63	0.83	2	4	2.24 ± 0.01	1.65 ± 0.02	2.60 ± 0.12	0.343 ± 0.001	0.23	–7.9 ± 0.2	472	6.5
30.59	0.92	2	3	2.36 ± 0.01	1.71 ± 0.02	2.77 ± 0.12	0.286 ± 0.001	0.24	–10.5 ± 0.3	455	5.0
						ζ Gem					
32.70	0.04	2	3	–3.82 ± 0.02	–5.04 ± 0.04	–3.05 ± 0.33	0.313 ± 0.001	0.27	–18.2 ± 0.7	196	2.9
33.62	0.14	2	3	–4.67 ± 0.01	–6.02 ± 0.02	–3.55 ± 0.19	0.292 ± 0.001	0.31	–21.9 ± 0.4	330	7.7
23.65	0.15	1	4	–4.00 ± 0.01	–4.89 ± 0.02	–3.35 ± 0.13	0.276 ± 0.001	0.31	–15.0 ± 0.3	338	4.2
34.65	0.23	2	3	1.53 ± 0.01	1.23 ± 0.02	1.97 ± 0.15	0.248 ± 0.001	0.37	–5.7 ± 0.3	334	6.0
35.65	0.34	2	3	9.44 ± 0.01	9.73 ± 0.02	9.41 ± 0.18	0.239 ± 0.001	0.39	5.8 ± 0.3	299	2.6
25.69	0.35	1	3	10.86 ± 0.01	11.22 ± 0.03	10.84 ± 0.35	0.256 ± 0.001	0.37	6.6 ± 0.4	195	1.9
15.71	0.37	1	3	12.29 ± 0.01	12.81 ± 0.02	12.12 ± 0.25	0.259 ± 0.001	0.38	9.4 ± 0.3	253	1.6
36.66	0.43	2	2	17.10 ± 0.01	17.87 ± 0.03	16.92 ± 0.46	0.304 ± 0.001	0.34	11.7 ± 0.5	255	2.3
26.60	0.44	2	3	17.69 ± 0.01	18.53 ± 0.02	17.48 ± 0.29	0.308 ± 0.001	0.33	12.4 ± 0.3	353	3.1
16.69	0.46	1	3	19.06 ± 0.02	20.11 ± 0.04	18.71 ± 0.50	0.324 ± 0.001	0.31	14.6 ± 0.6	189	1.4
37.66	0.53	3	2	21.81 ± 0.01	23.27 ± 0.03	21.40 ± 0.45	0.397 ± 0.001	0.28	16.4 ± 0.4	341	3.1
17.70	0.56	1	3	21.79 ± 0.01	23.25 ± 0.02	21.35 ± 0.33	0.439 ± 0.001	0.27	14.9 ± 0.2	446	3.1
28.68	0.62	2	2	16.11 ± 0.02	16.81 ± 0.06	16.02 ± 0.59	0.449 ± 0.001	0.24	7.0 ± 0.6	243	1.4
29.64	0.74	2	2	6.25 ± 0.03	5.98 ± 0.07	6.53 ± 0.53	0.372 ± 0.001	0.26	–3.3 ± 0.8	169	1.7
30.60	0.84	2	3	1.64 ± 0.01	1.06 ± 0.02	2.09 ± 0.16	0.321 ± 0.001	0.28	–8.5 ± 0.3	407	7.2
31.64	0.94	2	3	0.49 ± 0.01	–0.13 ± 0.02	0.98 ± 0.15	0.282 ± 0.001	0.28	–10.2 ± 0.3	372	8.3
21.70	0.96	1	5	0.18 ± 0.01	–0.54 ± 0.03	0.59 ± 0.15	0.271 ± 0.001	0.27	–12.1 ± 0.5	229	2.3
						Y Oph					
216.75	0.29	4	1	–9.75 ± 0.02	–9.83 ± 0.05	–9.72 ± 0.46	0.205 ± 0.001	0.32	–1.9 ± 1.1	189	1.2
201.63	0.41	4	1	–4.48 ± 0.03	-4.31 ± 0.08	–4.57 ± 0.43	0.202 ± 0.002	0.31	4.0 ± 1.8	119	1.4
150.78	0.44	1	1	–3.15 ± 0.02	–2.87 ± 0.04	–3.37 ± 0.27	0.223 ± 0.001	0.33	5.9 ± 0.7	262	2.9
203.65	0.53	4	1	0.57 ± 0.02	1.06 ± 0.04	0.20 ± 0.22	0.238 ± 0.001	0.31	9.7 ± 0.7	296	4.3
152.80	0.56	1	1	1.37 ± 0.02	1.80 ± 0.04	1.09 ± 0.24	0.244 ± 0.001	0.30	8.3 ± 0.7	297	3.8
154.75	0.67	1	1	2.89 ± 0.03	3.30 ± 0.07	2.47 ± 0.41	0.263 ± 0.001	0.27	7.4 ± 1.1	208	3.6
156.71	0.79	1	1	–1.85 ± 0.04	–1.62 ± 0.10	–2.13 ± 0.63	0.259 ± 0.002	0.26	4.1 ± 1.6	142	2.5
						RZ Vel					
204.44	0.00	3	1	13.05 ± 0.23	12.50 ± 0.58	14.39 ± 4.04	0.588 ± 0.012	0.14	–4.4 ± 4.0	76	1.3
205.44	0.05	3	1	–0.47 ± 0.07	–3.76 ± 0.16	0.69 ± 0.78	0.457 ± 0.009	0.16	–32.0 ± 2.7	210	1.5
206.44	0.10	3	1	–1.90 ± 0.08	–6.21 ± 0.17	–0.30 ± 0.96	0.459 ± 0.016	0.17	–42.7 ± 4.9	162	2.5
150.49	0.36	1	1	18.65 ± 0.01	18.46 ± 0.03	18.76 ± 0.38	0.219 ± 0.001	0.38	–3.9 ± 0.5	309	7.8
152.51	0.46	1	1	28.82 ± 0.01	28.83 ± 0.02	28.61 ± 0.60	0.231 ± 0.001	0.41	0.8 ± 0.5	205	2.8
154.50	0.55	1	1	45.64 ± 0.02	47.66 ± 0.05	44.86 ± 1.46	0.369 ± 0.002	0.32	24.7 ± 0.9	239	3.2
156.49	0.65	1	1	43.14 ± 0.05	43.91 ± 0.14	42.87 ± 2.31	0.526 ± 0.003	0.23	6.4 ± 1.1	178	1.8
201.44	0.86	3	1	39.12 ± 0.04	39.87 ± 0.09	38.93 ± 1.45	0.411 ± 0.002	0.24	8.1 ± 1.0	224	2.7
202.45	0.90	3	1	29.54 ± 0.06	29.84 ± 0.15	29.26 ± 1.09	0.483 ± 0.003	0.14	2.8 ± 1.2	271	1.2
203.44	0.95	3	1	13.05 ± 0.23	12.50 ± 0.58	14.39 ± 4.04	0.588 ± 0.012	0.14	–4.4 ± 4.0	76	1.3

Table 5. HARPS observations results for ℓ Car and RS Pup. See Table 3 for legend.

JD_c (a)	phase (b)	Cy. (c)	Sp. (d)	RV_g (e)	RV_m (f)	RV_c (g)	*FWHM* (h)	*D* (i)	*A* (j)	*SNR* (k)	χ^2_{red} (l)
						ℓ Car					
37.65	0.02	1	7	–13.40 ± 0.01	–15.70 ± 0.02	–12.19 ± 0.18	0.416 ± 0.001	0.26	–25.4 ± 0.3	354	3.5
40.63	0.10	1	5	–12.24 ± 0.01	–14.22 ± 0.02	–11.10 ± 0.17	0.362 ± 0.001	0.31	–25.2 ± 0.3	333	3.6
47.69	0.30	1	2	–1.57 ± 0.01	–2.51 ± 0.02	–0.61 ± 0.24	0.274 ± 0.001	0.42	–16.4 ± 0.4	275	7.5
48.62	0.33	1	2	–0.01 ± 0.01	–0.76 ± 0.01	0.59 ± 0.10	0.257 ± 0.001	0.40	–13.7 ± 0.2	438	10.3
49.67	0.36	1	2	1.79 ± 0.01	1.09 ± 0.02	2.34 ± 0.13	0.260 ± 0.001	0.40	–12.7 ± 0.3	374	6.0
15.72	0.40	1	3	4.92 ± 0.00	4.33 ± 0.01	5.42 ± 0.12	0.276 ± 0.001	0.40	–10.2 ± 0.2	405	7.0
51.68	0.41	2	4	5.23 ± 0.00	4.62 ± 0.01	5.75 ± 0.13	0.274 ± 0.001	0.39	–10.4 ± 0.2	352	6.0
16.69	0.43	1	3	6.64 ± 0.01	6.13 ± 0.02	7.15 ± 0.21	0.289 ± 0.001	0.39	–8.3 ± 0.3	293	5.6
52.64	0.44	2	2	6.93 ± 0.01	6.30 ± 0.02	7.42 ± 0.18	0.285 ± 0.001	0.39	–10.3 ± 0.3	376	5.4
17.71	0.46	1	3	8.46 ± 0.01	8.11 ± 0.01	8.86 ± 0.15	0.300 ± 0.001	0.38	–5.5 ± 0.2	444	8.7
53.69	0.47	2	2	8.70 ± 0.01	8.31 ± 0.02	9.00 ± 0.18	0.288 ± 0.001	0.37	–6.3 ± 0.3	390	5.0
54.67	0.50	2	2	10.36 ± 0.01	10.18 ± 0.02	10.52 ± 0.22	0.296 ± 0.001	0.35	–2.9 ± 0.3	340	4.7
55.70	0.53	2	2	11.99 ± 0.01	12.04 ± 0.02	12.08 ± 0.20	0.316 ± 0.001	0.35	0.6 ± 0.2	418	4.5
20.84	0.54	1	3	14.11 ± 0.01	14.65 ± 0.03	13.93 ± 0.35	0.335 ± 0.001	0.33	7.4 ± 0.4	218	2.2
56.70	0.55	2	2	13.46 ± 0.01	13.75 ± 0.02	13.42 ± 0.25	0.331 ± 0.001	0.34	4.0 ± 0.3	378	4.2
21.85	0.57	1	3	15.01 ± 0.01	15.66 ± 0.02	14.76 ± 0.22	0.358 ± 0.001	0.32	8.3 ± 0.2	379	3.6
57.70	0.58	2	2	14.82 ± 0.01	15.35 ± 0.02	14.67 ± 0.27	0.347 ± 0.001	0.34	7.0 ± 0.3	384	3.7
58.71	0.61	2	2	16.00 ± 0.01	16.83 ± 0.02	15.70 ± 0.27	0.365 ± 0.001	0.33	10.5 ± 0.3	412	5.3
23.66	0.62	1	4	16.98 ± 0.01	17.92 ± 0.02	16.55 ± 0.20	0.388 ± 0.001	0.31	11.1 ± 0.2	428	3.5
24.85	0.66	1	4	17.94 ± 0.01	19.15 ± 0.02	17.43 ± 0.22	0.389 ± 0.001	0.30	14.0 ± 0.2	374	3.6
25.87	0.69	1	4	18.52 ± 0.01	19.63 ± 0.02	18.00 ± 0.19	0.404 ± 0.001	0.30	12.4 ± 0.2	492	4.2
26.85	0.71	1	5	19.03 ± 0.01	20.27 ± 0.02	18.50 ± 0.24	0.426 ± 0.001	0.31	13.4 ± 0.2	436	5.9
28.69	0.77	1	5	20.12 ± 0.01	21.26 ± 0.02	19.50 ± 0.22	0.426 ± 0.001	0.29	12.2 ± 0.2	433	3.1
29.65	0.79	1	5	20.33 ± 0.01	21.61 ± 0.02	19.63 ± 0.23	0.445 ± 0.001	0.29	13.2 ± 0.2	439	4.7
30.80	0.83	1	7	19.76 ± 0.01	20.83 ± 0.01	19.05 ± 0.19	0.450 ± 0.001	0.28	11.0 ± 0.1	446	6.6
31.66	0.85	1	5	17.77 ± 0.01	18.65 ± 0.02	17.15 ± 0.24	0.458 ± 0.001	0.27	8.9 ± 0.2	391	5.3
32.72	0.88	1	5	11.81 ± 0.01	12.17 ± 0.02	11.51 ± 0.20	0.481 ± 0.001	0.24	3.4 ± 0.2	431	3.8
33.63	0.91	1	5	3.92 ± 0.01	3.06 ± 0.03	4.31 ± 0.20	0.483 ± 0.001	0.23	–8.2 ± 0.2	371	4.1
34.67	0.93	1	5	–4.93 ± 0.01	–6.89 ± 0.02	–3.99 ± 0.15	0.460 ± 0.001	0.24	–19.5 ± 0.2	486	8.3
35.66	0.96	1	7	–9.85 ± 0.01	–11.93 ± 0.02	–8.81 ± 0.14	0.434 ± 0.001	0.24	–21.8 ± 0.2	421	6.0
36.65	0.99	1	6	–12.39 ± 0.01	–14.56 ± 0.02	–11.29 ± 0.21	0.423 ± 0.001	0.24	–23.4 ± 0.3	327	2.8
						RS Pup					
56.68	0.02	1	1	3.58 ± 0.03	1.58 ± 0.07	4.33 ± 0.41	0.433 ± 0.003	0.20	–20.1 ± 0.9	347	2.1
58.69	0.07	1	1	5.31 ± 0.03	3.78 ± 0.07	5.94 ± 0.46	0.395 ± 0.002	0.23	–17.1 ± 0.9	277	2.0
60.68	0.12	1	1	7.95 ± 0.02	6.97 ± 0.05	8.50 ± 0.42	0.370 ± 0.001	0.26	–11.0 ± 0.7	315	2.3
62.67	0.17	1	1	10.99 ± 0.02	10.28 ± 0.05	11.48 ± 0.55	0.343 ± 0.001	0.29	–8.5 ± 0.7	258	2.8
64.68	0.22	1	1	14.21 ± 0.01	13.70 ± 0.04	14.55 ± 0.41	0.307 ± 0.001	0.32	–6.8 ± 0.5	328	3.2
66.66	0.26	1	1	17.46 ± 0.01	16.96 ± 0.03	17.96 ± 0.58	0.296 ± 0.001	0.36	–6.9 ± 0.5	308	3.8
150.48	0.28	3	1	18.43 ± 0.01	17.89 ± 0.03	18.96 ± 0.64	0.317 ± 0.001	0.37	–6.5 ± 0.5	310	2.9
152.49	0.33	3	1	21.56 ± 0.02	21.15 ± 0.04	21.79 ± 0.59	0.269 ± 0.001	0.34	–6.9 ± 0.7	249	7.2
154.49	0.38	3	1	24.80 ± 0.02	24.38 ± 0.05	25.12 ± 0.89	0.271 ± 0.001	0.36	–6.9 ± 0.7	211	3.0
156.48	0.43	3	2	27.90 ± 0.01	27.52 ± 0.04	28.12 ± 0.67	0.264 ± 0.001	0.34	–6.5 ± 0.6	202	4.1
48.61	0.83	1	1	47.56 ± 0.04	50.66 ± 0.09	46.52 ± 1.69	0.499 ± 0.004	0.24	27.3 ± 1.1	239	3.3
51.64	0.90	1	1	30.44 ± 0.11	25.29 ± 0.27	31.52 ± 2.02	0.955 ± 0.010	0.12	–22.6 ± 1.6	249	2.6
52.63	0.93	1	1	16.40 ± 0.12	12.85 ± 0.30	18.39 ± 1.97	0.681 ± 0.012	0.13	–22.8 ± 2.5	173	1.3
54.66	0.97	1	1	5.26 ± 0.05	2.97 ± 0.13	6.07 ± 0.71	0.479 ± 0.005	0.17	–20.9 ± 1.5	247	1.0

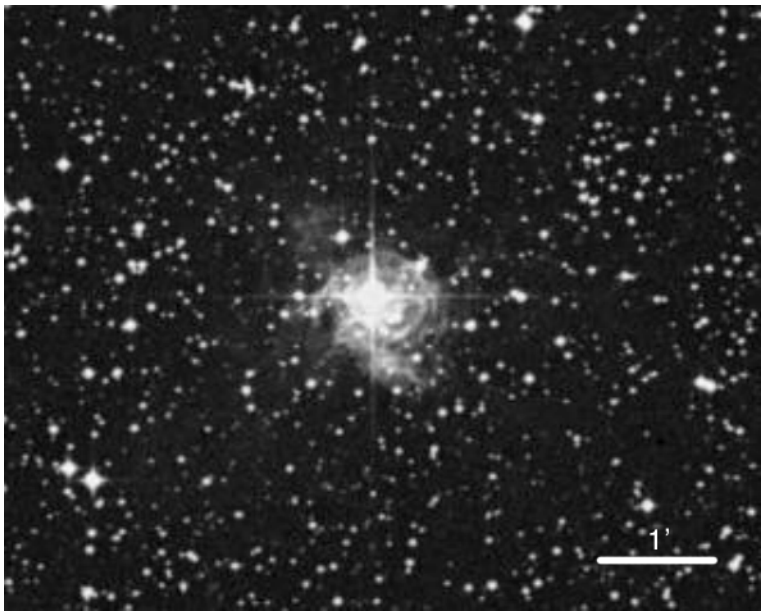

FIG. 2.11 – Enveloppe circumstellaire de la Céphéide RS Pup (image DSS).

2.3 L'environnement circumstellaire des Céphéides

2.3.1 Des indices convergents...

Plusieurs observations indiquent que les Céphéides sont de bonnes candidates pour présenter des enveloppes circumstellaires : la présence de matière au voisinage de RS Pup, la perte de masse observée par spectrographie, et l'excès infrarouge de certaines étoiles. Je développe ces différents indices ci-après, dans le but de positionner nos observations interférométriques récentes, qui sont rapportées dans les articles présentés dans les Sect. 2.3.2 et 2.3.3.

Matière circumstellaire

Avant notre travail sur ℓ Car, on ne connaissait qu'une seule Céphéide présentant une enveloppe circumstellaire (ECS), RS Pup (Fig. 2.11). Une autre de ces étoiles, SU Cas est située à proximité d'une nébuleuse, mais l'association physique est incertaine. Le mécanisme ayant conduit à la formation des coquilles autour de RS Pup est actuellement inconnu. Deasy (1988) a proposé plusieurs scenarios relatifs à l'évolution de l'étoile avant la séquence principale, ou bien à de la perte de masse episodique au cours de plusieurs traversées de la bande d'instabilité classique. Havlen (1972) et Szabados (2003) remarquent qu'il est improbable que RS Pup soit la seule Céphéide associée à une nébuleuse, mais du fait de la très grande luminosité intrinsèque de ces étoiles, elles sont très difficiles à détecter par imagerie classique.

Perte de masse

Sur la base de photométrie infrarouge du satellite IRAS et de spectres IUE dans l'ultraviolet, Deasy (1988) a mis en évidence de la perte de masse sur plusieurs Céphéides. Le taus le plus élevé est attribué par cet auteur à RS Pup ($10^{-6}\,M_{\odot}.\mathrm{yr}^{-1}$). The taux est très significatif, et explique la structure en "bulles" qui a été creusée par l'étoile dans le milieu interstellaire environnant. ζ Gem est aussi citée comme présentant un vent stellaire important, induisant un taux de perte

de masse de $\simeq 10^{-10} M_\odot.\mathrm{yr}^{-1}$, plusieurs ordres de grandeur plus faible que RS Pup. Pour cet auteur, ℓ Car montre aussi une perte de masse significative, avec un taux de l'ordre de trois fois plus élevé que ζ Gem. Böhm-Vitense & Love (1994) obtiennent même une valeur beaucoup plus grande, de $\simeq 2.10^{-5} M_\odot.\mathrm{yr}^{-1}$, encore plus élevée que RS Pup. Ils suggèrent également que la composante fixe (non pulsante) de la raie Hα observée en absorption est causée par une ECS d'une taille de l'ordre de 1000 UA. A la distance de ℓ Car (570 pc, cf. Sect. 2.1.4), cela correspond à une extension angulaire de 0.5".

Excès infrarouge

Plusieurs Céphéides ont montré un excès infrarouge modéré lié à la présence de matière circumstellaire. Un tel excès de flux dans l'infrarouge moyen est caractéristique d'un environnement relativement chaud situé près de l'étoile. Deasy (1988) a observé un excès du rapport $F(60\,\mu\mathrm{m})/F(12\,\mu\mathrm{m})$ dans les mesures du satellite IRAS sur plusieurs Céphéides brillantes, parmis lesquelles : α UMi (faible excès), SU Cas (très important), ℓ Car (faible), β Dor (important), S Mus (important), RS Pup (très important). Il est aussi intéressant de noter la détection par IRAS d'une émission infrarouge étendue autour de X Pup, située à seulement $\simeq 1$ kpc de RS Pup. Toujours sur la base de données IRAS, McAlary & Welch (1986) ont étudié un large échantillon de Céphéides à la recherche d'un excès infrarouge. Ils ont obtenu une détection claire pour RS Pup et SU Cas.

2.3.2 Article A&A : "Extended envelopes around Galactic Cepheids. I. ℓ Carinae from near and mid-infrared interferometry with the VLTI" (2006)

Cet article rapporte notre découverte d'une enveloppe autour de ℓ Car. Il s'agit de la première mise en évidence de matière circumstellaire autour d'une Céphéide par interférométrie. Une seule autre Céphéide (RS Pup) est clairement associée à une nébuleuse circumstellaire (visible à grande distance de l'étoile). Nos observations à l'aide des instruments VINCI et MIDI montrent que cet environnement possède une dimension caractéristique de l'ordre de quelques rayons stellaires, et une contribution au flux total de l'étoile de quelques pourcents en bande K. En infrarouge moyen (bande N), il semble dominer l'émission de l'étoile elle-même.

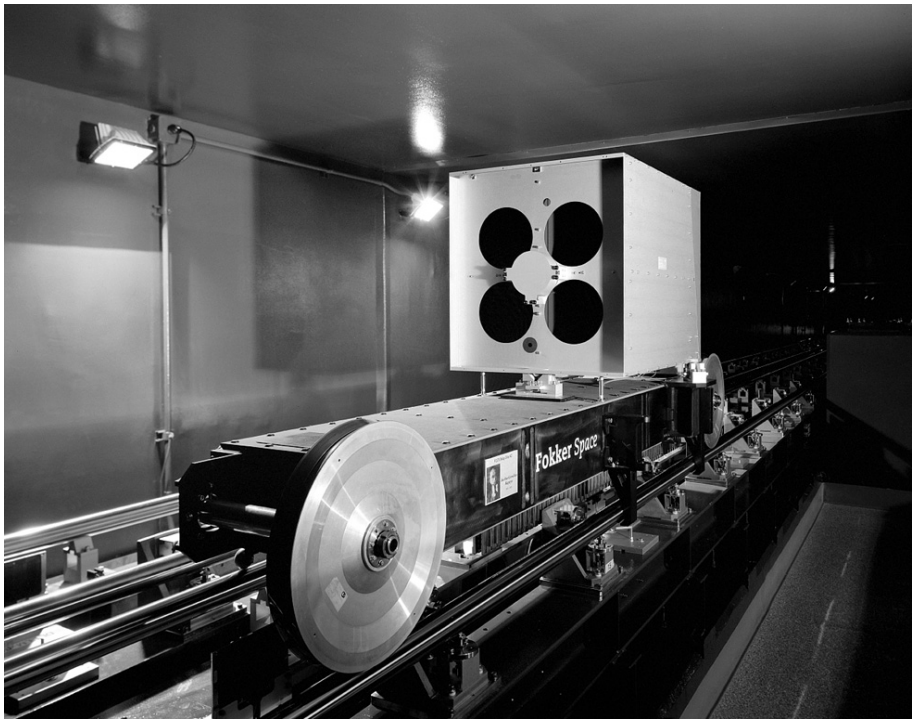

FIG. 2.12 – Une des lignes à retard du VLTI.

A&A 448, 623–631 (2006)
DOI: 10.1051/0004-6361:20053603

Astronomy & Astrophysics

Extended envelopes around Galactic Cepheids

I. ℓ Carinae from near and mid-infrared interferometry with the VLTI

P. Kervella, A. Mérand, G. Perrin, and V. Coudé du Foresto

LESIA, UMR 8109, Observatoire de Paris-Meudon, 5 place Jules Janssen, 92195 Meudon Cedex, France
e-mail: Pierre.Kervella@obspm.fr

Received 9 June 2005 / Accepted 25 October 2005

ABSTRACT

We present the results of long-baseline interferometric observations of the bright southern Cepheid ℓ Carinae in the infrared N (8−13 μm) and K (2.0−2.4 μm) bands, using the MIDI and VINCI instruments of the VLT Interferometer. We resolve in the N band a large circumstellar envelope (CSE) that we model with a Gaussian of 3 $R_\star$ ($\approx$500 $R_\odot$ $\approx$ 2−3 AU) half width at half maximum. The signature of this envelope is also detected in our K band data as a deviation from a single limb darkened disk visibility function. The superimposition of a Gaussian CSE on the limb darkened disk model of the Cepheid star results in a significantly better fit of our VINCI data. The extracted CSE parameters in the K band are a half width at half maximum of 2 $R_\star$, comparable to the N band model, and a total brightness of 4% of the stellar photosphere. A possibility is that this CSE is linked to the relatively large mass loss rate of ℓ Car. Though its physical nature cannot be determined from our data, we discuss an analogy with the molecular envelopes of RV Tauri, red supergiants and Miras.

Key words. Cepheids – techniques: interferometric – stars: circumstellar matter – stars: individual: ℓ Car

1. Introduction

Cepheids are commonly used as distance indicators, thanks to their well-established Period-Luminosity (P–L) law. Discovered almost one century ago, this empirical relation relates the absolute brightness of a Cepheid to its variation period. Measuring the period and apparent brightness of a Cepheid thus gives its distance. As they are intrisically very bright stars, and can be observed in distant galaxies, this remarkable property has turned these yellow supergiant stars into primary standard candles for extragalactic distance estimations.

The calibration of the P–L zero point itself relies essentially on the Baade-Wesselink (BW) method. This classical method (Baade 1926; Wesselink 1946) establishes the distances to Cepheids by determining simultaneously the change in linear and angular size over the pulsation. The linear size change is obtained from an integration of spectrographic radial velocity measurements, while the change in angular size can be obtained either from surface brightness considerations (classical method) or directly by interferometry. One potential weakness of the BW technique is that it relies implicitely on the asumption that the star radiates as a blackbody (surface brightness method) or can be resolved directly as a single, "naked" star (interferometric BW method). A deviation from these hypotheses, caused for instance by the presence of a circumstellar envelope (CSE), can lead to a bias in the resulting distance estimation.

We present here an interferometric investigation of the close environment of the bright southern Cepheid ℓ Car (HD 84810, HR 3884). As it is the brightest Cepheid in the sky, it was extensively studied using a variety of techniques. For instance, applications of the classical and interferometric BW method to this star can be found in Taylor et al. (1997) and Kervella et al. (2004c). We present in Sect. 2 our interferometric observations that were obtained using the VINCI and MIDI instruments of the VLTI. Section 3 is dedicated to the interpretation of the measured visibilities in terms of simple flux distribution models. In Sects. 4 and 5, we discuss the different physical processes that are likely to play a role in the formation of a CSE around ℓ Car, and we compare it to two variable star classes related to Cepheids (RV Tauri and Miras) that are known to host dusty environments.

2. Observations

2.1. VINCI

2.1.1. Raw data acquisition and processing

The European Southern Observatory's Very Large Telescope Interferometer (VLTI; Glindemann et al. 2004) has been operated on top of the Cerro Paranal, in Northern Chile since March 2001. For the new observations reported in this paper, the light coming from two test siderostats (0.35 m aperture) or two 8 m Unit Telescopes (UTs) was recombined coherently

in VINCI, the VLT INterferometer Commissioning Instrument (Kervella et al. 2000; Kervella et al. 2003). We used a regular K band filter ($\lambda = 2.0-2.4$ μm), and processed the data using the standard VINCI data reduction software version 3.0 (Kervella et al. 2004a). As part of our programme of Cepheid observations by interferometry, we have observed ℓ Car in January-February and April-May 2003. These measurements, obtained using the VLTI test siderostats on the B3-M0 baseline (140 m ground length, ≈125 m projected on the sky), were already reported in Kervella et al. (2004b, hereafter Paper I).

During the early VLTI commissioning (Jan.−Feb. 2002), additional visibility measurements of ℓ Car were obtained using the 8 m Unit Telescopes UT1 and UT3 (102 m ground length, ≈85 m projected), and with the test siderostats on the short E0-G0 baseline (16 m ground length, ≈14.5 m projected). The Unit Telescopes were not equipped at the time with adaptive optics systems (seeing limited regime). These new data are listed in Tables 1 and 2. The reference Julian date epoch (T_0 = 2 452 290.4158) and pulsation period (P = 35.551341 days) used to compute the phase are taken from Szabados (1989), and are identical to Paper I. The calibrators were chosen from the Cohen et al. (1999) catalogue (Table 3). As demonstrated by Bordé et al. (2002), the star diameters in this list have been estimated homogeneously to a relative precision of 1% and agree well with other angular diameter estimation methods.

2.1.2. Medium vs. long baselines: a discrepancy?

A first indication that a simple stellar disk model is not the most adequate for ℓ Car comes from the comparison of the observations obtained using the medium (UT1-UT3, ≈85 m) and long (B3-M0, ≈125 m) baselines. In order to derive angular diameters from the VINCI visibilities, we used the limb darkening model from Claret (2000), in the same way as described in Paper I. Figure 1 shows the evolution of the limb darkened angular diameter of ℓ Car as a function of phase. The solid curve is the result of the fit of the integrated radial velocity curve of this star to the B3-M0 data only (as described in Paper I). It appears clearly that the new angular diameter measurements from the UT1-UT3 baseline, represented as open squares, are larger by 3σ than those obtained with the siderostats.

We now examine the possible calibration or instrumental causes for this difference. It is improbable that it comes from an incorrect estimation of the angular diameter of the calibrators, as two different reference stars were used for the UT measurements (HR 4080 for phase 0.376 and HR 4831 for phase 0.490), with consistent results. Moreover, HR 4831 was also used for part of the siderostat observations (Table 2) with no detectable bias compared to other calibrators. The calibrators were all chosen from the catalogue by Bordé et al. (2002). This is a filtered version of the reference work by Cohen et al. (1999) that was adapted specifically for interferometry. All these calibrators are believed to be single stars, and do not show infrared excess.

It is also unlikely that a systematically different behavior between the siderostats and the UTs can create such a difference. Firstly, previous observations demonstrated a good agreement between these two types of light collectors for well-known stars (see e.g. Di Folco et al. 2004). Secondly, the visibility measurements being differential in nature (between the Cepheid and its calibrator), the existence of a "telescope type" bias would require a differential effect between the star and its calibrator. This is unlikely as the brightness and colors are chosen to be similar. The main difference between UTs and siderostats is the pupil size (8 m vs. 0.35 m). The field of view coupled in the single-mode fibers is 1.5″ with the siderostats (i.e. limited by the diffraction), and of the order of 1″ with the UTs in the K band (limited by the atmospheric seeing, see Guyon 2002 for details). Given the characteristic size of the

Table 1. Squared visibilities of ℓ Car in the K band from VINCI. The stations of the new measurements are marked in bold characters. The calibrators are given in italic characters. The stated Julian date JD_0 is JD−2.452 10^6. The azimuth is counted in degrees clockwise from North (N = 0 deg, E = 90 deg), and B is the projected baseline in meters. The pulsation phase ϕ is computed using the P and T_0 parameters from Szabados (1989).

JD_0	ϕ	B (m)	Az.	$V^2 \pm$ stat $\pm$ syst (%)
E0-G0				*HR 4546*
792.486	0.122	14.560	19.03	95.32 ± 3.97 ± 0.05
792.499	0.123	14.308	21.32	98.82 ± 3.68 ± 0.05
792.545	0.124	13.316	27.30	93.28 ± 3.91 ± 0.05
792.576	0.125	12.644	29.50	99.20 ± 6.14 ± 0.04
792.582	0.125	12.533	29.74	102.08 ± 6.63 ± 0.04
792.587	0.125	12.433	29.94	94.12 ± 6.53 ± 0.04
793.544	0.152	13.287	27.42	97.95 ± 2.83 ± 0.04
793.555	0.152	13.048	28.32	97.24 ± 2.68 ± 0.04
793.560	0.153	12.930	28.71	95.72 ± 2.75 ± 0.04
B3-M0				*HR 4546*
765.523	0.364	125.951	75.96	9.64 ± 0.41 ± 0.49
765.528	0.364	125.063	77.50	10.89 ± 0.54 ± 0.55
765.534	0.364	124.029	79.24	11.46 ± 0.72 ± 0.58
765.575	0.365	115.637	91.95	16.57 ± 0.63 ± 0.85
765.580	0.366	114.483	93.59	18.73 ± 1.68 ± 0.96
765.588	0.366	112.611	96.21	17.62 ± 0.46 ± 0.91
U1-U3				*HR 4080*
303.772	0.376	84.682	45.25	38.28 ± 0.73 ± 0.28
303.775	0.376	84.399	45.81	38.80 ± 0.78 ± 0.28
303.776	0.376	84.254	46.10	40.13 ± 0.86 ± 0.29
303.778	0.376	84.023	46.55	37.58 ± 0.72 ± 0.27
B3-M0				*HR 4546*
766.516	0.392	126.748	74.53	9.52 ± 0.50 ± 0.49
766.521	0.392	125.889	76.07	12.08 ± 0.86 ± 0.62
766.526	0.392	125.045	77.53	11.36 ± 0.94 ± 0.58
766.544	0.393	121.582	83.16	12.24 ± 0.45 ± 0.62
766.576	0.394	114.779	93.17	16.23 ± 0.56 ± 0.80
766.581	0.394	113.604	94.82	17.47 ± 0.63 ± 0.86
766.586	0.394	112.390	96.52	17.72 ± 0.66 ± 0.87

Table 2. Continued from Table 1.

JD_0	ϕ	B (m)	Az.	$V^2 \pm$ stat $\pm$ syst (%)
B3-M0				*HR 4546*
768.523	0.448	124.548	78.38	11.66 ± 0.50 ± 0.58
768.528	0.448	123.683	79.81	13.28 ± 1.31 ± 0.66
768.536	0.449	122.082	82.38	12.85 ± 1.59 ± 0.64
768.581	0.450	112.204	96.78	18.42 ± 0.55 ± 0.81
768.591	0.450	109.878	100.01	19.75 ± 0.52 ± 0.87
768.599	0.450	107.804	102.89	21.07 ± 0.60 ± 0.93
768.607	0.451	105.748	105.77	23.35 ± 0.60 ± 1.03
B3-M0				*HR 3046, HR 4831*
769.570	0.478	114.286	93.86	17.31 ± 0.69 ± 0.27
769.574	0.478	113.127	95.49	17.83 ± 0.75 ± 0.27
769.580	0.478	111.834	97.29	18.66 ± 0.74 ± 0.29
U1-U3				*HR 4831*
307.822	0.490	75.924	59.76	46.98 ± 1.06 ± 0.35
307.823	0.490	75.666	60.12	47.33 ± 0.88 ± 0.35
307.825	0.490	75.342	60.58	47.26 ± 0.84 ± 0.35
307.827	0.490	74.989	61.07	48.13 ± 0.91 ± 0.36
B3-M0				*HR 3046, HR 4831*
770.533	0.505	121.671	83.02	13.30 ± 0.56 ± 0.18
770.538	0.505	120.634	84.62	14.24 ± 0.61 ± 0.20

source of a few mas, this small difference cannot be the cause of a significant bias.

This systematic difference between the visibility data obtained on the B3-M0 and UT1-UT3 baselines is therefore unlikely to have an instrumental origin. In Sect. 3, we present a model of ℓ Car surrounded by a circumstellar environment (CSE) that can reproduce the data from both medium and long baselines, as well as the shorter (≈14.5 m projected) E0-G0 data.

2.2. MIDI

2.2.1. Raw data acquisition and processing

The MIDI observations of ℓ Car were obtained on the night of 8−9 April 2004, using the UT2-UT3 baseline of the VLTI. This baseline has a ground length of 46.6 m, but due to the low declination of ℓ Car and its calibrator, the projected baseline was 40.0 m. The raw data were processed using the MIDI Data Reduction Software developed by the Paris Observatory and distributed by the JMMC[1] in order to extract first the instrumental squared coherence factors and then the calibrated squared visibilities $V^2(\lambda)$. As MIDI operates in the diffraction limited regime of the UTs, the effective field of view diameter is equal to approximately 0.26″ at $\lambda = 10\,\mu$m. This is much larger than the typical angular size of the star and of its CSE (≈10 mas) discussed in Sect. 3. Perrin et al. (2005b) describe the steps to calibrate the MIDI data carried out by the software. This software also outputs the spectra of the source and calibrator over the N band. The presence of a strong ozone atmospheric absorption band over the range $\lambda = 9.3{-}10.0\,\mu$m (Lord 1992) can make the visibilities unreliable in this wavelength domain, as the photometric calibration is made more difficult by the lower flux level.

[1] Jean-Marie Mariotti Center (`http://mariotti.fr`).

2.2.2. Spectral energy distribution

The absolutely calibrated spectrum of ℓ Car presented in Fig. 2 was obtained by dividing the average observed with MIDI by the average spectrum of its calibrator HR 3187, and then multiplying the result by the absolutely calibrated template spectrum of HR 3187 given by Cohen et al. (1999). The agreement with the IRAS spectrum obtained on this star (Volk & Cohen 1989) is satisfactory. At the date of the MIDI observations (JD = 2 453 104.6), the pulsation phase of ℓ Car was $\phi = 0.901$: the star was just starting its inflation phase, shortly after its minimum diameter ($\phi = 0.89$).

While ℓ Car is rising towards maximum light in the visible ($\phi = 1.00$ by definition), it is almost at minimum light in the K band. Using the temperature scale from Kiss & Szàtmary (1998), with $B - V$ photometry and the color excess from Fernie (1990), we derive $T_{\rm eff} = 5500$ K for phase 0.901. Together with the extrapolated VINCI LD angular diameter for this phase ($\theta_{\rm LD} \simeq 2.70$ mas), we obtain the blackbody spectrum represented as a solid curve in Fig. 2. It is in excellent agreement with the IRAS observations, as well as with the MIDI spectrum. In the infrared, the photometry of a Cepheid is essentially determined by its change in apparent size, as opposed to the visible where its effective temperature plays the leading role. For instance, the amplitude of the photometric variation of ℓ Car in the K band is $\Delta m_K = 0.32$, corresponding to a ≃16% amplitude in terms of angular size. This is consistent with the pulsation amplitude of 18% measured with VINCI (Paper I). The small remaining difference between the IRAS and MIDI spectra can be explained by a pulsational variation of the radius of ℓ Car between the two observations. Unfortunately, the date at which the IRAS spectra were obtained is not available in the IRAS LRS catalogue, and we cannot compute the phase to check this hypothesis.

2.2.3. Calibration

The calibrator star used for the MIDI observations, HR 3187, was selected from the Cohen et al. (1999) catalogue, as the VINCI calibrators. This star is unresolved by the interferometer at the wavelengths sampled by MIDI (8−13 μm), with an angular diameter of only 2.4 mas (Table 3).

Figure 3 shows the result of the calibration of the ℓ Car observations using two different calibration hypotheses. In this figure, *Cal1* and *Cal2* refer to the first and second series of observations of HR 3187, while *Sci1* and *Sci2* refer to the first and second series of ℓ Car (Table 4). The first hypothesis is to consider the average transfer function (TF) of the interferometer over all calibrator observations, and apply it to all observations of ℓ Car. In the second case, *Cal1* is associated with *Sci1* and *Cal2* with *Sci2*. These two calibration choices

Table 3. Relevant parameters of the calibrators of ℓ Car (F6Ib-K0Ib), taken from Bordé et al. (2002).

HR	HD	m_V	m_K	m_N	Sp. Type	$T_{\rm eff}$(K)	$\log g$	π (mas)[a]	$\theta_{\rm LD}$(mas)[b]	$\theta_{{\rm UD}\,K}$(mas)[c]
HR 3046	HD 63744	4.70	2.31	2.42	K0III	4720	2.6	14.36 ± 0.48	1.67 ± 0.025	1.63 ± 0.024
HR 3187	HD 67582	5.04	2.04	2.24	K3III	4250	2.4	2.63 ± 0.51	2.39 ± 0.062	2.32 ± 0.061
HR 4080	HD 89998	4.83	2.40	2.44	K1III	4580	2.5	16.26 ± 0.56	1.72 ± 0.020	1.68 ± 0.019
HR 4546	HD 102964	4.47	1.56	1.67	K3III	4210	2.2	7.03 ± 0.72	2.48 ± 0.036[d]	2.41 ± 0.035[d]
HR 4831	HD 110458	4.67	2.28	2.39	K0III	4720	2.6	17.31 ± 0.65	1.70 ± 0.018	1.66 ± 0.018

[a] Parallaxes from the HIPPARCOS catalogue (Perryman et al. 1997).
[b] Catalogue values from Cohen et al. (1999).
[c] Linear limb darkening coefficients factors from Claret et al. (1995).
[d] The angular diameter of HR 4546 has been measured separately with VINCI.

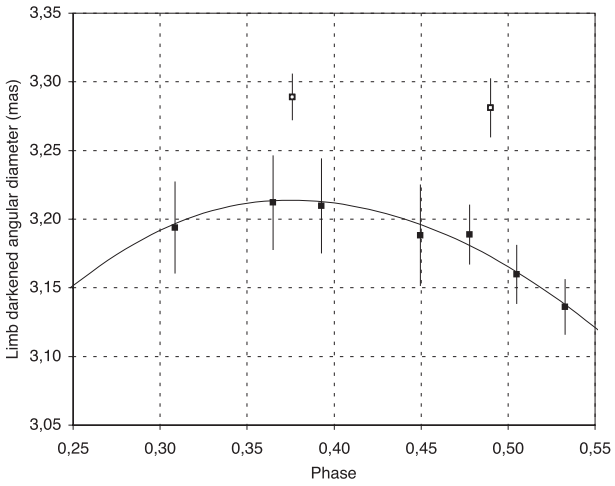

Fig. 1. Limb darkened disk angular diameter of ℓ Car deduced from VINCI observations on the B3-M0 siderostat baseline (filled squares) and the UT1-UT3 baseline (open squares). The solid curve is the best-fit model from Paper I, using the siderostat data only.

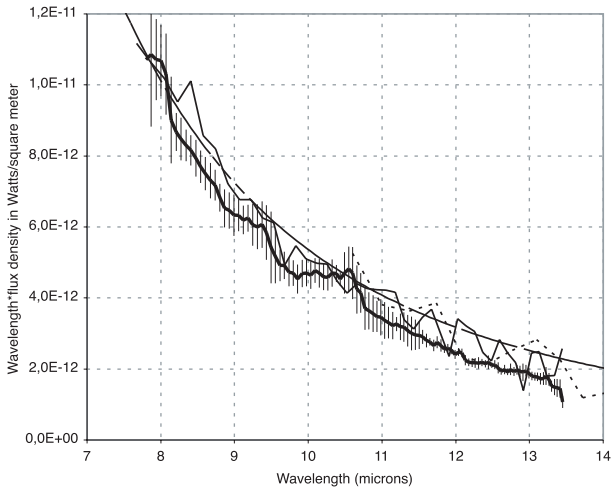

Fig. 2. Absolutely calibrated MIDI (thick curve) and IRAS LRS spectra (thin solid and dotted curves) of ℓ Car, using HR 3187 as a spectrophotometric standard star. The theoretical spectrum of a blackbody with $T = 5500$ K and an angular diameter of 2.70 mas is superimposed for reference (solid curve).

simply result in a vertical shift of the $V^2(\lambda)$ spectrum, leaving its shape qualitatively the same (rising from short to long wavelengths). This shows that independent of the calibration hypothesis, ℓ Car is significantly resolved by the interferometer. In the following, we have chosen to keep the association *Cal1-Sci1* and *Cal2-Sci2*, as the target and calibrator observations are slightly closer in time in this case. Qualitatively, the choice of the first hypothesis (average TF over the night) would have resulted in slightly lower visibilities, meaning that the object would appear even more resolved.

3. Model fitting

3.1. K band model

We model the visibility curve using a limb darkened disk (LD) representing the star, and a superimposed Gaussian shape representing the CSE. The stellar disk has only one parameter, the LD angular diameter ($\theta_{\rm LD}$), while the Gaussian shape has a variable full width at half maximum (FWHM) $D_{\rm CSE\,K}$ and total intensity $I_{\rm CSE\,K}$, normalized to the stellar brightness at center. The limb darkening profile for the star is taken from Claret (2000), considering the physical parameters of ℓ Car detailed in Paper I ($T_{\rm eff}, \log g, ...$). The visibility model is computed taking into account the bandwidth smearing effect (Davis et al. 2000; Kervella et al. 2004a) that is due to the broadband operation of VINCI. This is one of the simplest models to account for the contribution of a diffuse CSE, together with the photospheric emission from the star itself. Radiative transfer is not modeled at this stage. The model is purely geometric to ease the interpretation of the measured visibility points. The resulting $V^2(D_{\rm CSE\,K}, I_{\rm CSE\,K}, B)$ model is adjusted numerically to the observed $(B, V^2)_i$ data using a classical χ^2 minimization process. Figures 4 and 5 show the best fit model to the VINCI data.

For this fitting process, we considered only the VINCI measurements obtained between phases 0.36 and 0.51 on the B3-M0 baseline (≈125 m). We limited our selection to this range as it covers the phases of the intermediate baseline observations with the UTs. This way, we can separate the pulsation of the star from the presence of a CSE, and study the spatial light distribution of the star for a given phase of its pulsation. The data obtained on the E0-G0 baseline (≈14.5 m) are

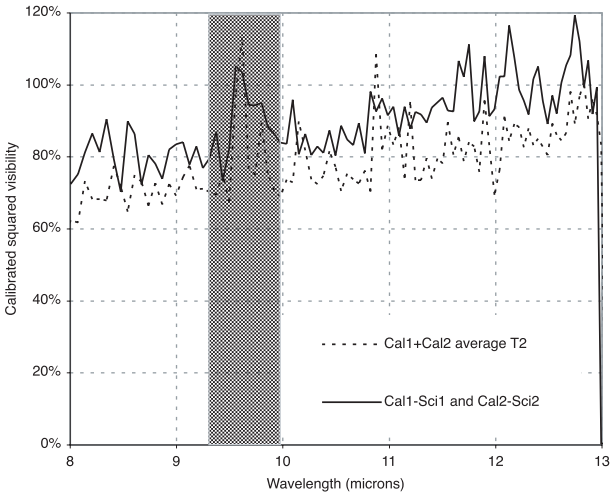

Fig. 3. Result of different calibration hypotheses for ℓ Car (see text for explanation). The shaded area corresponds to an atmospheric absorption feature of ozone ($\lambda = 9.3{-}10.0\,\mu$m, Lord 1992), where the data can be unreliable.

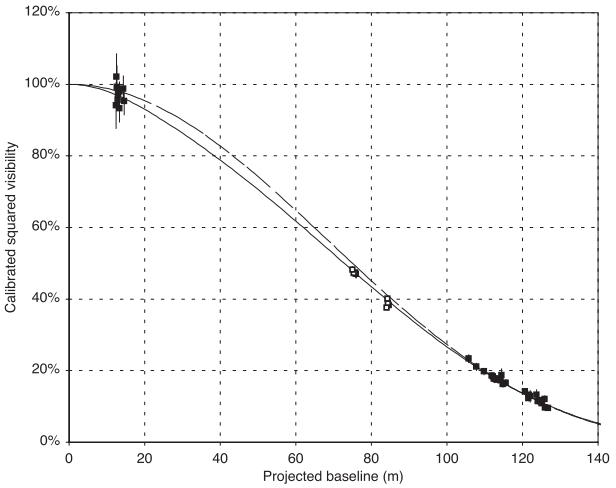

Fig. 4. Observed squared visibilities of ℓ Car with VINCI, and best fit model composed of a Gaussian CSE superimposed on a limb darkened disk (solid curve). The dashed curve is a simple uniform disk model fit to the B3-M0 siderostat data only (longest baseline). The data obtained with the UTs are marked with open squares, while the siderostat data are represented by filled squares.

Table 4. Journal of MIDI observations of ℓ Car on the UT2-UT3 baseline. JD_1 is defined as JD−2 453 104 (pulsation phase $\phi = 0.901$). B is the projected baseline length, Alt. the altitude of the star and PA is the position angle of the projected baseline ($N = 0°$, $E = 90°$).

UTC	JD_1	Target	Alt. (°)	B (m)	PA (°)
01:25:47	0.559	ℓ Car	52.07	40.85	48.52
01:26:40	0.560	ℓ Car	52.07	40.82	48.68
01:27:33	0.561	ℓ Car	52.07	40.79	48.84
01:48:28	0.575	HR 3187*	56.60	38.95	58.75
01:49:21	0.576	HR 3187	56.60	38.89	58.85
01:50:14	0.577	HR 3187	56.60	38.83	58.95
02:08:35	0.589	ℓ Car	51.11	39.22	56.25
02:09:28	0.590	ℓ Car	51.11	39.18	56.41
02:10:21	0.591	ℓ Car	51.11	39.14	56.57
02:28:55	0.603	HR 3187	49.98	35.92	63.40
02:29:48	0.604	HR 3187	49.98	35.85	63.50
02:30:41	0.605	HR 3187	49.98	35.78	63.60

* These data show a deficit in terms of photometry, and were not used in the calibration process.

not affected by the pulsation phase, as the K band photosphere remains largely unresolved on this short baseline ($V^2 \simeq 98\%$), and these data are thus sensitive only to extended emission.

We obtain the model parameters listed in Table 5. In terms of stellar radii, the CSE reaches $R_{\mathrm{CSE\,K}} = 1.9 \pm 1.4\ R_\star$ or $330 \pm 270\ R_\odot$, in the K band (assuming $R_\star = 179\,R_\odot$ from Kervella et al. 2004c). The large uncertainty on this radius is due to the relative lack of interferometric data for baselines between 15 and 75 m. The main constraint is the deficit, in term of visibilities, at baselines between 75 and 85 m. The total brightness of this environment represents 4% of the stellar brightness. The LD size of ℓ Car considering only the B3-M0 baseline measurements is $\theta_{\mathrm{LD}} = 3.093 \pm 0.009$ mas, only 0.6% away in terms of angular diameter from the best fit model with a CSE. Therefore, the results in terms of average diameter and distance reported by Kervella et al. (2004c) are not modified by the presence of this CSE.

3.2. N band model

From the VINCI observations in the K band reported in Paper I, we know that the angular diameter of the star at pulsation phase $\phi = 0.901$ is $\theta_{\mathrm{LD}} \simeq 2.70$ mas. This is beyond the resolution capabilities of MIDI on the UT2-UT3 baseline, and the squared visibility spectrum $V^2(\lambda)$ should therefore appear as the thin solid curve in Fig. 6 (top). The presence of a significant slope and squared visibilities as low as 80% at $\lambda = 8\,\mu$m however shows that a CSE is resolved by the interferometer.

Fitting the data with a Gaussian model results in an average FWHM of $D_{\mathrm{CSE\,N}} = 8 \pm 3$ mas. In this fitting process, the error bars of each $V^2(\lambda)$ value were not averaged, as it is currently not possible to separate the systematic and statistical contributions to these errors. We therefore chose this conservative approach to avoid underestimating the final error bars. The apparent size of the CSE appears to vary slightly over the N band, with a maximum size between 8 and 11 μm.

While the CSE appears to be relatively faint in the K band, it becomes much more visible in the N band, even dominating the star itself. The typical size of the CSE is similar in the two bands with a half FWHM of about $2{-}3\ R_\star$.

4. Nature of the CSE of ℓ Car

4.1. Circumstellar matter

Only one Cepheid is currently known to be associated with a CSE, RS Pup. Another Cepheid, SU Cas, appears to be located

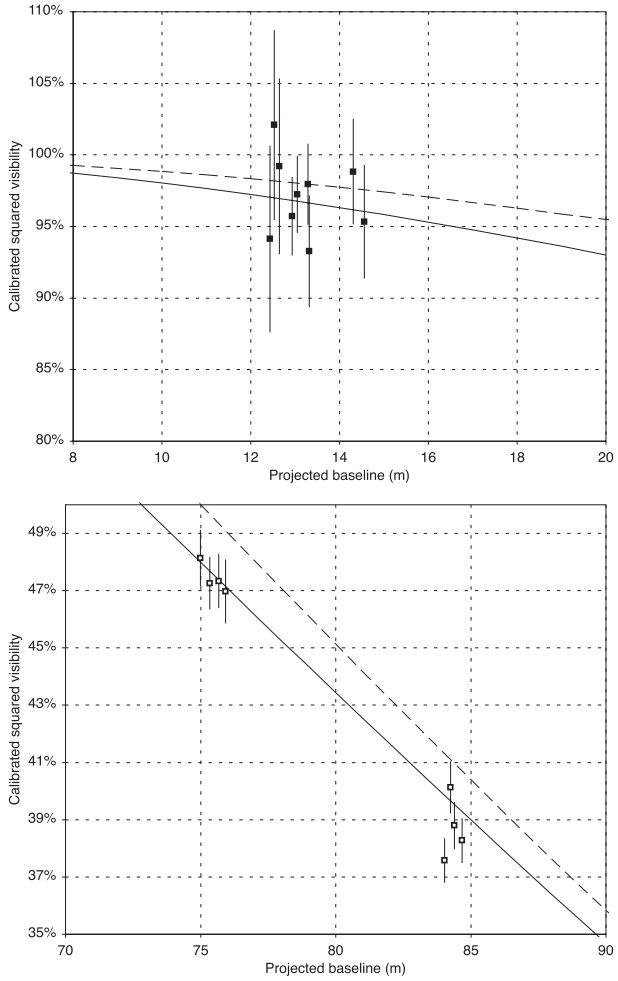

Fig. 5. Enlargements of Fig. 4 showing the squared visibility measurements obtained. *Top*: short E0-G0 siderostat baseline. *Bottom*: intermediate UT1-UT3 baseline.

Table 5. Best fit model parameters for the VINCI data in the K band. The adjusted model is the superimposition of a limb darkened disk representing the stellar photosphere and a Gaussian representing a CSE. $\theta_{\rm LD}$ is the LD angular diameter of the star, $D_{\rm CSE\,K}$ is the FWHM of the Gaussian (in mas), and $I_{\rm CSE\,K}$ is the ratio of the CSE brightness to the stellar brightness in the K band.

$\theta_{\rm LD}$ (mas)	$D_{\rm CSE\,K}$ (mas)	$I_{\rm CSE\,K}$	Reduced χ^2
3.11 ± 0.03	5.8 ± 4.5	4.2 ± 0.2%	0.65

close to a nebula, but the association is uncertain. The mechanism for the formation of the RS Pup shells is currently unknown. Deasy (1988) has proposed several scenarios, ranging from an evolution of the star before its Cepheid phase to mass loss during multiple crossings of the instability strip. As pointed out by Havlen (1972) and Szabados (2003), it is unlikely that RS Pup is the only existing Cepheid-nebula association. The detection of such nebulae is made particularly difficult by the large intrinsic brightness of the Cepheids themselves. They are extremely bright supergiants, and therefore they largely outshine their close environment, including possible associated nebulae.

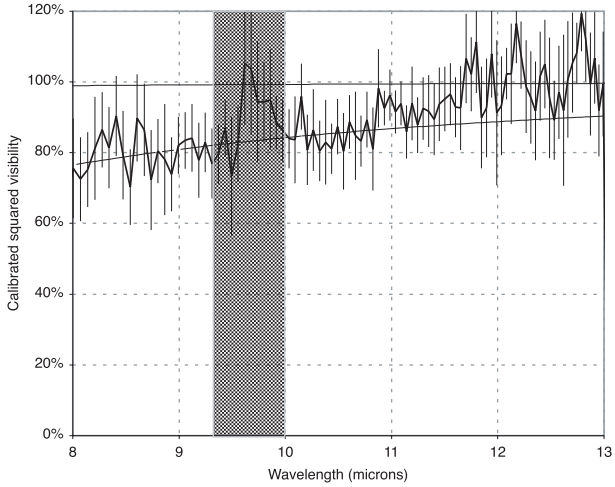

Fig. 6. Calibrated squared visibility $V^2(\lambda)$ of ℓ Car using the UT2-UT3 baseline (40 m projected length). The dashed curve is the best fit Gaussian model with a FWHM of $r_{\rm CSE}(N) = 8 \pm 3$ mas. The thin, almost linear solid curve close to 100% represents the visibility function of the K band photosphere of ℓ Car ($\theta_{\rm LD} = 2.70$ mas), at the phase of the MIDI observations ($\phi = 0.901$).

4.2. Mass loss

Based on IRAS photometry and IUE ultraviolet spectra, Deasy (1988) has identified mass loss in a number of Cepheids. The highest mass loss is attributed by this author to RS Pup ($10^{-6}\,M_\odot\,{\rm yr}^{-1}$). This level is very significant, and explains the "bubble" structures that have been carved by this star in the interstellar medium. ζ Gem is also quoted as exhibiting evidence of stellar wind in its ultraviolet spectra, inducing a mass loss of $\simeq 10^{-10}\ M_\odot\,{\rm yr}^{-1}$, several magnitudes smaller than RS Pup. ℓ Car shows also a significant mass loss, with a rate about three times as large as ζ Gem. Böhm-Vitense & Love (1994) even obtained a much higher value of $\simeq 2 \times 10^{-5}\ M_\odot\,{\rm yr}^{-1}$ for this star, even larger than RS Pup. They suggest that the fixed (non pulsating) Hα absorption feature that they detect is caused by a CSE with a size of the order of 1000 AU. At the distance of ℓ Car (570 pc, Kervella et al. 2004c), this corresponds to an angular extension of 0.5″. In addition, they detect "blobs" of OI emission up to a distance of several arcseconds from the star. The MIDI observations are sensitive to the central, hotter part of this CSE. Finally, these authors suggest in their conclusions that the mass loss rate may be larger for long period Cepheids than for short periods. This is also the conclusion of Willson (1988) based on theoretical pulsation computations: larger mass stars are associated with more mass loss: ℓ Car, with $P = 35.5$ days, is thus a prime candidate for a bright CSE.

4.3. Infrared excess

A number of Cepheids have shown moderate infrared excesses that are related to the presence of circumstellar matter. An excessive brightness at mid-infrared wavelengths is characteristic of a relatively warm, dusty environment. Deasy (1988) compared the IRAS excess ratios $F(60\,\mu{\rm m})/F(12\,\mu{\rm m})$ to predicted values for several bright Cepheids. Interestingly, an

extended infrared emission is identified around X Pup, located only $\simeq$1 kpc from RS Pup, and probably associated with the same nebula. Using IRAS data in the mid-IR, McAlary & Welch (1986) have studied a broad sample of Cepheids in order to detect infrared excesses. They obtained a clear detection in the case of RS Pup and SU Cas (two classical Cepheids). For ℓ Car however, we confirm their conclusion that no significant mid-IR excess is present in ℓ Car from our N band spectrum presented in Sect. 2.2.2.

Depending on its composition and temperature, the contribution from the CSE in the mid-IR could be small, especially as it may essentially diffuse the K band light from the star itself. Such a limited excess may well have remained below the sensitivity limit of the photometric detection methods. Moreover, this IR excess could be variable due to the change in effective temperature of the star, and the propagation of shock waves in the CSE around the minimum diameter phase. A cold temperature could for instance result in an excess at even longer wavelengths than the mid-infrared sampled with MIDI, up to the millimetric domain. No IR excess has been found with IRAS down to 60 μm, but Cepheids have never been studied at longer wavelengths.

The Gaussian model that we use in Sect. 3 for the CSE of ℓ Car should not be considered as physically realistic. In particular, it is clear that dust cannot exist within several radii of the star itself, as it would be sublimated. Nevertheless, we have chosen this simplified distribution in order to fit our limited data set with the smallest possible number of parameters. In order to establish the true geometry of the CSE, we plan to obtain in the future more visibility measurements over a broader range of spatial frequencies, as well as closure phases to search for deviations from central symmetry.

4.4. Polarization

Bastien et al. (1988) measured a significant fraction of polarized flux on ℓ Car with $1.58 \pm 0.01\%$ in the visible, at a position angle of 99.8 ± 0.2 deg. These authors noted that this polarization level is exactly the same as what was found by Serkowski, Matthewson & Ford (1975), 18 years before. A quick search through the catalogue compiled by Heiles (2000) reveals that several nearby Cepheids show a significant level of polarization (Table 6). Some fainter Cepheids located further away are known to present larger polarizations, but the fraction of the polarization introduced by the interstellar dust becomes uncertain.

Polyakova (1990) proposed that the observed polarization of Cepheids may be caused by the presence of a CSE that is 20 to 30% larger in the equatorial direction than along its pole. It would be interesting to measure interferometrically the shape of the CSE, using for instance the AMBER instrument (Petrov et al. 2000) to test this hypothesis.

Table 6. Fraction of polarized flux (p) for bright Cepheids. This list is limited to Cepheids brighter than $m_V = 6.0$ at maximum present in the catalogue assembled by Heiles (2000), apart from RS Pup. The color excess $E(B-V)$ reported by Fernie (1990) is given for each star, and the p values larger than 1% are marked in bold characters.

Star	m_V	$E(B-V)$	$p \pm \sigma(p)$ (%)
FF Aql	5.2	0.22	0.620 ± 0.006
η Aql	3.5	0.15	$\mathbf{1.685 \pm 0.003}$
RT Aur	5.0	0.05	0.490 ± 0.120
U Car	5.7	0.28	0.560 ± 0.100
v382 Car	3.8	–	0.510 ± 0.100
v399 Car	4.6	–	$\mathbf{1.425 \pm 0.090}$
ℓ Car*	3.3	0.17	$\mathbf{1.580 \pm 0.010}$
SU Cas	5.7	0.29	$\mathbf{1.853 \pm 0.036}$
δ Cep	3.5	0.09	0.440 ± 0.083
BG Cru	5.3	0.05	0.660 ± 0.035
X Cyg	5.8	0.29	0.410 ± 0.120
DT Cyg	5.6	0.04	0.280 ± 0.120
β Dor	3.5	0.04	0.440 ± 0.035
ζ Gem	3.6	0.02	0.110 ± 0.100
ω Gem	5.1	–	0.090 ± 0.120
T Mon	5.6	0.21	0.320 ± 0.120
Y Oph	5.9	0.66	$\mathbf{1.340 \pm 0.120}$
MY Pup	5.5	0.06	0.400 ± 0.035
RS Pup	7.0	0.45	0.440 ± 0.100
S Sge	5.2	0.13	0.689 ± 0.009
W Sgr	4.3	0.11	0.775 ± 0.016
X Sgr	4.2	0.20	$\mathbf{1.708 \pm 0.232}$
Y Sgr	5.2	0.21	0.220 ± 0.120
AH Vel	5.5	0.07	0.100 ± 0.100
T Vul	5.4	0.06	0.220 ± 0.120

* The value of p for ℓ Car is taken from Bastien et al. (1988).

5. Envelopes around stars related to Cepheids

5.1. The RV Tauri star AC Her

According to the General Catalogue of Variable Stars (Kholopov et al. 1998), variables of the RV Tauri class are pulsating yellow supergiants having spectral types F-G at maximum visible light and K-M at minimum. Their light curve shows alternating deep and shallow minima with a period (measured between one deep minimum and the next) of 30 to 150 days and an amplitude of 3 to 4 mag in the visible. RV Tau stars are particularly interesting as they seem to be intermediates between Cepheids and Mira variables. They are included in the broad group of "Type II Cepheids" (Wallerstein 2004). They are generally surrounded by dust shells that have been studied by several authors, including for instance Gherz (1972) and Jura (1986). On the theoretical side, Moskalik & Buchler (1991) have shown that an RV Tau-like pulsational behavior can be observed in long period Cepheids ($P = 25$–40 days), based on numerical models of Cepheids.

Shenton et al. (1992) have analyzed multi-wavelength photometry and spectroscopy of the short period RV Tauri star AC Her, from the ultraviolet to the infrared. This star is especially interesting as it pulsates with a very regular "double period" of 75.4 days, meaning that the time between

two consecutive minima (37.7 days) is close to the period of ℓ Car (35.6 days). However, it is clearly less massive, as Bono et al. (1997) give a probable mass below 1 $M_\odot$ for AC Her, compared to $M_{\ell\mathrm{Car}} \approx 13\,M_\odot$ (Caputo et al. 2005). In addition, AC Her was confirmed to be a binary star with a separation of 1.4 AU by Van Winckel et al. (1998) from radial velocity data. These authors also deduce an effective temperature of 5500 ± 250 K for the primary, comparable to ℓ Car ($\simeq$5100 K). AC Her also presents a very strong millimetric continuum flux (Van der Veen et al. 1994) that indicates the presence of large dust grains. Its spectrum shows a clear infrared excess in the N band, including a strong silicate emission feature between 8 and 12 μm (see e.g. Molster et al. 2002). Jura et al. (2000) have obtained mid-IR adaptive optics images of AC Her and detected two compact sources separated by 0.6″. These authors conclude that the best model to explain these observations is an edge-on ring of dust with a radius of 300 AU. However, this result was not confirmed by Close et al. (2003), who exclude any extended emission from high Strehl ratio AO images in the mid-IR domain. Exploring longer wavelengths, De Ruyter et al. (2005) have considered the spectral energy distribution of six bright RV Tau stars up to the millimetric domain in order to characterize the properties of the circumstellar dust. In the case of AC Her, they obtain a best-fit dust model consisting of a shell with an inner radius of 50 $R_\star$ and an external radius of 900 $R_\star$, and a total mass of the order of $3 \times 10^{-5}\,M_\odot$.

While ℓ Car does not present the same infrared excess as AC Her, and is significantly more massive, its physical properties place it at an interesting location in the H−R diagram close to the dusty pulsating RV Tau stars. By analogy with this class of stars, a significant millimetric excess could be present in the spectrum of ℓ Car. Unfortunately, to our knowledge, there are no millimetric observation of this star (or of any classical Cepheid) in the literature.

5.2. Mira stars and red supergiants

Recent observations making use of interferometers and combined with spectroscopic data have shed new light on the atmospheric structure of Miras and red supergiants, and on the interplay between atmospheric structure and dust formation. It is therefore interesting to compare Cepheids to these stars.

Cepheids and Miras undergo regular and large amplitude pulsations with comparable photospheric velocities of a few 10 km s^{-1}. Pulsations are efficient to expand the atmospheric volume and increase the scale height, making the atmosphere of these stars much more extended than for static objects.

Pulsations are mandatory in our current understanding of these objects to levitate material high enough in the atmosphere to allow for dust to condensate and drive the mass loss. Cepheids, as yellow supergiants, are very luminous and naturally have extended atmospheres. The driving mechanism for mass loss in red supergiants could be the production of acoustic energy by large convective cells as supported by Josselin & Plez (2003). Because they pulsate and they are supergiants, Cepheids can potentially use the two mechanisms to lose mass: pulsation and convection.

Perrin et al. (2004a,b, 2005a) have shown that the structure of the atmosphere of Mira stars and of the red supergiants Betelgeuse and μ Cep share some similarities. In both cases, a warm molecular layer with H_2O and CO was described at a short distance from the photosphere, at about 2 $R_\star$ for Mira stars and 1.4 $R_\star$ for red supergiants. The temperatures are also quite similar, of the order of 2000 K. Simultaneous modeling of interferometric and spectroscopic data by Weiner (2004) and Ohnaka (2004b) for Mira stars and by Ohnaka (2004a) for red supergiants confirmed the presence of water vapor in the molecular layer. Recently, Verhoelst et al. (2005) have shown that a consistent view of both interferometric and spectroscopic data of Betelgeuse requires the presence of corondum in the layer, thus providing a seed for silicate dust nucleation. A similar structure could exist around ℓ Car.

As a simple experiment, the properties of the CSE of ℓ Car can be extrapolated to that of Betelgeuse. Assuming thermal equilibrium in the atmosphere of Betelgeuse and assigning a fixed and common distance to all molecules in the atmosphere, a radial temperature law can be derived. The photosphere radiates a flux proportional to $R_\star^2\,T_\star^2$ of which a fraction $\mathrm{e}^{-\tau_l}$ is absorbed by the layer. As a very crude approximation it is assumed that τ_l does not vary with wavelength. Because of thermal equilibrium, the layer radiates a flux proportional to $(1-\mathrm{e}^{-\tau_l})\,R_\mathrm{l}^2\,T_\mathrm{l}^2$. Equating parameters to the values derived in Perrin et al. (2004a) yields $\tau_\mathrm{l} = 1.94$. Using this same optical depth for a hypothetical layer around ℓ Car yields a distance at which the temperature drops to 2000 K of 3.1 $R_\star$. Should the atmospheric contents detected with the interferometric K and N band measurements be water vapor, temperatures of 2000 K or less are required to produce a significant opacity. This simple experiment shows that the parameters derived in this paper for the CSE of ℓ Car a priori make sense physically, and are likely to be in agreement with what could be a general scheme for evolved stars.

One may now wonder at what characteristic distance sillicate dust could condensate, i.e. at what distance does the temperature drop below 1000 K. With the same rationale on thermal equilibrium and assigning an optical depth of 1 to the dust layer, the dust condensation radius order of magnitude is 21 $R_\star$, corresponding to 30 mas at the distance of ℓ Car. Given the resolution of MIDI during the observation, such a structure should have been detected if it exists. The current observations thus point towards a rather poor dusty environment around ℓ Car, a conclusion compatible with the absence of an infrared excess for the star.

6. Conclusion

Based on combined observations in the near and mid infrared domains with the VINCI and MIDI instruments of the VLTI, we have detected a circumstellar envelope around the massive Cepheid ℓ Car. Its typical size is 2−3 $R_\star$, and its contribution to the total near-infrared flux is 4%. Extended dusty environments are known to be present around other types of variable stars related to Cepheids that are located near ℓ Car in the Hertzsprung-Russell diagram. The physical process that created the CSE could be linked to the relatively large mass loss rate of ℓ Car

that could be enhanced by pulsation and convection. Although our data are still insufficient to study the nature of this CSE, a molecular layer could be a plausible explanation for our observations, by analogy with red supergiants and Miras.

Acknowledgements. Based on observations collected with the VLT Interferometer, Cerro Paranal, Chile, in the framework of the ESO programmes 071.D-0425 and 073.D-0142. This research has made use of the SIMBAD database at CDS, Strasbourg (France).

References

Baade, W. 1926, Astron. Nachr., 228, 359
Bastien, P., Drissen, L., Ménard, F., et al. 1988, AJ, 95, 900
Böhm-Vitense, E., & Love, S. G. 1994, ApJ, 420, 201
Bono, G., Caputo, F., & Santolamazza, P. 1997, A&A, 317, 171
Bordé, P., Coudé du Foresto, V., Chagnon, G., & Perrin, G. 2002, A&A, 393, 183
Caputo, F., Bono, G., Fiorentino, G., Marconi, M., & Musella, I. 2005, ApJ, 629, 1021
Claret, A. 2000, A&A, 363, 1081
Claret, A., Diaz-Cordovez, J., & Gimenez, A. 1995, A&AS, 114, 247
Close, L. M., Biller, B., Hoffmann, W. F., et al. 2003, ApJ, 598, L35
Cohen, M., Walker, R. G., et al. 1999, AJ, 117, 1864
Davis, J., Tango, W. J., & Booth, A. J. 2000, MNRAS, 318, 387
Deasy, H. P. 1988, MNRAS, 231, 673
De Ruyter, S., Van Winckel, H., Dominik, C., Waters, L. B. F. M., & Dejonghe, H. 2005, A&A, 435, 161
Di Folco, E., Thévenin, F., Kervella, P., et al. 2004, A&A, 426, 601
Fernie, J. D. 1990, ApJS, 72, 153
Gherz, R. D. 1972, ApJ, 178, 715
Glindemann, A., Albertsen, M., Andolfato, L., et al. 2004, SPIE, 5491, 447
Guyon, O. 2002, A&A, 387, 366
Josselin, É., & Plez, B. 2003, SF2A
Hanbury Brown, R., Davis, J., Lake, R. J. W., & Thompson, R. J. 1974, MNRAS, 167, 475
Havlen, R. J. 1972, A&A, 16, 257
Heiles, C. 2000, ApJ, 119, 923
Jura, M. 1986, ApJ, 309, 732
Jura, M., Chen, C., & Werner, M. W. 2000, ApJ, 541, 264
Kervella, P., Coudé du Foresto, V., Glindemann, A., & Hofmann, R. 2000, SPIE, 4006, 31
Kervella, P., Gitton, Ph., Ségransan, D., et al. 2003, SPIE, 4838, 858
Kervella, P., Ségransan, D., & Coudé du Foresto, V. 2004a, A&A, 425, 1161
Kervella, P., Nardetto, N., Bersier, D., Mourard, D., & Coudé du Foresto, V. 2004b, A&A, 416, 941 (Paper I)
Kervella, P., Fouqué, P., Storm, J., et al. 2004c, ApJ, 604, L113
Kholopov, P. N., Samus, N. N., Frolov, M. S., et al. 1998, Combined General Catalogue of Variable Stars, 4.1 edition (GCVS)
Kiss, L. L., & Szàtmary, K. 1998, MNRAS, 300, 616
Lord, S. 1992, NASA Tech. Mem., 103957
Marengo, M., Sasselov, D. D., Karovska, M., & Papaliolios, C. 2002, ApJ, 567, 1131
Marengo, M., Karovska, M., Sasselov, D. D., et al. 2003, ApJ, 589, 968
McAlary, C. W., & Welch, D. L. 1986, AJ, 91, 1209
Molster, F. J., Waters, L. B. F. M., & Tielens, A. G. G. M. 2002, A&A, 382, 222
Moskalik, P., & Buchler, J. R. 1991, ApJ, 366, 300
Ohnaka, K. 2004a, A&A, 421, 1149
Ohnaka, K. 2004b, A&A, 424, 1011
Perryman, M. A. C., Lindegren, L., Kovalevsky, J., et al., The HIPPARCOS Catalogue 1997, A&A, 323, 49
Perrin, G., et al., in preparation
Perrin, G., Ridgway, S. T., Mennesson, B., et al. 2004, A&A, 426, 279
Perrin, G., Ridgway, S. T., Verhoelst, T., et al. 2005, A&A, 436, 317
Perrin, G., Ridgway, S. T., Coudé du Foresto, V., et al. 2004, A&A, 418, 675
Petrov, R., Malbet, F., Richichi, A., et al. 2000, SPIE, 4006, 68
Polyakova, T. A. 1990, Pis'ma Astron. Zh., 16, 916
Serkowski, K., Mathewson, D. S., & Ford, V. L. 1975, ApJ, 196, 261
Shenton, M., Albinson, J. S., Barrett, P., et al. 1992, A&A, 262, 138
Szabados, L. 1989, Commmunications of the Konkoly Observatory Hungary, 94, 1
Szabados, L. 2003, Comm. Konkoly Obs., 103, 115
Taylor, M. M., Albrow, M. D., Booth, A. J., & Cottrell, P. L. 1997, MNRAS, 292, 662
Van der Veen, W. E. C. J., Waters, L. B. F. M., Trams, N. R., & Matthews, H. E. 1994, A&A, 285, 551
Van Winckel, H., Waelkens, C., Waters, L. B. F. M., et al. 1998, A&A, 336, L17
Verhoelst, T., Decin, L., Van Malderen, R., et al. 2005, A&A, submitted
Volk, K., & Cohen, M. 1989, AJ, 98, 1918
Wallerstein, G. 2004, PASP, 114, 689
Weiner, J. 2004, ApJ, 611, L37
Wesselink, A. 1946, Bull. Astron. Inst. Netherlands, 10, 91
Willson, L. A. 1988, Pulsation and Mass loss in Stars (Kluwer), 285

2.3.3 Article A&A : "II. Polaris and δ Cep from near-infrared interferometry with CHARA/FLUOR" (2006)

Notre détection d'une enveloppe autour de ℓ Car a démontré pour la première fois la présence de matière au voisinage immédiat de cette étoile. Nous rapportons dans cet article nos observations interférométriques de Polaris et δ Cep à l'aide de l'instrument CHARA/FLUOR. Nous avons établi que ces deux Céphéides possèdent des enveloppes similaires à celle de ℓ Car. Ceci indique que des enveloppes circumstellaires existent probablement autour de nombreuses Céphéides, sinon de la majorité d'entre elles.

FIG. 2.13 – Coucher de Soleil depuis l'Observatoire du Mont Wilson.

A&A 453, 155–162 (2006)
DOI: 10.1051/0004-6361:20054466

Astronomy & Astrophysics

Extended envelopes around Galactic Cepheids

II. Polaris and δ Cephei from near-infrared interferometry with CHARA/FLUOR⋆

A. Mérand[1,3], P. Kervella[1], V. Coudé du Foresto[1], G. Perrin[1], S. T. Ridgway[2,3], J. P. Aufdenberg[2], T. A. ten Brummelaar[3], H. A. McAlister[3], L. Sturmann[3], J. Sturmann[3], N. H. Turner[3], and D. H. Berger[3]

[1] LESIA, UMR 8109, Observatoire de Paris, 5 place Jules Janssen, 92195 Meudon, France
e-mail: antoine.merand@obspm.fr
[2] National Optical Astronomy Observatories 950 North Cherry Avenue, Tucson, AZ 85719, USA
[3] Center for High Angular Resolution Astronomy, Georgia State University, PO Box 3965, Atlanta, Georgia 30302-3965, USA

Received 3 November 2005 / Accepted 11 March 2006

ABSTRACT

We present the results of long-baseline interferometric observations of the classical Cepheids Polaris and δ Cep in the near infrared K' band (1.9−2.3 μm), using the FLUOR instrument of the CHARA Array. Following our previous detection of a circumstellar envelope (CSE) around ℓ Car (Kervella et al. 2006), we report similar detections around Polaris and δ Cep. Owing to the large data set acquired on Polaris, in both the first and second lobes of visibility function, we have detected the presence of a circum-stellar envelope (CSE), located at 2.4 ± 0.1 stellar radii, accounting for $1.5 \pm 0.4\%$ of the stellar flux in the K band. A similar model is applied to the δ Cep data, which shows improved agreement compared to a model without CSE. Finally, we find that the bias in estimating the angular diameter of δ Cep in the framework of the Baade-Wesselink method (Mérand et al. 2005b) is of the order of 1% or less in the K band. A complete study of the influence of the CSE is proposed in this context, showing that at the optimum baseline for angular diameter variation detection, the bias is of the order of the formal precision in the determination of the δ Cep pulsation amplitude (1.6%).

Key words. stars: variables: Cepheids – stars: circumstellar matter – stars: individual: Polaris (α Ursae Minoris) – stars: individual: δ Cephei – techniques: interferometric – techniques: high angular resolution

1. Introduction

Using low resolution interferometry (e.g. small baselines at which the star is under resolved) in the near infrared and mid-infrared, we recently reported the discovery of a circumstellar envelope (CSE) around the 35 day period Cepheid ℓ Car (Kervella et al. 2006). The presence of this feature may disturb the application of the classical Baade-Wesselink (BW) method, which aims at determining distances by measuring simultaneously the variations of angular and linear diameters.

Stellar interferometry has demonstrated a capability to measure precise Cepheid distances and the calibration zero point of the their Period-Luminosity relation (Kervella et al. 2004a). With the recent calibration of the BW method, thanks to the direct p-factor measurement by interferometry (Mérand et al. 2005b), it is now mandatory to study the Cepheid center-to-limb darkening (CLD) and the possible presence of CSEs in order to constrain two of the last sources of possible bias in the interferometric BW method. A morphological model is required in order to derive the angular diameter from a single baseline visibility measurement. If the assumed CLD differs from the actual one, or if the circumstellar emission is present, the derived angular diameters can be biased, possibly leading to a biased distance estimation in the BW method.

Following our recent study of ℓ Car, we present in this work near infrared observations of Polaris (α UMi, HR 424, HD 8890) and complementary observations of δ Cep (HR 8571, HD 213306) using the FLUOR (Fiber Link Unit for Optical Recombination) beam combiner installed at the CHARA (Center for High Angular Resolution Astronomy) Array. Polaris is the brightest Cepheid in the northern skies and offers the best opportunity to measure the CLD and detect the presence of a CSE. A great amount of data was collected, 65 calibrated data points using 4 different baselines (projected length from 19 to 246 m), to disentangle the CLD and CSE characterization from the possible close companion and radial pulsation detection. We show that these two latter effects have not been detected in our dataset, whereas the presence of a CSE is mandatory to explain a visibility deficit observed at $V^2 \sim 50\%$, as in ℓ Car.

We also present complementary observations of the Cepheid δ Cep with medium baselines ($B \approx 150$ m), following our determination of its p-factor using very long baselines (Mérand et al. 2005b). The final characteristics of the CSEs detected around Polaris and δ Cep are qualitatively in agreement with what has been found for ℓ Car.

Finally, we present a formal analysis of the bias introduced to the BW method in presence of the CSE.

2. Observational setup

2.1. CHARA/FLUOR

Observations were undertaken in the near infrared (K' band, $1.9 \leq \lambda \leq 2.3$ μm) at the CHARA Array (ten Brummelaar et al. 2005) using FLUOR, the Fiber Linked Unit for Optical

⋆ Table 4 is only available in electronic form at the CDS via anonymous ftp to cdsarc.u-strasbg.fr (130.79.128.5) or via http://cdsweb.u-strasbg.fr/cgi-bin/qcat?J/A+A/453/155

Recombination (Coudé du Foresto et al. 2003). The FLUOR Data reduction software (DRS) (Coudé du Foresto et al. 1997; Kervella et al. 2004b), was used to extract the squared modulus of the coherence factor between the two independent apertures from the fringe pattern.

2.2. Baselines

The baselines were chosen according to the Polaris and δ Cep angular sizes (approximately 3 and 1.5 mas, respectively), wavelength of observation and desired spatial resolution. Polaris must be observed at i) low spatial resolution ($V^2 \sim 50\%$) in order to detect the CSE and the possible faint companion, ii) high resolution (in the first lobe of the visibility profile, near the first null) in order to detect the pulsation with optimum sensitivity and iii) at the top of the second lobe in order to measure the CLD. This led to the choice of CHARA baselines i) S1-S2 ($b = 33$ m), E1-E2 ($b = 66$ m), ii) W2-E2 ($b = 156$ m) and iii) W1-E2 ($b = 251$ m). Concerning δ Cep, the only requirement for the complementary data was to reach $V^2 \sim 50\%$, where the CSE is believed to be easily detectable. This criteria led to projected baselines of roughly 150 m, corresponding to W2-E2 and S2-W2 at the CHARA Array. These latter baselines were chosen with similar length but different orientation, in order to investigate possible asymmetry in the CSE, if present.

2.3. Calibrators

Calibrator stars were chosen in two different catalogs: B02 (Bordé et al. 2002) for stars larger than 2.0 mas in diameter and M05 (Mérand et al. 2005a) for stars smaller than 2.0 mas using criteria defined in this latter work (see Table 1). We used calibrators from B02 for baselines smaller than 100 m, while for larger baselines we used calibrators from M05. The two catalogs are very similar by their characteristics: M05 is an extension of B02 using the very same procedure to estimate angular diameters. Therefore no trend is expected when using data calibrated with stars coming from these two catalogs.

3. Observations of Polaris

3.1. Context

Polaris has the largest angular size of all northern population I Cepheids. This star is therefore the best candidate for CLD measurements using an interferometer.

Because Polaris lies near the North celestial pole, the projected baseline remains almost constant in length while varying in position angle during the night (see Fig. 1).

3.2. Expected hydrostatic CLD profile

Claret (2000) tabulated limb darkening coefficients from hydrostatic ATLAS models. If we use the following parameters $T_{\rm eff} = 6000$ K, $\log g = 2.5$ and solar metallicity, we get in the database the following LD coefficients for the K band:

$$a_1 = 0.6404, a_2 = -0.1182, a_2 = -0.2786, a_4 = 0.1802$$

describing the center to limb variations:

$$I(\mu)/I(1) = 1 - \sum_{k=1}^{4} a_k \left(1 - \mu^{k/2}\right). \quad (1)$$

Table 1. Calibrators used for the observations. "SP" stands for spectral type. Uniform Disk diameters, given in mas, are only intended for computing the expected squared visibility in the K band.

	SP	UD diam.	Baseline	Notes
HD 5848	K2 II-III	$2.440_{\pm 0.064}$	S1-S2	B02, 1
HD 5848	K2 II-III	$2.440_{\pm 0.064}$	E1-E2	B02, 1
HD 81817	K3 III	$3.260_{\pm 0.085}$	–	–
HD 139669	K5 III	$2.890_{\pm 0.035}$	–	–
HD 222404	K1 III-IV	$3.290_{\pm 0.051}$	–	–
HD 83550	K2 III	$1.160_{\pm 0.015}$	W2-E2	M05, 1
HD 91190	K0 III	$1.330_{\pm 0.018}$	–	–
HD 118904	K2 III	$1.411_{\pm 0.018}$	–	–
HD 176527	K2 III	$1.721_{\pm 0.024}$	–	M05, 2
HD 218452	K5 III	$2.080_{\pm 0.024}$	–	–
HD 162211	K2 III	$1.598_{\pm 0.020}$	S2-W2	M05, 2
HD 165760	G8 III	$1.500_{\pm 0.020}$	–	–
HD 207130	K1 III	$1.331_{\pm 0.017}$	–	–
HD 217673	K1 II	$1.411_{\pm 0.020}$	–	–
HD 9022	K3 III	$1.050_{\pm 0.014}$	W1-E2	M05, 1
HD 42855	K3 III	$0.803_{\pm 0.010}$	–	–
HD 217673	K1 II	$1.411_{\pm 0.020}$	–	–
HD 206842	K1 III	$1.214_{\pm 0.016}$	–	M05, 2

Notes: B02 refers to Bordé et al. (2002) catalog; M05 to Mérand et al. (2005a) catalog; 1 refers to Polaris observations and 2 refers to δ Cep ones.

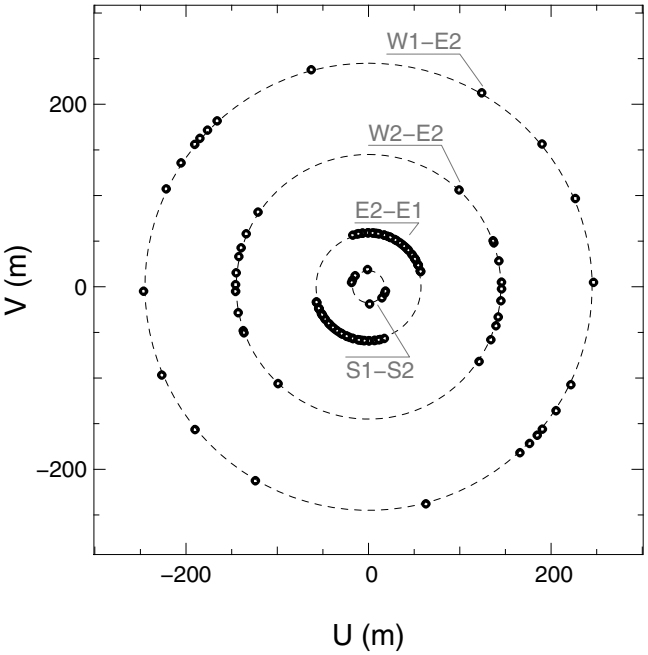

Fig. 1. $u-v$ map, in meters. Up is north and right is east. Each data point lies on a circle corresponding to the baseline because of the near-polar position in the sky of Polaris.

It is necessary to take into account the bandwidth smearing. Once the monochromatic visibility $v(\sigma, b)$ is computed from the intensity profile $I(\mu)/I(1)$ for a given wavenumber $\sigma = 1/\lambda$ and baseline b, the wide-band squared visibility is obtained by computing:

$$\mathcal{V}^2_{\rm FLUOR}(b) = \frac{\int T_r^2(\sigma)\ (B(\sigma)/\sigma)^2\ v^2(\sigma, b)\ {\rm d}\sigma}{\int T_r^2(\sigma)\ (B(\sigma)/\sigma)^2\ {\rm d}\sigma} \quad (2)$$

where $B(\sigma)/\sigma$ is the black body Planck function, in number of photons per unit of time, frequency and surface area for the effective temperature of the star (since FLUOR uses a detector that

Table 2. Best fit model parameters for Polaris and its CSE. $\theta_\star$ is the stellar angular diameter (mas), α the CLD coefficient, θ_s the shell angular diameter (mas), w the shell width (mas) and $F_s/F_\star$ the relative brightness (Fig. 3). Last column tabulates the reduced χ^2. Only parameters with error bars (lower scripts) have been fitted. The first line is the hydrostatic model; the second line is the adjusted CLD; the model of the last line includes a shell.

$\theta_\star$	α	θ_s	w	$F_s/F_\star$	χ^2
$3.152_{\pm 0.003}$	0.16	–	–	–	4.5
$3.189_{\pm 0.005}$	$0.26_{\pm 0.01}$	–	–	–	2.5
$3.123_{\pm 0.008}$	0.16	$7.5_{\pm 0.2}$	0.5	$1.5_{\pm 0.4}\%$	1.4

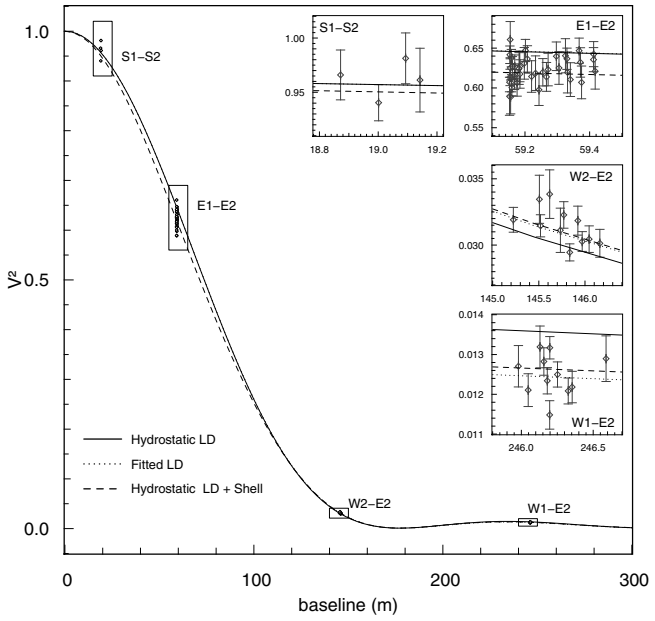

Fig. 2. Results of fit for different models. Squared visibility with respect to baseline. Solid line is the hydrostatic CLD from Claret (2000), dotted line is a fitted power law CLD while the dashed line is the hydrostatic model surrounded by the shell (see Table 2 for the models parameters). Note that solid and dotted line overlap in the main panel, the S1-S2 and E1-E2 small panels.

measures the flux as a number of photons); T_r is the chromatic instrumental transmission, which has been measured internally (a standard atmospheric transmission model is also applied).

The only parameter adjusted in the fit is the angular diameter of the star, which is found to be $\theta_\star = 3.152 \pm 0.003$ mas. The corresponding reduced χ^2 is 4.5 (Table 2). Note that we take into account the correlations between error bars of different data points. These correlations come from the multiple use of a single calibrator in the dataset. They are properly treated according to the formalism developed by Perrin (2003).

In Fig. 2, we display the data points and the models. The solid line corresponds to the hydrostatic CLD model for Polaris from Claret (2000). It appears that the model fails to reproduce the data in the second lobe (see W1-E1 baseline) and marginally intermediate baselines (E1-E2), where $V^2 \sim 50\%$.

3.3. Adjusted center-to-limb variation

Because the second lobe is not well reproduced by the hydrostatic model, a simple way to improve the model is to adjust the strength of the CLD. Indeed, the CLD profile changes the scale of the first lobe (not its shape) and the height of the second lobe. For this purpose we chose a single parameter CLD law, the power law: $I(\mu)/I(1) = \mu^\alpha$ (Michelson & Pease 1921; Hestroffer 1997). The hydrostatic model computed from Claret coefficients for Polaris corresponds to $\alpha = 0.16$. Even using a single parameter CLD model compared to the 4-parameters Claret's law, corresponding V^2 only differ at most by 10^{-3} (relative) in the first two lobes. We therefore prefer to use a single parameter CLD law (the power law), for the sake of simplicity.

The best fit, adjusting α as a free parameter, leads to $\theta_\star = 3.189 \pm 0.005$ mas and $\alpha = 0.26 \pm 0.01$; the reduced χ^2 is then 2.5 (Table 2, second line). Based on the χ^2, the fit is significantly better: the hydrostatic CLD led to χ^2 of 4.5. The CLD is stronger than predicted by hydrostatic models and the corresponding angular diameter is thus larger, as expected. However, before trying to interpret this result in terms of photospheric characteristics, one should notice that this model still fails to fit the mid-first lobe (see E1-E2 panel in Fig. 2, dotted line, which actually overlaps with the solid line). The measured V^2 data are lower than computed for a limb darkened disk. A change in CLD affects primarily the second lobe (higher spatial frequencies), and only the scale of the first lobe. In order to change the shape of the first lobe, one has to invoke something larger that Polaris itself to disturb the lower spatial frequencies. Thus, we think that this strong CLD is not realistic.

3.4. Companion and pulsation

When seeking possible explanations for the departure around $V^2 \sim 50\%$, two obvious possibilities must be considered before invoking a CSE: Polaris is a pulsating star and a spectroscopic-astrometric binary as well (Wielen et al. 2000). We shall now show that neither of these two hypotheses can explain the discrepancy in the first lobe.

If the departure detected at V^2 is believed to be due to the companion, it should vary with the position angle angle of the projected baseline. Our sampled range in projection angle is quite large and densely populated for E1-E2 (Fig. 1). However the departure does not change significantly with respect to projection angle of the baselines. As seen in Fig. 2: the V^2 recorded using E1-E2 are consistent within their errors. Because our typical V^2 precision is of the order of 3%, the companion must be as faint as 1.5% of the main star flux, or less (in the K band), in order to remain undetected by CHARA/FLUOR. Moreover, based on non detection in UV and X-ray, Evans et al. (2002) estimate that the companion mass is between 1.7 and 1.4 solar masses. Thus, this star is most likely a main sequence star of similar spectral type (but lower luminosity) to Polaris. Wielen et al. (2000), in their study of the astrometric orbit, conclude that the difference in magnitude between the two components is $\Delta V = 6.5$ from which we deduce, because of the similarity in spectral type, $\Delta K \approx 6.5$. This corresponds to a flux ratio of 2.5×10^{-3} which translates into an interferometric V^2 modulation twice as large, 5×10^{-3} or half a percent.

According to the latest radial velocity surveys, the radial pulsation of Polaris is of the order of 0.4% in diameter (Moskalik & Gorynya 2005). In the case of FLUOR, for which the relative error in squared visibility (σ_{V^2}/V^2) is almost constant, the most effective baseline to search for diameter variations maximizes the following criterion: for a given baseline b and angular diameter θ, a diameter increase of $\delta\theta$ should lead to the maximum relative increase in squared visibility $\delta V^2/V^2$. Thus, the

optimum baseline maximizes (in absolute value) the dimensionless quantity A_f, which we call the amplification factor:

$$A_\mathrm{f} = \frac{\partial V^2(b,\theta)}{\partial \theta} \frac{\theta}{V^2(b,\theta)}. \quad (3)$$

If the angular diameter θ increases by the very small amount $\delta\theta$, then, the visibility increases by $\delta V^2/V^2 = A_\mathrm{f} \times \delta\theta/\theta$. If we compute A_f for the four projected baselines for which Polaris has been observed, we get -0.1, -1, -11.5 and -3.7 for S1-S2, E1-E2, W2-E2 and W1-E2 respectively. Note that A_f is negative in the first lobe: an increase in diameter leads to a decrease in visibility, a well known effect of the Fourier transform. Our best baseline to detect the pulsation on Polaris is W2-E2 with an amplification factor of -11.5. Our relative average calibrated V^2 uncertainty is of the order of 3.5% for this baseline, thus we should be able to detect a 0.3% pulsation amplitude within one sigma (respectively 1% within 3 sigmas), assuming good phase coverage. In our case, data were recorded on three nights within a week. Because the pulsation is almost a multiple of 1 day ($P \approx 3.97$ days), it was not possible to explore more than three different epochs, one quarter phase apart. Fitting a uniform non-pulsating disk to W2-E2 data leads to a reduced χ^2 of 1.05, which means the pulsation was not detected due to poor phase coverage or because its amplitude was slightly shallower than expected (0.5%).

3.5. CSE model

We demonstrated that neither the companion nor the pulsation can be detected in our dataset. These phenomena cannot explain the visibility departure we observed at $V^2 \sim 50\%$ and can be therfore neglected.

Following the study on ℓ Car, we shall now explore the possible presence of a CSE around Polaris. We will adopt a ring-like model for the CSE. The image of the object, as seen by the interferometer, is supposed to be a limb-darkened star, surrounded by a ring. Note that the ring does not represent a flat disk, it is the two dimensional projection of the surrounding shell. This model contains five parameters (see Fig. 3): the star angular diameter ($\theta_\star$), its limb darkening coefficient (α), the ring mean diameter (θ_s), its width (w) and the flux ratio between the two components $F_\mathrm{s}/F_\star$. Apart from a star surrounded by a ring, this model can reproduce a single star ($F_\mathrm{s}/F_\star = 0$) or a star with an uniformly bright environment ($\theta_\mathrm{s} - w = \theta_\star$).

3.6. Results

The number of parameters (5) is too large compared to our dataset. Not that we do not have enough data points, but because these data points are bundled in four sets, one for each baseline. This is due to the particular position of Polaris in the sky (near the pole) and because our model is centro-symmetric. We choose to fix the center to limb darkening coefficient to the value predicted by hydrostatic models ($\alpha = 0.16$). Moreover, we also realized that the ring width does not play a significant role in the minimization: we fixed this parameter to different values, from 0.01 mas (very sharp ring) to 1 mas (diluted ring) and always obtained results for the other parameters within one sigma error bar. This is probably due to our lack of spatial resolution, which prevented us to actually resolve the ring width. Finally, only three parameters were adjusted: the stellar angular diameter, the shell angular diameter and its flux ratio. The best model is a CSE accounting for $1.5 \pm 0.4\%$ of the stellar flux and 7.6 ± 0.2 mas in angular diameter, whereas the stellar angular diameter is 3.123 ± 0.008 mas. The reduced χ^2 is 1.4 (Table 2).

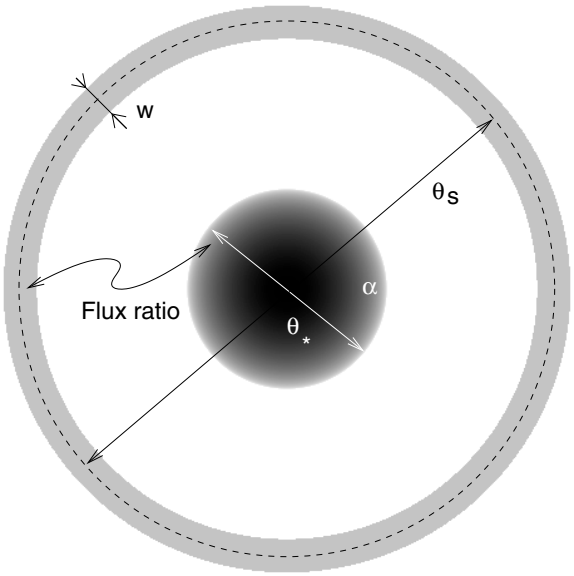

Fig. 3. Our simple CSE model: a star and a ring, as seen by the interferometer. The star (in the center) is characterized by its angular diameter $\theta_\star$ and CLD coefficient α (darker means brighter), whereas the shell is characterized by its angular diameter θ_s, width w and flux ratio.

Interestingly, though the CLD has the same as before ($\alpha = 0.16$, solid line in the same figure), the second lobe is lower than in the model without an envelope: the shell lowers the second lobe. This can be explained easily: since the shell is completely resolved at these baselines (its own visibility is extremely low), it only contributes as an uncorrelated flux and reduces the visibility by a factor $F_\star/(F_\mathrm{s} + F_\star)$ where $F_\star$ and F_s are the total fluxes of the two components (star and shell respectively).

3.7. Influence of the CLD

The CLD cannot be constrained from our data, not because they are not sensitive to it (we do have data in the second lobe), but rather owing to the limited number of free parameters the $u - v$ coverage authorizes. In terms of least square minimization, the reduced χ^2 is already close to its reasonable minimum. Adding a free parameter does not improve the fit – worse, it complicates the minimization algorithm and the error bar estimations. The only thing allowed, is to explore changes in the fixed value for the CLD parameter.

The χ^2 does not change much but it is still interesting to watch the behavior of the free parameters. The main effect of changing the CLD is to change the stellar diameter accordingly. Indeed, this is just a well known effect of the limb darkening, as the equivalent uniform disk diameter remains the same. The second lobe changes slightly, as expected: increasing the strength of the CLD lowers the second lobe. More interestingly, the flux ratio between the CSE and the star changes significantly. We previously noted that the shell would lower the second lobe. If the CLD lowers it too, the shell does not have to be as bright to compensate the effects of a shallow CLD. Yet it is not possible to let the shell disappear completely: the V^2 deficit still has to be fitted. Furthermore, the size of the shell does not change, since it is not constrained by the second lobe but by the position (in term of baseline) of the deficit at low spatial frequencies.

Therefore it is not possible to draw conclusions regarding Polaris' intrinsic CLD. We chose not to constrain this parameter and fixed it to a plausible value. Firstly, the quality of the fit is good enough (as judged by χ^2) to conclude that this value is compatible with our data set. Secondly, our model is not realistic enough that we can hope measuring the CLD with good accuracy. However, we suggest that the CLD of Polaris is probably consistent with the value expected from hydrostatic simulations.

3.8. Nature of the ring

We tested our best fit geometry with a physical model, such as the one used by Perrin et al. (2004) for Mira stars: this model is a simple radiative transfer calculation for a single layer shell surrounding a star. The shell is a self emitting black body, like the star itself. This type of model and our ring model lead to similar geometries for the object, as seen by the interferometer. In the model described by Perrin et al. (2004), the shell temperature can be computed using a simple radiative equilibrium model, such as presented in Ireland et al. (2005). Using silicate opacities (Suh 1999) and a black body spectrum for the Cepheid ($T_{\rm eff} \approx 6000$ K), we found an equilibrium temperature of the order of 2500 K at 3 stellar radii, which does not allow silicate dust grains to survive. Based on this test, the observed circumstellar emission is unlikely to be due to thermal emission from a silicate dust shell. This conclusion does not apply to Mira stars ($T_{\rm eff} \approx 2800$ K), for which the equilibrium temperature is much lower for a shell at the same distance.

3.9. Conclusion

A model consisting in a limb darkened star surrounded by a shell is an important improvement compared over the simple darkened disk model. The first lobe visibility deficit, for E1-E2 baseline, is understood to be due to the presence of a CSE consisting of a dim ring 2.4 ± 0.1 times larger than the star itself. The width of the ring is not known, and can be either thin or extended. However, the flux ratio between the CSE and the star is accurately known and does not depends on the width of the adopted ring: $1.5 \pm 0.4\%$. It is not possible to well constrain the intrinsic CLD of the star. However, our choice of a CLD computed from hydrostatic model (Claret 2000), combined with a CSE lead to a model consistent with the interferometric data.

4. Observations of δ Cep

4.1. Additional observations

In a recent study, we observed δ Cep (Mérand et al. 2005b) and applied the Baade-Wesselink (BW) method to the interferometric V^2 measurements. These measurements were obtained at very long baselines, between 235 and 315 m where $0.02 \leq V^2 \leq 0.15$. This range was chosen from among the whole dataset because it maximized the amplification factor criterion. The remaining data, acquired at medium baselines, did not contribute significantly to the angular diameter determination; moreover, their phase coverage was poor.

It was not possible to even suspect the presence of a shell based only on the longest baseline observations. Considering the experience with Polaris (above) and previously with ℓ Car, it appears the the CSE is only detectable using a combination of several different spatial frequencies. Thus, we here combine the sparse medium baseline data acquired on δ Cep in 2004 with more recent observations, obtained in 2005, at baselines where the CSE should show up clearly, if it exists: $V^2 \approx 50\%$. We shall also use the data set presented in Mérand et al. (2005b) in order to have consistent spatial frequency coverage between $V^2 \approx 50\%$ and the first visibility minimum. The purpose of these observations was to detect the presence of a CSE and study the impact on the angular diameter estimation.

Table 3. Best fit model parameters for δ Cep and its CSE. $\theta_\star$ is the stellar angular diameter (mas), α the CLD coefficient, $\theta_{\rm s}$ the shell angular diameter (mas), w the shell width (mas) and $F_{\rm s}/F_\star$ the relative brightness (Fig. 3). Last column tabulates the reduced χ^2. Only parameters with error bars (lower scripts) have been fitted. Note that in the second line, $\theta_{\rm s}/\theta_\star$, α, w and $F_{\rm s}/F_\star$, are set to the values found for Polaris (see Table 2).

$\theta_\star$	α	$\theta_{\rm s}$	w	$F_{\rm s}/F_\star$	χ^2
$1.480_{\pm 0.002}$	0.16	–	–	–	1.9
$1.476_{\pm 0.003}$	0.16	3.54	0.5	1.5%	1.1

4.2. Disentangling the CSE from the pulsation

In order to disentangle the presence of the CSE from the visibility time-modulation caused by the angular radial pulsation $\theta(\phi)$, we define the pseudo baseline B_{θ_0} as:

$$B_{\theta_0} = B\frac{\theta_0}{\theta(\phi)} \tag{4}$$

where $\theta(\phi)$, the angular diameter variation, is known from our previous BW study, which combined very long baseline observations with high precision radial velocity measurements. If the squared visibility data are plotted with respect to B_{θ_0}, they will match the profile of a star with an angular diameter of θ_0. The choice of θ_0 is arbitrary, and does not change the conclusions of the following discussion: we will use $\theta_0 = 1.475$ mas, the average angular diameter we reported in our precedent work (Mérand et al. 2005b).

4.3. CSE Model

It should be possible, in principle, to fit to δ Cep data a CSE model similar to the one we used for Polaris. However, we realize that the lack of data at the shortest baselines, where $V^2 \approx 90\%$, leads to large uncertainty on the CSE size. Indeed, the estimation of this size relies on the determination of the shape of the V^2 departure from the single star model. Even if the departure is obvious at $V^2 \approx 50\%$ compared to longer baselines, one needs data at short baselines, where V^2 approaches unity. While data collected at medium baselines compared to long baselines determine the lower limit for the CSE size, the comparison between short baselines and medium baselines leads to an upper limit.

Owing of the incompleteness of the δ Cep data set, compared to Polaris, we must use a simpler model, especially concerning the size of the CSE. As a first approximation, we choose to adopt the Polaris model, scaled to the appropriate angular diameter. Compared to parameter values given in Table 2, only $\theta_\star$ is adjusted, while $\theta_{\rm s}/\theta_\star$ is fixed to the value found for Polaris. In parallel, we will fit the angular diameter using a the CLD model adopted in Mérand et al. (2005b). The important result will lie in the difference between the two stellar angular diameter estimates.

The results of the fit (Table 3), as well as the visibility data points with respect to the pseudo baseline, are presented

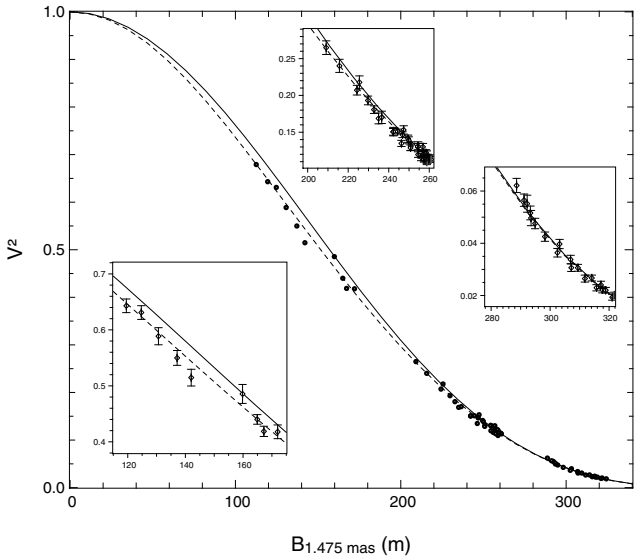

Fig. 4. All δ Cep squared visibility data with respect to the pseudo baseline $B_{\theta_0=1.475\,\mathrm{mas}}$. The limb darkened disk fit appears as a continuous line, while the rescaled Polaris model appears as a dashed line. Both models are fitted to the whole data set, while the rescaling function (pseudo baseline) only affects the longest baselines ($B_{1.475\,\mathrm{mas}} > 200$ m).

in Fig. 4. The revised diameter, using the CSE model, is $\theta_{\mathrm{CLD+CSE}} = 1.476 \pm 0.003$ mas ($\chi^2 = 1.1$) to be compared to $\theta_{\mathrm{CLD}} = 1.480 \pm 0.002$ mas ($\chi^2 = 1.93$) with no CSE. The quantity of interest is the diameter bias β:

$$\beta = \frac{\theta_{\mathrm{CLD}} - \theta_{\mathrm{CLD+CSE}}}{\theta_{\mathrm{CLD+CSE}}}. \quad (5)$$

For our case, considering the whole data set, we found β statistically compatible with 0. This means that omitting the CSE in the morphological model used to derive the angular diameter from our complete δ Cep dataset does not lead to a bias.

It is interesting to note that the Polaris model fits exactly the δ Cep data without any modifications, except for the angular scale.

4.4. CSE symmetry and variability

Two different aspects of the δ Cep CSE can now to be studied: its possible asymmetry and possible relative brightness change during the pulsation phase. The first aspect requires a study at different baseline projection angles of the visibility deficit at $V^2 \approx 50\%$, whereas the second requires a good phase coverage. Our data set contains data at $V^2 \approx 50\%$ with a baseline projection angle range of ninety degrees and with excellent phase coverage (considering our data were acquired at five different epochs).

In order to estimate the possible asymmetry or variability, we should consider the deficit between the measured visibility and that expected from the limb darkened model: $V^2 - V^2_{\mathrm{CLD}}$ at $B_{1.5\,\mathrm{mas}} \sim 140$ m (lower left sub-plot in Fig. 4). This deficit is plotted with respect to the baseline projection angle and pulsation phase in Fig. 5. At our level of precision, the CSE seems to be symmetric and stable through the pulsation. A more elaborate model is thus not justified.

A similar examination of the Polaris measurements leads to the same conclusion – the Polaris CSE appears symmetric and constant in time.

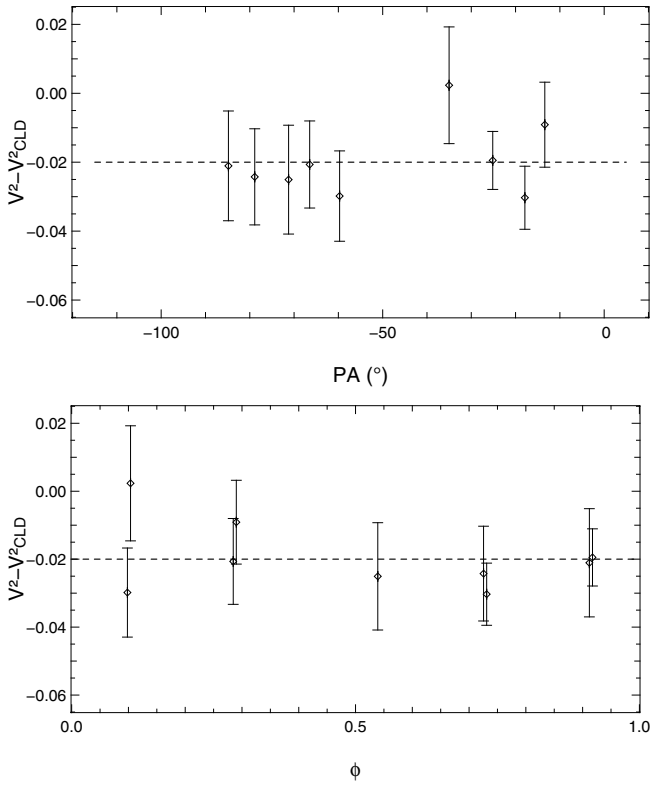

Fig. 5. δ Cep visibility deficit $V^2 - V^2_{\mathrm{CLD}}$ with respect to baseline projection angle (*upper panel*) and pulsation phase (*lower panel*). The dashed line represents a constant deficit. Neither an asymmetry nor a variability of the CSE is detected.

5. Consequences for the Baade-Wesselink method

5.1. De-biasing the stellar diameter measurement

Interferometric angular diameter measurements are always model dependent. In the case of stars without shells, it is necessary to correct for the CLD. In the case of single baseline observations of Cepheids, if a shell has to be taken into account the correction is no longer straightforward and depends on what baseline is used.

To understand this, we should evaluate the multiplicative bias introduced when measuring an angular diameter using a single baseline and not allowing for the presence of the CSE. This approach differs from the previous section, where we considered the whole δ Cep data set. Most Cepheid studies have not benefited from a similarly extensive coverage of spatial frequencies: e.g. Kervella et al. (2004a) or Mérand et al. (2005b). In these latter cases, in order to optimize the use of observing time, interferometric observations were recorded over a very restricted range of baselines.

Let us call $V^2_{\mathrm{CLD}}(b)$ the squared visibility of the star without the shell when observed at the baseline b, and $V^2_{\mathrm{CLD+CSE}}(b)$ for the star with the CSE, at the same baseline. Then, the bias $\beta(b)$ in diameter is, at the first approximation:

$$\beta(b) = \frac{\theta_{\mathrm{CLD}} - \theta_{\mathrm{CLD+CSE}}}{\theta_{\mathrm{CLD+CSE}}} \quad (6)$$

$$= \frac{V^2_{\mathrm{CLD}}(b) - V^2_{\mathrm{CLD+CSE}}(b)}{V^2_{\mathrm{CLD+CSE}}(b)} \times \frac{1}{A_{\mathrm{f}}(b)} \quad (7)$$

where $A_{\mathrm{f}}(b)$ is the amplification factor as defined previously. Note that β is negative: $V^2_{\mathrm{CLD}} > V^2_{\mathrm{CLD+CSE}}$ and $A_{\mathrm{f}} < 0$. In order

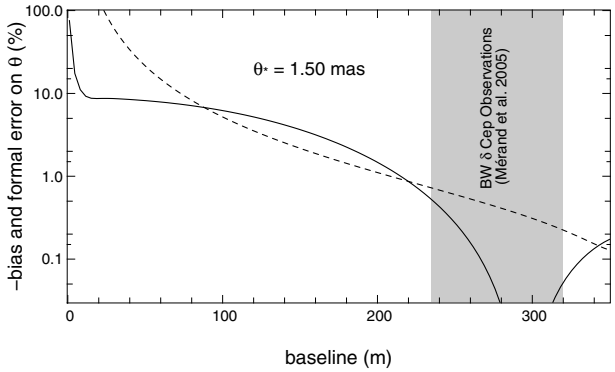

Fig. 6. Bias introduced when determining a Cepheid angular diameter using a single V^2 measurement at a given baseline and not taking into account the presence of the CSE, as a function of projected baseline (solid line). The dashed line is the formal error when deriving the angular diameter from a single V^2 measurement, assuming a 3% error on that measurement. The angular size chosen for this example is the average angular size of δ Cep and its CSE parameters (Table 3). The δ Cep diameter measurements, which took place between 235 and 313 m baselines (gray band), are biased at most at the 1% level, slightly lower than the formal error.

to compare this bias with respect to the formal error in the diameter estimation, we should compute the precision on the angular diameter σ_θ/θ, for a given error in squared visibility σ_{V^2}/V^2:

$$\sigma_\theta/\theta = \left| \frac{\sigma_{V^2}/V^2}{A_\mathrm{f}(b)} \right|. \quad (8)$$

Here, the $V^2_{\mathrm{CLD+CSE}}$ and V^2_{CLD} are essentially equivalent. For numerical application, we will consider the typical result we obtained for Mérand et al. (2005a): $\sigma_{V^2}/V^2 = 0.03$.

Figure 6 shows $-\beta$ for the δ Cep CSE parameters reported in Table 3. Our Baade-Wesselink observations used angular diameters determined at baselines ranging from 235 to 313 m (Mérand et al. 2005b). At such baselines, it appears that the bias is at most of the order of -1%, whereas the diameter formal error is slightly larger. One should notice this is not the case at the shortest baselines, where the bias exceeds the formal error.

5.2. Distance estimation bias

It is important to take into account this bias when applying the BW pulsation parallax method. Indeed, any multiplicative bias in angular diameter will lead to a multiplicative bias in distance, by the same amount. The pulsation parallax equation is (Mérand et al. 2005b):

$$\theta(\phi) - \theta_0 = -2\,\frac{p}{d}\int_0^\phi V_{\mathrm{rad.}}(t)\,\mathrm{d}t \quad (9)$$

where d is the distance, p the projection factor, θ the angular diameter, $V_{\mathrm{rad.}}$ the radial velocity, in the spectroscopic sense – note that we assume that the systematic velocity has been subtracted. The fitted parameters in this equation are θ_0 and d when determining the distance and assuming a given value for p (Kervella et al. 2004a) or θ_0 and p when knowing the distance and determining p (Mérand et al. 2005b). In the case of a multiplicative bias $1+\beta$ on the diameter, the projection factor is biased by the same amount, whereas the distance is biased by $1/(1+\beta)$.

In the case of δ Cep, the angular diameter was at most overestimated by a factor 1.01. Since the star appears larger than it actually is, our formal distance would have been under-estimated. In the case of our previous study, d has been fixed to the estimation of Benedict et al. (2002), $d = 274 \pm 11$ pc. We evaluated p, the projection factor, instead (Eq. (9)). Our value $p = 1.27 \pm 0.06$, should at most be revised to the lower value of 1.26 ± 0.06.

In future high precision interferometric BW observations, it will be necessary to determine and allow for the CSE bias. The best choice, in terms of spatial resolution, will be to observe in the first visibility lobe near the first minimum, in order to maximize the amplification factor. These observations will lead to the best formal angular diameter precision and the lowest bias due to the shell.

This conclusion relies on what we think the CSE looks like in the near-infrared K band. However, it seems likely that the CSE effects on the interferometric angular diameter estimation are less important at shorter wavelengths.

6. Conclusion and discussion

After ℓ Car, we report the interferometric detection in the near infrared of circumstellar emission around two additional Cepheids: Polaris and δ Cep. Polaris was studied in detail and we were able to apply a simple CSE model consisting in a star limb darkened according to hydrostatic models, surrounded by a dim ($1.5 \pm 0.4\%$ of the stellar flux), 2.4 ± 0.1 stellar diameters CSE. This model also explains the deficit in the visibility profile detected for δ Cep. The three Cepheids have quite different characteristics: Polaris has a small amplitude and a short period; δ Cep has a large amplitude, short period whereas ℓ Car has a large amplitude and long period. The (limited) measurements are consistent with similar circumstellar emission geometries in the three cases studied.

We computed the bias due to the presence of the CSE in the Baade-Wesselink method framework. The bias, in terms of distance, is smallest when the largest first-lobe baselines are used ($V^2 \approx 3\%$), and is at most 1%, under the current error contribution of interferometric measurements (Mérand et al. 2005b).

The presence of CSEs, with similar characteristics, around all Cepheids for which sufficient interferometric data are available, raises the possibility that this is a widespread phenomenon. Possible mass loss from Cepheids has been reviewed by Szabados (2003): slight infrared excesses have been detected for almost all Cepheids observed by IRAS, independently of the pulsating period. These observational constraints lead to a mass loss rate of the order of 10^{-10} to 10^{-8} $M_\odot$ yr^{-1}.

Mass loss is expected for Cepheids. This is a consequence of the theoretical Cepheid mass deficit. The deficit is the ratio between two different mass estimates: the evolutionary mass and the pulsational mass. The first, M_e, is derived from the Mass-Luminosity ($M-L$) relation computed from evolutionary numerical codes; the second, M_p, is derived using the Period-Mass-Radius relation (P-M-R), computed from non-linear pulsation numerical codes. The ratio $M_\mathrm{p}/M_\mathrm{e}$ is known to be smaller than unity. Even if the problem has been known for a long time and partially solved by refinements in numerical codes (Cox 1980), recent numerical investigations led to $M_\mathrm{p}/M_\mathrm{e} \approx 0.9$ for galactic Cepheids (Bono et al. 2001). According to these authors, this discrepancy between M_e and M_p might be explained by the fact that evolutionary codes do not take into account mass loss in the He-burning phase (post main sequence). The phase lasts 25 My For a 5 $M_\odot$ Cepheid and 2.5 My for a 11 $M_\odot$, assuming a 10% mass loss, a rough calculation leads to mass loss rates of the order of what is deduced from IRAS measurements.

The direct detection of CSEs around Cepheids at distances of only a few stellar radii is a confirmation that these stars are

experiencing substantial mass loss. The three Cepheids are significantly different one from another: we have three different periods (~4, ~5.4 and ~35 days), thus different masses; different pulsation amplitude (<1% for Polaris and ~15% for ℓ Car and δ Cep). This phenomenon cannot be neglected in future Cepheid studies, presumably having implications for evolutionary and pulsational codes, or while determining distances using the BW method.

Acknowledgements. The authors would like to thank all the CHARA Array and Mount Wilson Observatory day-time and night-time staff for their support during the installation of the FLUOR beam combiner and during the observations presented in this work. The CHARA Array was constructed with funding from Georgia State University, the National Science Foundation, the W. M. Keck Foundation, and the David and Lucile Packard Foundation. The CHARA Array is operated by Georgia State University with support from the College of Arts and Sciences, from the Research Program Enhancement Fund administered by the Vice President for Research, and from the National Science Foundation under NSF Grant AST 0307562.

References

Benedict, G. F., McArthur, B. E., Fredrick, L. W., et al. 2002, AJ, 124, 1695
Bono, G., Gieren, W. P., Marconi, M., Fouqué, P., & Caputo, F. 2001, ApJ, 563, 319
Bordé, P., Coudé du Foresto, V., Chagnon, G., & Perrin, G. 2002, A&A, 393, 183
Claret, A. 2000, A&A, 363, 1081
Coudé du Foresto, V., Ridgway, S., & Mariotti, J.-M. 1997, A&A, 121, 379
Coudé du Foresto, V., Bordé, P. J., Mérand, A., et al. 2003, in Interferometry for Optical Astronomy II, ed. W. A. Traub, Proc. SPIE, 4838, 280
Cox, A. N. 1980, ARA&A, 18, 15
Evans, N. R., Sasselov, D., & Short, C. I. 2002, AJ, 567, 1121
Hestroffer, D. 1997, A&A, 327, 199
Ireland, M. J., Tuthill, P. G., Davis, J., & Tango, W. 2005, MNRAS, 361, 337
Kervella, P., Nardetto, N., Bersier, D., Mourard, D., & Coudé du Foresto, V. 2004a, A&A, 416, 941
Kervella, P., Ségransan, D., & Coudé du Foresto, V. 2004b, A&A, 425, 1161
Kervella, P., Mérand, A., Coudé du Foresto, V., & Perrin, G. 2006, A&A, 448, 623
Mérand, A., Bordé, P., & Coudé du Foresto, V. 2005a, A&A, 433, 1555
Mérand, A., Kervella, P., Coudé Du Foresto, V., et al. 2005b, A&A, 438, L9
Michelson, A. A., & Pease, F. G. 1921, ApJ, 53, 249
Moskalik, & Gorynya 2005, Acta Astronomica, 55, 247
Perrin, G. 2003, A&A, 596, 702
Perrin, G., Ridgway, S. T., Mennesson, B., et al. 2004, A&A, 426, 279
Suh, K.-W. 1999, MNRAS, 304, 389
Szabados, L. 2003, Commmunications of the Konkoly Observatory Hungary, 103, 115
ten Brummelaar, T. A., McAlister, H. A., Ridgway, S. T., et al. 2005, ApJ, 628, 453
Wielen, R., Jahreiss, H., Dettbarn, C., Lenhardt, H., & Schawn, H. 2000, A&A, 360, 399

2.4 Projets de recherche

2.4.1 Etalonnage de l'échelle de distance des Céphéides

Le projet d'étalonnage interférométrique du point zéro de la relation P–L par interférométrie va se poursuivre par un programme important (60 h) inscrit dans le temps garanti de l'équipe AMBER, avec les télescopes auxiliaires du VLTI. Faisant partie de l'équipe proposante, je prévois de contribuer à l'obtention et à la réduction de ces observations. Elles seront complétées par des demandes dans le temps ouvert du VLTI. La conclusion de ce grand programme est prévue en 2009, avec la publication de notre nouvel étalonnage des relations Période-Luminosité, Période-Rayon et du facteur de projection des Céphéides proches.

Au total, une quarantaine de Céphéides sont résolvables avec AMBER et les plus longues bases du VLTI (Kervella 2001). Elles fourniront une base solide pour l'application de la méthode BW interférométrique et l'étalonnage de la relation P–L. La question de la mesure directe du facteur de projection est également à mon programme, avec en particulier une approche coordonnée entre les mesures de parallaxe HST-FGS en cours de l'équipe de F. Benedict (Université du Texas) et des observations interférométriques avec les interféromètres CHARA et VLTI. En complément de ces mesures, je prévois de poursuivre l'analyse des données obtenues avec le spectrographe HARPS sur dix Céphéides brillantes, de manière à identifier les meilleures observables pour mesurer la vitesse radiale de la photosphère. L'absence de biais dans les mesures spectroscopiques de vitesse radiale est un facteur d'une importance égale à la précision des mesures interférométriques pour obtenir une mesure juste de la distance.

2.4.2 Spectro-interférométrie avec MIDI et AMBER

Nos observations de l'enveloppe de ℓ Car en infrarouge moyen avec l'instrument MIDI du VLTI ont été décisives pour confirmer la présence de matière autour de cette étoile. Nous projetons dans les prochaines années de développer l'étude des enveloppes des Céphéides dans l'infrarouge moyen avec MIDI. Une extension dans le domaine millimétrique est également envisagée, par exemple à l'aide de l'interféromètre de l'IRAM, pour les Céphéides les plus proches et les plus brillantes. A titre exploratoire, des observations de Polaris et δ Cep dans la raie de l'hydrogène neutre à 21 cm ont été réalisées en 2006 avec le radiotélescope de Nançay.

AMBER est un instrument spectro-interférométrique qui permet d'obtenir des mesures de visibilité et de cloture de phase en fonction de la longueur d'onde pour les bandes JHK et avec trois résolutions spectrales ($R = 30$, 1 500, et 10 000, voir Petrov et al. 2000 pour plus de détails). Ce recombinateur est donc très bien adapté à l'étude de la dynamique interne de l'atmosphère des Céphéides au cours de leur pulsation. ℓ Car est en particulier une cible de choix, car elle présente le plus grand diamètre angulaire de toutes les Céphéides ce qui rend sa résolution par le VLTI plus facile. En étudiant par exemple le comportement de la raie Brγ de l'hydrogène, il sera possible de sonder les mouvements de matière dans l'atmosphère, ainsi que la rotation de l'étoile. La géométrie de la répartition de la matière autour de l'étoile pourra également être étudiée, avec notamment une grande sensibilité à une éventuelle asymmétrie par la cloture de phase.

Chapitre 3

La séquence principale

La classe des naines est de loin la plus nombreuse de l'Univers. Alors qu'elles réalisent la fusion de l'hydrogène en leur coeur, les étoiles de la séquence principale se trouvent dans une configuration relativement stable, qu'elles conservent pendant la majeure partie de leur existence. Le meilleur exemple d'une telle étoile est bien sûr le Soleil, mais la séquence principale recouvre en réalité une très grande variété d'étoiles. Par exemple, les naines massives en rotation rapide dont il sera question au Chapitre suivant appartiennent aussi à la séquence principale, tout comme les minuscules naines rouges de la Sect. 3.1. La taille de ces étoiles est naturellement très variable, et l'interférométrie permet de mesurer avec précision cette caractéristique physique fondamentale. En combinaison avec des mesures astérosismiques, il est possible de construire des modèles numériques très bien contraints, qui permettent d'étudier la structure et l'état évolutif des étoiles de manière raffinée (Sect. 3.2). La structure même de l'atmosphère des étoiles de type solaire comme α Cen B est maintenant accessible, comme le montre notre article reproduit à la Sect. 3.3. Enfin, les étoiles naines, par leur relative stabilité sont d'excellents étalons pour les observations interférométriques. Je présente à la Sect. 3.4 les relations de brillance de surface obtenues grâce aux observations obtenues avec le VLTI. Elles permettent d'estimer le diamètre angulaire des étoiles naines et sous-géantes avec une incertitude de seulement 1% à partir de simple photométrie large bande.

3.1 Les étoiles de très faible masse

Les naines rouges les moins massives sont particulièrement importantes car elles se situent à l'interface entre les étoiles et les naines brunes. Présentant une structure interne essentiellement convective, elles permettent d'étudier ce mode de transport de l'énergie de manière raffinée. Par ailleurs, leur densité élevée implique une équation d'état de la matière les composant bien spécifique. La Fig. 3.1 montre la relation masse-rayon tirée des modèles de Baraffe et al. (1998) pour deux âges discincts : 400 millions d'années pour la courbe en tireté et 5 milliards pour la courbe continue. Les mesures que nous avons obtenues avec le VLTI, et qui sont rapportées à la Sect. 3.1.1, confirment que les modèles sont satisfaisants pour les étoiles les moins massives. Il est intéressant de noter sur cette figure que l'on approche avec Proxima de la limite de dégénérescence : le gaz constituant l'étoile offre une résistance à la compression supérieure à celle d'un gaz parfait. Ceci explique pourquoi les étoiles et les planètes géantes comme Jupiter ont une taille similaire, alors que leur masse est extrêmement différente.

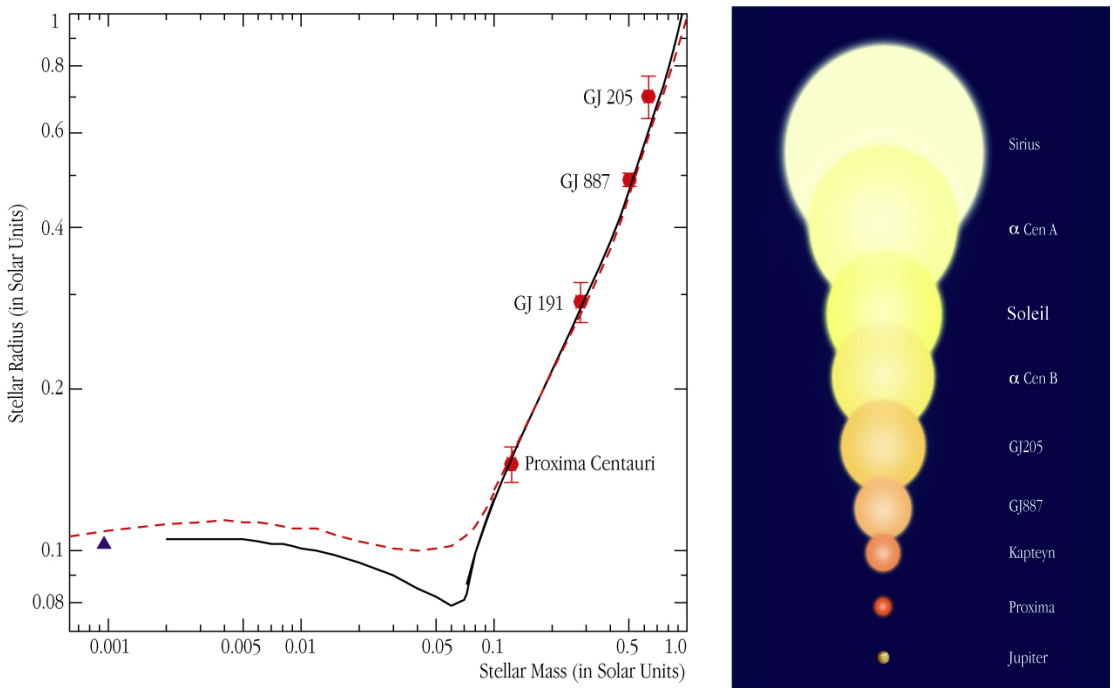

FIG. 3.1 – La partie gauche de cette figure montre la relation masse-rayon des quatre naines de très faible masse que nous avons mesurées à l'aide de l'instrument VINCI du VLTI. Le triangle indique la position de Jupiter. La partie droite montre la taille comparée de quelques étoiles mesurées avec VINCI, de Jupiter et du Soleil.

3.1.1 Lettre A&A : "First radius measurements of very low mass stars with the VLTI" (2003)

Dans cette lettre, nous rapportons la mesure du diamètre angulaire de quatre naines de faible masse à l'aide de l'instrument VINCI du VLTI. En complétant les mesures existantes, notamment vers les plus faibles masses avec *Proxima*, ces nouvelles mesures ont permis de confirmer que les modèles de structure stellaire sont globalement satisfaisants. Une légère tendance à sous-estimer les rayons semble cependant apparaître pour les étoiles de masse intermédiaire.

FIG. 3.2 – La plate-forme du VLT et le Soleil couchant sur le Pacifique, photographiés depuis le site du télescope VISTA.

A&A 397, L5–L8 (2003)
DOI: 10.1051/0004-6361:20021714

Astronomy & Astrophysics

Letter to the Editor

First radius measurements of very low mass stars with the VLTI⋆

D. Ségransan[1], P. Kervella[2], T. Forveille[3,4], and D. Queloz[1]

[1] Observatoire de Genève, 51 chemin des maillettes, 1290 Sauverny, Switzerland
[2] European Southern Observatory, Casilla 19001, Vitacura, Santiago 19, Chile
[3] Observatoire de Grenoble, BP 53X, 38041 Grenoble Cedex, France
[4] Canada-France-Hawaii Telescope Corporation, PO Box 1597, Kamuela, HI 96743, USA

Received 15 October 2002 / Accepted 21 November 2002

Abstract. We present 4 very low mass stars radii measured with the VLTI using the 2.2 μm VINCI test instrument. The observations were carried out during the commissioning of the 104-meter-baseline with two 8-meter-telescopes. We measure angular diameters of 0.7–1.5 mas with accuracies of 0.04–0.11 mas, and for spectral type ranging from M0V to M5.5V. We determine an empirical mass-radius relation for M dwarfs based on all available radius measurements. The observed relation agrees well with theoretical models at the present accuracy level, with possible discrepancy around 0.5–0.8 $M_{\odot}$ that needs to be confirmed. In the near future, dozens of M dwarfs radii will be measured with 0.1–1% accuracy, with the VLTI, thanks to the improvements expected from the near infrared instrument AMBER. This will bring strong observational constraints on both atmosphere and interior physics.

Key words. stars: low-mass, brown dwarfs – stars: fundamental parameters – techniques: interferometric

1. Introduction

Mass, radius, luminosity and chemical composition are the basic physical properties of a star. For a given mass and chemical composition, theory can predict most of the stellar physical parameters at a given age. Accurate stellar mass, radius and luminosity measurements thus provide a crucial test of our understanding of stellar physics. To be relevant, these parameters must be determined with an accuracy of the order of 1% (Andersen 1991).The previously rather noisy Mass-Luminosity relation for M dwarfs has recently been greatly improved (Delfosse et al. 2000; Ségransan et al. 2003). By contrast, the empirical Mass-Radius relation remains poorly constrained, since it is based on the observations of just two of the three known M-type eclipsing binaries, plus three M dwarfs radii measured at the Palomar Testbed Interferometer (PTI) with accuracies of 2–4% (Lane et al. 2001).

In this paper we present direct angular diameter measurements of four M dwarfs with spectral types ranging from M0V to M5.5V obtained with the Very Large Telescope Interferometer (VLTI) and two 8-meter-telescopes (Glindemann et al. 2001). The first two sections describe the observations and the data reduction. The third section presents the visibility calibration and the angular diameter determination. In the last section we compare presently known M dwarfs radiis and masses to theoretical models.

Send offprint requests to: D. Ségransan,
e-mail: Damien.Segransan@obs.unige.ch

⋆ Based on observations made with the European Southern Observatory telescopes and obtained from the ESO/ST-ECF Science Archive Facility.

2. Observations

Gl887, Gl205 and Gl191 were observed during the first commissioning run of the VLTI with 8-meter-telescopes in early November 2001, on the second and third nights after the "first fringes" with these telescopes. The observations of Gl551 were obtained in February 2002.

VINCI is the commissioning instrument of the VLTI (Kervella et al. 2000). It uses single-mode optical fibers to recombine the light from two telescopes of the Paranal Observatory, and modulates the optical path difference around its zero position to produce interference fringes. This recombination scheme was first used in the FLUOR instrument (Coudé du Foresto et al. 1998) and produces high precision visibility values, thanks to the efficient spatial filtering of the incoming beams and to the photometric monitoring of the filtered wavefronts.

Transfer function calibrators (Table 1) were selected based on their spectral type, distance to the target and known diameter (Cohen et al. 1999). Calibration tests show that a $\pm 1\,\sigma$ shift in the calibrator angular diameter values modify the measured M dwarf radii by less than $0.8\,\sigma$.

The M dwarfs science targets and their calibrators were observed in series of a few hundred interferograms, recorded at a frequency of 500–700 Hz. Due to many down times associated with the technical commissioning of the array, the observations of calibrator stars were not possible to the extent usually required to monitor extensively the transfer function. Nevertheless, the calibration measurements proved sufficient to estimate the transfer function with a good accuracy. The global interferometric efficiency of the VLTI mostly depends on two

Table 1. Calibrators and instrumental+atmospherical transfer function. Calibrator uniform disk angular diameters come from Cohen et al. (1999). Internal error and external error on the transfer function are given for each calibrator. Fomalhaut angular diameter was redetermined using the VLTI. (*) calibrator was not used due low visibilities or poor accuracy on their diameters.

		Spec.	Diameter	Transfer function		
Targets	Calib.	Type	$\theta_{\rm UD}$[mas]	$\lvert T_{\rm a+i}\rvert^2$	$\sigma_{\rm tot}$	$(\sigma_{\rm stat}/\sigma_{\rm cal})$
GJ205	39-Eri	K3III	1.81 ± 0.02	0.478	0.005	(.002/.005)
	HD36167*	K5III	3.55 ± 0.06	0.486	0.037	(.006/.036)
GJ887	HR8685	M0III	2.01 ± 0.02	0.448	0.005	(.003/.004)
	Fomalhaut*	A3V	2.13 ± 0.06	0.433	0.013	(.004/.013)
GJ191	39-Eri	K3III	1.81 ± 0.02	0.420	0.005	(.004/.004)
	Gam02 Vol*	K0III	2.45 ± 0.06	0.411	0.014	(.006/.013)
GJ551	HD110458	K0III	1.6 ± 0.02	0.509	0.006	(.004/.004)

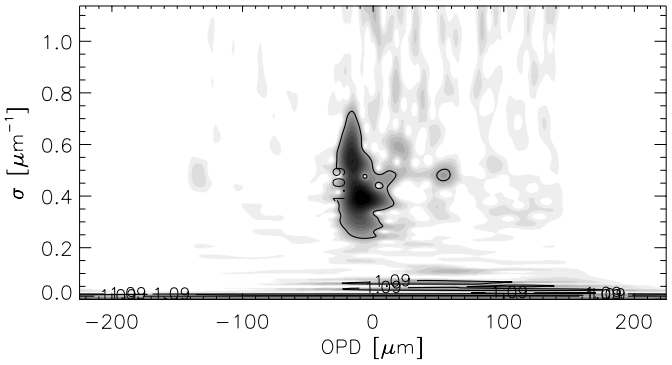

Fig. 1. Wavelet Spectral density of a pistonned interferogram. The effect of strong differential piston is to distort the interferogram fringe peak in the time-frequency space. Part of the interferogram's energy is spread out in both time and frequency, preventing a good measurement of the total energy.

parameters: the atmospheric coherence time, which varies over timescales sometimes as short as a few minutes, and the instrumental efficiency which changes over timescales of a week. Our effective calibration rate oversamples the instrumental efficiency variations by orders of magnitude, but risks undersampling the atmospheric coherence time. Fortunately, the Paranal observatory site is heavily monitored, and we could rely on continuous measurement of the atmospherical coherence time (Sandrock et al. 2000) to discard data intervals when the coherence time changed significantly between the observation of the calibrators and science targets.

3. From fringes to visibilities

We used a customised version of the VLTI/VINCI data reduction pipeline, whose general principle is based on the original FLUOR algorithm (Coudé du Foresto et al. 1997). Despite the high modulation frequency of the fringes, many recorded interferograms present a differential piston signature, as well as strong photometric fluctuations. The latter are expected for large apertures without adaptive optics correction, as individual speckle come in and out of the fiber input aperture. To overcome the noise amplification caused by low photometry data points, which could strongly bias the resulting visibilities, interferograms were calibrated by the average value of the photometry over the fringe packet. The two calibrated output interferograms were then subtracted to remove residual photometric fluctuations (Kervella, in prep).

In parallel to the FLUOR algorithm, based on Fourier analysis, we implemented a time-frequency analysis (Ségransan et al. 1999) based on the continuous wavelet transform (Farge 1992). Instead of the projection onto a sine wave of the Fourier transform, the wavelet transform decomposes it onto a function, *ie.* the Wavelet, that is localised in both time and frequency. We use as a basis the Morlet Wavelet, a Gaussian enveloppe multiplied by sine wave. With the proper choice of the number of oscillations inside the Gaussian envelope, the Morlet wavelet closely matches a VINCI interferogram. It is therefore extremely efficient at localizing the signal in both time and frequency.

As illustrated in Fig. 1, differential piston strongly affects the amplitude and the shape of the fringe peak in the wavelet power spectrum. We therefore select on the shape of fringe peak in the time-frequency domain to efficiently reject "pistonned" interferograms. We then derive visibilities from the wavelet spectral density, after removing the residual photon and detector noise.

4. Angular diameter and limb darkening

Stellar angular diameters are usually quoted for both a uniform disk and a limb-darkened disk, though only the latter is directly comparable to actual stellar models. The monochromatic visibility of a limb darkened disk is (Davis et al. 2000):

$$V_\lambda = \frac{\int_0^1 {\rm d}\mu I(\mu)\,\mu J_0\left(\pi B\theta_{LD}/\lambda\left(1-\mu^2\right)^{1/2}\right)}{\int_0^1 {\rm d}\mu I(\mu)} \quad (1)$$

where $I(\mu)$ is the surface brightness, J_0 is the zeroth order Bessel function, B the projected baseline, λ the wavelength, and $\theta_{\rm LD}$ the limb darkened diameter (in radian).

The VINCI instrument has no spectral resolution, and a bandpass defined by a K' filter (2–2.3 μm). For marginally resolved disks ($B\theta/\lambda << 1$), Eq. (1) remains approximately valid for polychromatic measurements, with λ then being the effective wavelength of the system. It differs from the mean wavelength of the filter through the wavelength-dependency of fiber coupling, combiner transmission, and the stellar spectrum. Since interferograms are Fourier transforms of the instrumental bandpass, they provide, in principle, an accurate measurement of the effective wavelength, obtained as the average barycenter of the fringe peak in the spectral density space. We computed such effective wavelengths for each star and compared them to the one given by the VINCI instrument modelisation ($\lambda_{\rm eff} = 2.195 \pm 0.010$ μm). Our estimations of $\lambda_{\rm eff}$ present a large scatter which is due to atmosperical differential piston and photometric fluctuations. We thus used the VLTI/VINCI effective wavelength provided by ESO and the effective temperature of each star to compute an accurate $\lambda_{\rm eff}$ for each target and calibrator.

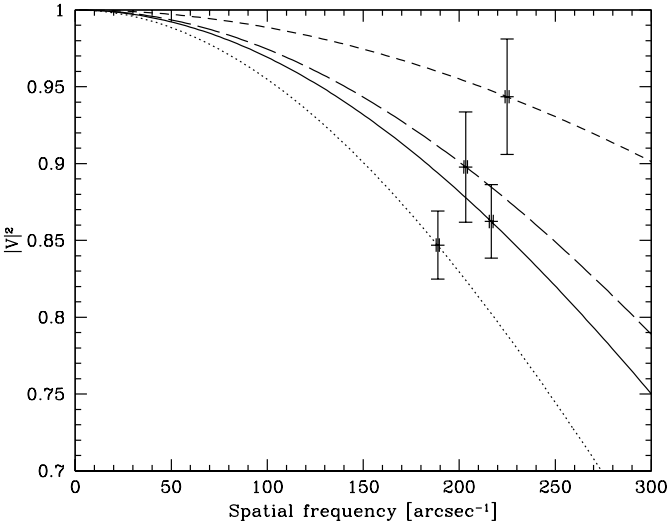

Fig. 2. Measured visibilities (data points) and best-fit model (curves, Eq. (2)) for GJ 205 (plain), GJ887 (dots), Gl191 (short dash), and Gl191 (long dash).

Due to their relatively short baselines, and limited uv-coverage, these observations cannot discriminate between an unphysical uniform star and a more realistic slightly larger limb-darkened star. To correct for limb-darkening, we therefore have to use a theoretical limb-darkening law. We adopt the non-linear limb-darkening coefficients from Claret (2000), Eq. (2), based on atmospheric models from Allard et al. (1997). We use gravities and effective temperatures from Baraffe et al. (1998) isochrones at 5 Gyr (Table 2) to select the apropriate entry in the Claret (2000) tables.

$$I(\mu) = I(1)\left[1 - \sum_{k=1}^{4} a_k \left(1 - \mu^{k/2}\right)\right]. \quad (2)$$

In Eq. (2), the a_k are the limb-darkening coefficients and $\mu = \cos(\gamma)$, with γ the angle between the line of sight and the emergent ray. The limb-darkening correction that we apply is in principle model-dependent. Fortunately, it is also quite small for M dwarfs, only 1–2% (Table 2). The correction itself is at best marginally relevant at our current accuracy level for individual diameters, and its theoretical uncertainties can for now be safely neglected. Future observations with longer baselines, at shorter wavelengths, and with a more accurate calibration, will need to consider the issue more carefully, but they will also directly measure the limb-darkening law for the closest M dwarfs.

5. Mass-radius relation

An accurate empirical mass-radius relation is an essential constraint on stellar interior structure, evolutionnary models and atmospheric physics. The interior structure is largely determined by the equation of state, whose derivation for very low mass stars, brown dwarfs, and planets involves the complex physics of strongly correlated and partially degenerated quantum plasma (Chabrier & Baraffe 2000).

To obtain the empirical mass-radius relation we need to convert angular diameter into linear radius, which is easily done thanks to accurate HIPPARCOS parallaxes for all sources, and we need accurate masses. For these single stars masses can only be estimated, from IR photometric measurements and accurate mass-luminosity relations. Fortunately, the K-band mass-luminosity relation has very little intrinsic dispersion for M dwarfs. We estimated the masses of the stars listed in Table 2 using an update (Ségransan et al. 2003) of the (Delfosse et al. 2000) empirical K band mass-luminosity relation, now based on 27 accurate masses and luminosities. The data dispersion around the average empirical relation corresponds to a mass error of ∼5%. Masses and radii are summarized in Table 2.

Figure 3 compares the empirical radii & masses with 5 Gyr and 1 Gyr theoretical isochrones from Baraffe et al. (1998). The Baraffe et al. (1998) models reproduce the observation fairly well in the sampled range, between 0.65 and 0.12 $M_\odot$. At a more detailed level though, one notices that the models underestimate the radii for YY Gem, V818 Tau and GJ 205, with masses in the 0.5–0.65 $M_\odot$ range. The discrepancy is highly significant for the eclipsing binaries, as extensively discussed by Torres & Ribas (2002) and is more marginal for long baseline interferometry data. There is an indication in Fig. 3 that the model reproduces the observations well below 0.5 $M_\odot$, and only become discrepant above that value. If real, this suggests that the shortcomings of current models have to be searched in the energy transport (convection description, opacities), rather than in the equation of state (EOS). As their mass decreases, stars at the bottom of the main sequence have increasingly simple transport properties (they are fully convective below ∼0.3 $M_\odot$), and an increasingly correlated and degenerate EOS. EOS shortcomings are therefore expected to show up most prominently at the lowest masses, and transport problems at higher masses. That result obviously needs confirmation from additional data points and from more accurate measurements, but the consistency between the eclipsing binary and the resolved single stars is comforting, as these two datasets were obtained through completely independent methods.

In addition to providing physical radii, the angular radii can be combined with integrated flux measurement to obtain the effective temperature from the Stefan-Boltzmann law. Up to now that process has typically been inversed, to derive radii for stars whose effective temperatures were obtained from comparison with model spectra (e.g. Leggett et al. 2000). Amongst the sources in Table 2, only GJ 699 has an integrated flux measurement (Leggett et al. 2000), and we thus have to rely on the bolometric correction polynomial fit of (Leggett et al. 2000) to estimate it for the other targets.

In spite of these increased uncertainties on the bolometric flux, the resulting effective temperatures have fairly small error bars (Table 2). With increasingly precise direct angular radii, and with integrated flux measurements for all targets, this test can become a very discriminating validation of model atmospheres, with potential accuracies at the ∼1% level on both $T_{\rm eff}$ and $\log(g)$. The present diameter measurements, which have similar precisions to those obtained at PTI (Lane et al. 2001), have been obtained during the commissioning phase of

Table 2. Measured angular diameter for the target stars. The uniform disk diameters for GJ 699, GJ 15A, GJ 411, GJ 380, GJ 105A are from Lane et al. (2001). For consistency with our measurements, we recomputed their limb darkened diameters, masses and radii. The masses for Gl 380 and Gl105A are based on the Baraffe et al. (1998) M-L relation, with an arbitrary 5% error bar.

	Spectral	Photometry & Masses		Limb Darkening, K band (models)						Diameter [mas]			Radius [$R_\odot$]		Atm. prop.			
Object	Type	M_K	$M/M_\odot$	g	$T_{\rm eff}$	a_1	a_2	a_3	a_4	$\theta_{\rm UD}$	$\theta_{\rm LD}$	σ_θ	R	σ_R	$T_{\rm eff}$	$\sigma_{T_{\rm eff}}$	g	σ_g
GJ205	M1.5V	5.09	0.631 ± 0.031	4.70	3894	1.11	−1.11	0.92	−0.31	1.124	1.149	0.11	0.702	0.063	3520	170	4.54	0.06
GJ887	M0.5V	5.79	0.503 ± 0.025	4.80	3645	1.61	−2.35	2.00	−0.68	1.366	1.388	0.04	0.491	0.014	3626	56	4.76	0.03
GJ191	M1V	7.08	0.281 ± 0.014	4.98	3419	1.76	−2.72	2.39	−0.82	0.681	0.692	0.06	0.291	0.025	3570	156	4.96	0.13
GJ551	M5.5V	8.80	0.123 ± 0.006	5.19	3006	1.94	−2.80	2.39	−0.81	1.023	1.044	0.08	0.145	0.011	3042	117	5.20	0.23
GJ699	M4V	8.21	0.158 ± .008	5.11	3193	1.87	−2.88	2.54	−0.88	0.987	1.004	0.04	0.196	0.008	3163	65	5.05	0.09
GJ15A	M2V	6.27	0.414 ± .021	4.87	3541	1.66	−2.48	2.14	−0.73	0.984	1.000	0.05	0.383	0.02	3698	95	4.89	0.06
GJ411	M1.5V	6.33	0.403 ± .020	4.88	3533	1.67	−2.50	2.16	−0.73	1.413	1.436	0.03	0.393	0.008	3570	42	4.85	0.03
GJ380	K7V	4.77	0.670 ± .033*	4.65	4106	1.09	−1.01	0.83	−0.28	1.268	1.155	0.04	0.605	0.02	–	–	4.70	0.03
GJ105A	K3V	4.17	0.790 ± .039*	4.56	4603	0.86	−0.53	0.38	−0.13	0.914	0.936	0.07	0.708	0.05	–	–	4.63	0.05

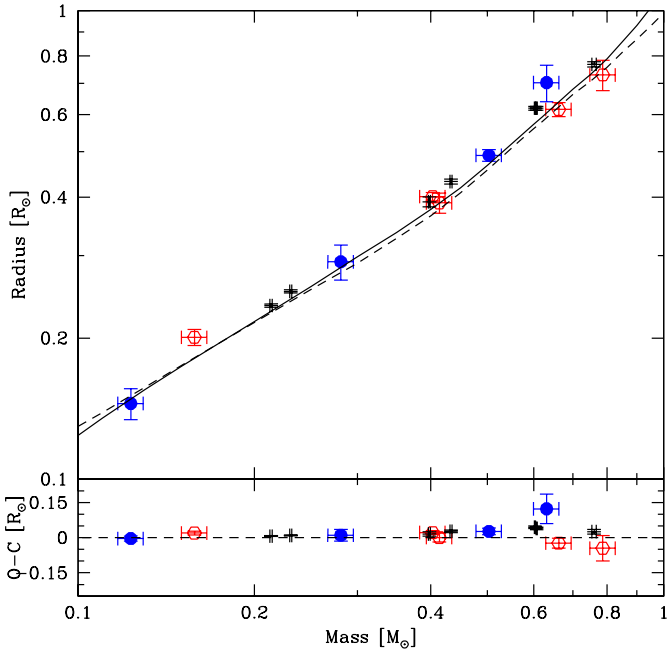

Fig. 3. Comparison between observational radii & masses measurements and the theoretical mass-radius relation. The solid and dashed curves are the 5 Gyr and 0.4–1 Gyr theoretical isochrones of Baraffe et al. (1998), which do not differ much over the present mass range. The filled circles are radius measurements from this paper, the open circles are PTI measurements by Lane et al. (2001), and the dots are masses and radii of three eclipsing binaries (Metcalfe et al. 1996; Torres & Ribas 2002; Ribas 2002). The error bars and the residuals from the model are shown at the bottom of the figure.

the VLTI interferometer, with a recombiner that was specified to validate and debug the interferometer, and not for an optimum scientific output. With the improvements expected from the near infrared scientific recombiner, AMBER (Petrov et al. 2001), from adaptive optics on the unit telescopes, the VLTI will measure dozens of M dwarfs with 0.1–1% accuracy. This will bring very strong observational constraints on models of both stellar interiors and atmospheres.

Acknowledgements. This research has made use of the SIMBAD database operated by CDS, Strasbourg, France. D.S. acknowledges the support of the *Fonds National Suisse de la Recherche Scientifique*. We thank the VLTI team for the commissioning and the data acquisition.

References

Allard, F., Hauschildt, P. H., Alexander, D. R., & Starrfield, S. 1997, ARA&A, 35, 137
Andersen, J. 1991, A&A Rev., 3, 91
Baraffe, I., Chabrier, G., Allard, F., & Hauschildt, P. H. 1998, A&A, 337, 403
Chabrier, G., & Baraffe, I. 2000, ARA&A, 38, 337
Claret, A. 2000, A&A, 363, 1081
Cohen, M., Walker, R. G., Carter, B., et al. 1999, AJ, 117, 1864
Coudé du Foresto, V., Perrin, G., Ruilier, C., et al. 1998, in Astronomical Interferometry, Proc. SPIE, 3350, 856
Coudé du Foresto, V., Ridgway, S., & Mariotti, J. 1997, A&AS, 121, 379
Davis, J., Tango, W. J., & Booth, A. J. 2000, MNRAS, 318, 387
Delfosse, X., Forveille, T., Ségransan, D., et al. 2000, A&A, 364, 217
Farge, M. 1992, Annual Review of Fluid Mechanics, 24, 395
Glindemann, A., Ballester, P., Bauvir, B., et al. 2001, The Messenger, 106, 1
Kervella, P., Coudé du Foresto, V., Glindemann, A., & Hofmann, R. 2000, in Interferometry in Optical Astronomy, Proc. SPIE, 4006, 31
Lane, B. F., Boden, A. F., & Kulkarni, S. R. 2001, ApJ, 551, L81
Leggett, S. K., Allard, F., Dahn, C., et al. 2000, ApJ, 535, 965
Metcalfe, T. S., Mathieu, R. D., Latham, D. W., & Torres, G. 1996, ApJ, 456, 356
Petrov, R. G., Malbet, F., Weigelt, G., et al. 2001, in SF2A-2001: Semaine de l'Astrophysique Française, 615
Ribas, I. 2002, A&A, accepted
Ségransan, D., Forveille, T., Millan-Gabet, C. P. R., & Traub, W. A. 1999, in Working on the Fringe: Optical and IR Interferometry from Ground and Space, ASP Conf. Ser., 194, 290
Sandrock, S., Amestica, R., Duhoux, P., Navarrete, J., & Sarazin, M. S. 2000, in Advanced Telescope and Instrumentation Control Software, Proc. SPIE, 4009, 338
Ségransan, D., Delfosse, X., Forveille, T., et al. 2003, in Brown Dwarfs, IAU Symp., 211, 211
Torres, G., & Ribas, I. 2002, ApJ, 567, 1140

3.2 Interférométrie et astérosismologie

Dans l'article rapportant nos mesures interférométriques à haute précision de α Cen A et B (reproduit à la Sect. 3.2.1), je présente le premier rapprochement de l'interférométrie et de l'astérosismologie.

Ces deux techniques sont remarquablement complémentaires pour l'étude des intérieurs et de l'évolution stellaires, par la nature même de leurs observables. L'astérosismologie permet ainsi d'accéder, via la grande séparation $\Delta\nu_0$, à la *densité* de l'étoile. Une mesure interférométrique du diamètre angulaire couplée à la parallaxe donne le rayon photosphérique, et donc le *volume* de l'étoile (la parallaxe *Hipparcos* est très précise pour les étoiles proches considérées). On obtient ainsi, par une simple multiplication, une excellente estimation de la masse de l'étoile.

Par ailleurs, la connaissance du diamètre linéaire de l'étoile se traduit dans le diagramme Hertzsprung-Russell par une "boite d'incertitude" beaucoup plus petite que les contraintes habituelles de température effective et de flux bolométrique. Ceci permet une estimation précise de l'âge et de l'état évolutif de l'étoile par cette nouvelle contrainte. Nous avons aussi appliqué cette méthode à Procyon (Sect. 3.2.2), δ Eri, ξ Hya et η Boo (Sect. 3.2.3).

3.2.1 Article A&A : "The diameters of α Centauri A and B. A comparison of the asteroseismic and VINCI/VLTI views" (2003)

Grâce à une bonne adaptation de la longueur des bases utilisées pour les observations de α Cen A et B rapportées dans cet article, nous avons pu obtenir des mesures de leurs diamètres angulaires d'une précision remarquable : respectivement 0,2 et 0,6%. Couplés aux mesures sismiques existantes, les diamètres obtenus nous ont permis de conclure que α Cen B a une masse relativement faible de 0,91 $M_\odot$. Les mesures de visibilité de α Cen A et B présentées dans cet article (Fig. 6 et 7) ont été reproduites en couverture du journal A&A.

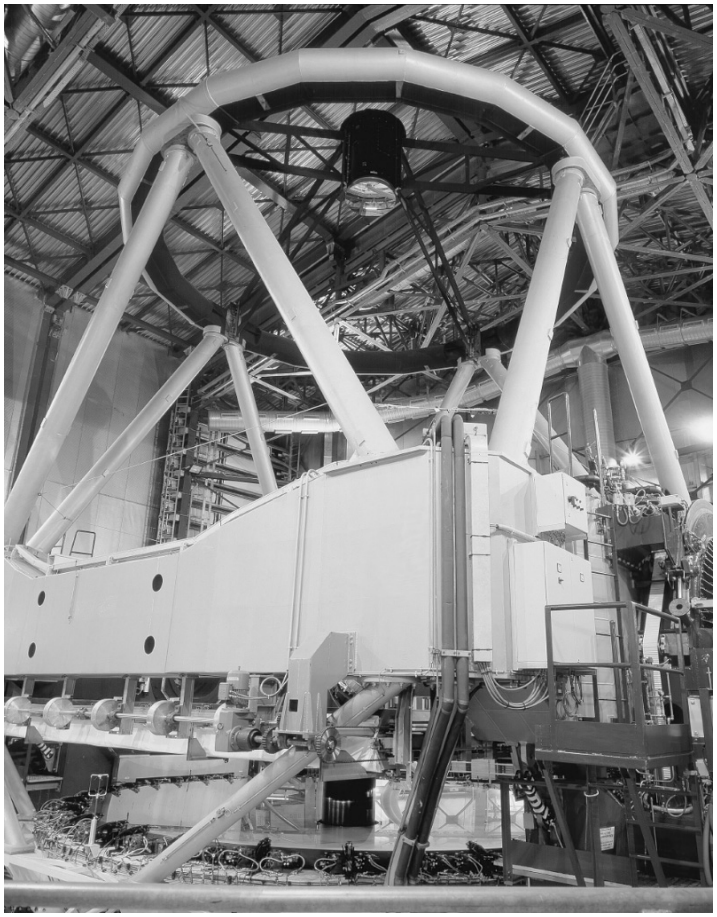

FIG. 3.3 – Un des télescopes unitaires de 8m du Very Large Telescope.

A&A 404, 1087–1097 (2003)
DOI: 10.1051/0004-6361:20030570

Astronomy & Astrophysics

The diameters of α Centauri A and B

A comparison of the asteroseismic and VINCI/VLTI views

P. Kervella[1], F. Thévenin[2], D. Ségransan[3], G. Berthomieu[2], B. Lopez[4], P. Morel[2], and J. Provost[2]

[1] European Southern Observatory, Alonso de Cordova 3107, Casilla 19001, Santiago 19, Chile
[2] Département Cassini, UMR CNRS 6529, Observatoire de la Côte d'Azur, BP 4229, 06304 Nice Cedex 4, France
[3] Observatoire de Genève, 1290 Sauverny, Switzerland
[4] Département Fresnel, UMR CNRS 6528, Observatoire de la Côte d'Azur, BP 4229, 06304 Nice Cedex 4, France

Received 20 January 2003 / Accepted 9 April 2003

Abstract. We compare the first direct angular diameter measurements obtained on our closest stellar neighbour, α Centauri, to recent model diameters constrained by asteroseismic observations. Using the VINCI instrument installed at ESO's VLT Interferometer (VLTI), the angular diameters of the two main components of the system, α Cen A and B, were measured with a relative precision of 0.2% and 0.6% respectively. Particular care has been taken in the calibration of these measurements, considering that VINCI is estimating the fringe visibility using a broadband K filter. We obtain uniform disk angular diameters for α Cen A and B of $\theta_{\rm UD}$[A] = 8.314 ± 0.016 mas and $\theta_{\rm UD}$[B] = 5.856 ± 0.027 mas, and limb darkened angular diameters of $\theta_{\rm LD}$[A] = 8.511 ± 0.020 mas and $\theta_{\rm LD}$[B] = 6.001 ± 0.034 mas. Combining these values with the parallax from Söderhjelm (1999), we derive linear diameters of D[A] = 1.224 ± 0.003 $D_\odot$ and D[B] = 0.863 ± 0.005 $D_\odot$. These values are compatible with the masses published by Thévenin et al. (2002) for both stars.

Key words. techniques: interferometric – stars: binaries: visual – stars: evolution – stars: oscillations – stars: fundamental parameters – stars: individual: α Cen

1. Introduction

The α Centauri triple star system is our closest stellar neighbour. The main components are G2V and K1V solar-like stars, while the third member is the red dwarf *Proxima* (M5.5V). α Cen A (HD 128620) and B (HD 128621) offer the unique possibility to study the stellar physics at play in conditions just slightly different from the solar ones. Their masses bracket nicely the Sun's value, while they are slightly older. In spite of their high interest, proximity and brightness, the two main components have never been resolved by long baseline stellar interferometry, due to their particularly southern position in the sky. We report in this paper the first direct measurement of their angular diameters. As a remark, the angular diameter of *Proxima* has also been measured recently for the first time ($\theta_{\rm LD}$ = 1.02 ± 0.08 mas) using two 8-meters Unit Telescopes and the VINCI instrument (Ségransan et al. 2003).

More than fourty years after the discovery of the solar seismic frequencies by Leighton (1960), and Evans & Michard (1962), solar-like *p* oscillations have been identified on α Cen A & B by Bouchy & Carrier (2001, 2002) with the CORALIE fiber-fed spectrograph. Today, asteroseismic frequencies have been detected in several additional stars. All these observations provide constraints, on one hand on stellar interior studies, and on the other hand on macroscopic stellar parameters like mass and radius. Several binary systems like α Cen (see Morel et al. 2001 for references) have been calibrated using spectro-photometry constraints. Recently, α Cen A has been calibrated using photometry, astrometry, spectroscopy and asteroseismic frequencies (Thévenin et al. 2002). These authors derived the age of the couple, the initial helium abundance $Y_{\rm i}$, and the radii of both stars. This calibration was based on stellar evolution models computed using the CESAM code (Morel 1997). One of the main results of this calibration was to constrain the masses of both stars, and in particular the mass of B. It had to be diminished by 3%, compared to the mass proposed by Pourbaix et al. (2002), leading to a smaller diameter of the star B. The high precision interferometric measurements of the angular diameters of α Cen A and B with VINCI/VLTI are a direct test of these refined models.

Send offprint requests to: P. Kervella,
e-mail: pierre.kervella@eso.org

2. Depscription of the instrument

2.1. The VLT Interferometer and VINCI

The European Southern Observatory's Very Large Telescope Interferometer (Glindemann et al. 2000) is operated on top of the Cerro Paranal, in Northern Chile, since March 2001.

In its current state of completion, the light coming from two telescopes can be combined coherently in VINCI, the VLT Interferometer Commissioning Instrument (Kervella et al. 2000, 2003a), or in the mid-infrared instrument MIDI (Leinert et al. 2000). A three ways beam combiner, AMBER (Petrov et al. 2000), will soon be installed in addition to these instruments. VINCI uses in general a regular K band filter (λ = 2.0−2.4 μm), as this was the case for our α Cen observations, but can also be operated in the H band (λ = 1.4−1.8 μm) using an integrated optics beam combiner (Berger et al. 2001). The K band setup effective wavelength changes slightly, depending on the spectral type of the observed target, between 2.174 and 2.184 μm for $3000 \leq T_{\rm eff} \leq 100\,000$ K. For α Cen A and B, $\lambda_{\rm eff} = 2.178 \pm 0.003$ μm (see Sect. 3.3 for details).

2.2. Interferometer configuration

We used as primary light collectors the two 0.35 m Test Siderostats of the VLTI. After being delayed by the VLTI optical delay lines, the stellar light was recombined in the interferometric laboratory using the VINCI instrument. A large number of baselines are accessible on the Cerro Paranal summit. Two of them were used for this study: E0-G0 and E0-G1, respectively of 16 and 66 meters ground length. The 16 m baseline observations were obtained during the early commissioning phase, from two days to a few weeks after the first fringes in March 2001. At the time, the effective aperture of the siderostats was limited to 0.10 m due to the unavailability of optical beam compression devices. Later in 2001, their installation allowed to recover the full 0.35 m primary mirror aperture of the siderostats, and all the 66 m baseline observations reported here were done with the full mirror. The shorter 16 m baseline is useful in the case of α Cen A to determine unequivocally the position of the 66 m measurements on the visibility curve, but does not bring a significant contribution to the final angular diameter precision (see Sect. 7).

2.3. Visibility calibration

During observations, the interferometric efficiency (visibility produced by the system when observing a point source) varies slowly over a timescale of hours. This means that the scientific target observations have to be calibrated periodically using observations of a star with a known angular diameter. The data reduction software of VINCI yields accurate estimates of the squared modulus of the coherence factor μ^2, which is linked to the object visibility V by the relationship

$$V^2 = \frac{\mu^2}{T^2} \tag{1}$$

where T is the interferometric efficiency. T is estimated by bracketing the science target with observations of calibrator stars whose V is supposed to be known a priori. The precision of our knowledge of the calibrator's angular diameter is therefore decisive for the final quality of the calibrated visibility value. For our observations, we have applied a constant transfer function T^2 between calibrator stars. This assumption has been validated during routine VLTI observations. A detailed description of the calibration observations can be found in Sect. 4.

3. Data processing

3.1. Data processing algorithm

We used a customized version of the standard VINCI data reduction pipeline (Kervella et al. 2003b), whose general principle is based on the original FLUOR algorithm (Coudé du Foresto et al. 1997). The two calibrated output interferograms are subtracted to remove residual photometric fluctuations. We implemented in this code a time-frequency analysis (Ségransan et al. 1999) based on the continuous wavelet transform (Farge 1992). Instead of the projection of the signal onto a sine wave of the Fourier transform, the wavelet transform decomposes it onto a function, i.e. the wavelet, that is localised in both time and frequency. We used as a basis the Morlet wavelet, a Gaussian envelope multiplied by a sinus wave. With the proper choice of the number of oscillations inside the Gaussian envelope, the Morlet wavelet closely matches a VINCI interferogram. It is therefore very efficient at localizing the signal in both time and frequency.

3.2. Data quality control

In spite of the relatively high modulation frequency of the fringes (296 Hz for the 66m baseline measurements), a fraction of the recorded interferograms present a differential piston signature between the two apertures. This is due to the relatively low coherence time observed at Paranal (1–4 ms at λ = 500 nm). These interferograms are rejected in the VINCI data processing by comparing the frequency of the measured fringe peak with the expected frequency from the K band filter of VINCI. If the measured fringe frequency is different by more than 20% from the expected frequency, the interferogram is ignored. The fringe packet extensions in the time and frequency domains are also used for the selection. This process allows to keep only the best quality interferograms and reduces the final dispersion of the visibilities. Finally, we rejected the observations that presented an abnormally low photometric signal to noise ratio, that is a typical symptom of an inaccuracy in the pointing of the siderostats.

The total numbers of selected and processed interferograms are 7854 on α Cen A (2427 on the 66 m baseline and 5427 on the 16 m baseline) and 1833 on α Cen B (66 m baseline only). For the calibration of the α Cen observations, we processed 2998 interferograms of θ Cen. Several calibrators (including θ Cen) were used for the 16 m baseline measurements of α Cen A, for a total of 8059 processed interferograms. The separate measurement of θ Cen was achieved using 1750 interferograms of this star and 789 interferograms of the secondary calibrator 58 Hya.

After the processing of a series of interferograms (100 to 500 scans), the mean squared coherence factor is derived from the average wavelets power spectral density of the selected interferograms. Figure 1 shows the average wavelets

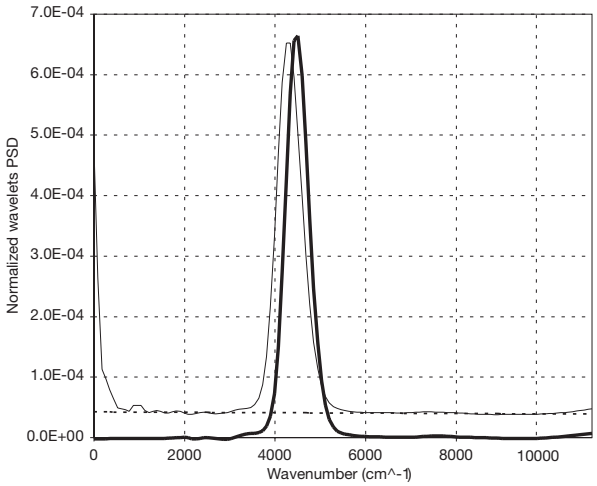

Fig. 1. Wavelets power spectral density (PSD) of a processed series of 418 interferograms obtained on α Cen A, before (thin line) and after (thick line) recentering of the fringe peak and subtraction of the background noise (dashed line).

power spectral density (PSD) of 418 processed interferograms, summed over the time extent of the fringe packet to obtain a one dimensional vector. In spite of the very low visibility of the fringes of α Cen A on the 66 m baseline ($V^2 \simeq 1\%$), the fringe peak is well defined.

The noise background (residual detector and photon shot noise) is estimated directly from the higher and lower frequencies of the average PSD of the interferogram, and then subtracted. As shown in Fig. 1, the subtraction is very efficient and gives a clean final PSD. The individual interferogram PSDs are summed after recentering of the fringe peak maximum, to reduce the power spread due to piston effect. This avoids that energy is lost in the integration process and allows a more precise estimation of the background level. We have chosen not to use the background removal method described by Perrin (2003), as we are simultaneously removing both the photon shot noise and detector noise contributions.

In Fig. 1, the recentered and background corrected fringe peak is shifted slightly towards higher wavenumber values due to the variation of α Cen A visibility over the K band. For simplicity reasons, the data reduction software assumes a fixed wavelength of 2.195 μm of the fringe peak maximum for the recentering process for all stars, but the exact target value has no effect on the final visibility.

3.3. Instrumental transmission

3.3.1. Transmission model

When using VINCI, the observations are carried out using a full K band filter, accepting the star light from 2.0 to 2.4 μm. In order to obtain a precise fit of the calibrated visibilities measured on sky, we computed the transmission of the interferometer taking into account the atmospheric transmission (Lord 1992), the fluoride glass optical fibers, the K band filter and the quantum efficiency of the HAWAII detector. This gave us a first approximation of the transmission of the interferometer $F_0(\lambda)$.

Table 1. Determination of the transmission correction slope γ of the VINCI/VLTI combination as observed on bright stars with two 8-meters telescopes.

	Peak position (μm)	γ (μm^{-1})
α PsA	2.198 ± 0.002	1.140
HR 8685 (1)	2.190 ± 0.003	0.911
HR 8685 (2)	2.202 ± 0.008	1.119
γ^2 Vol	2.198 ± 0.007	1.076
ϵ Eri	2.197 ± 0.010	1.065
39 Eri	2.196 ± 0.010	1.076
	Weighted average	1.076 ± 0.081

3.3.2. On-sky calibration

The instrumental uncertainties led us to compare directly this theoretical VINCI/VLTI transmission model to the real transmission of the system on sky. This has been achieved through the precise estimation of the effective wavenumber of a series of bright stars observations obtained with VINCI and two 8 meters Unit Telescopes (Table 1). A multiplicative slope γ (expressed in μm^{-1}) is superimposed to the theoretical transmission $F_0(\lambda)$ in order to match the observed average position of the PSD fringe peak. It is the only variable adjusted to match the observations. The photometric signal to noise ratio of the UTs observations being very high, we obtain a good precision on the average fringe peak frequency and thus on the estimation of γ, as shown in Table 1. The total photometric transmission of the interferometer $F(\lambda)$ is then given by:

$$F(\lambda) = \gamma(\lambda - \lambda_0)\, F_0(\lambda). \quad (2)$$

The reference wavelength λ_0 was set arbitrarily to 1.90 μm in our computation, but has no influence on the transmission calibration. $F(\lambda)$ is not normalized and gives only relative transmission values over the K band, but the absolute transmission is not needed to derive the model visibilities. It should be stressed that the sensitivity of the final angular diameter to γ is low, a ±0.08 μm^{-1} change of this parameter resulting only in a ±0.010 mas change on $\theta_{\rm UD}$ for α Cen A, and ±0.007 mas for B. These uncertainties were quadratically added to the final errors of the UD and LD angular diameter values given further in this paper. As a remark, we can also express this as a ±0.003 μm uncertainty on the average value of $\lambda_{\rm eff} = 2.178$ μm that we derive from $F(\lambda)$ for α Cen A and B.

3.3.3. Discussion

The observations of α Cen have been obtained with the siderostats, that have a slightly different optical setup than the UTs. There are 26 reflections for the UTs configuration in each arm of the interferometer, compared to 20 for the siderostats. Out of these, 15 mirrors are common between the two configurations. The remaining difference is therefore between the additional 11 reflections of the UTs and the additional 5 reflexions of the siderostats. Even assuming a very conservative mismatch of 1% between the extreme wavelengths reflectivity of each mirror of the UT train compared to the siderostats, we obtain a relative difference on γ of only 3%

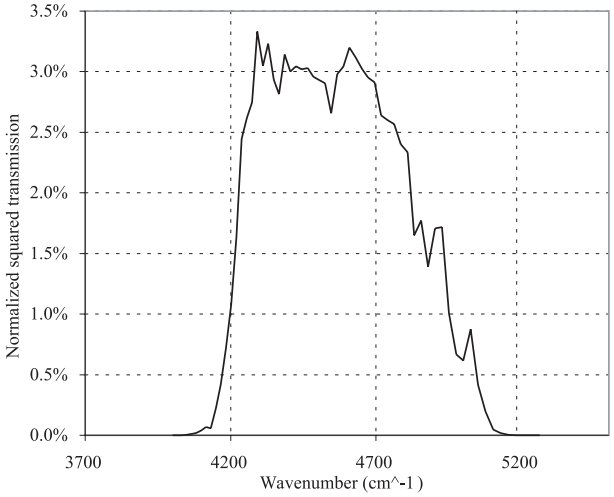

Fig. 2. Model PSD of α Cen A fringes for a zero baseline, including the spectrum of the star, atmosphere, fluoride glass fibers, *K* band filter, detector quantum efficiency and the correction function $F_1(\lambda)$ (see Sect. 3.3). A total precipitable water vapor of 3.0 mm (median for Paranal) is assumed for this plot. The curve for α Cen B is almost identical.

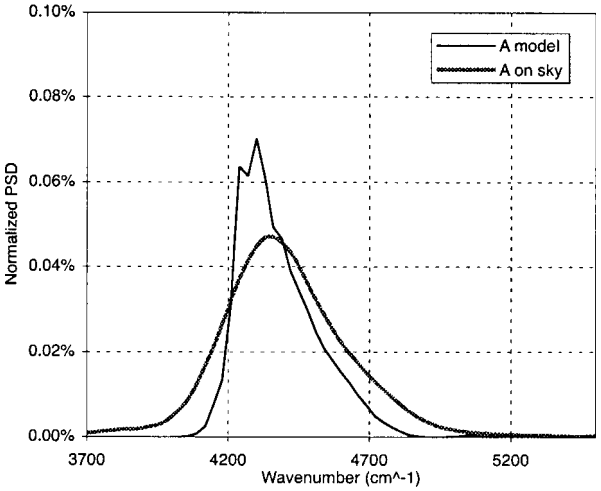

Fig. 3. Model (black line) and observed (grey line) PSDs of α Cen A fringes on the 66m baseline (61 m projected). The visibility loss for larger wavenumbers is clearly visible. The observed Fourier PSD, smoothed by the differential piston, shows the expected asymmetry. The on-sky and model vertical scales are arbitrary.

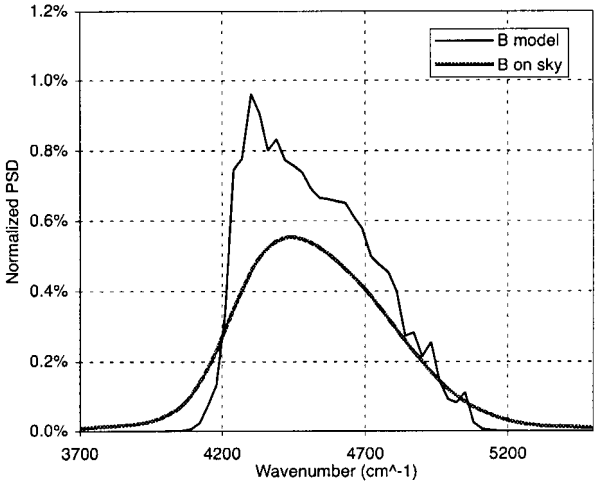

Fig. 4. Model (black line) and observed (grey line) PSDs of α Cen B fringes on the E0-G1 baseline. α Cen B being significantly less resolved than A, the squared visibility is more uniform over the *K* band than for α Cen A (Fig. 3). The asymmetry of the power spectrum is therefore smaller, though still present. The on-sky and model vertical scales are arbitrary.

that is significantly less than our quoted statistical uncertainty (7.5%). We have therefore considered this diffference negligible in our study.

A possible reason for the observed wavelength drift is the aging of the 20 mirror coatings necessary to bring the star light into the VINCI instrument (for each of the two beams). This process may have affected differentially the reflectivity of one end of the *K* band compared to the other. A difference in reflectivity of only 1% between the two extreme wavelengths will result in an 18% difference on the final transmission, after 20 mirrors (siderostats configuration). Also, the transmission curves provided by the manufacturer of the fiber optics used in VINCI do not have a sufficient precision to constrain accurately the instrument transmission model, and an error of several tens of percent is not to be excluded. To a lesser extent, the engineering grade HAWAII infrared array used in VINCI may have a quantum efficiency curve differing from the science grade versions by several percent. Finally, the MONA triple coupler used to recombine the light has also shown some birefringence during laboratory tests. This effect could result in a shift of the effective observation wavelength.

To secure the internal wavelength calibration of VINCI itself, crucial for the accuracy of the estimation of γ, we have obtained laboratory fringes with a *K* band laser ($\lambda = 2.304\ \mu$m). This gave us a precise wavelength reference to verify the scanning speed and the camera acquisition frequency.

3.3.4. Source spectrum

In addition to the constant term of the instrumental transmission, the shape of the source spectrum for each star was taken into account using its effective temperature. We computed synthetic spectra for α Cen A and B using Kurucz models, but considering the absence of any large absorption feature in the *K* band, we did not include spectral features in our final transmission model. The simulated spectrum of α Cen A fringes for a zero baseline is shown in Fig. 2.

3.4. Bandwidth smearing

An important effect of the relatively large spectral bandwidth of the VINCI filter is that several spatial frequencies are observed simultaneously by the interferometer. This effect is called *bandwidth smearing*. In the case of α Cen A, it is particularly strong as the visibilities are close to the first minimum of the visibility function, and this effect cannot be neglected. With a 60 m projected baseline, the short wavelength edge of the *K* band ($\lambda \simeq 2.0\ \mu$m) is already at the null of visibility, while the V^2 for the long wavelength edge ($\lambda \simeq 2.4\ \mu$m) is still

Table 2. Calibration observations of θ Cen and 58 Hya. The expected visibilities given in this table include the bandwidth smearing effect. The resulting interferometric efficiencies assumed for the calibration of the α Cen and θ Cen observations are given in bold characters, with the corresponding statistical and systematic error bars for each observing session. The calibrated visibilities can be found in Table 3 for θ Cen, and in Tables 5 and 6 for α Cen A and α Cen B.

JD − 2 450 000	Scans	B (m)	Azim. ($N = 0$)	μ^2 (%) ± stat. err.	Expected V^2 (%) ± syst. err.	IE (μ^2/V^2, %) ± stat. ± syst.	Target(s)
						52.08 ± 0.69 ± 0.63	θ Cen
2452.63024	45	65.2509	161.90	30.72 ± 0.75	58.90 ± 0.71	52.17 ± 1.27 ± 0.63	58 Hya
2452.63324	166	65.2011	162.55	31.56 ± 0.74	58.95 ± 0.71	53.54 ± 1.25 ± 0.64	58 Hya
2452.64109	269	65.0719	164.26	30.66 ± 0.31	59.08 ± 0.71	51.91 ± 0.52 ± 0.62	58 Hya
2452.64527	256	65.0047	165.18	30.73 ± 0.37	59.15 ± 0.71	51.95 ± 0.62 ± 0.62	58 Hya
						52.13 ± 0.69 ± 0.63	θ Cen
2452.67563	53	64.5970	174.54	31.42 ± 0.77	59.56 ± 0.70	52.77 ± 1.29 ± 0.62	58 Hya
2462.53152	389	65.7824	153.61	8.58 ± 0.17	18.13 ± 0.28	47.33 ± 0.93 ± 0.72	θ Cen
2462.60245	88	65.8892	168.69	8.63 ± 0.15	18.01 ± 0.27	47.94 ± 0.86 ± 0.73	θ Cen
						47.51 ± 0.49 ± 0.72	α Cen A, α Cen B
2462.60554	283	65.8801	169.39	8.46 ± 0.21	18.02 ± 0.27	46.97 ± 1.18 ± 0.72	θ Cen
2465.56068	94	65.9551	161.27	8.67 ± 0.14	17.93 ± 0.27	48.33 ± 0.80 ± 0.74	θ Cen
2465.56377	355	65.9541	161.93	8.58 ± 0.24	17.93 ± 0.27	47.87 ± 1.31 ± 0.73	θ Cen
2465.57390	241	65.9413	164.14	8.98 ± 0.50	17.95 ± 0.27	50.06 ± 2.80 ± 0.77	θ Cen
2465.57838	317	65.9320	165.13	8.85 ± 0.29	17.96 ± 0.27	49.31 ± 1.64 ± 0.75	θ Cen
						48.64 ± 1.50 ± 0.76	α Cen A, α Cen B
2465.65159	69	65.8006	1.99	9.35 ± 0.44	18.11 ± 0.28	51.66 ± 2.43 ± 0.79	θ Cen
2470.56229	87	65.9373	164.59	9.01 ± 0.13	17.95 ± 0.27	50.19 ± 0.73 ± 0.77	θ Cen
2470.56609	386	65.9289	165.43	9.00 ± 0.05	17.96 ± 0.27	50.09 ± 0.30 ± 0.77	θ Cen
2470.57010	341	65.9188	166.32	9.06 ± 0.15	17.97 ± 0.27	50.44 ± 0.83 ± 0.77	θ Cen
2470.57433	348	65.9073	167.27	8.73 ± 0.14	17.99 ± 0.27	48.53 ± 0.77 ± 0.74	θ Cen
						49.97 ± 0.87 ± 0.76	α Cen A, α Cen B

above 1%. The photons at the null of visibility have interfered destructively. Therefore, the fringe peak becomes very asymmetric in the PSD of the interferograms. As shown in Figs. 3 and 4, the observed and model PSDs agree well in general shape. The on-sky power spectrum is blurred by the differential piston and therefore appears "smoothed", but the characteristic asymmetry for low visibilities is clearly visible.

3.5. Baseline smearing

When the aperture of the light collectors is a significant fraction of the baseline, an effect similar to the bandwidth smearing appears on the visibility measurements. It comes from the fact that the baselines defined between different parts of the two primary mirrors cover a non-zero range of lengths and orientations. Therefore, several spatial frequencies are measured simultaneously by the beam combiner. In the case of the E0-G0 baseline (16 m) observations of α Cen A, the effective aperture was 0.10 m, and therefore the ratio of the primary mirror diameter to the baseline was only $D/B \approx 0.6\%$. For the E0-G1 baseline (66 m), this ratio is similar due to the larger 0.35 m apertures. Even in the difficult case of the α Cen A observations, this effect accounts at most for a relative shift of the visibility of 0.1%, to be compared to our relative systematic calibration error of 1.5%. In the case of α Cen B, we expect at most a 0.05% shift, for a relative systematic calibration error also of 1.5%. We have therefore neglected this effect in the rest of our study.

4. Calibration observations

The calibration of the interferometric efficiency (IE) of the interferometer is a critical step of the observations. We present in Table 2 the measurements that we obtained on the calibrators and the corresponding values of the IE for the three nights of observations of the α Cen pair (JD = 2 452 462-70) on the E0-G1 baseline, and the separate night used to measure θ Cen (JD = 2452452).

The primary calibrator θ Cen is located at a distance of 24 degrees from the α Cen pair, mostly in declination, while only 9 degrees separate θ Cen and the secondary calibrator 58 Hya. During the observations, the largest difference between the altitudes of θ Cen and α Cen happens at the crossing of the meridian, and is approximately 24 degrees (respective altitudes of about 55 and 80 degrees at Paranal). The airmasses of the two stars at meridian crossing are 1.25 and 1.03 respectively for α Cen and θ Cen. The difference is even smaller in the case of 58 Hya and θ Cen. As we obtained the E0-G1 baseline observations close to the meridian crossing, we do not expect any significant variation of IE due to the difference of airmass between the calibrators and the scientific targets.

5. The primary calibrator θ Centauri

The most important calibrator for the 66 meters baseline measurements is the giant star θ Cen (K0III). This calibrator was chosen for its stability and brightness in the list of standard stars compiled by Cohen et al. (1999) and verified by

Table 3. θ Cen squared visibilities.

JD − 2 450 000	B (m)	Azim. ($N = 0$)	V^2 (%) ± stat. ± syst.
E0-G1			
2452.60644	65.9464	163.49	17.74 ± 0.69 ± 0.21
2452.60943	65.9413	164.15	17.86 ± 0.36 ± 0.22
2452.61396	65.9318	165.15	17.72 ± 0.34 ± 0.21
2452.61906	65.9193	166.28	18.08 ± 0.29 ± 0.22
2452.65518	65.8220	174.54	18.20 ± 0.38 ± 0.22
2452.65855	65.8156	175.32	18.25 ± 0.40 ± 0.22
2452.66275	65.8088	176.30	18.08 ± 0.38 ± 0.22
2452.66685	65.8037	177.26	18.13 ± 0.39 ± 0.22

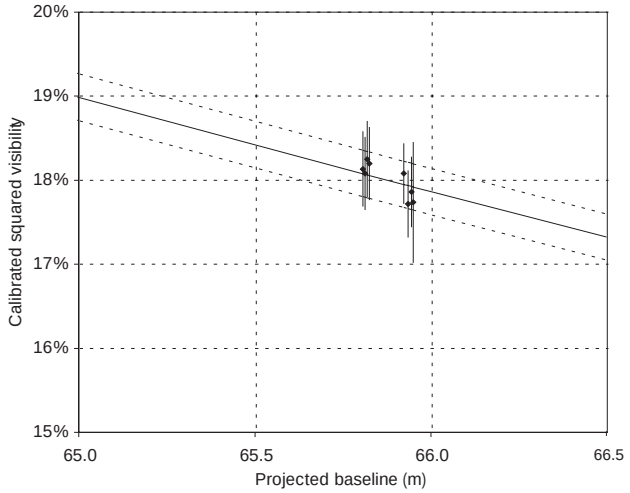

Fig. 5. Detail of θ Cen squared visibilities and uniform disk model. The continuous line is the UD diameter fit (5.305 ± 0.020 mas), and the dotted lines represent the limits of the $\pm 1\sigma$ error domain.

Bordé et al. (2002). This choice is critical in the sense that any departure of the true visibility of the calibrator from the assumed model will contaminate the calibrated visibility of the scientific target. This is the reason why one should avoid to use as calibrators pulsating variables (such as many M type giants, Cepheids,...), double or multiple stars, magnetically active objects (photospheric spots) or fast rotators (ellipticity of the star disk). The properties of all the stars listed in the Cohen et al. (1999) catalogue have been checked carefully and their diameters are believed to be constant to a very good accuracy. In addition, θ Cen is not classified as double, variable or active in any catalogue, and is a slow rotator ($V \sin i = 1.2$ km s^{-1}, Glebocki et al. 2000).

Unfortunately, the typical 1% precision of the Cohen et al. (1999) catalogue on the angular diameters, though very good in itself, is not sufficient due to the large size of this star and the correspondingly low visibility on the 66 meters baseline. After the first processing of our α Cen data, it appeared that the error bars on the final angular diameters were dominated by the systematic uncertainty on the angular size of θ Cen. Therefore, we reduced additional archived data obtained on θ Cen on a separate night, using the secondary calibrator 58 Hya and the 66 meters baseline. 58 Hya has a much smaller angular diameter than θ Cen and therefore provides a precise calibration

Table 4. Parameters of the primary (θ Cen) and secondary (58 Hya) calibrators.

	θ Cen HD 123139	58 Hya HD 130694
m_V	2.06	4.42
m_K	−0.10	1.13
Spectral type	K0IIIb	K4III
$T_{\rm eff}$ (K)[a]	4980	4040
Measurement λ (μm)	2.181	2.181
$\log g$ [a]	2.75	1.85
$\theta_{\rm LD}$ (mas)[b]	5.46 ± 0.058	3.22 ± 0.035
$\theta_{\rm UD}$ (mas)[c]	5.33 ± 0.057	3.12 ± 0.034
Measured $\theta_{\rm UD}$ (mas)	**5.305 ± 0.020**	

[a] $T_{\rm eff}$ and $\log g$ from Cayrel de Strobel et al. (1997).
[b] Catalogue value from Cohen et al. (1999).
[c] Linear limb darkening from Claret (2000).

of the interferometric efficiency. The calibrated squared visibility values obtained on θ Cen are listed in Table 3, and the angular diameter fit is shown in Fig. 5. The parameters for both stars and the measured uniform disk (UD) angular diameter of θ Cen are presented in Table 4. The VINCI/VLTI angular diameter found for this star agrees very well with the Cohen et al. (1999) value, while reducing significantly its uncertainty.

6. Calibrated visibilities

The list of the observations of α Cen A and B, with the resulting calibrated squared visibilities, is presented in Tables 5 and 6. The azimuth of the projected baseline is counted clockwise (cw) from north, and corresponds to the baseline orientation as seen from the star. Two error bars are given for each V^2 value:

- one statistical error bar, computed from the dispersion of the visibility values obtained during the observation,
- one systematic error bar defined by the uncertainty on the knowledge of the calibrator angular size.

While the statistical error can be diminished by repeatedly observing the target, the systematic error cannot be reduced by averaging measurements obtained using the same calibrator. This is taken into account in our model fitting by checking that the final uncertainty of the fit is larger than the systematic errors of each measured visibility value. This conservative approach ensures that we are not underestimating the systematic calibration errors.

7. Angular diameters

7.1. Uniform disk

Due to the spectrum shape variation with baseline described in Sect. 3.4, the classical monochromatic uniform disk (UD) model visibility curve is not applicable and can lead to very large UD size errors for low visibilities. We therefore adopted a direct fitting method in the broadband regime. For this

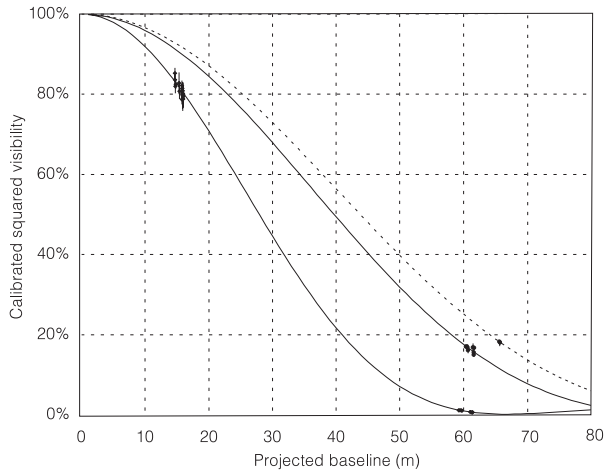

Fig. 6. Overview of the α Cen and θ Cen squared visibilities and UD models. From bottom to top: α Cen A, α Cen B and θ Cen (primary calibrator). The angular diameter of θ Cen was measured using 58 Hya as secondary calibrator.

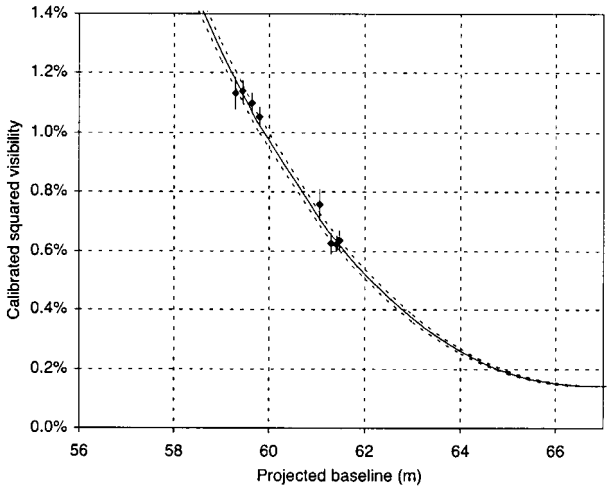

Fig. 7. Detail of α Cen A squared visibility. The continuous line is the uniform disk diameter fit (8.314 ± 0.016 mas), and the dotted lines represent the limits of the $\pm 1\sigma$ error domain. The visibility curve never goes to zero due to the bandwidth smearing effect.

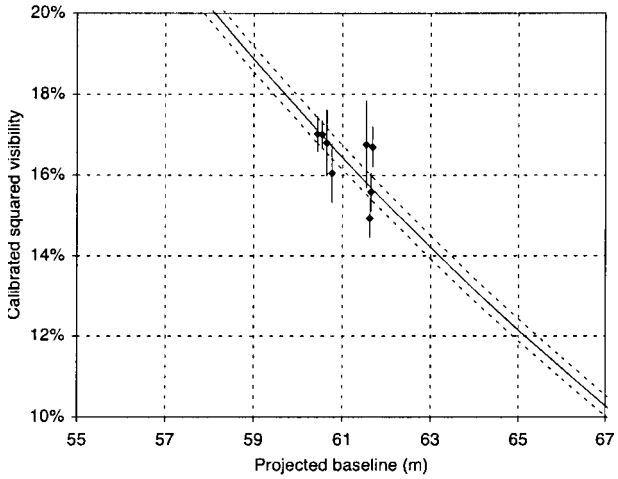

Fig. 8. Detail of α Cen B squared visibility. The continuous line is the uniform disk diameter fit (5.856 ± 0.027 mas), and the dotted lines represent the limits of the $\pm 1\sigma$ error domain.

Table 5. α Cen A squared visibilities, expressed in percents.

JD − 2 450 000	B (m)	Azim. ($N = 0$)	V^2 (%) ± stat. ± syst.
E0-G0			
1988.78108	15.9201	64.95	78.99 ± 1.48 ± 2.81
1988.78380	15.9071	65.79	79.61 ± 1.46 ± 2.83
1988.78652	15.8930	66.62	79.82 ± 1.42 ± 2.84
1988.78901	15.8793	67.39	79.80 ± 1.47 ± 2.84
1995.76493	15.9058	65.86	80.15 ± 1.03 ± 0.66
1996.63335	15.7916	24.31	78.66 ± 1.10 ± 0.42
1996.63970	15.8129	26.48	82.19 ± 1.12 ± 0.44
1996.64733	15.8390	29.06	80.33 ± 1.29 ± 0.43
1996.65492	15.8650	31.61	81.49 ± 1.15 ± 0.44
1996.67842	15.9399	39.40	80.87 ± 1.10 ± 0.43
1996.68327	15.9532	40.99	79.40 ± 1.10 ± 0.43
2001.80688	15.3644	83.76	80.71 ± 1.94 ± 0.05
2001.80954	15.3273	84.59	82.77 ± 2.69 ± 0.04
2002.70376	16.0062	52.80	78.76 ± 0.74 ± 0.05
2002.70640	16.0057	53.63	80.01 ± 1.07 ± 0.05
2003.83537	14.8150	94.44	82.49 ± 1.10 ± 0.05
2003.83780	14.7695	95.22	82.01 ± 1.80 ± 0.04
2003.84099	14.7088	96.25	85.30 ± 1.28 ± 0.05
2003.84356	14.6589	97.08	83.64 ± 1.77 ± 0.04
E0-G1			
2462.55258	59.2848	150.05	1.132 ± 0.051 ± 0.017
2462.55613	59.4391	150.91	1.139 ± 0.032 ± 0.017
2462.56087	59.6365	152.05	1.099 ± 0.031 ± 0.017
2462.56493	59.7975	153.04	1.054 ± 0.029 ± 0.016
2465.61044	61.2943	166.21	0.626 ± 0.035 ± 0.010
2470.58454	61.0497	163.19	0.758 ± 0.052 ± 0.012
2470.60337	61.4043	167.84	0.624 ± 0.023 ± 0.010
2470.60778	61.4696	168.93	0.637 ± 0.033 ± 0.010

Table 6. α Cen B squared visibilities.

JD − 2 450 000	B (m)	Azim. ($N = 0$)	V^2 (%) ± stat. ± syst.
E0-G1			
2462.58356	60.4413	157.57	17.02 ± 0.36 ± 0.26
2462.58697	60.5443	158.40	17.01 ± 0.23 ± 0.26
2462.59047	60.6453	159.26	16.80 ± 0.77 ± 0.26
2462.59490	60.7665	160.35	16.05 ± 0.68 ± 0.24
2465.62682	61.5409	170.27	16.76 ± 1.05 ± 0.26
2470.62033	61.6208	172.05	14.94 ± 0.44 ± 0.23
2470.62342	61.6500	172.82	15.59 ± 0.42 ± 0.24
2470.62783	61.6866	173.92	16.70 ± 0.44 ± 0.25

Table 7. Uniform disk angular diameters of α Cen A and B in the K band derived from the VINCI/VLTI observations.

	α Cen A	α Cen B
$\theta_{\rm UD}$ (mas)	8.314 ± 0.016	5.856 ± 0.027

purpose, the PSD of the stellar fringes is computed numerically over the K band using 10 nm spectral bins. We take here into account the total transmission of the interferometer

and the visibility of the fringes for each wavelength. The total power is then integrated and gives a numerical broadband visibility function ${V_K}^2(B, \theta_{\rm UD})$ where B is the projected baseline, and $\theta_{\rm UD}$ the UD angular diameter. To derive the α Cen UD diameters, we make a classical χ^2 minimization between our $(B, {V_K}^2)$ measurements and the ${V_K}^2(B, \theta_{\rm UD})$ function while changing the value of $\theta_{\rm UD}$.

Figure 6 shows the complete visibility curve of the UD model fit to the α Cen data, together with the primary calibrator θ Cen. The detail of the visibility curve of α Cen A shown in Fig. 7 demonstrates that the visibility never goes down to zero for any baseline, due to the bandwidth smearing effect. The minimum squared visibility is 0.15%, for a baseline length of aproximately 66.5 m. Figure 8 shows an enlargement of the visibility points obtained on α Cen B. The final UD angular diameters for the two stars and the corresponding effective wavelengths are given in Table 7.

7.2. Limb darkened angular diameters

In this section, we describe two methods to compute the LD angular diameter: through a conversion factor (classical approach), and through a visibility fit taking directly the limb darkening into account.

7.2.1. LD/UD conversion factor

The simplest approach to retrieve the limb darkened diameter from an interferometric UD measurement goes through the computation of the conversion factor ρ defined by:

$$\rho = \frac{\theta_{\rm LD}}{\theta_{\rm UD}} \tag{3}$$

ρ is deduced from stellar atmosphere luminosity profiles that are computed using radiative transfer modeling codes. These profiles are published in tables as a function of the wavelength band (e.g. Claret 2000). One limitation of the description of the LD visibility curve of the star by a single parameter is that it assumes that the visibility curve of the UD and LD models have the same intrinsic shape. This is not exactly the case near and especially after the first minimum of the visibility function. However, this approximation is satisfactory for compact stellar atmospheres such as the ones of α Cen stars. Hanbury Brown et al. (1974) have shown that the linear limb darkening coefficient u can be translated into the conversion factor ρ through the approximate formula:

$$\rho = \sqrt{\frac{1 - u/3}{1 - 7u/15}}. \tag{4}$$

These authors quote a maximum error of ±0.2% for this approximate formula, that is in general very satisfactory, but for the particular case of α Cen A, this uncertainty is comparable to our final error bar on the UD diameter. Different values of linear limb darkening conversion factors are given in Table 8, based on successive versions of the Claret et al. models (1995, 1998, 2000). Except for the older Claret (1995) values, that do not take metallicity and turbulence velocity into account, the two other results are very close to each other.

Table 8. Linear LD/UD conversion factors for α Centauri. The assumed physical parameters to match Claret's (2000) grid are the closest ones to those of Thévenin et al. (2002).

Model from Claret (2000)	α Cen A	α Cen B
$T_{\rm eff}$ (K)	5750	5250
$\log(g)$ (cm s^{-2})	4.5	4.5
$\log(M/H)$ (dex)	0.2	0.2
V_T (km s^{-1})	2.0	2.0
Reference	$\rho_{\rm A}$	$\rho_{\rm B}$
Claret et al. (1995)	102.047%	102.299%
Claret (1998)	102.388%	102.723%
Claret (2000)	102.355%	102.635%

In order to account for a possible systematic error in the determination of the limb darkening parameter, we allow a ±0.1% uncertainty to propagate into the computation of the limb darkened diameter of α Cen. It should be noted that the coefficients for both stars originate from the same Kurucz's model atmosphere computations of Claret (2000), and are therefore likely to have a good intrinsic consistency.

7.2.2. Limb darkened disk visibility fit

Hestroffer (1997) has chosen another approach by computing the analytical expression of the visibility function for a single-parameter power law intensity profile $I_\lambda(\mu) = \mu^\alpha$ (with $\alpha \geq 0$) where $\mu = \cos(\theta)$ is the cosine of the azimuth of a surface element of the star. This simplification allows this author to derive the analytical expression of the visibility function corresponding to a power law limb darkened disk:

$$V_\nu(x) = \Gamma(\nu + 1)\frac{J_\nu(x)}{(x/2)^\nu} \tag{5}$$

where $x = \pi B\theta/\lambda$ is the spatial frequency, $\nu = \alpha/2+1$, and $J_\nu(x)$ is the Bessel function of the first kind. As the intensity profiles produced by the most recent atmosphere models are close to power laws, as shown in Fig. 9, the power law fitting procedure gives good results. Claret (2000) has computed a four parameters law that aproximates very well the most recent Kurucz models for observations in the K band. Using this law gives a value of $\alpha = 0.1417$ for α Cen A and $\alpha = 0.1598$ for α Cen B.

The final precision on ρ is better than with the previous linear approximation, but as for the conversion coefficient approach presented in Sect. 7.2.1, we propagate an uncertainty of ±0.1% to the final LD angular diameter to account for a possible bias.

Practically, the fit is achieved on the calibrated visibilities listed in Tables 5 and 6 by a classical χ^2 minimization procedure. The product of this fit is directly the LD angular diameter of the star, without the intermediate step of the uniform disk model.

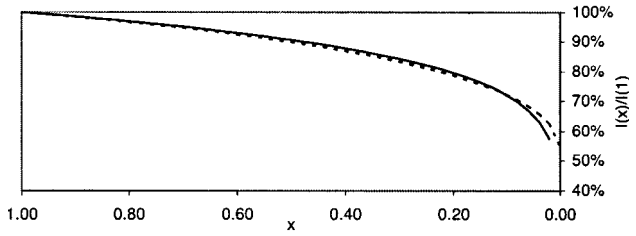

Fig. 9. Intensity profile of α Cen A from the four-parameters limb darkening law of Claret (2000) (dashed line) and the corresponding $\alpha = 0.1417$ power law.

Table 9. Summary of limb-darkened angular diameters from different computation methods. Both methods are based on the Claret (2000) coefficients. The fitting results using the analytical Hestroffer (1997) formula are assumed in the rest of this paper.

LD computation method	α Cen A (mas)
Hanbury Brown et al. (1974)	8.517 ± 0.021
Hestroffer (1997) analytical	**8.511 ± 0.020**
	α Cen B (mas)
Hanbury Brown et al. (1974)	6.010 ± 0.030
Hestroffer (1997) analytical	**6.001 ± 0.034**

7.3. Rotational distortions

As the VINCI/VLTI measurements have been obtained mostly at the same azimuth (roughly N-S), a possible source of bias could be the presence of flattening on the stellar disks due to rotational distortion. The estimated equatorial rotation periods for α Cen A and B are 22 and 41 days respectively (Morel et al. 2000), bracketing the solar value. The corresponding small rotational velocities rule out any flattening at a significant level, and therefore no correction has been applied to our measurements.

7.4. Summary of angular diameter values

Table 9 gives the limb darkened angular diameters derived from the LD/UD conversion factors and from the analytical LD visibility function (Hestroffer 1997). This last method is assumed in the following sections. All values take the bandwidth smearing effect into account.

8. Comparison of asteroseismic and interferometric linear diameters

8.1. Parallax from the literature

To convert the angular diameter into a linear value, it is necessary to know the parallax of the star. The α Cen system being very nearby ($D = 1.3$ pc), the precision on the measurement of its trigonometric parallax is potentially very good. Unfortunately, some discrepancies have appeared between the most recently published values (Table 10). In particular, the original *Hipparcos* parallax (Perryman et al. 1997) and the value by Pourbaix et al. (1999) are significantly different from the reprocessing of the *Hipparcos* data by Söderhjelm (1999), by more than 3σ. A difficulty with the *Hipparcos* satellite measurement is due to the large brightness of the α Cen pair. The light from one of the stars possibly contaminated the measurement on the other, leading to a systematic bias that may not have been propagated properly to the final error bars. In Sect. 8.2, we adopt the parallax value from Söderhjelm (1999), who took this effect into account.

Table 10. Parallax values of α Cen from the litterature.

Value (mas)	Author
750	Heintz (1958, 1982)
749 ± 5	Kamper & Wesselink (1978)
750.6 ± 4.6	Demarque et al. (1986)
742.1 ± 1.4	Perryman et al. (1997)
737.0 ± 2.6	Pourbaix et al. (1999)
747.1 ± 1.2	Söderhjelm (1999)

As a remark, the semi-major axis of the orbit of the two stars $a = 17.59 \pm 0.03$ AU (Pourbaix et al. 1999) is totally negligible compared to the distance D to the couple ($a/D = 0.006\%$), therefore the two stars can be considered at the same distance.

8.2. Linear diameters

Considering the parallax of 747.1 ± 1.2 mas from Söderhjelm (1999), it is now possible to compute the linear diameters of α Cen A and B (in solar units) from the two LD angular diameters determined interferometrically. They are found to be:

$$D[\mathrm{A}] = 1.224 \pm 0.003\ D_\odot \quad (6)$$

$$D[\mathrm{B}] = 0.863 \pm 0.005\ D_\odot \quad (7)$$

and can be compared to the linear diameters proposed by Thévenin et al. (2002):

$$D[\mathrm{A}] = 1.230 \pm 0.003\ D_\odot \quad (8)$$

$$D[\mathrm{B}] = 0.857 \pm 0.007\ D_\odot \quad (9)$$

The theoretical diameters are only $+1.3\sigma$ and -0.7σ away from the observed values. Both interferometric diameters and those deduced from the photometric calibration constrained by asteroseismic frequencies therefore agree very well.

These two model diameters are derived using the CESAM code, and are defined as the radii at which the temperature in the atmosphere is equal to the effective temperature of the star. Computing the layer where the continuum at 2.2 μm is formed leads to temperatures close to $T_{\rm eff}$, therefore the CESAM diameters can be directly compared to those measured by the VLTI at 2.2 μm.

8.3. Self consistent parallax

From our angular diameter measurements and the asteroseismic diameter estimations, we can also derive directly the parallax of the couple. The simple formula linking the limb darkened angular diameter $\theta_{\rm LD}$ (in mas), the linear diameter D (in $D_\odot$) and the parallax π (in mas) is:

$$\theta_{\rm LD} = 9.305 \times 10^{-3}\ D\ \pi. \quad (10)$$

Table 11. Parallax of α Cen from VINCI/VLTI and asteroseismological observations, and the corresponding self-consistent stellar parameters. Linear diameters are taken from the asteroseismology study by Thévenin et al. (2002).

Derived parallax	745.3 ± 2.5 mas	
	α Cen A	α Cen B
VINCI LD size (mas)	8.511 ± 0.020	6.001 ± 0.034
Model LD size (mas)	8.530 ± 0.035	5.943 ± 0.052
VINCI diameter ($D_\odot$)	1.227 ± 0.005	0.865 ± 0.006
Model diameter ($D_\odot$)	1.230 ± 0.003	0.857 ± 0.007

A least squares fit is computed between the LD angular diameters from the VLTI and the linear diameters from Thévenin et al. (2002). We find an optimal parallax of 745.3 ± 2.5 mas, that differs slightly from the original *Hipparcos* value by $+1.1\sigma$ (Perryman et al. 1997), from Pourbaix et al. (1999) by $+2.3\sigma$, and from Söderhjelm (1999) by only -0.7σ. The resulting values of angular and linear diameters are given in Table 11. The difference between theoretical and linear diameters for the self-consistent parallax is limited to $+0.5\sigma$ and -0.9σ, respectively for α Cen A and B.

8.4. Ratio of α Cen A and B radii

Contrary to the linear diameters themselves, their ratio is independent of the actual parallax of the system. Therefore, part of the systematic uncertainties can be removed by using this observable as a comparison basis between the observations and the models. For α Cen A and B, we have access to a very good quality parallax, and the uncertainty introduced there is relatively small. On the other hand, when measuring a farther double or multiple star, the parallax may be unknown, or known only with a bad precision. In this case, comparing the ratio of the stellar diameters will give much stronger constraints to the stellar structure models than the individual values. This technique is also applicable to the interferometric measurement of stars in clusters, within which the distance can be assumed to be uniform. From the limb-darkened values listed in Table 9, we obtain the following ratio between the angular diameters of α Cen A and B:

$$\frac{\theta_{\rm LD}[{\rm A}]}{\theta_{\rm LD}[{\rm B}]} = 1.418 \pm 0.009. \quad (11)$$

This value can be compared to the ratio of linear radii from the Thévenin et al. (2002) models that is:

$$\frac{R[{\rm A}]}{R[{\rm B}]} = 1.435 \pm 0.014. \quad (12)$$

We therefore find a slight diameter excess of α Cen B at a level of 1.0σ.

8.5. Masses and evolutionary models

As emphasized by Thévenin et al. (2002), the seismological analysis gives strong constraints on masses and on the age of the system when combined with spectro-photometric measurements. To achieve this, one derives from the set of oscillation frequencies, one "large" and two "small" frequency spacings. The large frequency spacing is a difference between frequencies of modes with consecutive radial order n: $\Delta\nu_\ell(n) \equiv \nu_{n,\ell} - \nu_{n-1,\ell}$. In the high frequency range, i.e. large radial orders, $\Delta\nu_\ell$ is almost constant with a mean value $\Delta\nu_0$, strongly related to the mean density of the star, i.e. to the mass and the radius. The small separations are very sensitive to the physical conditions in the core of the star and consequently to its age. These frequencies measured for the star A have largely forced the spectro-photometric calibration to decrease the masses of the stellar system α Cen, leading to the following values: $M_{\rm A} = 1.100 \pm 0.006\, M_\odot$ and $M_{\rm B} = 0.907 \pm 0.006\, M_\odot$ (Thévenin et al. 2002) close to those adopted by Guenther & Demarque (2000) and Kim (2000). The mass of the B component departs significantly by 3% from the value published by Pourbaix et al. (2002).

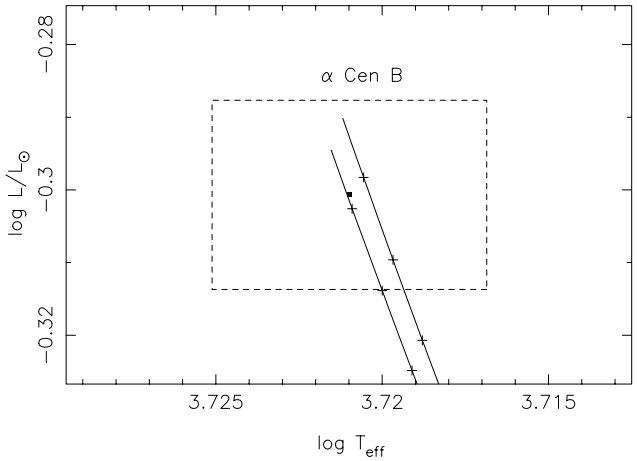

Fig. 10. HR diagram of α Cen B. The line on the right corresponds to a mixing length of $\lambda = 0.96$ and a mass of 0.909 $M_\odot$, the line on the left corresponds to the values published in Thévenin et al. 2002 ($\lambda = 0.98$, 0.907 $M_\odot$).

Using the orbital properties of the binary and also spectro-velocimetric curves, Pourbaix et al. (2002) have derived the masses of each components ($M_{\rm A} = 1.105 \pm 0.007\, M_\odot$, $M_{\rm B} = 0.934 \pm 0.006\, M_\odot$). We note that Thoul et al. (2003) have recently proposed a model of the binary system using these masses and spectro-photometric constraints different from that of Thévenin et al. (2002). They were able to reproduce the seismic frequencies of α Cen A, but the model they propose does not take into account the helium and heavy elements diffusion.

Because the interferometric diameter of α Cen B is a little larger than those deduced from the CESAM model, we explored the possibility to decrease this difference by changing the mixing length of the B model from $\lambda = 0.98$ to $\lambda = 0.96$, and by increasing the mass of the star from 0.907 to 0.909 $M_\odot$. These modifications do not change the calibration of α Cen A. We took care in this process to keep the star B in its error box on the HR diagram (Fig. 10). It results from this new mass a diameter that is closer to the interferometric one: 0.863 $D_\odot$ or 5.999 ± 0.050 mas (parallax from Söderhjelm 1999). The effective temperature is found to be 5262 K, identical to the

adopted spectroscopic one $T_{\rm eff}$ = 5260 K. Our results confirm that the mass of the B component is probably close to 0.907 $M_\odot$, as reported by Thévenin et al. (2002). A similar exercice is not possible if we adopt the mass of 0.934 $M_\odot$ derived by Pourbaix et al. (2002).

9. Conclusion

We have determined the angular diameters of α Cen A and B using the VINCI/VLTI instrument, to a relative precision of 0.2% and 0.6%, respectively. The low values of the α Cen A visibilities allowed us to match our statistical visibility error to the calibration uncertainty. This is an optimal situation for the angular diameter measurement, that would not have been feasible with a higher visibility. Calibrating with a fainter and smaller unresolved star would also not have been efficient, as we would have degraded significantly our statistical precision. There is still a compromise, as the low visibilities of α Cen A imply a slightly degraded statistical precision, but E0-G1 has proved to be a well suited baseline for the simultaneous measurement of the angular diameters of α Cen A and B.

The comparison of these interferometric diameters with the values derived using asteroseismic constraints shows a good agreement when adopting the parallax determined by Söderhjelm (1999). In particular, our diameters are compatible with the masses proposed by Thévenin et al. (2002) for both stars. In the near future, asteroseismic observations of the large frequencies spacing $\Delta\nu_\ell$ of α Cen B will complete the calibration of this binary system. Simultaneously, the very long baselines of the VLTI (up to 200 m) will allow us to measure directly the limb darkening of these two stars, and therefore derive the photospheric diameter without using a stellar atmosphere model. This work demonstrates that the combination of the interferometry and asteroseismology techniques can provide strong constraints on stellar masses and other fundamental parameters of stars.

Acknowledgements. We are grateful to V. Coudé du Foresto and G. Perrin for fruitful discussions regarding the analysis of the VINCI data, and to M. Wittkowski for his useful comments on the limb darkening question. We thank also the ESO VLTI team for operating the VLTI, and for making the commissioning data publicly available.

The interferometric measurements have been obtained using the Very Large Telescope Interferometer, operated by the European Southern Observatory at Cerro Paranal, Chile. The VINCI public commissioning data used in this paper has been retrieved from the ESO/ST-ECF Archive (Garching, Germany). This research has also made use of the SIMBAD database at CDS, Strasbourg (France) and of the WDS database at USNO, Washington, DC (USA).

References

Berger, J.-P., Haguenauer, P., Kern, P., et al. 2001, A&A, 376, 31
Bordé, P., Coudé du Foresto, V., Chagnon, G., & Perrin, G. 2002, A&A, 393, 183
Bouchy, F., & Carrier, F. 2001, A&A, 374, L5
Bouchy, F., & Carrier, F. 2002, A&A, 390, 205
Bouchy, F., & Carrier, F. 2002, Eddington Workshop, ESA SP-485, 253
Cayrel de Strobel, G., Soubiran, C., Friel, E. D., Ralite, N., & Francois, P. 1997, A&AS, 124, 299
Claret, A., Diaz-Cordovez, J., & Gimenez, A. 1995, A&AS, 114, 247
Claret, A. 1998, A&A, 335, 647
Claret, A. 2000, A&A, 363, 1081
Cohen, M., Walker, R. G., Carter, B., et al. 1999, AJ, 117, 1864
Coudé du Foresto, V., Ridgway, S., & Mariotti, J.-M. 1997, A&AS, 121, 379
Demarque, P., Guenter, D. B., & van Altena, W. F. 1986, ApJ, 300, 773
Evans, J. W., & Michard, R. 1962, ApJ, 136, 493
Farge, M.. 1992, Ann. Rev. Fluid Mech., 24, 395
Glebocki, R., Gnacinski, P., & Stawikowski, A. 2000, Acta Astron., 50, 509
Glindemann, A., Abuter, R., Carbognani, F., et al. 2000, SPIE, 4006, 2
Guenther, D. B., & Demarque, P. 2000, ApJ, 531, 503
Hanbury Brown, R., Davis, J., Lake, R. J. W., & Thompson, R. J. 1974, MNRAS, 167, 475
Heintz, W. 1958, Veröff. Münch. Observ., 5, 100
Heintz, W. 1982, Veröff. Münch. Observ., 102, 42
Hestroffer, D. 1997, A&A, 327, 199
Kamper, K. W., & Wesselink, A. J. 1978, AJ, 83, 1653
Kervella, P., Coudé du Foresto, V., Glindemann, A., & Hofmann, R. 2000, SPIE, 4006, 31
Kervella, P., Gitton, Ph., Ségransan, D., et al. 2003a, SPIE, 4838, 858
Kervella P., Ségransan, D., & Coudé du Foresto, V. 2003b, in preparation
Kim, J. C. 1999, JKAS, 32, 119
Leighton, R. B. 1960, in Proc. IAU Symp., 12, 321
Leinert, C., Graser, U., Waters, L. B. F. M., et al. 2000, SPIE, 4006, 43
Lord, S. D. 1992, NASA Technical Memor. 103957, data available at `http://www.gemini.edu`
Morel, P. 1997, A&AS, 124, 597
Morel, P., Provost, J., Lebreton, Y., Thévenin, F., & Berthomieu, G. 2000, A&A, 363, 675
Morel, P., Berthomieu, G., Provost, J., & Thévenin, F. 2001, A&A, 379, 245
Perrin G., 2003, A&A, 398, 385
Perryman, M. A. C., Lindegren, L., Kovalevsky, J., et al. 1997, A&A, 323, 49
Petrov, R., Malbet, F., Richichi, A., et al. 2000, SPIE, 4006, 68
Pourbaix, D., Neuforge-Verheecke, C., & Noels, A. 1999, A&A, 344, 172
Pourbaix, D., Nidever, D., McCarthy, C., et al. 2002, A&A, 386, 280
Ségransan, D., Forveille, T., Millan-Gabet, C. P. R., & Traub, W. A. 1999, in ASP Conf. Ser., 194, 290
Ségransan, D., Kervella, P., Forveille, T., & Queloz, D. 2003, A&A, 397, L5
Söderhjelm, S. 1999, A&A, 341, 121
Thévenin, F., Provost, J., Morel, P., et al. 2002, A&A, 392, L9
Thoul, A., Scufflaire, R., Noels, B., et al. 2003, A&A, submitted [`astro-ph/0303467`]

3.2.2 Article A&A : "The diameter and evolutionary state of Procyon A. Multi-technique modeling using asteroseismic and interferometric constraints" (2003)

Procyon est une étoile d'une importance toute particulière, car elle est régulièrement utilisée comme étalon photométrique. Nous présentons dans cet article notre mesure de diamètre angulaire de cette étoile à l'aide de l'instrument VINCI. La modélisation de cette étoile à l'aide du code CESAM, contrainte en particulier par le rayon mesuré et les fréquences sismiques, nous a permis de conclure que Procyon possède une masse d'environ 1,4 $M_\odot$ et un âge de 2,3 milliards d'années.

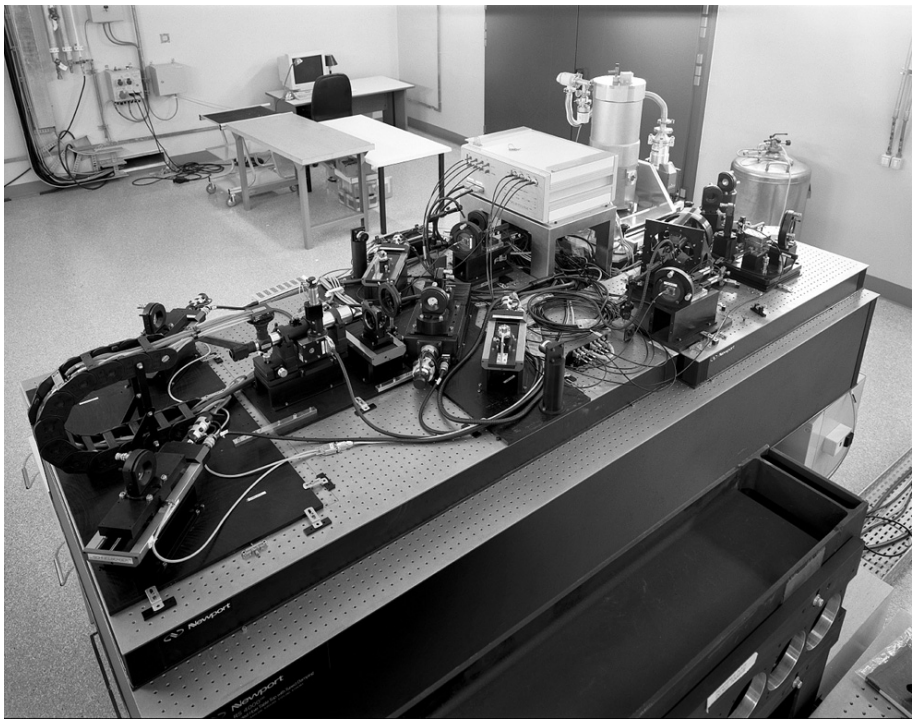

FIG. 3.4 – L'instrument VINCI, installé dans le laboratoire interférométrique à Paranal (photo prise en 2001, alors qu'AMBER et MIDI n'étaient pas encore installés).

A&A 413, 251–256 (2004)
DOI: 10.1051/0004-6361:20031527

Astronomy & Astrophysics

The diameter and evolutionary state of Procyon A

Multi-technique modeling using asteroseismic and interferometric constraints

P. Kervella[1], F. Thévenin[2], P. Morel[2], G. Berthomieu[2], P. Bordé[3], and J. Provost[2]

[1] European Southern Observatory, Casilla 19001, Vitacura, Santiago 19, Chile
[2] Département Cassini, UMR CNRS 6529, Observatoire de la Côte d'Azur, BP 4229, 06304 Nice Cedex 4, France
[3] LESIA, Observatoire de Paris-Meudon, 5, place Jules Janssen, 92195 Meudon Cedex, France

Received 19 May 2003 / Accepted 20 August 2003

Abstract. We report the angular diameter measurement obtained with the VINCI/VLTI instrument on the nearby star Procyon A (α CMi A, F5IV–V), at a relative precision of ±0.9%. We obtain a uniform disk angular diameter in the K band of $\theta_{\rm UD}$ = 5.376 ± 0.047 mas and a limb darkened value of $\theta_{\rm LD}$ = 5.448 ± 0.053 mas. Together with the HIPPARCOS parallax, this gives a linear diameter of 2.048 ± 0.025 $D_\odot$. We use this result in combination with spectroscopic, photometric and asteroseismic constraints to model this star with the CESAM code. One set of modeling parameters that reproduces the observations within their error bars are an age of 2314 Myr, an initial helium mass fraction $Y_{\rm i}$ = 0.301 and an initial mass ratio of heavy elements to hydrogen $(\frac{Z}{X})_{\rm i}$ = 0.0314. We also computed the adiabatic oscillation spectrum of our model of Procyon A, giving a mean large frequency separation of $\overline{\Delta\nu_0} \approx 54.7\,\mu$Hz. This value is in agreement with the seismic observations by Martić et al. (1999, 2001). The interferometric diameter and the asteroseismic large frequency spacing together suggest a mass closer to 1.4 $M_\odot$ than to 1.5 $M_\odot$. We conclude that Procyon is currently ending its life on the main sequence, as its luminosity class indicates.

Key words. stars: individual: α CMi – stars: fundamental parameters – stars: evolution – techniques: interferometric

1. Introduction

Procyon A (α CMi, HD 61421, HIP 37279) is among the brightest stars in the sky and is easily visible to the naked eye. This made it an ideal target for a number of spectro-photometric calibration works. It is also a visual binary star (ADS 6251A) classified F5 IV–V, with a white dwarf (WD) companion orbiting the main component in 40 years. The influence of this massive companion on the apparent motion of Procyon was discovered by Bessel (1844). Girard et al. (2000) have measured precisely the orbit of the pair, and obtained masses of 1.497 ± 0.037 $M_\odot$ and 0.602 ± 0.015 $M_\odot$, respectively for Procyon A and B. It has also been an asteroseismic target since a decade and Martic et al. (1999 and 2001 hereafter M99 and M01) have measured a large frequency spacing of respectively 55 and 54 μHz. These asteroseismic observations provide strong constraints on stellar interior models, and on macroscopic stellar parameters like mass and radius. Comparing the direct interferometric measurements of this star to its model diameter is therefore important to cross-validate both approaches.

Matching Procyon's position in the HR diagram has been recognized as of great difficulty by Guenther & Demarque (1993, hereafter GD93). The reason is the poorly known mass and metallicity Z of the star. We note that among the computed models only their model b is close to the mean large frequency spacing measured by M99–M01. Because numerous new studies and observational constraints (like the direct diameter) exist today, we re-examine the status of Procyon A in helium content Y and in age. We first review and present the adopted fundamental parameters of Procyon A in Sect.2, part of them being used for the limb-darkening in Sect. 3, where we present our new interferometric observations and the associated data processing. In Sect. 4, we detail several models of Procyon computed with the CESAM code (Morel 1997). These models are constrained using the spectroscopic effective temperature and the linear diameter value that we derived from the VINCI/VLTI observations. Thus, we avoid to fit the luminosity for which bolometric corrections are rather uncertain for stellar luminosity class IV–V. A study of the asteroseismic frequencies is then presented in Sect. 5, before the conclusion.

Send offprint requests to: P. Kervella,
e-mail: Pierre.Kervella@eso.org

2. Fundamental parameters

Physical properties of Procyon A are well known thanks to the carefully measured orbit of the system and accurate HIPPARCOS parallax. Its mass has been recently measured by Girard et al. (2000) at $M_{\rm A}$ = 1.497 ± 0.037 $M_\odot$, adopting a parallax of

283.2 ± 1.5 mas. This mass is computed using a large number of observations of inhomogeneous quality. The same authors, when they limit their observation sample to the excellent images obtained with the WFPC2, found $M_A = 1.465 \pm 0.041\,M_\odot$. If we replace the parallax used by Girard et al. (2000) by the parallax from the HIPPARCOS catalogue, 285.93 ± 0.88 mas, the sum of the masses of the binary decreases by 2.9%. Consequently, masses become respectively $M_A = 1.42 \pm 0.04\,M_\odot$ for Procyon A and $M_B = 0.575 \pm 0.017\,M_\odot$ for the white dwarf Procyon B. Allende Prieto et al. (2002, hereafter AP02), using the HIPPARCOS parallax of Procyon A, have estimated its mass to be $1.42 \pm 0.06\,M_\odot$. From these works, we can conclude that the mass of Procyon is probably between 1.4 and 1.5 $M_\odot$. Consequently, we investigate these two values in our study. The other adopted stellar parameters are summarized in Table 1.

The bolometric luminosity is given by Steffen (1985) $\log(L_\star/L_\odot) = 0.85 \pm 0.06$. The photospheric properties of Procyon have been carefully studied by AP02, who derived an effective temperature $T_{\rm eff} = 6512$ K. This value is based on the angular diameter measured in the visible by the Mark III optical interferometer (Mozurkewich et al. 1991). Detailed 3D stellar atmosphere simulations have led AP02 to correct this value of $T_{\rm eff}$ by 80 K. Following their results, we adopt $T_{\rm eff} = 6530 \pm 50$ K in our computations with a surface gravity of $\log g = 3.96 \pm 0.02$. It is interesting to notice that over the last twenty years, the effective temperature estimates for Procyon are spread between 6545 and 6811 K (Cayrel et al. 1997). Adopting a color index of $B - V = 0.421$ and using the calibration by Alonso (1996) we find $T_{\rm eff} = 6551$ K which is very close to the value proposed by AP02.

The iron abundance at surface of [Fe/H] = −0.05 ± 0.03 dex with respect to the solar one is also taken from AP02. Therefore we adopt for the modeling of the internal structure of Procyon A a chemical mixture which is calculated from the iron abundance using the approximation:

$$[\mathrm{Fe/H}]_s \equiv \log\left(\frac{Z_{\rm Fe}}{Z}\right)_s + \log\left(\frac{Z}{X}\right)_s - \log\left(\frac{Z_{\rm Fe}}{X}\right)_\odot \simeq \log\left(\frac{Z}{X}\right)_s - \log\left(\frac{Z}{X}\right)_\odot \quad (1)$$

where $\left(\frac{Z_{\rm Fe}}{Z}\right)_s$ is the iron mass fraction within Z. We use the solar mixture of Grevesse & Noels (1993) then $\left(\frac{Z}{X}\right)_\odot = 0.0245$. As we shall see in Sect. 4, we adopt at the age of Procyon A a surface abundance $\left(\frac{Z}{X}\right)_s = 0.0217 \pm 0.0017$. Note that this adopted error bar of AP02 is very small. Because the white dwarf (WD) Procyon B has already experienced the AGB phase, it is not excluded that material coming from this star can have contaminated the narrow surface convection layer of Procyon A. However, there is no evidence of such an effect in the published table of abundances of Procyon A (Steffen 1985). Enriched elements like "s" or other elements coming from Procyon B during its post-AGB phase do not seem to have migrated as gas or dust in the atmosphere of Procyon A. The mass transfer during this short period of the WD progenitor life could not exceed the accretion of the wind passing close to the star. Therefore, except if the two stars have filled their Roche lobe, the mass of Procyon A has only been changed by a negligible amount.

Table 1. Relevant parameters of α CMi (Procyon) and its calibrator α CMa (Sirius). For Sirius, see also Kervella et al. (2003d).

	α CMi HD 61421	α CMa HD 48915
m_V	0.34	−1.47
m_K	−0.65	−1.31
Spectral Type	F5IV–V	A1Vm
$M(M_\odot)$	1.42 ± 0.04	2.12 ± 0.02
$T_{\rm eff}$ (K)	6530 ± 50	9900 ± 200
$\log g$	3.96	4.30
[Fe/H]	−0.05 ± 0.03	0.50 ± 0.20
$v \sin i$	3.16 ± 0.50	16.0 ± 1.0
π^a (mas)	285.93 ± 0.88	379.22 ± 1.58
$\theta_{\rm UD}$ (mas)	**5.376 ± 0.047**	5.94 ± 0.02[b]
$\theta_{\rm LD}$ (mas)	**5.448 ± 0.053**	6.04 ± 0.02[b]

[a] Parallax values from HIPPARCOS (Perryman et al. 1997).
[b] Sirius $\theta_{\rm UD}$ and $\theta_{\rm LD}$ are taken from Kervella et al. (2003d).

The projected rotational velocity of Procyon A has been determined by many authors who derived values smaller than 5.0 km s^{-1}. Considering in particular the value proposed by AP02, $v \sin i = 3.2 \pm 0.5$ km s^{-1}, we conclude that Procyon A is a slow rotator and we neglect the rotational velocity in our modeling of its internal structure. The semi-major axis of the Procyon orbit being $\alpha \simeq 4\farcs5$ (Girard et al. 2000), the distance between the two companions amounts to ≃16 AU. The tidal interaction between the two components is therefore negligible.

3. Interferometric angular diameter

3.1. Instrumental setup and data processing

The European Southern Observatory's Very Large Telescope Interferometer (Glindemann et al. 2000) is operated on top of the Cerro Paranal, in Northern Chile, since March 2001. The observations reported here were done with two test siderostats (0.35 m aperture) and the VINCI beam combiner (Kervella et al. 2000, 2003a). The Procyon visibility measurements were all obtained on the B3–D3 baseline, 24 m in ground length. We used a regular K band filter ($\lambda = 2.0$–$2.4\,\mu$m) for these observations. The effective wavelength changes slightly depending on the spectral type of the observed target. For Procyon, we estimate $\lambda_{\rm eff} = 2.178 \pm 0.003\,\mu$m. This error bar adds quadratically a relative systematic uncertainty of 0.15% on the final limb darkened angular diameter error bar.

The raw data processing has been achieved using an improved version of the standard data reduction pipeline (Kervella et al. 2003c), whose general principle is similar to the original FLUOR algorithm (Coudé du Foresto et al. 1997). The two calibrated output interferograms are subtracted to remove residual photometric fluctuations. Instead of the classical Fourier analysis, we implemented a wavelet based time-frequency analysis (Ségransan et al. 1999). The output of the

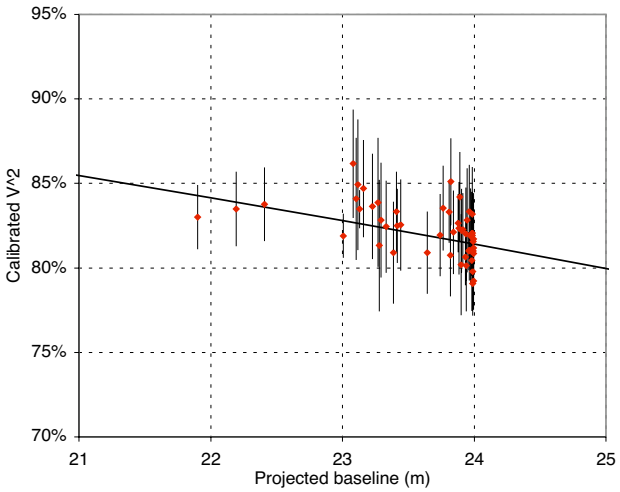

Fig. 1. Squared visibility measurements obtained on Procyon and best fit model (solid line).

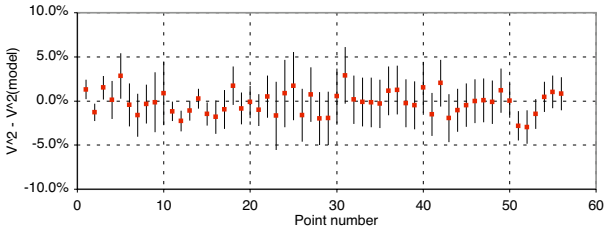

Fig. 2. Scattering of the Procyon measured visibilities around the best fit V^2 model. The plotted error bars are the quadratic sum of the statistical and systematic contributions.

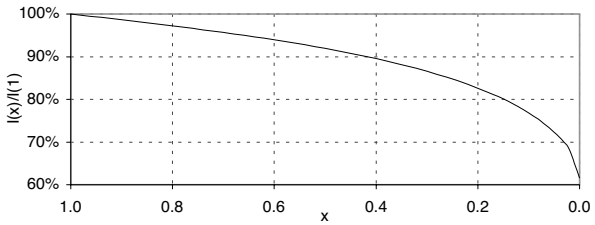

Fig. 3. Intensity profile of Procyon, from the four parameters law of Claret (2000).

processing pipeline is a single value of the squared coherence factor μ^2 for each series of 500 interferograms and the bootstrapped error bar.

3.2. Visibility calibration

Sirius was chosen as the calibrator for Procyon observations as its limb darkened (LD) angular diameter has been measured recently with high precision by Kervella et al. (2003d), using VINCI and the 66m E0-G1 baseline. Table 1 gives the relevant parameters of Procyon and Sirius. The interferometric efficiency (IE) of the instrument was estimated from the μ^2 values obtained on Sirius a short time before and after Procyon (typically 15 min). Thanks to the very high SNR of the Sirius interferograms, we were able to obtain very small relative errors on the IE values, typically 0.2% for a series of 500 interferograms. The error bar on the angular diameter of Sirius is treated as a systematic error in the calibration process, and is therefore not averaged for multiple observations. For the visibility fit, we took into account simultaneously the limb darkening and the bandwidth smearing, as described in Kervella et al. (2003b, 2003d).

Our February 2003 observation campaign of Procyon resulted in a total of 53 calibrated V^2 measurements, from 23 256 processed interferograms. In the calibration process, we separated clearly the statistical and systematic error contributions. This is essential to avoid underestimating the final error bars of the fit. The latter corresponds to the uncertainty on the angular diameter of Sirius. In spite of the fact that the angular size of Sirius is larger than Procyon's, the small error on its measured value (±0.3%) translates into a small calibration error. As a consequence, the global error on the angular size of Procyon is dominated by the statistical contribution by a factor of two compared to the systematic calibration error: the uncertainty on the angular size of Sirius is not limiting our final precision. The visibility points as a function of the projected baseline are presented in Fig. 1, and their residual scattering around the best fit model in Fig. 2.

3.3. Limb darkened angular diameter and linear size

The intensity profile $I(\mu)/I(1)$ that we chose for Procyon was computed by Claret et al. (2000), based on the ATLAS9 model atmospheres (Kurucz 1992). It is a four parameters law:

$$I(x)/I(1) = 1 - \sum_{k=1}^{4} a_k \left(1 - x^{\frac{k}{2}}\right) \quad (2)$$

which coefficients are $a_1 = 0.5089$, $a_2 = 0.0822$, $a_3 = -0.3978$, and $a_4 = 0.1967$. The parameter $x = \cos(\theta)$ is the cosine of the azimuth of a surface element of the star. The resulting profile is shown in Fig. 3. AP02 have identified an influence of the convective granulation of Procyon on its limb darkening at visible wavelengths. Though, the amplitude of this effect is already very small at $\lambda = 1.0\,\mu$m, and we neglect it for our observations at $\lambda = 2.2\,\mu$m.

We obtain directly the LD angular diameter of Procyon from a classical χ^2 minimization, $\theta_{\rm LD} = 5.448 \pm 0.053$ mas. Using a simple uniform disk model, we find a value of $\theta_{\rm UD} = 5.376 \pm 0.047$ mas.

We can compare the LD value with the previously published interferometric measurements, listed in Table 2. Our value of $\theta_{\rm LD}$ is compatible with previous measurements, that were all obtained using visible wavelength observations. It is also in excellent agreement with the average of all published values. From the VINCI/VLTI value of $\theta_{\rm LD}$ and the HIPPARCOS parallax, we deduce a linear diameter of $2.048 \pm 0.025\,D_\odot$. Computing the average of all published $\theta_{\rm LD}$ values, we obtain a linear radius of $R_\star = 2.047 \pm 0.020\,R_\odot$ for Procyon A, statistically identical to our result.

4. Modeling

The modeling of Procyon A is based on the matching of spectroscopic effective temperature, surface metallicity and

Table 2. Interferometric measurements of the angular diameter of Procyon A from the literature.

Instrument	λ (μm)	θ_{UD} (mas)	θ_{LD} (mas)
Intensity interf.[a]	0.45	5.10 ± 0.16	5.41 ± 0.17
Mark III[b]	0.80	5.26 ± 0.05	
Mark III[b]	0.45	5.14 ± 0.05	
Mark III[c]	0.80		5.46 ± 0.08
NPOI[c]	0.74	5.19 ± 0.04	5.43 ± 0.07
VINCI/VLTI	2.18	**5.38 ± 0.05**	**5.45 ± 0.05**
Average value			5.445 ± 0.035

[a] Hanbury Brown et al. (1974).
[b] Mozurkewich et al. (1991).
[c] Nordgren et al. (2001).

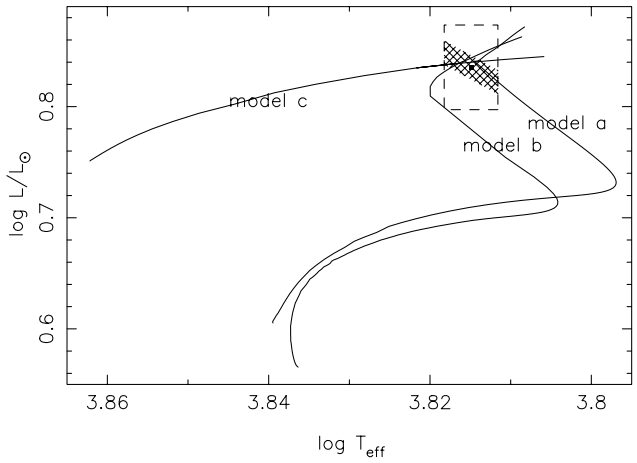

Fig. 4. Evolutionary tracks in the HR diagram of models of Procyon A (see Table 3). Dashed rectangle delimits the uncertainty domain for luminosity and effective temperature, while the hatched area delimits the uncertainty domain for effective temperature and the interferometric radius.

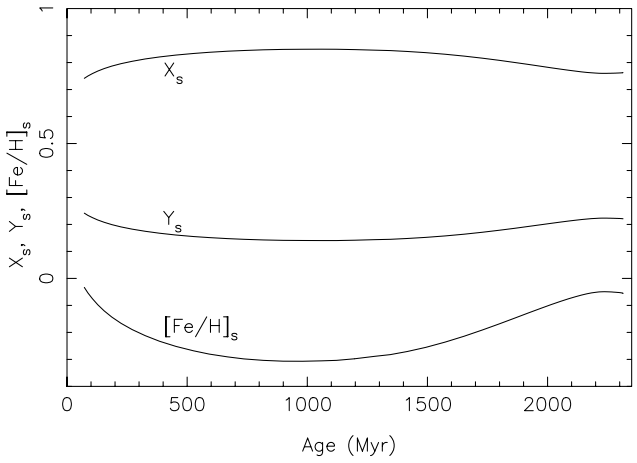

Fig. 5. Changes with respect to time for X_s, Y_s and $[Fe/H]_s$ for model *a* of Procyon.

interferometric radius by a "satisfactory" evolutionary model for a given mass. The constraint between $R_\star$ and $T_{\rm eff}$ within their error bars is illustrated in Fig. 4 by the hatched parallelogram, while the constraint between the $T_{\rm eff}$ and $L_\star$ is illustrated by the dashed rectangle. That emphazises the advantage of the use of the measured $R_\star$ instead of the $L_\star$ which depends of photometric calibrations and bolometric corrections.

Table 3 shows the characteristic and initial modeling parameters of the star. The ordinary assumptions of stellar modeling are made, i.e. spherical symmetry, no rotation, no magnetic field and no mass loss. The relevant nuclear reaction rates are taken from the NACRE compilation by Angulo et al. (1999). The equation of state adopted is taken from Eggleton et al. (1973), and the opacities are from the OPAL database (Iglesias & Rogers 1996), using the Grevesse & Noels (1993) mixture. The microscopic diffusion is described using the formalism of Burgers (1969) with the resistance coefficients of Paquette et al. (1986). We take into account the radiative diffusivity as recommended by Morel & Thévenin (2002), that limits the efficiency of the microscopic diffusion in outer-layers of stars with intermediate masses. The atmosphere is restored using Hopf's law (Mihalas 1978). The definition of the radius of the star is the bolometric radius, where $T(R_\star) = T_{\rm eff}$. In the convection zones the temperature gradient is computed according to the $\rm MLT_{CM}$ convection theory with a mixing length parameter of $\Lambda = 1$ (Canuto & Mazzitelli 1991, 1992).

Following the discussion of Sect. 2 we investigate the sensitivity of our models to a variation of the mass of Procyon in the range 1.4 to 1.5 $M_\odot$. We obtained a "satisfactory" model *a* (Fig. 4), detailed in Table 3, which reaches the hatched parallelogram corresponding to an age of 2314 Myr. Its evolutionary state corresponds closely to the end of the main sequence, when the convective core has disappeared owing to the exhaustion of the hydrogen at center. We present in Fig. 5 the variation for model *a* of X_s, Y_s and of $[Fe/H]_s$ as a function of the age. From the ZAMS until about 1 Gyr, due to the gravitational settling, the surface abundances of helium and heavy elements (*resp.* hydrogen) decrease (*resp.* increases). After 1 Gyr, the density in the envelope decreases due to the enlargement of radius. This leads to an increase of the radiative mixing, with the consequence of a dredge-up which increases (*resp.* decreases) Y_s and $[Fe/H]_s$ (*resp.* X_s) at the surface.

We also computed a "satisfactory" model *b* without microscopic diffusion in order to estimate its effect on the age of the star and we found that suppressing the diffusion increases the age by ~400 Myr. The evolutionary state of this model is the beginning of H burning in a shell.

Following the prescriptions of Schaller et al. (1992) we have computed additional models that include overshooting of the convective core of radius $R_{\rm co}$ over the distance $O_{\rm v} = A \min(H_{\rm p}, R_{\rm co})$. It has been impossible to find a "satisfactory" model reaching the narrow hatched area of the HR diagram with parameters $A > 0.03$.

Finally, we computed a model *c* with Girard et al. (2000) mass: 1.50 $M_\odot$ and find an age of 1.3 Gyr without overshoot. We also computed a model with an overshoot of 0.15 in agreement with Ribas et al. (2000) for stars of mass lower than 1.5 $M_\odot$ resulting in a model which increases the age of the star to 1.55 Gyr.

Table 3. Procyon A models (without overshoot, see text) lying within uncertainty box in the HR diagram. The subscripts "$_i$" and "$_s$" respectively refer to initial values and surface quantity at present day. "$_c$" refers to the central value.

Model	*a*	*b*	*c*
$m/M_\odot$	1.42	1.42	1.50
Y_i	0.3012	0.2580	0.345
Y_s	0.2209	0.2580	0.202
$\left(\frac{Z}{X}\right)_i$	0.03140	0.0218	0.0450
$\left(\frac{Z}{X}\right)_s$	0.02157	0.0218	0.0220
diffusion	yes	no	yes
X_c	0.00051	0.00000	0.2180
age (Myr)	2 314	2 710	1 300
$T_{\rm eff}$ (K)	6524	6547	6553
$\log g$	3.960	3.967	3.994
$[{\rm Fe/H}]_i$	+0.107	–0.051	+0.264
$[{\rm Fe/H}]_s$	–0.055	–0.051	–0.043
$\log(L/L_\odot)$	0.8409	0.8405	0.8390
$R/R_\odot$	2.0649	2.0495	2.0420
$\overline{\Delta\nu_0}$ (μHz)	54.7	55.4	56.4

The parameters for all models are listed in Table 3. Figure 4 shows the corresponding evolutionary tracks in the HR diagram. We note that our models fit the value of $\log g = 3.96$ proposed by AP02.

5. Asteroseismology

Asteroseismic observations of Procyon A have been reported by M99 and M01 and indicate an excess of power around 1 milliHertz with a probable frequency spacing of 54 to 55 μHz.

The narrow convective envelope of the star we consider may stochastically excite solar-like oscillations. As in the Sun, these oscillations will have quasi equidistant frequencies at given degree.

For all the models, we have computed a set of adiabatic frequencies of the normal modes for degrees $\ell = 0, 1, 2, 3$. The set of frequencies of model *a* are given in the frequency range 450 to 1600 μHz in Table 4.

The large frequency spacing is defined as the difference between frequencies of modes with consecutive radial order *n*: $\Delta\nu_\ell(n) \equiv \nu_{n,\ell} - \nu_{n-1,\ell}$. In the high frequency range, i.e. large radial orders, $\Delta\nu_\ell$ is almost constant with a mean value $\overline{\Delta\nu_0}$, strongly related to the mean density of the star. The computed frequencies are fitted to the following asymptotic relation (Berthomieu et al. 1993): $\nu_{n,\ell} = \nu_0 + \overline{\Delta\nu_\ell}(n - n_0) + a_\ell(n - n_0)^2$. With $n_0 = 21$, $\ell = 0$ and radial order *n* between 17 and 26 we obtain an estimate of the mean large difference $\overline{\Delta\nu_0}$.

The mean large spacing of model *a* is 54.7 μHz which fits well observational predictions of M99 & M01 ($\overline{\Delta\nu_0} \sim$ 54–55 μHz). For the model *c*, the mean large spacing is found to be 56.4 μHz, significantly different from the observed value. A mass as large as 1.5 $M_\odot$ for Procyon A seems therefore improbable. Adopting the VINCI/VLTI radius, and looking at the scaling of Kjeldsen & Bedding (2003),

$$\overline{\Delta\nu_{\rm osc}} \sim 134.9 \sqrt{\frac{m/M_\odot}{(R_\star/R_\odot)^3}}\ (\mu{\rm Hz}), \qquad (3)$$

Table 4. Asteroseismic frequencies (μHz) of Procyon A for model *a*. The "$\star$" correspond to "*g*" modes which are presents in the frequency domain due to the evolutionary state of the star.

$\ell = 0$	$\ell = 1$	$\ell = 2$	$\ell = 3$	*n*
485.35	513.36	532.31	551.46	8
–	–	–	597.20	$\star$
537.93	563.43	585.90	605.61	9
591.09	615.78	638.60	657.72	10
643.23	666.79	689.80	708.98	11
694.17	717.44	741.00	760.87	12
745.32	769.15	793.75	814.22	13
798.11	822.24	847.62	868.87	14
–	–	896.38	–	$\star$
852.14	876.76	904.48	923.72	15
906.98	931.22	957.38	978.12	16
961.42	985.26	1011.19	1031.92	17
–	–	–	1075.73	$\star$
1015.27	1038.85	1065.03	1086.34	18
1069.16	1092.64	1119.00	1140.31	19
1123.16	1146.76	1173.64	1195.27	20
1177.86	1201.57	1228.79	1250.68	21
1233.05	1256.82	1284.20	1306.18	22
1288.46	1312.09	1339.65	1361.81	23
1343.91	1367.55	1395.21	1417.43	24
1399.42	1422.95	1450.65	1472.94	25
1454.83	1478.24	1506.00	1528.39	26
1510.12	1533.53	1561.40	1583.89	27

the most straightforward way to decrease $\overline{\Delta\nu_0}$ is to decrease the mass of Procyon A.

Because the luminosity *L* is in relation with $T_{\rm eff}$ and with the radius *R* through the formula $L/L_\odot = (R/R_\odot)^2(T_{\rm eff}/T_{\rm eff}^\odot)^4$ we find from Eq. (3) the expression of the mean large spacing as a function of *L* and $T_{\rm eff}$,

$$\overline{\Delta\nu_{\rm osc}} \sim 134.9 \frac{\sqrt{m/M_\odot}}{(L/L_\odot)^{3/4}(T/T_{\rm eff})^3}\ (\mu{\rm Hz})\,. \qquad (4)$$

From this formula it is easy, if needed, to estimate the derivatives of the mean large spacing with respect to the mass, the effective temperature and the luminosity. To estimate the dependance between $\overline{\Delta\nu_{\rm osc}}$ and Z_i we have computed a modified model *a* with $\Delta Z_i = 0.001$ and found a variation in the parallelogram error box of: $\Delta T_{\rm eff} = 22$ K, $\Delta L/L = 0.008$, and $\Delta_{\rm age} = 33$ Myr. There were no significant changes with Z_i of $\overline{\Delta\nu_{\rm osc}}$ as can be expected from Eq. (3).

6. Discussion and conclusions

We have reported in this paper our modelisation of Procyon A based on observations by long-baseline interferometry and asteroseismology. The use of the measured stellar diameter allows to reduce significantly the error bar on the luminosity of the star, as it does not require any bolometric corrections. This advantage has been demonstrated in this study and in the modeling of Sirius by Kervella et al. (2003d).

Our model shows that using the given set of parameters and given physics, Procyon A is currently finishing to burn its central hydrogen, and is at the phase where the convective core

is disappearing. The error on the measured radius gives a narrow uncertainty of 10 Myr on the deduced age. Provencal et al. (2002) have discussed the cooling time of the WD Procyon B and found that the progenitor ended its lifetime 1.7 ± 0.1 Gyr ago. We derive an age of 2314 Myr for Procyon A. Subtracting the cooling age of the WD companion to our determination of the age of Procyon A leads to a lifetime of 614 Myr for the progenitor of Procyon B. This indicates that the mass of the progenitor is approximately $2.5\,M_{\odot}$. This value yields a mass of $\sim 0.57\,M_{\odot}$ for the core of the corresponding Thermal-Pulsating-AGB star (for $Z = 0.020$) (Bressan et al. 1993), which is the minimum possible value for the final mass of the WD (see also Jeffries 1997). This estimate of $0.57\,M_{\odot}$ agrees very well with the mass of Procyon B that we deduced from Girard et al. (2000). We note that the age obtained with model *c* is younger than the cooling age of Procyon B. This argument suggests a mass lower than $1.5\,M_{\odot}$ for Procyon A and strengthens the asteroseismology results.

Further progress on the modeling of Procyon will be possible when the accuracy on the flux of the star is improved to less than 1%. Waiting for such accuracy, the uniqueness of the solutions resulting from computed models fitting a narrow box in the HR diagram will come from future detailed asteroseismic studies. For example, other linear combinations of frequencies such as the small frequency spacings (see e.g. Gough 1991) will constrain the age and the mass of the star. We therefore encourage observers to progress on the asteroseismology of this star.

Large uncertainties also come from the adopted chemical abundance mixture $Z_{\rm s}$ which is still rather uncertain. Only a few chemical element abundances are measured today and most of them with a low accuracy. This uncertainty on $Z_{\rm s}$ is the largest source of error on the estimated initial helium content $Y_{\rm i}$ and on the age of Procyon. Thus, we recommend that surface abundances should be derived from 3D atmosphere studies, in particular for oxygen and other important donors of electrons.

Acknowledgements. The VLTI is operated by the European Southern Observatory at Cerro Paranal, Chile. The VINCI public commissioning data reported in this paper has been retrieved from the ESO/ST-ECF Archive. The VINCI pipeline includes the wavelets processing technique, developed by D. Ségransan (Obs. de Genève). No VLTI observation would have been possible without the efforts of the ESO VLTI team, to whom we are grateful. This research has made use of the SIMBAD database at CDS, Strasbourg (France).

References

Allende Prieto, C., Asplund, M., Garcia López, R. J., & Lambert, D. L. 2002, ApJ, 567, 544
Alonso, A., Arribas, S., & Martínez-Roger, C. 1996, A&A, 313, 873
Angulo, C., Arnould, M., Rayet, M., et al. 1999, Nucl. Phys. A, 656, 3
Berthomieu, G., Provost, J., Morel, P., & Lebreton, Y. 1993, A&A, 262, 775
Bessel, F. W. 1844, MNRAS, 6, 136
Bressan, A., Fagotto, F., Bertelli, G., & Chiosi, C. 1993, A&AS, 100, 674
Burgers, J. M. 1969, Flow Equations for Composite Gases (New York: Academic Press)
Canuto, V. M., & Mazitelli, I. 1991, ApJ, 370, 295
Canuto, V. M., & Mazitelli, I. 1992, ApJ, 389, 729
Cayrel de Strobel, G., Soubiran, C., Friel, E. D., Ralite, N., & Francois, P. 1997, A&AS, 124, 299
Claret, A. 2000, A&A, 363, 1081
Cohen, M., Walker, R. G., Barlow, M. J., & Deacon, J. R. 1992, AJ, 104, 1650
Cohen, M., Walker, R. G., Carter, B., et al. 1999, AJ, 117, 1864
Coudé du Foresto, V., Ridgway, S., & Mariotti, J.-M. 1997, A&AS, 121, 379
Eggleton, P. P., Faulkner, J., & Flannery, B. P. 1973, A&A, 23, 325
Girard, T. M., Wu, H., Lee, J. T., et al. 2000, AJ, 119, 2428
Glindemann, A., Abuter, R., Carbognani, F., et al. 2000, SPIE, 4006, 2
Gough, D. O. 1991, in Comments on Helioseismic Inference, ed. Y. Osaki, & H. Shibahashi, Progress of Seismology of the Sun and Stars (Springer Verlag, 283)
Grevesse, N., & Noels, A. 1993, in Cosmic Abundances of the Elements, ed. N. Prantzos, E. Vangioni-Flam, & M. Cassé, Origin and Evolution of the Elements (Cambridge University Press), 14
Guenther, D. B., & Demarque, P. 1993, ApJ, 405, 298
Hanbury Brown, R., Davis, J., Lake, J. W., & Thompson, R. J. 1974, MNRAS, 167, 475
Iglesias, C. A., & Rogers, F. J. 1996, ApJ, 464, 943
Jeffries, R. D. 1997, MNRAS, 288, 585
Kervella, P., Coudé du Foresto, V., Glindemann, A., & Hofmann, R. 2000, SPIE, 4006, 31
Kervella, P., Gitton, Ph., Ségransan, D., et al. 2003a, SPIE, 4838, 858
Kervella, P., Thévenin, F., Ségransan, D., et al. 2003b, A&A, 404, 1087
Kervella, P., Ségransan, D., & Coudé du Foresto, V. 2003c, in preparation
Kervella, P., Thévenin, F., Morel, P., et al. 2003d, A&A, 408, 681
Kjeldsen, H., & Bedding, T. 1995, A&A, 293, 87
Kurucz, R. L. 1992, The Stellar Populations of Galaxies, IAU Symp., 149, 225
Lemke, M. 1989, A&A, 225, 125
Martic, M., Schmitt, J., Lebrun, J., et al. 1999, A&A, 351, 993
Martic, M., Lebrun, J.-C., Schmit, J., Appourchaux, Th., & Bertaux, J.-L. 2001, in SOHO 10 / GONG 2000 Workshop, ed. A. Wilson, ESA SP-464, 431
Mihalas, D. 1978, Stellar Atmospheres, 2nd ed. (San Francisco: W. H. Freeman and Co)
Mozurkewich, D., Johnston, K. J., Simon, R. S., et al. 1991, AJ, 101, 2207
Morel, P. 1997, A&AS, 124, 597
Morel, P., & Thévenin, F. 2002, A&A, 390, 611
Nordgren, T. E., Sudol, J. J., & Mozurkewich, D. 2001, AJ, 122. 2707
Paquette, C., Pelletier, C., Fontaine, G., & Michaud, G. 1986, ApJS, 61, 177
Provencal, J. L., Shipman, H. L., Koester, D., Wesemael, F., & Bergeron, P. 2002, ApJ, 568, 324
Perryman, M. A. C., Lindegren, L., Kovalevsky, J., et al. 1997, The HIPPARCOS Catalogue, A&A, 323, 49
Ribas, I., Jordi, C., & Giménez, À. 2000, MNRAS, 318, L55
Schaller, G., Schaerer, D., Meynet, G., & Maeder, A. 1992, A&AS, 96, 269
Ségransan, D., Forveille, T., Millan-Gabet, C. P. R., & Traub, W. A. 1999, ASP Conf. Ser., 194, 290
Ségransan, D. 2001, Ph.D. Thesis, Grenoble
Steffen, M. 1985, A&AS, 59, 403

3.2.3 Article A&A : "VLTI/VINCI diameter constraints on the evolutionary status of δ Eri, ξ Hya, η Boo" (2005)

Avec la mesure du diamètre angulaire de ces trois étoiles possédant des mesures de fréquences astérosismiques, nous avons été en mesure d'estimer précisément leur état évolutif par la modélisation. Dans le cas de l'étoile géante ξ Hya, qui est dans une phase d'évolution rapide hors de la séquence principale, la contrainte apportée par la mesure du diamètre permet d'estimer l'âge de cette étoile avec une incertitude formelle de seulement 100 000 ans.

FIG. 3.5 – Les quatre télescopes de 8m du Very Large Telescope.

A&A 436, 253–262 (2005)
DOI: 10.1051/0004-6361:20042075

Astronomy & Astrophysics

VLTI/VINCI diameter constraints on the evolutionary status of δ Eri, ξ Hya, η Boo

F. Thévenin[1], P. Kervella[2], B. Pichon[1], P. Morel[1], E. Di Folco[3], and Y. Lebreton[4]

[1] Laboratoire Cassiopée, UMR 6202 CNRS, Observatoire de la Côte d'Azur, BP 4229, 06304 Nice Cedex 4, France
[2] Laboratoire d'Études Spatiales et d'Instrumentation Astrophysique (LESIA), UMR 8109 du CNRS, Observatoire de Paris, Section de Meudon, 5 place Jules Janssen, 92195 Meudon Cedex, France
[3] European Southern Observatory, Karl-Schwarzschild Strasse 2, 85748 Garching, Germany
[4] GEPI, UMR 8111 CNRS, Observatoire de Paris, Section de Meudon, 5 place Jules Janssen, 92195 Meudon Cedex, France

Received 27 September 2004 / Accepted 16 January 2005

Abstract. Using VLTI/VINCI angular diameter measurements, we constrain the evolutionary status of three asteroseismic targets: the stars δ Eri, ξ Hya, η Boo. Our predictions of the mean large frequency spacing of these stars are in agreement with published observational estimations. Looking without success for a companion of δ Eri, we doubt its classification as an RS CVn star.

Key words. stars: evolution – stars: fundamental parameters – techniques: interferometric

1. Introduction

After two years of operation, the commissioning instrument VINCI of the VLTI has provided valuable stellar diameter measurements. Among the impact of these diameters are the studies of main sequence stars, where diameters combined with asteroseismic frequencies can be used to constrain evolutionary status and mass. Several papers have been published (Ségransan et al. 2003; Kervella et al. 2003a,b; 2004a; Di Folco et al. 2004) with important results on stellar fundamental parameters prior to the use of the dedicated VLTI light combiner AMBER (Petrov et al. 2003). The aim of the present paper is to complete previous studies using VINCI to measure the diameter of three subgiant and giant stars that are among selected asteroseismic targets for ground-based observations and space missions: δ Eri, ξ Hya, η Boo. We perform a preliminary study of their evolutionary status by constraining their mass, their helium content and their age. One of the purposes of this paper is to show that in the future, the use of stellar diameters will be a significant constraint for evolutionary models for given input physics. We first describe the characteristics of each of the three stars (Sect. 2) and then we present diameter measurements (Sect. 3) for each star. We construct evolutionary models satisfying spectro-photometric observable constraints and we compare asteroseismic large frequencies with measured ones. We present these models (Sect. 4) and we draw some conclusions on the classification and fundamental parameters of the three stars.

2. Global characteristics of the stars

The first part of Table 1 presents the observational data of the three stars. The second part of this table summarizes some input parameters and output data of the models.

2.1. δ Eri

δ Eri (HD 23249, HR 1136, HIP 17378) has been thoroughly studied by photometry and spectroscopy and is classified as a K0 IV star (Keenan & Pitts 1980). It belongs to the group of the nearest stars with an accurate Hipparcos parallax of 110.58 ± 0.88 mas (Perryman et al. 1997). The star has been classified as a weakly active and X-ray soft source (Huensch et al. 1999) after a lengthy search for its activity. Wilson & Bappu (1957) concluded that the possible detection of emission in the H&K lines is "*exceedingly weak*" – so weak that it is questionable. It took more than 20 years to inconclusively detect its activity with Copernicus, revealing a weak emission in MgII (Weiler & Oegerle 1979). Fisher et al. (1983) tried to detect a periodic variation in the photometric data and concluded that, if it exists, the amplitude is below ±0.02 mag with a period of 10 days. They suggested that δ Eri could be classified as an RS CVn star. An RS CVn is defined as a F-G binary star having a period shorter than 14 days, with chromospheric activity and with a period of rotation synchronized with its orbital period (Linsky 1984), giving the star high rotational velocity inducing strong activity. This is in contrast with the low level

Table 1. Observable characteristics of the stars and best model reproducing them. The subscripts "$_{\rm ini}$" and "$_{\rm surf}$" respectively refer to initial values and current surface quantities. Note that the presented errors of VLTI/VINCI angular diameters are the statistical ones followed by the systematical ones. Note also that $D/D_\odot$ is equal to $R/R_\odot$.

	δ Eri	ξ Hya	η Boo
V	3.51 ± 0.02	3.54 ± 0.01	2.68 ± 0.01
BC	−0.24 ± 0.01	−0.26 ± 0.01	−0.06 ± 0.01
$T_{\rm eff}$(K)	5074 ± 60	5010 ± 100	6050 ± 150
$L/L_\odot$	3.19 ± 0.06	60.7 ± 4.1	8.95 ± 0.20
$[{\rm Fe/H}]_{\rm surf}$	0.13 ± 0.08	−0.04 ± 0.12	0.24 ± 0.07
$\log g$	3.77 ± 0.16	2.93 ± 0.30	3.66 ± 0.20
$\theta_{\rm LD}$(mas)	2.394 ± 0.014 ±0.025	2.386 ± 0.009 ±0.019	2.200 ± 0.027 ±0.016
$D/D_\odot$	2.33 ± 0.03	10.3 ± 0.3	2.68 ± 0.05
π(mas)	110.58 ± 0.88	25.23 ± 0.83	88.17 ± 0.75
$\Delta\nu_0(\mu$Hz)	43.8 ± 0.3	7.1	40.47 ± 0.05

	δ Eri diffusion	δ Eri no diffusion	ξ Hya diffusion	ξ Hya no diffusion	η Boo diffusion	η Boo no diffusion
$M/M_\odot$	1.215	1.215	2.65	2.65	1.70	1.70
Age of the ZAMS (Myr)	20.14	20.06	2.724	2.719	12.68	12.67
Age (from ZAMS) (Myr)	6194.	6196.	509.52	505.34	2738.5	2355.
$Y_{\rm ini}$	0.28	0.28	0.275	0.275	0.260	0.260
$[Z/X]_{\rm ini}$	0.148	0.148	0.00	0.00	0.367	0.367
$T_{\rm eff}$(K)	5055.	5066.	5037.	5034.	6050.	6090.
$L/L_\odot$	3.176	3.230	61.23	61.0	8.944	8.978
$R/R_\odot$	2.328	2.337	10.30	10.30	2.728	2.697
$\log g$	3.788	3.785	2.835	2.832	3.796	3.806
$Y_{\rm surf}$	0.266	0.28	0.274	0.275	0.228	0.260
$[Z/X]_{\rm surf}$	0.123	0.148	0.00	0.00	0.303	0.367
$M_{\rm CZ}(M_\star)$	0.729	0.727	0.608	0.596	0.9994	0.9994
$R_{\rm CZ}(R_\star)$	0.475	0.475	0.422	0.417	0.8388	0.8505
$\Delta\nu_0(\mu$Hz)	45.27	44.91	7.23	7.28	41.91	42.47

of activity detected for δ Eri making doubtful its classification as an RS CVn star. δ Eri has a projected rotational velocity of $v \sin i = 1.0\,{\rm km\,s^{-1}}$ (de Meideros & Mayor 1999) and the hypothetical RS CVn classification forces us to conclude that the binary is seen pole-on therefore explaining the lack of photometric variation and also of any variation of the radial velocity (Santos et al. 2004). To reveal the presence of a close companion around δ Eri, we set several VLTI/VINCI observations at different baselines (see Sect. 3).

We estimate its bolometric luminosity $L_\star/L_\odot = 3.19 \pm 0.06$ using the Alonso et al. (1999) empirical bolometric corrections (BC, BC = -0.24 ± 0.01 for giants, this is the dominant source of uncertainty on the luminosity). We adopt the Santos et al. (2004) values for the effective temperature $T_{\rm eff} = 5074 \pm 60$ K, logarithmic surface gravity $\log g = 3.77 \pm 0.16$ and surface iron abundance [Fe/H] = 0.13±0.03. These parameters are different from – but within the error bars of – the parameters proposed by Pijpers (2003) for this star, except the metallicity which is 0.24 dex higher. Bouchy & Carrier (2003) have measured a mean large frequency spacing of 43.8 μHz that we will try to reproduce with our model. We recall that the large frequency spacing is defined as the difference between frequencies of modes with consecutive radial order n: $\Delta\nu_l(n) = \nu_{n,l} - \nu_{n-1,l}$. In the high frequency range, i.e. large radial orders, $\Delta\nu_l(n)$ is almost constant with a mean value strongly related to the square root of the mean density of the star. To obtain the mean large frequency separation, we average over $l = 0$–2.

2.2. ξ Hya

ξ Hya (HD 100407, HR 4450, HIP 56343) is a giant star (G7 III) which has been considered by Eggen (1977) as a spurious member of the Hyades group because it departs slightly from the regression line of giant stars in the colour diagrams ($b-y$, $R-I$) and (M_1, $R-I$) of that stellar group.

Its Hipparcos parallax is 25.23 ± 0.83 mas. We estimate its bolometric luminosity $L_\star/L_\odot = 60.7 \pm 4.1$ using BC (BC = -0.26 ± 0.01) from Alonso et al. (1999). We adopt the spectroscopic parameters derived by Mc William (1990): effective temperature $T_{\rm eff} = 5010 \pm 100$ K, $\log g = 2.93 \pm 0.30$ and [Fe/H] = -0.04 ± 0.12. These parameters are different from – but within the error bars of – the parameters adopted by Frandsen et al. (2002) for this star. The star belongs to the HR diagram at the lowest part of the giant branch

corresponding to an evolved star with a mass around 3 $M_\odot$. Using a set of CORALIE spectra, Frandsen et al. (2002) detected solar-like oscillations suggesting radial modes with the largest amplitudes almost equidistant around 7.1 μHz. That important detection opens the possibility of better constraining the model of this star for which the mass is not well-known.

2.3. η Boo

η Boo (HD 121370, HR 5235, HIP 67927) is a subgiant (G0 IV) spectroscopic binary (SB1) studied recently by Di Mauro et al. (2003, 2004) and Guenther (2004). Its Hipparcos parallax is 88.17 ± 0.75 mas. Having large overabundances of Si, Na, S, Ni and Fe, it has been considered as super-metal-rich by Feltzing & Gonzales (2001). We adopt here a luminosity $L_\star/L_\odot = 8.95 \pm 0.20$ using BC (BC $= -0.06 \pm 0.01$, this is the dominant source of uncertainty on the luminosity) from Vandenberg & Clem (2003) for this subgiant, with an effective temperature $T_{\rm eff} = 6050 \pm 150$ K representing the average of five effective temperature determinations in the [Fe/H] catalogue of Cayrel de Strobel et al. (2001) and the spectroscopic $\log g = 3.66 \pm 0.20$ and [Fe/H] $= 0.24 \pm 0.07$ from Feltzing & Gonzales (2001). These parameters are different from – but within the error bars of – the parameters adopted by Di Mauro et al. (2003, 2004) for this star. Asteroseismic observations of δ Eri have been reported by Carrier et al. (2005) with $\Delta\nu_0 = 39.9 \pm 0.1$ μHz and by Kjeldsen et al. (2003) with $\Delta\nu_0 = 40.47 \pm 0.05$ μHz.

3. Diameter interferometric measurements

3.1. VINCI and the VLTI

The European Southern Observatory's Very Large Telescope Interferometer (Glindemann et al. 2000) has been operated on top of the Cerro Paranal, in Northern Chile since March 2001. For the observations reported in this work, the light coming from two telescopes (two 0.35 m test siderostats or VLT/UT1-UT3) was combined coherently in VINCI, the VLT Interferometer Commissioning Instrument (Kervella et al. 2000). We used a regular K band filter ($\lambda = 2.0$–2.4 μm) for these observations.

3.2. Data reduction

We used an improved version of the standard VINCI data reduction pipeline (Kervella et al. 2004b), whose general principle is based on the original FLUOR algorithm (Coudé du Foresto et al. 1997). The two calibrated output interferograms are subtracted to remove residual photometric fluctuations. Instead of the classical Fourier analysis, we implemented a time-frequency analysis (Ségransan et al. 1999) based on a continuous wavelet transform.

The atmospheric piston effect between the two telescopes corrupts the amplitude and the shape of the fringe peak in the wavelet power spectrum. As described in Kervella et al. (2004b), the properties of the fringe peaks in the time and frequency domains are monitored automatically, in order to reject from the processing the interferograms that are strongly affected by the atmospheric piston. This selection reduces the statistical dispersion of the squared coherence factors (μ^2) measurement, and avoids biases from corrupted interferograms. The final μ^2 values are derived by integrating the average wavelet power spectral density (PSD) of the interferograms at the position and frequency of the fringes. The residual photon and detector noise backgrounds are removed using a linear least squares fit of the PSD at high and low frequency. The statistical error bars on μ^2 are computed from the series of μ^2 values obtained on each target star (typically a few hundred interferograms) using the bootstrapping technique.

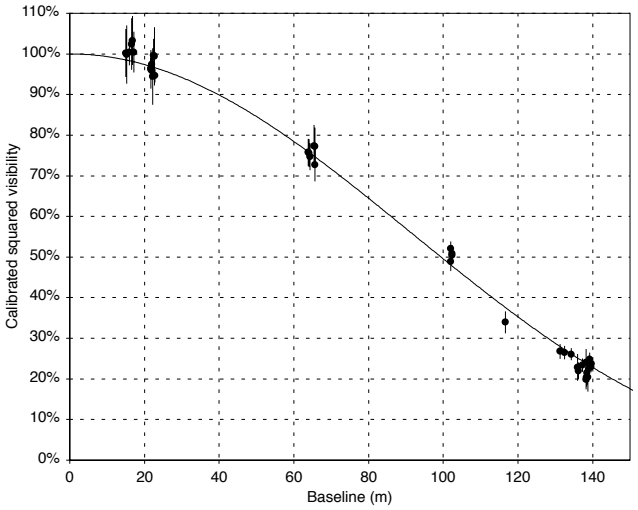

Fig. 1. Squared visibility measurements obtained on δ Eri. The solid line is a limb darkened disk model with $\theta_{\rm LD} = 2.394 \pm 0.014 \pm 0.025$ mas (statistical and systematic errors).

3.3. Measured visibilities and angular diameters

The visibility values obtained on δ Eri, ξ Hya and η Boo are listed in Tables 2 to 5, and plotted in Figs. 1 to 3.

The calibration of the visibilities obtained on δ Eri and η Boo was done using well-known calibrator stars that were selected from the Cohen et al. (1999) catalogue. The uniform disk (UD) angular diameter of these stars was converted into a limb darkened value and then to a K band uniform disk angular diameter using the recent non-linear law coefficients taken from Claret et al. (2000). As demonstrated by Bordé et al. (2002), the star diameters in this list have been measured very homogeneously to a relative precision of approximately 1%.

The VINCI instrument has no spectral dispersion and its bandpass corresponds to the K band filter (2–2.4 μm). It is thus important to compute the precise effective wavelength of the instrument in order to determine the angular resolution at which we are observing the targets. The effective wavelength differs from the filter mean wavelength because of the detector quantum efficiency curve, the fiber beam combiner transmission and the object spectrum. It is only weakly variable as a function of the spectral type.

To derive the effective wavelength of our observations, we computed a model taking into account the star spectrum and the VLTI transmission. The instrumental transmission of VINCI

Table 2. δ Eri squared visibilities.

Julian Date	Stations	N	B (m)	Az. (deg)	$V^2 \pm$ stat $\pm$ syst	Calibrator
2 452 682.528	B3-D1	74	22.638	14.95	0.9941 ± 0.0712 ± 0.0014	δ Lep
2 452 682.541	B3-D1	460	21.963	14.63	0.9740 ± 0.0140 ± 0.0014	δ Lep
2 452 682.545	B3-D1	281	21.735	14.55	0.9639 ± 0.0264 ± 0.0014	δ Lep
2 452 682.607	B3-D1	140	16.514	14.78	1.0242 ± 0.0632 ± 0.0014	δ Lep
2 452 682.612	B3-D1	340	15.954	14.99	1.0045 ± 0.0321 ± 0.0014	δ Lep
2 452 682.618	B3-D1	133	15.285	15.27	0.9987 ± 0.0715 ± 0.0013	δ Lep
2 452 671.562	B3-D1	233	22.437	14.84	0.9960 ± 0.0409 ± 0.0031	δ Lep
2 452 671.567	B3-D1	95	22.164	14.71	0.9442 ± 0.0697 ± 0.0029	δ Lep
2 452 671.574	B3-D1	210	21.749	14.55	0.9623 ± 0.0474 ± 0.0030	δ Lep
2 452 671.631	B3-D1	397	17.152	14.59	1.0042 ± 0.0501 ± 0.0014	δ Lep
2 452 671.635	B3-D1	206	16.756	14.71	1.0331 ± 0.0604 ± 0.0014	δ Lep
2 452 671.651	B3-D1	237	14.947	15.44	1.0023 ± 0.0588 ± 0.0014	δ Lep
2 452 672.553	B3-D1	401	22.756	15.02	0.9465 ± 0.0164 ± 0.0014	δ Lep
2 452 672.567	B3-D1	426	22.013	14.65	0.9585 ± 0.0153 ± 0.0014	δ Lep
2 452 672.603	B3-D1	379	19.478	14.26	0.9911 ± 0.0235 ± 0.0014	δ Lep
2 452 672.607	B3-D1	237	19.086	14.28	1.0134 ± 0.0540 ± 0.0015	δ Lep
2 452 673.567	B3-D1	236	21.898	14.60	0.9780 ± 0.0322 ± 0.0014	δ Lep
2 452 673.579	B3-D1	264	21.130	14.39	0.9940 ± 0.0264 ± 0.0015	δ Lep
2 452 673.609	B3-D1	441	18.693	14.31	1.0197 ± 0.0253 ± 0.0015	δ Lep
2 452 674.527	B3-D1	262	23.527	15.78	0.9718 ± 0.0294 ± 0.0014	δ Lep
2 452 674.557	B3-D1	415	22.253	14.75	0.9757 ± 0.0241 ± 0.0015	δ Lep
2 452 674.562	B3-D1	405	22.003	14.64	0.9833 ± 0.0249 ± 0.0015	δ Lep
2 452 674.566	B3-D1	314	21.756	14.55	0.9778 ± 0.0281 ± 0.0015	δ Lep
2 452 675.547	B3-D1	432	22.640	14.95	0.9731 ± 0.0213 ± 0.0014	δ Lep
2 452 676.557	B3-D1	383	21.997	14.64	0.9674 ± 0.0203 ± 0.0014	δ Lep
2 452 676.561	B3-D1	402	21.734	14.55	0.9813 ± 0.0201 ± 0.0015	δ Lep
2 452 676.565	B3-D1	259	21.474	14.47	0.9678 ± 0.0338 ± 0.0014	δ Lep
2 452 676.590	B3-D1	447	19.612	14.26	0.9883 ± 0.0227 ± 0.0014	δ Lep
2 452 676.602	B3-D1	328	18.603	14.32	0.9453 ± 0.0318 ± 0.0013	δ Lep
2 452 677.543	B3-D1	480	22.582	14.92	0.9651 ± 0.0283 ± 0.0014	δ Lep
2 452 677.547	B3-D1	445	22.366	14.80	0.9695 ± 0.0294 ± 0.0014	δ Lep
2 452 677.551	B3-D1	256	22.137	14.70	0.9283 ± 0.0407 ± 0.0013	δ Lep
2 452 677.587	B3-D1	267	19.633	14.26	1.0093 ± 0.0407 ± 0.0015	δ Lep
2 452 677.598	B3-D1	381	18.695	14.31	1.0013 ± 0.0384 ± 0.0015	δ Lep
2 452 677.603	B3-D1	287	18.286	14.36	1.0432 ± 0.0455 ± 0.0015	δ Lep
2 452 678.537	B3-D1	230	22.746	15.02	1.0024 ± 0.0382 ± 0.0014	δ Lep
2 452 678.548	B3-D1	121	22.186	14.72	0.9746 ± 0.0520 ± 0.0014	δ Lep
2 452 678.559	B3-D1	168	21.531	14.49	0.9900 ± 0.0492 ± 0.0014	δ Lep
2 452 678.584	B3-D1	422	19.649	14.26	1.0167 ± 0.0354 ± 0.0011	δ Lep
2 452 678.593	B3-D1	150	18.893	14.29	1.0966 ± 0.0618 ± 0.0012	δ Lep
2 452 679.561	B3-D1	402	21.184	14.40	0.9800 ± 0.0353 ± 0.0014	δ Lep
2 452 679.566	B3-D1	278	20.892	14.35	1.0211 ± 0.0435 ± 0.0015	δ Lep
2 452 683.578	B3-D1	374	19.065	14.28	0.9596 ± 0.0152 ± 0.0012	δ Lep
2 452 683.582	B3-D1	449	18.708	14.31	0.9900 ± 0.0147 ± 0.0013	δ Lep
2 452 683.586	B3-D1	283	18.316	14.36	0.9378 ± 0.0232 ± 0.0012	δ Lep
2 452 683.593	B3-D1	269	17.654	14.48	0.9915 ± 0.0274 ± 0.0013	δ Lep
2 452 683.598	B3-D1	250	17.167	14.59	0.9693 ± 0.0290 ± 0.0012	δ Lep
2 452 683.602	B3-D1	261	16.783	14.70	0.9154 ± 0.0274 ± 0.0012	δ Lep
2 452 684.516	B3-D1	296	22.937	15.15	0.9431 ± 0.0287 ± 0.0014	δ Lep
2 452 684.527	B3-D1	400	22.396	14.82	0.9473 ± 0.0220 ± 0.0014	δ Lep
2 452 684.562	B3-D1	439	20.148	14.27	0.9859 ± 0.0225 ± 0.0013	δ Lep
2 452 684.579	B3-D1	415	18.747	14.30	0.9882 ± 0.0232 ± 0.0013	δ Lep
2 452 685.587	B3-D1	206	17.669	14.47	1.0318 ± 0.0277 ± 0.0013	δ Lep

and the VLTI was first modeled taking into account all known effects and then calibrated based on several bright reference star observations with the UTs (see Kervella et al. 2003b, for details).

Taking the weighted average wavelength of this model spectrum gives an effective wavelength of $\lambda_{\rm eff} = 2.178 \pm 0.003\,\mu$m for δ Eri, ξ Hya and η Boo. The visibility fits were computed taking into account the limb darkening of the stellar

Table 3. δ Eri squared visibilities (continued from Table 2).

Julian Date	Stations	N	B (m)	Az. (deg)	$V^2 \pm$ stat $\pm$ syst	Calibrator
2 452 524.854	E0-G1	350	65.689	307.62	0.7271 ± 0.0400 ± 0.0054	70 Aql, 31 Ori
2 452 524.858	E0-G1	336	65.583	307.23	0.7720 ± 0.0464 ± 0.0057	70 Aql, 31 Ori
2 452 524.863	E0-G1	239	65.450	306.79	0.7729 ± 0.0521 ± 0.0057	70 Aql, 31 Ori
2 452 524.890	E0-G1	452	64.342	303.74	0.7467 ± 0.0329 ± 0.0055	70 Aql, 31 Ori
2 452 524.895	E0-G1	456	64.115	303.16	0.7561 ± 0.0336 ± 0.0056	70 Aql, 31 Ori
2 452 524.899	E0-G1	452	63.877	302.56	0.7579 ± 0.0332 ± 0.0056	70 Aql, 31 Ori
2 452 555.889	B3-M0	312	132.444	27.46	0.2742 ± 0.0150 ± 0.0055	δ Phe
2 452 555.893	B3-M0	275	131.275	27.44	0.2769 ± 0.0168 ± 0.0056	δ Phe
2 452 556.810	B3-M0	200	139.144	30.60	0.2477 ± 0.0152 ± 0.0067	δ Phe
2 452 556.817	B3-M0	395	139.500	30.10	0.2294 ± 0.0113 ± 0.0062	δ Phe
2 452 556.822	B3-M0	373	139.635	29.80	0.2370 ± 0.0117 ± 0.0064	δ Phe
2 452 564.830	B3-M0	146	138.416	28.23	0.2047 ± 0.0228 ± 0.0019	HR 8685
2 452 567.762	B3-M0	236	137.272	32.21	0.2245 ± 0.0153 ± 0.0044	HR 8685
2 452 577.789	B3-M0	173	138.926	28.46	0.2248 ± 0.0314 ± 0.0070	45 Eri, HR 2549
2 452 577.794	B3-M0	187	138.426	28.23	0.2156 ± 0.0289 ± 0.0067	45 Eri, HR 2549
2 452 213.776	UT1-UT3	73	101.996	232.98	0.4883 ± 0.0203 ± 0.0102	χ Phe
2 452 213.777	UT1-UT3	332	102.056	232.83	0.5207 ± 0.0138 ± 0.0109	χ Phe
2 452 213.791	UT1-UT3	69	102.374	231.76	0.5089 ± 0.0172 ± 0.0106	χ Phe
2 452 213.793	UT1-UT3	312	102.394	231.65	0.5044 ± 0.0150 ± 0.0105	χ Phe
2 452 578.723	B3-M0	269	135.965	33.09	0.2393 ± 0.0257 ± 0.0063	τ Cet
2 452 578.740	B3-M0	169	138.202	31.51	0.2520 ± 0.0246 ± 0.0066	τ Cet
2 452 578.745	B3-M0	74	138.752	31.02	0.2133 ± 0.0307 ± 0.0056	τ Cet
2 452 585.799	B3-M0	298	134.322	27.55	0.2608 ± 0.0134 ± 0.0071	τ Cet
2 452 601.810	B3-M0	206	116.676	28.41	0.3674 ± 0.0290 ± 0.0082	τ Cet
2 452 602.728	B3-M0	123	138.193	28.15	0.2183 ± 0.0241 ± 0.0056	τ Cet
2 452 602.742	B3-M0	396	136.193	27.73	0.2412 ± 0.0174 ± 0.0062	τ Cet

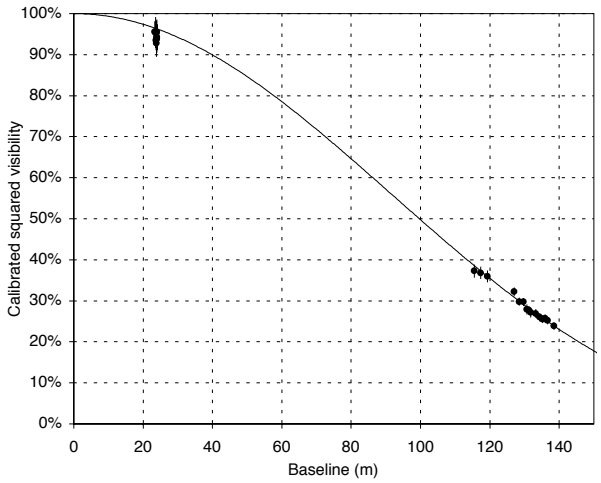

Fig. 2. Squared visibility measurements obtained on ξ Hya. The solid line is a limb darkened disk model with $\theta_{\rm LD} = 2.386 \pm 0.009 \pm 0.019$ mas (statistical and systematic errors).

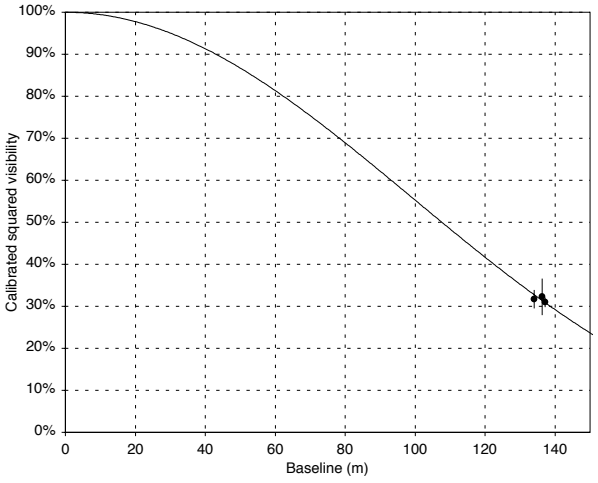

Fig. 3. Squared visibility measurements obtained on η Boo. The solid line is a limb darkened disk model with $\theta_{\rm LD} = 2.200 \pm 0.027 \pm 0.016$ mas (statistical and systematic errors).

disk of each stars. We used power law intensity profiles derived from the limb darkening models of Claret (2000) in the K band.

The resulting limb darkened diameters for the three program stars are given in Table 1. The statistical error bars were computed from the statistical dispersion of the series of μ^2 values obtained on each star (typically a few hundred), using the bootstrapping technique. The systematic error bars come from the uncertainties on the angular diameters of the calibrators that were used for the observation. They impact the precision of the interferometric transfer function measurement, and thus affect the final visibility value. Naturally, these calibration error bars do not get smaller when the number of observations increases, as the statistical errors do. The detailed methods and hypothesis used to compute these error bars are given in Kervella et al. (2004b).

Table 4. ξ Hya squared visibilities.

Julian Date	Stations	N	B (m)	Az. (deg)	$V^2 \pm$ stat $\pm$ syst	Calibrators
2 452 681.743	B3-D1	333	23.650	27.39	0.9539 ± 0.0376 ± 0.0008	α Crt
2 452 681.747	B3-D1	460	23.727	26.48	0.9520 ± 0.0305 ± 0.0008	α Crt
2 452 681.751	B3-D1	343	23.801	25.51	0.9281 ± 0.0334 ± 0.0007	α Crt
2 452 681.777	B3-D1	452	23.995	20.50	0.9555 ± 0.0304 ± 0.0008	α Crt
2 452 681.781	B3-D1	332	23.989	19.60	0.9383 ± 0.0337 ± 0.0008	α Crt
2 452 681.785	B3-D1	427	23.975	18.89	0.9424 ± 0.0305 ± 0.0008	α Crt
2 452 682.729	B3-D1	354	23.407	29.82	0.9560 ± 0.0251 ± 0.0009	α Crt
2 452 682.752	B3-D1	295	23.846	24.85	0.9519 ± 0.0280 ± 0.0009	α Crt
2 452 682.792	B3-D1	297	23.904	17.19	0.9420 ± 0.0317 ± 0.0007	α Crt
2 452 682.801	B3-D1	403	23.773	15.47	0.9351 ± 0.0237 ± 0.0007	α Crt
2 452 760.583	B3-M0	350	138.521	60.37	0.2383 ± 0.0058 ± 0.0069	α Crt
2 452 760.600	B3-M0	343	136.690	63.11	0.2520 ± 0.0061 ± 0.0073	α Crt
2 452 760.605	B3-M0	391	135.918	63.96	0.2568 ± 0.0059 ± 0.0075	α Crt
2 452 760.635	B3-M0	433	129.762	68.49	0.2971 ± 0.0058 ± 0.0077	α Crt
2 452 760.640	B3-M0	388	128.458	69.20	0.2978 ± 0.0061 ± 0.0077	α Crt
2 452 760.645	B3-M0	284	127.037	69.92	0.3221 ± 0.0071 ± 0.0084	α Crt
2 452 761.624	B3-M0	429	131.833	67.24	0.2714 ± 0.0063 ± 0.0097	51 Hya
2 452 761.628	B3-M0	303	130.716	67.94	0.2787 ± 0.0077 ± 0.0100	51 Hya
2 452 761.665	B3-M0	421	119.296	73.16	0.3592 ± 0.0063 ± 0.0131	51 Hya
2 452 761.671	B3-M0	402	117.300	73.87	0.3681 ± 0.0067 ± 0.0135	51 Hya
2 452 761.675	B3-M0	340	115.485	74.49	0.3727 ± 0.0087 ± 0.0136	51 Hya
2 452 762.604	B3-M0	470	135.192	64.66	0.2554 ± 0.0021 ± 0.0092	51 Hya
2 452 762.609	B3-M0	454	134.296	65.44	0.2600 ± 0.0022 ± 0.0094	51 Hya
2 452 762.614	B3-M0	386	133.310	66.21	0.2689 ± 0.0049 ± 0.0097	51 Hya
2 452 762.623	B3-M0	441	131.274	67.59	0.2771 ± 0.0027 ± 0.0100	51 Hya

Table 5. η Boo squared visibilities.

Julian Date	Stations	N	B (m)	Az. (deg)	$V^2 \pm$ stat $\pm$ syst	Calibrators
2 452 760.684	B3-M0	131	134.046	64.22	0.3167 ± 0.0187 ± 0.0119	α Crt
2 452 760.696	B3-M0	50	136.318	63.31	0.3227 ± 0.0415 ± 0.0121	α Crt
2 452 763.693	B3-M0	187	137.132	62.88	0.3095 ± 0.0092 ± 0.0064	μ Vir

3.4. Search for a companion to δ Eri

δ Eri is classified as an RS CVn variable (Kholopov et al. 1998), and has shown a small amplitude photometric variability (m_V = 3.51 to 3.56). Fisher et al. (1983) have also reported photometric variations with an amplitude $\Delta m_V = 0.02$ over a period of 10 days. This small amplitude and the apparent absence of periodic radial velocity modulation lead these authors to propose that δ Eri is a close binary star seen nearly pole on ($i \leq 5$ deg). Following this idea, we can suggest three hypotheses to explain the observed photometric variations:

1. The main star is ellipsoidal. This would result in a modulation of its projected surface along the line of sight during its rotation. This deformation would be caused by the close gravitational interaction of the main star with the unseen companion.
2. The companion creates a hot spot on the hemisphere of the main star that is facing it. It is changing in apparent surface when the system rotates, probably synchronously.
3. The pole of the main component has a dark spot that changes in apparent surface during the rotation of the star.

The period of the photometric variations, if attributed to the presence of an orbiting companion, allows us to deduce the distance between the two components through Kepler's third law. At the distance of δ Eri, this corresponds to an angular separation of approximately 9 mas, easily resolvable using the moderately long baselines of the VLTI. Using the B3-D1 stations of the VLTI, we have taken advantage of the fact that the azimuth of the projected baseline is almost constant for observations of δ Eri to monitor the evolution of its visibility over a period of 13 nights. The projected length is also very well suited to the expected separation. Our interferometric data (Fig. 4) does not show any systematic deviation from the uniform disk model fit obtained using the longer baselines, at a level of 0.2 ± 0.3%, consistent with zero. From these measurements, we conclude that no companion is detected at a level of about ±2% of the luminosity of the primary star. This result is consistent with the fact that δ Eri does not deviate significantly from the surface-brightness relations determined by Kervella et al. (2004c).

4. Models and results

In order to obtain a rapid estimate of the improvements brought by the new interferometric constraints on the radius on the determination of the mass and age of the three stars, we have

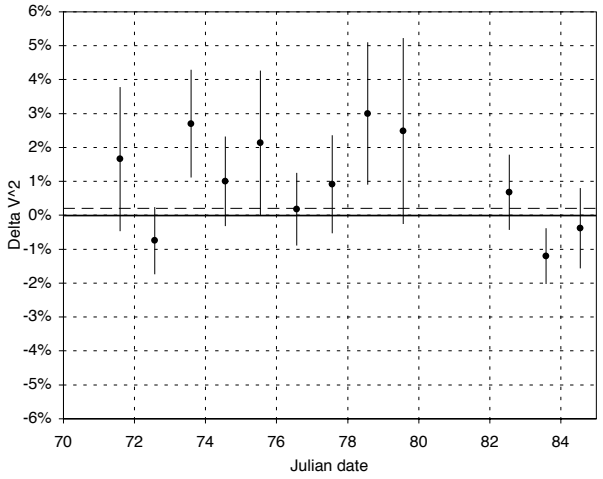

Fig. 4. Observed deviation of the squared visibilities of δ Eri (B3-D1 baseline only) with respect to the visibility model of a $\theta_{\rm UD}$ = 2.394 mas uniform disk model. The dashed line represents the average deviation over all observations (0.21%).

calculated evolutionary stellar models that we compare to observations. In these models we have adopted a given set of standard input physics and the observational parameters described in Sect. 2 and Table 1. We do not intend to examine in detail the effects on the uncertainties of the details of the models (envelope, convection, overshooting or other extra mixing) on the results presented here.

The parameters used to construct our CESAM (Morel 1997) evolutionary models are summarized in Table 1. The convection is described by Canuto & Mazitelli's theory (1991, 1992) and the atmospheres are restored on the basis of Kurucz's atlas models (1992). The other input physics are identical to those adopted for the star Procyon (see Kervella et al. 2004a). The adopted metallicity Z/X, which is an input parameter for the evolutionary computations, is given by the iron abundance measured in the atmosphere with the help of the following approximation: $\log\left(\frac{Z}{X}\right) \simeq$ [Fe/H] + $\log\left(\frac{Z}{X}\right)_\odot$. We use the solar mixture of Grevesse & Noels (1993): $\left(\frac{Z}{X}\right)_\odot = 0.0245$.

The evolutionary tracks are initialized at the Pre-Main Sequence stage. Note that the age is counted from the ZAMS. In CESAM, the ZAMS is defined as the stage of the end of the Pre-Main Sequence where the gravitational energy release is equal to the nuclear one. We have computed models with and without microscopic diffusion of chemical species.

To fit observational data (effective temperature $T_{\rm eff}$, luminosity L and surface metallicity $[Z/X]_{\rm surf}$) with corresponding results of various computations, we adjust the main stellar modeling parameters: mass, age and metallicity. In figures representing the zoom of HR diagram (Figs. 6, 8, 10 and 12), the (rectangular) error boxes are derived from the values and accuracies of the stellar parameters quoted in Table 1. The present (new) values of radii, presented in this paper, select sub-areas in these error boxes and hence the new measures of diameters are used to discriminate between our models (see Table 1). Our best model is the one that satisfies first the luminosity and radius constraint and second the effective temperature constraint. On the zooms of the HR diagrams (see Figs. 6, 8, 10 and 12), the measured radius and its confidence interval appear as diagonal lines. We notice that the addition of the radius measurement reduces significantly the uncertainty domain, and in some cases tightens the allowed range for ages by a factor of three (see below). We have computed models that include overshooting of the convective core (radius $R_{\rm co}$) over the distance $O_{\rm v} = A_{\rm ov}\,\min(H_{\rm p}, R_{\rm co})$ where $R_{\rm co}$ is the core radius, following the prescriptions of Schaller et al. (1992).

4.1. δ Eri

First, we adopt an initial helium content similar to the Sun, $Y_{\rm ini} = 0.28$ and $[Z/X]_{\rm ini} = 0.148$, both stars having similar ages and abundances (this will be confirmed hereafter).

Then, with mass and metallicity as free parameters, we have computed a grid of evolutionary tracks in order to reproduce observational data. Our best model without diffusion and without overshooting gives $M = 1.215\,M_\odot$ and an age (from the ZAMS) of 6196 Myr. Our best model with diffusion and an overshooting value of $A_{\rm ov} = 0.15$ in agreement with the results of Ribas et al. (2000) gives $M = 1.215\,M_\odot$, an age (from the ZAMS) of 6194 Myr and a diameter of $D = 2.328\,D_\odot$. See Figs. 5 and 6.

The mean large frequency splitting found for our best model is 45.27 μHz. This result is in agreeement within two per cent with the value of 43.8 μHz of the mean large frequency splitting reported by Carrier et al. (2003).

4.2. ξ Hya

We have computed a grid of evolutionary tracks (with and without diffusion) in order to reproduce observational data. Hence, we derived the following parameters: $M = 2.65\,M_\odot$, $Y_{\rm ini} = 0.275$ and $[Z/X]_{\rm ini} \equiv 0.0$. Our best model with diffusion and an overshooting value of $A_{\rm ov} = 0.20$ in agreement with the results of Ribas et al. (2000) gives us an age (from the ZAMS) of 509.5 Myr and a diameter of $D = 10.3\,D_\odot$. To improve the modeling, a better precision of the diameter is required as it is the case for the two other stars discussed in this paper, for which the accuracy is better by an order of magnitude. See Figs. 7 and 8.

Solar-like oscillations of that star were discovered by Frandsen et al. (2002) with a mean spacing of 7.1 μHz; see also Teixeira et al. (2003). From our model, we computed a value of 7.2 μHz similar to the theoretical value presented by Frandsen et al. or Teixeira et al.

4.3. η Boo

Concerning the values of $T_{\rm eff}$ and its corresponding uncertainty, we have chosen conservative values based upon various determinations: Feltzing & Gonzales (2001) gives $T_{\rm eff} = 6000 \pm 100$ K whereas Cayrel de Strobel (2001) gives a range between 5943 and 6219 K . We notice that DiMauro et al. adopt $T_{\rm eff} = 6028 \pm 45$ K but in our study, we take advantage of the constraint given by the new diameter value which reduces the uncertainty as shown in Figs. 10 or 12.

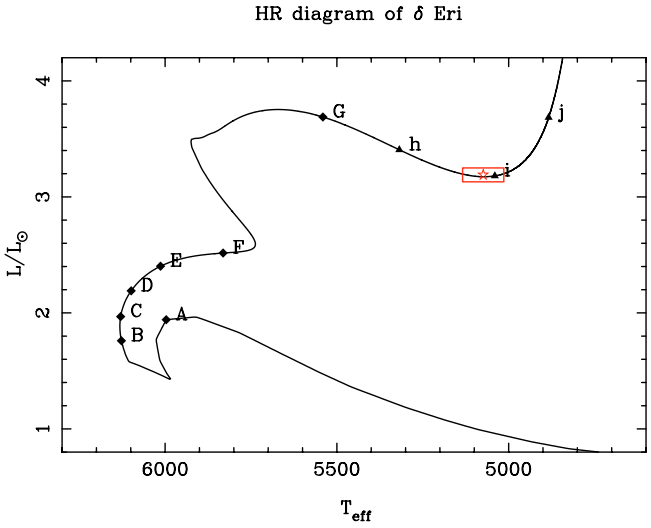

Fig. 5. Evolutionary tracks in the H-R diagram for δ Eri from label "A" (0 Myr) to label "G" (6000 Myr), shown by upper case letters and squares with time steps of 1000 Myr; from label "h" (6100 Myr) to label "j" (6300 Myr), shown by lower case letters and triangles with time steps of 100 Myr.

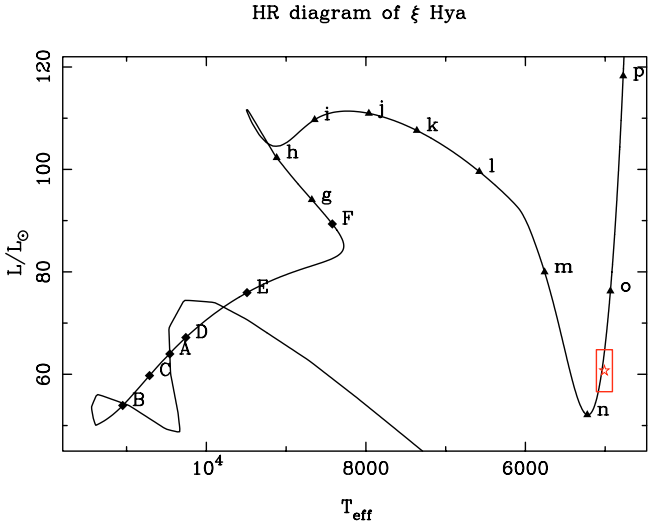

Fig. 7. Evolutionary tracks in the H-R diagram for ξ Hya from label "A" (0 Myr) to "F" (500 Myr), shown by upper case letters and squares with time steps of 100 Myr; from label "g" (502 Myr) to "p" (511 Myr), show by lower case letters and triangles with time steps of 1 Myr.

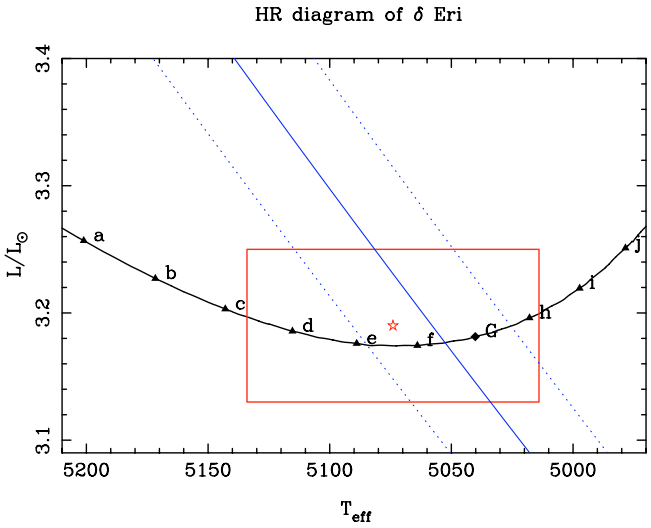

Fig. 6. Zoom of the evolutionary tracks in the H-R diagram for δ Eri from label "a" (6140 Myr) to label "j" (6230 Myr), shown by lower case letters and triangles with time steps of 10 Myr (except label "G" at 6200 Myr shown by an upper case letter and a square). Our best model is close to label "f" at 6194 Myr (see Table 1).

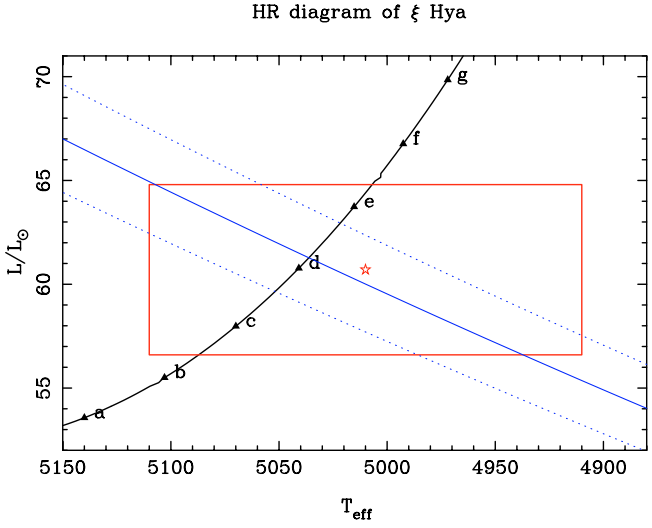

Fig. 8. Zoom of the evolutionary tracks in the H-R diagram for ξ Hya. from label "a" (509.2 Myr) to "g" (509.8 Myr), shown by lower case letters and triangles with time steps of 0.1 Myr. Our best model is close to label "d" at 509.5 Myr (see Table 1).

In a first attempt to characterize this star, DiMauro et al. (2003) limit the range of mass between 1.64 $M_\odot$ and 1.75 $M_\odot$. Guenther (2004) adopted in his conclusion a mass of 1.706 $M_\odot$ with an initial chemical composition: $X_{\rm ini}$ = 0.71 , $Y_{\rm ini}$ = 0.25 and $Z_{\rm ini}$ = 0.04. In the present study, we have computed a grid of models and it appears that the best fitting parameters are M = 1.70 $M_\odot$ with an initial chemical composition $X_{\rm ini}$ = 0.70, $Y_{\rm ini}$ = 0.26 and Z$_{\rm ini}$ = 0.04. A first set of models have been computed with the simplest available reliable physics (and therefore without diffusion, as probably done by the previously cited authors). A second set of models have also been computed with improved physics. Thus, we include convective overshooting (with $A_{\rm ov}$ = 0.15, see previous discussion), diffusion and radiative diffusivity (see Morel & Thévenin 2002) which controls diffusion of chemical elements in intermediate mass stars. The two sets of results give similar results except for the ages: the age of the best model with diffusion (2738.5 Myr) is higher than the age of the best model without diffusion (2355.0 Myr).

As shown, for example, in Fig. 10, without the constraint given by the diameter, the age would range from 2295 Myr (between label "b" and label "c") to 2410 Myr (close to label "n"), with a derived uncertainty of 115 Myr. For a given set of input physics, the constraint on diameter reduces the uncertainty on the age by about a factor of three: the age would

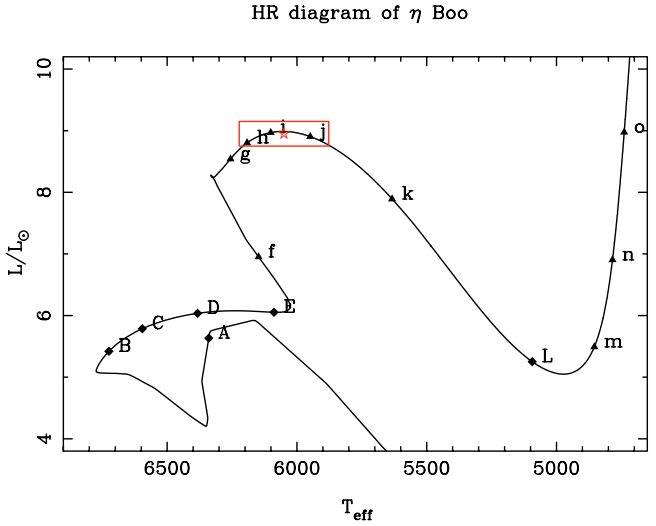

Fig. 9. Evolutionary tracks in the H-R diagram for η Boo (model without diffusion) from label "A" (0 Myr) to "E" (2000 Myr), shown by upper case letters and squares with time steps of 500 Myr; from label "f" (2200 Myr) to "o" (2650 Myr), shown by lower case letters and triangles with time steps of 50 Myr (except label "L" at 2500 Myr shown by an upper case letter and a square).

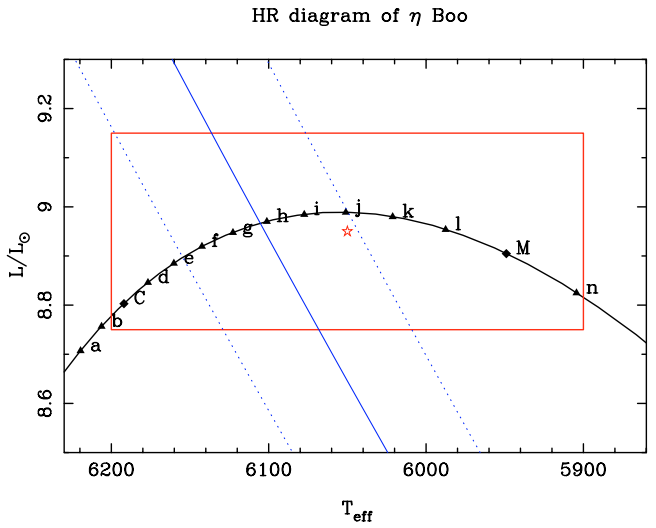

Fig. 10. Zoom of the evolutionary tracks in the H-R diagram for η Boo (model without diffusion) from label "a" (2280 Myr) to "n" (2410 Myr), shown by lower case letters and triangles with time steps of 10 Myr (except labels "C" at 2300 Myr and label "M" a 2400 Myr shown by an upper case letters and squares). Our best model is close to label "h" at 2350 Myr (see Table 1).

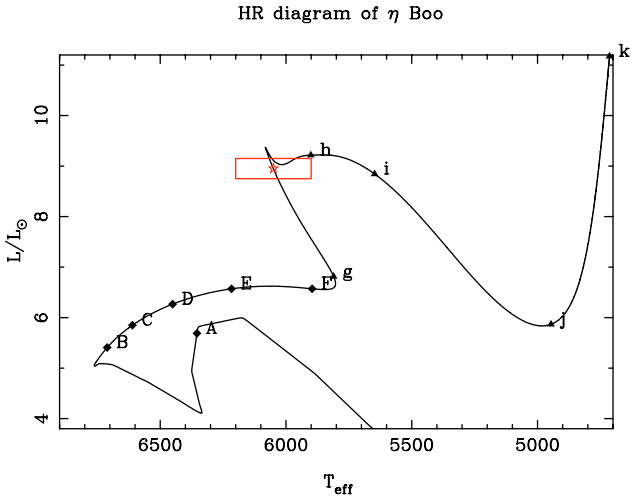

Fig. 11. Evolutionary tracks in the H-R diagram for η Boo (model with diffusion) from label "A" (0 Myr) to label "F" (2500 Myr), shown by upper case letters and squares with a time step of 500 Myr; label "g" at 2700 Myr shown by a triangle; from label "h" (2750 Myr) to label "k" (2900 Myr), shown by lower case letters and triangles with a time step of 50 Myr.

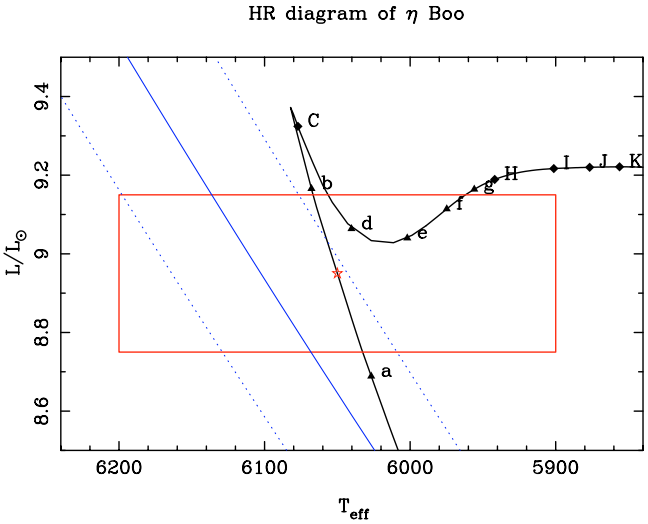

Fig. 12. Zoom of the evolutionary tracks in the H-R diagram for η Boo (model with diffusion) from label "a" (2738 Myr) to label "g" (2744 Myr), shown by lower case letters and triangles with time steps of 1 Myr (except label "C" at 2740 Myr shown by a square); from label "H" (2745 Myr) to label "K" (2760 Myr), shown by upper case letters and squares with time steps of 5 Myr. Our best model is between label "a" (at 2738 Myr) and label "b" (at 2739 Myr) (see Table 1).

be ranging from 2323 Myr (close to label "e") to 2370 Myr (close to label "j"), corresponding to a (reduced) uncertainty of 47 Myr (Figs. 9–12). Note that our model for η Boo with diffusion (Figs. 11 and 12) has the star in a very short-lived phase of evolution (which is, of course, possible but with a small, but non zero, probability).

5. Concluding remarks

We have measured with the instrument VLTI/VINCI the angular diameters of three subgiant and giant stars and used them as an additive constraint to the spectro-photometric and asteroseismic ones to perform a study of the stellar evolutionary status.

Owing the position of the three stars in the HR diagram, the determination of the modeling parameters, in particulary the age, is very sensitive to the input physics, due to the rapidity of the stellar evolution compared to the size of the error boxes.

With our input physics and observational constraints, δ Eri is a star at the end of the subgiant phase ($M = 1.215\ M_{\odot}$) with an age of 6.2 Gyr. We attempt without success to detect a close

companion forcing us to conclude that the classification of δ Eri as an RS CVn star is doubtful.

ξ Hya has been constrained with success with a model adopting a mass of 2.65 $M_{\odot}$ and an age of 510 Myr.

η Boo is a subgiant slightly more evolved than Procyon with a similar age of 2.7 Gyr. With a mass of at $M = 1.7\,M_{\odot}$ (similar to the mass adopted by Di Mauro et al. 2003), we were able to reproduce the VLTI/VINCI radius. We notice that because of the short evolutionary time scales of a model crossing rather large error boxes, the results of the models – in particular the age – are very sensitive to the input physics (for instance, the core mixing. Some progress in the asteroseismic observations is now required to better constrain the evolutionary state of giant stars for which the frequency spacings (Bouchy & Carrier 2003; Bedding & Kjeldsen 2003) are still relatively imprecise. The improvement of the angular diameter estimations in the future will further tighten the uncertainty domain in the HR diagram, especially as detailed modeling of the atmosphere will be required. This improvement will naturally require a higher precision on the parallax value to derive the linear diameters.

Acknowledgements. The VINCI public commissioning data reported in this paper has been retrieved from the ESO/ST-ECF Archive. The VINCI pipeline includes the wavelets processing technique, developed by D. Ségransan (Obs. de Genève). No VLTI observation would have been possible without the efforts of the ESO VLTI team, to whom we are grateful. This work has been performed using the computing facilities provided by the program Simulations Interactives et Visualisation en Astronomie et Mécanique (SIVAM) at the computer center of the Observatoire de la Côte d'Azur. This research has made use of the Simbad database operated at CDS, Strasbourg, France. We thank the referee, T. R. Bedding, for his suggested improvements of this paper.

References

Alonso, A., Arribas, S., & Martínez-Roger, C. 1999, A&AS, 140, 261
Bedding, T. R., & Kjeldsen, H. 2003, PASA, 20, 203
Bordé, P., Coudé du Foresto, V., Chagnon, G., & Perrin, G. 2002, A&A, 393, 183
Bouchy, F., & Carrier, F. 2003, Ap&SS, 284, 21
Canuto, V. M., & Mazitelli, I. 1991, ApJ, 370, 295
Canuto, V. M., & Mazitelli, I. 1992, ApJ, 389, 729
Carrier, F., Bouchy, F., & Eggenberger, P. 2003, in Asteroseismology across the HR diagram, ed. M. J. Thompson, M. S., Cunha, & M. J. Monteiro (Kluwer Academic Publishers) 311
Carrier, F., Eggenberger, P., & Bouchy, F. 2005, A&A, 434, 1085
Cayrel de Strobel, G., Soubiran, C., & Ralite, N. 2001, A&A, 373, 159
Claret, A. 2000, A&A, 363, 1081
Cohen, M., Walker, R. G., Carter, B., et al. 1999, AJ, 117, 1864
Coudé du Foresto, V., Ridgway, S., & Mariotti, J.-M. 1997, A&AS, 121, 379
Di Folco, E., Thévenin, F., Kervella, P., et al. 2004, A&A, 426, 601
Di Mauro, M. P., Christensen-Dalsgaard, J., Kjeldsen, H., Bedding, T. R., & Paternò, L. 2003, A&A, 404, 341
Di Mauro, M. P., Christensen-Dalsgaard, J., Paternò, L., & D'Antona, F. 2004, Sol. Phys., 220, 185
Eggen O. J., ApJ, 215, 812
Feltzing, S., & Gonzales, G. 2001, A&A, 367, 251
Fisher, G. F., Hall, D. S., Henry, G. W., et al. 1983, IBVS, 2259, 1
Frandsen, S., Carrier, F., Aerts, C., et al. 2002, A&A, 394, L5
Glindemann, A., Abuter, R., Carbognani, F., et al. 2000, SPIE, 4006, 2
Grevesse, N., & Noels, A. 1993, Cosmic Abundances of the Elements, in Origin and Evolution of the Elements, ed. N. Prantzos, E. Vangioni-Flam, & M. Cassé (Cambridge University Press), 14
Guenther, D. B. 2004, ApJ, 612, 454
Huensch, M., Schmitt, J. H. M. M., & Voges, W. 1999, A&AS, 132, 155
Keenan, P. C., & Pitts, R. E. 1980, ApJS, 42, 541
Kervella, P., Coudé du Foresto, V., Glindemann, A., & Hofmann, R. 2000, SPIE, 4006, 31
Kervella, P., Thévenin, F., Ségransan, D., et al. 2003a, A&A, 404, 1087
Kervella, P., Thévenin, F., Morel, P., Bordé, P., & Di Folco, E. 2003b, A&A, 408, 681
Kervella, P., Thévenin, F., Morel, P., et al. 2004a, A&A, 413, 251
Kervella, P., Ségransan, D., & Coudé du Foresto, V. 2004b, A&A, 425, 1161
Kervella, P., Thévenin, F., Ségransan, D., & Di Folco, E. 2004c, A&A, 426, 297
Kholopov, P. N., et al., The Combined General Catalogue of Variable Stars, 1998, 4th Edition
Kjeldsen, H., Bedding, T. R., Baldry, I. K., et al. 2003, AJ, 126, 1483
Kurucz, R. L. 1992, The Stellar Populations of Galaxies, IAU Symp., 149, 225
Linsky, J. L. 1984, LNP, 193, 244
McWilliam, A. 1990, ApJS, 74, 1075
de Medeiros, J., & Mayor, M. 1999, A&AS, 139, 433
Morel, P. 1997, A&AS, 124, 597
Morel, P., & Thévenin, F. 2002, A&A, 390, 611
Perryman, M. A. C., Lindegren, L., Kovalevsky, J., et al. 1997, A&A, 323, 49
Petrov, R., Amber consortium 2003, EAS Pub. Series, 6, 111
Pijpers, F. P. 2003, A&A, 400, 241
Ribas, I., Jordi, C., & Giménez, À. 2000, MNRAS, 318, L55
Santos, N. C., Israelian, G., & Mayor, M. 2004, A&A, 415, 1153
Schaller, G., Schaerer, D., Meynet, G., & Maeder, A. 1992, A&AS, 96, 269
Ségransan, D., Forveille, T., Millan-Gabet, C. P. R., & Traub, W. A. 1999, in ASP Conf. Ser., 194, 290
Ségransan, D., Kervella, P., Forveille, T., & Queloz, D. 2003, A&A, 397, L5
Teixeira, T. C., Christensen-Dalsgaard, J., Carrier, F., et al. 2003, Ap&SS, 284, 233
VandenBerg, D. A., & Clem, J. L. 2003, AJ, 126, 778
Weiler, E. J., & Oegerle, W. R. 1979, ApJS, 39, 537
Wilson, O. C., & Vainu Bappu, M. K. 1957, ApJ, 125, 661

3.3 Assombrissement centre-bord

L'assombrissement centre-bord (ACB) est une des caractéristiques observationnelles les plus importantes des atmosphères stellaires. ll s'agit cependant d'un effet particulièrement difficile à mesurer directement sur les étoiles autres que le Soleil (Fig. 3.6), car il se manifeste comme une faible modulation de la visibilité interférométrique avec la fréquence spatiale ou la longueur de la base utilisée (Fig. 3.3).

Pourtant, une bonne connaissance de l'ACB est indispensable pour traduire correctement des visibilités interférométriques en une mesure de diamètre angulaire photosphérique. Jusqu'à présent, on utilise en général les résultats de modèles numériques d'atmosphère du type de ceux de Kurucz (1992). Même s'ils ont donné de bons résultats pour les étoiles géantes mesurées par interférométrie (voir par exemple l'étude de la géante rouge ψ Phe par Wittkowski et al. 2004), le cas des étoiles naines n'est pas aussi bien étudié.

La raison à cela est essentiellement la petite taille des étoiles de la séquence principale. Avec les interféromètres existant actuellement ($B \leq 330\,\mathrm{m}$), et pour des étoiles plus petites angulairement que 2 mas, il est très difficile d'atteindre une résolution angulaire suffisante pour se trouver dans la partie de leur courbe de visibilité sensible à l'ACB : le second lobe. Si la mesure de la taille d'une étoile demande typiquement un seul élément de résolution de l'interféromètre sur le disque de l'étoile, la mesure de l'ACB en réclame au minimum 2, ce qui implique une longueur de base deux fois plus grande. Il faut comprendre que la limite de 2 mas donnée ci-dessus correspond à la taille apparente du Soleil à une distance de seulement 4,5 parsec. Dans un tel volume restreint, le nombre d'étoiles accessible à une mesure interférométrique d'ACB est naturellement assez faible. Les étoile naines les plus favorables pour ce type d'étude sont α Cen A et B (Sect. 3.3.1).

Une discussion de l'ACB de l'étoile naine Véga est présentée à la Sect. 4.4. Elle est dissociée de ce chapitre sur les étoiles de la séquence principale car l'ACB de Véga est fortement affecté par la rotation de l'étoile.

FIG. 3.6 – Photographie du Soleil en lumière blanche montrant son assombrissement centre-bord (crédit photo : P. Hyndman).

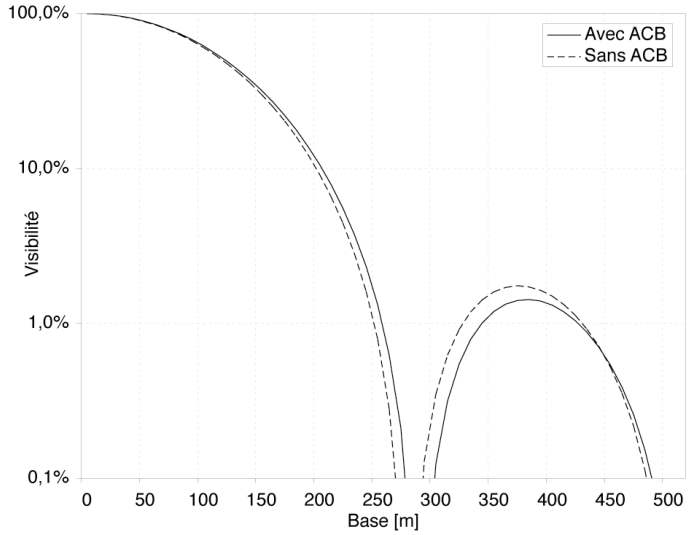

FIG. 3.7 – Fonction de visibilité interférométrique d'une étoile de type solaire d'un diamètre angulaire de 2 mas, en bande K, avec et sans prise en compte de son assombrissement centre-bord (modèle linéaire avec $u = 0,28$).

3.3.1 Article A&A : "The limb darkening of α Cen B. Matching 3D hydrodynamical models with interferometric measurements" (2006)

Nous avons obtenu avec VINCI une mesure de la visibilité de α Cen B dans le second lobe de sa fonction de visibilité, ainsi que des observations supplémentaires dans le premier lobe par rapport à notre article de 2003 (Sect. 3.2.1). Dans le but d'améliorer notre connaissance de l'ACB de cette étoile, nous avons calculé un modèle hydrodynamique tridimensionnel (3D hydro) de la partie supérieure de l'atmosphère stellaire. Le résultat de cette modélisation est comparé aux mesures interférométriques, ainsi qu'à un modèle 1D plus simple de type Kurucz (1992). Même si la quantité et la précision des données n'est pas encore suffisante pour conclure, l'approche 3D hydro reproduit mieux les observations que l'approche 1D classique.

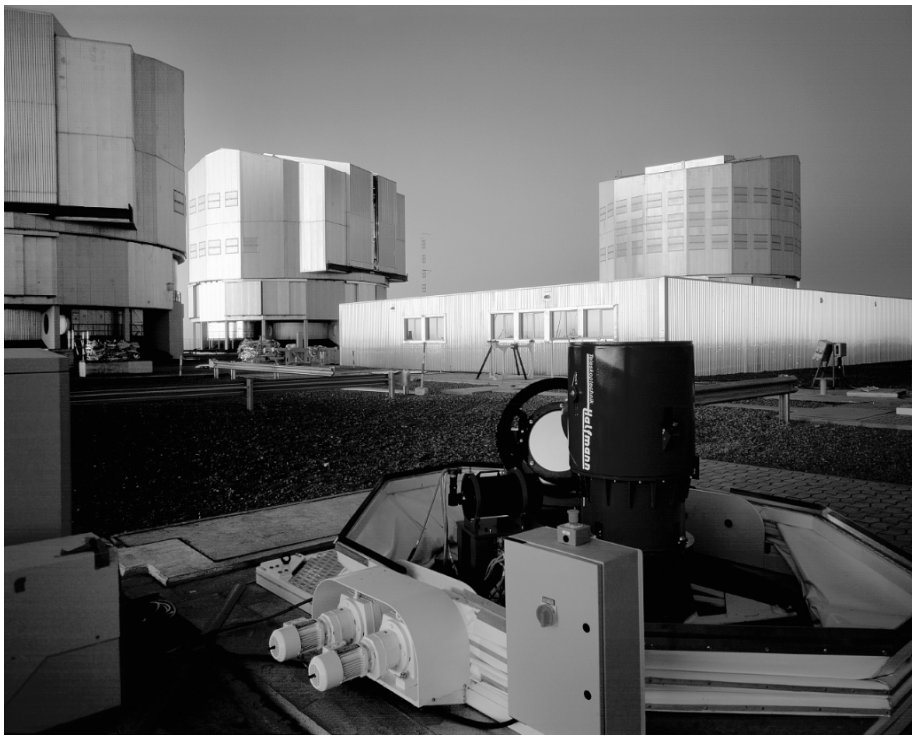

FIG. 3.8 – Au premier plan, un sidérostats de test du VLTI (35cm de diamètre), et en arrière plan les trois grands télescopes UT2, UT3 et UT4. Le bâtiment du laboratoire interférométrique est visible à droite.

A&A 446, 635–641 (2006)
DOI: 10.1051/0004-6361:20053187

Astronomy & Astrophysics

The limb darkening of α Centauri B

Matching 3D hydrodynamical models with interferometric measurements

L. Bigot[1], P. Kervella[2], F. Thévenin[1], and D. Ségransan[3]

[1] Département Cassiopée, UMR 6202, Observatoire de la Côte d'Azur, BP 4229, 06304 Nice Cedex 4, France
e-mail: lbigot@obs-nice.fr
[2] LESIA, UMR 8109, Observatoire de Paris-Meudon, 5 place Jules Janssen, 92195 Meudon Cedex, France
[3] Observatoire de Genève, 1290 Sauverny, Switzerland

Received 4 April 2005 / Accepted 12 September 2005

ABSTRACT

For the nearby dwarf star α Cen B (K1 V), we present limb-darkening predictions from a 3D hydrodynamical radiative transfer model of its atmosphere. We first compared the results of this model to a standard Kurucz's atmosphere. Then we used both predictions to fit the new interferometric visibility measurements of α Cen B obtained with the VINCI instrument of the VLT Interferometer. Part of these new visibility measurements were obtained in the second lobe of the visibility function, which is sensitive to stellar limb-darkening. The best agreement is found for the 3D atmosphere limb-darkening model and a limb-darkened angular diameter of $\theta_{3D} = 6.000 \pm 0.021$ mas, corresponding to a linear radius of $0.863 \pm 0.003\,R_\odot$ (assuming $\pi = 747.1 \pm 1.2$ mas). Our new linear radius agrees well with the asteroseismic value predicted by Thévenin et al. (2002, A&A, 392, L9). In view of future observations of this star with the VLTI/AMBER instrument, we also present limb-darkening predictions in the J, H, and K bands.

Key words. instrumentation: interferometers – stars: atmospheres

1. Introduction

Limb-darkening (hereafter LD) is a well-known effect in stellar physics. Its manifestation is a non-uniform brightness of the disk, whose edges appear fainter than the center. This effect occurs because of the decrease in the source function outwards in the atmosphere. The disk center then shows deeper and warmer layers, whereas the edges show higher and cooler material. This means that analysis of the intensity $I_\lambda(\mu)$ at different latitudinal angles $\mu = \cos\theta$ provides information on the temperature variation with depth in the external layers of the star. This is therefore an excellent constraint for testing atmospheric models, to validate or invalidate assumptions used to derive these models (like NLTE/LTE), and to provide suggestions for improving the input physics (equation-of-state and/or opacities in particular). The center-to-limb variation of the Sun has been known for many years and been measured for numerous μ and λ (e.g. Pierce & Slaughter 1977; Neckel & Labs 1994; Hestroffer & Magnan 1998) leading to a plethora of theoretical works that have improved our knowledge of the external layers of the Sun.

Traditionally, analysis of solar and stellar LD is made by adopting an approximated law for $I_\lambda(\mu)$, generally a polynomial expansion in μ that are either linear or non-linear (see e.g. Claret 2000, for recent developments) and with coefficients determined from 1D atmospheric models, like ATLAS (Kurucz 1992) or Phoenix (Hauschildt 1999). However, in spite of the detailed physics included in these codes, their 1D nature is a limitation for deriving realistic emergent intensities. Indeed, these codes contain free parameters, like the well-known mixing length parameter, which are injected artificially in order to reproduce the properties of the turbulent convection at the stellar surface. As a consequence, the comparison between these 1D models and observations depends on the input parameters, which thereby creates an important source of uncertainties. Moreover, convection is by nature a 3D process. Its manifestation is the presence of bright granules and dark intergranular lanes. Reducing it to a 1D process, i.e. ignoring horizontal flows and temperature inhomogeneities, changes the pressure scale height, the location of the surface, and therefore also the emergent intensity (see e.g. Allende-Prieto et al. 2004; and Asplund et al. 2000a, for a comparison of multi-dimensional simulations).

The precise measurements of the center-to-limb variation achieved nowadays require realistic stellar atmospheric models that take all the complexity of the stellar surface into account, and motivates the use of the new generation of 3D radiative hydrodynamical (hereafter RHD) simulations.

In this paper we propose a study of α Cen B (HD128621), a nearby K1V dwarf star. It is part of a visual triple star

system whose brightest component, α Cen A (HD128620), is a G2V dwarf. Both theoretical and observational considerations motivated the selection of this star in the present work. From the interferometric point of view, the proximity (1.3 pc) of the star is a rare opportunity for interferometric measurements, since most of the nearby dwarfs have angular diameters that are too small to be measured. Our interest in this star grew recently since our new measurements provided data points in the second lobe of the visibility function, which is sensitive to the LD of the star. From a theoretical point of view, this star is important for various reasons. In particular, recent detection of solar-like oscillations in α Cen A and B (Bouchy & Carrier 2001, 2002; Carrier & Bourban 2003) have led several authors (e.g. Morel et al. 2000; Thévenin et al. 2002; Thoul et al. 2004; Eggenberger et al. 2004) to build evolution models of these two stars that are strongly constrained by the measured frequency spacings. The result is a better, but still debated, determination of the fundamental parameters of the system.

In Sect. 2, we report the new interferometric measurements of α Cen B obtained since 2003 using the VINCI instrument. Section 3 describes our 3D simulations to derive self-consistent stellar limb-darkening of α Cen B. They are subsequently used to compute visibility curves in the near-infrared (Sect. 4) in order to interpret our measurements in terms of stellar angular diameter and to discuss the agreement between the 3D limb-darkening model and our second lobe visibility measurements. We also use our simulations to predict future observations (J, H, and K bands) that will be made with the next generation of instruments of the VLTI, such as the new AMBER instrument (Petrov et al. 2000; Robbe-Dubois et al. 2004).

2. New interferometric observations

A total of 37 new interferometric measurements of α Cen B were obtained in 2003 on two baselines, D1-B3 (24 m in ground length) and B3-M0 (140 m), using the VINCI instrument (Kervella et al. 2000; Kervella et al. 2003a). The points obtained on the longer baseline are located in the second lobe of the visibility function of α Cen B, whose shape depends on the limb-darkening. We obtained 1000 interferograms on the B3-M0 baseline in two series. Out of these, 534 were processed by the VINCI pipeline. The B3-M0 baseline observations are made difficult by the very low V^2 of the interferometric fringes, less than 2%. However, Fig. 1 shows an example of the power spectral density of these very low visibility fringes where no bias is present. On the D1-B3 baseline, we recorded 17 500 interferograms in 35 series (15 141 processed). These new measurements were added to the V^2 values obtained on the E0-G1 baseline and have already been published in Kervella et al. (2003b, hereafter Paper I). The resulting squared visibilities are listed in Tables 2 and 3.

We used several stars from the Cohen et al. (1999) catalog as calibrators to estimate the point source response of the interferometer. They were observed immediately before or after α Cen B. On the D1-B3 baseline, we used HD 119193 ($\theta_{\rm UD}$ = 2.03 ± 0.022 mas), 58 Hya ($\theta_{\rm UD}$ = 3.13 ± 0.030 mas) and HD 112213 ($\theta_{\rm UD}$ = 3.14 ± 0.025 mas). Approximately one third of the measurements were obtained with each of these

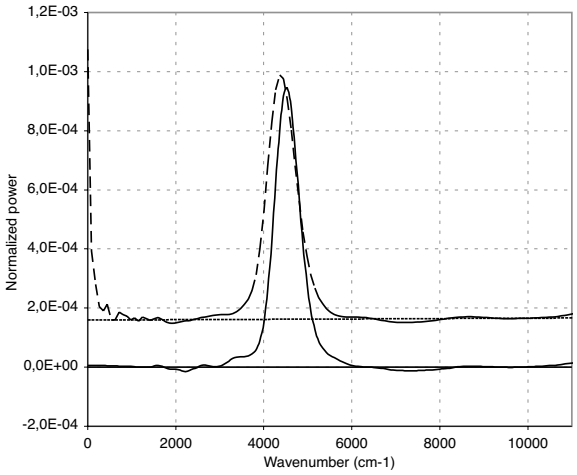

Fig. 1. The average wavelet power spectral density (WPSD) of 299 interferograms of α Cen B obtained on JD 2 452 770.6605 (11 May 2003). In spite of the very low visibility (V^2 = 1.38%), subtraction of the background noise (dotted line) from the processed fringe's power peak (dashed line) leaves no residual bias on the final WPSD (solid line). The power integration is done between wave numbers 1970 and 7950 cm^{-1}.

calibrators. On the B3-M0 baseline, we relied on HR 4831 ($\theta_{\rm UD}$ = 1.66 ± 0.018 mas), whose small size results in a low systematic uncertainty on the calibrated V^2 values. The angular diameter estimates from Cohen et al. (1999) have been verified by Bordé et al. (2002) as reliable within their stated error bars. The squared visibilities were derived using the processing methods described in Kervella et al. (2004). As an example, the calibration sequence used for the longest baseline B3-M0 is presented in Table 1.

3. Simulation of a 3D atmosphere

In order to model the intensity profile of α Cen B, we performed realistic, time-dependent, 3D radiative hydrodynamical simulations of its surface. The emerging intensity of the atmospheric model in different directions was used to build theoretical monochromatic limb-darkening profiles for various wavelengths covering the spectral domains of interest for the VINCI and AMBER instruments (in the 1.0−2.4 μm range).

3.1. The stellar atmosphere modelling

The numerical code used for this work belongs to a new generation of 3D atmospheric codes developed for the study of solar (e.g. Stein & Nordlund 1989, 1998) and stellar (e.g. Nordlund & Dravins 1990; Asplund et al. 2000; Allende-Prieto et al. 2002; Ludwig et al. 2002) granulation and line formations (e.g. Asplund et al. 2000a,b,c, 2004, 2005). The code solves the non-linear, compressible equations of mass, momentum, and energy conservation on a Eulerian mesh. The 3D radiative transfer was solved at each time step along different inclined rays for which we assumed local thermodynamical equilibrium (LTE). We considered 10 latitudinal μ points and 4 longitudinal φ points, and checked that a finer grid in (μ, φ) does not change the properties of the model. Realistic equation-of-state

Table 1. Calibration sequence of α Cen B on the B3-M0 baseline (140 m ground length). The expected visibilities $V^2_{\rm theo}$ given in this table include the bandwidth smearing effect. The interferometric efficiency given in italics corresponds to the value assumed for the calibration of these particular α Cen B observations (see Tables 2 and 3). The HR 4831 data marked with (*) were taken 2 h before α Cen B, and are listed to show the stability of the IE, but were not used for the IE estimation.

JD	Scans	B (m)	Azim.	$\mu^2 \pm$ stat. (%)	$V^2_{\rm theo} \pm$ syst. (%)	$IE \pm$ stat. $\pm$ syst. (%)	Target
2 452 770.5474	365	139.309	49.24	29.37 ± 0.39	49.93 ± 0.80	58.83 ± 0.79 ± 0.94*	HR 4831*
2 452 770.5523	316	139.131	50.51	29.38 ± 0.51	50.06 ± 0.80	58.70 ± 1.02 ± 0.93*	HR 4831*
2 452 770.5572	296	138.913	51.77	30.05 ± 0.67	50.19 ± 0.80	59.88 ± 1.34 ± 0.95*	HR 4831*
2 452 770.6368	405	128.934	71.28	32.05 ± 0.35	55.48 ± 0.75	57.78 ± 0.62 ± 0.77	HR 4831
2 452 770.6419	408	127.841	72.49	31.60 ± 0.36	56.01 ± 0.74	56.42 ± 0.64 ± 0.74	HR 4831
2 452 770.6469	392	126.698	73.69	32.72 ± 0.36	56.54 ± 0.73	57.87 ± 0.64 ± 0.74	HR 4831
2 452 770.6605	299	133.838	59.85	0.791 ± 0.039		*57.36 ± 0.82 ± 0.74*	α Cen B
2 452 770.6656	235	133.277	61.33	0.777 ± 0.082		*57.36 ± 0.82 ± 0.74*	α Cen B

Table 2. α Cen B squared visibilities.

JD	B (m)	Azim.	$V^2 \pm$ stat. $\pm$ syst. (%)
D1-B3			
2 452 720.9141	20.891	108.36	81.24 ± 3.03 ± 0.09
2 452 720.9081	21.095	106.30	83.40 ± 2.80 ± 0.09
2 452 725.8927	21.152	105.72	80.48 ± 1.83 ± 0.04
2 452 720.9029	21.270	104.52	83.89 ± 2.66 ± 0.09
2 452 725.8878	21.315	104.05	79.99 ± 1.81 ± 0.04
2 452 725.8828	21.479	102.36	80.95 ± 1.84 ± 0.04
2 452 720.8627	22.462	91.40	83.75 ± 3.84 ± 0.10
2 452 725.8408	22.669	88.80	79.26 ± 2.54 ± 0.06
2 452 725.8358	22.786	87.24	78.79 ± 2.52 ± 0.06
2 452 720.8489	22.799	87.08	82.95 ± 3.88 ± 0.10
2 452 725.8306	22.903	85.63	79.32 ± 2.54 ± 0.06
2 452 720.8434	22.921	85.36	82.06 ± 3.76 ± 0.10
2 452 726.8032	23.375	77.99	77.19 ± 0.64 ± 0.07
2 452 703.8642	23.405	77.43	80.79 ± 2.25 ± 0.05
2 452 726.7983	23.452	76.49	78.82 ± 0.60 ± 0.07
2 452 703.8599	23.470	76.13	80.05 ± 2.23 ± 0.05
2 452 726.7933	23.525	74.96	77.69 ± 0.59 ± 0.07
2 452 703.8555	23.534	74.77	81.05 ± 2.23 ± 0.05
2 452 723.7937	23.627	72.58	77.60 ± 0.93 ± 0.10
2 452 723.7885	23.688	71.00	77.11 ± 0.86 ± 0.10
2 452 723.7835	23.741	69.46	78.76 ± 0.81 ± 0.10
2 452 723.7521	23.953	59.81	78.42 ± 0.77 ± 0.10
2 452 703.8019	23.970	58.32	79.61 ± 2.50 ± 0.05
2 452 723.7469	23.970	58.20	78.20 ± 0.83 ± 0.10
2 452 704.7984	23.971	58.09	81.26 ± 0.98 ± 0.05
2 452 703.7979	23.980	57.06	80.38 ± 2.46 ± 0.05
2 452 704.7940	23.982	56.70	81.38 ± 0.97 ± 0.05
2 452 723.7419	23.982	56.63	77.93 ± 0.55 ± 0.10
2 452 709.7555	23.985	48.87	82.93 ± 3.59 ± 0.10
2 452 704.7896	23.989	55.34	80.51 ± 1.01 ± 0.05
2 452 716.7402	23.990	50.10	77.55 ± 3.22 ± 0.08
2 452 709.7596	23.991	50.19	81.43 ± 3.55 ± 0.10
2 452 726.7251	23.994	53.95	76.95 ± 0.90 ± 0.08
2 452 716.7448	23.994	51.55	76.31 ± 3.22 ± 0.08
2 452 709.7640	23.994	51.57	77.31 ± 3.73 ± 0.09

Table 3. α Cen B squared visibilities (continued).

JD	B (m)	Azim.	$V^2 \pm$ stat. $\pm$ syst. (%)
E0-G1*			
2 452 462.5836	60.441	157.57	17.02 ± 0.36 ± 0.26
2 452 462.5870	60.544	158.40	17.01 ± 0.23 ± 0.26
2 452 462.5905	60.645	159.26	16.80 ± 0.77 ± 0.26
2 452 462.5949	60.767	160.35	16.05 ± 0.68 ± 0.24
2 452 465.6268	61.541	170.27	16.76 ± 1.05 ± 0.26
2 452 470.6203	61.621	172.05	14.94 ± 0.44 ± 0.23
2 452 470.6234	61.650	172.82	15.59 ± 0.42 ± 0.24
2 452 470.6278	61.687	173.92	16.70 ± 0.44 ± 0.25
B3-M0			
2 452 770.6605	133.838	59.85	1.379 ± 0.07 ± 0.02
2 452 770.6656	133.277	61.33	1.356 ± 0.14 ± 0.02

* E0-G1 measurements reported by Kervella et al. (2003b).

(including ionization, dissociation, and recombination) and opacities (Uppsala opacity package, Gustafsson et al. 1975) were used. The line-blanketing was taken into account through the opacity binning technique (Nordlund 1982). In the present simulation we considered a Cartesian grid of $(x, y, z) = 125 \times 125 \times 82$ points. The geometrical sizes are 6×6 Mm for the horizontal directions and 5 Mm for the vertical one. The dimensions of this domain are large enough to include a sufficiently large number of granules ($n \geq 20$) simultaneously, which prevents statistical bias. A periodic boundary condition was applied for the horizontal directions, and transmitting vertical boundaries were used at the top and bottom of the domain. The base of the domain was adjusted to have a nearly adiabatic, isentropic, and featureless convective transport. The upper boundary was placed sufficiently high in the atmosphere so that it does not influence the property of the model.

A detailed description of the current version of the code used in this paper may be found in Stein & Nordlund (1998). Unlike 1D hydrostatic models that reduce all hydrodynamics to a single adjustable parameter, the present simulations were done ab initio by solving the complete set of RHD equations in a self-consistent way. All the dynamics and turbulence of the model came naturally from the equations of physics. Nothing was adjusted, such as the convective flux in the MLT formalism. The diagnostic made by such RHD simulations is, therefore, much more realistic than the 1D models. We emphasize that the realism of these 3D simulations has been intensively

Table 4. limb-darkening $I(\lambda, \mu)$ for various wavelengths over the *JHK* range.

λ (μm) / μ	0.0	0.1	0.2	0.3	0.4	0.5	0.6	0.7	0.8	0.9	1.0
1.050	0.4434	0.5745	0.6453	0.7069	0.7605	0.8087	0.8527	0.8932	0.9311	0.9667	1.0000
1.270	0.4646	0.6017	0.6738	0.7347	0.7860	0.8310	0.8711	0.9074	0.9406	0.9715	1.0000
1.650	0.4838	0.6752	0.7487	0.8039	0.8462	0.8812	0.9110	0.9369	0.9601	0.9811	1.0000
2.000	0.5442	0.7063	0.7707	0.8202	0.8585	0.8905	0.9178	0.9417	0.9630	0.9825	1.0000
2.200	0.5729	0.7220	0.7817	0.8283	0.8646	0.8950	0.9211	0.9439	0.9645	0.9831	1.0000
2.400	0.5968	0.7353	0.7912	0.8352	0.8698	0.8988	0.9239	0.9458	0.9656	0.9836	1.0000

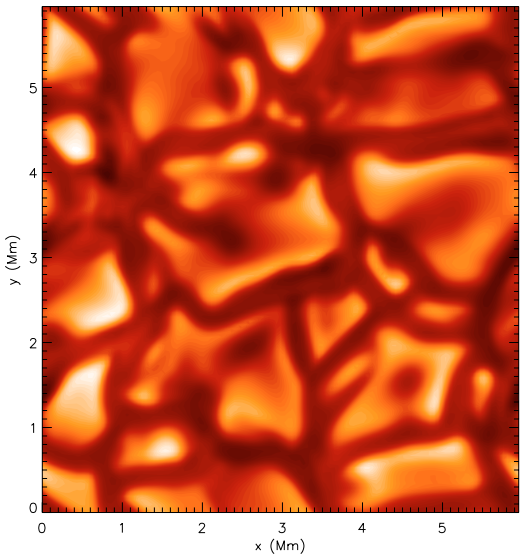

Fig. 2. Snapshot of the disk-center ($\mu = 1$) intensity emerging at the stellar surface at a representative time.

checked for solar line formations (e.g. Asplund et al. 2000b,c, 2004), helioseismology (e.g. Rosenthal et al. 1999), and also for stellar line formations (e.g. Allende-Prieto et al. 2002).

The adopted atmospheric parameters are those of Morel et al. (2000), i.e. $T_{\rm eff}$ = 5260 K, $\log g$ = 4.51 and [Fe/H] = +0.2. The simulation was run for a few hours of stellar time that covered several convective turn-over times. The result is a 3D, time-dependent box representing the stellar surface. A snapshot of the disk-center surface intensity is represented in Fig. 2. The structure of our model is similar to the one obtained by Nordlund & Dravins (1990) but is even more realistic, since the present version of the code solves compressible equations of hydrodynamics and uses more grid-points, which allows a better treatment of the turbulence.

3.2. 3D limb-darkening

The monochromatic surface intensity was computed for various latitudinal μ and longitudinal φ directions at the stellar surface. The limb-darkening $I_\lambda(\mu)$ was obtained by horizontal (x, y), longitudinal and time averages of the surface intensity. For the time average, we considered a sequence of 2 hours of stellar time. The results are plotted in Fig. 3 for the two extreme wavelengths of our spectral domain, 1.0 and 2.4 μm. For comparison, we overplot limb-darkening obtained from a 1D ATLAS9 model for the same wavelengths and for the same stellar fundamental parameters. It appears that 3D RHD produces a less significant center-to-limb variation than a 1D static model. The departure from a 1D model increases with decreasing wavelengths. Such behavior was also found by Allende Prieto et al. (2002) for Procyon. However, in the case of α Cen B, the departure from 1D to 3D limb-darkening is smaller, as a consequence of a less efficient convection in K dwarfs as compared to F stars.

The reason the emergent intensity differs between 1D and 3D models is that the properties of the superadiabatic and surface convective layers cannot be described well by the mixing length formalism, whatever parameter we choose. The temperature inhomogeneities (granulation) together with the strong sensitivity of the opacity (H^-) to the temperature make the warm ascending flows more opaque than they would be for a homogeneous 1D model. This purely 3D effect, added to the contribution of the turbulent pressure, pushes the location of the surface to lower densities. The temperature gradient in these regions is steeper than in the 1D case (see Nordlund & Dravins 1990). Since the continuum is formed in these layers, the emergent intensity is different.

The correction due to 3D simulations (a few percents) is small but not negligible with respect to the precision obtained by the new generation of interferometric instruments like VINCI or AMBER. This improvement is essential for deriving an accurate angular diameter of the star. We report our limb-darkening predictions in Table 4 for a series of continuum wavelengths between 1.0 and 2.4 μm, corresponding to the *JHK* range accessible to the AMBER instrument.

4. Visibility model and angular diameter of α Cen B

In this section, we describe the application of our 3D limb-darkening models to the interpretation of the VINCI measurements of α Cen B.

4.1. Limb-darkened disk visibility model

In the simple case of a centro-symmetric star such as α Cen B, the visibility function measured using a broadband interferometric instrument such as VINCI is defined by three wavelength-dependent functions:

1. The spectral energy distribution $S(\lambda)$ of the star, expressed in terms of photons (VINCI uses a photon counting detector).

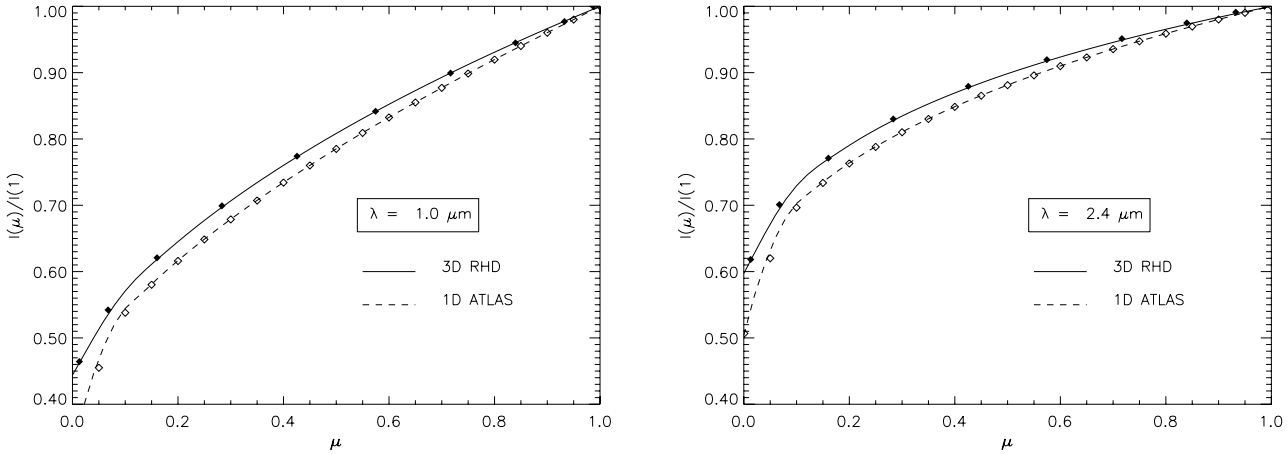

Fig. 3. Normalized monochromatic center-to-limb variation $I_\lambda(\mu)/I_\lambda(1)$ of the surface intensity obtained by 3D RHD simulations of α Cen B as a function of μ for two different wavelengths: 1 μm (*left panel*) and 2.4 μm (*right panel*), which correspond to the extreme limits of the spectral domain we have considered in this paper. The solid lines represent the 3D RHD limb-darkening, whereas the dashed lines represent limb darkening derived from 1D ATLAS atmospheric models. In both case, the symbols $\diamond$ represent the values extracted from both 1D (white) and 3D (black) simulations.

2. The wavelength-dependent intensity profile of the star: $I(\lambda,\mu)/I(\lambda,1)$.
3. The spectral transmission $T(\lambda)$ of the instrument, including the atmosphere, all optical elements and the detector quantum efficiency.

Out of these three functions, $T(\lambda)$ is known from the conception of the instrument, as well as from calibrations obtained on the sky (see Kervella et al. 2003b, for details). The spectral energy distribution of the star $S(\lambda)$ can be measured directly using a spectrograph or taken from atmospheric numerical models.

From the 3D RHD simulations presented in Sect. 3, we obtained intensity profiles for ten distinct wavelengths over the K band (chosen in the continuum). For each of these profiles, ten values of μ were computed. The resulting 10×10 element 2D table $I(\lambda,\mu)/I(\lambda,1)$ was then interpolated to a larger 60×50 element table, with a 10 nm step in wavelength (over the 1.90−2.50 μm range) and a 0.02 step in μ. This interpolation preserves the smooth shape of the intensity profile function well. This procedure was also used to build the $I(\lambda,\mu)/I(\lambda,1)$ table based on the 1D Kurucz model. The original sample (10×20) was interpolated to the same final grid as the 3D model.

We can derive the monochromatic visibility law $V_\lambda(B,\theta)$ from the monochromatic intensity profile $I(\lambda,\mu)$ using the Hankel integral:

$$V_\lambda(B,\theta) = \frac{1}{A}\int_0^1 I(\lambda,\mu) J_0\left(\frac{\pi\, B\, \theta_{\rm LD}}{\lambda}\sqrt{1-\mu^2}\right)\mu\,\mathrm{d}\mu, \quad (1)$$

where B is the baseline (in meters), θ the limb darkened angular diameter (in radians), J_0 the zeroth order of the Bessel function, λ the wavelength (in meters), $\mu = \cos\theta$ the cosine of the azimuth of a surface element of the star, and A the normalization factor:

$$A = \int_0^1 I(\lambda,\mu)\,\mu\,\mathrm{d}\mu. \quad (2)$$

To obtain the visibility function observed by VINCI in broadband, we have to integrate this function taking the transmission of the instrument and the spectral energy distribution of the star into account:

$$V_K(B,\theta) = \frac{\int_K [V_\lambda(B,\theta)\, T(\lambda)\, S(\lambda)]^2\ \lambda^2\,\mathrm{d}\lambda}{\int_K [T(\lambda)\, S(\lambda)]^2\ \lambda^2\,\mathrm{d}\lambda}. \quad (3)$$

Note the λ^2 term that is necessary, as the actual integration of the squared visibility by VINCI over the K band is done in the Fourier conjugate space of the optical path difference (expressed in meters), and is therefore done in wavenumber $\sigma = 1/\lambda$. This corrective term ensures that the integration of the star's spectrum is done precisely in the same way as in the instrument.

This formulation is very general, as it does not make any particular assumption about the spectrum of the star or about the wavelength dependence of its intensity profile $I(\lambda,\mu)$.

4.2. Fit of the interferometric data and angular diameter of α Cen B

Considering the model discussed in Sect. 4.1, we now derive the limb-darkened angular diameter $\theta_{\rm LD}$ of α Cen B. It is obtained by a standard χ^2 analysis of the data. We define the reduced χ^2 of our fit by

$$\chi^2_{\rm red} = \frac{1}{N-n}\sum_{i=1}^{N}\left(\frac{V_i^2 - V^2_{\rm model}}{\sigma_i}\right)^2, \quad (4)$$

where n is the number of variables ($n = 1$ for our fit), N the total number of measurements, i the index of a particular measurement, and σ_i the standard deviation of the measurement with index i.

The χ^2 minimization was computed for three center-to-limb models: uniform disk (UD), 1D ATLAS, and 3D RHD. In each case, the broadband square visibility curve $V^2_K(B,\theta)$ is shown in Figs. 4 and 5. In addition to the purely statistical error, we must

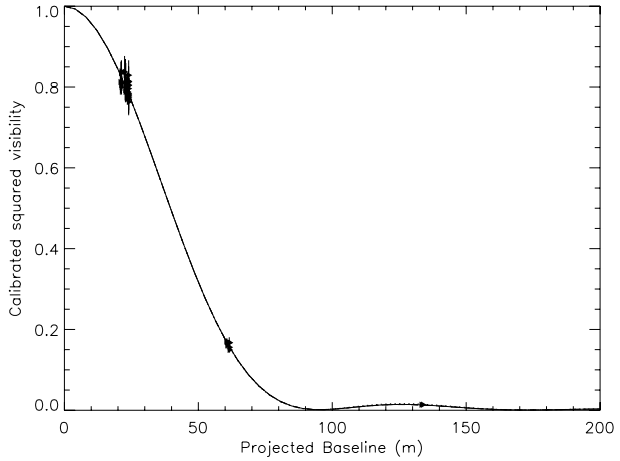

Fig. 4. Overview of α Cen B squared visibilities. The continuous line represents the broadband, limb darkened disk visibility model derived from the 3D RHD with $\theta_{3D} = 6.000$ mas.

also take two systematic error sources into account: the calibration uncertainty and the wavelength uncertainty. The calibration uncertainty comes from the errors on the a priori angular sizes of the five calibrators that were used for the VINCI observations. It amounts to 0.012 mas on the final angular diameter. The wavelength uncertainty comes from the imperfect knowledge of the transmission of VINCI, in particular of its fluoride glass optical fibers. This transmission was calibrated on the sky (Paper I), and the uncertainty on this measurement is estimated to be 0.15%. As it impacts linearly on the angular diameter value, it corresponds to 0.009 mas. These two systematic factors add up quadratically to the 0.013 mas statistical uncertainty and result in a total error of 0.021 mas on the angular diameters of α Cen B. The best fit angular diameter that we derive using our 3D limb-darkening model is $\theta_{3D} = 6.000 \pm 0.021$ mas. The 1D model produces a slightly larger diameter, $\theta_{1D} = 6.017 \pm 0.021$ mas, and the UD disk produces naturally a much smaller diameter, $\theta_{UD} = 5.881 \pm 0.021$ mas.

There is no significant difference between the three models in the first lobe of visibility. However, different amplitudes of the second lobe were observed. While the UD model produces higher visibilities, the 1D limb-darkened model leads to visibilities that are slightly too low compared to our observations. Overall, the 3D model leads to a slightly better agreement with observations.

As expected, the difference 3D/1D is rather small, since we are working in the near-infrared (K-band) and with a dwarf star. It is nonetheless comparable to σ_{stat} and therefore significant.

4.3. Linear diameter

Assuming the parallax value of Söderhjelm (1999), $\pi = 747.1 \pm 1.2$ mas[1], we found a linear radius of $0.863 \pm 0.003\,R_\odot$ which agrees with results presented in Paper 1. We estimated that the adopted uncertainty in T_{eff} (=50 K) leads to an error of about $0.0003\,R_\odot$, i.e. ten times smaller than the derived uncertainties. From the 1D analysis, we derived a radius of $0.865 \pm 0.003\,R_\odot$, larger than the radius found by the RHD approach by about $1\,\sigma_{stat}$. In addition to the corrections it provides, the use of 3D simulations was also motivated by the absence of adjustable parameters, which is not the case for 1D models.

This slightly smaller linear radius obtained from 3D RHD simulations, compared with the one derived from 1D ATLAS model, supports the suggestion of a smaller mass ($M = 0.907\,M_\odot$, Kervella et al. 2003) rather than the larger one ($M = 0.934 \pm 0.007\,M_\odot$) proposed by Pourbaix et al. (2002). However, stellar evolution models are sensitive to many parameters, and a smaller radius does not always lead to a smaller mass. More investigations are thus needed before we can reach a definite conclusion about the mass of α Cen B. In this context, our improved radius provides an additional constraint on asteroseismic diagnostics.

5. Conclusion

In this paper we improve determination of the radius of α Cen B in two respects. Firstly, we report the first interferometric measurements in the second lobe of visibility. Secondly, in order to derive a reliable value of the angular diameter of the star, we performed realistic 3D RHD simulations of the surface of α Cen B. By comparison with observations, we found a radius of $0.863 \pm 0.003\,R_\odot$. The correction provided by the 3D approach is small but significant (especially in the K band probed with VINCI), since it provides a radius that is smaller by roughly $1\,\sigma_{stat}$ compared with what can be obtained by 1D models. Moreover, the use of 3D RHD is preferable since it does not introduce adjustable parameters to describe convection. We also emphasize that for hotter A–F stars the correction due to 3D analysis will be larger than for α Cen B. We have shown that even for a K-dwarf like α Cen B, though it is small, the correction obtained by the use of RHD simulations should not be neglected for very high precision interferometric measurements. In the next few years, the combination of high visibility precision and long baselines will require the use of realistic theoretical models of the stellar limb-darkening to extract the true photospheric angular diameter of the observed stars from the observed visibilities. Conversely, observations beyond the first minimum of the visibility function will directly sample the light distribution on the surface of the stars, therefore providing constraints for the atmosphere structure models. Future observations with the VLTI will allow to sample tightly the second lobe of the visibility function of several solar analogs (including α Cen A and B), and therefore to derive their intensity profiles with high accuracy. Comparisons between our theoretical predictions of limb-darkening and the future observations made by AMBER will be an excellent test of our modelling of the surface of α Cen B. Indeed, AMBER will provide new interferometric data that will contain much more information

[1] One should note that there is a rather broad distribution of parallax values for α Cen in the literature, as discussed in Paper I. While the value from Söderhjelm (1999) is the result of a careful reprocessing of the *Hipparcos* data, the possibility of a bias beyond the stated $1\,\sigma$ error cannot be completely excluded, in particular, due to the extreme brightness and binarity of α Cen.

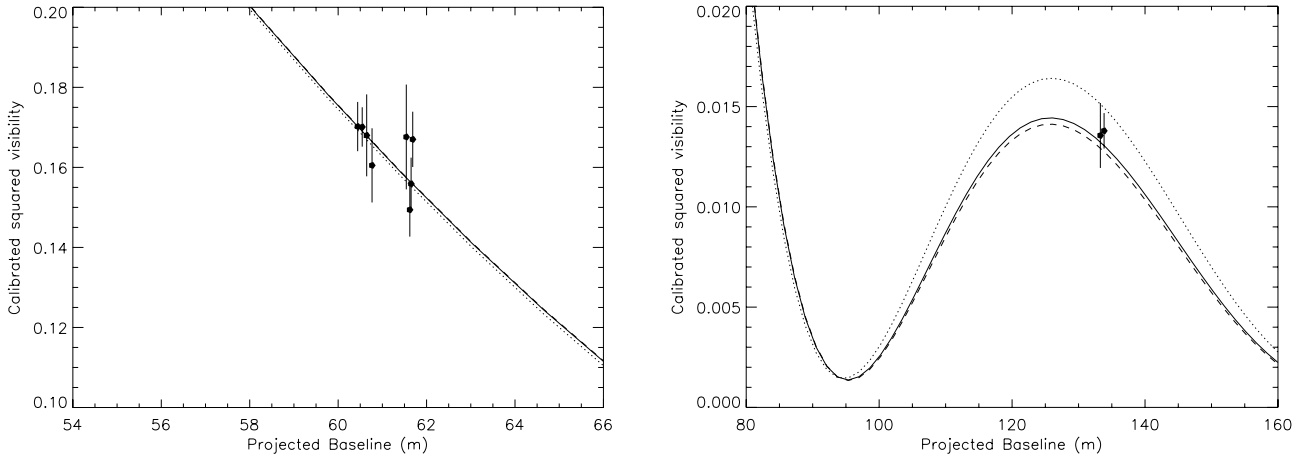

Fig. 5. Close-up views of the squared visibilities of α Cen B in the lower part of the first lobe (*left panel*) and the second lobe (*right panel*). The continuous line represents the broadband, limb darkened disk visibility model derived from the 3D RHD with $\theta_{3D} = 6.000$ mas. The dashed lines correspond to results obtained from the 1D ATLAS model with $\theta_{1D} = 6.017$ mas. The upper dotted curve is a UD model with $\theta_{UD} = 5.881$ mas.

compared with VINCI. There will be two major advantages with AMBER:

- It will provide a wavelength dependence of the visibility ([1.9−2.4] μm) therefore allowing differential studies of limb-darkening as a function of wavelength.
- AMBER can simultaneously combine the light from three telescopes and therefore measure the closure phase. This gives an advantage to determining the angular size of the star when observing in the minima of the visibility function.

These improvements will lead to better constrained angular diameters of α Cen A and B and, therefore, to high precision measurement of the ratio of the linear radii of A and B, independent of the parallax.

Acknowledgements. We thank Vincent Coudé du Foresto for important remarks that led to improvements at an early stage of this paper. We thank the anonymous referee for constructive remarks. These interferometric measurements were obtained using the VLTI (ESO Paranal, Chile), and were retrieved from the ESO/ST-ECF Archive (Garching, Germany). LB thanks the CNES for financial support and Å. Nordlund for providing his RHD code. We also thank Claude Van't Veer for providing the ATLAS model.

References

Allende Prieto, C., Asplund, M., Garcia Lòpez, R. J., & Lambert, D. L. 2002, ApJ, 567, 544
Allende Prieto, C., Asplund, M., & Fabiani Bendicho, P. 2004, A&A, 423, 1109
Asplund, M., Nordlund, Å., Trampedach, R., & Stein, R. F. 1999, A&A, 346L, 17
Asplund, M., Ludwig, H.-G., Nordlund, Å., & Stein, R. F. 2000a, A&A, 359, 669
Asplund, M., Nordlund, Å., Trampedach, R., Allende Prieto, C., & Stein, R. F. 2000b, A&A, 359, 729
Asplund, M., Nordlund, Å., Trampedach, R., & Stein, R. F. 2000c, A&A, 359, 743
Asplund, M., Grevesse, N., Sauval, A. J., Allende Prieto, C., & Kiselman, D. 2004, A&A, 417, 751
Asplund, M., Grevesse, N., Sauval, A. J., Allende Prieto, C., & Blomme, R. 2005, A&A, 431, 693
Bordé, P., Coudé du Foresto, V., Chagnon, G., & Perrin, G. 2002, A&A, 393, 183
Bouchy, F., & Carrier, F. 2001, A&A, 374, L5
Bouchy, F., & Carrier, F. 2002, A&A, 390, 205
Carrier, F., & Bourban, G. 2003, A&A, 406, 23
Claret, A. 2000, A&A, 363, 1081
Cohen, M., Walker, R. G., Carter, B., et al. 1999, AJ, 117, 1864
Eggenberger, P., Charbonnel, C., Talon, S., et al. 2004, A&A, 417, 235
Gustafsson, B., Bell, R. A., Eriksson, K., & Nordlund, Å. 1975, A&A, 42, 407
Hauschildt, P. H., Allard, F., & Baron, E. 1999, ApJ, 512, 377
Hestroffer, D., & Magnant, C. 1998, A&A, 333, 338
Kervella, P., Coudé du Foresto, V., Glindemann, A., & Hofmann, R. 2000, SPIE, 4006, 31
Kervella, P., Gitton, Ph., Ségransan, D., et al. 2003a, SPIE, 4838, 858
Kervella, P., Thévenin, F., Ségransan, D., et al. 2003b, A&A, 404, 1087 (Paper I)
Kervella, P., Ségransan, D., & Coudé du Foresto, V. 2004, A&A, 425, 1161
Kurucz, R. L. 1992, The Stellar Populations of Galaxies, IAU Symp., 149, 225
Ludwig, H., Allard, F., & Hauschildt, P. H. 2002, A&A, 395, 99
Morel, P., Provost, J., Lebreton, Y., Thévenin, F., & Berthomieu, G. 2000, A&A, 363, 675
Neckel, H., & Labs, D. 1994, SoPh, 153, 91
Nordlund, Å. 1982, A&A, 107, 1
Nordlund, Å., & Dravins, D. 1990, A&A, 228, 155
Petrov, R. G., Malbet, F., Richichi, A., et al. 2000, SPIE, 4006, 68
Pierce, A. K., & Slaughter, C. D. 1977, SoPh, 51, 25
Pourbaix, D., Nidever, D., McCarthy, C., et al. 2002, A&A, 386, 280
Robbe-Dubois, S., Petrov, R. G., Lagarde, S., et al. 2004, SPIE, 5491, 1089
Rosenthal, C. S., Christensen-Dalsgaard, J., Nordlund, Å., Stein, R. F., & Trampedach, R. 1999, A&A, 351, 689
Stein, R. F., & Nordlund, Å. 1989, ApJ, 342, L95
Stein, R. F., & Nordlund, Å. 1998, ApJ, 499, 914
Söderhjelm, S. 1999, A&A, 341, 121
Thévenin, F., Provost, J., Morel, P., et al. 2002, A&A, 392, L9
Thoul, A., Scuflaire, R., Noels, A., et al. 2003, A&A, 402, 293

3.4 La brillance de surface des étoiles naines

La brillance de surface d'une étoile est une grandeur particulièrement intéressante à étalonner, car elle se conserve avec la distance (en l'absence d'extinction) : lorsque la distance est doublée, sa surface apparente est divisée par quatre, comme son flux apparent. Par définition, la brillance de surface bolométrique d'une étoile f est liée à sa température effective $T_{\rm eff}$ par $f \simeq L/R^2 \simeq T_{\rm eff}^4$ (avec R le rayon bolométrique de l'étoile et L son flux bolométrique). Exprimée en valeur logarithmique, $F = \log f$ est donc une fonction linéaire des indices de couleur. Fouqué & Gieren (1997) donnent la définition suivante de la brillance de surface à la longueur d'onde λ :

$$F_\lambda = 4,2207 - 0,1 m_\lambda - 0,5 \log \theta_{\rm LD} \tag{3.1}$$

La constante est simplement une normalisation au flux bolométrique solaire ($f_\odot$) et à la magnitude absolue solaire ($M_{\rm bol\,\odot}$) :

$$4,2207 = 0,1 M_{\rm bol\,\odot} + 1 + 0,25 \log \frac{4 f_\odot}{\sigma} \tag{3.2}$$

Une conséquence de cette conservation est que le diamètre angulaire d'une étoile peut être calculé à partir de seulement deux magnitudes mesurées dans deux bandes distinctes. Ceci est très utile pour estimer *a priori* la taille angulaire des étoiles d'étalonnage utilisées en interférométrie. Les relations entre la brillance de surface et une combinaison de magnitudes visible et infrarouge sont en particulier très faiblement dispersées. La Fig. 1 de l'article reproduit à la Sect. 3.4.1 montre une des meilleures relations, basée sur la couleur $B - L$.

3.4.1 Article A&A : "The angular sizes of dwarf stars and subgiants. Surface brightness relations calibrated by interferometry" (2004)

Je présente dans cet article une analyse de l'ensemble des mesures interférométriques existantes d'étoiles naines et sous-géantes, dans le but de réaliser un étalonnage des relations couleur-brillance de surface pour ces classes d'étoiles. Plus de la moitié de ces mesures proviennent d'observations réalisées avec l'instrument VINCI du VLTI. Les relations les plus adaptées à la prédiction de diamètres angulaires sont obtenues pour les indices de couleur visible-infrarouge : leur dispersion intrinsèque est inférieure à 1%. Il est intéressant de noter que ces relations ont éte utilisées très récemment avec succès par Bouchy et al. (2005) pour préciser les propriétés de l'étoile HD 189733 occultée par une planète de 1,15 M_J. L'accord avec les observations du transit de la planète est excellent.

FIG. 3.9 – Deux des charriots mobiles des lignes à retard du VLTI. Leur longueur totale est d'environ 2m.

A&A 426, 297–307 (2004)
DOI: 10.1051/0004-6361:20035930

Astronomy & Astrophysics

The angular sizes of dwarf stars and subgiants

Surface brightness relations calibrated by interferometry⋆

P. Kervella[1,2], F. Thévenin[3], E. Di Folco[4], and D. Ségransan[5]

[1] LESIA, UMR 8109, Observatoire de Paris-Meudon, 5 place Jules Janssen, 92195 Meudon Cedex, France
e-mail: Pierre.Kervella@obspm.fr
[2] European Southern Observatory, Alonso de Cordova 3107, Casilla 19001, Vitacura, Santiago 19, Chile
[3] Observatoire de la Côte d'Azur, BP 4229, 06304 Nice Cedex 4, France
[4] European Southern Observatory, Karl-Schwarzschild-str. 2, 85748 Garching, Germany
[5] Observatoire de Genève, 1290 Sauverny, Switzerland

Received 22 December 2003 / Accepted 17 June 2004

Abstract. The availability of a number of new interferometric measurements of Main Sequence and subgiant stars makes it possible to calibrate the surface brightness relations of these stars using exclusively direct angular diameter measurements. These empirical laws make it possible to predict the limb darkened angular diameters $\theta_{\rm LD}$ of dwarfs and subgiants using their dereddened Johnson magnitudes, or their effective temperature. The smallest intrinsic dispersions of $\sigma \leq 1\%$ in $\theta_{\rm LD}$ are obtained for the relations based on the K and L magnitudes, for instance $\log \theta_{\rm LD} = 0.0502\,(B-L) + 0.5133 - 0.2\,L$ or $\log \theta_{\rm LD} = 0.0755\,(V-K) + 0.5170 - 0.2\,{\rm K}$. Our calibrations are valid between the spectral types A0 and M2 for dwarf stars (with a possible extension to later types when using the effective temperature), and between A0 and K0 for subgiants. Such relations are particularly useful for estimating the angular sizes of calibrators for long-baseline interferometry from readily available broadband photometry.

Key words. stars: fundamental parameters – techniques: interferometric

1. Introduction

The surface brightness (hereafter SB) relations link the emerging flux per solid angle unit of a light-emitting body to its color, or effective temperature. These relations are of considerable astrophysical interest, as a well-defined relation between a particular color index and the surface brightness can provide accurate predictions of the stellar angular diameters. Such predictions are essential for the calibration of long-baseline interferometric observations. We propose in the present paper new and accurate calibrations of the SB-color relations of dwarfs and subgiants based on direct interferometric measurements of nearby members of these two luminosity classes. Our primary purpose is to establish reliable relations that can be used to predict the angular sizes of calibrator stars for long-baseline interferometry.

After defining the surface brightness relations (Sect. 2), we discuss in Sect. 3 the sample of measurements that we selected for our calibrations (interferometric and photometric data). Section 4 is dedicated to the calibration of the empirical SB relations, relative to the color indices and to the effective temperature, for stars of spectral types A0 to M2. We also derive inverse relations to estimate the effective temperature from broadband photometry and angular diameter measurements. As the established relations are intended to be used primarily to predict angular diameters, we discuss in Sect. 5 their associated errors in this context. In Sect. 6, we search for a possible instrumental bias linked to one of the five interferometric instruments represented in our sample. Numerous versions of the SB relations have been established in the literature, mostly for giants and supergiants, and we discuss them in Sect. 7. Main Sequence stars are potentially very good calibrators for long-baseline interferometry, and we discuss this particular application of our SB relations in Sect. 8.

2. Direct and inverse surface brightness relations

By definition, the bolometric surface flux $f \sim L/D^2$ is linearly proportional to $T_{\rm eff}^4$, where L is the bolometric flux of the star, D its bolometric diameter and $T_{\rm eff}$ its effective temperature. In consequence, $F = \log f$ is a linear function of the stellar color indices expressed in magnitudes (logarithmic scale), and

⋆ Tables 3–6 are only available in electronic form at
http://www.edpsciences.org

SB relations can be fitted using (for example) the following expressions:

$$F_B = a_0\,(B-V)_0 + b_0 \quad (1)$$

$$F_V = a_1\,(V-K)_0 + b_1 \quad (2)$$

$$F_H = a_2\,(B-H)_0 + b_2 \quad (3)$$

where F_λ is the surface brightness. When considering a perfect blackbody curve, any color can in principle be used to obtain the SB. The index 0 designates the dereddened magnitudes, and the a_i and b_i coefficients represent respectively the slopes and zero points of the different versions of the SB relation. The particular expression of the SB relation $F_V(V-R)$ is also known as the Barnes-Evans (B-E) relation, and is historically the first version to have been calibrated empirically (Barnes et al. 1976). However, the relatively large intrinsic dispersion of the visible B-E relation has led many authors to prefer its infrared counterparts, in particular those based on the K band magnitudes ($\lambda = 2.0$–$2.4\ \mu$m), as infrared wavelengths are less affected by interstellar extinction. The surface brightness F_λ is given by the following expression (Fouqué & Gieren 1997):

$$F_\lambda = 4.2207 - 0.1\,m_{\lambda_0} - 0.5\,\log\theta_{\rm LD} \quad (4)$$

where $\theta_{\rm LD}$ is the limb darkened angular diameter, i.e. the angular size of the stellar photosphere.

The linear expressions of the SB can be inverted easily to predict angular diameters, and give linear relations such as:

$$\log\theta_{\rm LD} = c_1\,(V-K) + d_1 - 0.2\,V \quad (5)$$

for the $F_V(V-K)$ inversion. We have in this example:

$$c_1 = -2\,a_1 \quad (6)$$

$$d_1 = 2\,(4.2207 - b_1). \quad (7)$$

In the present paper, we will refer to both the direct and inverse relations as "SB relations".

3. Selected measurement sample

3.1. Angular diameters

Over the past two years, sixteen new angular diameter measurements of nearby Main Sequence and subgiant stars were obtained with the VLT Interferometer (Glindemann et al. 2000, 2003a,b) equipped with the fiber-based beam combiner VINCI (Kervella et al. 2000, 2003a). To complement this sample, we have searched the literature, and added to our list the measurements related to the stars of luminosity classes IV and V. Most of the visible and infrared interferometers are represented in our sample, with measurements from the NII (*Narrabri Intensity Interferometer*, Hanbury Brown et al. 1967), the Mk III (Shao et al. 1988), the PTI (*Palomar Testbed Interferometer*, Colavita et al. 1999) and the NPOI (*Navy Prototype Optical Interferometer*, Armstrong et al. 1998). Our findings originally included a few lunar occultation measurements, but they were rejected as they were related to variable or multiple stars, or their precision was not sufficient to give them any weight in the fitting process.

To obtain a consistent sample of limb darkened (LD) angular diameters we have retained solely the uniform disk (UD) values from the literature. The conversion of these model-independent measurements to LD values was achieved using the linear LD coefficients u from Claret (2000), and the conversion formula from Hanbury Brown et al. (1974a). These coefficients are broadband, single-parameter approximations of the Kurucz (1992) model atmospheres. They are tabulated for a grid of temperatures, metallicities and surface gravities and we have chosen the closest models to the physical properties of the stars. We have considered a uniform microturbulent velocity of $2\,{\rm km\ s^{-1}}$ for all stars. This single source for limb darkening corrections ensures the self-consistency of our final sample.

3.2. Photometry

All the apparent magnitudes that we have retained from the literature are expressed in the Johnson system. When available, we have preferentially kept the uncertainties given by the original authors, otherwise we adopted arbitrarily a conservative error bar. The U band magnitudes were obtained from Morel et al. (1978) and Mermilliod (1986), and we adopted a ± 0.02 error. The B, V, R and I bands were obtained from several online catalogues available through VIZIER (Ochsenbein et al. 2000), and we also adopted a ± 0.02 uncertainty. For the J to L infrared bands, references are not so easy to find, as many bright stars are unfortunately absent from the recent infrared surveys, like 2MASS (Cutri et al. 2003) or DENIS (Fouqué et al. 2000). We have relied on the VIZIER database to obtain the infrared magnitudes of our sample of stars. In some cases, the references we used are 30 years old, but many of them have small and reliable uncertainties. The original references of the measurements are given in the footnotes of Table 3.

3.3. Data selection

The SB relations rely on the assumption that stars behave like black bodies, i.e. that their colors are mainly governed by their effective temperature. A severe deviation from this assumption will cause a discrepancy between the actual flux per surface unit and the temperature of the star.

For instance, if there is a second, unresolved star near the main object, its additional flux will bias the spectral energy distribution. For this reason, we have rejected the binary and multiple objects for which separate photometry of the components is not available.

The presence of warm material in the circumstellar environment can also create an excess at infrared wavelengths. While this signature is most useful for identifying the stars surrounded by protoplanetary disks, it creates a bias in the measured color of the star. Some of the stars we selected are surrounded by debris disks (ϵ Eri, α PsA, τ Cet, β Leo), but the contribution of the circumstellar material is negligible, even in the infrared J to L bands. The material surrounding these stars is very cold and radiates mostly in the far infrared domain. We have rejected

the measurement of β Pic from Di Folco et al. (in preparation), due to its large uncertainty ($\simeq$10%) and to the relatively high density of its edge-on circumstellar disk that could cause significant extinction.

The fast rotating stars can deviate significantly from the black body assumption. As demonstrated by the VINCI observations of the nearby Be star α Eri (Domiciano de Souza et al. 2003), the photosphere of these objects can be deformed by their fast rotation. This creates differential limb darkening between the pole and the equator which appear to have different effective temperatures. This makes it particularly difficult to define the true photometric solid angle subtended by these objects. In addition, many fast rotating stars go through episodes of mass loss, that are likely to create a warm circumstellar environment. The presence of such hot material around the star will create a bias in the flux and color of the star. For these reasons, we have chosen to reject the known fast rotators ($v \sin i \geq 100\,\mathrm{km\,s^{-1}}$) and the Be stars from our list.

The very low mass stars *Proxima* (GJ 551, M5.5V) and *Barnard's star* (GJ 699, M4V) have been excluded from our fitting procedures for three reasons. The first is that because of their very low effective temperatures the molecular absorption bands dominate their spectra and lead to a significant discrepancy with the hotter stars. Second, these stars are variable, presenting occasional flares that make it difficult to estimate their magnitudes. Third, they present chromospheric activity that could bias their magnitudes in the U to V colors. However, we have kept these two stars on the SB relation figures for comparison.

The spectroscopic and eclipsing binaries are less useful for the estimation of the surface brightness relation, as it is in general impossible to measure separately the magnitudes of these stars with the required precision. For this reason, we have not included in our sample the angular diameter measurements obtained by spectroscopic or photometric methods. For the interested reader, a rather complete compilation of the measurements using these techniques can be found in the CADARS catalogue by Pasinetti-Fracassini et al. (2001).

3.4. Final sample

We report in Tables 1 and 2 the complete set of measurements that we have considered for our fit. In this table, the angular diameters $\theta_{\rm UD}$ (uniform disk) and $\theta_{\rm LD}$ (limb-darkened disk) are expressed in milliarcseconds (mas). The limb darkening conversion coefficient $k = \theta_{\rm LD}/\theta_{\rm UD}$ was computed for each star based on the tables of Claret (2000). When a physical parameter was not available in the literature, it has been estimated approximately, and appears in *italic* characters. The observation wavelength λ is given as either the name of the photometric band (V, H, K) or the actual wavelength in μm. The error bar in the angular diameter of the Sun (G2V) has been set arbitrarily to ±0.1%. The parallaxes are from the *Hipparcos* catalogue (Perryman et al. 1997), except the α Cen value that was taken from Söderhjelm (1999), who derived it from reprocessed *Hipparcos* data. The interferometer used for each measurement is indicated in the "Instr." column.

4. Surface brightness relations

4.1. Fitting procedure

For each angular diameter measurement $\theta_{\rm LD}$, and based on the observed apparent magnitudes m_λ, we have computed the surface brightness F_λ in all bands, using the definition of Eq. (4). The resulting F_λ values were then fitted relative to the colors $(C_0 - C_1)$, using a linear model. This fit was achieved using a classical χ^2 minimization taking into account the errors in both the colors and F_λ. The minimized quantity, using the slope a and zero point b as variables, is the reduced χ^2 expression:

$$\chi^2_{\rm red}(a,b) = \frac{1}{N-2}\sum_{i=1}^{N}\frac{\left[(F_0)_i - a\,(C_0-C_1)_i - b\right]^2}{(\sigma_{F\,i})^2 + a^2\,(\sigma_{C\,i})^2} \tag{8}$$

where we have:

- N the total number of measurements in our sample;
- $(F_0)_i$ the surface brightness of star i in band C_0;
- $(C_0 - C_1)_i$ the color of the star of index i computed between bands C_0 and C_1;
- $\sigma_{C\,i}$ the 1 σ error bar in the chosen color of star i;
- $\sigma_{F\,i}$ the 1 σ error bar in the surface brightness F_0.

The 1σ errors σ_a and σ_b are subsequently estimated from the best fit values a and b by solving numerically the expression:

$$\chi^2_{\rm red}(a+\sigma_a, b+\sigma_b) = \chi^2_{\rm red}(a,b) + 1. \tag{9}$$

The solutions of this equation correspond to an elliptic contour, due to the correlation between the a and b variables. It has to be projected on the a and b axis to give the errors. The residuals $\Delta F_i = F_i - F_{\rm model}$ are used to estimate the intrinsic dispersion $\sigma_{\rm int}(F)$ of the surface brightness relation from:

$$\sigma^2_{\rm int}(F) = \frac{1}{N}\sum_{i=1}^{N}\left[(\Delta F_i)^2 - (\sigma_{F\,i})^2\right]. \tag{10}$$

This process gives a total number of 72 (a,b) best fit pairs, with their associated errors (σ_a, σ_b), and the intrinsic dispersion $\sigma_{\rm int}$ of the data around the best fit model.

From there, we can invert these relations easily to obtain their angular diameter counterparts:

$$\log\theta_{\rm LD} = c\,(C_0 - C_1) + d - 0.2\,C_0. \tag{11}$$

The slopes and zero points are computed from the (a,b) pairs through:

$$c = -2\,a, \quad \sigma_c = 2\,\sigma_a \tag{12}$$

$$d = 2\,(4.2207 - b), \quad \sigma_d = 2\,\sigma_b \tag{13}$$

and the intrinsic dispersions $\sigma_{\rm int}(\log\theta_{\rm LD})$ are given by:

$$\sigma_{\rm int}(\log\theta_{\rm LD}) = 2\,\sigma_{\rm int}(F_\lambda). \tag{14}$$

The same method was used for the fits using the effective temperature, except that no error bar was considered on the $T_{\rm eff}$ values from the literature (equal weighting), and we used a second degree polynomial model instead of a linear one.

Table 1. Angular diameters of dwarf stars (luminosity class V) measured by long-baseline interferometry (apart from the Sun). They are expressed in mas, and $T_{\rm eff}$ is in K. "Ref.$_1$" designates the reference used for $T_{\rm eff}$, $\log g$ and [Fe/H]. When unavailable, the metallicity has been set arbitrarily to the solar value. "Ref.$_2$" designates the reference used for each angular diameter measurement (expressed in mas). The errors are given in superscript close to each value.

Star	Spect.	π (mas)	Ref.$_1$	$T_{\rm eff}$	$\log g$	[Fe/H]	Instr.	Ref.$_2$	λ	$\theta_{\rm UD}$	k	$\theta_{\rm LD}$
α Lyr	A0V	$128.93^{0.55}$	(a, e)	9522	3.98	−0.33	PTI	(8)	K	$3.24^{0.01}$	1.012	$3.28^{0.01}$
α Lyr	A0V	$128.93^{0.55}$	(a, e)	9522	3.98	−0.33	NII	(1)	V	$3.08^{0.07}$	1.046	$3.22^{0.07}$
α Lyr	A0V	$128.93^{0.55}$	(a, e)	9522	3.98	−0.33	Mk III	(4)	0.8	$3.15^{0.03}$	1.028	$3.24^{0.03}$
α Lyr	A0V	$128.93^{0.55}$	(a, e)	9522	3.98	−0.33	Mk III	(4)	0.55	$3.00^{0.05}$	1.046	$3.13^{0.05}$
α CMa A	A1V	$379.21^{1.58}$	(b)	9800	4.30	0.40	NII	(16)	V	$5.60^{0.07}$	1.045	$5.85^{0.07}$
α CMa A	A1V	$379.21^{1.58}$	(b)	9800	4.30	0.40	VLTI	(9)	K	$5.94^{0.02}$	1.012	$6.01^{0.02}$
α CMa A	A1V	$379.21^{1.58}$	(b)	9800	4.30	0.40	Mk III	(4)	0.8	$5.82^{0.11}$	1.027	$5.98^{0.11}$
β Leo	A3V	$90.16^{0.89}$	(g)	8570	4.26	0.20	VLTI	(10)	K	$1.43^{0.03}$	1.015	$1.45^{0.03}$
β Leo	A3V	$90.16^{0.89}$	(g)	8570	4.26	0.20	NII	(1)	V	$1.25^{0.09}$	1.052	$1.31^{0.09}$
α PsA	A3V	$130.08^{0.92}$	(g)	8760	4.22	0.43	NII	(1)	V	$1.98^{0.13}$	1.050	$2.08^{0.14}$
α PsA	A3V	$130.08^{0.92}$	(g)	8760	4.22	0.43	VLTI	(10)	K	$2.20^{0.02}$	1.014	$2.23^{0.02}$
α Cen A	G2V	$747.10^{1.20}$	(k)	5790	4.32	0.20	VLTI	(13)	K	$8.31^{0.02}$	1.024	$8.51^{0.02}$
Sun	G2V			5770								$1919260^{0.1\%}$
τ Cet	G8V	$274.18^{0.80}$	(i)	5400	4.55	−0.40	VLTI	(10)	K	$2.03^{0.03}$	1.024	$2.08^{0.03}$
GJ 166 A	K1V	$198.25^{0.84}$	(a)	5073	4.19	−0.31	VLTI	(15)	K	$1.60^{0.06}$	1.029	$1.65^{0.06}$
α Cen B	K1V	$747.10^{1.20}$	(k)	5260	4.51	0.23	VLTI	(13)	K	$5.86^{0.03}$	1.026	$6.01^{0.03}$
ϵ Eri	K2V	$310.74^{0.85}$	(a)	5052	4.57	−0.15	VLTI	(10)	K	$2.09^{0.03}$	1.027	$2.15^{0.03}$
GJ 105 A	K3V	$138.72^{1.04}$	(a)	4718	4.50	−0.07	PTI	(12)	H, K	$0.91^{0.07}$	1.032	$0.94^{0.07}$
GJ 570 A	K4V	$169.31^{1.67}$	(a)	4533	4.79	0.02	VLTI	(15)	K	$1.19^{0.03}$	1.030	$1.23^{0.03}$
ϵ Ind A	K4.5V	$275.49^{0.69}$	(b)	4500	4.50	−0.10	VLTI	(15)	K	$1.84^{0.02}$	1.030	$1.89^{0.02}$
GJ 380	K7V	$205.23^{0.81}$	(a)	3861	4.68	−0.93	PTI	(12)	H, K	$1.27^{0.04}$	1.018	$1.29^{0.04}$
GJ 191	M1V	$255.12^{0.86}$	(b)	3524	4.87	−0.50	VLTI	(14)	K	$0.68^{0.06}$	1.016	$0.69^{0.06}$
GJ 887	M0.5V	$303.89^{0.87}$	(f)	3645	4.80	*0.00*	VLTI	(14)	K	$1.37^{0.04}$	1.018	$1.39^{0.04}$
GJ 205	M1.5V	$175.72^{1.20}$	(b)	3626	4.80	0.60	VLTI	(14)	K	$1.12^{0.11}$	1.020	$1.15^{0.11}$
GJ 15 A	M2V	$280.26^{1.05}$	(a)	3721	5.00	−1.40	PTI	(12)	H, K	$0.98^{0.05}$	1.017	$1.00^{0.05}$
GJ 411	M1.5V	$392.52^{0.91}$	(h)	3620	4.90	−0.20	PTI	(12)	H, K	$1.41^{0.03}$	1.019	$1.44^{0.03}$
GJ 699	M4Ve	$549.30^{1.58}$	(a)	3201	5.00	−0.90	PTI	(12)	H, K	$0.99^{0.04}$	1.018	$1.00^{0.04}$
Proxima	M5.5V	$772.33^{2.42}$	(f)	3006	5.19	*0.00*	VLTI	(14)	K	$1.02^{0.08}$	1.030	$1.05^{0.08}$

– Ref.$_1$ for $T_{\rm eff}$, $\log g$ and [Fe/H]:(a) Cenarro et al. (2001); (b) Cayrel de Strobel et al. (1997); (c) Allende Prieto et al. (2002); (d) Gray et al. (2001); (e) Thévenin & Idiart (1999); (f) Ségransan et al. (2003); (g) Erspamer & North (2003); (h) Cayrel de Strobel et al. (2001); (i) Di Folco et al. (in preparation); (j) Morel et al. (2001); (k) Morel et al. (2000).

– Ref.$_2$ for angular diameters:(1) Hanbury Brown et al. (1974b); (2) Kervella et al. (2004a); (3) Nordgren et al. (2001); (4) Mozurkewich et al. (2003); (5) Thévenin et al. (in preparation); (6) Boden et al. (1998); (7) Nordgren et al. (1999); (8) Ciardi et al. (2001); (9) Kervella et al. (2003b); (10) Di Folco et al. (in preparation); (11) Nordgren et al. (2001); (12) Lane et al. (2001); (13) Kervella et al. (2003c); (14) Ségransan et al. (2003); (15) Ségransan et al. (in preparation); (16) Davis et al. (1986).

We minimized numerically the following $\chi^2_{\rm red}$ expression using a, b, c as variables:

$$\chi^2_{\rm red}(a,b,c) = \frac{1}{N-3}\sum_{i=1}^{N}\frac{[F_i - F_{\rm model}(T_{\rm eff})_i]^2}{\sigma_F^2} \quad (15)$$

where

$$F_{\rm model}(T_{\rm eff})_i = a\,(\log T_{\rm eff})_i^2 + b\,(\log T_{\rm eff})_i + c. \quad (16)$$

The errors in each of the a, b and c coefficients were not computed, as the correlations existing between these coefficients make it very difficult to determine them accurately. This is justified by the fact that the astrophysical dispersion of the measurements is largely dominant over the 1σ fitting errors of the model, and the systematic errors in these coefficients can thus be considered negligible. The inversion of the resulting $T_{\rm eff}$ based relations is straightforward. With an expression of the form:

$$\log\theta_{\rm LD} = d(\log T_{\rm eff})^2 + e(\log T_{\rm eff}) + f - 0.2C_\lambda \quad (17)$$

we have by definition:

$$d = -2\,a, \quad e = -2\,b \quad (18)$$

$$f = 2\,(4.2207 - c). \quad (19)$$

As in the previous case based on colors, the intrinsic dispersions $\sigma_{\rm int}(\log\theta_{\rm LD})$ of the angular diameter relations are given by:

$$\sigma_{\rm int}(\log\theta_{\rm LD}) = 2\,\sigma_{\rm int}(F). \quad (20)$$

In some cases, we could derive only upper limits of the intrinsic dispersion $\sigma_{\rm int}$, as it was found to be smaller than the average

Table 2. Angular diameters of subgiant stars (luminosity class IV) measured by interferometry. The references and notations are given in Table 1.

Star	Spect.	π (mas)	Ref.$_1$	$T_{\rm eff}$	$\log g$	[Fe/H]	Instr.	Ref.$_2$	λ	$\theta_{\rm UD}$	k	$\theta_{\rm LD}$
γ Gem	A0IV	$31.12^{2.33}$	(b)	9260	3.60	−0.12	NII	(1)	V	$1.32^{0.09}$	1.047	$1.38^{0.09}$
α CMi A	F5IV-V	$285.93^{0.88}$	(c)	6530	3.96	−0.05	VLTI	(2)	K	$5.38^{0.05}$	1.019	$5.48^{0.05}$
α CMi A	F5IV-V	$285.93^{0.88}$	(c)	6530	3.96	−0.05	NPOI	(11)	V	$5.19^{0.04}$	1.057	$5.49^{0.04}$
α CMi A	F5IV-V	$285.93^{0.88}$	(c)	6530	3.96	−0.05	Mk III	(4)	0.8	$5.32^{0.08}$	1.039	$5.53^{0.08}$
α CMi A	F5IV-V	$285.93^{0.88}$	(c)	6530	3.96	−0.05	Mk III	(4)	0.55	$5.30^{0.11}$	1.057	$5.60^{0.11}$
η Boo	G0IV	$88.17^{0.75}$	(a)	6003	3.62	0.25	VLTI	(5)	K	$2.15^{0.03}$	1.022	$2.20^{0.03}$
η Boo	G0IV	$88.17^{0.75}$	(a)	6003	3.62	0.25	Mk III	(4)	0.8	$2.18^{0.02}$	1.044	$2.27^{0.03}$
η Boo	G0IV	$88.17^{0.75}$	(a)	6003	3.62	0.25	Mk III	(4)	0.55	$2.13^{0.03}$	1.063	$2.26^{0.03}$
η Boo	G0IV	$88.17^{0.75}$	(a)	6003	3.62	0.25	NPOI	(11)	V	$2.17^{0.06}$	1.064	$2.31^{0.06}$
ζ Her A	G0IV	$92.64^{0.60}$	(j)	5820	3.85	0.04	Mk III	(4)	0.8	$2.26^{0.05}$	1.045	$2.36^{0.05}$
ζ Her A	G0IV	$92.64^{0.60}$	(j)	5820	3.85	0.04	Mk III	(4)	0.55	$2.13^{0.03}$	1.065	$2.27^{0.03}$
ζ Her A	G0IV	$92.64^{0.60}$	(j)	5820	3.85	0.04	NPOI	(11)	V	$2.37^{0.08}$	1.065	$2.52^{0.09}$
μ Her	G5IV	$119.05^{0.62}$	(a)	5411	3.87	0.16	Mk III	(4)	0.8	$1.86^{0.04}$	1.049	$1.95^{0.04}$
μ Her	G5IV	$119.05^{0.62}$	(a)	5411	3.87	0.16	Mk III	(4)	0.55	$1.81^{0.03}$	1.070	$1.93^{0.03}$
β Aql	G8IV	$72.95^{0.83}$	(a)	5041	3.04	−0.04	NPOI	(7)	V	$2.07^{0.09}$	1.075	$2.23^{0.10}$
η Cep	K0IV	$69.73^{0.49}$	(a)	5013	3.19	−0.19	NPOI	(7)	V	$2.51^{0.04}$	1.064	$2.67^{0.04}$
δ Eri	K0IV	$110.58^{0.88}$	(a)	4884	3.40	−0.11	VLTI	(5)	K	$2.33^{0.03}$	1.027	$2.39^{0.03}$

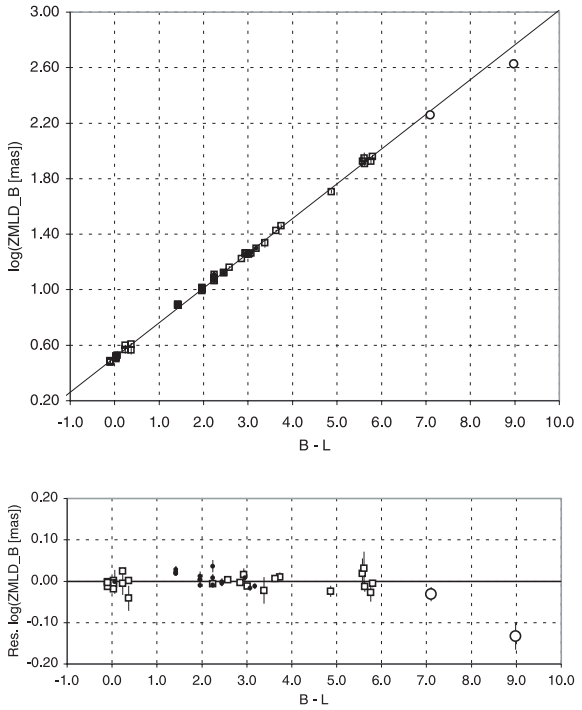

Fig. 1. Linear fit of the surface brightness relation $\log \mathrm{ZMLD}_B(B-L)$ (*upper part*), and the corresponding residuals (*lower part*). The intrinsic dispersion in the relation is ±0.004 on $\log$ ZMLD, equivalent to a systematic error of less than 1% in the predicted angular diameters. The open circles designate GJ 699 and *Proxima*, which were excluded from the fitting procedure.

error of the measurements (in such cases, Eq. (10) gives a negative value for $\sigma^2_{\rm int}$). For these relations, such as $\log \theta_{\rm LD}(T_{\rm eff}, L)$, we conclude that the intrinsic dispersion is undetectable at our level of sensitivity.

4.2. Angular diameter relations based on colors

The SB relations for *UBVRIJHKL* colors are listed in Table 4. They take the form:

$$\log \theta_{\rm LD}(C_0, C_1) = c_\lambda (C_0 - C_1) + d_\lambda - 0.2\, C_0 \tag{21}$$

where C_0 and C_1 are any two distinct colors of the Johnson system. In many cases, the dependence of the zero magnitude limb darkened angular diameter (ZMLD), defined for $C_0 = 0$, as a function of the color is not linear in reality. Thus, the linear model that we fit does not represent the observations well. In this case, we have added a note "*nl*" after the obtained residual dispersion. The non-linear relations should preferably not be used for predictions, though the stated dispersions include the non-linearity.

In theory, there should be a perfect diagonal symmetry between the dispersions listed in Table 4. In reality, the symmetry is only approximate, because C_0 and C_1 are not symmetric in the expression of $\log \theta_{\rm LD}(C_0, C_1)$. Therefore, an increased dispersion of the apparent magnitudes in one band C_1 will be reflected preferentially in the $\theta_{\rm LD}(C_0, C_1)$ dispersion, rather than in $\theta_{\rm LD}(C_1, C_0)$. For this reason, we provide both versions in Table 4, including the quasi-symmetric pairs. The best relations based on the K band (showing residual dispersions below 1% on the angular diameter $\theta_{\rm LD}$) are the following:

$$\log \theta_{\rm LD} = 0.0535\,(B-K) + 0.5159 - 0.2\,K \tag{22}$$

$$\log \theta_{\rm LD} = 0.0755\,(V-K) + 0.5170 - 0.2\,K, \tag{23}$$

and the best relations for the L band are:

$$\log \theta_{\rm LD} = 0.0412\,(U-L) + 0.5167 - 0.2\,L \tag{24}$$

$$\log \theta_{\rm LD} = 0.0502\,(B-L) + 0.5133 - 0.2\,L \tag{25}$$

$$\log \theta_{\rm LD} = 0.0701\,(V-L) + 0.5139 - 0.2\,L \tag{26}$$

$$\log \theta_{\rm LD} = 0.1075\,(R-L) + 0.5128 - 0.2\,L. \tag{27}$$

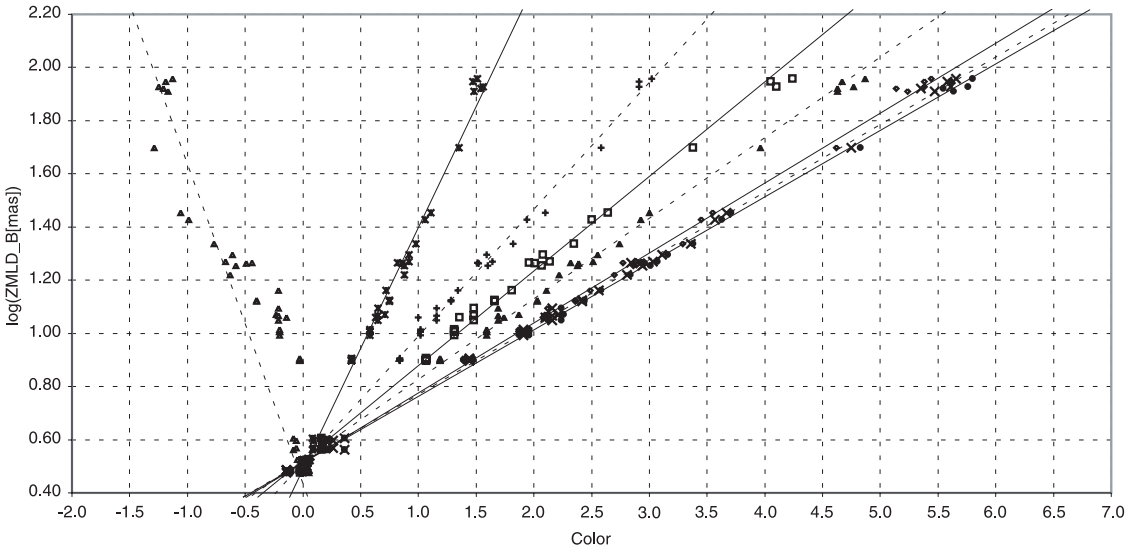

Fig. 2. Johnson B band ZMLD_B relations as a function of color. The errors bars have been omitted for clarity, and the fitted models are represented alternatively as solid and dashed lines. From left to right, using the colors: $(B-U)$, $(B-V)$, $(B-R)$, $(B-I)$, $(B-J)$, $(B-H)$, $(B-K)$, $(B-L)$. A clear non-linearity is visible on the $(B-U)$ based relation.

These expressions are valid at least over the range of colors defined by our sample (Tables 1 and 2). In terms of spectral types, the angular diameter predictions can be considered reliable between A0 and M2 for dwarfs, and between A0 and K0 for subgiants. There are indications (Fig. 1) that the infrared relations are valid down to the spectral type M4V of GJ 699, but show some discrepancy for the M 5.5V star *Proxima*. The established relations are likely to be valid also for subgiants of spectral types later than K0IV, but this cannot be verified from our sample. It should be stressed that they are applicable only to single stars, and the presence of a non-resolved stellar companion contributing a significant fraction of the measured flux will bias the predicted angular diameters. As more than half of the Main Sequence stars are binary or multiple stars, care should be taken in the application of these relations.

4.3. Angular diameter relations based on effective temperatures

Table 5 gives the best fit model coefficients for the relations $\theta_{\mathrm{LD}}(T_{\mathrm{eff}}, C_\lambda)$, defined as:

$$\log \theta_{\mathrm{LD}} = d\,(\log T_{\mathrm{eff}})^2 + e\,(\log T_{\mathrm{eff}}) + f - 0.2\,C_\lambda. \quad (28)$$

The smallest residuals are obtained for the relations based on T_{eff} and the K or L magnitudes, with an upper limit on the 1σ dispersion of 1.0% (the true dispersion is undetectable from our data):

$$\log \theta_{\mathrm{LD}} = 0.8470\,x^2 - 7.0790\,x + 15.2731 - 0.2\,K$$

$$\log \theta_{\mathrm{LD}} = 0.6662\,x^2 - 5.6609\,x + 12.4902 - 0.2\,L,$$

where $x = \log T_{\mathrm{eff}}$. The range of validity of the T_{eff} based relations is 3600–10 000 K for dwarfs, and 4900–9500 K for subgiants. As shown in Fig. 3, there are indications that the infrared relations are valid for dwarfs with T_{eff} down to ∼3000 K.

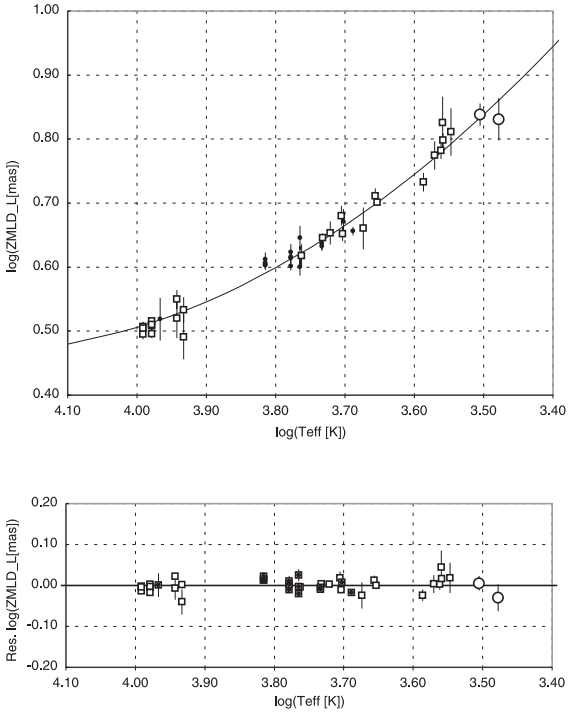

Fig. 3. Second degree polynomial fit of $\mathrm{ZMLD}_L(\log T_{\mathrm{eff}})$ (*upper part*) and the corresponding residuals (*lower part*). The coefficients are given in Table 5, and correspond to a relation of the form $\log \mathrm{ZMLD}_L = d(\log T_{\mathrm{eff}})^2 + e(\log T_{\mathrm{eff}}) + f$. The open circles designate GJ 699 and *Proxima*, which were excluded from the fit (see Sect. 3.3), though they are consistent with the model within their error bars.

4.4. $T_{\mathrm{eff}}(\theta_{LD}, m_\lambda)$ relations

By inverting the relations established in Sect. 4.3, it is possible to predict the effective temperature of the observed stars based on their angular diameter and broadband magnitude in a single band. As in the previous sections, we assume zero interstellar extinction, and the relations are valid only for dereddened

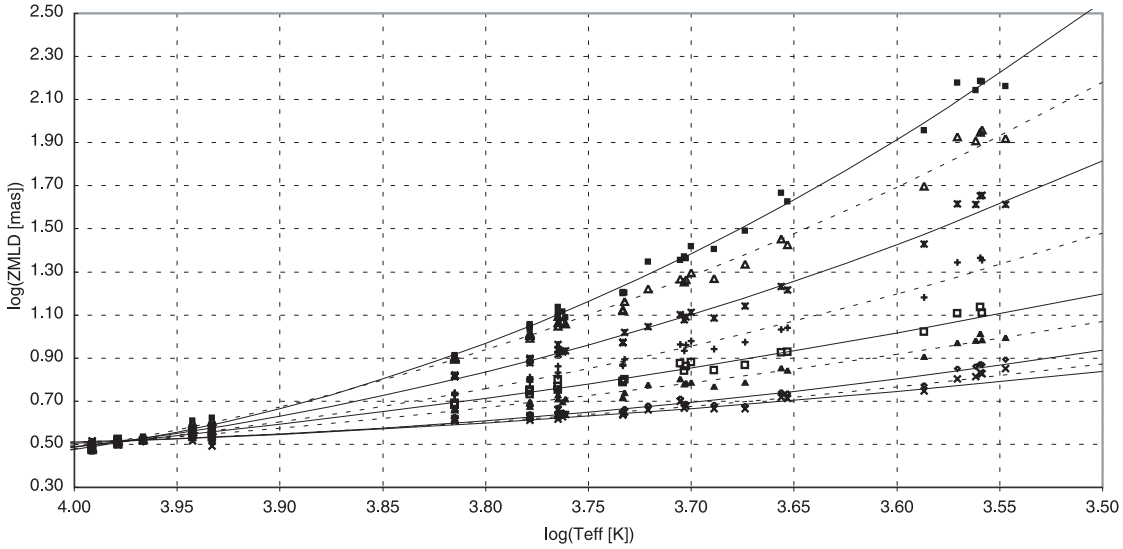

Fig. 4. ZMLD$_\lambda$ relations as a function of the effective temperature. The error bars have been omitted for clarity, and the fitted models are represented alternatively as solid and dashed lines. From top to bottom, using the zero magnitude reference colors U, B, V, R, I, J, H, K and L.

magnitudes. The formulation of the $T_{\rm eff}(\theta_{\rm LD}, m_\lambda)$ laws is easily derived analytically. From Eq. (28), we obtain $\log T_{\rm eff}$ through the expression:

$$\log T_{\rm eff} = \frac{-\sqrt{4d\log\theta_{\rm LD} + 0.8d\,C_\lambda + e^2 - 4df} - e}{2d} \quad (29)$$

that can be rewritten as

$$\log T_{\rm eff} = -\sqrt{g\log\theta_{\rm LD} + h\,C_\lambda + i} + j \quad (30)$$

where

$$g = \frac{1}{d}, \quad h = \frac{0.2}{d}, \quad (31)$$

$$i = \frac{e^2}{4d^2} - \frac{f}{d}, \quad j = \frac{-e}{2\,d}. \quad (32)$$

The intrinsic dispersion of the $\log T_{\rm eff}$ relations can be approximated from the intrinsic dispersion of the $\log\theta_{\rm LD}$ relations, as we have $\sigma_{\rm int}(\log\theta_{\rm LD}) \ll 1$:

$$\sigma_{\rm int}(\log T_{\rm eff}) = 0.5\ \sqrt{g}\ \sigma_{\rm int}(\log\theta_{\rm LD}). \quad (33)$$

The corresponding coefficients and dispersions are given in Table 6. The K band relation presents the smallest intrinsic dispersion ($\sigma \leq 0.60\%$), corresponding to a systematic uncertainty of less than 40 K in the predicted temperature of a G2V star:

$$\log T_{\rm eff} = 4.1788 - \sqrt{1.1806\log\theta_{\rm LD} + 0.2361\,K - 0.5695}.$$

However, we would like to stress that the uncertainty in the measured apparent magnitudes can easily be dominant, as a ± 0.03 error in K will translate into a $\pm 1.7\%$ error in $T_{\rm eff}$, nearly three times as large as the intrinsic dispersion.

Considering that photometry at an absolute level of ± 0.01 is not available for all stars, the $T_{\rm eff}$ predictions from different bands can be averaged, taking carefully into account the statistical and systematic errors of each relation used, in order to reach the intrinsic dispersion level. In addition, such an averaging process should not be done for stars affected by interstellar or circumstellar extinction, as it will affect differently each photometric band.

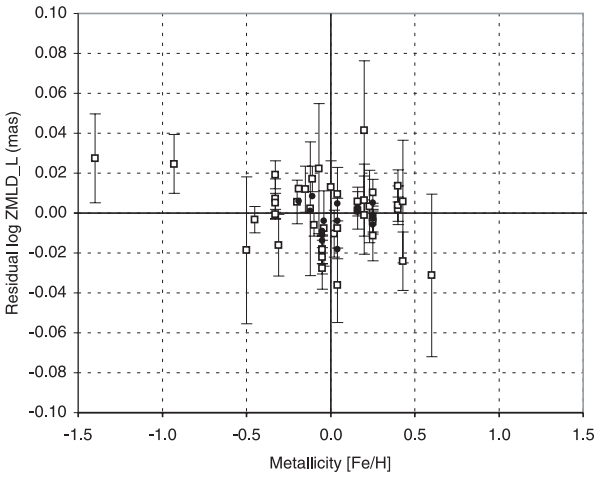

Fig. 5. Residuals of the fit of ZMLD$_L(L,\ B-L)$ as a function of the metallicity [Fe/H] of the star. Dwarfs are represented by open squares, and subgiants by solid dots. No correlation is visible among the stars of our sample.

4.5. Metallicity

A possible source of natural dispersion of the SB relations is the presence of deep absorption lines in the spectra of the stars. This effect is stronger for stars that have a high metal content. However, as shown in Fig. 5, there is no clear evidence of a correlation between the residuals of the least dispersed relation $\theta_{\rm LD}(L,\ B-L)$ and the metallicity [Fe/H]. This is an indication that our SB relations are valid at least for metallicities between -0.5 and $+0.5$ dex, and probably also for lower values. The two metal-deficient stars of Fig. 5 are GJ 15 A ([Fe/H] = -1.40 dex) and GJ 699 ([Fe/H]= -0.90 dex, not included in our fits). For typical stars of the solar neighborhood our relations are thus always applicable.

5. Sources of uncertainty in the predicted diameters

Several observational and astrophysical sources of uncertainty add up to create the total error in the predicted angular diameters:

- *Intrinsic dispersion of the empirical relation:* as discussed above, the best relations have intrinsic dispersions below 1%. It should be stressed that their predictions cannot be averaged to reduce this systematic uncertainty. However, the predictions from independent colors (such as $V-K$ and $B-L$) can be averaged to reduce the statistical uncertainty in the predictions due to the errors in the photometric measurements. In this process, the systematic uncertainties of each relation *cannot* be reduced and have to be carefully taken into account. This is essential as the calibrations have been obtained for all colors from the same sample of stars, and the resulting systematic errors are therefore highly correlated.
- *Uncertainties in the apparent magnitudes:* combining the high precision magnitudes available in the visible with the infrared magnitudes produced by the 2MASS and DENIS surveys should make it possible to retrieve the visible-infrared color indices with a precision better than ±0.02 mag. However, we would like to stress that the uncertainty in the apparent magnitude measurements can easily be the largest contributor to the predicted angular diameter errors. The true errors in the photometric measurements have to be estimated accurately in order to obtain reasonable uncertainties in the predicted angular sizes.
- *Interstellar extinction and circumstellar matter:* for the sample of nearby stars that was considered for our fits, the interstellar extinction is negligible: apart from γ Gem at 32 pc, all stars are located closer than 15 pc. However, our SB relations are strictly valid only for extinction-corrected magnitudes. The uncertainty in the assumed color excess $E(B-V)$ (for instance) will translate into an additional uncertainty in the dereddened magnitudes. The presence of a significant amount of circumstellar matter around the star will also affect its spectral properties, and can be difficult to detect.

6. Comparison between interferometers

The residuals of the fits of the least dispersed relations (based on infrared colors) allow us to examine if systematic discrepancies are detectable between the five interferometers represented in our sample. For each instrument we have computed the average residuals of its measurements, and the 1 σ error resulting from the averaging of their respective errors. The results are presented in Table 7.

We observe that the average residuals are below 1.5% in terms of ZMLD for all instruments. In addition, all the deviations are below 1σ, and can therefore be fully explained by random statistical dispersion. As a remark, the agreement between the VLTI/VINCI results and the Mk III is remarkable, with no systematic deviation detectable at a level of a few tenths of a percent. This is especially encouraging as these two instruments are observing at very different wavelengths (visible and K band, respectively).

This comparison exercise relies implicitly on the assumption that the considered $\mathrm{ZMLD}_0(C_0-C_1)$ relations are applicable to each instrument's subsample of stars, down to the precision of each individual measurement. This may not be the case for all stars, but the agreement that we observe is a worst case, and the true agreement is in any case very satisfactory.

7. Previous calibrations and other luminosity classes

Previous calibrations of the SB relations for dwarfs have been derived by Di Benedetto (1998) and Van Belle (1999a). These two authors relied on the limited sample of hot dwarfs observed with the Narrabri intensity interferometer (Hanbury Brown et al. 1974a,b). The agreement of our calibration with the work by Van Belle (1999a) is satisfactory within 1σ for the $(V, V-K)$ relation, but there is a difference of about 2σ in the slope of the $(B, B-K)$ relation. As the fit obtained by this author is based on a small range of colors, we attribute this moderate discrepancy to an underestimation of the true error bar in the slope, even in the restricted quoted range of validity ($-0.6 \leq B-K \leq +2.0$).

Several calibrations of the SB relations for giants have been proposed in recent years, thanks to the availability of a number of direct interferometric measurements of this class of stars. Van Belle (1999a) used a sample of 190 giants, complemented by 67 carbon stars and Miras measured with the PTI (Van Belle et al. 1999b), IOTA (e.g., Dyck et al. 1998) and lunar occultation observations (e.g., Ridgway et al. 1982) to calibrate the $F_V(V-K)$ relation of giant and supergiant stars. Welch (1994) and Fouqué & Gieren (1997) proposed a calibration of the SB relations of Cepheids based on an extrapolation of the corresponding relations of giants. Among the supergiants, Cepheids occupy a particular place. The observations of these variable stars by interferometry, intended primarily to study their pulsation, have resulted in the measurement of several of these objects (Mourard et al. 1997; Lane et al. 2000; Nordgren et al. 2000; Kervella et al. 2001; Lane et al. 2002; Kervella et al. 2004b). Based on these observations, Nordgren et al. (2002) have established dedicated SB relations for Cepheids, and they find a satisfactory agreement with previous works. From these studies, it appears that the SB relations found for giants and supergiants are similar to the ones determined in the present paper for dwarfs and subgiants, especially their visible-infrared versions. This means qualitatively that any two stars of class I–V with similar magnitudes in two bands will present approximately the same angular diameters.

8. Main Sequence stars as calibrators for long-baseline interferometry

8.1. The need for small and nearby calibrators

Interferometric observations are generally based on interleaved observations of a scientific target and a calibrator. The angular size of the calibrator is supposed to be known a priori, and

Table 7. Comparison between interferometers. The average residuals of the fits of $ZMLD_B$ and $ZMLD_V$ for the K and L based colors are given together with the corresponding 1σ error bars. All values are expressed in percents of the ZMLD values. All the residuals are compatible with zero within their 1σ error bars.

Instrument	N	$\Delta ZMLD_B(B-K)$	$\Delta ZMLD_V(V-K)$	$\Delta ZMLD_B(B-L)$	$\Delta ZMLD_V(V-L)$
PTI	5	$+0.48 \pm 0.89\%$	$+0.82 \pm 0.94\%$	$+0.63 \pm 0.89\%$	$+0.89 \pm 0.93\%$
NII	5	$+1.02 \pm 1.42\%$	$+1.03 \pm 1.46\%$	$+1.03 \pm 1.58\%$	$+1.02 \pm 1.63\%$
Mk III	11	$-0.11 \pm 0.56\%$	$-0.12 \pm 0.57\%$	$-0.06 \pm 0.64\%$	$-0.11 \pm 0.66\%$
NPOI	5	$-1.20 \pm 1.20\%$	$-1.23 \pm 1.24\%$	$-1.23 \pm 1.24\%$	$-1.39 \pm 1.53\%$
VLTI/VINCI	16	$-0.05 \pm 0.49\%$	$-0.07 \pm 0.51\%$	$-0.07 \pm 0.51\%$	$-0.11 \pm 0.68\%$

the observed fringe contrast is used to estimate the instrumental transfer function (also called system visibility). The catalogue of calibrators assembled by Cohen et al. (1999), and customized to interferometry by Bordé et al. (2002), consists mainly of K giants with angular diameters of about 2 mas. While this size is well adapted to short baseline observations (up to a few tens of meters in the infrared), these stars are too large angularly to serve as calibrators for the hectometric baselines of the VLTI, the CHARA array (McAlister et al. 2000) or the NPOI (Armstrong et al. 1998). In addition, it is foreseen that shorter wavelengths will be implemented on the VLTI than the K band currently accessible with VINCI. For instance, the AMBER instrument (Petrov et al. 2000) will allow observations in the J band. The two-fold increase in angular resolution will naturally require significantly smaller calibrators than those in the Cohen et al. (1999) catalogue.

A fundamental problem with distant stars is that the reddening corrections are uncertain. This means that it is highly desirable to use nearby stars as calibrators, located within a few tens of parsecs. In this respect, giant stars are not well suited due to their large linear dimensions, but dwarfs and subgiants are ideally suited to provide small and well-defined calibrators.

Another advantage of Main Sequence stars is that their strong surface gravity results in a compact atmosphere and a well-defined photosphere. Their disk appears sharper than that of the giants, for which the precise definition of the limb darkened disk angular diameter at a level of less than 1% can be difficult, in particular for the later spectral types. As an example, a discussion of the M4III giant ψ Phe can be found in Wittkowski et al. (2004).

8.2. Calibration precision vs. brightness

It is possible to estimate the maximum angular size of calibrator stars in order to obtain a given relative precision in the calibration of the interferometric efficiency. Figure 6 shows the achievable precision in the interferometric efficiency using the $(B, B-L)$ relation determined in Sect. 4.2 ($\sigma \leq 1.0\%$), as a function of the angular diameter of the calibrator star, for four different baselines (100, 200, 400 and 800 m), in the H band. These baselines are representative of the existing or foreseen interferometers (Keck, PTI, VLTI, CHARA, NPOI and OHANA, sorted by increasing maximum baseline). The horizontal scale of Fig. 6 can be adapted for other wavelengths or other baselines by scaling it linearly while maintaining constant the B/λ ratio.

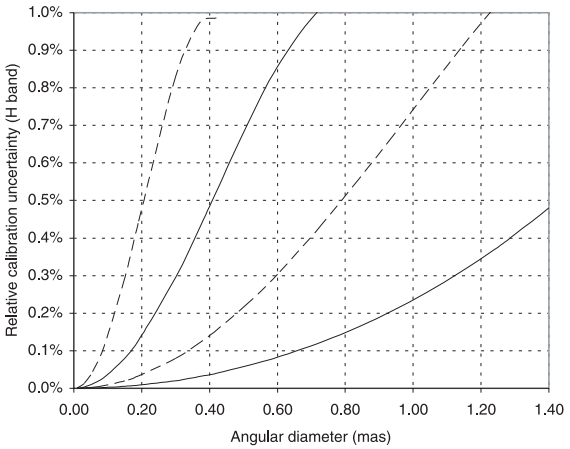

Fig. 6. Precision achievable in the measurement of the interferometric efficiency as a function of the angular diameter of the calibrator, predicted using the $(B, B-L)$ SB relation ($\leq$1.0% dispersion). From left to right, the curves refer to baselines of 800, 400, 200 and 100 m, in the H band.

If we now set a limit of 0.5% on the acceptable systematic uncertainty in the interferometric efficiency, we can compute the apparent magnitude of the Main Sequence calibrators that should be used as a function of their color. The result is presented in Fig. 7 as a function of the $B-H$ color, for different baseline lengths and interferometric observations in the H band. From this figure, it can be concluded that suitable calibrators for extremely long baseline observations will have to be faint. Let us consider the example of the OHANA interferometer (original idea proposed by Mariotti et al. 1996), whose longest foreseen baseline is 800 m. The H band magnitude of the calibrators necessary to obtain a relative systematic visibility error of 0.5% will be between $m_H = 6$ and 8, depending on the spectral type. This is rather faint, even for large aperture light collectors, but it is feasible with OHANA.

As an alternative, it is possible to build (through time consuming observations) a secondary network of brighter and larger calibrators based on the small angular diameter ones, but there will always be a limitation attached to the fact that calibrators have to be observed in the first lobe of their visibility function. For OHANA, this sets a hard limit of $\simeq$0.5 mas on the calibrator angular size, and even $\leq$0.4 mas to obtain a visibility of at least 0.3. This corresponds to apparent magnitudes of $m_H = 5$ to 7 in the H band, one magnitude brighter than the primary network.

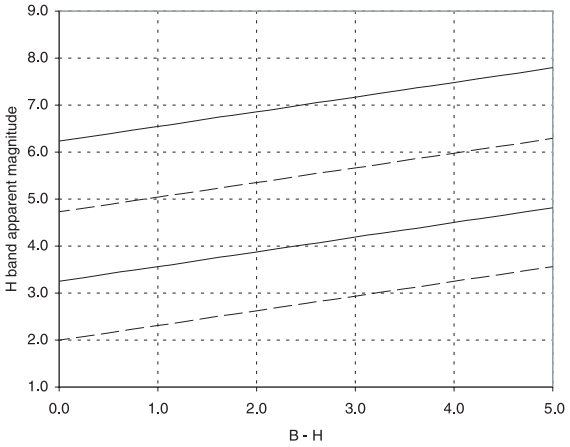

Fig. 7. Apparent magnitude in the H band of the calibrators suitable for obtaining a relative precision of 0.5% in the calibration of the interferometric efficiency, as a function of the $B - H$ color. From top to bottom, the curves refer to baselines of 800, 400, 200 and 100 m, in the H band.

For the longest baseline of the VLTI (200 m), calibrator magnitudes between $m_H = 3$ and 5 will be sufficient, clearly in the accessible domain of the AMBER beam combiner (Petrov et al. 2000) with the 1.8 m Auxiliary Telescopes (Koehler et al. 2002). The creation of a secondary network of calibrators should therefore not be necessary.

It should be stressed that the present conclusions regarding magnitudes are not limited to dwarf stars, as giants and supergiants follow comparable surface brightness relations. This means that the magnitude ranges defined above will be almost the same for other luminosity classes. A decisive advantage of dwarfs is that for the same apparent magnitude, they will be much closer than the more luminous classes, and therefore significantly less affected by interstellar extinction.

8.3. Example of diameter prediction

As a practical application, we have chosen the two stars 51 Peg A (HD 217014) and HD 209458 A. The former hosts the first planet discovered around a solar type star (Mayor & Queloz 1995), and the latter presents planetary transits (Charbonneau et al. 2000). We selected these two stars because they have been observed extensively using different techniques and did not show any large amplitude photometric variability. They therefore represent good examples of stable, well known stars, and are ideal candidates for the prediction of their angular size using the SB relations determined in the present paper.

Table 8 presents the predicted angular diameters of the two stars for the (V, $V - K$) version of the SB relation. The m_V magnitudes are from *Hipparcos* (Perryman et al. 1997) for both stars, with an arbitrary error bar of ±0.01, while the K band infrared magnitudes were taken from Ducati et al. (2002) for 51 Peg A, and from the 2MASS catalogue (Cutri et al. 2003) for HD 209458 A.

For 51 Peg A, we obtain a predicted angular diameter of $\theta_{\rm LD} = 0.689 \pm 0.011$ mas. The corresponding value for HD 209458 A is $\theta_{\rm LD} = 0.228 \pm 0.004$ mas. These angular sizes

Table 8. Photometry (*upper part*) and predicted limb darkened angular diameters $\theta_{\rm LD}$ (*lower part*) of the planet-hosting stars 51 Peg A and HD 209458 A.

	51 Peg A	HD 209458 A
m_V	5.50 ± 0.01	7.65 ± 0.01
m_K	3.97 ± 0.01	6.31 ± 0.03
$\theta_{\rm LD}(K,\ V-K)$	0.689 ± 0.011 mas	0.228 ± 0.004 mas

can be translated into linear radii using the *Hipparcos* parallaxes (Perryman et al. 1997), $\pi_{51\,\rm Peg\,A} = 65.10 \pm 0.76$ mas and $\pi_{\rm HD\,209458\,A} = 21.24 \pm 1.00$ mas. We obtain $R_{51\,\rm Peg\,A} = 1.138 \pm 0.023\,R_\odot$ and $R_{\rm HD\,209458\,A} = 1.154 \pm 0.059\,R_\odot$. HD 209458 A is a particularly interesting object, as Brown et al. (2001) have been able to estimate directly its linear radius through the deconvolution of the light curve of the transit. They obtain a value of $R_{\rm HD\,209458\,A} = 1.146 \pm 0.050\,R_\odot$, in remarkable agreement with our (K, $V - K$) prediction. The bulk of the ±5% uncertainty comes from the error in the *Hipparcos* parallax, the relative error in the angular size being only ±2%.

The direct measurement of the angular diameter of 51 Peg A is within the capabilities of the existing very long baseline interferometers (several hundred meters), but this is not true for HD 209458 A. Its 0.228 mas size would require baselines of more than 800 m to be resolved at visible wavelengths (several kilometers in the infrared). Such baselines are not presently available or scheduled. And even so, the calibration of these observations would be extremely difficult, as the calibrator would have to be very faint. More generally, carefully calibrated surface brightness relations are currently the only method to estimate precisely (±1%) the angular size of solar type stars fainter than $m_V = 7$.

9. Conclusion

The laws that we established between the angular size and broadband colors (or effective temperature) are strictly empirical. Our best relations present a very small intrinsic dispersion, down to less than 1%. They can be used to predict the angular sizes of A0–M2 dwarfs and A0–K0 subgiants from simple, readily available broadband photometry. On the one hand, Gray et al. (2003) have recently published an extensive survey of the spectral properties of nearby stars within 40 pc, including estimates of their effective temperatures. On the other hand, several large catalogues (2MASS, DENIS,...) provide high precision magnitudes of these stars in the infrared. From the cross-comparison of these sources, the SB relations determined in the present paper make it possible to assemble a catalogue of calibrators for interferometry that will be practically unaffected by interstellar extinction, multiplicity or circumstellar material biases. These resulting angular diameter predictions will provide a reliable basis for the calibration of long-baseline interferometric observations.

Acknowledgements. P.K. acknowledges partial support from the European Southern Observatory through a post-doctoral fellowship. D.S. acknowledges the support of the Swiss FNRS. This research has

made extensive use of the SIMBAD and VIZIER online databases at CDS, Strasbourg (France).

References

Allende Prieto, C., Asplund, M., Garcia Lòpez, R. J., & Lambert, D. L. 2002, ApJ, 567, 544

Armstrong, J. T., Mozurkewich, D., Rickard, L. J., et al. 1998, ApJ, 496, 550

Barnes, T. G., Evans, D. S., & Parson, S. B. 1976, MNRAS, 174, 503

Bessell, M. S., Castelli, F., & Plez, B. 1998, A&A, 333, 231

Boden, A. F., Van Belle, G. T., Colavita, M. M. 1998, ApJ, 504, 39

Bordé, P., Coudé du Foresto, V., Chagnon, G., & Perrin, G. 2002, A&A, 393, 183

Brown, T. M., Charbonneau, D., Gilliland, R. L., Noyes, R. W., Burrows, A. 2001, ApJ, 552, 699

Cayrel de Strobel, G., Soubiran, C., Friel, E. D., Ralite, N., & Francois, P., 1997, A&AS, 124, 299

Cayrel de Strobel, G., Soubiran, C., & Ralite, N. 2001, A&A, 373, 159

Cenarro, A. J., Cardiel, N., Gorgas, J., et al. 2001, MNRAS, 326, 959

Charbonneau, D., Brown, T. M., Latham, D. W., & Mayor, M. 2000, ApJ, 522, L145

Ciardi, D. R., Van Belle, G. T., Akeson, R. L., et al. 2001, ApJ, 559, 1147

Claret, A. 2000, A&A, 363, 1081

Cohen, M., Walker, R. G., Carter, B., et al. 1999, AJ, 117, 1864

Colavita, M. M., Wallace, J. K., Hines, B. E., et al. 1999, ApJ, 510, 505

Colina, L., Bohlin, R. C., & Castelli, F. 1996, AJ, 112, 307

Cutri, R. M., Skrutskie, M. F., Van Dyk, S., et al. 2003, Univ. of Massachusetts and IPAC, http://www.ipac.caltech.edu/2mass

Davis, J., & Tango, W. J. 1986, Nature, 323, 234

Di Benedetto, G. P. 1998, A&A, 339, 858

Di Folco, E., Thévenin, F., Kervella, P., et al. 2004, in preparation

Domiciano de Souza, A., Kervella, P., Jankov, S., et al. 2003, A&A, 407, L47

Ducati, J. R. 2002, NASA Ref. Pub. 1294

Dyck, H. M., Van Belle, G. T., & Thompson, R. R. 1998, AJ, 116, 981

Erspamer, D., & North, P. 2003, A&A, 398, 1121

Fouqué, P., & Gieren, W. P. 1997, A&A, 320, 799

Fouqué, P., Chevallier, L., Cohen, M., et al. 2000, A&AS, 141, 313

Glass, I. S. 1974, Month. Not. of Astron. Soc. South Africa, 33, 53

Glass, I. S. 1975, MNRAS, 171, 19

Glindemann, A., Abuter, R., Carbognani, F., et al. 2000, Proc. SPIE, 4006, 2

Glindemann, A., Argomedo, J., Amestica, R., et al. 2003a, Proc. SPIE, 4838, 89

Glindemann, A., Argomedo, J., Amestica, R., et al. 2003b, Ap&SS, 286, 1

Gray, R. O., Graham, P. W., & Hoyt, S. R. 2001, AJ, 121, 2159

Gray, R. O., Corbally, C. J., Garrison, R. F., Mc Fadden, M. T., & Robinson, P. E. 2003, AJ, 126, 2048

Hanbury Brown, R., Davis, J., Allen, L. R. 1967, MNRAS, 137, 375

Hanbury Brown, R., Davis, J., Lake, J. W., & Thompson, R. J. 1974a, MNRAS, 167, 475

Hanbury Brown, R., Davis, J., & Allen, L. R. 1974b, MNRAS, 167, 121

Hoffleit, D., & Warren, W. H. 1991, The Bright Star Catalogue, 5th Revised Ed., Astronomical Data Center, NSSDC/ADC

Kervella, P., Coudé du Foresto, V., Glindemann, A., Hofmann, R. 2000, Proc. SPIE, 4006, 31

Kervella, P., Coudé du Foresto, V., Perrin, G., et al. 2001, A&A, 367, 876

Kervella, P., Gitton, Ph., Ségransan, D., et al. 2003a, Proc. SPIE, 4838, 858

Kervella, P., Thévenin, F., Morel, P., Bordé, P., & Di Folco, E. 2003b, A&A, 408, 681

Kervella, P., Thévenin, F., Ségransan, D., et al. 2003c, A&A, 404, 1087

Kervella, P., Thévenin, F., Morel, P., et al. 2004a, A&A, 413, 251

Kervella, P., Nardetto, N., Bersier, D., Mourard, D., & Coudé du Foresto, V. 2004b, A&A, 416, 941

Kidger, M. R., & Martín-Luis, F. 2003, AJ, 125, 3311

Koehler, B., Flebus, C., Dierickx, P., et al. 2002, ESO Messenger, 110, 21

Kurucz, R. L. 1992, The Stellar Populations of Galaxies, IAU Symp., 149, 225

Lane, B. F., Kuchner, M. J., Boden, A. F., Creech-Eakman, M., & Kulkarni, S. R. 2000, Nature, 407, 485

Lane, B. F., Boden, A. F., & Kulkarni, S. R., 2001, ApJ, 551, L81

Lane, B. F., Creech-Eakman, M., & Nordgren, T. E. 2002, ApJ, 573, 330

Leggett, S. K. 1992, ApJS, 82, 35

Mariotti, J.-M., Coudé du Foresto, V., Perrin, G., Peiqian Zhao, & Léna, P. 1996, A&AS, 116, 381

McAlister, H. A., Bagnuolo, W. G., ten Brummelaar, T. A., et al. 2000, Proc. SPIE, 4006, 465

Mayor, M., & Queloz, D. 1995, Nature, 378, 355

Mermilliod, J.-C. 1986, Catalogue of Eggen's UBV data, unpublished, available through SIMBAD

Morel, M., & Magnenat, P. 1978, A&AS, 34, 477

Morel, P., Provost, J., Lebreton, Y., Thévenin, F., & Berthomieu, G. 2000, A&A, 363, 675

Morel, P., Berthomieu, G., Provost, J., & Thévenin, F. 2001, A&A, 379, 245

Mould, J. R., & Hyland, A. R. 1976, ApJ, 208, 399

Mourard, D., Bonneau, D., Koechlin, L., et al. 1997, A&A, 317, 789

Mozurkewich, D., Armstrong, J. T., Hindsley, R. B., et al. 2003, AJ, 126, 2502

Nordgren, T. E., Germain, M. E., Benson, J. A., et al. 1999, AJ, 118, 3032

Nordgren, T. E., Armstrong, J. T., Germain, M. E., et al. 2000, ApJ, 543, 972

Nordgren, T. E., Sudol, J. J., & Mozurkewich, D. 2001, AJ, 122, 2707

Nordgren, T. E., Lane, B. F., Hindsley, R. B., & Kervella, P. 2002, AJ, 123, 3380

Ochsenbein, F., Bauer, P., Marcout, J. 2000, A&AS, 143, 221

Pasinetti-Fracassini, L. E., Pastori, L., Covino, S., & Pozzi, A. 2001, A&A, 367, 521

Petrov, R., Malbet, F., Richichi, A., et al. 2000, Proc. SPIE, 4006, 68

Perryman, M. A. C., Lindegren, L., Kovalevsky, J., et al., The Hipparcos Catalogue 1997, A&A, 323, 49

Ridgway, S. T., Jacoby, G. H., Joyce, R. R., & Wells, D. C. 1982, AJ, 87, 1044

Shao, M., Colavita, M. M., Hines, B. E., et al. 1988, ApJ, 327, 905

Ségransan, D., Kervella, P., Forveille, T., Queloz, D. 2003, A&A, 397, L5

Ségransan, D., Kervella, P., et al., in preparation

Söderhjelm, S. 1999, A&A, 341, 121

Thévenin, F., & Idiart, T. P. 1999, ApJ, 521, 753

Thévenin, F., Kervella, P., et al., in preparation

Van Belle, G. T. 1999a, PASP, 11, 1515

Van Belle, G. T., Lane, B. F., Thompson, R. R., et al. 1999b, AJ, 117, 521

Welch, D. L. 1994, AJ, 108, 1421

Wittkowski, M., Aufdenberg, J. P., & Kervella, P. 2004, A&A, 413, 711

Table 3. Apparent magnitudes of the dwarf stars (upper part) and subgiants (lower part) of our sample. The uncertainty adopted for each apparent magnitude value is given in superscript.

Star	m_U [a]	m_B [b]	m_V [b]	m_R [c]	m_I [c]	m_J [d]	m_H [d]	m_K [d]	m_L [d]
α Lyr	$0.03^{0.02}$	$0.03^{0.02}$	$0.03^{0.02}$	$0.04^{0.02}$	$0.03^{0.02}$	$0.00^{0.02}$	$0.00^{0.01}$	$0.00^{0.01}$	$0.00^{0.01}$
α CMa A	$-1.51^{0.02}$	$-1.46^{0.02}$	$-1.46^{0.02}$	$-1.46^{0.02}$	$-1.45^{0.02}$	$-1.34^{0.03}$	$-1.32^{0.03}$	$-1.32^{0.02}$	$-1.36^{0.03}$
β Leo	$2.30^{0.02}$	$2.22^{0.02}$	$2.14^{0.02}$	$2.08^{0.02}$	$2.06^{0.02}$	$2.02^{0.01}$	$1.99^{0.09}$	$1.86^{0.09}$	$1.86^{0.09}$
α PsA	$1.31^{0.02}$	$1.25^{0.02}$	$1.16^{0.02}$	$1.10^{0.02}$	$1.08^{0.02}$	$1.06^{0.05}$	$1.05^{0.06}$	$0.99^{0.03}$	$1.01^{0.07}$
α Cen A	$0.92^{0.02}$	$0.70^{0.02}$	$-0.01^{0.02}$			$-1.16^{0.02}$	$-1.39^{0.09}$	$-1.50^{0.02}$	$-1.55^{0.09}$
Sun [e]	$-25.98^{0.02}$	$-26.12^{0.02}$	$-26.75^{0.02}$	$-27.12^{0.02}$	$-27.48^{0.02}$	$-27.86^{0.02}$	$-28.20^{0.02}$	$-28.22^{0.02}$	
τ Cet	$4.43^{0.02}$	$4.22^{0.02}$	$3.50^{0.02}$	$2.88^{0.01}$	$2.41^{0.01}$	$2.11^{0.01}$	$1.73^{0.01}$	$1.66^{0.01}$	$1.64^{0.01}$
GJ 166 A	$5.69^{0.02}$	$5.25^{0.02}$	$4.43^{0.02}$	$3.72^{0.01}$	$3.27^{0.01}$	$2.91^{0.03}$	$2.46^{0.01}$	$2.39^{0.02}$	$2.30^{0.02}$
α Cen B	$2.86^{0.02}$	$2.21^{0.02}$	$1.33^{0.02}$			$-0.01^{0.02}$	$-0.49^{0.09}$	$-0.60^{0.02}$	$-0.63^{0.09}$
ϵ Eri	$5.19^{0.02}$	$4.61^{0.02}$	$3.73^{0.02}$	$3.01^{0.02}$	$2.54^{0.02}$	$2.23^{0.03}$	$1.75^{0.03}$	$1.67^{0.01}$	$1.60^{0.05}$
GJ 105 A	$7.58^{0.02}$	$6.81^{0.02}$	$5.83^{0.02}$	$4.99^{0.02}$	$4.46^{0.02}$	$4.07^{0.03}$	$3.52^{0.03}$	$3.45^{0.03}$	$3.43^{0.03}$
GJ 570 A	$7.88^{0.02}$	$6.82^{0.02}$	$5.71^{0.02}$	$4.72^{0.02}$	$4.18^{0.02}$	$3.82^{0.02}$	$3.27^{0.02}$	$3.15^{0.02}$	$3.11^{0.02}$
ϵ Ind A	$6.74^{0.02}$	$5.75^{0.02}$	$4.69^{0.02}$	$3.81^{0.02}$	$3.25^{0.02}$	$2.83^{0.02}$	$2.30^{0.02}$	$2.18^{0.02}$	$2.12^{0.02}$
GJ 380	$9.23^{0.02}$	$7.94^{0.02}$	$6.59^{0.02}$	$5.36^{0.02}$	$4.56^{0.02}$	$3.98^{0.03}$	$3.32^{0.03}$	$3.19^{0.03}$	$3.11^{0.03}$
GJ 191	$11.64^{0.02}$	$10.40^{0.02}$	$8.86^{0.02}$			$5.77^{0.02}$	$5.27^{0.02}$	$5.05^{0.02}$	$4.86^{0.02}$
GJ 887	$9.99^{0.02}$	$8.83^{0.02}$	$7.35^{0.02}$			$4.20^{0.02}$	$3.60^{0.02}$	$3.36^{0.02}$	$3.20^{0.02}$
GJ 205	$10.63^{0.02}$	$9.44^{0.02}$	$7.97^{0.02}$	$6.53^{0.02}$	$5.39^{0.02}$	$4.77^{0.02}$	$4.06^{0.02}$	$3.86^{0.02}$	$3.83^{0.02}$
GJ 15 A	$10.88^{0.02}$	$9.63^{0.02}$	$8.07^{0.02}$	$6.72^{0.02}$	$5.53^{0.02}$	$4.86^{0.03}$	$4.25^{0.03}$	$4.02^{0.02}$	$3.87^{0.03}$
GJ 411	$10.13^{0.02}$	$9.00^{0.02}$	$7.49^{0.02}$	$5.98^{0.02}$	$4.76^{0.02}$	$4.13^{0.03}$	$3.56^{0.03}$	$3.35^{0.03}$	$3.20^{0.03}$
GJ 699	$12.57^{0.02}$	$11.28^{0.02}$	$9.54^{0.02}$	$7.71^{0.02}$	$6.10^{0.02}$	$5.30^{0.02}$	$4.77^{0.02}$	$4.52^{0.02}$	$4.18^{0.02}$
Proxima	$14.56^{0.02}$	$13.02^{0.02}$	$11.05^{0.02}$	$8.68^{0.02}$	$6.42^{0.02}$	$5.33^{0.02}$	$4.73^{0.02}$	$4.36^{0.03}$	$4.04^{0.02}$
γ Gem	$1.97^{0.02}$	$1.92^{0.02}$	$1.92^{0.02}$	$1.86^{0.02}$	$1.87^{0.02}$	$1.87^{0.02}$	$1.83^{0.02}$	$1.85^{0.03}$	$1.87^{0.09}$
α CMi A	$0.82^{0.02}$	$0.79^{0.02}$	$0.37^{0.02}$	$-0.05^{0.02}$	$-0.28^{0.02}$	$-0.40^{0.03}$	$-0.60^{0.03}$	$-0.65^{0.03}$	$-0.68^{0.03}$
η Boo	$3.46^{0.02}$	$3.26^{0.02}$	$2.68^{0.02}$	$2.24^{0.02}$	$1.95^{0.02}$	$1.67^{0.02}$	$1.39^{0.01}$	$1.35^{0.01}$	$1.30^{0.02}$
ζ Her A	$3.67^{0.02}$	$3.46^{0.02}$	$2.81^{0.02}$	$2.30^{0.02}$	$1.98^{0.02}$	$1.77^{0.01}$	$1.42^{0.01}$	$1.38^{0.01}$	$1.30^{0.06}$
μ Her	$4.57^{0.02}$	$4.17^{0.02}$	$3.42^{0.02}$	$2.89^{0.02}$	$2.51^{0.02}$	$2.13^{0.01}$	$1.80^{0.01}$	$1.74^{0.01}$	$1.72^{0.02}$
β Aql	$5.07^{0.02}$	$4.58^{0.02}$	$3.72^{0.02}$	$3.06^{0.02}$	$2.57^{0.02}$	$2.19^{0.02}$	$1.70^{0.01}$	$1.65^{0.02}$	$1.61^{0.02}$
η Cep	$4.96^{0.02}$	$4.35^{0.02}$	$3.43^{0.02}$	$2.76^{0.02}$	$2.27^{0.02}$	$1.80^{0.05}$		$1.22^{0.02}$	$1.17^{0.09}$
δ Eri	$5.13^{0.02}$	$4.46^{0.02}$	$3.54^{0.02}$	$2.82^{0.02}$	$2.32^{0.02}$	$1.95^{0.01}$	$1.49^{0.02}$	$1.40^{0.01}$	$1.36^{0.02}$

– References:

(*a*) Morel et al. (1978); Mermilliod (1986).

(*b*) Morel et al. (1978); Hoffleit & Warren (1991); Perryman et al. (1997).

(*c*) Morel et al. (1978); Bessell et al. (1998); Ducati et al. (2002).

(*d*) Glass (1974); Glass (1975); Mould & Hyland (1976); Morel et al. (1978); Leggett (1992); Ducati et al. (2002); Kidger & Martín-Luis (2003); the 2MASS catalogue (Cutri et al. 2003).

(*e*) We refered to Colina et al. (1996) for the apparent magnitudes of the Sun.

Table 4. Surface brightness relations using *UBVRIJHKL* based colors to obtain the limb darkened angular diameter $\theta_{\rm LD}$ (in mas) as a function of the magnitude and color of the star through: $\log \theta_{\rm LD}(C_0, C_1) = c_\lambda(C_0 - C_1) + d_\lambda - 0.2\,C_0$. The residual dispersions are given in percents of the LD angular diameter. The 1σ errors in each coefficient are given in superscript, *multiplied by 1000* to reduce the length of each line, i.e. $0.5822^{3.2}$ stands for 0.5822 ± 0.0032. When the data depart significantly from our linear fit and present a detectable non-linearity, the dispersion is mentioned in *italic* characters, and we have added the note "*nl*". The dispersions smaller than 5% are mentioned in bold characters: they mark the relations that are the most suitable for predicting stellar angular sizes.

C_0 ↓	$C_1 \rightarrow U$	B	V	R	I	J	H	K	L
c_U		$1.2701^{11.8}$	$0.5822^{3.2}$	$0.3925^{1.7}$	$0.3178^{1.1}$	$0.2805^{1.0}$	$0.2509^{0.8}$	$0.2437^{0.8}$	$0.2407^{0.8}$
d_U		$0.6607^{7.9}$	$0.5532^{4.5}$	$0.5393^{3.5}$	$0.5384^{3.1}$	$0.5351^{3.0}$	$0.5206^{2.9}$	$0.5217^{2.7}$	$0.5184^{2.9}$
σ_U		*57.8% nl*	*17.9% nl*	*10.6% nl*	*7.88% nl*	*5.05% nl*	**3.06%**	**2.76%**	**1.92%**
c_B	$-1.0923^{10.4}$		$0.9095^{6.9}$	$0.4771^{2.2}$	$0.3557^{1.4}$	$0.3029^{1.0}$	$0.2630^{0.8}$	$0.2538^{0.7}$	$0.2501^{0.9}$
d_B	$0.6542^{7.0}$		$0.4889^{1.1}$	$0.5116^{0.1}$	$0.5235^{0.1}$	$0.5242^{0.1}$	$0.5134^{1.0}$	$0.5158^{0.1}$	$0.5133^{0.1}$
σ_B	*59.2% nl*		*9.17% nl*	*4.75% nl*	*4.98% nl*	**3.07%**	**1.89%**	**≤1.00%**	**≤1.00%**
c_V	$-0.3846^{2.3}$	$-0.7083^{7.4}$		$0.7900^{8.4}$	$0.4550^{2.9}$	$0.3547^{2.0}$	$0.2893^{1.6}$	$0.2753^{1.4}$	$0.2694^{1.4}$
d_V	$0.5513^{3.4}$	$0.4889^{5.7}$		$0.5217^{6.4}$	$0.5332^{4.0}$	$0.5310^{3.6}$	$0.5148^{3.2}$	$0.5175^{2.9}$	$0.5146^{3.1}$
σ_V	*18.0% nl*	*9.18% nl*		*8.53% nl*	*8.30% nl*	**4.75%**	**1.85%**	**1.01%**	**≤1.00%**
c_R	$-0.1966^{1.0}$	$-0.2792^{1.7}$	$-0.5842^{5.1}$		$0.7404^{6.4}$	$0.4647^{3.2}$	$0.3405^{2.5}$	$0.3158^{1.9}$	$0.3041^{1.8}$
d_R	$0.5351^{2.4}$	$0.5109^{3.0}$	$0.5251^{4.7}$		$0.5570^{5.2}$	$0.5392^{4.0}$	$0.5119^{3.8}$	$0.5158^{3.1}$	$0.5144^{3.3}$
σ_R	*11.1% nl*	*5.02% nl*	*8.63% nl*		*14.5% nl*	*8.43% nl*	**2.88%**	**2.05%**	**2.52%**
c_I	$-0.1210^{0.7}$	$-0.1587^{1.1}$	$-0.2609^{2.0}$	$-0.5998^{7.6}$		$0.9079^{19.8}$	$0.4318^{6.0}$	$0.3833^{4.5}$	$0.3707^{4.6}$
d_I	$0.5351^{1.9}$	$0.5207^{2.3}$	$0.5296^{2.8}$	$0.5416^{4.7}$		$0.5233^{7.6}$	$0.5089^{4.4}$	$0.5140^{3.7}$	$0.5097^{4.0}$
σ_I	*8.30% nl*	*5.34% nl*	*8.73% nl*	*12.1% nl*		*10.8% nl*	*5.83% nl*	**3.84%**	**3.30%**
c_J	$-0.0818^{0.6}$	$-0.1043^{0.9}$	$-0.1581^{1.4}$	$-0.2842^{3.2}$	$-0.7198^{16.9}$		$0.6280^{16.0}$	$0.5214^{10.6}$	$0.4840^{9.4}$
d_J	$0.5325^{1.9}$	$0.5216^{2.2}$	$0.5276^{2.4}$	$0.5299^{3.2}$	$0.5197^{6.5}$		$0.4990^{5.8}$	$0.5066^{4.9}$	$0.5078^{4.8}$
σ_J	*5.13% nl*	**3.12%**	**4.98%**	*7.26% nl*	*10.9% nl*		*10.44% nl*	*5.86% nl*	**4.08%**
c_H	$-0.0513^{0.5}$	$-0.0625^{0.6}$	$-0.0892^{0.9}$	$-0.1376^{1.8}$	$-0.2290^{4.0}$	$-0.4312^{12.1}$		$1.8747^{58.8}$	$1.1714^{27.7}$
d_H	$0.5189^{1.6}$	$0.5138^{1.8}$	$0.5145^{1.9}$	$0.5138^{2.3}$	$0.5093^{2.9}$	$0.5013^{4.4}$		$0.5352^{7.5}$	$0.5271^{6.2}$
σ_H	**2.67%**	**1.24%**	**1.12%**	**2.06%**	*5.53% nl*	*10.31% nl*		*17.2% nl*	*13.0% nl*
c_K	$-0.0440^{0.4}$	$-0.0535^{0.6}$	$-0.0755^{0.8}$	$-0.1144^{1.4}$	$-0.1805^{2.8}$	$-0.3192^{7.4}$	$-1.7040^{55.1}$		$3.0857^{33.9}$
d_K	$0.5202^{1.6}$	$0.5159^{1.6}$	$0.5170^{1.7}$	$0.5168^{1.9}$	$0.5149^{2.3}$	$0.5089^{3.4}$	$0.5336^{7.0}$		$0.6258^{3.6}$
σ_K	**2.58%**	**≤1.00%**	**≤1.00%**	**1.60%**	**3.67%**	*5.87% nl*	*17.6% nl*		*26.9% nl*
c_L	$-0.0412^{0.5}$	$-0.0502^{0.6}$	$-0.0701^{0.8}$	$-0.1075^{1.4}$	$-0.1696^{2.9}$	$-0.2826^{6.4}$	$-0.9843^{24.1}$	$-2.8950^{115.7}$	
d_L	$0.5167^{1.7}$	$0.5133^{1.8}$	$0.5139^{1.9}$	$0.5128^{2.1}$	$0.5101^{2.5}$	$0.5081^{3.3}$	$0.5245^{5.4}$	$0.5309^{12.4}$	
σ_L	**≤1.00%**	**≤1.00%**	**≤1.00%**	**≤1.00%**	**2.43%**	**3.61%**	*13.1% nl*	*26.3% nl*	

Table 5. SB relations using the magnitude C_λ and the effective temperature $T_{\rm eff}$ of the star to obtain the limb darkened angular diameter $\theta_{\rm LD}$ (in mas): $\log \theta_{\rm LD}(T_{\rm eff}, C_\lambda) = d(\log T_{\rm eff})^2 + e \log T_{\rm eff} + f - 0.2\,C_\lambda$. The 1σ residual dispersions are given in percents of the LD angular diameter.

C_λ	σ	d	e	f
U	5.93%	5.6391	−46.4505	96.0513
B	6.33%	3.6753	−30.9671	65.5421
V	5.90%	3.0415	−25.4696	53.7010
R	4.76%	2.1394	−18.0221	38.3497
I	2.28%	0.9847	−8.7985	19.9281
J	1.19%	0.9598	−8.3451	18.5204
H	1.38%	1.1684	−9.6156	20.2779
K	≤1.00%	0.8470	−7.0790	15.2731
L	≤1.00%	0.6662	−5.6609	12.4902

Table 6. $T_{\rm eff}(\theta_{\rm LD}, m_\lambda)$ relations to obtain the effective temperature: $\log T_{\rm eff} = -\sqrt{g \log \theta_{\rm LD} + h\,C_\lambda + i} + j$. The 1σ residual dispersions are given in percents of the effective temperature $T_{\rm eff}$ (expressed in K).

C_λ	σ	g	h	i	j
U	1.19%	0.1773	0.0355	−0.0703	4.1186
B	1.57%	0.2721	0.0544	−0.0850	4.2128
V	1.61%	0.3288	0.0658	−0.1249	4.1870
R	1.57%	0.4674	0.0935	−0.1848	4.2120
I	1.13%	1.0155	0.2031	−0.2788	4.4675
J	0.60%	1.0419	0.2084	−0.3975	4.3472
H	0.63%	0.8559	0.1712	−0.4230	4.1149
K	≤0.60%	1.1806	0.2361	−0.5695	4.1788
L	≤0.60%	1.5010	0.3002	−0.6977	4.2486

3.5 Projets de recherche

La précision des mesures interférométriques de diamètre angulaire des étoiles proches n'est plus aujourd'hui la limite à l'établissement de contraintes de rayons pour les modèles d'évolution. En effet, la précision des parallaxes Hipparcos ($\approx 1\,\mathrm{mas}$) est le facteur limitant pour calculer le rayon linéaire au delà des étoiles les plus proches ($d \geq 10\,\mathrm{pc}$). Dès lors, il n'est pas opportun de chercher des précisions sur le diamètre angulaire inférieures au pourcent pour contraindre le rayon linéaire.

En attendant les missions spatiales d'astrométrie SIM et GAIA, il reste cependant très utile de mesurer l'assombrissement centre-bord, de manière à valider le plus précisément possible les modèles d'atmosphère. En particulier, les modèles tridimensionnels hydrodynamiques sont très prometteurs, mais demandent une vérification observationnelle. Je projette de réaliser ce travail sur plusieurs étoiles naines proches, mais également sur d'autres classes de luminosité.

L'étude des étoiles déficientes en métaux est actuellement dans une période de fort développement, à la fois sur le plan de la modélisation, mais aussi par de nouvelles observations astérosismiques. Je prévois de contribuer à l'étude de ces étoiles par la mesure de la taille angulaire, et éventuellement de l'assombrissement centre-bord, de plusieurs de ces étoiles. Il est en effet possible qu'elles ne suivent pas les relations de brillance de surface établies sur les étoiles de métallicité solaire.

Chapitre 4

Les étoiles en rotation rapide

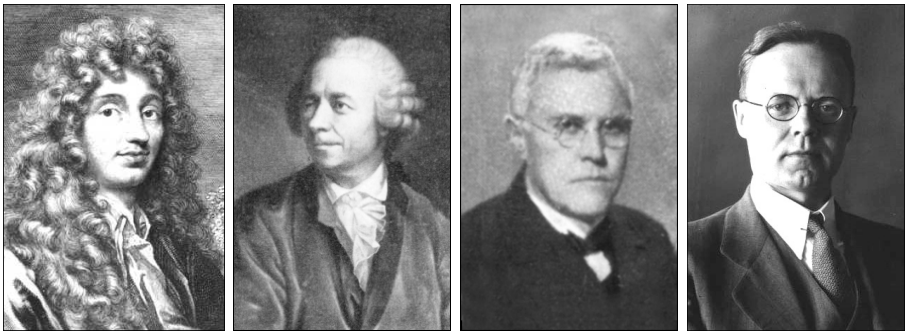

FIG. 4.1 – Portraits de personnalités importantes de l'étude des étoiles en rotation rapide : Christiaan Huygens (1629-1695), Leonhard Euler (1707-1783), Ernst Hugo Von Zeipel (1873-1959) et Otto Struve (1897-1963).

Beaucoup des astres qui nous sont familiers sont presque parfaitement sphériques. La Terre, la Lune, le Soleil présentent des formes indiscernables de sphères parfaites sauf à les mesurer avec précision à l'aide d'instruments. La forme de la sphère est le résultat d'un équilibre rassurant, et est perçue comme une image de la perfection. Pourtant, partout dans l'Univers, la rotation privilégie un axe de l'espace au détriment des deux autres, et brise ainsi l'équilibre et la symétrie de la sphère. Dans notre propre système solaire, les planètes géantes Saturne et Jupiter subissent une importante déformation de leur globe, du fait de leur courte période de rotation. Qu'en est-il des étoiles présentant des vitesses équatoriales de rotation cent fois, ou même deux-cent fois plus rapides que celle du Soleil ?

4.1 La rotation des masses fluides

4.1.1 Une question ancienne

L'étude de la rotation des masses fluides est un domaine très ancien, mais où les progrès ont été relativement lents. La raison en est que ce problème physique est simple dans son traitement approché (équilibre hydrostatique, densité uniforme,) mais devient peu à peu d'une grande complexité avec la prise en compte des phénomènes physiques les plus fins (rotation différentielle, transfert du rayonnement,). La progression générale des connaissances scientifiques au cours des quatre siècles passés a permis une remarquable amélioration de notre compréhension

des phénomènes astrophysiques en jeu dans les étoiles en rotation, parallèlement aux progrès en mathématiques et physique. Un historique détaillé se trouve dans les livres de Jean-Louis Tassoul (1978; 2000), dont je reprend ici les dates importantes.

C'est en 1610 que Galilée (1564-1642) a mesuré pour la première fois la période de rotation du Soleil, en interprétant correctement le passage des taches solaires sur le disque de notre étoile. A la fin du XIXème siècle, William de Wiveleslie Abney (1843-1920) a compris que l'élargissement des raies spectrales de certaines étoiles est causé par leur rotation rapide sur elle-même. Du fait de l'effet Doppler, les raies spectrales formées dans la partie du disque qui s'approche de nous sont décalées vers le bleu, et inversement vers le rouge pour la partie qui s'éloigne. Comme le spectre de l'étoile est la somme de la contribution de toutes les parties visibles du disque, les raies apparaissent élargies. La première moitié du XXème siècle a permis de généraliser cette explication à une grande variété d'étoiles simples ou binaires, notamment grâce à l'amélioration des spectrographes.

Sur le plan théorique, dès la fin du XVIIème siècle, Isaac Newton (1643-1727) a calculé l'ellipticité du globe terrestre en rotation avec l'hypothèse d'homogénéité. Pour ce problème particulier, il a obtenu la relation :

$$\Gamma = \frac{R_{\rm eq} - R_{\rm pol}}{R_{\rm pol}} = \frac{5}{4}\frac{C}{P} \tag{4.1}$$

avec $R_{\rm eq}$ et $R_{\rm pol}$ les rayons équatorial et polaire, C la force centrifuge, et P le poids. Peu après, Christiaan Huygens (1629-1695) a étendu ce calcul au cas d'une masse ponctuelle produisant un champ de gravitation dépendant inversement du carré de la distance, et entourée de matière non pesante en rotation uniforme de corps solide (on parlera plus tard d'hypothèse de Roche). Les équipotentielles présentent alors un aplatissement relatif de

$$\Gamma = \frac{1}{2}\frac{C}{P} \tag{4.2}$$

Au XVIIIème siècle, plusieurs grands mathématiciens ont travaillé sur la question de la forme théorique du géoïde terrestre, dont Alexis-Claude Clairaut (1713-1765), Colin Maclaurin (1698-1746) et surtout Leonhard Euler (1707-1783). Pour cela, ils ont établi les fondements de l'hydrostatique, plus tard développés par Pierre-Simon de Laplace (1749-1827) et Adrien Marie Legendre (1752-1833) peu avant la Révolution française. Les mathématiciens Carl Gustav Jacobi (1804-1851) et Joseph Liouville (1809-1882) ont ensuite démontré que les formes axi-symétriques ne sont pas les seuls équilibres possibles pour un corps en rotation.

Au début du XXème siècle, le domaine a connu un renouveau important sous l'impulsion de Aleksandr Mikhailovich Liapunov (1857-1918) et Henri Poincaré (1854-1912), qui ont établi la théorie générale de l'équilibre et de la stabilité des formes ellipsoïdales. Cette théorie a été particulièrement approfondie car on a cru un temps qu'elle permettait d'expliquer la formation des étoiles binaires. Après la première guerre mondiale, James Jeans (1877-1946) a construit une série de modèles pour différentes degrés de condensation centrale (des polytropes), conduisant Otto Struve (1897-1963) a proposer que les étoiles Be sont des étoiles en rotation uniforme rapide à la limite de disloquation, et entourées d'un anneau de matière gazeuse. En même temps que ces découvertes sur la physique des masses fluides en rotation, de grands progrès étaient faits sur l'explication du transport de l'énergie dans les étoiles, conduisant David Milne (1896-1950) puis Subrahmanyan Chandrasekhar (1910-1995) à construire les premiers modèles physiques complets de polytropes déformés pas la rotation. En 1924, Ernst Hugo Von Zeipel (1873-1959) a établi un théorème important donnant la quantité d'énergie émise en un point de la photosphère d'une étoile en rotation de corps solide. Arthur Eddington (1882-1944) en a déduit l'existence d'une circulation de matière entre le pôle et l'équateur d'une telle étoile, la circulation méridienne.

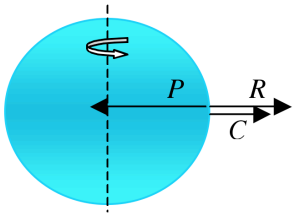

FIG. 4.2 – L'équilibre d'une étoile en rotation (voir notations dans le texte).

Avec l'amélioration considérable des moyens d'observation, et en particulier l'apparition des détecteurs électroniques à la fin du XXème siècle, de nouvelles questions sont apparues. Des différences sont ainsi apparues entre les modèles des étoiles chaudes (en particulier des types spectraux O et B) et les observations, en particulier concernant les abondances en hélium et en azote. Le raffinement des modèles d'évolution a aussi fait apparaître l'influence de la rotation sur le trajet suivi par l'étoile dans le diagramme Hertzprung-Russell. Sa durée de vie en particulier peut être augmentée de plus d'un quart du fait du mélange introduit par la circulation méridienne. Partant d'une évolution conditionnée essentiellement par la masse M de l'étoile et sa composition chimique Z, il est ainsi apparu indispensable d'introduire une variable supplémentaire : la vitesse angulaire de rotation Ω.

La richesse et la complexité des phénomènes physiques en jeu dans les étoiles en rotation ont abouti à différents modèles numériques reproduisant de mieux en mieux les contraintes issues de l'observation. Pourtant, tous les processus à l'œuvre dans les étoiles en rotation ne sont pas encore bien connus. Le transport du moment cinétique en général et le rôle de la turbulence en particulier sont encore des domaines de recherche très actifs. L'évolution de la prise en compte de la rotation différentielle est à ce titre remarquable : la plupart des modèles numériques considèrent encore comme hypothèse de départ la rotation de corps solide. La raison en est qu'il est pour l'instant très difficile de contraindre la rotation interne de l'étoile sur la base des mesures spectroscopiques seules.

Comme nous le verrons plus loin, les observations interférométriques récentes permettent maintenant de mesurer la forme de la photosphère des étoiles. Ceci nous a permis de montrer que la rotation de corps solide ne permet pas d'expliquer l'aplatissement extrême d'Achernar (Sect. 4.3). C'est un pas vers la construction de nouveaux modèles plus raffinés et une meilleure compréhension du transport de moment cinétique dans les étoiles.

4.1.2 L'équilibre d'une étoile en rotation

Une étoile est une masse de gaz chaud en équilibre sous l'effet de deux forces antagonistes (Fig. 4.2) : la gravitation, qui tend à la contracter par le poids (P), et la pression qui tend à la dilater (résultante R). La surface apparente de l'étoile, la photosphère, est une surface où cet équilibre est réalisé, avec la condition supplémentaire que l'opacité du gaz soit suffisamment faible pour que les photons émis par l'étoile s'en échappent en ligne droite. Dans une étoile en rotation, la force centrifuge crée une composante supplémentaire C dans cet équilibre. Son effet est équivalent à une diminution de la gravité locale, variable avec la latitude. Ceci crée un écart à la sphéricité avec une augmentation du rayon de l'étoile à l'équateur.

Le Soleil est une étoile en rotation lente : à l'équateur, il effectue un tour sur lui-même en 26 jours environ. De ce fait, la force centrifuge introduite par la rotation est très faible par rapport à la gravité : seulement $C = 0,006\,\mathrm{N}$ contre $P = 274\,\mathrm{N}$ pour le poids d'une masse de $1\,\mathrm{kg}$ à l'équateur, soit un rapport de $C/P = 0.002\%$. La moitié de ce rapport donne un ordre de

grandeur de l'aplatissement réel très faible de notre étoile (approximation de Huygens) :

$$\Gamma_\odot = \left[\frac{R_{\rm eq} - R_{\rm pol}}{R_{\rm pol}}\right]_\odot = 0,001\% \tag{4.3}$$

soit moins de 10 km ! Nous avons utilisé cette approximation pour illustrer ce calcul approché car la masse des étoiles en général, et des plus massives en particulier, est très concentrée près de leur centre. En réalité, la période de rotation du Soleil est différente aux pôles et à l'équateur et il existe un champ magnétique non-homogène, rendant l'explication théorique complète de l'aplatissement très complexe, mais l'ordre de grandeur est correct.

Reprenons maintenant l'approximation de Huyghens (4.2) :

$$\Gamma = \frac{R_{\rm eq} - R_{\rm pol}}{R_{\rm pol}} = \frac{1}{2}\frac{C}{P} \tag{4.4}$$

On peut la réécrire sous la forme suivante

$$\Gamma = \frac{1}{2}\frac{\Omega^2 R}{GM/R^2} = \left(\frac{3}{8\pi G}\right)\frac{\Omega^2}{\rho} \tag{4.5}$$

avec Ω la vitesse angulaire de rotation (supposée uniforme), G la constante universelle de gravitation, R le rayon à l'équateur, M la masse de l'étoile et $\rho = 3M/(4\pi R^3)$ sa densité moyenne (aplatissement faible). Pour une même vitesse angulaire, l'aplatissement est donc inversement proportionnel à la densité de l'étoile considérée.

Avec un rayon équatorial de $12\,R_\odot$, la force de gravitation de Achernar est beaucoup moins importante : $P = 12\,\mathrm{N}$ pour une masse de 1 kg. Par contre, on estime la vitesse équatoriale de Achernar à 290 km/s (compte tenu de l'angle de projection), ce qui donne une force centrifuge colossale de $C = 10\,\mathrm{N}$ sur cette même masse. Le demi-rapport des deux forces est de $1/2\ C/P = 44\%$ soit une valeur proche du rapport d'aplatissement $\Gamma(\text{Achernar}) = 56\%$ obtenu grâce aux mesures interférométriques. Il est intéressant de remarquer que la force résultante totale sur la masse de 1 kg est de seulement 2 N, ce qui signifie que la matière située à l'équateur d'Achernar peut très facilement s'en échapper sous l'effet d'une éruption stellaire. Ceci explique que Achernar soit parfois entourée de matière diffuse, lors des épisodes Be (le spectre de l'étoile présente alors des raies spectrales en émission). Altaïr, plus petite se contente d'un rapport $1/2\ C/P = 17\%$, là encore proche de la valeur réellement observée de $\Gamma(\text{Altair}) = 14\%$.

4.1.3 Deux exemples de rotateurs rapides proches de nous : Saturne et Jupiter

Saturne en tête, les planètes géantes du système solaire donnent un exemple de déformation rotationnelle analogue à celle des étoiles en rotation rapide. Saturne boucle un tour sur elle-même en 10,5 h, ce qui cause un aplatissement de $\Gamma_{\saturn} = 11\%$. Jupiter tourne encore plus vite, en seulement 9,9 h, mais son aplatissement est plus faible : $\Gamma_{\jupiter} = 7\%$. La vitesse lineaire à l'équateur de Saturne est de 9,9 km/s, contre 12,6 km/s pour Jupiter. Ces chiffres sont bien sûr très inférieurs à ce qu'on observe par exemple pour Altaïr ($v \sin i \approx 200\,\mathrm{km/s}$, $R = 1,8\,R_\odot$), mais Saturne est en fait un assez bon analogue d'Altaïr : sa période de rotation ($P_{\saturn} \approx 10,5\,\mathrm{h}$) est tout à fait comparable à la période de rotation supposée d'Altaïr ($P_{\rm Altair} \approx 10\,\mathrm{h}$).

La masse d'Altaïr est de $1,7\,M_\odot$, son rayon équatorial de $1,9\,R_\odot$, et son rayon polaire de $1,7\,R_\odot$ ce qui lui confère une densité moyenne de $\rho_{\rm Altair} \approx 30\%\,\rho_\odot$. La densité moyenne de Saturne est de 690 kg/m3, et celle du Soleil est de 1 400 kg/m3, soit $\rho_{\saturn} \approx 50\%\,\rho_\odot$. Du fait de sa

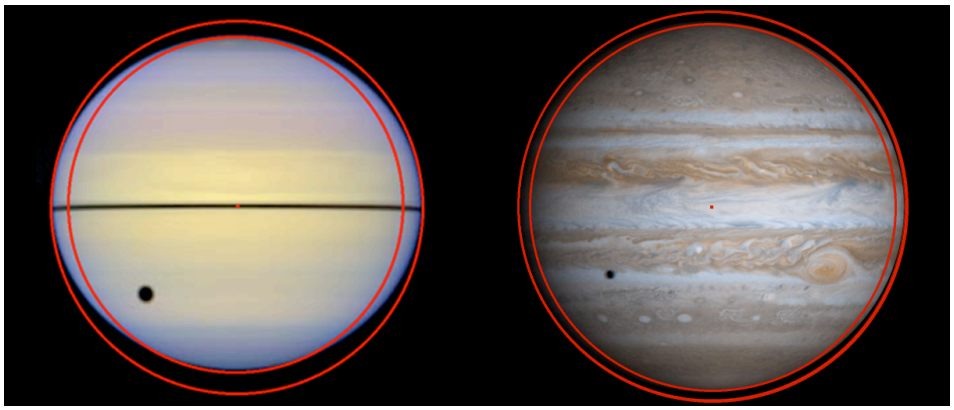

FIG. 4.3 – Photographies de Saturne et Jupiter montrant leur déformation rotationnelle. L'image de gauche a été obtenue par le télescope Hubble lors du passage de la Terre dans le plan des anneaux, qui est aussi le plan équatorial de la planète. On distingue clairement l'aplatissement polaire très important : $\Gamma = 11\%$. Jupiter (photo de droite, obtenue par la sonde européenne *Ulysses*), malgré sa rotation plus rapide que celle de Saturne, présente un aplatissement moins important ($\Gamma = 7\%$) du fait de sa plus grande densité. Les cercles tangents à l'équateur et aux pôles de la planète ont été tracés pour mieux visualiser la déformation (photos NASA).

plus grande densité, l'aplatissement $\Gamma_{\saturn} = 11\%$ de Saturne est un peu plus faible que celui mesuré pour Altaïr, $\Gamma(\text{Altair}) = 14\%$. Ceci est dû à l'influence proportionnellement plus importante de la gravité comparée à la force centrifuge. Le même calcul pour la planète Jupiter donne une densité plus forte ($\rho_{\jupiter} = 94\%\,\rho_\odot$), et un aplatissement plus faible ($\Gamma_{\jupiter} = 7\%$). L'aplatissement différent des deux planètes est clairement visible sur la Fig. 4.3.

Cette analogie entre les étoiles en rotation rapide et les planètes géantes a cependant ses limites. La première est bien entendu que les planètes gazeuses sont des objets de masses beaucoup plus faibles : Saturne par exemple, ne représente que 0.03% de la masse du Soleil. Par ailleurs, le champ magnétique par unité de masse est beaucoup plus intense pour les planètes joviennes que pour les étoiles comme Altaïr ou Achernar. La présence de ce champ magnétique tend à uniformiser la rotation de la planète, alors que la rotation différentielle semble jouer un rôle important dans les étoiles massives. Enfin, la matière constituant les étoiles et les planètes géantes, si elle est relativement semblable en composition (essentiellement de l'hydrogène et de l'hélium) est dans un état physique très différent : un plasma dans les étoiles, mais un gaz, un liquide ou même un solide (hydrogène métallique) pour Jupiter et Saturne. Les effets mécaniques de la rotation rapide sont ainsi similaires entre étoiles et planètes, mais la comparaison fine de leurs formes réclame la mise en œuvre de modèles spécifiques.

4.2 Altaïr (α Aql)

4.2.1 Observations interférométriques et modélisation

Les premières observations interférométriques de Altaïr obtenues par van Belle et al. (2001) à l'aide du *Palomar Testbed Interferometer* (PTI) ont montré un aplatissement de $\Gamma = 14\%$. La partie gauche de la Fig. 4.4 montre les mesures et le meilleur modèle obtenu par ces auteurs. Il est à noter que les observations du PTI ont été obtenues essentiellement selon deux azimuths, et elles ne permettent pas de déterminer à elles seules l'aplatissement de l'étoile (par le fit d'une

ellipse par exemple) et son orientation sur le ciel. C'est pourquoi il a été nécessaire à ces auteurs de prendre en compte les données spectrales et de faire des hypothèses sur l'étoile pour aboutir à ce modèle. *A contrario*, nos observations de Achernar présentées à la Sect. 4.3 ont permis de déterminer de manière directe à la fois la forme de l'étoile et son orientation sur le ciel.

A la suite de ces premiers résultats, des observations obtenues par Ohishi et al. (2004) avec l'interféromètre à trois télescopes NPOI (*Navy Prototype Optical Interferometer*) ont permis de détecter la présence d'un excès de lumière au pôle de l'étoile dû à l'effet Von Zeipel (Fig. 4.4 à droite). Pour l'instant, ces observations sont encore trop parcellaires pour permettre de contraindre suffisamment les modèles, mais elles sont en accord avec les prévisions.

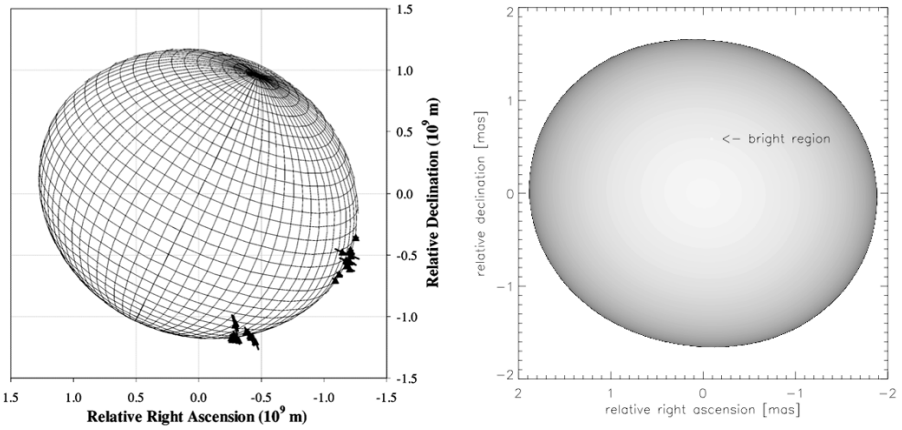

FIG. 4.4 – Modèles de Altaïr obtenus par Van Belle et al. (2001, à gauche) et Ohishi et al. (2004, à droite).

L'aplatissement de Altaïr relativement modéré est convenablement reproduit par les modèles faisant l'hypothèse de Roche, même si nous avons montré dans l'article joint (Sect. 4.2.2) que des différences inexpliquées existent entre les observations en infrarouge et dans le visible. Cette étoile possède une masse relativement faible ($1{,}7\,M_\odot$) et une vitesse équatoriale de rotation limitée à $v \sin i \approx 225\,\mathrm{km/s}$. La faible inclinaison de son axe de rotation sur la ligne de visée (mesurée par interférométrie) indique que cette vitesse projetée est proche de la vitesse réelle.

4.2.2 Article A&A : "Gravitational darkening of Altair from interferometry" (2005)

Cette article présente une synthèse de mesures interférométriques existantes et nouvelles (obtenues avec VINCI en bandes H et K) de l'étoile en rotation rapide Altaïr. Il s'agit de la première étude de ce type confrontant des données obtenues en visible et en infrarouge. Il apparaît quelques différences significatives entre ces deux domaines de longueur d'onde, mais leur explication est encore incertaine. Cette étoile présente un assombrissement gravitationnel dû à l'effet Von Zeipel compatible avec la théorie classique.

FIG. 4.5 – Paysage du Cerro Paranal (Chili).

A&A 442, 567–578 (2005)
DOI: 10.1051/0004-6361:20042476

Astronomy & Astrophysics

Gravitational-darkening of Altair from interferometry

A. Domiciano de Souza[1], P. Kervella[2], S. Jankov[3,4], F. Vakili[3], N. Ohishi[5], T. E. Nordgren[6], and L. Abe[5]

[1] Max-Planck-Institut für Radioastronomie, Auf dem Hügel 69, 53121 Bonn, Germany
e-mail: adomicia@mpifr-bonn.mpg.de
[2] LESIA, UMR 8109, Observatoire de Paris-Meudon, 5 place Jules Janssen, 92195 Meudon Cedex, France
[3] Lab. Univ. d'Astrophysique de Nice (LUAN), UMR 6525, UNSA, Parc Valrose, 06108 Nice Cedex 02, France
[4] Astronomical Observatory Belgrade, MNTRS 1940, Volgina 7, 11050 Beograd, Serbia and Montenegro
[5] National Astronomical Observatory of Japan, 2-21-1 Osawa, Mitaka, Tokyo 181-8588, Japan
[6] Department of Physics, University of Redlands, 1200 East Colton Avenue, Redlands, CA 92373, USA

Received 3 December 2004 / Accepted 13 June 2005

ABSTRACT

Interferometric observations have revealed that the rapid rotator Altair is a flattened star with a non-centrally symmetric intensity distribution. In this work we perform for the first time a physically consistent analysis of all interferometric data available so far, corresponding to three different interferometers operating in several spectral bands. These observations include new data (squared visibilities in the H and K bands from VLTI-VINCI) as well as previously published data (squared visibilities in the K band from PTI and squared visibilities, triple amplitudes, and closure phases in the visible between 520 nm and 850 nm from NPOI). To analyze these data we perform a χ^2 minimization using an interferometry-oriented model for fast rotators, which includes Roche approximation, limb-darkening, and von Zeipel-like gravity-darkening. Thanks to the rich interferometric data set available and to this physical model, the main uniqueness problems were avoided. As a result, we show that the observations can only be explained if Altair has a gravity-darkening compatible with the expected value for hot stars, i.e., the von Zeipel effect ($T_{\rm eff} \propto g^{0.25}$).

Key words. techniques: high angular resolution – techniques: interferometric – methods: data analysis – stars: rotation – stars: individual: Altair

1. Introduction

Altair (α Aql, HR 7557, HD 187642) is a bright ($V = 0.77$), rapidly rotating A7IV-V star, which has been studied by many authors. For example, Buzasi et al. (2005) recently detected several oscillating frequencies in Altair and proved that this star is a variable of the δ Scuti type, as expected by its location within the instability strip. Several basic physical parameters of Altair are summarized by Buzasi et al. (2005) in their introduction. One important characteristic of Altair is its fast rotation. Spectroscopic and interferometric observations indicate a $v_{\rm eq} \sin i$ value between 190 km s^{-1} and 250 km s^{-1} (Abt & Morrell 1995; van Belle et al. 2001; Royer et al. 2002; among others); most recently Reiners & Royer (2004) determined $v_{\rm eq} \sin i = 227 \pm 11$ km s^{-1} from spectroscopy.

Theories foresee that such a high rotation velocity can lead to many modifications in the physical structure of a star like Altair. In particular, the star is expected (1) to be oblate because of a strong centrifugal force and (2) to exhibit gravity-darkening (after the seminal work of von Zeipel 1924). These theoretically expected modifications are now measured by modern observing techniques, notably those based on long baseline interferometry. See, for example, Domiciano de Souza et al. (2003) for the case of another rapidly rotating star (Achernar).

For Altair, van Belle et al. (2001) measured the rotational flattening projected onto the sky-plane using the Palomar Testbed Interferometer (PTI, Colavita et al. 1999). By adopting an equivalent limb-darkened ellipse model these authors derived major and minor axes of $2a = 3.461 \pm 0.038$ mas and $2b = 3.037 \pm 0.069$ mas, respectively, which means an axial ratio of $a/b = 1.140 \pm 0.029$. van Belle et al. (2001) used a Roche model (solid body rotation and mass M concentrated in a point at the center of the star) without gravity-darkening to analyze their observations of Altair. However, even with this relatively simplified model their analysis encountered several uniqueness problems caused by the limited coverage of spatial frequencies (observations inside the first visibility lobe only) and spectral information (only one broadband near-IR filter used). The important issue of uniqueness problems in interferometric studies of rapidly rotating stars is discussed by Domiciano de Souza et al. (2002).

More recently, Ohishi et al. (2004) used the Navy Prototype Optical Interferometer (NPOI, Armstrong et al. 1998) to observe Altair. In particular, they obtained closure phases and

squared visibilities around the first minimum. These observations suggest that Altair is not only oblate but also that it is a gravity-darkened star with a non-centrally symmetric intensity distribution. The nature of these data largely diminishes the uniqueness problems associated with the analysis of rapid rotators.

Even though the observations indicate that Altair is an oblate and gravity-darkened star, previous works did not adopt physically consistent models including these two effects. In the present work we use our interferometry-oriented model for fast rotators (Domiciano de Souza et al. 2002) to perform a χ^2 minimization including all interferometric data available up-to-date: new squared visibilities in the H and K bands from the Very Large Telescope Interferometer (VLTI, e.g., Glindemann et al. 2003); (2) squared visibilities in the K band from PTI; and (3) squared visibilities, triple amplitudes, and closure phases in the visible from NPOI.

In Sect. 2 we summarize the observations used here, and in Sect. 3 we describe the adopted model, which includes Roche approximation, a limb-darkening law compatible with Altair's effective temperature distribution, and a von Zeipel-like gravity-darkening law. In Sect. 4 we present the main results of our χ^2 analysis of the interferometric data. A critical discussion of our results is given in Sect. 5, while the conclusions of this work are summarized in Sect. 6.

2. Interferometric observations

The first attempt to measure the geometrical deformation of Altair was carried out with the Narrabri intensity interferometer (Hanbury Brown 1974). However, these observations remained too marginal to allow unambiguous conclusions to be drawn by the Australian group. Recent observations by at least three modern interferometers have resulted in several high-quality measurements becoming available. In the following section we briefly describe the three interferometric data sets (one new and two previously published and analyzed) used in this work to constrain a number of unknown physical parameters of Altair.

2.1. VLTI-VINCI near-IR observations

We first describe the new near-IR observations of Altair performed with the VLTI. These new data were obtained with two test siderostats (0.35 m aperture) and the VINCI[1] instrument (Kervella et al. 2000 and Kervella et al. 2003a). The visibility measurements were all recorded on the E0-G1 baseline of the VLTI (ground length of 66 m). We combined the stellar light using a classical fiber-based triple coupler (MONA) for the K band observations, and an integrated optics beam combiner (IONIC, Lebouquin et al. 2004) in the H band. Standard K ($2.0 < \lambda < 2.4\,\mu$m) and H ($1.5 < \lambda < 1.8\,\mu$m) band filters were used for these observations. The effective wavelength of the observations changes slightly depending on the spectral type of the observed target. For Altair, we determined $\lambda_{\rm eff} = 2.176 \pm 0.003\,\mu$m and $\lambda_{\rm eff} = 1.633 \pm 0.003\,\mu$m, respectively in the K and H bands.

[1] V(LT) IN(terferometer) C(ommissioning) I(nstrument).

The raw data processing has been achieved using a wavelet-based algorithm, integrated in an automated data reduction pipeline (Kervella et al. 2004a). The general principle is similar to the original FLUOR algorithm (Coudé du Foresto et al. 1997), but instead of the classical Fourier analysis, we implemented a wavelet-based time-frequency analysis (Ségransan et al. 1999). The two calibrated output interferograms are subtracted to correct for residual photometric fluctuations. The output of the pipeline is a single value of the squared coherence factor μ^2 for each series of 500 interferograms and the associated bootstrapped error bar. We obtained a total of 5500 interferograms of Altair in the K band and 4500 in the H band, among which 2749 and 1949 were reduced by the pipeline, respectively. All the VINCI data were obtained between July and September 2002. The final normalized squared visibilities V^2 and other observational information are given in Table 1.

We used three stars as calibrators for the K band observations (24 Cap, χ Phe, and 70 Aql) and one for the H band (α Ind). These stars were selected from Cohen et al. (1999) for their stability, and we took their sizes from the Bordé et al. (2002) catalogue. To obtain their equivalent uniform-disk diameters, we applied the broadband limb-darkening corrections provided by Claret (2000a), based on the ATLAS models (Kurucz 1992). In absence of data in the literature, the metallicity of the calibration stars was taken as solar. Note, however, that in the H and K bands the influence of metallicity on the limb-darkening is very weak. The relevant properties of the calibrators used for VINCI observations are listed in Table 2.

The choice of the calibrators is an important step for preparing interferometric observations, since significant departures of their actual visibilities from the expected model can propagate into biases on the calibrated visibilities of the scientific target. Among the possible reasons for such departures, binarity (or multiplicity in general) and deviations from spherical symmetry (due, for instance, to fast rotation or gravitational interaction) are the most critical. All stars in the Cohen et al. (1999) catalogue were carefully scrutinized by these authors for the presence of companions and are currently regarded as single stars. With respect to fast rotation, the value of $v_{\rm eq} \sin i$ is only available for one star, 70 Aql, which is also the most sensitive star to potential deformations as it is a bright giant. With $v_{\rm eq} \sin i = 1.9\,{\rm km\,s^{-1}}$, $\log g \approx 1.9$, and a radius of $\approx 200\,R_\odot$, a first order approximation of its flattening ratio (Roche model) is given by the following relation (e.g. Domiciano de Souza et al. 2002):

$$\frac{R_{\rm eq}}{R_{\rm p}} = 1 + \frac{v_{\rm eq}^2 R_{\rm eq}}{2GM} < 1 + 10^{-4}. \quad (1)$$

The effect of the rotation on the shape of this star is therefore taken as negligible. Measurements of the projected rotational velocities are not available for the other calibrators of our sample, but as they are giant stars, we assume that they are small enough so that their rotational deformation can be neglected. Our four calibrators are significantly resolved by the interferometer, but the a priori uncertainty on their angular diameters was carefully propagated to the final error bars on the calibrated squared visibilities of Altair. The errors in the calibrated V^2

Table 1. VLTI-VINCI observations of Altair performed in the H and K bands.

H band								
Date (JD)	Projected Baseline (m)	Position Angle[a] (deg)	Calib. V^2	Stat. V^2 error	Syst. V^2 error	Total V^2 error	Uniform disc diameter (mas)	Calibrator
2 452 477.655	62.110	139.77	0.388	±0.022	±0.008	±0.023	3.22 ± 0.09	α Ind
2 452 477.659	61.702	139.97	0.403	±0.023	±0.009	±0.024	3.18 ± 0.10	α Ind
2 452 479.561	65.950	140.66	0.336	±0.023	±0.006	±0.023	3.23 ± 0.09	α Ind
2 452 479.706	55.760	144.48	0.464	±0.027	±0.009	±0.028	3.26 ± 0.12	α Ind
2 452 482.726	52.131	148.77	0.510	±0.052	±0.012	±0.054	3.28 ± 0.24	α Ind
2 452 483.645	61.490	140.08	0.401	±0.024	±0.006	±0.024	3.20 ± 0.10	α Ind
2 452 484.699	54.905	145.37	0.539	±0.042	±0.010	±0.043	2.99 ± 0.18	α Ind
2 452 485.594	64.851	139.08	0.371	±0.032	±0.008	±0.033	3.15 ± 0.13	α Ind
2 452 485.598	64.627	139.07	0.358	±0.032	±0.008	±0.033	3.21 ± 0.13	α Ind
K band								
Date (JD)	Projected Baseline (m)	Position Angle (deg)	Calib. V^2	Stat. V^2 error	Syst. V^2 error	Total V^2 error	Uniform disc diameter (mas)	Calibrator
2 452 469.722	57.285	143.05	0.656	±0.017	±0.016	±0.023	3.18 ± 0.13	24 Cap
2 452 469.755	53.065	147.53	0.685	±0.015	±0.017	±0.023	3.26 ± 0.14	24 Cap
2 452 469.763	51.957	149.02	0.696	±0.017	±0.017	±0.024	3.26 ± 0.15	24 Cap
2 452 531.587	52.790	147.89	0.645	±0.072	±0.007	±0.072	3.52 ± 0.44	χ Phe
2 452 531.592	52.204	148.67	0.632	±0.076	±0.007	±0.076	3.64 ± 0.47	χ Phe
2 452 531.596	51.624	149.49	0.663	±0.076	±0.007	±0.076	3.49 ± 0.48	χ Phe
2 452 536.511	60.454	140.68	0.605	±0.028	±0.008	±0.029	3.28 ± 0.15	70 Aql
2 452 536.543	56.759	143.52	0.636	±0.031	±0.008	±0.032	3.32 ± 0.18	70 Aql
2 452 536.547	56.226	144.03	0.701	±0.033	±0.008	±0.034	2.98 ± 0.20	70 Aql
2 452 536.578	52.212	148.66	0.713	±0.049	±0.009	±0.050	3.14 ± 0.33	70 Aql
2 452 536.582	51.738	149.33	0.643	±0.043	±0.008	±0.043	3.60 ± 0.27	70 Aql

[a] 0° is North and 90° is East.

Table 2. Relevant parameters of the calibrators used for VINCI observations of Altair.

Name	24 Cap	χ Phe	70 Aql	α Ind
HD number	HD 200914	HD 12524	HD 196321	HD 196171
m_V	4.5	5.2	4.9	3.1
m_K	0.5	1.3	1.2	0.9
Sp. type	M0.5III	K5III	K5II	K0III
$T_{\rm eff}$ (K)[a]	3630	3780	3780	4720
$\log g$[a]	1.4	1.9	1.9	2.6
[Fe/H][c]	–	–	–	0.0
$v_{\rm eq} \sin i$ (km s^{-1})[d]	–	–	1.9	–
$\oslash_{\rm LD}$ (mas)[a]	4.43 ± 0.05	2.77 ± 0.03	3.27 ± 0.04	3.28 ± 0.03
$\oslash_{\rm UD}$ (mas)[b]	4.30 ± 0.05	2.69 ± 0.03	3.17 ± 0.04	3.20 ± 0.03

[a] From Cohen et al. (1999).
[b] Limb-darkened disc diameters $\oslash_{\rm LD}$ converted to uniform disc diameters $\oslash_{\rm UD}$ using the linear limb-darkening coefficients from Claret (2000a).
[c] From Cayrel de Strobel et al. (1997, 2001).
[d] From Glebocki et al. (2000).

(statistical, systematic, and total) are also listed in Table 1. The uncertainties in V^2 are dominated by the statistical errors.

2.2. PTI near-IR observations

Another data set used in this paper was obtained with PTI and was previously reported and analyzed by van Belle et al. (2001, hereafter vB2001). This data set corresponds to 27 measurements of V^2 on Altair performed in the K band for two distinct baselines (ground lengths of 85 m and 110 m).

2.3. NPOI visible observations

The third data set used in this work, which was previously reported and analyzed by Ohishi et al. (2004, hereafter ONH2004), corresponds to interferometric observations in the

visible obtained with NPOI. These observations of Altair were recorded simultaneously using three baselines forming a triangle (ground lengths of 30, 37, and 64 m), allowing measurements of V^2, triple amplitudes, and closure phases. In this work we use the NPOI observations of Altair performed on May 25 2001 (see Table 2 of ONH2004), which consist of 7 scans (Hummel et al. 1998). We use 18 spectral channels covering wavelengths from 520 to 850 nm; the data for $\lambda = 633$ nm are not used because they contain light from the metrology laser, and the data for $\lambda = 618$ nm are not used because they are not available for all NPOI observables.

3. Modeling Altair

3.1. Model of a rotating star

Since previous interferometric observations (vB2001 and ONH2004) indicate that Altair's flattening is compatible with uniform rotation, in this paper we adopt the classical Roche model. This model is described in more detail, for example, by Domiciano de Souza et al. (2002), who developed an interferometry-oriented model for rapid rotators. Once the surface equipotential (Ψ) and the corresponding local effective surface gravity ($g(\theta) = |\boldsymbol{\nabla}\Psi|$, where θ is the colatitude) in the Roche approximation are defined, the local effective temperature is given by the following von Zeipel-like gravity-darkening law (e.g. Collins 1965):

$$T_{\rm eff}\,(\theta) = T_{\rm p}\left(\frac{g\,(\theta)}{g_{\rm p}}\right)^{\beta} \qquad (2)$$

where $T_{\rm p}$ and $g_{\rm p}$ are the polar effective temperature and gravity, respectively. In this paper we adopt two theoretical limits for the gravity-darkening coefficient β, namely, $\beta = 0.25$ for hot stars with radiative external layers (von Zeipel 1924) and $\beta = 0.08$ for cold stars with convective external layers (Lucy 1967).

To compute our models of Altair the code BRUCE (Townsend 1997) is used to obtain a stellar grid ($\simeq$25 500 visible points) for the local values of effective temperature and gravity, velocity field, projected surface, and surface normal direction.

3.2. Intensity maps

Because of the geometrical deformation and gravity-darkening, the intensity maps are highly dependent on the inclination of the rotation axis i (Domiciano de Souza et al. 2002). In order to evaluate the intensity maps for Altair we first used Kurucz (1992) model atmospheres[2] as input for the SYNSPEC code (Hubeny 1988 and Hubeny & Lanz 1995) to generate a grid of synthetic specific intensities normal to the surface ($I(\mu = 1, \lambda)$, where μ and λ have their usual meanings). This grid corresponds to different values of $T_{\rm eff}$ and $\log g$ in steps of 250 K and 0.5 dex, respectively. To be consistent with recent spectroscopic observations the grids of $I(\mu = 1, \lambda)$ were calculated for microturbulent velocity $v_{\rm micro} = 2$ km s^{-1} and solar abundance, except for 14 elements between C and Cu (Erspamer & North 2002, 2003).

Since interferometric observations of Altair were performed within wide spectral bands, we integrated $I(1, \lambda)$ over the corresponding spectral channel/band to obtain a grid of integrated intensities normal to the surface $I(1)$. Before performing this integration we multiply $I(1, \lambda)$ by the atmospheric and instrumental transmissions. Because the computation of $I(1)$ influences the calculations of interferometric observables, we present further details of this integration procedure in Sect. 3.3.

Once $I(1)$ is defined, we can obtain the intensity at every μ ($I(\mu)$) through an appropriate limb-darkening law. Accurate modeling of limb-darkening is crucial to determine precise stellar diameters, in particular for rapidly rotating stars where we expect a non-uniform surface brightness distribution. To model Altair we adopted the four-parameter non-linear limb-darkening law proposed by Claret (2000a,b):

$$\frac{I(\mu)}{I(1)} = 1 - a_1(1-\mu^{\frac{1}{2}}) - a_2(1-\mu) - a_3(1-\mu^{\frac{3}{2}}) - a_4(1-\mu^2) \qquad (3)$$

where tabulated values of a_1, a_2, a_3, and a_4 are given by Claret for 12 commonly used photometric bands. For Altair we used those for the H and K bands to simulate PTI and VLTI-VINCI observations and those for the V (for $\lambda \leq 600$ nm) and R (for $\lambda > 600$ nm) bands to simulate NPOI observations.

Claret (2000a,b) argues that Eq. (3) is valid across the whole HR diagram, which is, in fact, an important requirement for a consistent modeling of Altair since this star could present an effective temperature distribution in the transition range between hot (radiative envelope) and cold (convective envelope) stars (e.g., Panzera et al. 1999).

Finally, we can now define the intensity maps $I(\boldsymbol{r})$, i.e., the visible stellar surface brightness distribution on the two-dimensional sky-plane at a position $\boldsymbol{r}$. To obtain $I(\boldsymbol{r})$ we thus perform a linear interpolation of the predefined grids of integrated intensities $I(1)$ and the limb-darkening coefficients a_1, a_2, a_3, and a_4, for each visible point of the stellar grid.

3.3. Complex visibilities

Once the intensity map is defined, the computation of complex visibilities is straightforward. Normalized complex visibilities $V(\boldsymbol{f})$ are obtained by the numerical counterpart of the following equation (for further details see Domiciano de Souza et al. 2002):

$$V(\boldsymbol{f}) = |V(\boldsymbol{f})|\,\mathrm{e}^{\mathrm{i}\phi(\boldsymbol{f})} = \frac{\widetilde{I}(\boldsymbol{f})}{\widetilde{I}(\boldsymbol{0})} \qquad (4)$$

where $|V|$ and ϕ are the visibility amplitude and phase, $\widetilde{I}(\boldsymbol{f})$ is the Fourier transform of the intensity map $I(\boldsymbol{r})$, and $\boldsymbol{f}$ is the spatial frequency coordinate associated with $\boldsymbol{r}$. From Eq. (4) we can directly obtain the interferometric observables: squared visibilities V^2, triple amplitudes $|V_1||V_2||V_3|$, and closure phases $\phi_1 + \phi_2 + \phi_3$. These observables are functions of the spatial frequency $\boldsymbol{f}$, and the indices 1, 2, and 3 denote the three interferometric baselines in a triangular configuration.

For each pair of telescopes, $\boldsymbol{f}$ is given by the ratio between the vector baseline projected onto the sky $\boldsymbol{B}_{\rm proj}$ and the

[2] From Dr. R. L. Kurucz model atmospheres and references publicly available at `http://kurucz.harvard.edu/grids/`

effective wavelength $\lambda_{\rm eff}$ of the considered spectral channel: $\boldsymbol{f} = \boldsymbol{B}_{\rm proj}/\lambda_{\rm eff}$. This dependence of the spatial frequency on $\lambda_{\rm eff}$ is responsible for an observational effect known as *bandwidth smearing* (e.g., Kervella et al. 2003b; and Wittkowski et al. 2004). Indeed, the wide spectral coverage in the H ($\simeq 0.3\,\mu$m) and K ($\simeq 0.4\,\mu$m) bands implies that several spatial frequencies are simultaneously observed by the interferometer (VLTI-VINCI and PTI in our case).

To account for the bandwidth smearing in the near-IR we divided the H and K bands into $N = 20$ spectral sub-channels and computed the stellar intensity distributions I_j integrated over each spectral sub-channel j. The corresponding Fourier transforms $\widetilde{I_j}$ are then calculated, and the final normalized squared visibilities in the H and K bands are given by:

$$V^2_{\rm IR\ band} = \frac{\sum_{j=1}^{N} \left|\widetilde{I_j}(\boldsymbol{B}_{\rm proj}/\lambda_{{\rm eff},j})\right|^2}{\sum_{j=1}^{N} \left|\widetilde{I_j}(\boldsymbol{0})\right|^2}. \quad (5)$$

The bandwidth smearing is negligible for the relatively narrow spectral channels of the NPOI observations.

4. Results from the χ^2 analysis

In this section we perform a χ^2 analysis to constrain a number of unknown physical parameters in our model for Altair from the available interferometric observations.

We investigate two test models corresponding to the theoretical limits for the gravity-darkening parameter β, namely, 0.08 (convective atmospheres) and 0.25 (radiative atmospheres). To obtain a mean effective temperature compatible with previous works (between $\simeq$7500 K and $\simeq$8000 K; see for example Esparmer & North 2003, vB2001; and Ferrero et al. 1995) the adopted polar temperatures $T_{\rm p}$ for the test models are 8000 K and 8500 K, corresponding to $\beta = 0.08$ and 0.25, respectively. The chosen stellar mass $M = 1.8\,M_\odot$ is given by Malagnini & Morossi (1990). Other slightly different mass estimates exist since determining the mass of a single star, particularly a rapid rotator, is not a simple task, but the main results of this work do not critically depend on this value. We adopted the projected equatorial velocity $v_{\rm eq}\sin i = 227\,{\rm km\,s^{-1}}$ determined by Reiners & Royer (2004) from high spectral resolution observations. Their value is compatible with other recent measurements of $v_{\rm eq}\sin i$ within their error bars (e.g. vB2001; and Royer et al. 2002).

In addition to the fixed physical parameters described above, the equatorial radius $R_{\rm eq}$ (or the polar one $R_{\rm p}$) is also needed to calculate the models of Altair. However, $R_{\rm eq}$ is related to the equatorial angular diameter $\oslash_{\rm eq}$ by means of the stellar distance ($d = R_{\rm eq}/\oslash_{\rm eq} = 5.143 \pm 0.025$ pc from Hipparcos; Perryman et al. 1997). Since $\oslash_{\rm eq}$ is one important output from our interferometric data analysis, $R_{\rm eq}$ has to be updated accordingly to each $\oslash_{\rm eq}$ value tested during the χ^2 minimization procedure. To avoid calculating a large number of models we performed a preliminary χ^2 minimization using a fixed $R_{\rm eq}$ in order to constraint the range of $\oslash_{\rm eq}$ close to the minimum χ^2. In the final χ^2 analysis, $\oslash_{\rm eq}$ (and the corresponding $R_{\rm eq}$) varies with steps of 0.01 mas within a range corresponding to the uncertainty in $\oslash_{\rm eq}$. Since this uncertainty is rather small ($\lesssim$2%), $R_{\rm eq}$ could be kept constant without introducing any significant changes in our modeling and results.

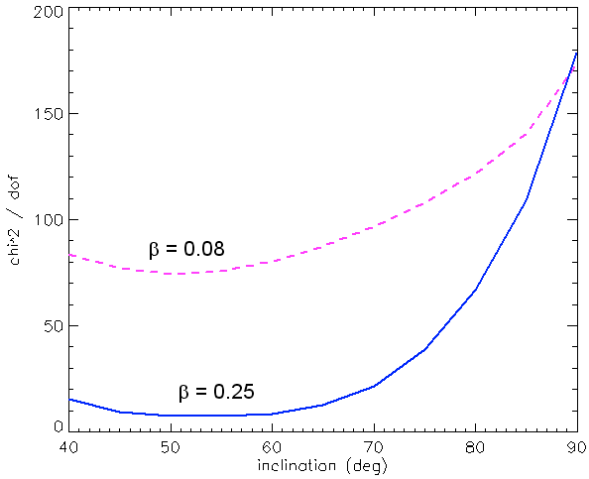

Fig. 1. Reduced χ^2 (χ^2/d.o.f.) as a function of the stellar inclination i computed from all interferometric observations described in Sect. 2 for the two test models (radiative and convective limits for the gravity-darkening). These values correspond to the best equatorial angular diameter $\oslash_{\rm eq}$ and major axis orientation η for a given i. Models with $\beta = 0.25$ (solid curve) are preferred compared to models with $\beta = 0.08$ (dashed curve). The minimum χ^2/d.o.f. ($\chi^2_{\rm min}$/d.o.f. = 7.3) is obtained for $\beta = 0.25$ and $i = 55°$. Further physical parameters for this best model from all data (BMAD) and the corresponding error bars are given in Table 3, together with the results of other χ^2 analyses.

Additionally, the major axis orientation (position angle) on the sky-plane η is allowed to vary in steps of 3°. The inclination of the rotation axis i can vary between 40° and 90° (steps of 5°). For $i < 40°$ the equatorial rotation velocity becomes higher than 90% of the critical limit ($v_{\rm crit}$) leading to unrealistically low equatorial temperatures as a consequence of the von Zeipel effect.

We thus have two test models (corresponding to $\beta = 0.08$ and $\beta = 0.25$) with three free parameters (i, $\oslash_{\rm eq}$, and η) for our χ^2 analysis whose results are presented below.

4.1. Analysis of all data

We present the results of our χ^2 analysis applied to all available interferometric data on Altair (cf. Sect. 2). This consists of 47 near-IR V^2 observations (VLTI-VINCI and PTI) together with 630 visible observations (NPOI). Figure 1 shows the reduced χ^2 (χ^2/d.o.f., where the degree of freedom (d.o.f.) is 674) as a function of the inclination i computed from all interferometric observations for the two test models. The values in Fig. 1 correspond to the best $\oslash_{\rm eq}$ and η for a given i.

An important result seen in Fig. 1 is that all models with a gravity-darkening coefficient for hot stars ($\beta = 0.25$) are preferred, i.e., have lower χ^2 in comparison to models with a gravity-darkening coefficient for cold stars ($\beta = 0.08$). This is model-dependent but still the first direct determination of the gravity-darkening coefficient for a rapid rotator, obtained

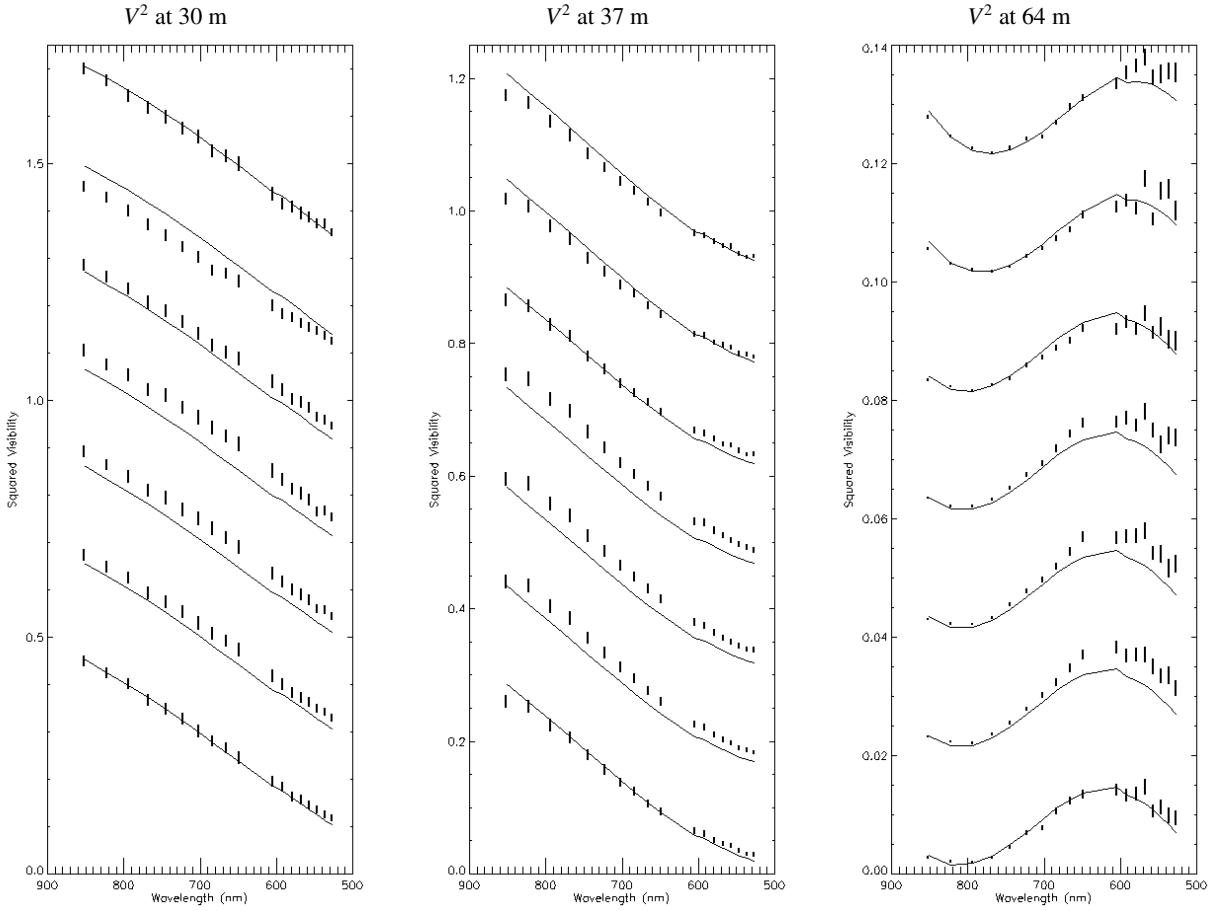

Fig. 2. Squared visibilities V^2 and corresponding errors versus the wavelength for the seven NPOI scans (see Sect. 2). Solid curves correspond to theoretical values obtained from our best model from the χ^2 analysis of all interferometric data (BMAD; see also Fig. 1). Plots for scans 2 to 7 were progressively shifted for better visualization.

thanks to a physically coherent modeling dedicated to stellar interferometry.

The minimum χ^2/d.o.f. is $\chi^2_{\rm min}$/d.o.f. = 7.3 obtained for an inclination $i = 55° \pm 8°$. This best model obtained from the χ^2 analysis of all data is hereafter refereed as BMAD (best model for all data). All free parameters ($\oslash_{\rm eq}$, η, and i) and uncertainties corresponding to the BMAD are given in Table 3 together with some selected dependent parameters. In Table 3 we also list the results from additional χ^2 analyses described in the following sections.

In order to avoid an underestimation of the uncertainties on the free parameters, we computed the limits of the confidence domain by searching for the region between χ^2/d.o.f. and χ^2/d.o.f. + 1. We used the reduced χ^2 and not the total χ^2 as we found it difficult to account for possible correlations between the error bars on each measurement, in particular for the NPOI data. By adopting χ^2/d.o.f., we chose the conservative approach to consider that all measurements are fully correlated with each other, i.e. that their error bars cannot be diminished by averaging in the fitting process. This means that our derived error bars may be overestimated, but this will avoid an over-interpretation of the data.

In Figs. 2 and 3 we compare the five NPOI observables (V^2 for three baselines, triple amplitudes, and closure phases) with the corresponding theoretical values derived from the BMAD. We note in particular that, although the uncertainties in the closure phases are quite small ($\lesssim$0.03 rad), there is a rather good agreement between the observed closure phases and those obtained from the BMAD (solid curves). Clearly, models with $\beta = 0.08$ (plotted as dashed curves for comparison) cannot reproduce these data, leading to χ^2/d.o.f. > 75 in Fig. 1. In Fig. 4 we compare the theoretical squared visibilities V^2 from the BMAD with the observed V^2 and corresponding errors from VLTI-VINCI (H and K bands) and PTI (K band), as described in Sect. 2.

Considering all these distinct interferometers, observables, wavelengths, and baselines (lengths and position angles), Figs. 2 to 4 show a good general agreement between observations and the BMAD, particularly for the closure phases. However, some discrepancies between theoretical and observed V^2 exist, leading to a relatively a high $\chi^2_{\rm min}$/d.o.f.(=7.3). This issue is discussed hereafter.

4.2. Analysis of selected data subsets

The high $\chi^2_{\rm min}$/d.o.f. obtained in the last section from the analysis of all interferometric data is partially due to an underestimation of long-term errors for the NPOI visibility amplitudes.

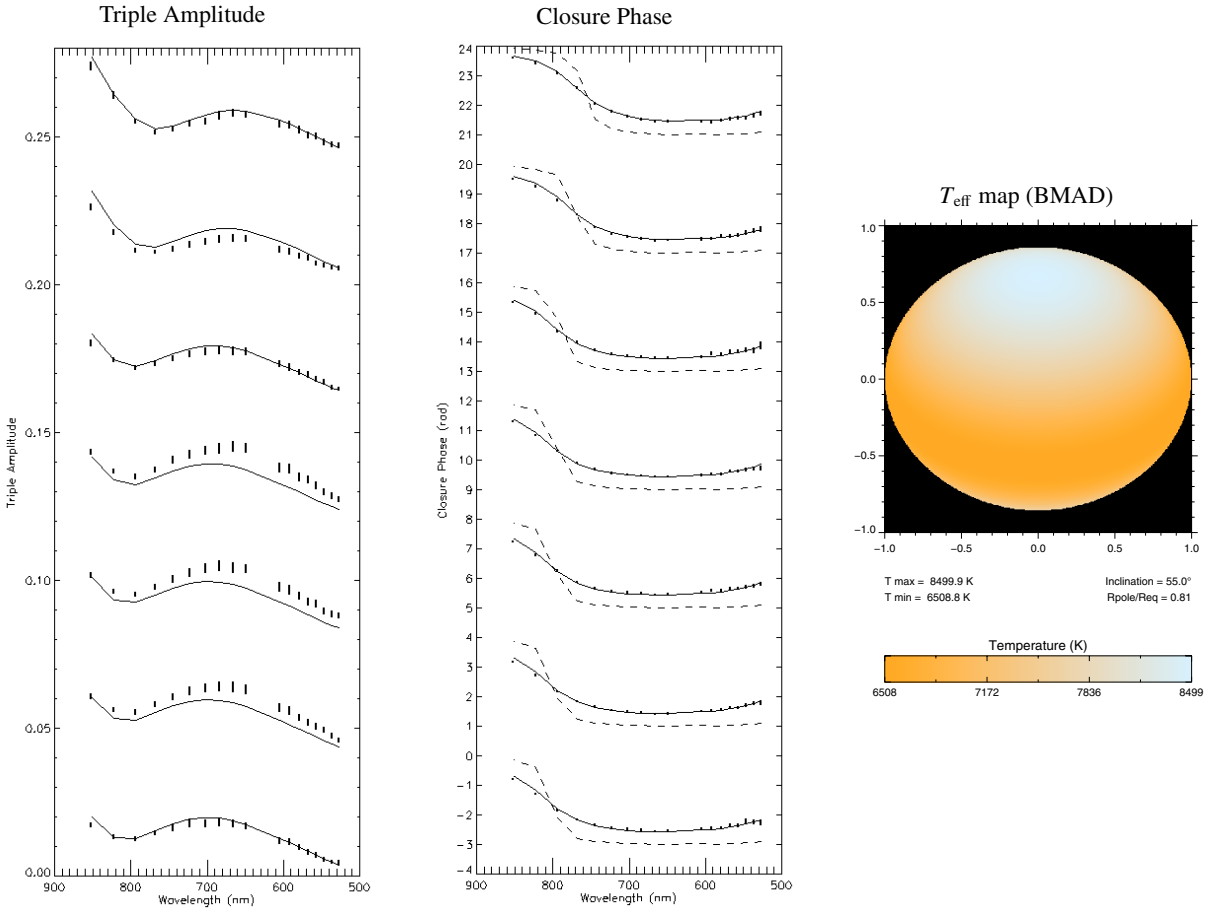

Fig. 3. Triple amplitudes $|V_1||V_2||V_3|$, closure phases $\phi_1 + \phi_2 + \phi_3$, and corresponding errors versus the wavelength for the seven NPOI scans (Sect. 2). Solid curves correspond to theoretical values obtained from our best model from the χ^2 analysis of all interferometric data (BMAD; see also Fig. 1). The closure phase is very sensitive to the stellar intensity distribution. Therefore, a comparison between a strong ($\beta = 0.25$; solid curves) and a weak ($\beta = 0.08$; dashed curves) gravity-darkened model shows that a highly non-uniform surface brightness distribution is mandatory to reproduce the observed closure phases. Note that the closure phases have small error bars ($\lesssim$0.03 rad). Plots for scans 2 to 7 were progressively shifted for better visualization. The picture in the right is the effective temperature map for the BMAD (Table 3).

This calibration problem is clearly present in Figs. 2 and 3 as a scatter of the observed V^2 and triple amplitudes relative to the model. The observations for a given scan are shifted in the same direction for all wavelengths. On the other hand, the closure phase is a more stable interferometric observable, being unaffected by this calibration problem as shown by the excellent agreement between observation and model in Fig. 3.

We have thus performed another χ^2 analysis including only the (7 scans)*(18 wavelengths) closure phases from NPOI, together with the 47 near-IR V^2 from PTI and VINCI. The χ^2/d.o.f. behavior is similar to that seen in Fig. 1, but the minimum reduced χ^2 is now $\gtrsim$2 times smaller than before, namely, $\chi^2_{\rm min}$/d.o.f. = 3.2. In agreement with the analysis of all data presented in the last section, we obtained $\beta = 0.25$ and $i = 55° \pm 14°$. Further physical parameters for this best model determined from the near-IR V^2 and closure phases (BMIRCP) are given in Table 3.

Even though this analysis showed that $\chi^2_{\rm min}$/d.o.f.(=3.2) diminishes when the NPOI V^2 and triple amplitudes are removed, the value obtained indicates that some non negligible discrepancies between model and observations still exist. Such discrepancies come from the fact that the near-IR V^2 for the BMAD and the BMIRCP systematically underestimate the observations from PTI and VINCI, as we can see in Fig. 4.

Because these near-IR V^2 include data from two distinct interferometers using different calibrators, one can hardly invoke some kind of calibration problem, such as those found on the NPOI data. These low theoretical near-IR V^2 seem to be due to the rather large equatorial angular diameter deduced from the χ^2 minimization, namely, $\oslash_{\rm eq} = 3.83 \pm 0.06$ mas for the BMAD and $\oslash_{\rm eq} = 3.88 \pm 0.08$ mas for the BMIRCP (Table 3). To investigate this point we performed two additional χ^2 analyses: one for the (7 scans)*(18 wavelengths) closure phases alone (NPOI data) and another for the 47 near-IR V^2 alone (VLTI-VINCI and PTI data). These results are also summarized in Table 3.

Our analysis result in $\chi^2_{\rm min}$/d.o.f. = 1.4 for the best model for the closure phases alone (BMCP). The χ^2/d.o.f. behavior is once more similar to that seen in Fig. 1, resulting in $\beta = 0.25$ and $i = 50° \pm 12°$. The derived equatorial diameter ($\oslash_{\rm eq} = 3.88 \pm 0.03$ mas) is compatible with those from the two previous analyses (BMAD and BMIRCP).

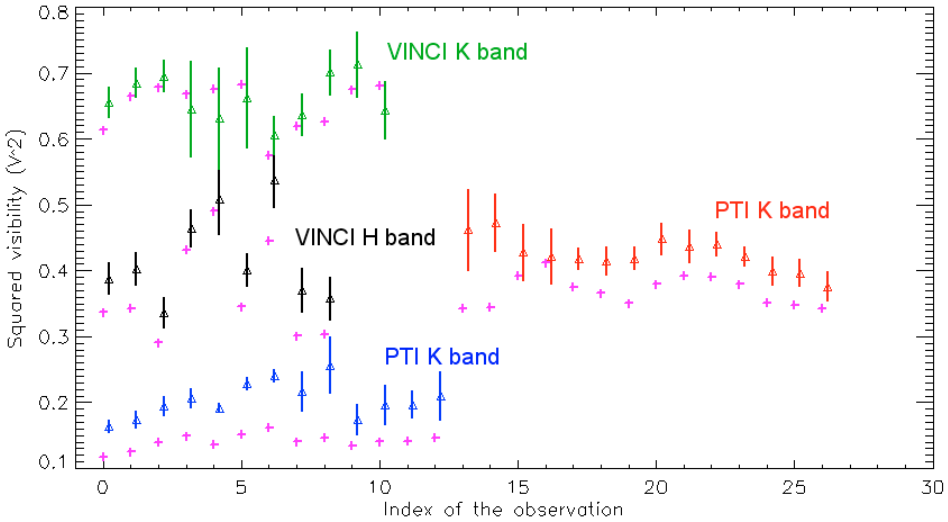

Fig. 4. Squared visibilities V^2 (triangles) and corresponding error bars from VLTI-VINCI (H and K bands) and PTI (K band; baselines 85 m and 110 m) as described in Sect. 2. The abscissa is an index (integer number) to label each group of V^2 data. The crosses correspond to theoretical V^2 obtained from the model with minimum χ^2 (best model; cf. Fig. 1). The abscissas of the V^2 data are slightly shifted to the right compared to those of the theoretical V^2 for better visualization.

Table 3. Input and derived parameters obtained from a χ^2 minimization procedure applied to several data sets: all data (BMAD), near-IR V^2 and closure phases (BMIRCP), closure phases alone (BMCP), and near-IR V^2 alone (BMIR). There is no uncertainty associated to β and T_p because they define two test models based on theoretical limits for the gravity darkening (see text for details). Selected dependent parameters for the best models are also listed.

Fixed input parameters	BMAD	BMIRCP	BMCP	BMIR
$v_{eq} \sin i$ (km s^{-1})	227	227	227	227
M ($M_\odot$)	1.8	1.8	1.8	1.8
i (deg)	–	–	–	50°
(β, T_p (K))	–	–	–	(0.25, 8500)
Results of the χ^2 analyses	**BMAD**	**BMIRCP**	**BMCP**	**BMIR**
χ^2_{min}/d.o.f.	7.3	3.2	1.5	0.50
(β, T_p (K)) [a]	(0.25, 8500)	(0.25, 8500)	(0.25, 8500)	–
i (deg)	55° ± 8°	55° ± 14°	50° ± 12°	–
$2a = \oslash_{eq}$ (mas)	3.83 ± 0.06	3.88 ± 0.08	3.88 ± 0.03	3.44 ± 0.05
R_{eq} [b] ($R_\odot$)	2.117 ± 0.035	2.145 ± 0.045	2.145 ± 0.020	1.902 ± 0.029
η (deg)	92° ± 6°	62° ± 17°	95° ± 23°	113° ± 12°
Dependent parameters	**BMAD**	**BMIRCP**	**BMCP**	**BMIR**
T_{eq} (K)	6509	6483	6171	6453
v_{eq} (km s^{-1})	277	277	296	296
v_{eq}/v_{crit}(%)	76%	76%	80%	77%
f_{rot} (cycles/day)	2.585	2.552	2.729	3.077
$2b = \oslash_p^{max}$ (mas)	3.29	3.33	3.32	2.99
$a/b = \oslash_{eq}/\oslash_p^{max}$	1.164	1.165	1.169	1.149
R_{eq}/R_p	1.237	1.240	1.275	1.243

[a] Theoretical limit preferred compared to (β, T_p (K)) = (0.08, 8000).
[b] From $\oslash_{eq}$ and Hipparcos distance (d = 5.143 ± 0.025 pc).

Before analyzing the near-IR V^2 alone, we should note that since VLTI-VINCI and PTI data correspond to observations in the first visibility lobe far from the first minimum and in a limited range of baseline position angles, this analysis suffers from a significant uniqueness problem (Domiciano de Souza et al. 2002). This means, in particular, that the stellar inclination cannot be derived from these data. Thus, we fixed β = 0.25 and i = 50°, compatibly with the values derived for the BMCP. The obtained χ^2_{min}/d.o.f. is 0.50 for the best model for the near-IR V^2 alone (BMIR). As expected, the derived equatorial diameter is significantly smaller ($\oslash_{eq}$ = 3.44 ± 0.05 mas) than all previous analyses, which included visible data from NPOI.

Figure 5 shows the fit to the closure phase for the BMCP (solid curves in the left panel) and the fit to the near-IR V^2

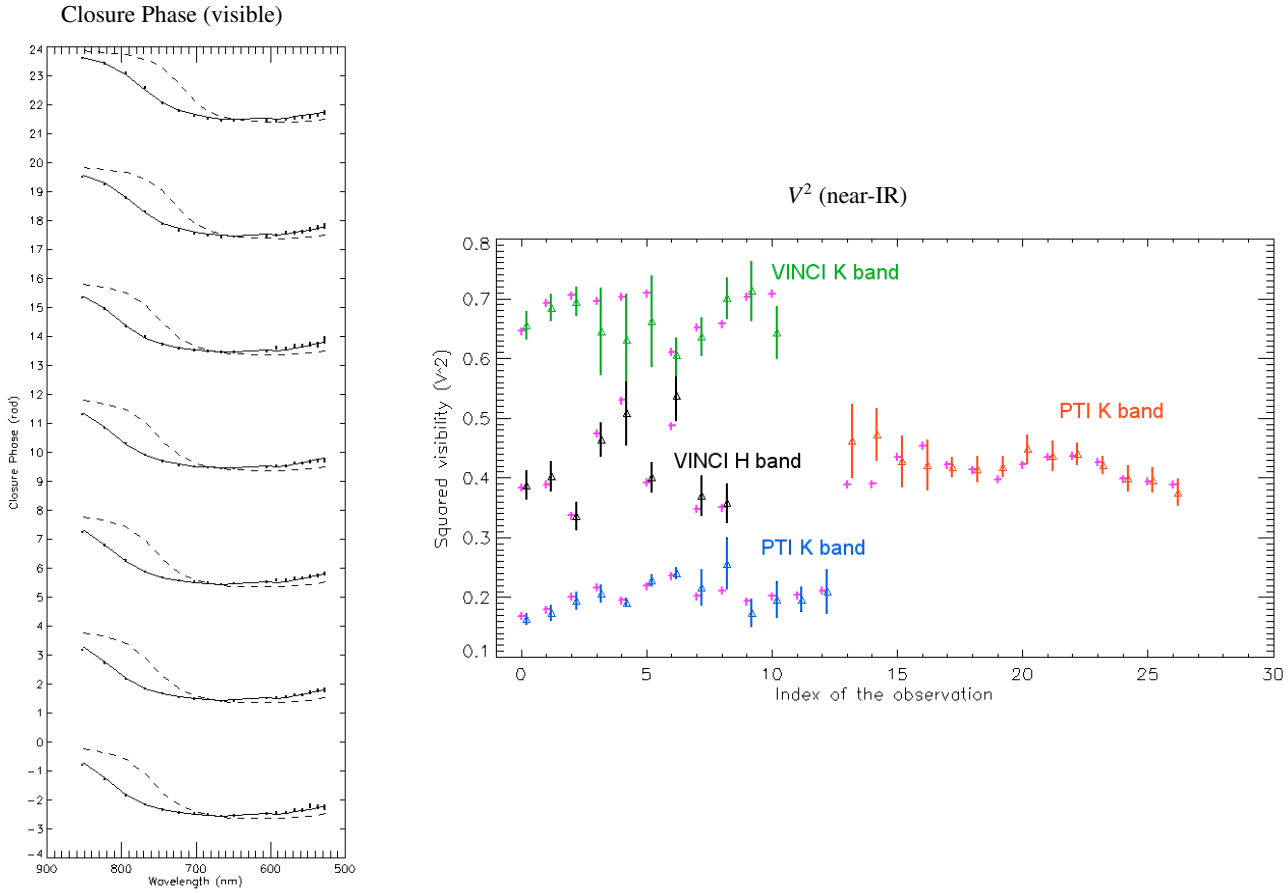

Fig. 5. The left panel shows the closure phases $\phi_1 + \phi_2 + \phi_3$ and corresponding errors versus the wavelength for the seven NPOI scans (Sect. 2). Solid curves correspond to theoretical values obtained from our best model from the χ^2 analysis of closure phases alone (BMCP; see Table 3). Dashed curves correspond to the theoretical closure phases obtained by fixing $i = 50°$, $\oslash_{eq} = 3.44$ mas, and $\eta = 113°$. These parameters were derived from the χ^2 analysis of near-IR V^2 alone (BMIR). The solid curves provide a much better fit to the observed closure phases because they correspond to an angular equatorial diameter larger ($\oslash_{eq} = 3.88$ mas) than the value for the dashed curves ($\oslash_{eq} = 3.44$ mas). On the other hand, a model (BMIR) with $\oslash_{eq} = 3.44$ mas nicely fits the near-IR V^2 as shown in the right panel (see also Fig. 4).

for the BMIR (right panel). Individually, these fits are rather good as one can see in Fig. 5 and also as indicated by the corresponding χ^2_{min}/d.o.f. (1.4 for the BMCP and 0.5 for the BMIR). However, it is clear that the large $\oslash_{eq}$ from the analyses including the closure phases cannot fit the near-IR V^2 (as already shown in Fig. 4).

Conversely, the smaller $\oslash_{eq}$ derived from the near-IR V^2 alone (BMIR) cannot fit the closure phases. This is shown as dashed curves in Fig. 5 (left panel), where we plotted the theoretical closure phases obtained by a model with fixed $i = 50°$, $\beta = 0.25$, $\oslash_{eq} = 3.44$ mas, and $\eta = 113°$ (values from the BMIR). Although this model certainly leads to a high χ^2, we note that models with $\beta = 0.08$ and free i, $\oslash_{eq}$, and η, lead to an even higher χ^2. Thus, the identification of the von Zeipel effect on Altair ($T_{eff} \propto g^{0.25}$), which is the main result of this work, is not affected or hampered by this discrepancy between the angular sizes derived from the visible and near-IR data.

In the following section we investigate this discrepancy and discuss some physical consequences of our results, in particular concerning the von Zeipel effect.

5. Discussion

5.1. The size of Altair

The results described in the last section and summarized in Table 3 reveal a discrepancy between the stellar angular diameters required to fit the visible and near-IR interferometric data. This discrepancy also appears when we compare the results obtained in the visible by ONH2004 (NPOI data) and in the K band by vB2001 (PTI data).

To investigate this issue we estimate the angular size of Altair using an independent method: the average surface brightness. Using the surface brightness relations from Kervella et al. (2004b), we can derive the mean equivalent limb-darkened angular diameter of Altair using only its photometric properties (Table 4). We adopted the apparent magnitudes in the visible and near-IR from Hipparcos (Perryman et al. 1997), Morel & Magnetat (1978), Ducati (2002), and the recent infrared catalogue from Kidger & Martín-Luis (2003). The error bars from the original authors on the apparent magnitudes are given for each band, except for the U, R, and I bands, where

Table 4. Apparent and absolute magnitudes of Altair, using the Hipparcos parallax (π = 194.45 ± 0.94 mas).

	U	B	V	R	I	J	H	K	L
m_λ	1.07	0.99	0.77	0.62	0.48	0.327	0.228	0.205	0.20
$\sigma(m_\lambda)$	0.05	0.01	0.01	0.05	0.05	0.009	0.008	0.005	0.01
M_λ	2.51	2.43	2.21	2.06	1.92	1.77	1.67	1.65	1.64

a conservative 0.05 mag error has been assumed. No interstellar extinction is taken into account for this nearby star ($d \simeq 5$ pc).

We obtain consistent limb-darkened disk angular diameters for all the visible-infrared colors, with, for instance, $\oslash_{\rm LD}(B, B-L) = 3.258 \pm 0.034$ mas. Considering the Hipparcos parallax of $\pi = 194.45 \pm 0.94$ mas (distance $d = 5.143 \pm 0.025$ pc), this translates into a photometric equivalent linear radius of $1.801 \pm 0.021\ R_\odot$. Erspamer & North (2003) obtain an effective temperature of $T_{\rm eff} = 7550$ K, averaged over the disk of Altair. The $\oslash_{\rm LD}(T_{\rm eff}, m_\lambda)$ relations from Kervella et al. (2004b) give the same LD angular diameter using the H, K, and L apparent magnitudes.

Let us compare the photometric-average angular size derived above ($\oslash_{\rm LD}(B, B-L) = 3.258 \pm 0.034$ mas) with an equivalent angular disk diameter leading to the same area of the stellar surface projected onto the sky-plane $\bar{\oslash}$ obtained from our models. For BMIR we obtain $\bar{\oslash} = 3.20$ mas, while for BMAD, BMIRCP, and BMCP we obtain $\bar{\oslash}$ between 3.53 and 3.58 mas. This comparison points towards a smaller size of Altair since there is a better agreement between the sizes estimated by the surface brightness method and by the χ^2 analysis including near-IR V^2 alone, with the latter still being slightly smaller.

From the present data it is not possible to determine whether the discrepancy between the stellar angular diameters in the visible and near-IR has a physical or an instrumental origin. Bias in the wavelength calibration could lead to a larger or smaller size since it affects the spatial frequency. Previous comparisons between stellar angular diameters measured by NPOI and other interferometers show no sign of systematic differences (Nordgren et al. 2001). On the other hand, the large angular size in the visible could also be explained, for example, by an extended emission only seen in the visible. To further investigate the origin of this discrepancy, more precise interferometric observations of Altair are required, preferably in the near-IR at the second visibility lobe and/or with phase closures. These observations should be made in such a way that the quality and the nature of the data in the visible and near-IR are similar and, thus, better comparable. Such observations are expected to be performed with the instrument VLTI-AMBER (e.g., Petrov et al. 2003).

5.2. Rotation and gravity darkening laws

In the present paper we consistently adopted the Roche approximation and a von Zeipel-like gravity-darkening (Eq. (2)). Nevertheless, other more subtle possibilities exist and should be considered in the future when more precise interferometric observations of Altair will be available.

For example, our results indicate that the effective temperature at Altair's equator could be low enough that the star presents convection in its external equatorial regions ($T_{\rm eq} \simeq$ 6500 K for the models with minimum χ^2). Such low $T_{\rm eq}$ requires a gravity-darkening exponent $\beta \simeq 0.08$ (Lucy 1967; Claret 2000c), so that a latitudinal dependent β parameter should be more convenient for Altair (e.g., a continuous variation from the radiative limit $\beta = 0.25$ to the convective limit $\beta = 0.08$ between the poles and the equator). The hypothesis of a convective equatorial region is supported by several works showing that Altair has a chromosphere and a corona, possibly linked to subphotospheric convective zones (e.g., Ferrero et al. 1995).

Other possibilities for a variable parameter β or even for an alternative gravity-darkening law is the presence of differential rotation (e.g., Connon Smith & Worley 1974; Kippenhahn 1977). Although Reiners & Royer (2004) found no signatures of external latitudinal-dependent differential rotation in Altair, we think that one cannot exclude internal differential rotation and/or external differential rotation not detected by the Fourier transform method used by those authors. In fact, the method used by Reiners & Royer (2004) is not very sensitive to differential rotation laws where polar regions rotate faster than layers closer to the equator (anti solar-like or negative differential rotation; e.g., Reiners & Schmitt 2002).

Interestingly enough, Stoekley (1968) found evidence of an anti-solar-like differential rotation in Altair. The presence of negative surface differential rotation is in fact compatible with the hypothesis of a convective equatorial region. For such cool regions, characteristic of F and later type stars, it is possible that some braking mechanism (magnetic effects and/or viscosity due to the onset of convection) could act preferentially close to Altair's equator, slowing these regions relative to those closer to the poles.

This important issue concerning the presence of differential rotation in Altair, and the corresponding gravity-darkening law, should be investigated in the future by additional studies, preferably with distinct and complementary techniques. For example, Domiciano de Souza et al. (2004) proposed a technique to detect both solar-like and anti-solar-like differential rotation by combining high angular resolution with high spectral resolution (differential interferometry). The forthcoming VLTI-AMBER will be able to operate in a differential interferometry mode in the near-IR (e.g., Petrov et al. 2003).

5.3. Inclination and rotation frequency

The results presented in Sect. 4 suggest an intermediate inclination for Altair (see Table 3). These results seem to disagree with the analysis from Reiners & Royer (2004), which points towards higher inclinations ($i > 68^\circ$ on a 1σ level). However, this discrepancy disappears if we consider 2σ confidence

levels in the results from Reiners & Royer (2004), which implies $i > 45°$. Additionally, Stoeckley (1968) derived an inclination angle between 30° and 50° from the analysis of line profiles of Mg II 4481 and Ca II 3934, which is in agreement with our results as well.

It is important that further studies investigate how subtle effects, such as differential rotation and gravity-darkening, influence the interferometric observables and, in particular, the line profiles. It would thus be possible to consistently combine interferometry and spectroscopy in order to determine the stellar inclination more precisely.

Once i, $R_{\rm eq}$, and $v_{\rm eq} \sin i$ are known, the rotation frequency can be determined, in the uniform rotation approximation, by:

$$f_{\rm rot} = \frac{1}{P_{\rm rot}} = \frac{(v_{\rm eq} \sin i)}{2\pi R_{\rm eq}(\sin i)}. \quad (6)$$

The rotation frequencies computed from the equation above and corresponding to our χ^2 analyses are listed in Table 3. Recently, Buzasi et al. (2005) detected several pulsation modes in WIRE (Wide-field InfraRed Explorer) observations, indicating that Altair is a low-amplitude δ Scuti star. The authors suggest that the two low-frequency modes found (f_1 = 2.570 ± 0.020 cycles/day and f_2 = 3.526 ± 0.020 cycles/day) may be associated with the stellar rotation frequency.

The theoretical $f_{\rm rot}$ values listed in Table 3 suggest that the frequency f_1 measured by Buzasi et al. (2005) is a better candidate for $f_{\rm rot}$. However, more precise measurements should be acquired before we can unambiguously identify f_1 = 2.570 ± 0.020 cycles/day as the rotation frequency of Altair.

5.4. On the age of Altair

This work, along with previous ones, has proven that long baseline interferometry is a powerful technique for studying rapidly rotating stars. In particular, this technique can provide important clues to the many unanswered questions concerning the structure and evolution of rapid rotators. For example, placing an intermediate-mass star like Altair in its evolutionary history is an interesting but difficult task requiring as much information as possible.

The age of a star can be derived using different indicators. Lachaume et al. (1999) have used five different methods to study main-sequence stars in the solar neighborhood: isochrones in the HR diagram, rotation, calcium emission lines, kinematics in the Galaxy, and iron abundance. Unfortunately, due to Altair's rapid rotation, its spectral lines are very broad, and this prevents the application of the Ca emission line and kinematic methods. The rotational velocity of a hot, fast rotator is not an accurate indicator of its age, because of the uncertainties on the initial rotational velocity and on the braking mechanisms possibly present.

To estimate the age of Altair, we took advantage of the recent models from Girardi et al. (2002). We read the tables of these authors for the following parameters: [Fe/H] = −0.34, $T_{\rm eff}$ = 7550 K, $\log g$ = 4.13 (Erspamer & North 2003), and Z = 0.008. We adopted the absolute magnitudes presented in Table 4, derived using the parallax from Hipparcos (Perryman et al. 1997): π = 194.45 ± 0.94 mas. The bolometric magnitude was estimated using the corrections provided by Girardi et al. (2002). The best fit of the models with the observed absolute magnitudes of Altair is obtained for an age between 1.2 and 1.4 Gyr.

The relatively old age of Altair suggests that it has kept a high rotation velocity for a long time, well into its lifetime on the main sequence. It does not seem that an efficient braking mechanism is acting to slow down the rotation velocity of this intermediate-mass star. Altair was searched for the presence of a debris disk by Kuchner et al. (1998) in the mid-infrared, without success. The absence of a disk could be one of the factors that prevented an efficient slow down of the star by magnetic coupling or turbulent friction. In any case we believe that further studies should be performed on the evolution of an intermediate-mass and fast rotating star such as Altair.

6. Summary and conclusions

We performed a physically consistent analysis of all available interferometric data on Altair using our interferometry-oriented model for fast rotators. This model includes Roche approximation, limb-darkening from Claret (2000a,b), and a von Zeipel-like gravity-darkening law, as described in Sect. 3 and also by Domiciano de Souza et al. (2002). The rich observational set analyzed here includes new data from VLTI-VINCI (V^2 in the H and K bands), as well as published data from PTI (V^2 in the K band) and NPOI (V^2, triple amplitudes, and closure phases in the visible between 520 nm and 850 nm).

In particular, and as already pointed out by ONH2004, the presence of gravity-darkening in Altair is revealed by the NPOI observations showing (1) a non-zero V^2 in the first minimum and (2) a smooth variation of the closure phase between 0 and π rad. Thanks to our interferometry-oriented model we were able, for the first time, to provide a physical interpretation of all observations from NPOI, PTI, and VLTI-VINCI combined. In particular, we could show that Altair exhibits a gravity-darkening compatible with the theoretically expected value for hot stars (von Zeipel effect): $T_{\rm eff} \propto g^{0.25}$.

Moreover, with the parameters and models considered here we were able to show that the observations of Altair are better reproduced by models with an intermediate inclination (between 40° and 65° including the error bars).

Our analysis also reveals a possible discrepancy between visible and near-IR angular diameters derived from the data that should be further investigated by visible and near-IR observations of high quality, preferably within the second visibility lobe and/or with closure phases.

Further observations should also be performed to investigate the presence of differential rotation on Altair and the corresponding gravity-darkening laws. Precise interferometric observations in the near-IR, allowing us to study differential rotation in particular (Domiciano de Souza et al. 2004), are soon expected for the VLTI spectro-interferometer AMBER (e.g., Petrov et al. 2003).

Acknowledgements. This work has been supported by a postdoctoral fellowship at the Max-Planck-Institut für Radioastronomie

(Infrared Interferometry Group). We acknowledge Drs. G. Weigelt and T. Driebe for their invaluable suggestions that allowed us to improve the quality of this work.

References

Abt, H. A., & Morrell, N. I. 1995, ApJS, 99, 135
Armstrong, J. T., Mozurkewich, D., Rickard, L. J., et al. 1998, ApJ, 496, 550
Bordé, P., Coudé du Foresto, V., Chagnon, G., & Perrin, G. 2002, A&A, 393, 183
Buzasi, D. L., Bruntt, H., Bedding, T. R., et al. 2005, ApJ, 619, 1072
Cayrel de Strobel, G., Soubiran, C., Friel, E. D., Ralite, N., & Francois, P. 1997, A&AS, 124, 299
Cayrel de Strobel G., Soubiran C., & Ralite N. 2001, A&A, 373, 159
Claret, A. 2000a, A&A, 363, 1081
Claret, A. 2000b, VizieR Online Data Catalog, 336, 31081
Claret, A. 2000c, A&A, 359, 289
Cohen, M., Walker, R. G., Carter, B., et al. 1999, AJ, 117, 1864
Colavita, M. M., Wallace, J. K., Hines, B. E., et al. 1999, ApJ, 510, 505
Collins, G. W. 1965, ApJ, 142, 265
Connon Smith, R., & Worley, R. 1974, MNRAS, 167, 199
Coudé du Foresto, V., Ridgway, S., & Mariotti, J.-M. 1997, A&AS, 121, 379
Domiciano de Souza, A., Vakili, F., Jankov, S., Janot-Pacheco, E. & Abe, L. 2002, A&A, 393, 345
Domiciano de Souza, A., Kervella, P., Jankov, S., et al. 2003, A&A, 407, L47
Domiciano de Souza, A., Zorec, J., Jankov, S., et al. 2004, A&A, 418, 781
Ducati, J. R. 2002, NASA Ref. Pub. 1294
Erspamer, D., & North, P. 2002, VizieR Online Data Catalog, 339, 81121
Erspamer, D., & North, P. 2003, A&A, 398, 1121
Ferrero, R. F., Gouttebroze, P., Catalano, S., et al. 1995, ApJ, 439, 1011
Girardi, L., Bertelli, G., Bressan, A., et al. 2002, A&A, 391, 195
Glebocki, R., Gnacinski, P., & Stawikowski, A. 2000, Acta Astron., 50, 509
Glindemann, A., Algomedo, J., Amestica, R., et al. 2003, Proc. SPIE, 4838, 89
Hanbury Brown, R. 1974, in The Intensity Interferometer (London: Taylor & Francis LTD), 151
Hubeny, I. 1988, Comp. Phys. Comm., 52, 103
Hubeny, I., & Lanz, T. 1995, ApJ, 439, 875
Hummel, C. A., Mozurkewich, D., Armstrong, J. T., et al. 1998, AJ, 116, 2536
Kervella, P., Coudé du Foresto, V., Glindemann, A., & Hofmann, R. 2000, SPIE, 4006, 31
Kervella, P., Gitton, Ph., Ségransan, D., et al. 2003a, SPIE, 4838, 858
Kervella, P., Thévenin, F., Morel, P., Bordé, P., & Di Folco, E. 2003b, A&A, 408, 681
Kervella, P., Ségransan, D., & Coudé du Foresto, V. 2004a, A&A, 425, 1171
Kervella, P., Thévenin, F., Di Folco, E., & Ségransan, D. 2004b, A&A, 426, 297
Kidger, M. R., & Martín-Luis, F. 2003, AJ, 125, 3311
Kippenhahn, R. 1977, A&A, 58, 267
Kuchner, M. J., Brown, M. E., & Koresko, C. D. 1998, PASP, 110, 1336
Kurucz, R. L. 1992, The Stellar Populations of Galaxies, IAU Symp. 149, 225
Lachaume, R., Dominik, C., Lanz, T., & Habing, H. J. 1999, A&A, 348, 897
Lebouquin, J. B., Rousselet-Perraut, K., Kern, P., et al. 2004, A&A, 424, 719
Lucy, L. B. 1967, Z. Astrophys., 65, 89
Malagnini, M. L., & Morossi, C. 1990, A&AS, 85, 1015
Morel, M., & Magnetat, P. 1978, A&AS, 34, 477
Nordgren, T. E., Sudol, J. J., & Mozurkewich, D. 2001, AJ, 122, 2707
Ohishi, N., Nordgren, T. E., & Hutter, D. J. 2004, ApJ, 612, 463
Panzera, M. R., Tagliaferri, G., Pasinetti, L., & Antonello, E. 1999, A&A, 348, 161
Perryman, M. A. C., Lindegren, L., Kovalevsky, J., et al., The Hipparcos Catalogue, 1997, A&A, 323, 49
Petrov, R. G., & Amber Consortium, The 2003, EAS Publications Series, Observing with the VLTI, ed. G. Perrin and F. Malbet, 6, 111
Reiners, A., & Schmitt, J. H. M. M. 2002, A&A, 384, 155
Reiners, A., & Royer, F. 2004, A&A, 428, 199
Royer, F., Grenier, S., Baylac, M.-O., Gómez, A. E., & Zorec, J. 2002, A&A, 393, 897
Ségransan, D., Forveille, T., Millan-Gabet, C. P. R., & Traub, W. A. 1999, in ASP Conf. Ser. 194, 290
Stoeckley, T. R. 1968, MNRAS, 140, 121
Townsend, R. H. D. 1997, MNRAS, 284, 839
van Belle, G. T., Ciardi, D. R., Thompson, R. R., Akeson, R. L., & Lada, E. A. 2001, ApJ, 559, 1155
von Zeipel, H. 1924, MNRAS, 84, 665
Wittkowski, M., Aufdenberg, J. P., & Kervella, P. 2004, A&A, 413, 711

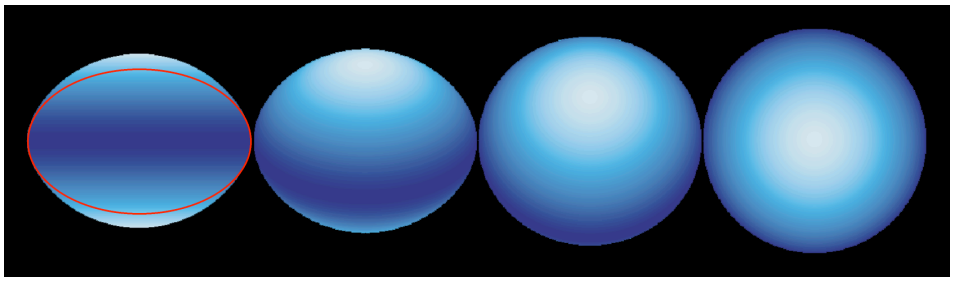

FIG. 4.6 – Modèle numérique d'Achernar obtenu par Domiciano et al. (2003) sur la base de l'hypothèse de Roche : vitesse de rotation uniforme et masse concentrée au centre de l'étoile. Le modèle est visualisé de gauche à droite pour des inclinaisons de 0 (plan équatorial), 30, 60 et 90 degrés (vue polaire). L'aplatissement minimum mesuré à l'aide du VLTI est représenté par l'ellipse superposée à la vue équatoriale (illustration de gauche).

4.3 Achernar (α Eri)

4.3.1 Observations avec le VLTI

Nous avons observé l'étoile Achernar (α Eri, HD 10144) en 2002-2003 à l'aide de l'instrument VINCI du VLTI. Le détail de ces observations est présenté dans la Lettre (Domiciano et al. 2003) et l'Article (Kervella & Domiciano 2006) que nous avons publiés dans A&A, et qui sont reproduits Sect. 4.3.3 et 4.3.4, respectivement.

Achernar est l'étoile la plus brillante ($m_V = 0,50$) et la plus proche représentante de la classe des étoiles *Be*, avec une distance de seulement $d = 44$ pc (Perryman et al. 1997). Ces étoiles de types spectraux *B* présentent des épisodes durant lesquels la raie H_α apparaît en émission dans leur spectre. Dans le but de mesurer la déformation rotationnelle de cette étoile, nous avons tiré partie de l'effet de supersynthèse dû à la rotation terrestre pour mesurer sa taille angulaire selon une large gamme d'azimuths (Fig 2 de la Lettre reproduite à la Sect. 4.3.3).

L'analyse des observations supplémentaires obtenues avec les grands télescopes de 8 m du VLTI nous a par ailleurs permis de mettre en évidence la présence d'une enveloppe circumstellaire allongée selon la direction des pôles de l'étoile (Sect. 4.3.4).

4.3.2 La nécessité de la rotation différentielle

Achernar est une étoile beaucoup plus massive ($6\,M_\odot$) et grosse ($12\,R_\odot$ à l'équateur) qu'Altaïr. Ceci conduit à une densité moyenne très faible d'environ $10\,\mathrm{kg/m^3}$, soit moins de 1% de celle du Soleil ! Il est donc attendu que son aplatissement rotationnel soit important. Cependant, l'aplatissement observé est tel qu'il est impossible à expliquer dans le cadre d'une rotation uniforme(Fig. 4.6).

Il apparaît donc indispensable d'introduire dans la modélisation la rotation différentielle. Mais comme nous n'avons pas d'information directe sur le profil de la vitesse de rotation interne par l'observation de la surface de l'étoile, il est très difficile de définir le type de loi à utiliser. En considérant des hypothèses simples sur la loi de rotation interne différentielle, Jackson et al. (2004) ont construit des modèles d'Achernar en utilisant comme contraintes le profil interférométrique obtenu avec le VLTI (Fig. 4.7). Leurs modèles sont basés sur l'hypothèse que l'étoile est en équilibre hydrostatique entre la gravitation et la force centrifuge. Du fait de la rotation ultra-rapide du cœur de l'étoile, les aplatissements obtenus peuvent être extrêmes sans que l'étoile n'atteigne la vitesse critique et ne se disloque. Les formes obtenues permettent de

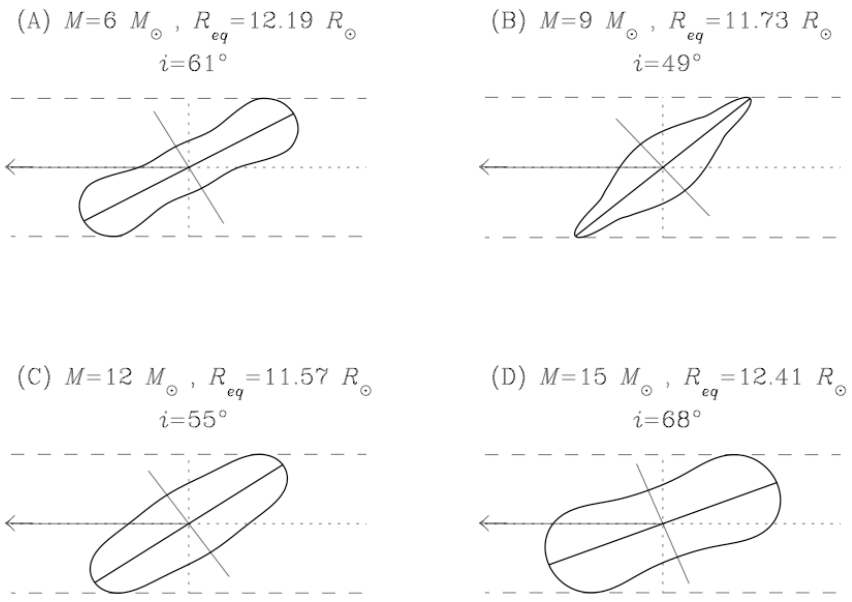

FIG. 4.7 – Quelques modèles numériques d'Achernar obtenus par Jackson et al. (2004) sur la base d'un profil de vitesse de rotation interne non uniforme. L'observateur est situé à gauche de l'illustration. Tous ces modèles sont compatibles avec les résultats interférométriques du VLTI, mais posent des problèmes pour l'interprétation du spectre de l'étoile.

reproduire l'aplatissement record de $\Gamma = 56\%$ observé par le VLTI, mais ne reproduisent pas les profils des raies spectrales de l'étoile.

En mesurant précisément la forme de la photosphère de l'étoile, ainsi que la répartition de lumière à sa surface, il est possible de contraindre les modèles de manière suffisamment forte pour en déduire la loi de rotation interne. Pour conclure sur la forme tridimensionnelle réelle d'Achernar, et donc sa loi de rotation interne, il est donc nécessaire d'obtenir la carte précise de la répartition de lumière sur l'étoile. Les observations actuelles à deux télescopes n'ont permis de reconstituer que le profil de l'étoile, mais Achernar sera bientôt une cible privilégiée pour le nouvel instrument AMBER du VLTI. Combinant la lumière de trois télescopes simultanément, il permettra de mesurer directement l'effet Von Zeipel sur cette étoile, une clé pour explorer la structure interne de cette étoile hors du commun.

4.3.3 Lettre A&A : "The spinning-top Be star Achernar from VLTI-VINCI" (2003)

Nos observations de l'étoile Be Achernar (α Eri) avec VINCI ont mis en évidence un aplatissement considérable de son disque apparent, au-delà de ce que prévoient les modèles de rotation basés sur l'hypothèse de corps solide. Ceci nous amène à conclure à la présence probable de rotation différentielle à l'intérieur de cette étoile. Nous examinons également la possibilité de présence d'un disque circumstellaire lors de nos observations, avec pour conclusion que celle-ci est improbable du fait de l'absence d'émission dans la raie Hα.

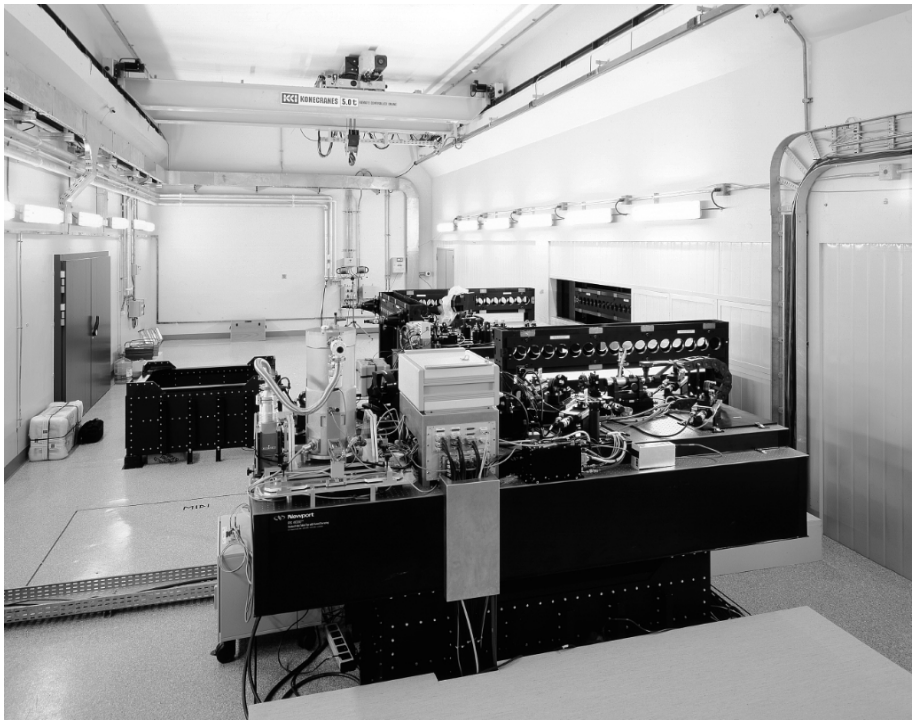

FIG. 4.8 – Le laboratoire interférométrique du VLTI début 2001, avec l'instrument VINCI au premier plan.

A&A 407, L47–L50 (2003)
DOI: 10.1051/0004-6361:20030786

Astronomy & Astrophysics

The spinning-top Be star Achernar from VLTI-VINCI

A. Domiciano de Souza[1], P. Kervella[2], S. Jankov[3], L. Abe[1], F. Vakili[1,3], E. di Folco[4], and F. Paresce[4]

[1] Laboratoire Univ. d'Astroph. de Nice (LUAN), CNRS UMR 6525, Parc Valrose, 06108 Nice Cedex 02, France
[2] European Southern Observatory (ESO), Alonso de Cordova 3107, Casilla 19001, Vitacura, Santiago 19, Chile
[3] Observatoire de la Côte d'Azur, Département FRESNEL, CNRS UMR 6528, Boulevard de l'Observatoire, BP 4229, 06304 Nice, France
[4] European Southern Observatory (ESO), Karl-Schwarzschild str. 2, 85748 Garching, Germany

Received 5 May 2003 / Accepted 22 May 2003

Abstract. We report here the first observations of a rapidly rotating Be star, α Eridani, using Earth-rotation synthesis on the Very Large Telescope (VLT) Interferometer. Our measures correspond to a $2a/2b = 1.56 \pm 0.05$ apparent oblate star, $2a$ and $2b$ being the equivalent uniform disc angular diameters in the equatorial and polar direction. Considering the presence of a circumstellar envelope (CSE) we argue that our measurement corresponds to a truly distorted star since α Eridani exhibited negligible Hα emission during the interferometric observations. In this framework we conclude that the commonly adopted Roche approximation (uniform rotation and centrally condensed mass) should not apply to α Eridani. This result opens new perspectives to basic astrophysical problems, such as rotationally enhanced mass loss and internal angular momentum distribution. In addition to its intimate relation with magnetism and pulsation, rapid rotation thus provides a key to the Be phenomenon: one of the outstanding non-resolved problems in stellar physics.

Key words. techniques: high angular resolution – techniques: interferometric – stars: rotation – stars: emission-line, Be – stars: individual: Achernar

1. Introduction

The southern star Achernar (α Eridani, HD 10144, spectral type B3Vpe) is the brightest Be star in the sky. A Be star is defined as a non-supergiant B type star that has presented episodic Balmer lines in emission (Jaschek et al. 1981), whose origin is attributed to a CSE ejected by the star itself. Physical mechanisms like non-radial pulsations, magnetic activity, or binarity are invoked to explain the CSE formation of Be stars in conjunction with their fundamental property of rapid rotation. Theoretically, rotation has several consequences on the star structure (Cassinelli 1987). The most obvious is the geometrical deformation that results in a larger radius at the equator than at the poles. Another well established effect, known as gravity darkening or the von Zeipel effect for hot stars (von Zeipel 1924), is that both surface gravity and emitted flux decrease from the poles to the equator. Although well studied in the literature, the effects of rotation have rarely been tested against accurate enough observations (Reiners & Schmitt 2003; van Belle et al. 2001), a gap bridged by our interferometric observations of Achernar.

Send offprint requests to: A. Domiciano de Souza,
e-mail: Armando.Domiciano@obs-azur.fr

2. Observations and data processing

Dedicated observations of Achernar have been carried out during the ESO period 70, from 11 September to 12 November 2002, with quasi-uniform time coverage, on the VLT Interferometer (VLTI, Glindemann et al. 2003) equipped with the VINCI beam combiner (Kervella et al. 2003a). This instrument recombines the light from two telescopes in the astronomical K band, which is centered at 2.2 μm and covers 0.4 μm. The observable measured by VINCI is the squared coherence factor μ^2 of the star light. It is derived from the raw interferograms after photometric calibration using a wavelet based method (Ségransan et al. 1999). The reduction procedure is detailed by Kervella et al. (2003b) and has successfully been applied to dwarf stars observations with the VLTI (Ségransan et al. 2003). The instrumental value of μ^2 is then calibrated through the observation of stable stars with known angular diameters. The calibrators chosen for Achernar are presented in Table 1. The final product of the processing is the squared visibility V^2 of the object for each baseline projected on the sky ($B_{\rm proj}$). V^2 is directly related to the Fourier transform of the brightness distribution of the object via the Zernike-Van Cittert theorem. For these observations, two interferometric baselines were used, 66 m (E0-G1; azimuth 147°, counted from North to East) and 140 m (B3-M0; 58°), equipped with 40 cm siderostats (Fig. 1 left). Their orientations are almost perpendicular to each other giving an excellent configuration for the

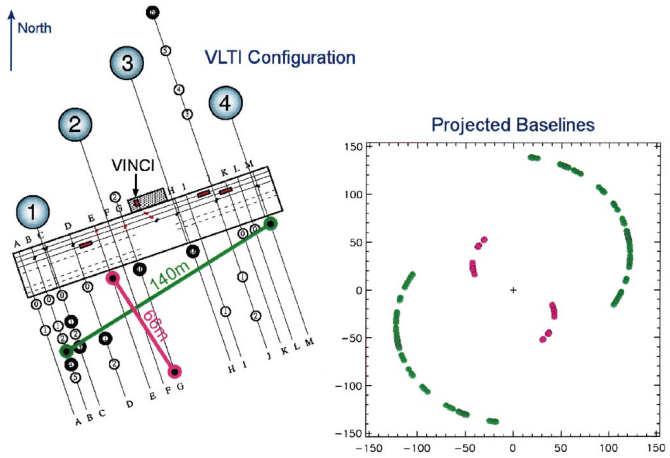

Fig. 1. VLTI ground baselines for Achernar observations and their corresponding projections onto the sky at different observing times. *Left*: Aerial view of VLTI ground baselines for the two pairs of 40 cm siderostats used for Achernar observations. Color magenta represents the 66 m (E0-G1; azimuth 147°, counted from North to East) and green the 140 m (B3-M0; 58°). *Right*: Corresponding baseline projections onto the sky ($B_{\rm proj}$) as seen from the star. Note the very efficient Earth-rotation synthesis resulting in a nearly complete coverage in azimuth angles.

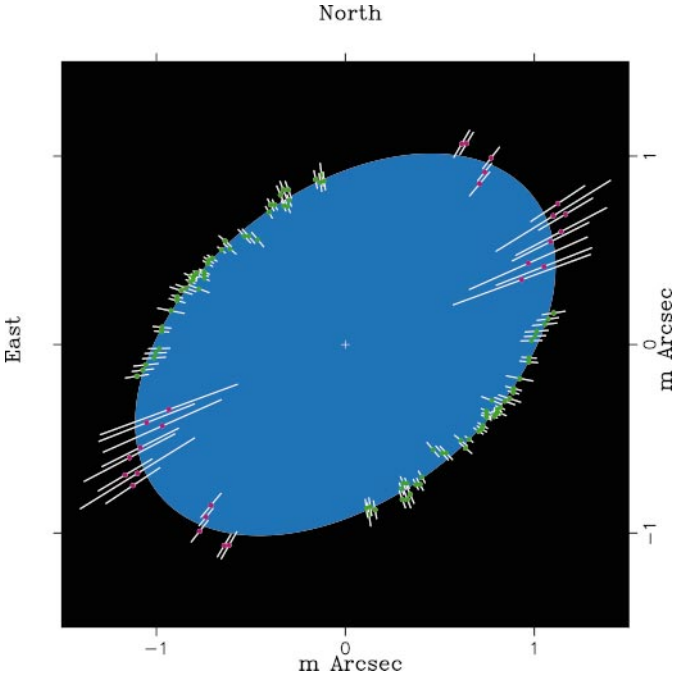

Fig. 2. Fit of an ellipse over the observed squared visibilities V^2 translated to equivalent uniform disc angular diameters. Each V^2 is plotted together with its symmetrical value in azimuth. Magenta points are for the 66 m baseline and green points are for the 140 m baseline. The fitted ellipse results in major axis $2a = 2.53 \pm 0.06$ milliarcsec, minor axis $2b = 1.62 \pm 0.01$ milliarcsec, and minor axis orientation $\alpha_0 = 39° \pm 1°$ (from North to East). The points distribution reveals an extremely oblate shape with a ratio $2a/2b = 1.56 \pm 0.05$.

detection of stellar asymmetries. Moreover, Earth-rotation has produced an efficient baseline synthesis effect (Fig. 1, right). A total of more than 20 000 interferograms were recorded on Achernar, and approximately as many on its calibrators, corresponding to more than 20 hours of integration. From these data, we obtained 60 individual V^2 estimates, at an effective wavelength of $\lambda_{\rm eff} = 2.175 \pm 0.003\,\mu$m.

3. Results

The determination of the shape of Achernar from our set of V^2 is not a straightforward task so that some prior assumptions need to be made in order to construct an initial solution for our observations. A convenient first approximation is to derive from each V^2 an equivalent uniform disc (UD) angular diameter $\oslash_{\rm UD}$ from the relation $V^2 = |2J_1(z)/z|^2$. Here, $z = \pi \oslash_{\rm UD}(\alpha) B_{\rm proj}(\alpha) \lambda_{\rm eff}^{-1}$, J_1 is the Bessel function of the first kind and of first order, and α is the azimuth angle of $B_{\rm proj}$ at different observing times due to Earth-rotation. The application of this simple procedure reveals the extremely oblate shape of Achernar from the distribution of $\oslash_{\rm UD}(\alpha)$ on an ellipse (Fig. 2). Since α, $B_{\rm proj}(\alpha)$, and $\lambda_{\rm eff}$ are known much better than 1%, the measured errors in V^2 are associated only to the uncertainties in $\oslash_{\rm UD}$. We performed a non-linear regression fit using the equation of an ellipse in polar coordinates. Although this equation can be linearized in Cartesian coordinates, such a procedure was preferred to preserve the original, and supposedly Gaussian, residuals distribution as well as to correctly determine the parameters and their expected errors. We find a major axis $2a = 2.53 \pm 0.06$ milliarcsec (mas), a minor axis $2b = 1.62 \pm 0.01$ mas, and a minor-axis orientation $\alpha_0 = 39° \pm 1°$. Note that the corresponding ratio $2a/2b = 1.56 \pm 0.05$ determines the equivalent star oblateness only in a first-order UD approximation. To interpret our data in terms of physical parameters of Achernar, a consistent scenario must be tailored from its basic known properties, so that we can safely establish the conditions where a coherent model can be built and discussed.

4. Discussion

Achernar's pronounced apparent asymmetry obtained in this first approximation, together with the fact that it is a Be star, raises the question of whether we observe the stellar photosphere with or without an additional contribution from a CSE.

For example, a flattened envelope in the equatorial plane would increase the apparent oblateness of the star if it were to introduce a significant infrared (IR) excess with respect to the photospheric continuum. Theoretical models (Poeckert & Marlborough 1978) predict a rather low CSE contribution in the K band especially for a star tilted at higher inclinations, which should be our case as discussed below. Indeed, Yudin (2001) reported a near IR excess (difference between observed and standard color indices in visible and L band centered at 3.6 μm) to be $E(V-L) = 0\overset{\rm m}{.}2$, with the same level of uncertainty. Moreover, this author reports a zero intrinsic polarization (p_*). These values are significantly smaller than mean values for Be stars earlier than B3 ($\overline{E}(V-L) > 0\overset{\rm m}{.}5$ and $\overline{p_*} > 0.6\%$), meaning that the Achernar's CSE is weaker than in other known Be stars. Further, an intermediate

Table 1. Relevant parameters of the calibrators of Achernar. $\oslash_{UD}$ is the equivalent uniform disc angular diameter. The value of $\oslash_{UD}$ for δ Phe and χ Phe is based on spectrophotometry (Cohen et al. 1999), while that for α PsA was measured separately with the VLTI and should appear in a forthcoming publication from one of us (E.F.).

Name	Spec. type	λ_{eff} (μm)	Baseline (m)	$\oslash_{UD}$ (mas)
δ Phe	K0IIIb	2.181	140	2.18 ± 0.02
α PsA	A3V	2.177	140	2.20 ± 0.07
χ Phe	K5III	2.182	66	2.69 ± 0.03

angular diameter of our elliptical fit (Fig. 2) is compatible with the $\oslash_{UD} = 1.85 \pm 0.07$ mas measured by Hanbury-Brown (1974) in the visible, in contrast to what is expected if the envelope were to contribute to our present IR observations. Finally, Chauville et al. (2001) report no emission in the Hγ line. Since the emission in Hγ and in the continuum are both formed roughly in the same layer of the CSE (Ballereau et al. 1995), the contribution from the nearby environment of the star should be considered below the limit of detection.

Of course, being classified as a Be star, Achernar can enhance the strength of its CSE due to episodic mass ejections, which are generally witnessed by increased Balmer line emission (e.g. de Freitas Pacheco 1982). This possibility was checked against a Hα spectrum (Leister & Janot-Pacheco 2003) taken in October 2002, during our VLTI-VINCI campaign presenting a photospheric absorption profile. To be sure that we observed a quiescent Achernar we synthesized a Hα profile from our model (Domiciano de Souza et al. 2002) compared to the observed line. We estimated the emission to be at most 3% across the whole line. Such an upper limit would correspond to a CSE emitting at most 12% of the photospheric continuum flux, due to free-free and free-bound emission (Poeckert & Marlborough 1978).

Thus, we assume hereafter that the observed asymmetry of Achernar mainly reflects its true photospheric distortion with a negligible CSE contribution. Under this assumption, and using the Hipparcos distance ($d = 44.1 \pm 1.1$ pc; Perryman et al. 1997), we derive an equatorial radius $R_{eq} = 12.0 \pm 0.4\ R_\odot$ and a maximum polar radius $R_{pol}^{max} = 7.7 \pm 0.2\ R_\odot$, respectively from $2a$ and $2b$ obtained from the elliptical fit on $\oslash_{UD}(\alpha)$. From simple geometrical considerations the actual polar radius R_{pol} will be smaller than R_{pol}^{max} for polar inclinations $i < 90°$, while R_{eq} is independent of i.

Based on these conclusions we applied our interferometry-oriented code (Domiciano de Souza et al. 2002) to Achernar. This code includes radiation transfer, the von Zeipel law ($T_{eff} \propto g_{eff}^{0.25}$, T_{eff} and g_{eff} being the effective temperature and gravity, respectively), and the Roche approximation (e.g. Roche 1837; Kopal 1987). In this approximation and noting that the stellar rotation must be kept smaller than its critical value, the adopted projected equatorial velocity $V_{eq} \sin i = 225$ km s^{-1} (Slettebak 1982) implies that $i > 46°$. At this limit T_{eff} and g_{eff} both attain zero at the equator, and the surface equipotential first derivatives become discontinuous. Therefore we chose to explore a parameter space between the representative limit

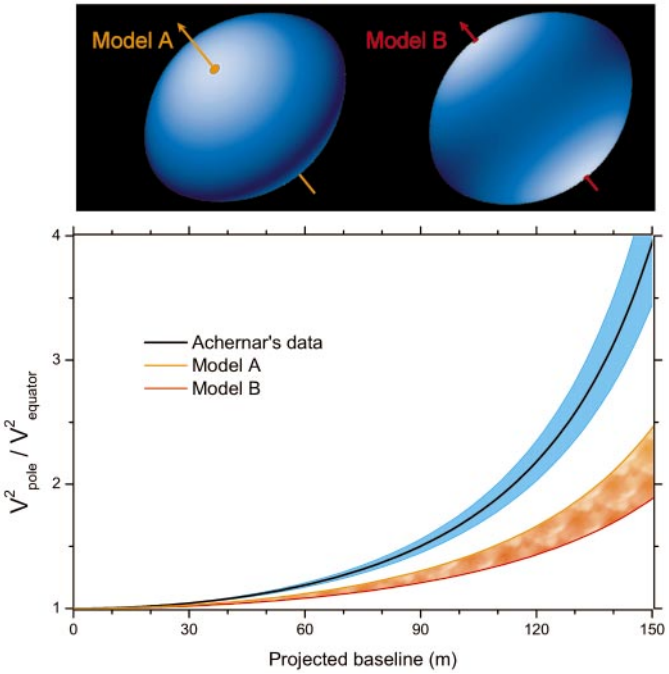

Fig. 3. Comparison of ratios of squared visibility curves between the polar and equatorial directions V^2_{pol}/V^2_{eq}. The black solid curve corresponds to V^2_{pol}/V^2_{eq} for the elliptical fit on Achernar's data, together with the corresponding uncertainties. Simply speaking V^2_{pol}/V^2_{eq} somehow reflects R_{eq}/R_{pol}^{max}, since interferometry is sensitive to the Fourier transform of the stellar brightness distribution. The colored region represents our attempt attain the black curve with our model for Achernar within the physically reasonable solutions A (orange; upper limit) and B (red; lower limit). This failure to reproduce the observations is a strong and direct indication that uniform rotation does not apply to rapidly rotating stars.

solution models A ($i = 50°$) and B ($i = 90°$). Table 2 summarizes the corresponding sets of fundamental parameters. Figure 3 clearly shows that the solutions enclosed between the models A and B cannot reproduce the observed highly oblate ellipse. We also checked, with negative result, whether the situation would improve significantly by varying the fundamental parameters of Achernar in a physically reasonable range (mass $\pm 1\ M_\odot$, $T_{pol} \pm 2000$ K, $V_{eq} \sin i \pm 25$ km s^{-1}).

Thus, in absence of Hα emission making a CSE contribution unlikely to reproduce the observed oblateness, the classical assumption of Roche approximation becomes questionable. Deviations from this gravitational potential and the presence of differential rotation, both intimately related to the internal angular momentum distribution, should be investigated. Indeed, several differential rotation theories predict surface deformations stronger than that of uniform rotation by considering that the angular velocity increases towards the stellar center. Two interesting examples are "shellular" rotation (Zahn 1992) and laws with angular momentum constant on cylinders (Bodenheimer 1971). In this context our result on Achernar's surface distortion should also impact other internal mechanisms like meridional circulation, turbulence, transport and diffusion of the chemical elements and angular momentum,

Table 2. Fundamental parameters for two limit solution models of Achernar. From the fixed parameters and in the Roche approximation, the minimum polar inclination is $i_{\rm min} = 46°$ where $V_{\rm eq} = V_{\rm crit} = 311$ km s^{-1} and $R_{\rm eq} = 1.5\ R_{\rm pol}$. In addition to these parameters we adopted a linear limb darkening coefficient from Claret (2000) compatible with the variable effective temperature and gravity over the stellar surface. The equatorial effective temperature is much lower than the polar one due to the von Zeipel effect.

Fixed parameters	Adopted value	Comments
$T_{\rm pol}$	20 000 K	~B3V star
Mass	6.07 $M_\odot$	Harmanec (1988)
$V_{\rm eq} \sin i$	225 km s^{-1}	Slettebak (1982)
$R_{\rm eq}$	12.0 $R_\odot$	this work
Model dependent parameters	Values for Model A	Values for Model B
$T_{\rm eq}$	9500 K	14 800 K
i	50°	90°
$V_{\rm crit}$	304 km s^{-1}	285 km s^{-1}
$V_{\rm eq}$	$0.96 V_{\rm crit}$	$0.79 V_{\rm crit}$
$R_{\rm pol}$	8.3 $R_\odot$	9.5 $R_\odot$

increase of mass loss with rotation as well as anisotropies in the mass ejection and wind density from rotating stars (Maeder 1999; Maeder & Meynet 2000).

Finally, the highly distorted shape of Achernar poses the question of Be stars rotation rate. As argued by several authors (e.g. Cassinelli 1987; Owocki 2003) the formation of out-flowing discs from Be stars remains their central puzzle, where rapid rotation is the crucial piece. Struve's (1931) original vision of a critically rotating star, ejecting material from its equator, has been discarded in the past by observing that Be stars rotate at most 70% or 80% of their critical velocity (typically ~500 km s^{-1} for a B0V star). However, this statistically observed limit might be biased by the fact that close to or beyond such velocities the diagnosis of Doppler-broadened spectral lines fails to determine the rotation value due to gravity darkening (Owocki 2003; Townsend 1997). We believe that only direct measures of Be star photospheres by interferometry can overcome the challenge to prove whether these objects rotate close, to a few percent, of their critical velocity or not. This have a profound impact on dynamical models of Be stars CSE formation from rapid rotation combined to mechanisms like pulsation, radiation pressure of photospheric hot spots, or expelled plasma by magnetic flares.

Acknowledgements. A.D.S., P.K. and L.A. acknowledge CAPES-Brazil, ESO and CNES-France for financial support respectively. The authors acknowledge support from D. Mourard and his team from OCA-France. LUAN is supported by UNSA and CNRS. Observations with the VLTI became possible thanks to the VLTI team. We are grateful to Drs. N. V. Leister and E. Janot-Pacheco for Achernar's spectra.

References

Ballereau, D., Chauville, J., & Zorec, J. 1995, A&AS, 111, 423
Bodenheimer, P. 1971, A&A, 167, 153
Cassinelli, J. P. 1987, in Physics of Be stars, ed. A. Slettebak, & T. P. Snow (Cambridge: Cambridge Univ. Press), 106
Chauville, J., Zorec, J., Ballereau, D., et al. 2001, A&A, 378, 861
Claret, A. 2000, A&A, 363, 1081
Cohen, M., Walker, R. G., Carter, B., et al. 1999, AJ, 117, 1864
de Freitas Pacheco, J. A. 1982, MNRAS, 199, 591
Domiciano de Souza, A., Vakili, F., Jankov, S., Janot-Pacheco, E., & Abe, L. 2002, A&A, 393, 345
Glindemann, A., Algomedo, J., Amestica, R., et al. 2003, Proc. SPIE, 4838, 89
Hanbury Brown, R., Davis, J., & Allen, L. R. 1974, MNRAS, 167, 121
Harmanec, P. 1988, Bull. Astron. Inst. Czechoslovakia, 39, 329
Jaschek, M., Slettebak, A., & Jaschek, C. 1981, Be Star Newsletter, 4, 9
Kervella, P., Gitton, Ph., Ségransan, D., et al. 2003a, Proc. SPIE, 4838, 858
Kervella, P., Thévenin, F., Ségransan, D., et al. 2003b, A&A, 404, 1087
Kopal, Z. 1987, Ap&SS, 133, 157
Leister, N. V., & Janot-Pacheco, E. 2003, private commun.
Maeder, A. 1999, A&A, 347, 185
Maeder, A., & Meynet, G. 2000, A&ARv, 38, 143
Owocki, S. P. 2003, Proc. IAU Symp. 215, ed. A. Maeder, & P. Eenens, in press
Perryman, M. A. C., Lindegren, L., Kovalevsky, J., et al. 1997, A&A, 323, L49
Poeckert, R., & Marlborough, J. M. 1978, ApJS, 38, 229
Reiners, A., & Schmitt, J. H. M. M. 2003, A&A, 398, 647
Roche, E. A. 1837, Mém. de l'Acad. de Montpellier (Section des Sciences), 8, 235
Ségransan, D., Kervella, P., Forveille, T., & Queloz, D. 2003, A&A, 397, L5
Ségransan, D., Forveille, T., Millan-Gabet, C. P. R., & Traub, W. A. 1999, ASP Conf. Ser., 194, 290
Slettebak, A. 1982, ApJ, 50, 55
Struve, O. 1931, ApJ, 73, 94
Townsend, R. H. D. 1997, Ph.D. Thesis, Univ. College London
van Belle, G. T., Ciardi, D. R., Thompson, R. R., Akeson, R. L., & Lada, E. A. 2001, ApJ, 559, 1155
von Zeipel, H. 1924, MNRAS, 84, 665
Yudin, R. V. 2001, A&A, 368, 912
Zahn, J.-P. 1992, A&A, 265, 115

4.3.4 Article A&A : "The polar wind of the fast rotating Be star Achernar. VINCI/VLTI interferometric observations of an elongated polar envelope" (2006)

L'analyse d'observations supplémentaires de Achernar obtenues avec les grands télescopes de 8 m du VLTI et VINCI a permis de mettre en évidence une enveloppe circumstellaire allongée selon la direction des pôles de l'étoile. Il s'agit de la première détection de l'émission "free-free" créée par le vent stellaire rapide expulsé des calottes polaires de l'étoile, surchauffées par l'effet Von Zeipel.

FIG. 4.9 – Coucher de Soleil à Paranal (photo R. Petrov).

A&A 453, 1059–1066 (2006)
DOI: 10.1051/0004-6361:20054771

Astronomy & Astrophysics

The polar wind of the fast rotating Be star Achernar

VINCI/VLTI interferometric observations of an elongated polar envelope

P. Kervella[1] and A. Domiciano de Souza[2,3]

[1] LESIA, CNRS UMR 8109, Observatoire de Paris-Meudon, 5 place Jules Janssen, 92195 Meudon Cedex, France
e-mail: Pierre.Kervella@obspm.fr
[2] Lab. Univ. d'Astrophysique de Nice (LUAN), CNRS UMR 6525, UNSA, Parc Valrose, 06108 Nice, France
[3] Observatoire de la Côte d'Azur, CNRS UMR 6203, Département GEMINI, BP 4229, 06304 Nice Cedex 4, France

Received 23 December 2005 / Accepted 20 February 2006

ABSTRACT

Context. Be stars show evidence of mass loss and circumstellar envelopes (CSE) from UV resonance lines, near-IR excesses, and the presence of episodic hydrogen emission lines. The geometry of these envelopes is still uncertain, although it is often assumed that they are formed by a disk around the stellar equator and a hot polar wind.
Aims. We probe the close environment of the fast rotating Be star Achernar at angular scales of a few milliarcseconds (mas) in the infrared, in order to constrain the geometry of a possible polar CSE.
Methods. We obtained long-baseline interferometric observations of Achernar with the VINCI/VLTI beam combiner in the H and K bands, using various telescope configurations and baseline lengths with a wide azimuthal coverage.
Results. The observed visibility measurements along the polar direction are significantly lower than the visibility function of the photosphere of the star alone, in particular at low spatial frequencies. This points to the presence of an asymmetric diffuse CSE elongated along the polar direction of the star. To our data, we fit a simple model consisting of two components: a 2D elliptical Gaussian superimposed on a uniform ellipse representing the distorted photosphere of the fast rotating star.
Conclusions. We clearly detected a CSE elongated along the polar axis of the star, as well as rotational flattening of the stellar photosphere. For the uniform-ellipse photosphere we derive a major axis of $\theta_{\rm eq} = 2.13 \pm 0.05$ mas and a minor axis of $\theta_{\rm pol} = 1.51 \pm 0.02$ mas. The relative near-IR flux measured for the CSE compared to the stellar photosphere is $f = 4.7 \pm 0.3\%$. Its angular dimensions are loosely constrained by the available data at $\rho_{\rm eq} = 2.7 \pm 1.3$ mas and $\rho_{\rm pol} = 17.6 \pm 4.9$ mas. This CSE could be linked to free-free emission from the radiative pressure driven wind originating from the hot polar caps of the star.

Key words. techniques: high angular resolution – techniques: interferometric – stars: emission-line, Be – stars: mass-loss – stars: rotation – stars: individual: Achernar

1. Introduction

The southern star Achernar (α Eridani, HD 10144) is the brightest of all Be stars ($V = 0.46$ mag). Depending on the author (and the technique used) the spectral type of Achernar ranges from B3-B4IIIe to B4Ve (e.g., Slettebak 1982; Balona et al. 1987). The estimated projected rotation velocity $v \sin i$ ranges from 220 to 270 km s^{-1} and the effective temperature $T_{\rm eff}$ from 15 000 to 20 000 K (e.g., Vinicius et al. 2006; Rivinius, priv. comm.; Chauville et al. 2001). The difficulty in deriving these parameters more precisely is a direct consequence of the rapid rotation of Achernar. Such rapid rotation (≥80% of the critical velocity) induces mainly two effects on the star structure: a rotational flattening and a gravity darkening, which can be described by the von Zeipel effect (von Zeipel 1924).

Domiciano de Souza et al. (2003, hereafter D03) measured the apparent rotational flattening of Achernar using the Very Large Telescope Interferometer (VLTI). They showed that the flattening ratio measured on this star cannot be explained in the Roche approximation, especially when taking the von Zeipel effect into account. Recently, this effect was revealed in two other rapidly rotating stars thanks to interferometric observations: Altair (A7V, Ohishi et al. 2004; Domiciano de Souza et al. 2005) and Regulus (B7V, McAlister et al. 2005).

Rapid rotation and gravity darkening seem to be important keys to explaining the two-component circumstellar environment (CSE) of Be stars: (1) a dense (particle densities $N \simeq 10^{11}$–10^{12} cm^{-3}), high mass-loss ($\simeq 10^{-8}$ $M_\odot$/yr) and low radial velocity ($\simeq$10–100 km s^{-1}) equatorial envelope and (2) a rarefied ($N \simeq 10^{9}$ cm^{-3}), low mass-loss ($\simeq 10^{-10}$ $M_\odot$/yr) and fast ($\simeq$1000 km s^{-1}) polar wind (e.g. Damineli Neto & de Freitas Pacheco 1982; Waters et al. 1987, and references therein). This picture of a two-component CSE is based on many observations of Be stars performed in the past few decades. For example, optical/IR data have shown emission lines and IR excesses that essentially probe the denser regions of the CSE (e.g. Waters 1986; Dougherty et al. 1994), while UV resonance lines of highly ionized species can probe regions of lower density (e.g. Snow 1981; Peters 1982). Gehrz et al. (1974) showed that the near-IR excess measured in Be stars is due to free-free radiation.

The disk-like shape of the dense equatorial CSE has been directly measured by interferometric observations in the radio and optical/IR (e.g. Dougherty & Taylor 1992; Stee et al. 1995; Quirrenbach et al. 1997). In a recent work, Tycner et al. (2005) explore the relationship between the angular size of the Hα emitting region (measured by interferometry) and the net Hα emission measured spectroscopically for seven Be stars. They find an interesting correlation between the two quantities, which they

Table 1. Relevant parameters of the calibrators used for VINCI observations of Achernar (continued in Table 2).

Name	α PsA	χ Phe	HR 1318	α Ind	HR 37	HR 2305	δ Phe
HD number	HD 216956	HD 12524	HD 26846	HD 196171	HD 787	HD 44951	HD 9362
m_V	1.2	5.2	4.9	3.1	5.3	5.2	4.0
m_K	1.0	1.3	2.3	0.9	1.8	2.3	1.7
Sp. type	A3V	K5III	K3III	K0III	K5III	K3III	K0IIIb
$T_{\rm eff}$ (K)[a]	8760	3780	6210	4720	3780	4250	4660
$\log g$[a]	4.2	1.9	2.2	2.6	1.9	2.4	2.9
$v \sin i$ (km s^{-1})[c]	85	–	20	–	2	20	–
$\theta_{\rm LD}$ (mas)[a]	2.23 ± 0.07	2.77 ± 0.03	1.86 ± 0.02	3.28 ± 0.03	2.52 ± 0.03	1.81 ± 0.03	2.24 ± 0.02
$\theta_{\rm UD}$ (mas)[b]	2.19 ± 0.07	2.69 ± 0.03	1.81 ± 0.02	3.20 ± 0.03	2.45 ± 0.03	1.76 ± 0.03	2.18 ± 0.02

[a] From Cohen et al. (1999) or Bordé et al. (2002), except α PsA which angular size was measured by Di Folco et al. (2004). [b] Linear limb darkening coefficients from Claret et al. (1995) or Claret (2000). [c] The projected rotational velocities were taken from the catalogue compiled by Glebocki et al. (2000).

attribute to an optically thick emission proportional to the effective area of the emitting disk. Because the equatorial disks are denser (≃100 times) than the polar winds and because the free-free emissivity is proportional to the density squared, the equatorial disk dominates the near-IR continuum emission when it is present.

However, it is still not clear if this free-free radiation comes only from the equatorial envelope or if it can also be formed, at least partially, in the polar wind. Modern high angular resolution techniques have the resolving power and sensitivity required to map the spatial distribution of the near-IR emission. In the present paper we investigate this issue by using all available interferometric observations of Achernar obtained with the VINCI/VLTI near-IR instrument (Sect. 2). These observations were performed during a phase where the equatorial disk was nearly absent. The adopted analytical model is presented in Sect. 3 and our results discussed in Sect. 4.

2. Interferometric observations

2.1. Instrumental setup and observations

The European Southern Observatory's VLTI (Glindemann et al. 2000, 2004) has been in operation on top of the Cerro Paranal, in Northern Chile since March 2001. For the observations reported in this paper, the light coming from two test siderostats (0.35 m aperture) or two Unit Telescopes (8 m aperture) was recombined coherently in VINCI, the VLT INterferometer Commissioning Instrument (Kervella et al. 2000, 2003). We used either a K band ($\lambda = 2.0{-}2.4\,\mu$m) or H band ($\lambda = 1.4{-}1.8\,\mu$m) filter, depending on the beam combiner. In the K band, we relied on the MONA beam combiner, based on fluoride glass optical fibers, while in the H band, we employed the IONIC integrated optics beam combiner (Berger et al. 2001; Kervella et al. 2003; Lebouquin et al. 2004). A total of nine VLTI baselines were used for this program, including five out of the six possible Unit Telescope baselines. Considering the transmission of the instrument and the average effective temperature of Achernar, the effective wavelength of our observations was $\lambda = 2.175\,\mu$m in the K band and $\lambda = 1.631\,\mu$m in the H band. The uncertainty on these wavelengths (≈0.2%) is negligible compared to the accuracy of our measurements.

2.2. Data processing and calibration

The raw data processing was achieved using a wavelet-based algorithm, integrated in an automated data reduction pipeline (Kervella et al. 2004a). The general principle is similar to the original FLUOR algorithm (Coudé du Foresto et al. 1997), but instead of the classical Fourier analysis, we implemented a wavelet-based time-frequency analysis (Ségransan et al. 1999). The output of this pipeline is a single value of the squared coherence factor μ^2 for each series of 500 interferograms and the associated bootstrapped error bar. We obtained a total of 49 500 interferograms of Achernar in the K band and 9500 in the H band, among which 32 394 and 3029 were reduced by the pipeline, respectively. The lower proportion of processed interferograms in the H band is explained by the fact that only one interferometric output is available in the IONIC component, instead of two for the MONA beam combiner. In both cases, two photometric outputs are present. This resulted in a total of 99 squared visibility measurements in the K band, and 19 in the H band, with their associated statistical and calibration uncertainties.

We used a number of calibrators taken mainly from the Bordé et al. (2002) catalogue, which is an adaptation of the Cohen et al. (1999) catalogue for interferometric observations. The observations of these stars were used to estimate the point source response of the interferometer immediately before or after the Achernar observations. Their properties are listed in Tables 1 and 2. The choice of the calibrators is an important step in the preparation of interferometric observations, as significant departures of their actual visibilities from the expected model can propagate into biases on the calibrated visibilities of the scientific target. Among the possible reasons for such departures, binarity (or multiplicity) and deviations from sphericity (due, for instance, to fast rotation or gravitational interaction) are the most critical. All stars in the Bordé et al. (2002) catalogue were carefully scrutinized by these authors for the presence of companions, and are currently regarded as single stars. With respect to fast rotation, the values of $v \sin i$ are generally low for all our calibrators. Spectroscopic measurements of the projected rotational velocities are missing for some of our calibrators; but as they are giant stars, we assume that they are small and, therefore, that the deformation of these stars can be neglected.

One of our calibrators, α PsA (Fomalhaut), is a moderately fast rotating dwarf (A3V, $v \sin i \approx 85\,$km s^{-1}, from Glebocki et al. 2000). We considered carefully the visibilities that were computed using this calibrator, and they show no deviation from the other measurements, in particular those calibrated by δ Phe that were obtained on the same baseline. Moreover, Di Folco et al. (2004) have measured the angular diameter of this star along the same projected baseline azimuth as during our observations of Achernar. Therefore, we do not expect any difference in terms of angular diameter. In any case, we considered a conservative ±0.07 mas (±3%) uncertainty on the asumed angular diameter of α PsA.

Table 2. Relevant parameters of the calibrators used for VINCI observations of Achernar (continued from Table 1). The references are the same as in Table 1.

Name	ϵ Ind A	α Cet	υ Cet
HD number	HD 209100	HD 18884	HD 12274
m_V	4.7	2.5	4.0
m_K	2.2	–1.7	0.0
Sp. type	K4.5V	M1.5IIIa	K5/M0III
T_{eff} (K)	4500	3730	–
$\log g$	4.5	–	–
$v \sin i$ (km s^{-1})	1	–	–
θ_{LD} (mas)[a]	1.89 ± 0.02	–	–
θ_{UD} (mas)[b]	1.84 ± 0.02	11.6 ± 0.40	5.3 ± 0.5

[a] The angular diameter of ϵ Ind A was measured by Kervella et al. (2004b). [b] The uniform disk angular sizes of α Cet and υ Cet were taken from Dyck et al. (1998) and Richichi & Percheron (2005), respectively.

The resulting calibrated squared visibilities are listed in Tables 3a–d. For each measurement, the calibrator is listed. No systematic deviation of the visibility was observed for any of our calibrators at a 1σ level.

3. Model fitting

3.1. Polar and equatorial visibilities

In order to define a plausible model for the light distribution of Achernar, we examine here the shape of the polar and equatorial visibility functions. The orientation of the minor axis of Achernar on the plane of the sky relative to the North was obtained by D03 using a subset of the data discussed in the present paper. Using a simplified analysis of the dependence of the equivalent uniform disk angular diameter with the azimuth of the projected baseline, they obtained an orientation of the minor axis of Achernar (assumed to be the polar axis) of $\alpha_0 = 39 \pm 1°$ east of North.

To visualize the polar visibility function of Achernar, we extracted the interferometric measurements with azimuth angles between 10° and 70°, i.e. $\simeq \pm 30°$ from the sky-projected polar axis of the star. As shown in Fig. 2 (left), it appears that the distribution of the measured visibilities does not follow that of a uniform disk, and there is a clear deficit of visibility at low spatial frequencies. Fitting a simple uniform disk model (through a classical least-square minimization) to these data leads to $\theta_{UD} = 1.78$ mas, but the reduced χ^2 of 6.2 is characteristic of a poor fit. The deficit of visibility at low spatial frequencies is typical of the presence of an extended, incoherent source that is already resolved by the interferometer on the short baselines. In other words, a diffuse and extended envelope appears to be present along the polar axis of the star.

The equatorial visibility function can be evaluated by restricting our sample to the visibility measurements obtained in the azimuth range $\alpha_1 = 129 \pm 30°$. As shown in Fig. 1, we do not have as many measurements at high spatial frequencies along this range of azimuth, due to the limitations in the available VLTI baselines during commissioning. Figure 2 (right) shows the distribution of squared visibilities observed in this azimuth range as a function of the spatial frequency. In this case, the fit of a simple uniform disk model with $\theta_{UD} = 2.38$ mas produces satisfactory results with a reduced χ^2 of only 0.6. In this case, we conclude that we do not detect any significant diffuse envelope along the equatorial plane of the star.

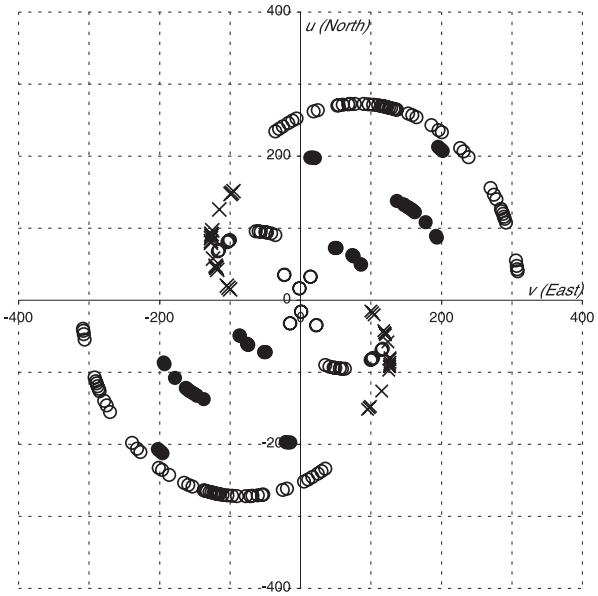

Fig. 1. Coverage of the (u, v) plane for the VINCI observations of Achernar. The K band observations (MONA beam combiner) are represented using circles (open for siderostat observations, solid for the Unit Telescopes), and the H band observations are represented using crosses. The scales are in units of B/λ, expressed in cycles/arcsec.

3.2. Star-envelope model description

As discussed in Sect. 3.1, it appears that a diffuse envelope, confined to the direction of its polar axis, is present around Achernar. In order to study the flux contribution of this envelope, we need to define a simple model to fit the observed visibility data. For this purpose, we considered the following components:

- the stellar photosphere is represented by a uniform ellipse. The parameters are the equatorial and polar angular sizes θ_{eq} and θ_{pol} and the azimuth orientation of the equatorial axis on the sky α_1;
- the diffuse envelope is represented by a bidimensional elliptical Gaussian. It is parametrized by its full widths at half maximum (FWHM) along the polar and equatorial axes of the star ρ_{pol} and ρ_{eq}, and its integrated flux relative to the stellar flux f. We make the assumption that its principal axes are aligned with the principal axes of the stellar photosphere.

Using a simple uniform ellipse model is naturally a very simplified approximation of the photospheric light distribution of Achernar. In reality, the rapid rotation of the star causes significant brightening of the polar caps of the star as a consequence of its flattening. Though numerical models can accurately predict the distribution of light on the photosphere of uniformly rotating stars (see e.g. Domiciano de Souza et al. 2002), the underlying Roche approximation is not necessarily verified for Achernar. In particular, Jackson et al. (2004) show that stellar models of Achernar including differential internal rotation result in better agreement with the interferometric profile obtained by D03. Though there are good prospects for differential rotation being constrained observationally by spectro-interferometry (Domiciano de Souza et al. 2004), the current uncertainties on the light distribution of the photosphere lead us to prefer the simple approach of a uniform ellipse. We also make the hypothesis that the axes of the envelope are aligned with the principal axes of the stellar photosphere. Due to the limited coverage of our data set in terms of azimuth angle at intermediate baselines, we

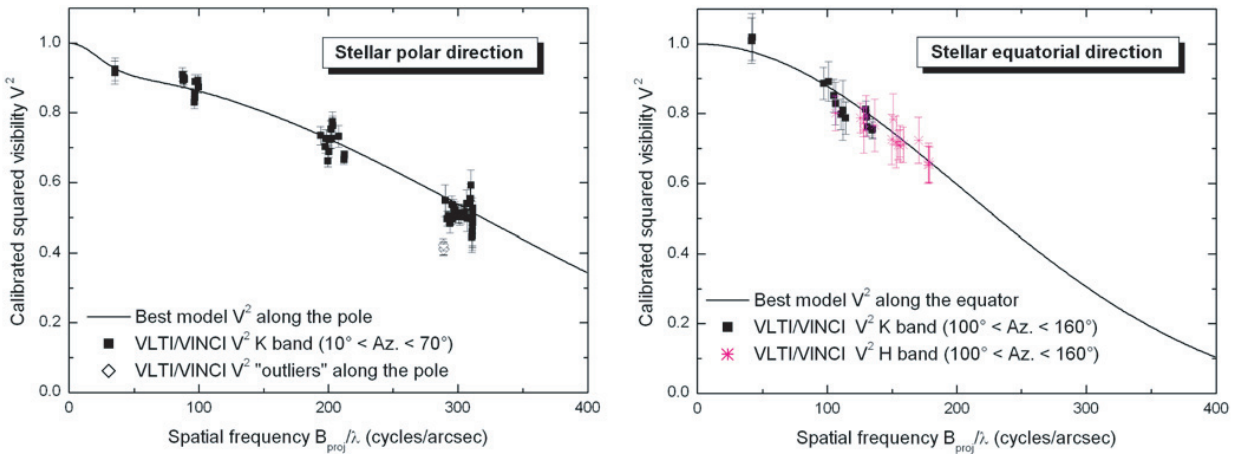

Fig. 2. *Left*: squared visibilities V^2 measured on Achernar and corresponding to projected baseline azimuth angles around the polar direction (values between 10° and 70°). *Right*: V^2 corresponding to projected baseline azimuth angles around the equatorial direction (values between 100° and 160°). The solid squares and crosses represent K and H band data, respectively. The solid curves represent theoretical V^2 along the pole (*left*) and the equator (*right*) obtained from the 2D fit of our two-component model (Sect. 3) to all measured V^2 (Tables 3a–d. Note also the V^2 outliers along the polar direction, which were not included in the fit (see text for details).

Table 3. (a) Squared visibilities of Achernar in the K band from VINCI, ordered by increasing azimuth angle of the projected baseline. The calibrators are named using their HR number, when no Bayer designation is available. The stated Julian date JD_0 is $JD - 2.452\times10^6$. The azimuth is counted in degrees clockwise from North ($N = 0$ deg, $E = 90$ deg), and B is the projected baseline in meters. The squared visibilities are followed in subscript by the statistical and calibration uncertainties.

JD_0	Cal.	Stations	B (m)	Az.	V^2 (%)
548.551	α PsA	B3-M0	139.44	7.3	$45.7_{\pm1.5\pm4.1}$
546.558	α PsA	B3-M0	139.48	7.9	$42.7_{\pm4.4\pm3.3}$
548.555	α PsA	B3-M0	139.46	8.7	$46.3_{\pm1.5\pm4.2}$
548.560	α PsA	B3-M0	139.48	10.2	$44.4_{\pm1.5\pm4.0}$
547.595	α PsA	B3-M0	139.61	20.2	$45.9_{\pm2.1\pm3.8}$
545.604	α PsA	B3-M0	139.69	21.2	$50.6_{\pm1.6\pm2.4}$
547.600	α PsA	B3-M0	139.63	21.8	$45.0_{\pm2.1\pm3.7}$
545.608	α PsA	B3-M0	139.70	22.6	$52.6_{\pm1.6\pm2.5}$
547.605	α PsA	B3-M0	139.65	23.3	$46.5_{\pm2.2\pm3.8}$
545.613	α PsA	B3-M0	139.72	24.0	$51.7_{\pm1.5\pm2.5}$
216.589	1318	U1-U3	95.29	24.2	$67.9_{\pm1.1\pm0.5}$
216.592	1318	U1-U3	95.15	24.8	$66.6_{\pm1.3\pm0.5}$
545.622	α PsA	B3-M0	139.72	26.7	$49.7_{\pm1.5\pm2.4}$
545.626	α PsA	B3-M0	139.72	28.0	$48.7_{\pm2.2\pm2.3}$
534.712	χ Phe	U1-U2	44.61	29.6	$87.3_{\pm1.6\pm0.4}$
545.632	α PsA	B3-M0	139.70	29.9	$51.3_{\pm2.2\pm2.4}$
534.714	χ Phe	U1-U2	44.56	30.1	$89.3_{\pm1.6\pm0.4}$
575.637	37, 2305	U1-U3	93.34	31.3	$73.2_{\pm2.8\pm1.3}$
213.654	χ Phe	U1-U3	91.22	36.9	$76.3_{\pm2.2\pm1.6}$
213.655	χ Phe	U1-U3	91.12	37.2	$77.4_{\pm2.3\pm1.6}$
213.658	χ Phe	U1-U3	90.79	37.9	$72.4_{\pm2.2\pm1.5}$
213.660	χ Phe	U1-U3	90.62	38.3	$75.2_{\pm2.0\pm1.6}$
534.749	χ Phe	U1-U2	43.54	38.7	$88.9_{\pm2.1\pm0.4}$
213.663	χ Phe	U1-U3	90.28	39.0	$72.3_{\pm2.0\pm1.5}$
534.750	χ Phe	U1-U2	43.48	39.1	$84.3_{\pm1.5\pm0.4}$
534.752	χ Phe	U1-U2	43.40	39.6	$85.4_{\pm1.6\pm0.4}$
556.635	δ Phe	B3-M0	139.20	39.8	$59.2_{\pm4.1\pm1.7}$
214.664	1318	U1-U3	89.89	39.9	$68.8_{\pm1.7\pm0.5}$
534.755	χ Phe	U1-U2	43.32	40.2	$82.9_{\pm1.7\pm0.4}$
214.667	1318	U1-U3	89.60	40.5	$66.2_{\pm1.6\pm0.5}$
556.642	δ Phe	B3-M0	139.02	41.7	$55.3_{\pm4.0\pm1.6}$
213.675	χ Phe	U1-U3	88.92	41.8	$72.6_{\pm2.0\pm1.5}$
214.675	1318	U1-U3	88.69	42.2	$70.2_{\pm1.7\pm0.5}$
556.646	δ Phe	B3-M0	138.88	42.9	$54.3_{\pm3.8\pm1.6}$
213.691	χ Phe	U1-U3	87.05	45.1	$73.5_{\pm2.2\pm1.5}$

Table 3. (b) Squared visibilities of Achernar in the K band from VINCI (continued from Table 3a).

JD_0	Cal.	Stations	B (m)	Az.	V^2 (%)
533.711	ϵ Ind	U1-U4	129.75	45.7	$41.3_{\pm1.2\pm1.4}$
533.713	ϵ Ind	U1-U4	129.70	46.1	$41.0_{\pm0.9\pm1.4}$
533.715	ϵ Ind	U1-U4	129.64	46.8	$41.0_{\pm0.9\pm1.4}$
533.717	ϵ Ind	U1-U4	129.57	47.4	$42.4_{\pm0.9\pm1.4}$
550.685	δ Phe	B3-M0	137.86	49.2	$49.8_{\pm3.4\pm1.4}$
550.688	δ Phe	B3-M0	137.64	50.3	$53.9_{\pm3.6\pm1.5}$
550.697	δ Phe	B3-M0	137.09	52.5	$51.5_{\pm1.6\pm1.4}$
534.898	χ Phe	U2-U3	39.87	54.7	$89.5_{\pm2.4\pm0.4}$
534.900	χ Phe	U2-U3	39.68	55.0	$89.9_{\pm1.8\pm0.4}$
534.902	χ Phe	U2-U3	39.44	55.4	$89.3_{\pm1.8\pm0.4}$
534.904	χ Phe	U2-U3	39.18	55.9	$91.0_{\pm1.9\pm0.4}$
556.696	δ Phe	B3-M0	135.77	56.9	$50.9_{\pm2.2\pm1.4}$
556.701	δ Phe	B3-M0	135.32	58.2	$50.3_{\pm2.1\pm1.3}$
556.705	δ Phe	B3-M0	134.87	59.5	$51.1_{\pm2.2\pm1.4}$
550.733	δ Phe	B3-M0	133.55	62.6	$52.1_{\pm2.0\pm1.5}$
590.625	δ Phe	B3-M0	133.37	63.0	$51.6_{\pm0.8\pm1.3}$
550.736	δ Phe	B3-M0	133.15	63.5	$52.9_{\pm1.8\pm1.5}$
590.629	δ Phe	B3-M0	132.83	64.2	$49.7_{\pm0.7\pm1.2}$
550.741	δ Phe	B3-M0	132.55	64.7	$53.7_{\pm1.8\pm1.5}$
569.691	δ Phe	B3-M0	132.25	65.3	$49.6_{\pm1.1\pm1.2}$
945.621	α PsA	E0-G0	15.95	65.4	$92.5_{\pm3.2\pm0.1}$
590.634	δ Phe	B3-M0	132.12	65.6	$49.5_{\pm0.8\pm1.2}$
554.735	α PsA	B3-M0	131.85	66.1	$48.4_{\pm1.9\pm2.0}$
569.695	δ Phe	B3-M0	131.58	66.6	$49.7_{\pm1.1\pm1.2}$
945.625	α PsA	E0-G0	15.93	66.7	$91.5_{\pm3.3\pm0.1}$
590.639	δ Phe	B3-M0	131.41	66.9	$50.4_{\pm0.8\pm1.3}$
569.700	δ Phe	B3-M0	130.94	67.8	$49.6_{\pm1.7\pm1.2}$
579.677	δ Phe	B3-M0	130.22	69.1	$54.8_{\pm4.4\pm1.1}$
579.682	δ Phe	B3-M0	129.41	70.4	$49.7_{\pm4.5\pm1.0}$
579.687	δ Phe	B3-M0	128.57	71.8	$48.7_{\pm4.7\pm1.0}$
555.761	δ Phe	B3-M0	127.04	74.1	$48.7_{\pm1.9\pm1.0}$
555.765	δ Phe	B3-M0	126.16	75.4	$49.7_{\pm3.3\pm1.0}$
577.707	δ Phe	B3-M0	125.74	75.9	$50.1_{\pm3.4\pm1.3}$
577.712	δ Phe	B3-M0	124.67	77.4	$49.8_{\pm3.4\pm1.3}$
577.717	δ Phe	B3-M0	123.75	78.6	$50.3_{\pm3.4\pm1.3}$
552.786	α PsA	B3-M0	123.47	79.0	$49.7_{\pm4.2\pm3.6}$
533.781	χ Phe	U2-U4	89.03	84.0	$64.6_{\pm2.9\pm1.2}$
533.783	χ Phe	U2-U4	88.98	84.5	$64.8_{\pm2.5\pm1.2}$
555.798	δ Phe	B3-M0	118.90	84.6	$49.7_{\pm3.5\pm1.0}$

Table 3. (c) Squared visibilities of Achernar in the K band from VINCI (continued from Table 3b).

JD_0	Cal.	Stations	B (m)	Az.	V^2 (%)
533.786	χ Phe	U2-U4	88.91	85.2	$63.6_{\pm 2.6 \pm 1.1}$
533.788	χ Phe	U2-U4	88.83	85.8	$62.9_{\pm 2.5 \pm 1.1}$
555.802	δ Phe	B3-M0	117.78	85.9	$50.3_{\pm 2.8 \pm 1.0}$
579.754	δ Phe	B3-M0	113.06	91.2	$52.6_{\pm 4.0 \pm 0.8}$
579.759	δ Phe	B3-M0	111.82	92.6	$52.0_{\pm 4.0 \pm 0.8}$
629.580	α Cet	B3-C3	7.37	93.1	$98.2_{\pm 2.7 \pm 0.0}$
579.763	δ Phe	B3-M0	110.48	94.0	$52.0_{\pm 4.3 \pm 0.8}$
629.585	α Cet	B3-C3	7.31	94.7	$102.1_{\pm 3.4 \pm 0.0}$
544.865	χ Phe	B3-M0	108.80	95.8	$50.2_{\pm 3.8 \pm 2.4}$
544.869	α PsA	B3-M0	107.50	97.2	$49.5_{\pm 3.2 \pm 2.4}$
544.873	α PsA	B3-M0	106.17	98.6	$48.2_{\pm 3.4 \pm 2.3}$
535.631	χ Phe	E0-G1	43.57	111.5	$88.7_{\pm 4.6 \pm 0.5}$
535.642	χ Phe	E0-G1	45.32	114.0	$89.2_{\pm 5.7 \pm 0.5}$
538.646	χ Phe	E0-G1	47.10	116.7	$85.1_{\pm 4.7 \pm 0.4}$
538.651	χ Phe	E0-G1	47.74	117.7	$82.9_{\pm 6.1 \pm 0.4}$
535.673	χ Phe	E0-G1	49.58	120.7	$79.8_{\pm 4.3 \pm 0.4}$
535.678	χ Phe	E0-G1	50.24	121.8	$80.9_{\pm 8.6 \pm 0.4}$
662.575	α Cet	E0-G0	18.82	122.1	$102.0_{\pm 4.3 \pm 5.3}$
535.686	χ Phe	E0-G1	51.24	123.6	$78.7_{\pm 4.6 \pm 0.4}$
662.579	υ Cet	E0-G0	18.65	123.6	$100.9_{\pm 6.0 \pm 2.5}$
528.781	χ Phe	E0-G1	58.21	140.2	$81.1_{\pm 2.5 \pm 0.6}$
528.785	χ Phe	E0-G1	58.49	141.1	$79.0_{\pm 1.8 \pm 0.6}$
528.790	χ Phe	E0-G1	58.76	142.1	$76.1_{\pm 2.4 \pm 0.6}$
528.820	χ Phe	E0-G1	60.41	149.0	$75.2_{\pm 2.2 \pm 0.7}$
528.824	χ Phe	E0-G1	60.60	150.0	$75.7_{\pm 2.8 \pm 0.7}$

Table 3. (d) Squared visibilitiess of Achernar in the H band from VINCI, equipped with the IONIC integrated optics beam combiner.

JD_0	Cal.	Stations	B (m)	Az.	V^2 (%)
475.861	α Ind	E0-G1	52.48	126.0	$70.8_{\pm 4.3 \pm 1.6}$
475.870	α Ind	E0-G1	53.39	127.8	$71.1_{\pm 4.8 \pm 1.6}$
477.781	α Ind	E0-G1	42.26	109.7	$78.7_{\pm 3.9 \pm 1.7}$
477.785	α Ind	E0-G1	42.98	110.7	$77.4_{\pm 3.7 \pm 1.7}$
479.941	α Ind	E0-G1	59.78	146.1	$65.3_{\pm 5.2 \pm 1.4}$
479.944	α Ind	E0-G1	59.95	146.8	$66.0_{\pm 5.4 \pm 1.4}$
479.949	α Ind	E0-G1	60.19	147.9	$65.3_{\pm 5.1 \pm 1.4}$
482.791	α Ind	E0-G1	45.98	115.0	$76.6_{\pm 7.3 \pm 1.7}$
482.824	α Ind	E0-G1	50.39	122.1	$72.5_{\pm 7.0 \pm 1.6}$
482.827	α Ind	E0-G1	50.80	122.8	$78.4_{\pm 7.1 \pm 1.8}$
483.718	α Ind	E0-G1	34.05	98.7	$82.0_{\pm 4.4 \pm 1.8}$
483.722	α Ind	E0-G1	34.83	99.7	$77.5_{\pm 4.1 \pm 1.7}$
483.727	α Ind	E0-G1	35.78	101.0	$80.1_{\pm 4.6 \pm 1.7}$
483.831	α Ind	E0-G1	51.56	124.2	$71.9_{\pm 7.2 \pm 1.7}$
483.835	α Ind	E0-G1	52.05	125.1	$70.9_{\pm 3.8 \pm 1.7}$
483.839	α Ind	E0-G1	52.51	126.0	$72.0_{\pm 4.2 \pm 1.7}$
484.767	α Ind	E0-G1	43.17	110.9	$75.3_{\pm 6.4 \pm 1.4}$
484.771	α Ind	E0-G1	43.72	111.7	$79.3_{\pm 5.7 \pm 1.4}$
485.887	χ Phe	E0-G1	57.36	137.5	$72.3_{\pm 6.5 \pm 1.2}$

choose this approach in order to reduce the number of fitted parameters, and therefore improve the stability of the convergence of the χ^2 minimization.

3.3. Photospheric visibility function

The visibility function of a uniform ellipse can be derived from the classical visibility function of a circular uniform disk with an angular diameter $\theta_{\rm UD}$:

$$V_{\rm UD}(u,v) = \frac{2\,J_1(x)}{x} \tag{1}$$

where $x = \pi\,\theta_{\rm UD}\,\sqrt{u^2+v^2}$, with u and v the spatial frequency coordinates in units of B/λ. In order to obtain the visibility function of the ellipse, we use a rotation of the (u,v) axes and a scaling of the (u,v) variables:

$$u' = u\,\cos\alpha_1 + v\,\sin\alpha_1 \qquad v' = -u\,\sin\alpha_1 + v\,\cos\alpha_1. \tag{2}$$

The visibility of the uniform ellipse with a major axis $\theta_{\rm eq}$, a minor axis $\theta_{\rm pol}$, and a major axis orientation relative to the u axis α_1 is therefore:

$$V_{\rm star}(u,v,\theta_{\rm eq},\theta_{\rm pol},\alpha_1) = \frac{2\,J_1(x')}{x'} \tag{3}$$

where $x' = \pi\,\sqrt{\theta_{\rm eq}^2\,u'^2 + \theta_{\rm pol}^2\,v'^2}$.

3.4. Envelope visibility function

As in Sect. 3.3, we can obtain the visibility function of an elliptical Gaussian brightness distribution from the circularly symmetric case for which we have

$$V_{\rm Gauss}(u,v) = \exp\left[-\frac{\left(\pi\,\rho\,\sqrt{u^2+v^2}\right)^2}{4\,\ln 2}\right] \tag{4}$$

where ρ is the FWHM. In the elliptical case, we therefore obtain

$$V_{\rm env}(u,v,\rho_{\rm eq},\rho_{\rm pol},\alpha_1) = \exp\left[-\frac{\left(\pi\,\sqrt{\rho_{\rm eq}^2u'^2 + \rho_{\rm pol}^2v'^2}\right)^2}{4\,\ln 2}\right] \tag{5}$$

with the same expression of u' and v' as in Sect. 3.3, as we assume that the axes of the Gaussian envelope are aligned with the axes of the photosphere. The indexes "eq" and "pol" refer to the equator and pole of the central star.

3.5. Extracted parameters

Combining the visibility expressions presented in Sects. 3.3 and 3.4, we obtain the following expression for our simple model of an elongated ellipse with a superimposed Gaussian envelope:

$$V_{\rm model}(u,v,\theta_{\rm eq},\theta_{\rm pol},\rho_{\rm eq},\rho_{\rm pol},\alpha_1,f) = \frac{V_{\rm star} + f\,V_{\rm env}}{1+f}. \tag{6}$$

To derive the six free parameters of our model, we proceed through a classical χ^2 minimization process, with

$$\chi^2_{\rm tot}(\theta_{\rm eq},\theta_{\rm pol},\rho_{\rm eq},\rho_{\rm pol},\alpha_1,f) = \sum_i \frac{\left[V_i^2 - V^2_{\rm model}(u_i,v_i,...)\right]^2}{\sigma_i^2} \tag{7}$$

where V_i^2 is one of the VINCI squared-visibility measurements, and σ_i^2 its associated total variance. The expression of the reduced χ^2 is:

$$\chi^2_{\rm red} = \frac{\chi^2_{\rm tot}}{N_{\rm obs} - \text{d.o.f.}} \tag{8}$$

where $N_{\rm obs}$ is the number of individual observations and d.o.f. = 6 the numbers of degrees of freedom, considering that we fit a total of six parameters.

The minimum $\chi^2_{\rm red}$ of 0.79 is reached for the parameters listed in Table 4. This low value is characteristic of a good correspondence of our model to the interferometric data. The best-fit

Table 4. Best fit parameters (and corresponding uncertainties) of our simple model consisting in a Gaussian elliptical envelope superimposed on a uniform ellipse representing the central star. The fit was computed on our complete H and K band data set.

$\theta_{\rm eq}$	2.13 ± 0.05 mas	stellar equatorial angular size
$\theta_{\rm pol}$	1.51 ± 0.02 mas	stellar polar angular size
α_1	131.6 ± 1.4 deg	azimuth of the stellar equator
$\rho_{\rm eq}$	2.7 ± 1.3 mas	envelope FWHM along stellar equator
$\rho_{\rm pol}$	17.6 ± 4.9 mas	envelope FWHM along stellar pole
f	$4.7 \pm 0.3\%$	relative (envelope to star) near-IR flux

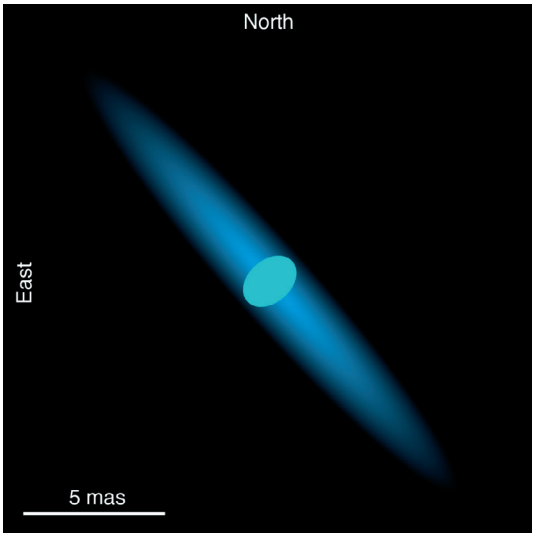

Fig. 3. Graphical representation of the best-fit model intensity distribution of Achernar. The relative flux contributions from the star and the envelope are not to scale. This illustration should not be considered as a true image of the star.

visibility function is a two-dimensional $V^2(u, v)$ map. Figure 2 shows the cuts of this best-fit $V^2(u, v)$ map along the stellar pole and the equator (solid curves). Note that the rapid visibility decrease observed at low spatial frequencies in the polar direction is reproduced well by the presence of the elongated polar envelope in the model.

A graphical representation of the star and its polar envelope based on the best-fit parameters is presented in Fig. 3. We emphasize that this figure is not a true image of the star, but only the representation of the best-fit light distribution with the a priori hypothesis that the star can be described by a uniform ellipse surrounded by an elliptical Gaussian envelope aligned with its principal axes. This intensity distribution reproduces the observed visibilities well, but several others could also fit. In particular, we cannot determine if the envelope is symmetric relative to the star, due to the baseline orientation ambiguity of 180°.

3.6. Excluded data points

In the fitting process, we chose to exclude the four data points obtained on the UT1-UT4 baseline (see Table 3b). With a position angle of ≈46 deg for the projected baseline, they correspond to a measurement that is almost aligned with the pole of the star ($\alpha_0 = 41.6 \pm 1.4$ deg). Although they satisfy the data quality criteria that we applied to the other data points, they are located $6{-}7\sigma$ away from the best-fit model. It should be noted that the 114 remaining data points are in excellent agreement with our CSE model, and the residuals of the fit present satisfactory statistical properties (see Sect. 3.7).

An instrumental origin for these outliers cannot be formally excluded, especially as these data points were obtained on the very first night of VLTI operations of the UT1-UT4 baseline. However, no particular technical problem was reported, and the other stars observed on this night showed consistent results. As we could not distinguish these measurements from the rest of our data, we chose to publish them all together for the sake of homogeneity. A possible astrophysical cause for these low visibilities would be a stellar eruption that could have suddenly increased the CSE brightness and/or angular extension.

3.7. Comparison with other models and residuals of the fit

In order to assess the level of adequation of our star+CSE model to the data, we also tried to fit them with two simpler models: a circular uniform disk and a uniform ellipse. The residuals for each of the three models are presented in Fig. 4 as a function of the projected baseline azimuth angle. We obtained in the first case a uniform disk angular diameter of $\theta_{\rm UD} = 1.78$ mas, with the large $\chi^2_{\rm red}$ of 4.9 characteristic of a bad fit. Fitting a uniform ellipse results in the following best-fit values: $\theta_{\rm eq} = 2.31$ mas, $\theta_{\rm pol} = 1.68$ mas, and $\alpha_1 = 135.7°$. Again, the $\chi^2_{\rm red}$ of 3.2 shows poor agreement of this model to our data. It thus appears that our star+Gaussian CSE model is a much better fit to our data set ($\chi^2_{\rm red} = 0.79$) than the models without CSE.

As shown in Fig. 4 (bottom), the residuals of our star+CSE fit appear to be homogeneous with respect to azimuth angle. Similarly, we do not detect any significant residual either with respect to projected baseline length or with time (Fig. 5). The H and K band data sets do not show any systematic deviation, which justifies a posteriori our combined treatment of these two data sets. Due to the relatively small number of measurements in the H band and their lower accuracy compared to the K band, their influence on the best-fit parameters is very limited. However, they are overall in excellent agreement with the best-fit model, with a specific reduced χ^2 of only 0.2. Considering the limited amount of H band data, we currently cannot investigate the wavelength dependence of the CSE properties, but additional observations with the AMBER instrument of the VLTI in the J and H bands will soon allow such studies. It should be noted that interferometric observations of the bright B0IVpe star γ Cas in the visible have shown that the apparent size of this star can vary considerably with wavelength (Stee et al. 1998). The scatter appears to be slightly larger along the polar direction than along the equator of the star (Fig. 5, top). This could be caused by deviations from our simple star-CSE model on small angular scales. For instance, the presence of clumps in the CSE could create this apparent instability of the visibility function. However, our data set is still too limited to constrain their properties significantly.

4. Nature of the CSE of Achernar

4.1. Total extension

As listed in Table 4, the angular sizes of the axes of the photosphere ellipse ($\theta_{\rm eq}$ and $\theta_{\rm pol}$) are well constrained, as is the flux ratio $f = 4.7 \pm 0.3\%$ between the star and the polar envelope. However, the angular dimensions of the envelope itself are poorly constrained. In particular, as visible in Fig. 2, we lack very short baseline measurements to estimate the total extension of the envelope in the polar direction. Considering our data, it could be much more extended than the

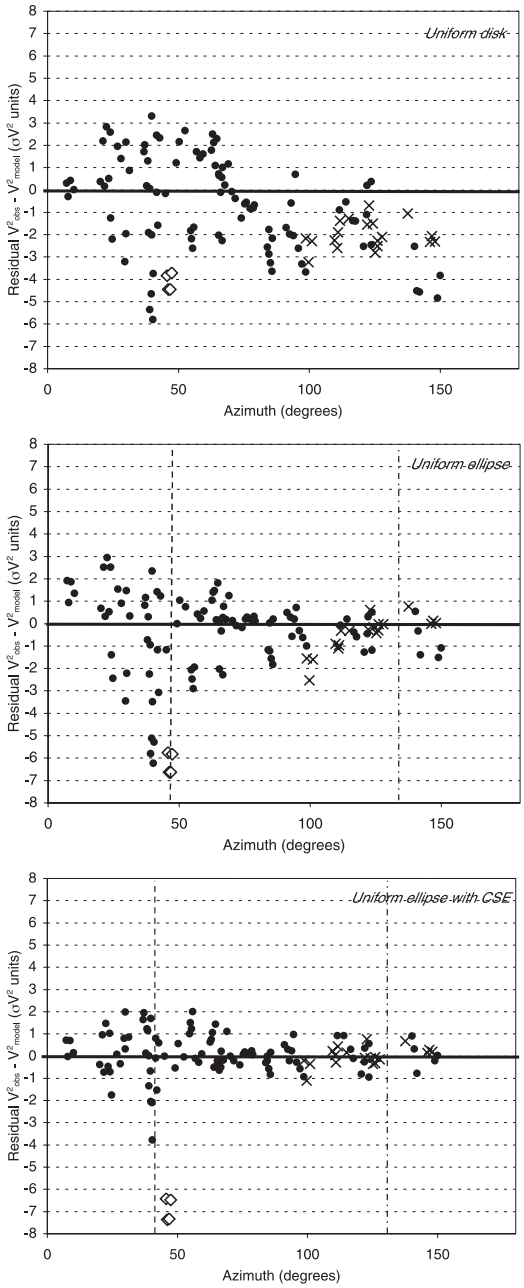

Fig. 4. Residuals of the visibility fit in units of V^2 standard deviation σ, as a function of azimuth angle, for a uniform disk (*top*), a uniform ellipse (*middle*), and our uniform ellipse with CSE model (*bottom*). The H band data are shown with crosses. The four outliers (open diamonds) were not included in the fit. The dashed and dot-dashed lines represent, respectively, the polar and equatorial directions of the models, including a uniform ellipse.

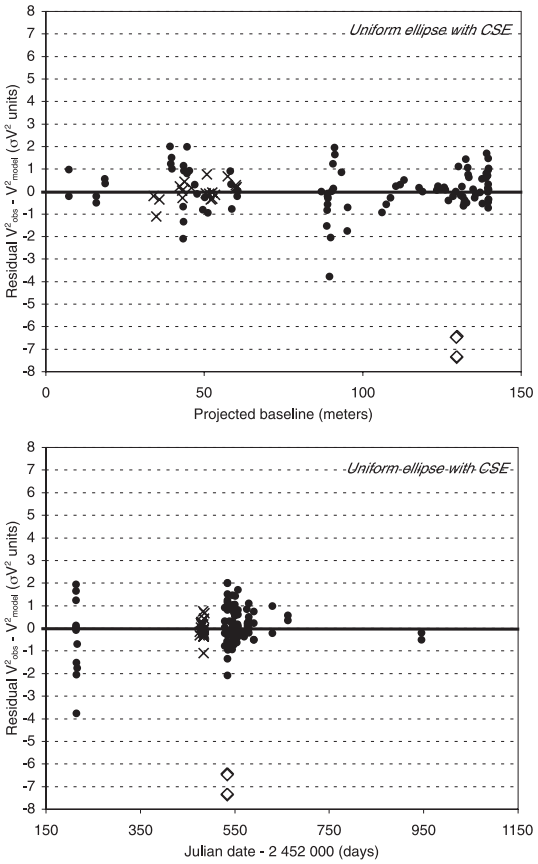

Fig. 5. Residuals of the visibility fit as a function of projected baseline length (*top*) and date of observation (*bottom*). The symbols are the same as in Fig. 4.

derived $\rho_{\rm pol} = 17.6 \pm 4.9$ mas, which should be considered as a lower limit. The angular extension of the envelope in the equatorial direction is also rather poorly constrained by our data, but appears to be small, and could be approximately the size of the star itself.

4.2. Photospheric flattening ratio

From the fit of our two-component model, we obtained a photospheric major- over minor-axis ratio of $\theta_{\rm eq}/\theta_{\rm pol} = 1.41 \pm 0.04$, while D03 measured a value of 1.56 ± 0.05, using part of the current data set. The 2.3σ difference between these two values can be explained by the difference in adopted model between these two approaches. D03 estimated the uniform disk equivalent angular diameter for each available azimuth and fitted an ellipse on the resulting values. In the present work, we directly fitted our two-component model to the visibilities in the (u, v) plane. In addition, D03 used a single-disk model that does not take the presence of the envelope into account.

Both approaches are valid and have their limitations and advantages. The important point where the main objective concerns the study of the flattening of the star is to compare the results to a physically realistic model including (at least) rotational deformation and gravity darkening, as was done by D03. In a future work we intend to perform a complete astrophysical analysis of the available interferometric and spectroscopic data on Achernar, including rotational effects (flattening and gravity darkening) and the CSE, both in the polar and equatorial directions.

4.3. Infrared free-free emission

From the measured flattening ratio, the polar temperature of Achernar could be higher than 20 000 K. In this context, the radiation pressure reaches very high values. As was demonstrated in the case of the luminous blue variable star η Carinae by Van Boekel et al. (2003), a stellar wind ejected from the poles can have a detectable signature in the interferometric visibilities in the near infrared. Recently, Meilland et al. (2006) showed that an elongated polar wind should be included with

a thin disk in order to explain the near-IR VLTI/AMBER (e.g., Petrov et al. 2003) observations of α Arae, another Be star that is very similar to Achernar (rotation velocity, spectral type). Although the central stars are similar, one important difference is that α Arae presented hydrogen lines in strong emission during the interferometric observations, while they were absent from the spectrum of Achernar. Both stars show an elongated polar wind responsible for a free-free and free-bound near-IR continuum emission, while only one of them (α Arae) shows a dense equatorial disk (resolved by VLTI/AMBER) where hydrogen emission lines are formed. This indicates that a significant (in terms of size and near-IR emission) polar wind exists independently if the star is in a normal B or in a Be phase; i.e., the polar wind does not seem to be completely related to the existence of a denser equatorial envelope.

In the hypothesis that the observed polar CSE near-IR emission is mostly caused by free-free radiation, we can roughly estimate the mean electron density as $n_e \simeq 2{-}3 \times 10^{10}\,\mathrm{cm}^{-3}$ for the H and K bands. This value was obtained from the free-free emissivity (e.g. Allen 1973) by considering an electron temperature of 20 000 K (the result does not depend strongly on this value) and by using the CSE parameters derived in this work (Table 4).

In a recent paper, Vinicius et al. (2006) estimated the 2.2 μm continuum emission based on a residual emission detected in the Hα absorption profile measured contemporaneously to the VINCI/VLTI campaign on Achernar. They proposed an explanation for the strong flattening measured on Achernar (Domiciano de Souza et al. 2003) by adopting the hypothesis that the residual Hα emission and the associated near-IR continuum emission are formed in the remaining equatorial disk. However, considering the results from the present work, a significant fraction of the near-IR emission appears to originate in the polar envelope.

5. Conclusion

We have detected a diffuse circumstellar envelope around the bright Be star Achernar, which accounts for approximately 5% of the flux of the star in the near-IR (H and K bands). This envelope presents clear asymmetry with a significantly larger extension along the polar direction of the star. The photosphere of the star itself is distorted by the fast rotation with a larger equatorial angular diameter. The elongation of the CSE points to a significant polar wind, most probably powered by the hot temperature at the stellar poles (von Zeipel effect). Its total extension is loosely constrained by our observations, and it could reach large distances from the star. It appears that a complete astrophysical model able to simultaneously explain all observations (spectroscopic and interferometric) of Achernar is required. We are also confident that spectro-interferometric observations of Achernar with the VLTI/AMBER instrument will bring new insight into the gravity darkening, actual shape and relative intensity of the central star and its immediate circumstellar environment.

Acknowledgements. The interferometric measurements were obtained using the VINCI instrument installed at the VLTI. The VLTI is operated by the European Southern Observatory at Cerro Paranal, Chile. These data were obtained under an unreferenced P70 shared-risk programme and during the technical commissioning of the interferometer. Their processing made use of the wavelet-based technique developed by D. Ségransan (Observatoire de Genève) and integrated into the VINCI pipeline. Observations with the VLTI are only made possible through the efforts of the VLTI team, for which we are grateful. The VINCI public commissioning data reported in this paper were retrieved from the ESO/ST-ECF Archive (Garching, Germany). This research made use of the SIMBAD and VIZIER databases at the CDS, Strasbourg (France), and NASA's Astrophysics Data System Bibliographic Services. We thank Drs. O. Chesneau and J. A. de Freitas Pacheco for their enlightening suggestions.

References

Allen, C. W. 1973, Astrophysical quantities (London: University of London, Athlone Press), 3rd edn.
Balona, L. A., Engelbrecht, C. A., & Marang, F. 1987, MNRAS, 227, 123
Berger, J.-P., Haguenauer, P., Kern, P., et al. 2001, A&A, 376, 31
Bordé, P., Coudé du Foresto, V., Chagnon, G., & Perrin, G. 2002, A&A, 393, 183
Chauville, J., Zorec, J., Ballereau, D., et al. 2001, A&A, 378, 861
Claret, A., Diaz-Cordovez, J., & Gimenez, A. 1995, A&AS, 114, 247
Claret, A. 2000, A&A, 363, 1081
Cohen, M., Walker, R. G., Carter, B., et al. 1999, AJ, 117, 1864
Coudé du Foresto, V., Ridgway, S., & Mariotti, J.-M. 1997, A&AS, 121, 379
Di Folco, E., Thévenin, F., Kervella, P., et al. 2004, A&A, 426, 601
Damineli Neto, A., & de Freitas-Pacheco, J. A. 1982, MNRAS, 198, 659
Domiciano de Souza, A., Vakili, F., Jankov, S., Janot-Pacheco, E., & Abe, L. 2002, A&A, 393, 345
Domiciano de Souza, A., Kervella, P., Jankov, S., et al. 2003, A&A, 407, L47
Domiciano de Souza, A., Zorec, J., Jankov, S., et al. 2004, A&A, 418, 781
Domiciano de Souza, A., Kervella, P., Jankov, S., et al. 2005, A&A, 442, 567
Dougherty, S. M., & Taylor, A. R. 1992, Nature, 359, 808
Dougherty, S. M., Waters, L. B. F. M., Burki, G., et al. 1994, A&A, 290, 609
Dyck, H. M., van Belle, G. T., & Thompson, R. R. 1998, AJ, 116, 981
Gehrz, R. D., Hackwell, J. A., & Jones, T. W. 1974, ApJ, 191, 675
Glebocki, R., Gnacinski, P., & Stawikowski, A. 2000, Acta Astron., 50, 509
Glindemann, A., Abuter, R., Carbognani, F., et al. 2000, SPIE, 4006, 2
Glindemann, A., Albertsen, M., Avila, G., et al. 2004, SPIE, 5491, 447
Jackson, S., MacGregor, K. B., & Skumanich, A. 2004, ApJ, 606, 1196
Kervella, P., Coudé du Foresto, V., Glindemann, A., & Hofmann, R. 2000, SPIE, 4006, 31
Kervella, P., Gitton, Ph., Ségransan, D., et al. 2003, SPIE, 4838, 858
Kervella, P., Ségransan, D., & Coudé du Foresto, V. 2004a, A&A, 425, 1171
Kervella, P., Thévenin, F., Di Folco, E., & Ségransan, D. 2004b, A&A, 426, 297
Lebouquin, J.-B., Rousselet-Perraut, K., Kern, P., et al. 2004, A&A, 424, 719
McAlister, H. A., ten Brummelaar, T. A., Gies, D. R, et al. 2005, ApJ, 628, 439
Meilland, A., Stee, Ph., Vannier, M., et al. 2006, A&A, submitted
Ohishi, N., Nordgren, T. E., & Hutter, D. J. 2004, ApJ, 612, 463
Peters, G. J. 1982, ApJ, 253, L33
Petrov, R. G., & Amber Consortium, The 2003, EAS Publications Series, Observing with the VLTI, ed. G. Perrin, & F. Malbet, 6, 111
Quirrenbach, A., Bjorkman, K. S., Bjorkman, J. E., et al. 1997, ApJ, 479, 477
Richichi, A., & Percheron, I. 2005, A&A, 434, 1201
Ségransan, D., Forveille, T., Millan-Gabet, C. P. R., & Traub, W. A. 1999, in ASP Conf. Ser., 194, 290
Slettebak, A. 1982, ApJS, 50, 55
Stee, Ph., de Araujo, F. X., Vakili, F., et al. 1995, A&A, 300, 219
Stee, Ph., Vakili, F., Bonneau, D., & Mourard, D. 1998, A&A, 332, 268
Snow, T. P. 1981, ApJ, 251, 139
Tycner, C., Lester, J. B., Hajian, A. R., et al. 2005, ApJ, 624, 359
Van Boekel, R., Kervella, P., Schöller, M., et al. 2003, A&A, 410, 37
Vinicius, M. M. F., Zorec, J., Leister, N. V., & Levenhagen, R. S. 2006, A&A, 446, 643
von Zeipel, H. 1924, MNRAS 84, 665
Waters, L. B. F. M. 1986, A&A, 162, 121
Waters, L. B. F. M., Cote, J., & Lamers, H. J. G. L. M. 1987, A&A, 185, 206

4.3.5 Article Pour La Science “Les étoiles, déformées par leur rotation” (2005)

Cet article grand public a pour objectif de diffuser l'idée que les étoiles, et notamment les étoiles chaudes, peuvent présenter des déformations importantes dues à leur rotation. Pour ce faire, je fais le point sur les mesures interférométriques existantes d'étoiles en rotation rapide. Ce domaine étant en évolution rapide, je présente également les perspectives d'observation futures sur ces objets étonnants.

Fig. 4.10 – L'observatoire de Paranal, sous la conjonction de trois planètes : Vénus au centre, Mercure en bas et Saturne à gauche (photo S. Guisard).

Les étoiles, déformées

À l'instar du Soleil, les étoiles sont supposées sphériques. Toutefois, les astres tournant très vite sur eux-mêmes subissent d'énormes forces centrifuges, qui engendrent d'étonnantes déformations et modifient leur évolution.

Pierre Kervella

Vingt-neuf octobre 2001. Au cœur du désert d'Atacama, au Nord du Chili, les deux télescopes de huit mètres de diamètre *Antu* et *Melipal* du *Very Large Telescope* s'ouvrent doucement. Pour la première fois, ils vont observer ensemble la même cible, selon une technique nommée interférométrie qui décuple leur pouvoir de résolution. Pour ce baptême, c'est vers Achernar, la neuvième étoile la plus brillante du ciel, que les astronomes dirigent les deux miroirs. Cette étoile tourne sur elle-même 50 fois plus vite que le Soleil, la vitesse à l'équateur dépassant 250 kilomètres par seconde, et les chercheurs veulent observer les déformations qu'entraîne cette rotation effrénée. Les résultats sont stupéfiants : Achernar est aplatie comme une dragée, son disque apparent étant plus d'une fois et demie plus long que large ! En comparaison, l'aplatissement du Soleil est infime, puisque son diamètre équatorial n'est que 1,00001 fois supérieur à son diamètre polaire. Quelle est la cause d'une telle déformation ? Pour le comprendre, détaillons les conséquences de la rotation des étoiles sur leur forme et sur leur fonctionnement. Après avoir évoqué les observations récentes, nous examinerons les modèles élaborés pour décrire ces objets atypiques, puis nous décrirons l'impact d'une rotation rapide sur la vie d'une étoile.

Beaucoup des astres familiers sont presque parfaitement sphériques. La Terre, la Lune, le Soleil présentent des formes indiscernables de sphères parfaites, sauf à les mesurer avec précision. La forme sphérique résulte d'un équilibre universel entre pression et gravité. Pourtant, dans l'Univers, tout est en mouvement. Les galaxies, les étoiles, les planètes tournent sur elles-mêmes. Cette rotation privilégie un axe de l'espace et brise la symétrie et l'équilibre de la sphère. Le Soleil tourne lentement sur lui-même en 26 jours, mais de nombreuses étoiles, en particulier les plus chaudes, tournent jusqu'à 100 fois plus vite, effectuant une révolution en seulement quelques heures. Leur vitesse de rotation atteint plusieurs centaines de kilomètres par seconde à l'équateur. Il en résulte une force centrifuge colossale, qui déforme ces boules de gaz tournoyantes et modifie leur machinerie.

Deux des plus brillantes étoiles en rotation rapide sont Achernar et Altaïr. Située à 144 années-lumière dans la constellation de l'Eridan, Achernar est une étoile naine bleue très chaude, dont la température de surface atteint 20 000 kelvins. Avec 8 500 kelvins, Altaïr est moins brûlante, mais néanmoins plus chaude que le Soleil (5 700 kelvins). Au-delà de ces deux exemples, on connaît aujourd'hui plusieurs milliers d'étoiles naines en rotation rapide, et ce phénomène est même la norme pour les étoiles les plus chaudes (les étoiles bleues).

La rotation d'une étoile se traduit par l'étalement de ses raies spectrales par effet Doppler. En raison de la rotation, les raies du spectre de rayonnement émis par la partie du disque de l'étoile qui se rapproche de l'observateur sont décalées vers le bleu ; inversement, ces mêmes raies produites par la partie qui s'éloigne sont décalées vers le rouge. Comme le spectre observé intègre la lumière provenant de l'ensemble du disque visible, les composantes décalées vers le rouge s'ajoutent à celles décalées vers le bleu, et les raies spectrales apparaissent élargies *(voir la figure 3)*. Cet effet permet d'estimer la vitesse de rotation apparente des étoiles. Les raies spectrales d'Achernar et Altaïr sont ainsi considérablement élargies, et correspondent à une vitesse de rotation de 225 kilomètres par seconde à l'équateur. En comparaison, la vitesse équatoriale du Soleil n'est que de deux kilomètres par seconde.

Ces vitesses endiablées ne sont de surcroît que des valeurs minimales. En effet, l'analyse spectroscopique n'indique pas l'inclinaison de l'axe de rotation des étoiles observées par rapport à la ligne de visée. La vitesse mesurée est la projection de la vitesse réelle sur la ligne de visée, et lui est donc inférieure. Elle correspond à la vitesse réelle si l'étoile est vue

par leur rotation

1. L'étoile bleue Achernar, une boule de gaz 12 fois plus grande et six fois plus massive que le Soleil, chauffée à 20 000 degrés, tournoie dans l'espace comme une toupie avec, à l'équateur, une vitesse dépassant 250 kilomètres par seconde. Cette rotation altère la forme de l'étoile : une énorme force centrifuge la rend plus d'une fois et demie plus large que haute, et la région équatoriale est refroidie tandis que les pôles rayonnent intensément.

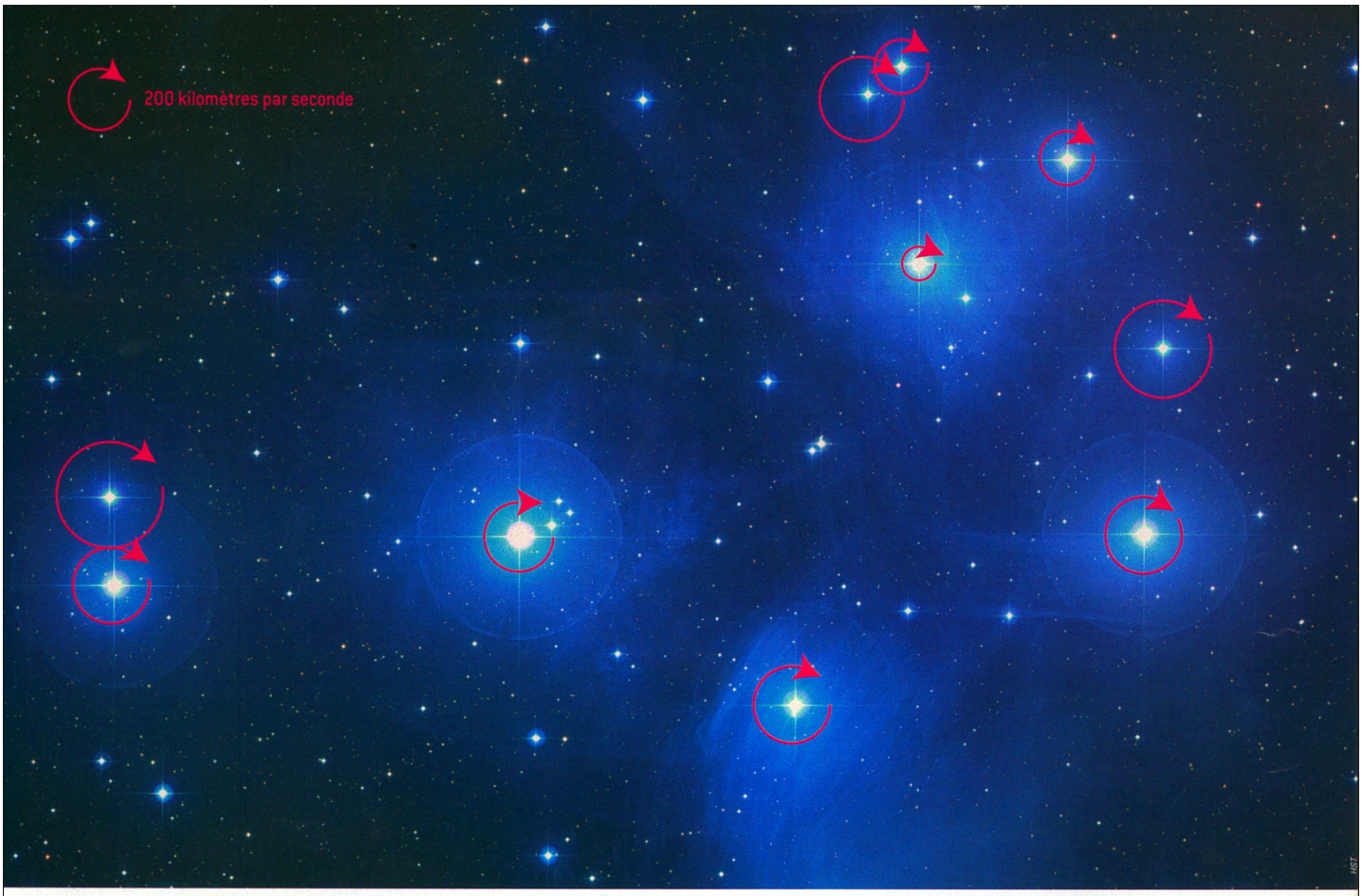

2. L'amas des Pléiades, situé à 440 années-lumière, est formé d'étoiles jeunes tournant rapidement sur elles-mêmes. Les étoiles les plus chaudes se sont allumées ensemble il y a seulement une centaine de millions d'années et la plupart gardent des vitesses de rotation atteignant 350 kilomètres par seconde. En raison de l'incertitude sur l'orientation de l'axe de rotation, les vitesses mesurées sont les valeurs minimales des vitesses réelles *(le diamètre des cercles rouges est proportionnel à la vitesse de rotation équatoriale)*. Cette uniformité suggère que la majorité des étoiles jeunes et massives tournent rapidement, et que les formes aplaties sont la norme plutôt que l'exception.

selon l'équateur et, *a contrario*, une étoile en rotation rapide vue depuis son pôle semble tourner très lentement. Véga, dans la constellation de la Lyre, présente ainsi un spectre semblable à celui d'une étoile normale et une forme circulaire, mais on pense qu'il s'agit d'une étoile en rotation rapide vue par le pôle. Austin Gulliver, de l'Université de Brandon au Canada, a en effet mis en évidence un léger élargissement des raies les plus faibles de son spectre. Ainsi, bien qu'Achernar et Altaïr aient la même vitesse de rotation apparente, peut-être ne tournent-elles pas au même rythme.

Observer directement la forme et la répartition de luminosité à la surface des étoiles permettrait de lever le voile sur leur vitesse de rotation réelle. Le diamètre apparent des étoiles, même les plus proches, ne dépasse cependant pas quelques millièmes de seconde d'angle, l'équivalent d'une pièce de un euro observée à 1 500 kilomètres. Seule l'interférométrie permet de les distinguer avec précision. Cette technique consiste à observer un objet céleste avec plusieurs télescopes espacés, puis à recombiner les images. L'infime décalage entre les trajets des rayons lumineux d'un télescope à l'autre provoque des figures d'interférence qui nous renseignent sur la taille, la forme et la luminosité de l'objet. La résolution théorique d'un interféromètre est celle d'un miroir virtuel d'un diamètre équivalent à la distance séparant les télescopes – la base –, tandis que la luminosité est la somme de celle des miroirs utilisés.

La dernière génération d'interféromètres, tels le VLTI européen (pour *Very large telescope interferometer*), le NPOI (*Navy prototype optical interferometer*, ou prototype d'interféromètre optique de la marine) et le PTI (interféromètre de test du mont Palomar) américains, dont les bases atteignent plusieurs dizaines à plusieurs centaines de mètres, a aujourd'hui un pouvoir de résolution angulaire suffisant pour mesurer la forme des étoiles proches.

Deux télescopes pour un profil

Cependant, même les mesures avec ces interféromètres sont incomplètes. La longueur de la base interférométrique imposée ne permet pas d'observer l'astre visé sous différentes échelles, et la luminosité du dispositif est très faible. Un interféromètre ne fournit en particulier qu'une information partielle sur la répartition de lumière à la surface de l'étoile – la photosphère. L'équipe d'Armando Domiciano de Souza, de l'Université de Nice, a néanmoins tiré parti d'une technique dite de supersynthèse pour mesurer en 2001 la taille d'Achernar selon différentes directions à l'aide du VLTI. En observant l'étoile continûment durant une nuit, on bénéficie de la rotation diurne de la Terre, qui fait varier l'orientation et la longueur de la base projetée sur le plan du ciel. On peut ainsi mesurer la taille de l'étoile sous différents angles. Les astronomes ont découvert que le disque

d'Achernar est 1,56 fois plus long que large. C'est de loin l'étoile la plus déformée connue à ce jour. De surcroît, la luminosité de sa photosphère n'est pas homogène.

L'effet de supersynthèse intervient également à une moindre échelle dans les observations d'Altaïr réalisées en 2001 par Gérard Van Belle, du *Jet propulsion laboratory* de la NASA, avec le PTI. Ces observations ont révélé que l'aplatissement de cette étoile naine n'est « que » de 1,14. L'effet intervient aussi dans les observations de Naoko Ohishi, de l'Observatoire du Japon, qui a mesuré avec le NPOI la répartition de lumière sur l'étoile, révélant l'existence d'une tache brillante dont nous verrons qu'elle indique sans doute la position du pôle. Ces dernières semaines, l'équipe de Hal McAlister, de l'Université de Géorgie, est entrée dans la course en annonçant avoir mesuré grâce au réseau de télescopes américain CHARA (*Center for High Angular Resolution Astronomy*, ou Centre pour l'astronomie à haute résolution angulaire) que l'aplatissement de Regulus, la plus brillante étoile de la constellation du Lion connue pour tourner sur elle-même à une vitesse record de 305 kilomètres par seconde, atteint 1,18.

La rotation bouscule l'équilibre

Bien que l'interférométrie donne accès à l'aplatissement apparent des étoiles en rotation, ces informations sont insuffisantes pour les caractériser totalement. Du seul profil de l'étoile et de sa vitesse de rotation apparente, il est impossible de déduire directement la forme de l'astre en trois dimensions. Si l'on arrivait à localiser les pôles de l'étoile, on en déduirait son inclinaison par rapport à la ligne de visée et donc sa vitesse de rotation et sa forme réelles. Cette idée est sur le point d'aboutir mais, pour l'instant, les astronomes sont contraints d'imaginer la structure des étoiles en rotation et de comparer ces modèles aux observations pour en estimer la pertinence.

La rotation joue un rôle primordial dans la vie des étoiles. Une étoile se forme à partir de l'effondrement gravitationnel d'un nuage de gaz sur lui-même. La matière du nuage tombe en formant un disque de poussière et de gaz en rotation, au centre duquel l'étoile se constitue. La « quantité de rotation » du nuage initial se transmet ainsi et se concentre dans l'étoile, dont la vitesse de rotation augmente en vertu de la conservation du moment cinétique. Le moment cinétique d'un objet ponctuel en rotation autour d'un axe extérieur est le produit de sa masse, de sa vitesse de rotation et de sa distance à l'axe de rotation (cette définition se généralise aux cas d'un objet non ponctuel et d'un axe passant par lui). Pour un système isolé, le moment cinétique est conservé. C'est pourquoi une patineuse tournant sur elle-même accélère sa rotation lorsqu'elle rapproche les bras le long de son corps.

Au cours de la vie d'une étoile, le moment cinétique hérité du nuage primordial se conserve globalement, mais est redistribué dans le système que forment l'étoile et son cortège de planètes. Dans le Système solaire, le mouvement orbital des planètes représente ainsi 97 pour cent du moment cinétique total, bien que 99 pour cent de la masse soient contenus dans le Soleil. D'autres mécanismes redistribuent le moment cinétique aussi bien à l'intérieur qu'à l'extérieur de l'étoile. Le champ magnétique, en particulier, joue un grand rôle dans le cas des étoiles peu massives comme le Soleil. Les lignes de champ internes à l'étoile exercent une résistance à la déformation de sorte qu'elles uniformisent et ralentissent la rotation de la matière au sein de l'étoile. Celles qui s'échappent à l'extérieur s'appuient sur le gaz ionisé du milieu environnant et freinent également la rotation de l'astre. La plupart des étoiles âgées tournent ainsi lentement. Le champ magnétique des jeunes étoiles massives comme Achernar est cependant beaucoup plus faible, de sorte que le transfert de moment cinétique vers l'extérieur est moins efficace. Ces étoiles conservent l'essentiel de leur vitesse de rotation initiale.

Quand elle est rapide, la rotation joue un rôle clé dans l'équilibre des étoiles. Une étoile est une masse de gaz chaud en équilibre sous l'effet de deux forces antagonistes : la gravitation, qui tend à la contracter, et la pression du gaz et du rayonnement engendrée par les réactions thermonucléaires qui se déroulent en son sein, qui tend à la dilater. La surface apparente de l'étoile, la photosphère, est l'endroit où cet équilibre est réalisé, avec la condition supplémentaire que le gaz y soit suffisamment peu dense et donc transparent pour que les photons s'en échappent en ligne droite sans être réabsorbés. Elle est habituellement sphérique. Dans une étoile en rotation, les forces centrifuges ajoutent une composante à cet équilibre. Son effet équivaut à une diminution locale de la gravité, variable selon la latitude ; c'est pourquoi le rayon de l'étoile à l'équateur, où cette diminution est maximale, augmente. Ainsi, la force centrifuge du Soleil à son équateur est égale à 0,002 pour cent de la force de gravité, et l'aplatissement de l'astre – le rapport entre le diamètre équatorial et le diamètre polaire – vaut 1,00001 ; cela correspond à une différence d'à peine dix kilomètres entre le rayon à l'équateur et celui aux pôles.

L'astronome hollandais Christiaan Huygens est le premier à étudier, au XVII^{e} siècle, le problème de la déformation d'une sphère de gaz en rotation. Pour ce faire, il néglige la masse du gaz, qu'il rassemble en un point au centre de la

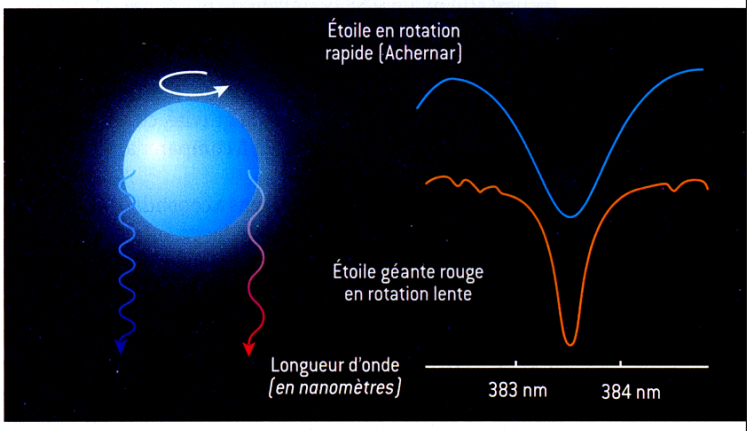

3. Le spectre d'une étoile en rotation rapide contient des raies élargies. Les raies émises par la partie du disque stellaire qui se rapproche de l'observateur lors de la rotation sont décalées vers le bleu par effet Doppler ; ces mêmes raies sont décalées vers le rouge lorsqu'elles sont produites par la partie qui s'éloigne *(à gauche)*. Le spectre observé regroupant la lumière de l'ensemble du disque, les raies obtenues, somme des composantes décalées, apparaissent élargies *(à droite)*. Cet effet indique la vitesse de rotation des étoiles, soumise à l'incertitude sur l'inclinaison de leur axe.

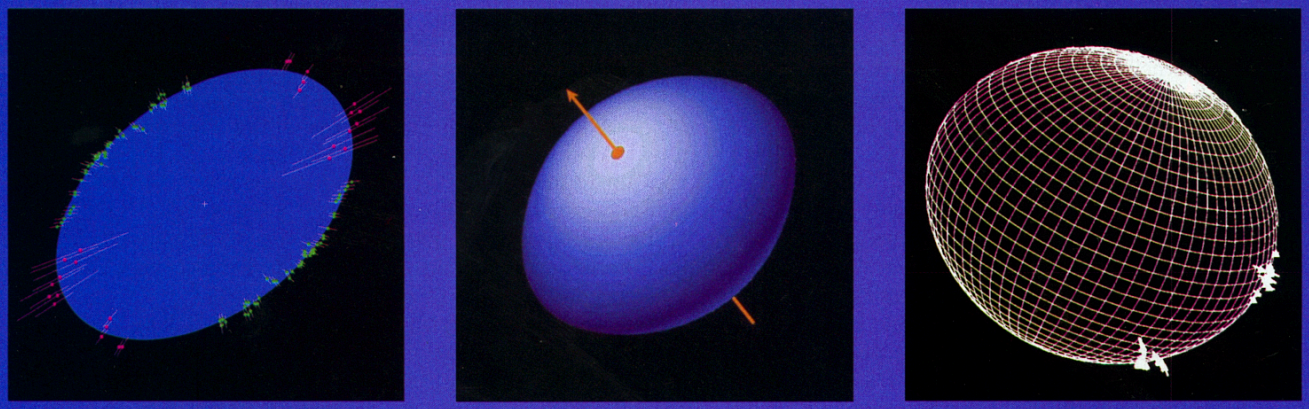

4. Le profil d'Achernar obtenu par l'interféromètre du Très grand télescope européen, le VLTI *(à gauche, les points de mesure sont en vert et en rouge)*, présente un aplatissement record : le rapport du grand et du petit axe de l'ellipse apparente vaut 1,56. Le modèle supposant que l'étoile tourne « d'un bloc » *(au centre)* n'explique pas totalement l'aplatissement. L'introduction d'une rotation différentielle – variant avec la distance à l'axe – est nécessaire. En revanche, pour Altaïr, un modèle de corps solide similaire reproduit l'aplatissement, égal à 1,14 *(à droite)*.

sphère et suppose que la boule de gaz tourne « en bloc » autour d'un axe passant par le centre. Lorsque chacun des éléments tourne à la même vitesse angulaire, on parle de corps solide en rotation. Dans un tel modèle où l'étoile est assimilée à un solide en rotation, l'aplatissement est égal à la moitié du rapport entre la force centrifuge et la gravité de surface, plus un. Cette loi est valable en première approximation, car l'essentiel de la masse d'une étoile est ramassé en son centre.

L'aplatissement d'Achernar est bien supérieur à celui du Soleil : avec un rayon équatorial 12 fois supérieur et une masse six fois plus élevée, la force de gravitation à l'équateur est du même ordre que celle régnant à la surface de la Terre. En revanche, sa vitesse équatoriale est estimée à 290 kilomètres par seconde à partir de la vitesse mesurée et de l'hypothèse qu'il s'agit d'un corps solide. La force centrifuge atteint alors 88 pour cent de la gravité. L'aplatissement donné par l'approximation de Huygens est de 1,44, une valeur proche de l'aplatissement mesuré par interférométrie (1,56). Sur Altaïr, plus petite, la force centrifuge n'est « que » de 34 pour cent de la gravité, ce qui donne un aplatissement théorique de 1,17, à comparer avec l'aplatissement observé, 1,14.

L'approche simple de Huygens a cependant ses limites, et ne permet pas d'expliquer de façon totalement satisfaisante les observations. Le physicien britannique James Hopwood Jeans a construit, après la Première Guerre mondiale, une série de modèles pour différentes équations d'état du gaz dont sont formées les étoiles en rotation (une équation d'état est une relation entre des grandeurs thermodynamiques telles que la température, la pression et le volume). Il a ainsi considéré des masses de gaz présentant différents degrés de condensation centrale. Ces modèles, dits polytropes, sont caractérisés par un indice polytropique d'autant plus petit que la masse est regroupée au centre de l'étoile. Si cet indice dépasse un certain seuil, c'est-à-dire si la masse devient moins concentrée au cœur de l'étoile, la force centrifuge surpasse la force de gravité à l'équateur et l'étoile perd de la masse. D'où l'hypothèse formulée en 1931 par l'astronome d'origine russe Otto Struve que les étoiles dites *Be*, des étoiles très chaudes dont la raie d'émission H_α de l'hydrogène est très prononcée, telle Achernar, tournent rapidement sur elles-mêmes à la limite de la dislocation, et qu'elles sont entourées d'un anneau de matière gazeuse qui s'échappe à l'équateur sous l'effet de la force centrifuge. De fait, la résultante de la gravité et de la force centrifuge à l'équateur d'Achernar n'atteint que deux newtons par kilogramme, si bien que de la matière s'en échappe parfois sous l'effet d'une éruption stellaire, même très modeste. Le gaz dilué éjecté de la surface est alors responsable de l'émission dans la raie H_α. Parallèlement à ces découvertes sur la physique des masses fluides en rotation, les études sur le transport de l'énergie dans les étoiles avaient progressé, ce qui a conduit l'Anglais Edward Milne, puis l'Indien Subrahmanyan Chandrasekhar à construire les premiers modèles physiques complets d'étoiles polytropiques déformés par la rotation.

La rotation allonge la durée de vie

En 1924, alors que la source d'énergie des étoiles était encore inconnue, l'astronome suédois Hugo von Zeipel démontre que le flux radiatif d'une étoile par unité de surface est proportionnel à la gravité effective locale. Plus la gravité est forte, plus la pression et la température de l'atmosphère stellaire doivent être élevées pour que l'équilibre soit maintenu, de sorte que le flux rayonné augmente. Il en déduit que l'énergie rayonnée par une étoile en rotation est plus élevée aux pôles qu'à l'équateur. La force centrifuge diminue en effet la gravité effective à l'équateur, de sorte que la température du gaz et la quantité de rayonnement y sont plus faibles. Von Zeipel prédit alors qu'une étoile écrasée par une rotation rapide doit présenter des taches chaudes et brillantes aux pôles. Cet effet commence aujourd'hui à

être vérifié grâce aux observations interférométriques, et nous verrons qu'il joue un rôle clé dans la compréhension des étoiles en rotation rapide.

Peu après ces prédictions, l'Anglais Arthur Eddington déduit l'existence d'une circulation de matière dite méridienne entre le pôle et l'équateur des étoiles en rotation. La matière se déplace lentement, dans les couches supérieures de l'étoile, des pôles chauds vers l'équateur plus froid, où elle replonge vers les couches profondes avant de ressortir à nouveau par les pôles. Ce brassage peut augmenter la durée de vie des étoiles en rotation rapide de plus de 25 pour cent par rapport à des astres de même masse et de même composition chimique tournant lentement, car il ramène l'hydrogène des couches externes vers le cœur où a lieu la fusion thermonucléaire.

De façon générale, plus une étoile tourne vite sur elle-même, plus elle vit longtemps. Partant d'une évolution conditionnée par la masse de l'étoile et par sa composition chimique, il est ainsi apparu indispensable d'introduire dans les modèles une variable supplémentaire, la vitesse de rotation.

Une palette de formes exotiques

Si les modèles de corps solides en rotation expliquent en première approximation l'aplatissement des étoiles, ils ont atteint leur limite avec les observations récentes d'Achernar. Un aplatissement de 1,56 ne peut s'expliquer dans le cadre d'une rotation uniforme. Cela impliquerait une vitesse de rotation dépassant le seuil au-delà duquel l'étoile se disloquerait. Dans le cas de Regulus, les calculs de H. McAlister montrent que si sa vitesse était supérieure de dix pour cent à la valeur actuelle, l'étoile se disloquerait.

La solution est de supposer que les différentes couches de l'étoile ne tournent pas toutes à la même vitesse. Une telle rotation, dite différentielle, se déroule par exemple dans le disque du Système solaire : la période de révolution des planètes est d'autant plus courte qu'elles sont proches de notre étoile. En introduisant une vitesse de rotation interne dépendant de la distance à l'axe polaire, les astrophysiciens construisent des modèles plus réalistes.

Il est cependant impossible de déterminer la rotation interne de l'étoile sur la base des seules mesures spectroscopiques. Les observations interférométriques actuellement disponibles ne permettent pas de résoudre ce problème : elles donnent la forme de l'étoile, qui n'apporte aucune information directe sur le profil radial de la vitesse de rotation interne, tandis que la répartition de lumière à la surface reste mal déterminée. La rotation différentielle n'est donc pas un paramètre facile à introduire dans un modèle et, de fait, la plupart des modèles numériques d'étoiles continuent de prendre comme hypothèse de départ un corps solide en rotation. Néanmoins, moyennant des mesures interférométriques précises de la répartition de lumière sur la photosphère de l'étoile, il est possible de déterminer des contraintes suffisamment fortes pour en déduire une loi approchée de rotation interne.

En considérant que la vitesse angulaire décroît en fonction de l'inverse du carré de la distance à l'axe de l'étoile, Stephen Jackson, du Centre de recherches sur l'atmosphère

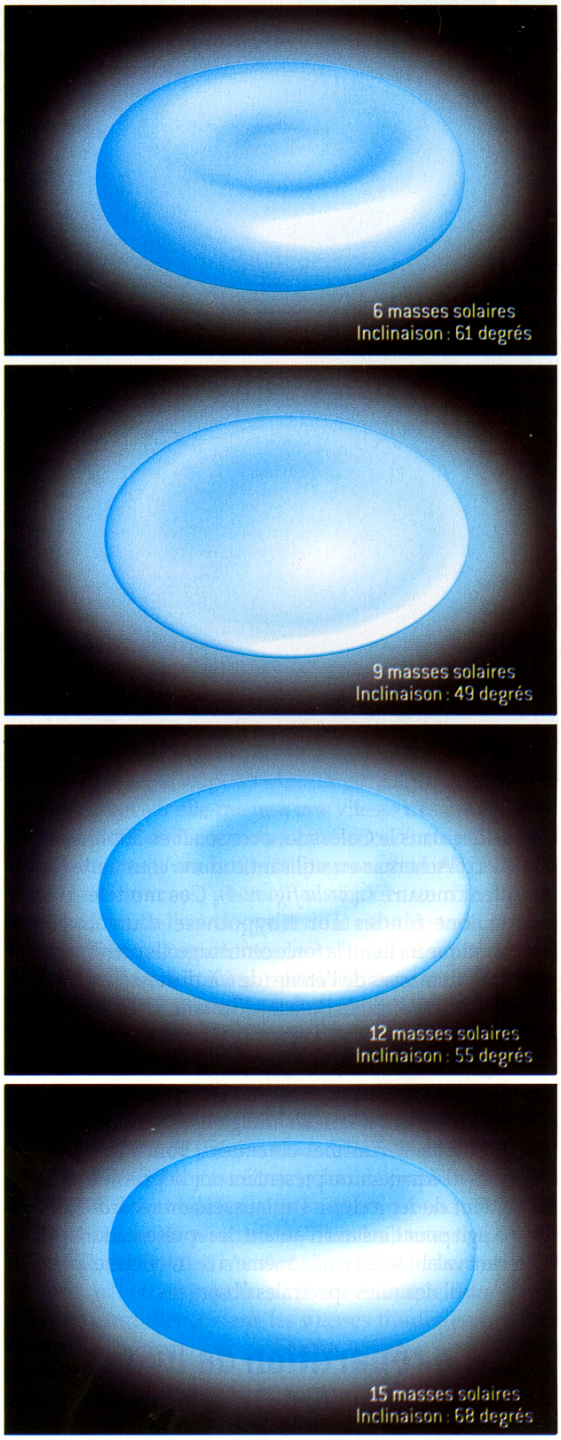

5. L'introduction de la rotation différentielle dans les modèles d'étoiles en rotation multiplie les structures compatibles avec les profils observés. En supposant que les différentes couches ne tournent pas à la même vitesse, les aplatissements obtenus peuvent être extrêmes sans que l'étoile ne se disloque. Les quatre modèles ci-dessus, fondés sur une vitesse angulaire interne décroissant comme l'inverse du carré de la distance à l'axe de l'étoile, reproduisent le profil observé d'Achernar. Ils correspondent à des étoiles de 6 à 15 masses solaires et à différents paramétrages de la rotation interne *(rapide au centre pour a et b, plus lente pour b et c)*. Toutefois, ces modèles reproduisent imparfaitement le spectre lumineux de l'étoile.

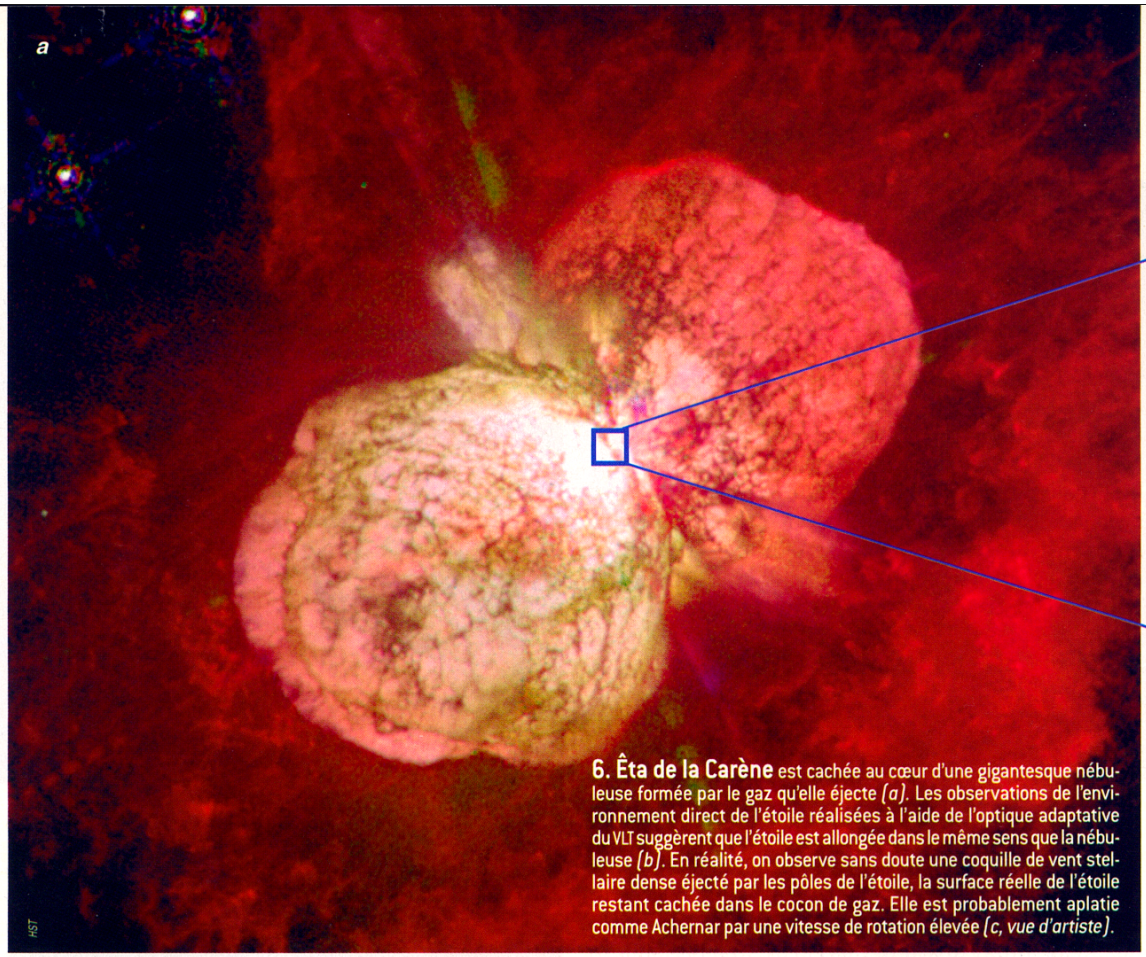

6. Êta de la Carène est cachée au cœur d'une gigantesque nébuleuse formée par le gaz qu'elle éjecte *(a)*. Les observations de l'environnement direct de l'étoile réalisées à l'aide de l'optique adaptative du VLT suggèrent que l'étoile est allongée dans le même sens que la nébuleuse *(b)*. En réalité, on observe sans doute une coquille de vent stellaire dense éjecté par les pôles de l'étoile, la surface réelle de l'étoile restant cachée dans le cocon de gaz. Elle est probablement aplatie comme Achernar par une vitesse de rotation élevée *(c, vue d'artiste)*.

de Boulder, dans le Colorado, a construit en 2004 plusieurs modèles d'Achernar en utilisant comme contrainte l'aplatissement mesuré *(voir la figure 4)*. Ces modèles numériques sont fondés sur l'hypothèse d'un équilibre hydrostatique incluant la force centrifuge. Ils correspondent à différentes masses de l'étoile (de 6 à 15 masses solaires) et différents paramétrages de la loi de rotation interne (plus ou moins rapide au centre de l'étoile). En raison de la rotation ultrarapide du cœur de l'étoile introduite arbitrairement dans ces modèles, les aplatissements obtenus peuvent être extrêmes sans que l'étoile n'atteigne la vitesse critique et ne se disloque. Les formes obtenues – bombées aux pôles et aplaties à l'équateur, ou présentant une dépression polaire – permettent de reproduire l'aplatissement record d'Achernar. Il s'agit pour l'instant d'autant de représentations potentiellement valables de l'étoile, même si ces modèles expliquent mal le profil des raies spectrales observées.

La répartition de luminosité éclaire l'orientation

Quel est le modèle qui correspond à la réalité ? Pour le savoir, des mesures supplémentaires sont indispensables. Comme l'ont démontré les observations d'Altaïr, l'interférométrie permet d'obtenir davantage que le simple profil de l'étoile. Grâce à la répartition de luminosité à la surface de l'astre, on peut préciser l'orientation de l'étoile. La surbrillance polaire due à l'effet Von Zeipel est l'une des clés pour explorer la structure interne des étoiles en rotation rapide. En la localisant, on déduit la position des pôles et donc l'inclinaison de l'étoile. Grâce à cette information supplémentaire, on déduit du profil la forme en trois dimensions et la vitesse de rotation réelle de l'étoile.

Cette méthode pourrait être appliquée pour déterminer l'aplatissement d'Altaïr. Au vu de la vitesse de rotation et de l'aplatissement mesurés, la tache brillante localisée par Naoko Ohishi est compatible avec la position attendue du pôle dans un modèle de corps solide. Ces observations sont cependant trop parcellaires (l'excès de lumière est faible) pour autoriser l'étalonnage des modèles. L'aplatissement de 1,14 d'Altaïr reste pour l'instant bien expliqué dans le cadre d'un modèle de corps solide, et cette étoile n'est pas un test suffisamment discriminant pour les modèles.

Les récentes observations de Regulus, qui suggèrent que la température de la photosphère atteint par endroits 15000 kelvins contre 10000 ailleurs, sont susceptibles de révéler la position de l'axe de rotation de cette étoile par le même principe. Dans le cas d'Achernar, les observations actuelles – à deux télescopes – n'ont permis de reconstituer que le profil de l'étoile, mais l'étoile sera bientôt une cible privilégiée pour le nouvel instrument AMBER du VLTI. Les observations combinées de trois télescopes seront à même de localiser une éventuelle surbrillance polaire, ce qui opérerait une sélection radicale parmi les différents modèles de l'étoile.

L'effet Von Zeipel n'est pas seulement une aubaine pour les observateurs. Il contribue aussi à la perte de masse des étoiles. Durant la plus grande partie de leur vie, les étoiles chaudes perdent leur moment cinétique essentiellement par l'émission d'un vent ténu de gaz et de particules chargées, le vent stellaire. Plus elles sont chaudes, plus leur vent stellaire est intense : le rayonnement très énergétique produit par la

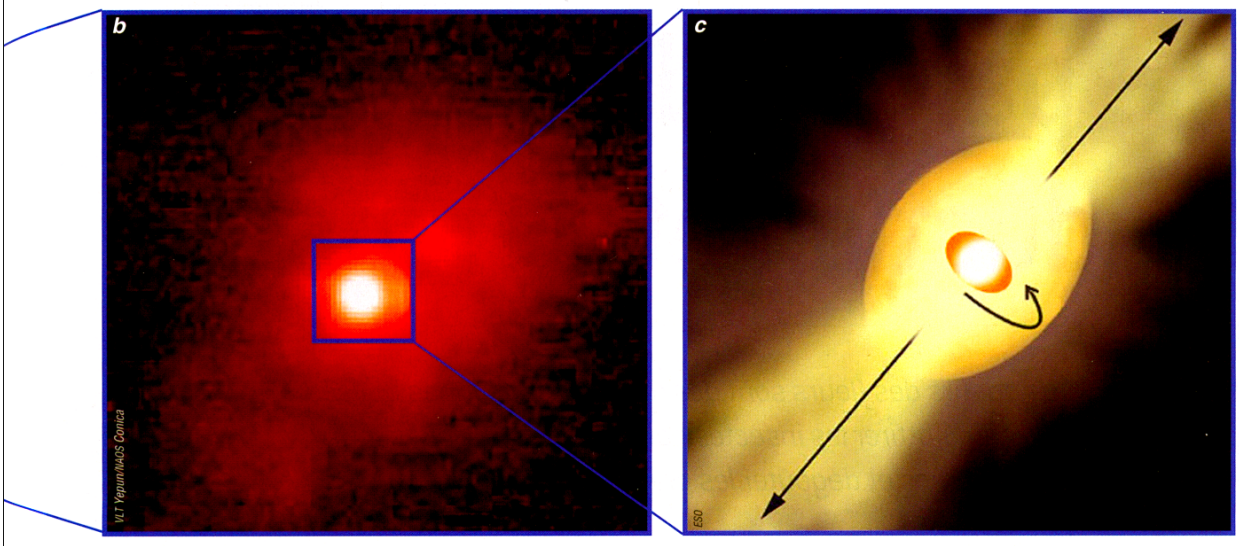

photosphère surchauffée pousse les atomes de gaz avec force et en arrache une partie à l'attraction de l'étoile pour les propulser dans l'espace interstellaire. Dans le cas des étoiles les plus chaudes en rotation rapide, l'énergie rayonnée étant plus grande aux pôles à cause de l'effet Von Zeipel, le vent stellaire est chaud et rapide au-dessus des pôles tandis qu'il est plus froid et lent à l'équateur. Contrairement à l'intuition, l'étoile perd de la masse essentiellement par les pôles, et non par l'éjection équatoriale due à la force centrifuge.

Êta de la Carène, un monstre au souffle chaud

Ce vent stellaire polaire est d'une importance capitale dans la vie des étoiles extrêmement massives comme Êta de la Carène. Située à environ 7 000 années-lumière, Êta de la Carène est intrinsèquement la plus brillante des étoiles de notre galaxie et est probablement plus de 100 fois plus massive que le Soleil. Son vent stellaire est si dense qu'il en devient opaque et la masque complètement. La perte de moment cinétique due à ce mécanisme est beaucoup plus importante que pour Achernar. Elle influe notablement sur son évolution, notamment du fait de pertes de masse rapides et violentes. On estime que la masse initiale d'Êta de la Carène atteignait environ 160 masses solaires, et qu'elle a perdu plusieurs dizaines de masses solaires en à peine trois millions d'années d'existence. Elle expulse, encore actuellement, l'équivalent de plusieurs fois la masse de la Terre chaque jour ! Êta de la Carène est entourée d'une nébuleuse en forme de sablier, fruit d'une gigantesque éruption stellaire survenue en 1841, et qui s'agrandit d'année en année. L'étoile connaîtra sans doute une fin très violente dans les prochains siècles ou millénaires.

Êta de la Carène a été observée en 2003 à l'aide du VLTI par l'équipe de Roy Van Boekel, de l'Observatoire austral européen (ESO), qui a employé comme pour Achernar la technique de supersynthèse interférométrique. L'étoile présente un aspect allongé, comme un ballon de rugby aligné avec l'axe de la nébuleuse bipolaire. Cet allongement selon l'axe de rotation semble paradoxal, mais, en réalité, le vent stellaire nous donne une image déformée d'Êta de la Carène. Nous observons le vent stellaire dense, chaud et opaque qui s'échappe à plusieurs centaines de kilomètres par seconde des pôles brillants de l'étoile, tandis que l'étoile elle-même reste masquée. Dissimulée dans son cocon opaque, elle est vraisemblablement aplatie comme Achernar. Pour que l'éjection de matière par les pôles soit si importante, l'étoile tourne probablement sur elle-même à une vitesse très proche de la vitesse critique de dislocation. La présence d'un disque équatorial, ou même d'une étoile compagnon comme le prédisent certains astronomes, pourrait aussi jouer un rôle dans la conformation de l'enveloppe et de la nébuleuse d'Êta de la Carène. Pratiquement toutes les nébuleuses entourant les étoiles chaudes et lumineuses présentent une structure bipolaire semblable à celle d'Êta de la Carène, dont la formation apparaît intimement liée à la rotation de l'objet central.

Les étoiles en rotation rapide présentent une remarquable variété de phénomènes physiques : déformation, rotation différentielle, circulation méridienne, effet Von Zeipel… Autant de précieux indices sur les mécanismes à l'œuvre dans ces objets célestes, dont la prise en compte a conduit à des modèles numériques reproduisant de mieux en mieux les observations. Tous les processus propres aux étoiles en rotation ne sont cependant pas encore bien compris, et le transport du moment cinétique ainsi que le rôle de la turbulence dans les masses fluides en rotation restent des domaines de recherche actifs.

Pierre KERVELLA est astronome adjoint à l'Observatoire de Paris-Meudon.

Auteur & Bibliographie

A. DOMICIANO DE SOUZA et *al.*, *The spinning-top Be star Achernar from VLTI-VINCI*, in *Astronomy and Astrophysic Letters*, vol. 407, pp. 47-50, 2003.

J.-L. TASSOUL, *Stellar rotation*, Cambridge University Press, 2000.

A. MAEDER et G. MEYNET, *The evolution of rotating stars*, in *Annual Review of Astronomy and Astrophysics*, vol. 38, pp. 143–90, 2000.

K. DAVIDSON et R. HUMPHREYS, *Eta Carinae and its environment*, in *Annual Review of Astronomy and Astrophysics*, vol. 35, pp. 1-32, 1997.

4.4 Véga (α Lyr)

4.4.1 Une géométrie particulière

Véga (A0V) est une étoile particulièrement importante car elle est restée longtemps la référence du système des magnitudes astronomiques. Les observations obtenues par Peterson et al. (2004) à l'aide de l'interféromètre NPOI (Fig. 4.11) ne montrent pas d'aplatissement du disque visible de cette étoile. La raison de cette absence de déformation est que la configuration géométrique de cette étoile naine (type spectral A0V) est très particulière : vue presque parfaitement par le pôle (inclinaison de 5° seulement sur la ligne de visée), son profil apparaît circulaire. Seule la répartition de la lumière à sa surface indique sa rotation rapide, car elle présente un profil d'assombrissement à l'équateur caractéristique de l'effet Von Zeipel. Grâce à ces mesures, on estime qu'elle tourne sur elle-même avec une vitesse équatoriale réelle de 230 km/s, et un aplatissement réel de $\Gamma = 24\%$.

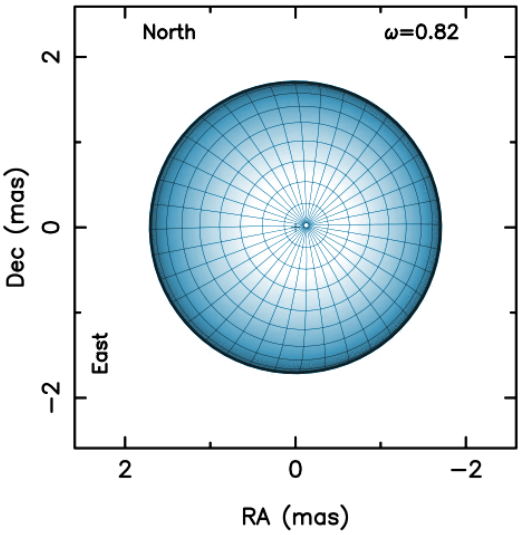

FIG. 4.11 – Modèle de Véga, construit à partir des observations de l'interféromètre NPOI enregistrées par Peterson et al. (2004). Cette étoile est vue pratiquement par le pôle.

4.4.2 Observations récentes avec CHARA

Grâce à des observations obtenues avec l'interféromètre CHARA et l'instrument FLUOR, nous avons pu mesurer avec précision le profil d'assombrissement centre-bord de Véga. Du fait de l'orientation particulière de Véga sur le ciel, ces observations permettent d'étudier l'effet Von Zeipel sans être gêné par l'incertitude sur l'orientation de l'étoile. La Fig. 4.12 montre le modèle d'assombrissement centre-bord et rotationnel de Véga obtenu à l'aide des observations de CHARA. La grande précision de ces mesures permet de montrer que l'assombrissement centre-bord n'est pas celui d'une étoile normale de ce type spectral sans rotation, et un modèle incluant la rotation explique les observations de manière satisfaisante.

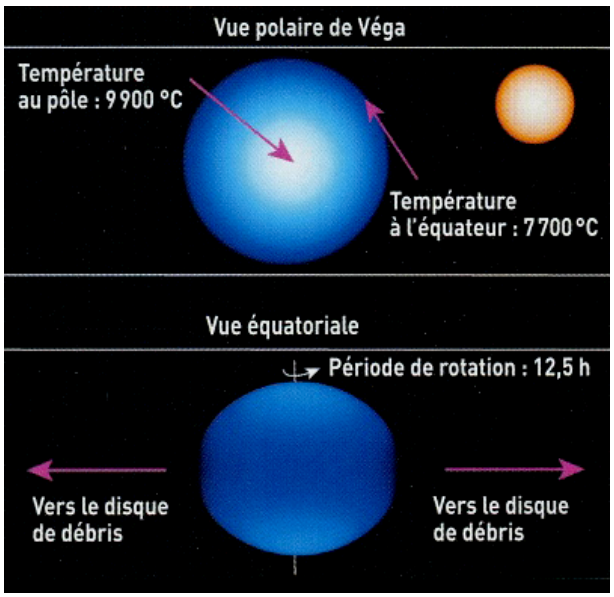

FIG. 4.12 – Modèle de Véga obtenu à l'aide des observations de l'interféromètre CHARA. Le Soleil est représenté en haut à droite pour donner l'échelle. Véga est par ailleurs entourée d'un disque de débris, probablement contenu dans son plan équatorial (figure du bas).

4.4.3 Article ApJ : "First results from the CHARA array. VII. Long-baseline interferometric measurements of Vega consistent with a pole-on, rapidly rotating star" (2006)

Les observations obtenues à l'aide de l'interféromètre CHARA ont mis clairement en évidence un assombrissement centre-bord anormal pour l'étoile Véga. Une modélisation adaptée a permis de conclure que l'effet Von Zeipel, caractéristique d'une rotation rapide de l'étoile, est la cause de ce phénomène. Nous avons pu déduire de ce modèle les paramètres physiques principaux de l'étoile (inclinaison, vitesse de rotation équatoriale,...).

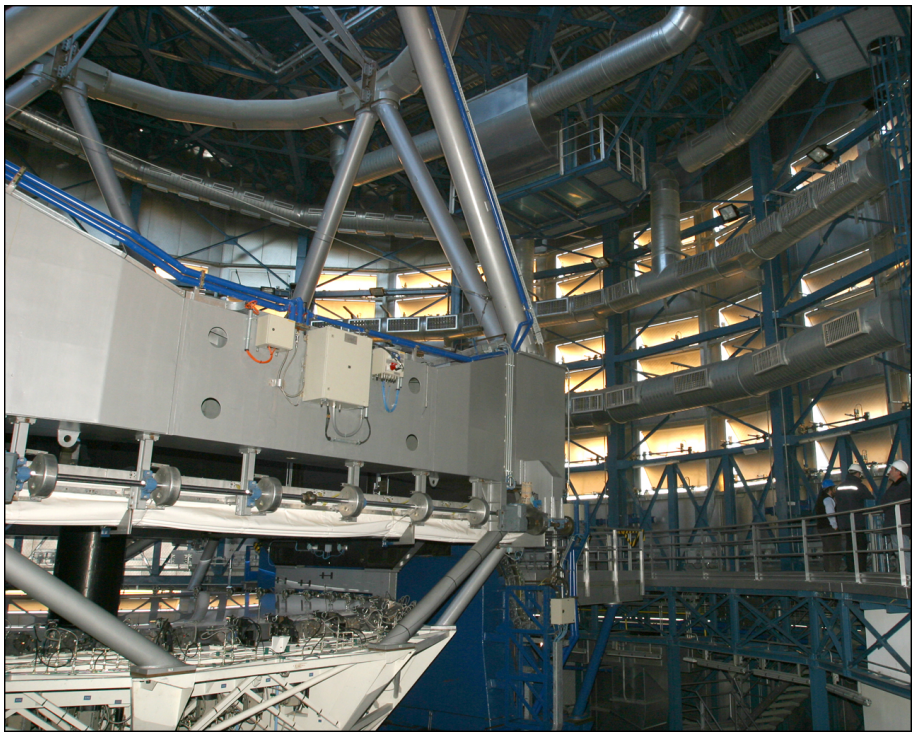

FIG. 4.13 – Le télescope UT1 du VLT (photo Y. Bresson).

The Astrophysical Journal, 645:664–675, 2006 July 1

FIRST RESULTS FROM THE CHARA ARRAY. VII. LONG-BASELINE INTERFEROMETRIC MEASUREMENTS OF VEGA CONSISTENT WITH A POLE-ON, RAPIDLY ROTATING STAR

J. P. Aufdenberg,[1,2] A. Mérand,[3] V. Coudé du Foresto,[3] O. Absil,[4] E. Di Folco,[3] P. Kervella,[3] S. T. Ridgway,[2,3] D. H. Berger,[5,6] T. A. ten Brummelaar,[6] H. A. McAlister,[7] J. Sturmann,[6] L. Sturmann,[6] and N. H. Turner[6]

Received 2006 January 5; accepted 2006 March 9

ABSTRACT

We have obtained high-precision interferometric measurements of Vega with the CHARA Array and FLUOR beam combiner in the K' band at projected baselines between 103 and 273 m. The measured visibility amplitudes beyond the first lobe are significantly weaker than expected for a slowly rotating star characterized by a single effective temperature and surface gravity. Our measurements, when compared to synthetic visibilities and synthetic spectrophotometry from a Roche–von Zeipel gravity-darkened model atmosphere, provide strong evidence for the model of Vega as a rapidly rotating star viewed very nearly pole-on. Our best-fitting model indicates that Vega is rotating at ~91% of its angular break-up rate with an equatorial velocity of 275 km s^{-1}. Together with the measured $v \sin i$, this velocity yields an inclination for the rotation axis of 5°. For this model the pole-to-equator effective temperature difference is ~2250 K, a value much larger than previously derived from spectral line analyses. A polar effective temperature of 10,150 K is derived from a fit to ultraviolet and optical spectrophotometry. The synthetic and observed spectral energy distributions are in reasonable agreement longward of 140 nm, where they agree to 5% or better. Shortward of 140 nm, the model is up to 10 times brighter than observed. The model has a luminosity of ~37 $L_\odot$, a value 35% lower than Vega's apparent luminosity based on its bolometric flux and parallax, assuming a slowly rotating star. Our model predicts the spectral energy distribution of Vega as viewed from its equatorial plane, and it may be employed in radiative models for the surrounding debris disk.

Subject headings: methods: numerical — stars: atmospheres — stars: fundamental parameters (radii, temperature) — stars: individual (Vega) — stars: rotation — techniques: interferometric

Online material: machine-readable table

1. INTRODUCTION

The bright star Vega (α Lyr, HR 7001, HD 172167, A0 V) has been a photometric standard for nearly 150 years. Hearnshaw (1996) describes Ludwig Seidel's visual comparative photometer measurements, beginning 1857, of 208 stars reduced to Vega as the primary standard. Today precise absolute spectrophotometric observations of Vega are available from the far-ultraviolet to the infrared (Bohlin & Gilliland 2004). The first signs that Vega may be anomalously luminous appeared in the 1960s after the calibration of the Hγ equivalent width to absolute visual magnitude [W(Hγ)-M_V] relationship (Petrie 1964). Millward & Walker (1985) confirmed Petrie's findings using better spectra and showed that Vega's M_V is 0.5 mag brighter than the mean A0 V star based on nearby star clusters. Petrie (1964) suggested the anomalous luminosity may indicate that Vega is a binary; however, the intensity interferometer measurements by Hanbury Brown et al. (1967) found no evidence for a close, bright companion, a result later confirmed by speckle observations (McAlister 1985). A faint companion cannot be ruled out (Absil et al. 2006), although the presence of such a companion would not solve the luminosity discrepancy. Hanbury Brown et al. (1967) also noted on the basis of their angular diameter measurements that Vega's radius is 70% larger than that of Sirius. Recent precise interferometric measurements show Vega's radius ($R = 2.73 \pm 0.01\ R_\odot$; Ciardi et al. 2001) to be 60% larger than that of Sirius ($R = 1.711 \pm 0.013\ R_\odot$, $M = 2.12 \pm 0.06\ M_\odot$; Kervella et al. 2003), while the mass-luminosity and mass-radius relations for Sirius, $L/L_\odot = (M/M_\odot)^{4.3\pm0.2}$ and $R/R_\odot = (M/M_\odot)^{0.715\pm0.035}$, yield a radius for Vega only ~12% larger.

Since the work of von Zeipel (1924a, 1924b), it has been expected that in order for rapidly rotating stars to achieve both hydrostatic and radiative equilibrium, these stars' surfaces will exhibit gravity darkening, a decrease in effective temperature from the pole to the equator. In the 1960s and 1970s considerable effort (see, e.g., Collins 1963, 1966; Hardorp & Strittmatter 1968; Maeder & Peytremann 1970; Collins & Sonneborn 1977) was put into the development of models for the accurate prediction of colors and spectra from the photospheres of rapidly rotating stars. These early models showed that in the special case in which one views these stars pole-on, they will appear more luminous than nonrotating stars, yet have very nearly the same colors and spectrum. The connection between Vega's anomalous properties and the predictions of rapidly rotating model atmospheres was made by Gray (1985, 1988), who noted that Vega must be nearly pole-on and rotating at 90% of its angular breakup rate to account for its excessive apparent luminosity. Gray (1988) also noted that Vega's apparent luminosity is inconsistant with its measured Strömgren color indices, which match those of a dwarf, while the apparent luminosity suggests an evolved subgiant.

[1] Michelson Postdoctoral Fellow.
[2] National Optical Astronomy Observatory, 950 North Cherry Avenue, Tucson, AZ 85719.
[3] LESIA, UMR 8109, Observatoire de Paris-Meudon, 5 place Jules Janssen, 92195 Meudon Cedex, France.
[4] Insitut d'Astrophysique et de Géophysique, University of Liège, 17 Allée du Six Août, 40000 Liège, Belgium.
[5] Department of Astronomy, University of Michigan, 917 Dennison Building, 500 Church Street, Ann Arbor, MI 48109-1042.
[6] CHARA Array, Mount Wilson Observatory, Mount Wilson, CA 91023.
[7] Center for High Angular Resolution Astronomy, Department of Physics and Astronomy, Georgia State University, P.O. Box 3969, Atlanta, GA 30302-3969.

Another anomalous aspect of Vega is the flat-bottomed appearance of many of its weak metal lines observed at high spectral resolution and very high signal-to-noise ratio (>2000; Gulliver et al. 1991). The modeling by Elste (1992) showed that such flat-bottomed or trapazoidal profiles could result from a strong center-to-limb variation in the equivalent width of a line coupled with a latitudinal temperature gradient on the surface of the star. Soon after, Gulliver et al. (1994) modeled these unusual line profiles together with Vega's spectral energy distribution (SED) and found a nearly pole-on ($i = 5\overset{\circ}{.}5$), rapidly rotating ($V_{\rm eq} = 245$ km s^{-1}) model to be a good match to these data.

Since the detection in the infrared of Vega's debris disk (Aumann et al. 1984), much of the attention paid to Vega has been focused in this regard (see, e.g., Su et al. 2005). However, not only has Vega's disk been spatially resolved, but photosphere has been as well. This was done first by Hanbury Brown et al. (1967), although attempts to measure Vega's angular diameter go back to Galileo (Hughes 2001). Recent interferometric measurements of Vega show nothing significantly out of the ordinary when compared to standard models for a slowly rotating A0 V star (Hill et al. 2004; $v \sin i = 21.9 \pm 0.2$ km s^{-1}). Specifically, uniform disk fits to data obtained in the first lobe of Vega's visibility curve, from the Mark III interferometer (Mozurkewich et al. 2003) at 500 and 800 nm and from the Palomar Testbed Interferometer (PTI; Ciardi et al. 2001) in the K band, show the expected progression due to standard wavelength-dependent limb darkening: 3.00 ± 0.05 mas (500 nm), 3.15 ± 0.03 mas (800 nm), and 3.24 ± 0.01 (K band). In addition, the first lobe data in the optical from the Navy Prototype Optical Interferometer (NPOI) yield 3.11 ± 0.01 mas ($\sim$650 nm; Ohishi et al. 2004), consistent with this picture. Ciardi et al. (2001) note small residuals in their angular diameter fits that may be due to Vega's disk.

Triple amplitude data from NPOI in May 2001 (Ohishi et al. 2004) sample the second lobe of Vega's visibility curve, where a gravity-darkening signature should be unambiguous. However, these data show the signature of limb darkening expected for a nonrotating star, as predicted by ATLAS9 limb-darkening models (van Hamme 1993). Most recently, a preliminary analysis of second-lobe NPOI data from 2003 October (Peterson et al. 2004) indicate that Vega is indeed strongly gravity darkened, a result inconsistent with Ohishi et al. (2004). Peterson et al. (2006) note that the NPOI Vega data are difficult to analyze due to detector nonlinearities for such a bright star. Peterson et al. (2006) do see a strong interferometric signal for gravity darkening from the rapid rotator Altair with an angular break-up rate 90% of critical. Since a similar rotation rate is expected for Vega on the basis of its apparently high luminosity (Gray 1988; Gulliver et al. 1994), a strong gravity darkening is expected for Vega as well.

There is clearly a need for additional high spatial resolution observations of Vega's photosphere to confirm the hypothesis of Gray (1988), confirm the 2003 NPOI observations, and test the theory of von Zeipel. We have employed the long baselines of the Center for High Angular Resolution Astronomy (CHARA) Array (ten Brummelaar et al. 2005) on Mount Wilson, together with the capabilties of the spatially filtered Fiber Linked Unit for Optical Recombination (FLUOR; Coudé du Foresto et al. 2003), as a means to probe the second lobe of Vega's visibility curve at high precision and accuracy in the K band. Our Vega campaign, part of the commissioning science (McAlister et al. 2005; Mérand et al. 2005b; van Belle et al. 2006) for the CHARA Array, obtained visibility data on baselines between 103 and 273 m that clearly show the signature of a strongly gravity darkened, pole-on, rapidly rotating star. In this paper we present these data and a detailed modeling effort to fit both our inteferometric data and the archival data of Vega's spectral energy distribution.

We introduce our observations in § 2. Sections 3, 4, and 5 describe the construction and fitting of one- and two-dimensional synthetic brightness distributions to our interferometic data and archival spectrophotometry. A discussion of our results follows in § 6. We conclude with a summary in § 7.

2. OBSERVATIONS

Our interferometric measurements were obtained using the CHARA Array in the infrared K' band (1.94–2.34 μm) with FLUOR. Our observations were obtained during six nights in the late spring of 2005 using four telescope pairs, E2-W2, S1-W2, E2-W1, and S1-E2 with maximum baselines of 156, 211, 251, and 279 m, respectively. The FLUOR Data Reduction Software (Kervella et al. 2004; Coudé du Foresto et al. 1997) was used to extract the squared modulus of the coherence factor between the two independent telescope aperatures. We obtained 25 calibrated observations of Vega, which are summarized in Table 1. The (u, v)-plane sampling is shown in Figure 1.

The calibrator stars were chosen from the catalog of Mérand et al. (2005a). The CHARA Array's tip-tilt adaptive optics system operates at visual wavelengths. Vega is sufficiently bright that it was necessary to reduce the gain on the tip-tilt detector system while observing Vega and return the gain to the nominal setting for the fainter calibrator stars. Calibrators chosen for this work are all K giants: HD 159501 (K1 III), HD 165683 (K0 III), HD 173780 (K3 III), HD 176567 (K2 III), and HD 162211 (K2 III). The spectral type difference between the calibrators and Vega does not significantly influence the final squared visibility estimate. The interferometric transfer function of CHARA/FLUOR was estimated by observing a calibration star before and after each Vega data point. In some cases a different calibrator was used on either side of the Vega data point (see Table 1). The inteferometric efficiency of CHARA/FLUOR was consistent between all calibrators and stable over each night at $\sim$85%.

3. ONE-DIMENSIONAL MODEL FITS

Under the initial assumption that Vega's projected photospheric disk is circularly symmetric in both shape and intensity, we have fit three models to the CHARA/FLUOR data set: (1) a uniform disk, where the intensity, assumed to be Planckian [$I(\lambda) = B(T_{\rm eff} = 9550\ {\rm K},\ \lambda)$], is independent of μ, the cosine of the angle between the line-of-sight and the surface normal; (2) an analytic limb-darkening law, $I(\mu,\ \lambda) = B(T_{\rm eff} = 9550\ {\rm K},\ \lambda)\mu^{\alpha}$; and (3) a PHOENIX (Hauschildt et al. 1999) model radiation field with stellar parameters [$T_{\rm eff} = 9550$ K, $\log(g) = 3.95$] consistent with the slowly rotating model that Bohlin & Gilliland (2004) show to be a good match to Vega's observed SED. The computation of the synthetic squared visibilities from these models takes into account the bandwidth smearing introduced by the nonmonochromatic FLUOR transmission (see § 4.2.1 below).

Figure 2 shows the synthetic squared visibilities from the three models in comparison with the CHARA/FLUOR data. The uniform disk angular diameter we derive ($\theta_{\rm UD} = 3.209 \pm 0.003$ mas) is not consistent with Ciardi et al. (2001; $\theta_{\rm UD} = 3.24 \pm 0.01$ mas). We find this is most likely because we do not assume a flat spectrum across the K'-band filter. Regardless, this uniform disk model is poor fit ($\chi^2_\nu = 38$) because it neglects limb darkening. The limb darkening expected for a slowly rotating star should be well predicted by the PHOENIX model, but this model is also a poor fit ($\chi^2_\nu = 20$, $\theta_{\rm LD} = 3.259 \pm 0.002$ mas). The second lobe

TABLE 1
CHARA/FLUOR K'-Band Vega Measurements

No.	Julian Date	Telescope Pair	u (m)	v (m)	Projected Baseline (m)	Position Angle (deg)	V^2 (×100)	$\sigma V^2_{\rm total}$ (×100)	Calibration Star(s) HD Number
1.....	2,453,511.261	E2-W2	−98.941	23.114	101.606	−76.85	21.1531	0.8846	176527
2.....	2,453,511.313	E2-W2	−127.859	−0.092	127.859	89.95	6.2229	0.2019	176527, 173780
3.....	2,453,511.347	E2-W2	−139.876	−18.250	141.062	82.56	2.6256	0.0742	173780
4.....	2,453,511.374	E2-W2	−144.773	−33.322	148.558	77.03	1.3567	0.0417	173780
5.....	2,453,512.266	E2-W2	−103.834	20.146	105.770	−79.02	18.2301	0.1976	159501
6.....	2,453,512.269	E2-W2	−106.062	18.698	107.698	−80.00	16.7627	0.1710	159501
7.....	2,453,512.277	E2-W2	−110.513	15.601	111.609	−81.96	14.4223	0.1493	159501
8.....	2,453,512.284	E2-W2	−114.716	12.396	115.384	−83.83	12.2229	0.1336	159501
9.....	2,453,512.291	E2-W2	−118.435	9.291	118.799	−85.51	10.3873	0.1168	159501
10.....	2,453,512.345	E2-W2	−140.179	−18.907	141.448	82.31	2.6399	0.0741	173780
11.....	2,453,512.349	E2-W2	−141.068	−20.951	142.615	81.55	2.3968	0.0676	173780
12.....	2,453,512.356	E2-W2	−142.577	−24.954	144.744	80.07	2.0041	0.0591	173780
13.....	2,453,516.258	E2-W1	−141.950	88.392	167.221	−58.08	0.1040	0.0059	159501
14.....	2,453,516.343	E2-W1	−224.986	25.325	226.407	−83.57	1.2148	0.0521	159501, 165683
15.....	2,453,517.248	E2-W1	−132.597	92.319	161.569	−55.15	0.2426	0.0194	159501, 173780
16.....	2,453,517.288	E2-W1	−180.244	67.502	192.469	−69.46	0.5913	0.0314	173780
17.....	2,453,517.342	E2-W1	−225.788	24.193	227.080	−83.88	1.1066	0.0670	173780
18.....	2,453,519.225	E2-S1	−169.006	−165.745	236.716	45.55	1.1361	0.0414	159501
19.....	2,453,519.252	E2-S1	−168.472	−183.482	249.095	42.55	0.9120	0.0344	159501
20.....	2,453,519.285	E2-S1	−161.265	−205.029	260.851	38.18	0.6047	0.0259	159501
21.....	2,453,519.316	E2-S1	−147.913	−224.292	268.673	33.40	0.5079	0.0238	159501
22.....	2,453,522.270	E2-S1	−163.306	−200.735	258.773	39.13	0.5911	0.0427	159501
23.....	2,453,522.306	E2-S1	−148.868	−223.205	268.295	33.70	0.4518	0.0241	159501
24.....	2,453,522.336	E2-S1	−131.105	−239.777	273.279	28.67	0.3788	0.0199	159501
25.....	2,453,538.206	W2-S1	56.624	202.948	210.699	15.59	0.9303	0.0682	162211

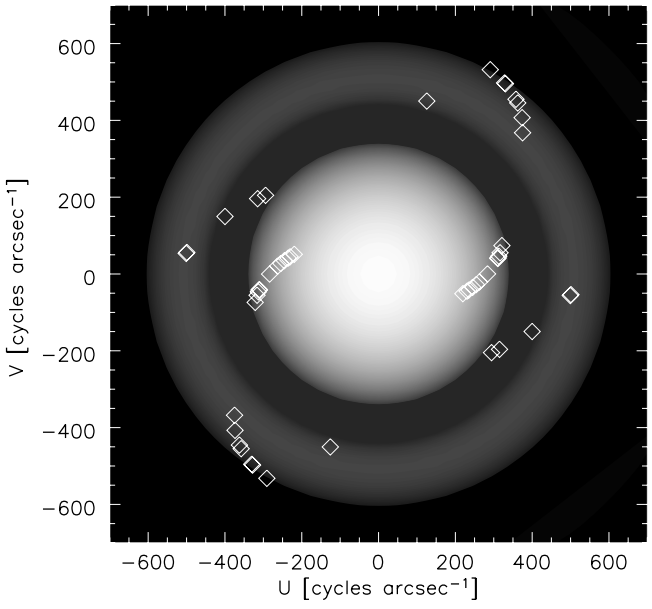

Fig. 1.—Sampling of the (u, v)-plane for the CHARA/FLUOR Vega data set. The diamonds represent the monochromatic sampling at 2.0 μm within the K' band. In the K' band, the CHARA baselines E2-W2, E2-W1, E2-S1, and W2-S1 sample the lower first lobe, first null, and second lobe of Vega's visibility curve. Two-telescope observations have a 180° ambiguity in the position angle, therefore we plot two coordinates, (u, v) and $(-u, -v)$, for each of the 25 data points. These (u, v) points overlay a model for Vega's two-dimensional monochromatic Fourier appearance. This squared visibility model is a Fast Fourier Transform (displayed with a logarithmic stretch) of a synthetic intensity map of Vega in the plane of the sky (see Fig. 3).

data indicate that Vega is significantly more limb darkened compared to this model. The nonphysical $I(\mu) = \mu^{\alpha}$ model yields a much better fit ($\chi^2_{\nu} = 1.5$) and a significantly larger angular diameter $\theta_{\rm LD} = 3.345 \pm 0.006$ ($\alpha = 0.341 \pm 0.013$), which suggests the limb-darkening correction in the K' band is ~2.5 times larger (4.2% vs. 1.6%) than expected for a slowly rotating Vega.

Absil et al. (2006) report that a small fraction ($f = 1.29\% \pm 0.16\%$) of Vega's K'-band flux comes from an extended structure,

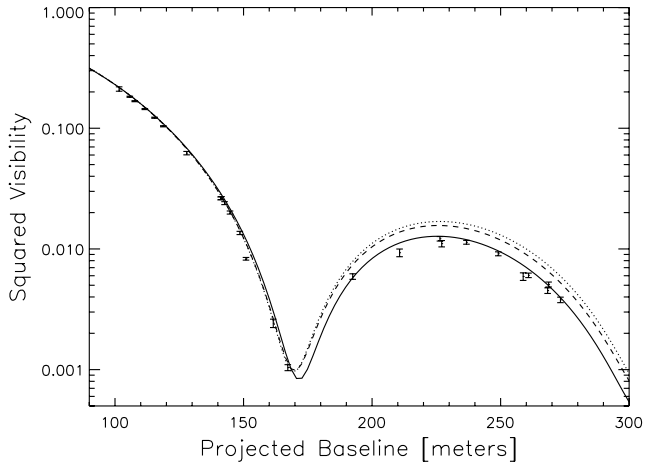

Fig. 2.—Best-fit one-dimensional, symmetric models in comparison with the CHARA/FLUOR data set. The dotted line is a bandwidth-smeared uniform disk ($\chi^2_{\nu} = 38$, $\theta_{\rm UD} = 3.209 \pm 0.003$ mas) The dashed line is a bandwidth-smeared PHOENIX model atmosphere with parameters consistent with a slowly rotating Vega [$T_{\rm eff} = 9550$ K, $\log(g) = 3.95$, $\chi^2_{\nu} = 20$, $\theta_{\rm LD} = 3.259 \pm 0.002$ mas], and the solid line a bandwidth-smeared analytic limb-darkening model, $I(\mu) = \mu^{\alpha}$ ($\chi^2_{\nu} = 1.5$, $\theta_{\rm LD} = 3.345 \pm 0.006$ mas, $\alpha = 0.341 \pm 0.013$). If extended emission in the K' band is present at the 1.3% level in the Vega system, these best angular diameters are systematically high by ~3 σ (see text).

most likely Vega's debris disk. In order to gauge the significance of this extra flux on the photospheric parameters derived above, the synthetic squared visibilities are reduced by an amount equal to the square of fraction of light coming from the debris disk. At long baselines, the visibility of the debris disk is essentially zero such that

$$V_{\rm obs}^2 = \left[(1-f)V_{\rm photosphere} + fV_{\rm disk}\right]^2 \approx 0.974 V_{\rm photosphere}^2. \quad (1)$$

The revised fits to $V_{\rm photosphere}^2$ are $\theta_{\rm UD} = 3.198 \pm 0.003$ ($\chi_\nu^2 = 38$) for the uniform disk, $\theta_{\rm LD} = 3.247 \pm 0.002$ ($\chi_\nu^2 = 19$) for the PHOENIX model, and $\theta_{\rm LD} = 3.329 \pm 0.006$ ($\alpha = 0.328 \pm 0.013$, $\chi_\nu^2 = 1.4$) for the $I(\mu) = \mu^\alpha$ model. The effect of removing the extended emission is to reduce the best-fit angular diameter for all three models by $\sim 3\,\sigma$; the correction for extended emission is therefore significant.

4. TWO-DIMENSIONAL MODEL CONSTRUCTION

In order to physically interpret the strong limb darkening we find for Vega, we have adapted a computer program written by S. Cranmer (2002, private communication) from Cranmer & Owocki (1995) that computes the effective temperature and surface gravity on the surface of a rotationally distorted star, specifically a star with an infinitely concentrated central mass under uniform angular rotation, a Roche–von Zeipel model. This azimuthally symmetric model is parameterized as a function of the colatitude given the mass, polar radius, luminosity, and fraction of the angular break-up rate.

Each two-dimensional intensity map is characterized by five variables: $\theta_{\rm equ}$, the angular size of the equator, equivalent to the angular size as viewed exactly pole-on; $\omega = \Omega/\Omega_{\rm crit}$, the fraction of the critical angular break-up rate; $T_{\rm eff}^{\rm pole}$, the effective temperature at the pole; $\log(g)_{\rm pole}$, the effective surface gravity at the pole; and ψ, the position angle of the pole on the sky measured east from north.

Given these input parameters, along with the measured trigonometric parallax $\pi_{\rm hip} = 128.93 \pm 0.55$ mas (Perryman et al. 1997), and the observed projected rotation velocity, $v \sin i = 21.9 \pm 0.2$ km s^{-1} (Hill et al. 2004), the parameterization of the intensity maps begins with

$$R_{\rm equ} = 107.48 \frac{\theta_{\rm equ}}{\pi_{\rm hip}}, \quad (2)$$

with the equatorial radius in solar units and both $\theta_{\rm equ}$ and $\pi_{\rm hip}$ in milliarcseconds. It follows from a Roche model (Cranmer & Owocki 1995; eq. [26]) that the corresponding polar radius is

$$R_{\rm pole} = \frac{\omega R_{\rm equ}}{3\cos\left[\frac{\pi + \cos^{-1}(\omega)}{3}\right]}$$

and the stellar mass is

$$M = \frac{g_{\rm pole} R_{\rm pole}^2}{G}, \quad (4)$$

where G is the universal gravitational constant. The luminosity is then

$$L = \frac{\sigma \Sigma \left(T_{\rm eff}^{\rm pole}\right)^4}{g_{\rm pole}}, \quad (5)$$

where σ is the Stefan-Boltzman constant and Σ is the surface-weighted gravity (Cranmer & Owocki 1995; eqs. [31] and [32]), expressed as a power series expansion in ω,

$$\Sigma \approx 4\pi GM\left(1.0 - 0.19696\omega^2 - 0.094292\omega^4 + 0.33812\omega^6 - 1.30660\omega^8 + 1.8286\omega^{10} - 0.92714\omega^{12}\right). \quad (6)$$

The ratio of the luminosity to Σ provides the proportional factor between the effective temperature and gravity for von Zeipel's radiative law for all colatitudes ϑ:

$$T_{\rm eff}(\vartheta) = \left[\frac{L}{\sigma\Sigma} g(\vartheta)\right]^\beta = T_{\rm eff}^{\rm pole}\left[\frac{g(\vartheta)}{g_{\rm pole}}\right]^\beta, \quad (7)$$

where the gravity darkening parameter, β, takes the value 0.25 in the purely radiative case (no convection). The effective temperature difference between the pole and equator, $\Delta T_{\rm eff}$, may be expressed in terms of $T_{\rm eff}^{\rm pole}$ and ω:

$$\Delta T_{\rm eff} = T_{\rm eff}^{\rm pole} - T_{\rm eff}^{\rm equ} = T_{\rm eff}^{\rm pole}\left[1 - \left(\frac{\omega^2}{\eta^2} - \frac{8}{27}\eta\omega\right)^\beta\right], \quad (8)$$

where

$$\eta = 3\cos\left[\frac{\pi + \cos^{-1}(\omega)}{3}\right].$$

The effective gravity as a function of ϑ is given by

$$g(\vartheta) = \left[g_r(\vartheta)^2 + g_\vartheta(\vartheta)^2\right]^{1/2}, \quad (9)$$

$$g_r(\vartheta) = \frac{-GM}{R(\vartheta)^2} + R(\vartheta)(\Omega\sin\vartheta)^2, \quad (10)$$

$$g_\vartheta(\vartheta) = R(\vartheta)\Omega^2 \sin\vartheta\cos\vartheta, \quad (11)$$

where g_r and g_ϑ are the radial and colatitudinal components of the gravity field. The colatitudinal dependence of the radius is given by

$$R(\vartheta) = 3\frac{R_{\rm pole}}{\omega\sin\vartheta}\cos\left[\frac{\pi + \cos^{-1}(\omega\sin\vartheta)}{3}\right] \quad (\omega > 0) \quad (12)$$

and angular rotation rate is related to the critical angular rotation rate[8] by

$$\Omega = \omega\Omega_{\rm crit} = \omega\left(\frac{8}{27}\frac{GM}{R_{\rm pole}^3}\right)^{1/2}. \quad (13)$$

At the critical rate ($\omega = 1$), $R_{\rm equ} = 1.5R_{\rm pole}$. The inclination follows from

$$i = \sin^{-1}\left(\frac{v\sin i}{V_{\rm equ}}\right), \quad (14)$$

[8] There is a typographical error in eq. (5) of Collins (1963), which is not in the paper's erratum (Collins 1964): $\omega_c^2 = GM/R_e$ should be $\omega_c^2 = GM/R_e^3$, where ω_c the critical angular rate and R_e is the equatorial radius at the critical rate.

where the equatorial velocity is

$$V_{\rm equ} = R_{\rm equ}\Omega. \tag{15}$$

4.1. *Building the Intensity Maps*

For each wavelength λ (185 total wavelength points: 1.9–2.4 μm in 0.005 μm steps, with additional points for H I and He I profiles calculated in non-LTE), an intensity map is computed as follows: $T_{\rm eff}(\vartheta)$ and $\log((g)\vartheta)$ are evaluated at 90 ϑ points from 0° to $90^\circ + i$. At each ϑ there are 1024 longitude φ points from 0° to 360° to finely sample the perimeter of the nearly pole-on view. For Vega's nearly pole-on orientation, the relatively high resolution in φ reduces numerical aliasing when the brightness map is later interpolated onto a uniformly gridded rectangular array as described below.

Each set of spherical coordinates $[R(\vartheta),\ \vartheta,\ \varphi]$ is first transformed to rectangular (x, y, z) coordinates with the Interactive Data Language (IDL) routine `POLEREC3D`.[9] Next, the z-axis of the coordinate system is rotated away from the observer by an angle equal to the inclination i (using the IDL routine `ROT_3D`) and then the (x, y)-plane is rotated by an angle equal to ψ, the position angle (east of north) of the pole on the sky (using the IDL routine `ROTATE_XY`).

At each point in the map, the cosine of the angle between the observer's line of sight and the local surface normal is

$$\begin{aligned}\mu(x,\ y) &= \mu(\vartheta,\ \varphi,\ i)\\ &= \frac{1}{g(\vartheta)}\Big[-g_r(\vartheta)(\sin\vartheta\sin i\cos\varphi + \cos\vartheta\cos i)\\ &\quad - g_\vartheta(\vartheta)(\sin i\cos\varphi\cos\vartheta - \sin\vartheta\cos i)\Big].\end{aligned} \tag{16}$$

The intensity at each point $(x,\ y)$ is interpolated from a grid of 170 spherical, hydrostatic PHOENIX (vers. 13.11.00B) stellar atmosphere models (Hauschildt et al. 1999) spanning 6500 to 10,500 K in $T_{\rm eff}$ and 3.25 to 4.15 in $\log(g)$:

$$\begin{aligned}T_j &= 6500 + 250j\ {\rm K}, \quad j = \{0,\ 1, \ldots,\ 16\},\\ \log(g_l) &= 3.25 + 0.1l, \quad l = \{0,\ 1, \ldots,\ 9\}.\end{aligned}$$

Four radiation fields, $I(\lambda,\ \mu)$ evaluated at 64 angles by PHOENIX, are selected from the model grid to bracket the local effective temperature and gravity values on the grid square,

$$\begin{aligned}T_j < T_{\rm eff}(\vartheta) < T_{j+1},\\ g_l < g(\vartheta) < g_{l+1}.\end{aligned}$$

The intensity vectors $I_\lambda(\mu)$ are linearly interpolated (in the log) at $\mu(x,\ y)$ around the grid square,

$$\begin{aligned}I_\lambda^{00} &= I_\lambda\big(T_j,\ g_l,\ \mu(x,\ y)\big),\\ I_\lambda^{10} &= I_\lambda\big(T_{j+1},\ g_l,\ \mu(x,\ y)\big),\\ I_\lambda^{11} &= I_\lambda\big(T_{j+1},\ g_{l+1},\ \mu(x,\ y)\big),\\ I_\lambda^{01} &= I_\lambda\big(T_j,\ g_{l+1},\ \mu(x,\ y)\big).\end{aligned}$$

[9] The coordinate transformation routines used here are from the JHU/APL/S1R IDL library of the Space Oceanography Group of the Applied Physics Laboratory of Johns Hopkins University.

Next, the intensity is bilinearly interpolated at the local $T_{\rm eff}$ and $\log(g)$ for each $(x,\ y)$ position in the map:

$$\begin{aligned}I_\lambda(x,\ y) &= I_\lambda[T_{\rm eff}(x,\ y),\ g(x,\ y),\ \mu(x,\ y)]\\ &= (1-a)(1-b)I_\lambda^{00} + a(1-b)I_\lambda^{10}\\ &\quad + abI_\lambda^{11} + (1-a)bI_\lambda^{01}\end{aligned} \tag{17}$$

where

$$\begin{aligned}a &= \big[T_{\rm eff}(x,\ y) - T_j\big]/\big(T_{j+1} - T_j\big),\\ b &= [\,g(x,\ y) - g_l\big]\big(g_{l+1} - g_l\big).\end{aligned}$$

Finally, a Delaunay triangulation is computed (using the IDL routine `TRIGRID`) to regrid the intensity map $I_\lambda(x,\ y)$, originally gridded in ϑ and φ, onto a regular 512×512 grid of points in x and y. The coordinates x and y have the units of milliarcseconds and correspond to offsets in right ascension and declination on the sky $(\Delta\alpha,\ \Delta\delta)$ relative to the origin, the subsolar point.

4.2. *Synthetic Squared Visibility Computation*

Due to the lack of symmetry in the synthetic intensity maps, we evaluate a set of discrete two-dimensional Fourier transforms in order to generate a set of synthetic squared visibilities comparable to the CHARA/FLUOR observations. The first step is to compute the discrete Fourier transform for each wavelength at each of the spatial frequency coordinates $(u,\ v)$ corresponding to the projected baseline and orientation of each data point (see Table 1). The mean $(u,\ v)$ coordinates for each data point, in units of meters, are converted to the corresponding spatial frequency coordinates $(u_k,\ v_k)$ in units of cycles per arcsecond for each wavelength λ_k. The Fourier transform

$$V_\lambda^2(u,\ v) = \left[\int_{-\infty}^{\infty}\int_{-\infty}^{\infty} S_\lambda I_\lambda(x,\ y)e^{i2\pi(ux+vy)}\,dx\,dy\right]^2 \tag{18}$$

is approximated by the integration rule of Gaussian quadrature (e.g., Stroud & Secrest 1966; Press et al. 1992):

$$\begin{aligned}V_k^2(u_k,\ v_k) \approx &\left\{\sum_{i=1}^{N} A_i \sum_{j=1}^{N} A_j S_k I_k(x_i,\ y_j)\cos\big[2\pi(u_k x_i + v_k y_j)\big]\right\}^2\\ &+ \left\{\sum_{i=1}^{N} A_i \sum_{j=1}^{N} A_j S_k I_k(x_i, y_j)\sin\big[2\pi(u_k x_i + v_k y_j)\big]\right\}^2,\end{aligned} \tag{19}$$

where S_k is the wavelength discretized value of the instrument sensitivity curve S_λ, and A_i, A_j and x_i, y_j are the weights and nodes of the quadrature, respectively. For our square grid, the x- and y-coordinate nodes and weights are indentical. The two-dimensional Gaussian quadrature is performed with a version of the IDL routine `INT_2D` modified to use an arbitrarily high number of nodes. The intensity at wavelength k, $I_k(x, y)$, is interpolated at $\big(x_i, y_j\big)$ from the regular 512×512 spacing to the quadrature node points using the IDL routine `INTERPOLATE` which uses a cubic convolution interpolation method employing 16 neighboring points. The synthetic squared visibility is normalized to unity at zero spatial frequency by

$$V_k^2(0,\ 0) \approx \left[\sum_{i=1}^{N} A_i \sum_{j=1}^{N} A_j S_k I_k\big(x_i,\ y_j\big)\right]^2. \tag{20}$$

We find $N = 512$ provides the degree of numerical accuracy sufficient in the case of a two-dimensional uniform disk (right circular cylinder) to yield V^2 values in agreement with the analytic result,

$$V_k^2(u_k,\ v_k) = \left[2J_1\left(\pi\theta\sqrt{u_k^2 + v_k^2}\right) \Big/ \left(\pi\theta\sqrt{u_k^2 + v_k^2}\right)\right]^2, \quad (21)$$

where J_1 is the first order Bessel function of the first kind, θ is the angular diameter of the uniform disk, and B is the projected baseline, to better than 1% for $V^2 > 10^{-3}$. We use the IDL function BESELJ for our J_1 computations. For $V^2 \lesssim 10^{-4}$, near the monochromatic first and second zeros, the numerical accuracy of the quadrature deteriorates to 10% or worse. The bandwidth-smeared V^2 minimum is at $\sim 10^{-3}$, so we find this quadrature method yields squared visibilities which are sufficiently accurate for our task, however observations with an even larger dynamic range (Perrin & Ridgway 2005) will require more accurate methods.

To test the two-dimensional Gaussian quadrature method in the case where no analytic solution is available, we computed the two-dimensional fast Fourier transform (IDL routine FFT) of a brightness map (see Fig. 3). First, we compared the results of the two-dimensional FFT to the analytic uniform disk (eq. [21]. To reduce aliasing we find it necessary to "zero-pad" the brightness map. With 12-to-1 zero padding (the 512×512 brightness map placed at the center of a larger 6144×6144 array of zeros), we find the two-dimensional FFT has very similar accuracy to the 512-point Gaussian quadrature: better than 1% down to $V^2 \gtrsim 10^{-3}$ inside the second null. For the brightness map shown in Figure 3, the two-dimensional FFT and Gaussian quadrature methods agree to better than 0.5% down to $V^2 \gtrsim 10^{-3}$, inside the second null. We find the computational time required to evaluate equation (19) at 25 $(u_k,\ v_k)$ points for 185 wavelengths is $\sim$6 times faster than the evaluation of the 185 zero-padded two-dimensional FFTs.

4.2.1. *Bandwidth Smearing*

Once we have computed $V_k^2(u_k,\ v_k)$ for the 185 wavelength points, we proceed to compute the bandwidth-smeared average squared visibility $V(B,\ \lambda_0)^2$,

$$V(B,\ \lambda_0)^2 = \frac{\int_0^\infty V(B,\ \lambda)^2 \lambda^2\, d\lambda}{\int_0^\infty V(0,\ \lambda)^2 \lambda^2\, d\lambda}. \quad (22)$$

This integral is performed by the IDL routine INT_TABULATED, a five-point Newton-Cotes formula. The λ^2 term is included so that the integral is equivalent to an integral over wavenumber (frequency), where

$$\lambda_0^{-1} = \frac{\int_0^\infty \lambda^{-1} S(\lambda) F_\lambda\, d\lambda}{\int_0^\infty S(\lambda) F_\lambda\, d\lambda} \quad (23)$$

is the mean wavenumber. This simulates the data collection and fringe processing algorithm used by FLUOR. In the discretized integrand $V(B,\ \lambda_k)^2$ is equivalent to $V_k^2(u_k,\ v_k)$, where $B = 206264.8\lambda_k \left(u_k^2 + v_k^2\right)^{1/2}$, with λ_k in units of meters and u_k and v_k in units of cycles per arcsecond.

4.3. *Synthetic Spectral Energy Distribution Construction*

To construct synthetic SEDs for Vega from the Roche–von Zeipel model, 170 radiation fields were computed from the same model grid used to construct the K'-band intensity maps. The wavelength resolution is 0.05 nm from 100 to 400 nm, 0.2 nm from 400 nm to 3 μm, and 10 nm from 3 to 50 μm. The higher resolution in the ultraviolet is needed to sample the strong line blanketing in this spectral region. From the resulting grid of radiation fields, intensity maps are computed (see § 4.1), and the flux is computed from

$$F_\lambda = \int_0^\pi \int_0^{2\pi} -\frac{g(\vartheta)}{g_r(\vartheta)} I_\lambda(R, \vartheta, \varphi) R(\vartheta)^2 \sin\vartheta \mu(\vartheta, \varphi, i)\, d\varphi\, d\vartheta. \quad (24)$$

This two-dimensional integral is performed with the IDL routine INT_TABULATED_2D (vers. 1.6), which first constructs a Delaunay triangulation of points in the $(\vartheta,\ \varphi)$-plane. For each triangle in the convex hull (defined as the smallest convex polygon completely enclosing the points), the volume of the triangular cylinder formed by six points (the triangle in the plane and three points above with heights equal to the integrand) is computed and summed. For computing the flux from the intensity maps, a coarser sampling in ϑ and φ (20×40), relative to that needed for the visibility computations, is sufficient for better than 1% flux accuracy. The numerical accuracy was checked by computing the SED of a nonrotating star ($\omega = 0$) and comparing this to a single effective temperature SED from a one-dimensional atmosphere. The interpolation and integration errors result in a flux deficit of less than 0.7% at all wavelengths relative to the one-dimensional model atmosphere.

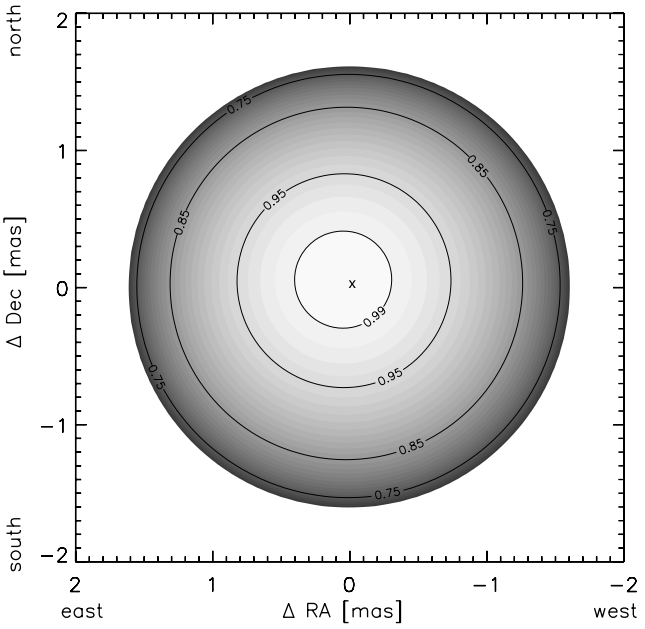

FIG. 3.—Synthetic brightness map (linear stretch) of Vega for our best-fitting parameters: $\omega = 0.91$, $\theta_{\rm equ} = 3.329$ mas, $T_{\rm eff}^{\rm pole} = 10,150$ K, $\log(g)_{\rm pole} = 4.10$. For this model, Vega's pole is inclined 5° toward a position angle of 40°, with the subsolar point marked with an "x." The labeled intensity contours are relative to the maximum intensity in the map.

5. TWO-DIMENSIONAL MODEL FITTING

5.1. *Initial Parameter Constraints*

The computation of each intensity map, the Fourier transforms, and the bandwidth-smearing for each set of input parameters [$\theta_{\rm equ}$, ω, $T_{\rm eff}^{\rm pole}$, $\log(g)_{\rm pole}$, ψ] is too computationally expensive to compute synthetic squared visibilities many hundreds of times as part

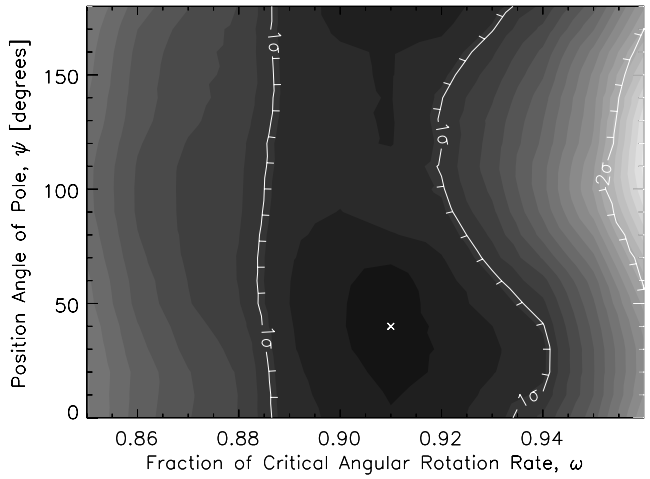

FIG. 4.—Contour plot of χ^2_ν in the $(\omega,\ \psi)$-plane for $T_{\rm eff}^{\rm pole} = 10,250$ K and $\log(g)_{\rm pole} = 4.1$. The labeled contours denote the lower and upper 1σ range, and a $2\ \sigma$ contour, from the F test. The cross marks the best fit, $\chi^2_\nu = 1.31$, while the brightest region has a $\chi^2_\nu = 3.25$ (see Fig. 6).

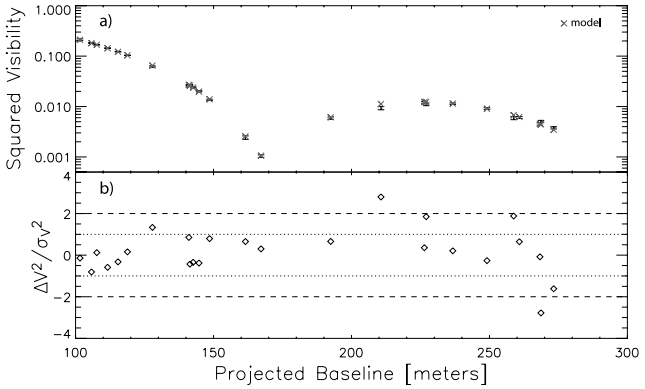

FIG. 5.—(*a*) CHARA/FLUOR V^2 data (error bars) plotted as a function of projected baseline (for a range of azimuths, see Table 1) together with the best-fitting Roche–von Zeipel synthetic squared visibilities. Model parameters: $\omega = 0.91$, $\theta_{\rm equ} = 3.329$ mas, $T_{\rm eff}^{\rm pole} = 10,250$ K, $\log(g)_{\rm pole} = 4.10$. The best-fit $\chi^2_\nu = 1.31$. (*b*) Deviations of the best-fit model from observed squared visibilities. The dotted and dashed lines indicated the 1 and 2 σ deviations.

of a gradient-search method over the vertices of a five-dimensional hypercube. Therefore, we must proceed with targeted trial searches to establish the sensitivity of χ^2_ν to each parameter after first establishing a reasonable range of values for each parameter.

The parameter $\theta_{\rm equ}$ is a physical angular diameter related to a uniform disk fit by a scale factor depending on the degree of gravity and limb darkening, which in turn depends on the parameters ω, $\log(g)_{\rm pole}$, and $T_{\rm eff}^{\rm pole}$, in order of importance. As shown above, a limb-darkening correction of 4% is significantly larger than the $\sim$1.5% value expected for a normal A0 V star at 2 μm (Davis et al. 2000). The analytic limb-darkening model fit is sufficiently good that we take $\theta_{\rm equ} = 3.36$ mas as a starting value. This corresponds to $R_{\rm equ} = 2.77\ R_\odot$ from equation (2).

Our starting value for ω is based on the assumption that Vega's *true* luminosity should be similar to that slowly rotating A0 V stars. Vega has an apparent luminosity, assuming a single effective temperature from all viewing angles, of 57 $L_\odot$ based on its bolometric flux and the parallax. In the pole-on rapidly rotating case, we would see Vega in its brightest projection. According to Millward & Walker (1985) the mean absolute visual magnitude, M_V, is 1.0 for spectral type A0 V. With a bolometric correction of -0.3, this translates to $L = 37.7\ L_\odot$. From equations (5) and (6) we expect $\omega > 0.8$ in order to account for the luminosity discrepancy assuming a minimum polar effective temperature of 9550 K, based on the nonrotating model fits to Vega's SED (Bohlin & Gilliland 2004). The range of effective temperatures and surface gravities for the model atmosphere grid described in § 4.1 sets our upper rotation limit at $\omega \leq 0.96$. For $\omega > 0.8$, $\Delta T_{\rm eff} > 1300$ K (see eq. [8]), and thus $T_{\rm eff}^{\rm pole}$ must be greater than 9550 K to compensate for the pole-to-equator temperature gradient and to reproduce the observed SED. So, given a mean apparent $T_{\rm eff}$ of 9550 K, a rough estimate of $T_{\rm eff}^{\rm pole}$ is 9550 K + $\frac{1}{2}\Delta T_{\rm eff} = 10,200$ K. We therefore limit the polar effective temperature to the range 10,050 K $< T_{\rm eff}^{\rm pole} <$ 10,350 K.

The relationship between ω and the true luminosity, through equations (5), (6), and (4), is independent of the polar surface gravity; yet we can constrain $\log(g)_{\rm pole}$ by assuming Vega follows the mass-luminosity relation we derive for the slowly rotating Sirius, $L/L_\odot = (M/M_\odot)^{4.3\pm0.2}$. Here we assume Vega's rapid rotation has no significant effect on its interior in relation to the luminosity from nuclear reactions in its core. Assuming $L =$ 37.7 $L_\odot$ from above, the mass-luminosity relation yields $M = 2.3 \pm 0.1\ M_\odot$. As ω increases, $R_{\rm pole}$ decreases relative to $R_{\rm equ}$, therefore choosing $M = 2.2\ M_\odot$ and $\omega = 0.8$ provides a lower limit of $\log(g)_{\rm pole} = 4.0$. For lower polar gravities, Vega's mass will be significantly lower than expected based on its luminosity; nevertheless, we choose a range $\log(g)_{\rm pole}$ values from 3.6 and 4.3 in order to check the effect of the gravity on our synthetic visibilities and SEDs.

Finally, the position angle of Vega's pole, ψ, should be important if Vega's inclination is sufficiently high *and* its rotation sufficiently rapid to produce an elliptical projection of the rotationally distorted photosphere on plane of the sky. Previous measurements (Ohishi et al. 2004; Ciardi et al. 2001) find no evidence for ellipticity. Preliminary results from the NPOI three-telescope observations of Peterson et al. (2004) suggest an asymmetric brightness distribution with $\psi = 281^\circ$.

5.2. *CHARA/FLUOR Data: Parameter Grid Search*

For the grid search we compute the χ^2_ν for a set of models defined by $\theta_{\rm equ}, \omega, T_{\rm eff}^{\rm pole}, \log(g)_{\rm pole}$, and ψ, adjusting $\theta_{\rm equ}$ slightly (<0.3%) to minimize χ^2_ν for each model (see below). Figure 4 shows a χ^2_ν map in the $(\omega,\ \psi)$-plane for a range of $\theta_{\rm equ}$ values with $T_{\rm eff}^{\rm pole} = 10,250$ K, $\log(g)_{\rm pole} = 4.1$. We find a best fit of $\chi^2_\nu = 1.31$ for parameters $\omega = 0.91$, $\theta_{\rm equ} = 3.329$ mas, and $\psi = 40^\circ$. A direct comparison of this model with the squared visibility data is shown in Figure 5.

The F-test provides a 1 σ lower limit on ω at $\simeq$0.89. For $\omega < 0.89$, the synthetic V^2 values are generally too high across the second lobe because the model is not sufficiently darkened toward the limb. Correspondingly, the upper limits on ω are constrained because the synthetic V^2 values are generally too low across the second lobe, due to very strong darkening toward the limb for $\omega \gtrsim 0.93$. In addition, the upper limit on ω is a function of ψ because the projected stellar disk appears sufficiently more elliptical, even at low inclinations $i \simeq 5^\circ$, as the model star rotates faster. The data from the nearly orthogonal E2-W1 and E2-S1 baselines constrain models with $\omega > 0.92$ to limited range of position angles, but these data provide no constraint on ψ at lower ω-values where the star is less distorted, $R_{\rm equ}/R_{\rm pole} < 1.24$.

As ω increases so does the darkening of the limb due to the increasing larger pole-to-equator effective temperature difference. As a result, the best-fit $\theta_{\rm equ}$ value increases with ω because

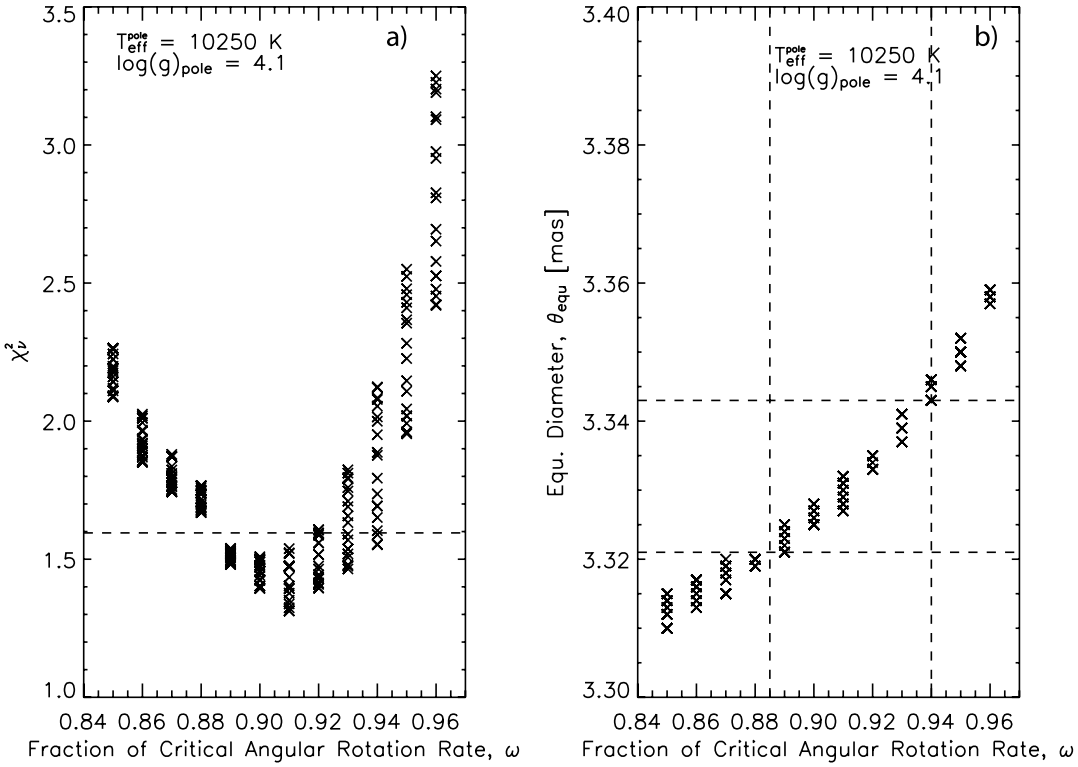

FIG. 6.—Constraints on model parameters from the CHARA/FLUOR data. (*a*) Reduced χ^2 values χ^2_ν from the Roche-von Zeipel model fit to the squared visibility data as a function the fraction of the critical angular break-up rate, $\omega = \Omega/\Omega_{crit}$, for fixed values of the polar effective temperature T_{eff}^{pole} and polar surface gravity $\log(g)_{pole}$. The dashed line denotes the 1 σ confidence region for ω from the F test for 24 degrees of freedom relative to the best fit at $\chi^2_\nu = 1.31$. For each ω, χ^2_ν values are plotted for 18 position angles ψ (0° to 170° in 10° steps; see Fig. 4). (*b*) Relationship between the best-fit equatorial angular diameter θ_{equ} at each ω for the range of position angles. The dashed lines provide an estimate for the 1 σ range in ω and the corresponding range in the equatorial angular diameter.

the effective "limb-darkening" correction increases. The best-fit values for θ_{equ} and ω are therefore correlated. To establish this correlation, we estimated the best-fitting θ_{equ} value for a given ω without recomputing the brightness map and Fourier components. While each intensity map is constructed for a fixed θ_{equ} value, we can approximate the squared visibilities for models with slightly (<0.5%) larger or smaller θ_{equ} values as follows. A small adjustment to V^2 due to a small adjustment in θ_{equ}, assuming the physical model for the star is not significantly changed and the model changes relatively slowly with wavelength, is equivalent to computing V^2 at a larger (smaller) wavelength for a larger (smaller) value of θ_{equ}. So, for a given projected baseline, we linearly interpolate (in the log) $V^2_\lambda(u, v)$ at $\lambda = \lambda_k(\theta_{fit}/\theta_{equ})$, a wavelength shift of 10 nm or less. Near the bandpass edges, the instrument transmission drops to zero, so there is no concern about interpolating outside of the wavelength grid with this scheme. The V^2 normalization, equation (20), must be scaled by the $(\theta_{fit}/\theta_{equ})^2$ to compensate for the revised surface area of the star. After one iteration, setting $\theta_{equ} = \theta_{fit}$, recomputing the Fourier map and refitting the data, the best-fit θ_{equ} value is within 0.25% of that found with the estimated model V^2 values.

Figure 6*a* shows the χ^2_ν values from Figure 4 projected on the ω axis, with a spread of values for the 18 position angles at each ω-value. This shows again that for the range $0.89 < \omega < 0.92$ there is no constraint on the position angle of the pole. The corresponding best-fit θ_{equ} values are shown in Figure 6*b*. The equatorial angular diameter is constrained to the range 3.32 mas < θ_{equ} < 3.34 mas. The best fit to the CHARA/FLUOR data is insensitive to T_{eff}^{pole}. This is because ΔT_{eff}, which determines the overall darkening, is quite sensitive to ω, but T_{eff}^{pole} is not (see eq. [8]). Thus, we cannot usefully constrain T_{eff}^{pole} or ψ from the CHARA/FLUOR data. As for the surface gravity, varying $\log(g)_{pole}$ over what we consider the most probable range, 4.1 ± 0.1, does not significantly effect the χ^2_ν minimum. Models with $\log(g)_{pole}$ values from 3.9 to 4.3 all fall within 1 σ of the best fit. The best-fit θ_{equ} values are essentially independent of T_{eff}^{pole} between 9800 and 10,450 K and weakly dependent on $\log(g)_{pole}$

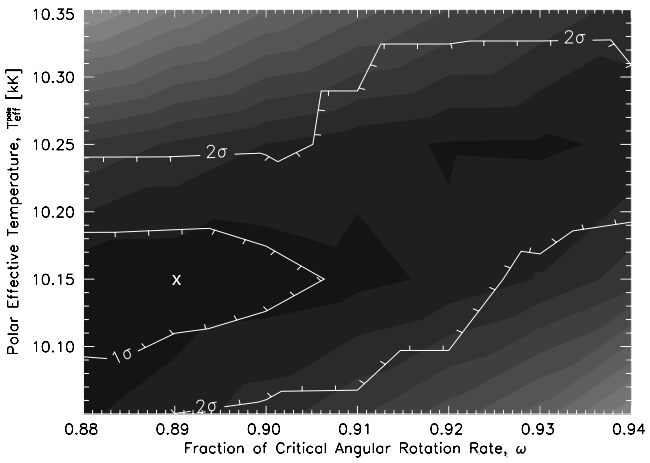

FIG. 7.—Contour plot of χ^2_ν for the SED fits in the (ω, T_{eff}^{pole})-plane. The ω range is limited to the 1 σ range from CHARA/FLUOR fits (see Fig. 6). The polar surface gravity is fixed at $\log(g)_{pole} = 4.1$. The labeled contours denote the 1 and 2 σ regions from the F test. The cross marks the location of the best-fit model, $\chi^2_\nu = 8.7$.

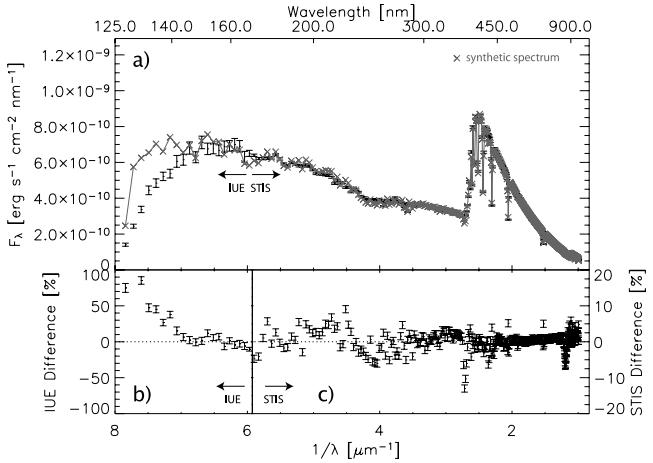

FIG. 8.—(*a*) Comparison between the SED of Bohlin & Gilliland (2004) and our best-fitting ($\chi^2_\nu = 8.7$) rapidly rotating SED model for Vega: $\omega = 0.91$, $T_{\rm eff}^{\rm pole} = 10,150$ K, and $\log(g)_{\rm pole} = 4.10$. Also shown are the differences between this model and the data in (*b*) the region at shorter wavelengths observed by the *IUE* and (*c*) the region observed by the *HST* Space Telescope Imaging Spectrograph at longer wavelengths. At wavenumbers $1/\lambda < 2.38$ μm^{-1} the "observed" SED is represented by a closely fitting Kurucz model spectrum (see Bohlin & Gilliland 2004).

between 3.8 and 4.3; all best-fit $\theta_{\rm equ}$ values fall well within the 1 σ range established in Figure 6.

5.3. *Spectral Energy Distribution: Parameter Grid Search*

Here we compare our synthetic SEDs to the absolute spectrophotometry of Vega. Specifically, we compare our models to the data-model composite SED[10] of Bohlin & Gilliland (2004), which includes *International Ultraviolet Explorer* (*IUE*) data from 125.5 to 167.5 nm, *Hubble Space Telescope* (*HST*) Space Telescope Imaging Spectrograph (STIS) data from 167.5 to 420 nm, and a specifically constructed Kurucz model shortward of *IUE* and longward 420 nm to match and replace data corrupted by CCD fringing in this wavelength region. To facilitate this comparison, first the synthetic spectra were convolved to the spectral resolution of the observations ($\lambda/\Delta\lambda = 500$), and then both the data and convolved synthetic spectra were binned: 2.0 nm wide bins in the UV (127.5–327.5 nm, 101 bins) and 2.0 nm bins in the optical and near-IR (330.0–1008 nm, 340 bins) for a total of 441 spectral bins.

[10] At ftp://ftp.stsci.edu/cdbs/cdbs2/calspec/alpha_lyr_stis_002.fits.

Figure 7 shows the χ^2_ν map in the (ω, $T_{\rm eff}^{\rm pole}$)-plane. These two parameters, apart from the angular diameter, most sensitively affect the fit to the observed SED. There is a clear positive correlation between ω and $T_{\rm eff}^{\rm pole}$. This makes sense if one considers that a more rapidly rotating star will be more gravity darkened and require a hotter pole to compensate for a cooler equator in order to match the same SED. Following this correlation, it is expected that a continuum of models from ($\omega = 0.89$, $T_{\rm eff}^{\rm pole} = 10,150$ K) to ($\omega = 0$, $T_{\rm eff}^{\rm pole} = 9550$ K) will provide a reasonable fit to the SED since the nonrotating ATLAS12 model of Kurucz fits the observed SED quite well (Bohlin & Gilliland 2004). However, we did not consider models with $\omega < 0.88$ in the SED analysis because such models are a poor match to the CHARA/FLUOR squared visibility data set as shown above. In other words, although the ATLAS12 model provides a good fit to the observed SED, it fails to predict the correct center-to-limb darkening for Vega.

The best-fit synthetic spectrum is shown in Figure 8. Considering the complexity of this synthetic SED relative to a single $T_{\rm eff}$ model, there is generally good agreement (±5%) between our best-fit model and the data longward of 300 nm, apart from larger mismatches at the Paschen and Balmer edges and in the Balmer lines. Longward of 140 nm, the model agrees with the observations to within ±10%. At wavelengths below 140 nm, as measured by the *IUE*, the data are up to a factor of 2 lower than predicted. Our best fit yields $\chi^2_\nu = 8.7$. The overprediction below 140 nm has only a small effect on the synthetic integrated flux between 127.5 and 1008 nm, 2.79×10^{-5} ergs cm^{-2} s^{-1}, which is within 1.2 σ of the value derived from an integration of the observed SED, $(2.748 \pm 0.036) \times 10^{-5}$ ergs cm^{-2} s^{-1}. The equatorial angular diameter derived from this SED fit, $\theta_{\rm equ} = 3.407$ mas, differs from the best fit to the CHARA/FLUOR data, $\theta_{\rm equ} = 3.329$ mas, by 2.4%, a value within the uncertainty of the absolute flux calibration.

6. DISCUSSION

The best-fit stellar parameters, based on the model fits to the CHARA/FLUOR data and archival spectrophotometry in § 5, are summarized in Table 2. As discussed in § 3, the effect of extended K'-band emission in the Vega system, if unaccounted for, is to increase the apparent angular diameter of Vega slightly, by ~0.3%. Correcting for this effect via equation (1), the best-fit equatorial diameter is shifted systematically lower by 0.3% (0.01 mas) to the range 3.31 mas $< \theta_{\rm equ} <$ 3.33 mas. We find that all other parameters in Table 2 are uneffected by the extended emission within the error bars given. The best-fit range for the fraction of the angular break-up rate, $0.89 < \omega < 0.92$, sensitive to

TABLE 2
FUNDAMENTAL STELLAR PARAMETERS FOR VEGA

Parameter	Symbol	Value	Reference
Fraction of the angular break-up rate	ω	0.91 ± 0.03	CHARA/FLUOR V^2 fit
Equatorial angular diameter (mas)	$\theta_{\rm equ}$	3.33 ± 0.01	CHARA/FLUOR V^2 fit
Parallax (mas)	$\pi_{\rm hip}$	128.93 ± 0.55	Perryman et al. (1997)
Equatorial radius ($R_\odot$)	$R_{\rm equ}$	2.78 ± 0.02	Eq. (2)
Polar radius ($R_\odot$)	$R_{\rm pole}$	2.26 ± 0.07	Eq. (3)
Pole-to-equator $T_{\rm eff}$ difference (K)	$\Delta T_{\rm eff}$	2250^{+400}_{-300}	Eq. (8)
Polar effective temperature (K)	$T_{\rm eff}^{\rm pole}$	10,150 ± 100	Fit to spectrophotometry (Bohlin & Gilliland 2004)
Luminosity ($L_\odot$)	L	37 ± 3	Eq. (5)
Mass ($M_\odot$)	M	2.3 ± 0.2	$(L/L_\odot) = (M/M_\odot)^{4.27\pm0.20}$ (from Sirius)
Polar surface gravity (cm s^{-2})	$\log(g)_{\rm pole}$	4.1 ± 0.1	Eq. (4)
Equatorial rotation velocity (km s^{-1})	$V_{\rm equ}$	270 ± 15	Eqs. (13) and (15)
Projected rotation velocity (km s^{-1})	$v \sin i$	21.9 ± 0.2	Hill et al. (2004)
Inclination of rotation axis (deg)	i	4.7 ± 0.3	Eq. (14)

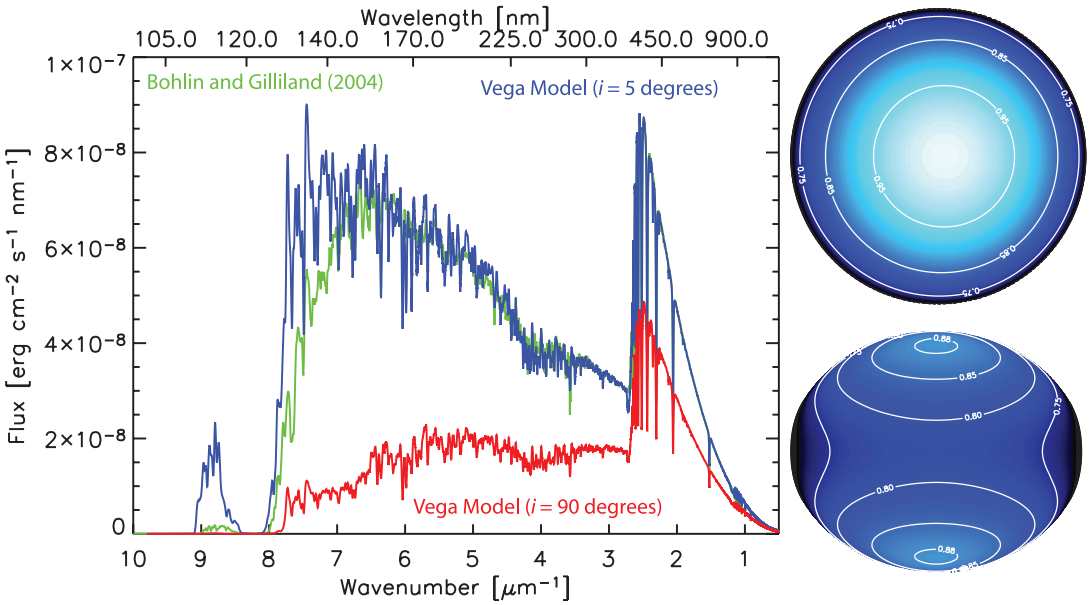

FIG. 9.—*Left*: Comparison between the SED from Bohlin & Gilliland (2004; *IUE* and *HST* observations supplemented by a slowly rotating model spectrum both below 127.5 nm and longward of 420 nm) and two rapidly rotating models for Vega's SED, one viewed from an inclination of 5° (nearly pole on) and one viewed from an inclination of 90° (equator on), from an integration of two intensity maps via eq. (24) for these inclinations. *Right*: Comparison of the best-fit brightness distributions for Vega with inclinations of 5° (*top*) and 90° (*bottom*). For the equator-on view, the poles appear 10% fainter than the pole-on view due to limb darkening.

the amplitude of the second lobe, is unaffected by the extended emission because the V^2 correction is quite small there, $\Delta V^2 < 0.0003$, relative to the first lobe, where the correction is up to 20 times larger.

One parameter that stands out is our large pole-to-equator effective temperature difference, $\Delta T_{\rm eff} = 2250^{+400}_{-300}$ K, relative to previous spectroscopic and spectrophotometric studies of Vega (Gulliver et al. 1994; Hill et al. 2004) for which $\Delta T_{\rm eff}$ falls into the range 300 to 400 K. Our larger $\Delta T_{\rm eff}$ yields a much cooler equatorial effective temperature, $T_{\rm eff}^{\rm equ} = 7900^{+500}_{-400}$ K, than most recently reported for Vega, 9330 K (Hill et al. 2004). The amplitude of the second-lobe visibility measurements as observed by CHARA/FLUOR is well fit by strong darkening toward the limb. In the context of the Roche-von Zeipel model, such darkening requires a large pole-to-equator $T_{\rm eff}$ gradient. Consequently, we predict that Vega's equator-on SED (that is, viewed as if $i = 90°$ and integrated over the visible stellar disk; see eq. [24]) has a significantly lower color temperature and overall lower flux, particularly in the midultraviolet where the flux is lower by a factor of 5, as shown in Figure 9. A debris disk, aligned with Vega's equatorial plane as suggested by our nearly pole-on model for the star and the recent observations of a circular disk in the mid-IR (Su et al. 2005), should see a significantly less luminous, cooler SED than we see from the Earth. In the literature to date, modeling of the heating, scattering, and emission of Vega's dusty debris disk has assumed an irradiating SED equal to the pole-on view of Vega (see, e.g., Absil et al. 2006; Su et al. 2005). Our synthetic photospheric equatorial spectrum for Vega is tabulated in Table 3. It should be interesting to investigate how our predicted equatorial spectrum used in such modeling will affect conclusions regarding the amount of dust and the grain-size distribution in the debris disk.

Several of Vega's fundamental stellar parameters ($\Delta T_{\rm eff}$, $V_{\rm equ}$, i) we derive differ significantly from those derived by Gulliver et al. (1994) and Hill et al. (2004) from high-dispersion spectroscopy. Regarding $\Delta T_{\rm eff}$, both spectroscopic studies find $\omega \simeq 0.5$, while we find $\omega = 0.91 \pm 0.03$. These two ω-values, along with the corresponding $T_{\rm eff}^{\rm pole}$ values, 9680 and 10,150 K, in equation (8), yield $\Delta T_{\rm eff}$ values of 350 and 2250 K. The reason the ω-values differ is at least partly linked to inconsistent parameters used in the spectroscopic studies. As noted in Hill et al. (2004), the Gulliver et al. (1994) study finds a low value for the polar gravity, $\log(g)_{\rm pole} = 3.75$, which yields a mass for Vega of only 1.34 $M_\odot$ and an inclination inconsistent with the expected equatorial velocity. The equatorial velocity of Hill et al. (2004), $V_{\rm equ} = 160$ km s^{-1}, is not consistent with their other parameters [$\omega = 0.47, \log(g)_{\rm pole} = 4.0, R_{\rm equ} = 2.73\,R_\odot, i = 7\overset{\circ}{.}9$] which should yield instead $V_{\rm equ} = 113$ km s^{-1} and $i = 11\overset{\circ}{.}1$. Values of $V_{\rm equ} = 160$ km s^{-1} and $i = 7\overset{\circ}{.}9$ are recovered if $\omega = 0.65$, which corresponds to $V_{\rm equ}/V_{\rm crit} = 0.47$. It is possible to confuse ω with $V_{\rm equ}/V_{\rm crit}$. The two are not equivalent:

$$\omega = \frac{\Omega}{\Omega_{\rm crit}}\frac{V_{\rm equ}}{V_{\rm crit}} = 2\cos\left[\frac{\pi + \cos^{-1}(\omega)}{3}\right]. \qquad (25)$$

TABLE 3

A MODEL EQUATORIAL PHOTOSPHERIC SPECTRAL ENERGY DISTRIBUTION FOR VEGA FROM 1020.5 Å TO 40 μm (R = 500)

Wavelength (Å) (1)	Flux (F_λ)[a] (ergs cm^{-2} s^{-1} Å^{-1}) (2)
1.020500000000000E+03	1.68027E+03
1.021000000000000E+03	1.65680E+03
1.021500000000000E+03	1.62296E+03
1.022000000000000E+03	1.57629E+03
1.022500000000000E+03	1.51370E+03

NOTE.—Table 3 is published in its entirety in the electronic edition of the *Astrophysical Journal*. A portion is shown here for guidance regarding its form and content.

[a] The flux at a distance d from Vega *in the equatorial plane* is the flux from col. (2) multiplied by the ratio $(R_{\rm equ}/d)^2$, the ratio squared of Vega's equatorial radius to the distance, or $(2.78/d)^2$ when d has the units of solar radii.

For $\omega = 0.65$, the corresponding $\Delta T_{\rm eff} = 757$ K, not 350 K. Therefore, there appears to be a mismatch between the $V_{\rm equ}$ and $\Delta T_{\rm eff}$ values used in the most recent spectral analyses, and this suggests the spectral data must be reanalyzed with a consistent model. A. Gulliver (2006, private communication) confirms that Hill et al. (2004) did confuse ω with $V_{\rm equ}/V_{\rm crit}$, and this group is now reanalyzing Vega's high-dispersion spectrum. Our best-fit value for ω, derived from the interferometric data, is appealing because, together with our derived polar effective temperature, it yields a luminosity consistent with that of slowly rotating A0 V stars. A more slowly rotating model for Vega will have a warmer equator and an overall higher true luminosity too large for its mass. Therefore, it seems that less rapidly rotating models for Vega do not offer an explanation for the apparent overluminosity with respect to its spectral type.

Our best-fit model, while it provides self-consistent parameters within the Roche–von Zeipel context, has several discrepancies, most notably producing too much flux below 140 nm relative to the observed SED. The limitations of the LTE metal-line blanketing for modeling Vega in the ultraviolet have recently been explored by García-Gil et al. (2005). They find that in the UV the line opacity is generally systematically too large in LTE because the overionization in non-LTE is neglected. Our best model flux below 140 nm is already too large, so a fully non-LTE treatment is not expected to improve this discrepancy. The Wien tail of Vega's SED will be the most sensitive to the warmest colatitudes near the pole. In our strictly radiative von Zeipel model, SEDs with $T_{\rm eff}^{\rm pole} < 10{,}050$ K produce too much flux in the optical and near-IR, so simply lowering $T_{\rm eff}^{\rm pole}$ will not solve the problem; the temperature gradient must differ from the $T_{\rm eff} \propto g_{\rm eff}^{0.25}$ relation. The equatorial effective temperature we derive, 7900 K, may indicate that Vega's equatorial region is convective. If so, von Zeipel's purely radiative gravity darkening exponent, $\beta = 0.25$, will not be valid near the equator. A more complex model, in which the gravity darkening transitions from purely radiative near the pole to partially convective near the equator, may be the next approach to take. Such a temperature profile may allow for a cooler $T_{\rm eff}^{\rm pole}$, reducing the flux discrepancy below 140 nm, while still matching the observed optical and near-IR fluxes. Such a gradient must also improve the match to the Balmer and Paschen edges and the Balmer lines.

7. SUMMARY

We have demonstrated that a Roche–von Zeipel model atmosphere rotating at 91% ± 3% of the angular break-up rate provides a very good match to K'-band long-baseline interferometric observations of Vega. These observations sample the second lobe of Vega's visibility curve and indicate a limb-darkening correction 2.5 times larger than expected for a slowly rotating A0 V star. In the context of the purely radiative von Zeipel gravity darkening model, the second-lobe visibility measurements imply a ∼22% reduction in the effective temperature from pole to equator. The model predicts an equatorial velocity of 270 ± 15 km s^{-1}, which together with the measured $v \sin i$ yields an inclination of $i \simeq 5^\circ$, confirming the pole-on model for Vega suggested by Gray (1988) to explain Vega's anomalous luminosity. Our model predicts a true luminosity for Vega of 37 ± 3 $L_\odot$, consistent with the mean luminosity of A0 V stars from $W(\mathrm{H}\gamma)$-M_V calibration (Millward & Walker 1985). We predict that Vega's spectral energy distribution viewed from its equatorial plane is significantly cooler than viewed from its pole. This equatorial spectrum may significantly impact conclusions derived from models for Vega's debris disk that have employed Vega's observed polar-view spectral energy distribution, rather than the equatorial one, which seems more appropriate given our observations.

We thank G. Romano and P.J. Goldfinger for their assistance with the operation of FLUOR and CHARA respectively. F. Schwab kindly provided advice on two-dimensional FFTs and aliasing. Thanks to T. Barman for discussions about numerical cubature and to the entire PHOENIX development team for their support and interest in this work. Thanks to referee A. Gulliver for his careful reading and suggestions. This work was performed in part under contract with the Jet Propulsion Laboratory (JPL), funded by NASA through the Michelson Fellowship Program. JPL is managed for NASA by the California Institute of Technology. The National Optical Astronomy Observatory is operated by the Association of Universities for Research in Astronomy (AURA), Inc., under cooperative agreement with the National Science Foundation (NSF). This research has been supported by NSF grants AST 02-05297 and AST 03-07562. Additional support has been received from the Research Program Enhancement program administered by the Vice-President for Research at Georgia State University. In addition, the CHARA Array is operated with support from the Keck Foundation and the Packard Foundation. This research has made use of NASA's Astrophysics Data System, and the SIMBAD database, operated at CDS, Strasbourg, France. Some of the data presented in this paper was obtained from the Multimission Archive (MAST) at the Space Telescope Science Institute (STScI). STScI is operated by AURA, Inc., under NASA contract NAS5-26555. Support for MAST for non-*HST* data is provided by the NASA Office of Space Science via grant NAG5-7584 and by other grants and contracts.

Facilities: CHARA (FLUOR)

REFERENCES

Absil, O., et al. 2006, A&A, 452, 237
Aumann, H. H., et al. 1984, ApJ, 278, L23
Bohlin, R. C., & Gilliland, R. L. 2004, AJ, 127, 3508
Ciardi, D. R., van Belle, G. T., Akeson, R. L., Thompson, R. R., Lada, E. A., & Howell, S. B. 2001, ApJ, 559, 1147
Collins, G. W. 1963, ApJ, 138, 1134
———. 1964, ApJ, 139, 1401
———. 1966, ApJ, 146, 914
Collins, G. W., & Sonneborn, G. H. 1977, ApJS, 34, 41
Coudé du Foresto, V., Ridgway, S., & Mariotti, J.-M. 1997, A&AS, 121, 379
Coudé du Foresto, V., et al. 2003, Proc. SPIE, 4838, 280
Cranmer, S. R., & Owocki, S. P. 1995, ApJ, 440, 308
Davis, J., Tango, W. J., & Booth, A. J. 2000, MNRAS, 318, 387
Elste, G. H. 1992, ApJ, 384, 284
García-Gil, A., García López, R. J., Allende Prieto, C., & Hubeny, I. 2005, ApJ, 623, 460
Gray, R. O. 1985, JRASC, 79, 237
———. 1988, JRASC, 82, 336
Gulliver, A. F., Adelman, S. J., Cowley, C. R., & Fletcher, J. M. 1991, ApJ, 380, 223
Gulliver, A. F., Hill, G., & Adelman, S. J. 1994, ApJ, 429, L81
Hanbury Brown, R., Davis, J., Allen, L. R., & Rome, J. M. 1967, MNRAS, 137, 393
Hardorp, J., & Strittmatter, P. A. 1968, ApJ, 151, 1057
Hauschildt, P. H., Allard, F., Ferguson, J., Baron, E., & Alexander, D. R. 1999, ApJ, 525, 871
Hearnshaw, J. B. 1996, The Measurement of Starlight: Two Centuries of Astronomical Photometry (Cambridge: Cambridge Univ. Press)
Hill, G., Gulliver, A. F., & Adelman, S. J. 2004, in IAU Symp. 224, The A-Star Puzzle, ed. J. Zverko, J. Ziznovsky, S. J. Adelman, & W. W. Weiss (Cambridge: Cambridge Univ. Press), 35
Hughes, D. W. 2001, J. British Astron. Assoc., 111, 266

Kervella, P., Ségransan, D., & Coudé du Foresto, V. 2004, A&A, 425, 1161
Kervella, P., Thévenin, F., Morel, P., Bordé, P., & Di Folco, E. 2003, A&A, 408, 681
Maeder, A., & Peytremann, E. 1970, A&A, 7, 120
McAlister, H. A. 1985, in IAU Symp. 111, Calibration of Fundamental Stellar Quantities, ed. D. S. Hayes & A. G. D. Philip (Dordrecht: Reidel), 97
McAlister, H. A., et al. 2005, ApJ, 628, 439
Mérand, A., Bordé, P., & Coudé du Foresto, V. 2005a, A&A, 433, 1155
Mérand, A., et al. 2005b, A&A, 438, L9
Millward, C. G., & Walker, G. A. H. 1985, ApJS, 57, 63
Mozurkewich, D., et al. 2003, AJ, 126, 2502
Ohishi, N., Nordgren, T. E., & Hutter, D. J. 2004, ApJ, 612, 463
Perrin, G., & Ridgway, S. T. 2005, ApJ, 626, 1138
Perryman, M. A. C., et al. 1997, A&A, 323, L49
Peterson, D. M., et al. 2004, Proc. SPIE, 5491, 65
———. 2006, ApJ, 636, 1087
Petrie, R. M. 1964, Publ. Dom. Astrophys. Obs. Victoria, 12, 317
Press, W. H., Teukolsky, S. A., Vetterling, W. T., & Flannery, B. P., ed. 1992, Numerical Recipes in FORTRAN (2nd ed.; Cambridge: Cambridge Univ. Press)
Stroud, A. H., & Secrest, D. 1966, Gaussian Quadrature Formulas (Englewood Cliffs: Practice Hall)
Su, K. Y. L., et al. 2005, ApJ, 628, 487
ten Brummelaar, T. A., et al. 2005, ApJ, 628, 453
van Belle, G. T., et al. 2006, ApJ, 637, 494
van Hamme, W. 1993, AJ, 106, 2096
von Zeipel, H. 1924a, MNRAS, 84, 665
———. 1924b, MNRAS, 84, 684

Note added in proof.—New closure phase operations of Vega at visual wavelenghts with the Navy Prototype Optical Interferometer (D. M. Peterson et al., Nature, 440, 896 [2006]) are also consistent with a rapidly rotating model for Vega. The Peterson et al. model establishes values for Vega's mass, equatorial velocity, polar surface gravity, inclination, angular velocity, polar radius, and equatorial effective temperature that overlap with our values within the uncertainties. While both the Peterson et al. model and our model appear to have the same Roche-von Zeipel formalism, the two data sets and models yield significantly different equatorial radii: $R_{\rm equ} = 2.78 \pm 0.02\ R_\odot$ (CHARA/FLUOR) versus $2.873 \pm 0.026\ R_\odot$ (NPOI). This difference is directly linked to a difference in the derived angular size of Vega's equator in two studies: $\theta_{\rm equ} = 3.33 \pm 0.01$ mas (CHARA/FLUOR) versus 3.446 ± 0.031 mas (NPOI). We do not at present understand the reason for this dependency.

4.5 Projets de recherche

Le domaine de l'étude des étoiles en rotation rapide par interférométrie est en développement très rapide. Tous les interféromètres à longue base actuellement opérationnels possèdent un grand programme d'observation de ces objets. Les déformations photosphériques spectaculaires observées jusqu'à présent ont en effet soulevé nombre de questions sur la structure interne de ces objets. Alors que pour les étoiles les moins massives, comme Altaïr, le modèle de rotation de corps solide (modèle de Roche) apparaît satisfaisant, il est insuffisant pour expliquer les observations d'Achernar, une étoile B plus massive.

L'introduction de la rotation différentielle n'est cependant pas aisée : comment définir la loi de variation radiale ? La seule contrainte observationnelle envisageable pour l'instant est la répartition de lumière à la surface de l'étoile, qui donne directement accès, via le théorème de Von Zeipel, à la gravité effective, c'est-à-dire à la somme de la gravitation et de la force centrifuge. Je prévois donc d'orienter mon travail vers une cartographie de la surface de plusieurs étoiles Be proches, avec notamment des observations AMBER de Achernar. D'autre part, la mise en évidence d'une enveloppe circumstellaire asymétrique autour d'Achernar implique que l'étude de la répartition de lumière photosphérique passe aussi par une meilleure compréhension de l'environnement proche des étoiles Be.

Chapitre 5

Perspectives scientifiques

5.1 Une technique de spécialistes ?

L'interférométrie optique a largement évolué dans les années 1990, passant d'une technique confidentielle, réservée à un petit nombre de spécialistes, à un moyen d'observation courant et accessible à tous les astronomes. Ceci est particulièrement vrai depuis l'ouverture du VLTI, et la première mise à la disposition d'une grande communauté de l'instrument VINCI, en 2001-2002. Les instrumentalistes spécialistes d'interférométrie ont par ailleurs fait des efforts importants pour rendre cette technique accessible, par des écoles de formation (Ecole d'été Michelson, Ecole de Goutelas,...), ainsi que de nombreux séminaires et conférences. Le Centre Jean-Marie Mariotti (JMMC), créé en 2000, permet aujourd'hui à tous les astronomes français de bénéficier du soutien de spécialistes. Le JMMC développe également des outils logiciels pour la préparation des observations (ASPRO) et la réduction des données (logiciel de réduction AMBER). Sur le plan pratique, les interféromètres les plus avancés (VLTI, CHARA par exemple) permettent une mise en oeuvre par un seul opérateur, voire même à distance. L'interférométrie stellaire à longue base n'est donc plus aujourd'hui une technique de spécialistes, même si les données interférométriques sont plus complexes à analyser que celles produites par un télescope monolithique. Elles présentent par ailleurs la caractéristique de n'être en général interprétables que dans une démarche d'ajustement d'un modèle aux résultats d'observation (sauf dans le cas de la synthèse d'images). L'augmentation rapide du nombre de publications rapportant des résultats d'observation témoigne de la vigueur de la recherche astronomique utilisant l'interférométrie (Fig. 5.1).

5.2 Un nouvel outil pour la physique stellaire

L'observation des étoiles repose historiquement sur trois techniques :
- la *photométrie*, en bande large ou en bande étroite, incluant l'imagerie,
- la *spectrographie* et la spectrophotométrie,
- la *polarimétrie* et la spectropolarimétrie.

L"interférométrie permet d'enrichir ces techniques classiques en levant, au moins partiellement, la dégénerescence spatiale de la mesure à petite échelle angulaire. Les trois techniques classiques appliquées à la lumière collectée par un télescope monolithique ne permettent que des mesures intégrées sur la tache de diffraction, qui est presque toujours beaucoup plus grande que la taille angulaire des étoiles observées. Le passage à la haute résolution angulaire permis par l'interférométrie permet de détailler la contribution de chaque partie de l'objet observé. Il est

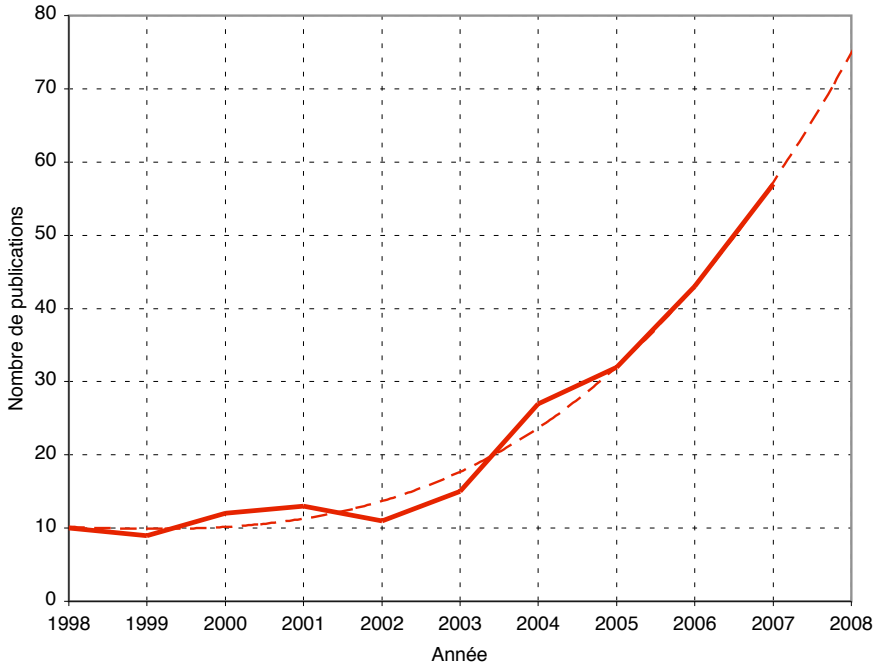

FIG. 5.1 – Evolution du nombre de publications rapportant des résultats d'observations obtenues par interférométrie optique et infrarouge sur une période de 10 ans.

important de noter qu'un interféromètre est simplement une forme particulière de télescope, les franges étant les images produites par ce télescope. Un interféromètre doit nécessairement alimenter un instrument d'un des trois types classiques pour réaliser des mesures physiques. VINCI, comme beaucoup des instruments interférométriques existants, est apparenté à un "photomètre interférométrique", alors que AMBER et MIDI sont plutôt des "spectrographes interférométriques". Un exemple de "spectro-polarimètre interférométrique" est l'instrument GI2T-REGAIN, fonctionnant en visible.

5.3 Combien d'étoiles mesurables ?

Les limitations de l'interférométrie sont, comme pour les télescopes monolithiques, liées à la résolution angulaire qu'il est possible d'atteindre et à la sensibilité photométrique. Ces deux paramètres imposent une limite au nombre de sources qu'il est possible de détailler. La courbe de la Fig. 5.2 montre le nombre total d'étoiles en fonction de leur diamètre angulaire, estimé par les relations de brillance de surface (Sect. 3.4). Sachant que le VLTI en bande H permet de résoudre complètement une étoile d'une taille angulaire de 2 mas environ, 1000 étoiles sont en principe résolvables, sur tout le ciel (environ les 2/3 sont observables depuis Paranal). La mesure de l'assombrissement centre-bord nécessite au moins deux éléments de résolution sur la photosphère de l'étoile, ce qui réduit l'échantillon mesurable à environ 200 étoiles. Ce chiffre relativement faible est la conséquence du fait que l'interférométrie, contrairement à la spectroscopie par exemple, est sensible à la distance des objets observés. Deux étoiles identiques dont l'une est 5 fois plus distante donneront le même spectre en posant 25 fois plus longtemps sur l'étoile la plus lointaine. Par contre, pour une précision de mesure donnée, si l'étoile lointaine est non résolue, poser plus longtemps une observation interférométrique ne permettra pas de la résoudre. Seule

l'augmentation de la longueur de base, et donc du pouvoir de résolution, permettra de réaliser cette mesure.

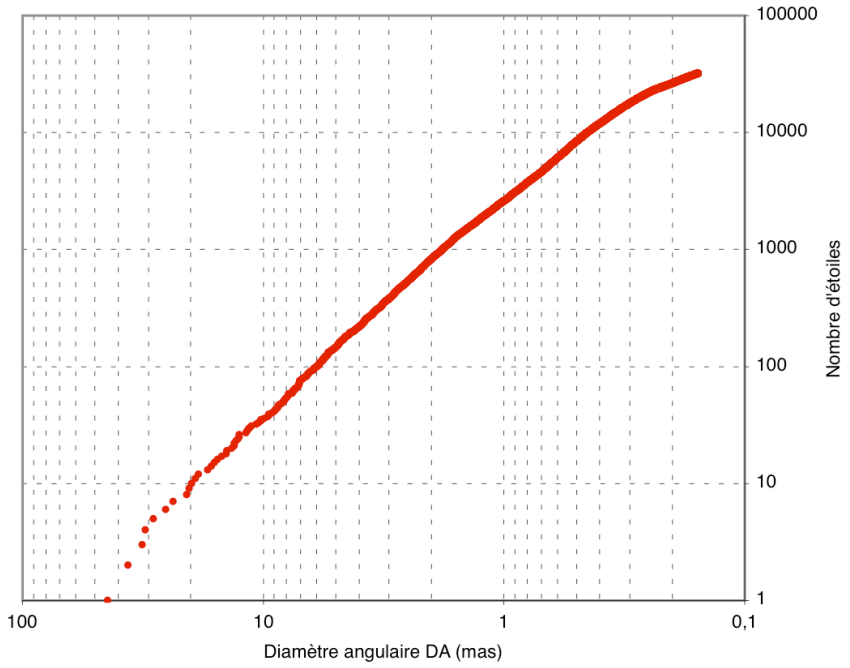

FIG. 5.2 – Nombre d'étoiles observables dont le diamètre angulaire est plus grand que la valeur indiquée en abcisse (échantillon des étoiles plus brillantes que $m_V = 8$ extrait du catalogue Hipparcos).

Par ailleurs, si l'on souhaite estimer le rayon lineaire de l'étoile, il faut de plus une mesure de distance. Un rayon linéaire est nécessaire par exemple pour modéliser les étoiles présentant des oscillations de type solaire (voir Sect. 3.2). En croisant le catalogue Hipparcos avec les relations de brillance de surface, il apparaît que le nombre total d'étoiles "utiles" dans ce cadre est relativement réduit (Fig. 5.3) et que les types spectraux accessibles ne couvrent pas tout le diagramme de Hertzsprung-Russell (Figs. 5.4).

De ces calculs simples, il ressort que l'interférométrie est limitée à un nombre de sources relativement faible avec les instruments actuels. Ceci met en lumière la nécessité d'imaginer une nouvelle génération d'interféromètres pour pouvoir aborder l'observation d'une plus grande variété d'objets célestes. Si la sensibilité des télescopes de 8 m du VLTI n'est pour l'instant pas limitante, la longueur de base maximale entre deux de ces télescopes (135 m) limite pour l'instant la résolution accessible à environ 1 mas.

5.4 La fiabilité, clef des grands réseaux

Les progrès technologiques permettent aujourd'hui de gérer les grands réseaux de télescopes, comme le VLTI ou CHARA, avec une fiabilité remarquable. Il est intéressant de noter par exemple que les derniers chiffres de la fiabilité du VLTI publiées par l'ESO font apparaître un taux de disponibilité de 75% environ, à comparer aux 90% d'un télescope unitaire. Considérant que le VLTI utilise au moins deux télescopes simultanément, des lignes à retard, et des instruments complexes, la performance est plus qu'honorable ! La même évolution est visible pour les

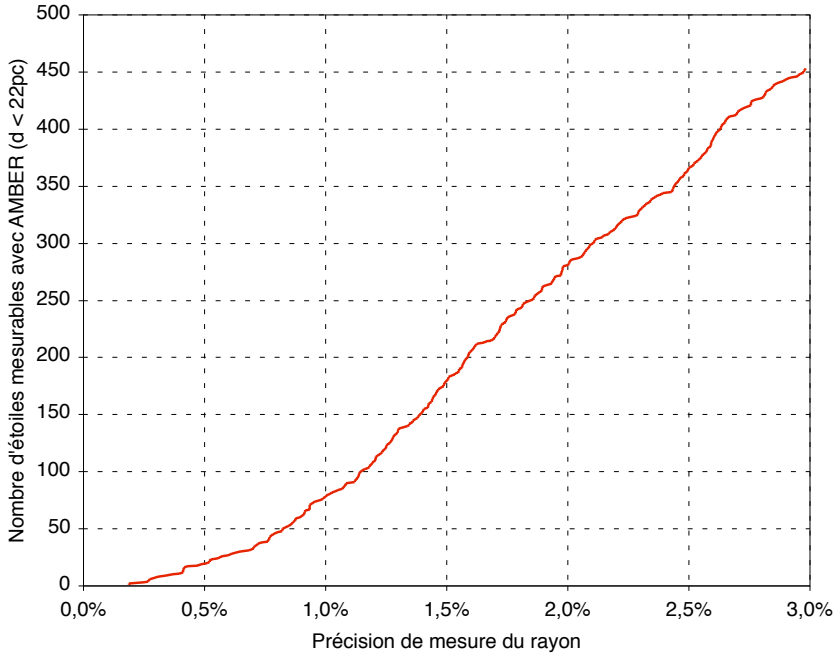

FIG. 5.3 – Nombre d'étoiles situées à moins de 22 pc en fonction de la précision atteignable sur la mesure de leur rayon linéaire, par la combinaison de mesures AMBER de diamètre angulaire (bande H, base de 200m) et de parallaxes Hipparcos.

autres interféromètres en opération : plus de fiabilité et plus de régularité dans l'obtention de données, elles-mêmes de meilleure qualité.

Cette phase de consolidation des technologies est très importante pour préparer la prochaine génération d'instruments du VLTI, le réseau OHANA et les missions d'interférométrie dans l'espace comme DARWIN. Le niveau de complexité d'un réseau de 8 télescopes, à l'image du VLTI, atteint un niveau tel que la fiabilité devient le point le plus critique de leur réalisation. Si chacun des éléments du système (télescope, lignes à retard,...) n'atteint "que" 95% de fiabilité, alors l'interféromètre ne sera opérationnel que la moitié du temps !

5.5 Vers le VLTI de seconde génération

Les premiers instruments du VLTI (VINCI, MIDI et AMBER) offrent dès aujourd'hui de vastes possibilités, mais apparaissent limités en terme de nombre de télescopes utilisables simultanément (2 ou 3 seulement), de sensibilité (VINCI permet $m_K = 10$), et de pouvoir de résolution.

La première de ces limitations, le nombre de télescopes, est particulièrement gênante pour l'observation des objets dont la répartition de lumière est complexe. Deux ou trois télescopes ne permettent pas de reconstituer une véritable image (c'est-à-dire une carte de la répartition de lumière indépendante d'un modèle), ce qui est clairement limitant par exemple dans le cas des noyaux actifs de galaxie (NAG), ou des étoiles évoluées dont les enveloppes sont complexes.

La sensibilité des instruments de première géneration est modérément pénalisante pour l'étude des exoplanètes, du centre de notre Galaxie, ou encore des NAG situés à des dis-

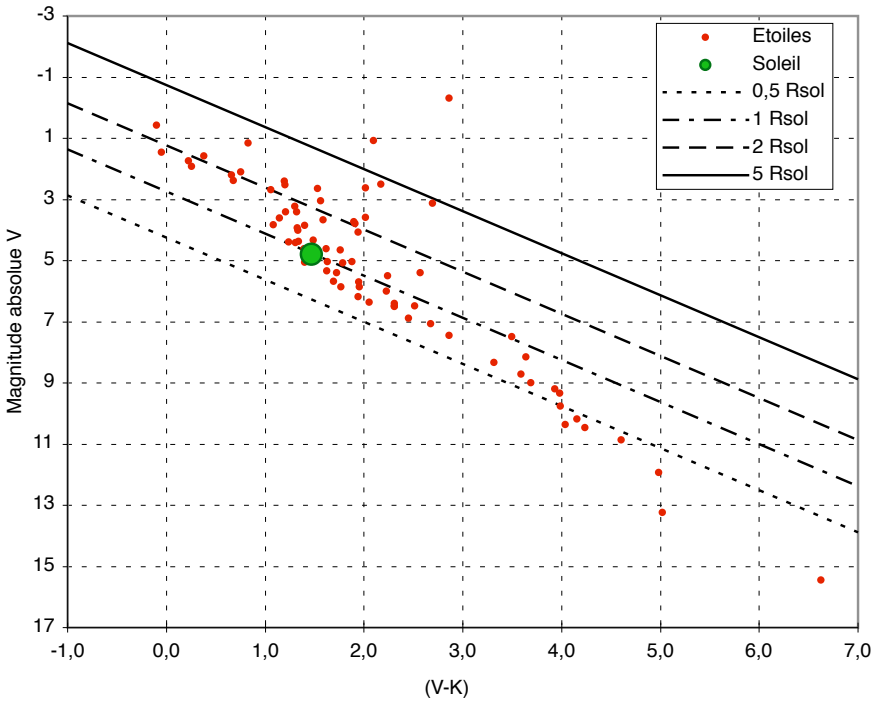

FIG. 5.4 – Positions dans le diagramme Hertzsprung-Russell des 79 étoiles situées à moins de 22 pc dont le rayon peut être mesuré avec une précision meilleure que 1% en combinant des mesures AMBER et Hipparcos. Les droites diagonales représentent les lieux de rayon linéaire constant (isorayons).

tances intermédiaires (magnitudes supérieures à 12). Deux solutions peuvent être envisagées pour améliorer la sensibilité : augmenter le flux lumineux utile, ou utiliser une référence de phase extérieure pour augmenter le temps d'intégration. Sur le premier point, il est intéressant de noter que la transmission totale du VLTI (incluant les instruments) est inférieure à 1%. Ce chiffre est faible, mais il est le résultat attendu de la complexité optique de cet instrument. Après plus de 20 réflexions, les faisceaux de lumière de l'étoile observée sont filtrés spatialement (VINCI et AMBER), avant d'être recombinés. Malgré l'utilisation d'optiques adaptatives pour les grands télescopes de 8 m, les pertes dues au filtrage spatial des faisceaux restent considérables.

Pour augmenter le flux utile à l'interférométrie, il apparaît souhaitable d'augmenter à la fois la transmission du train optique, et la qualité optique des images (rapport de Strehl et stabilité notamment). Ceci pourrait être envisagé grâce à un transport fibré des faisceaux, au lieu de l'actuel transport par train optique de miroirs (le projet OHANA fait déjà appel à cette technologie). Pour augmenter la qualité des images fournies par les télescopes, l'ajout d'une optique adaptative spécifique corrigeant les hauts ordres de la turbulence apparaît comme une solution prometteuse, surtout aux longueurs d'ondes infrarouges. Même si la qualité actuelle de la correction apportée par les systèmes d'optique adaptative MACAO du VLTI est en moyenne de bonne qualité (rapport de Strehl de l'ordre de 50% sur une étoile de magnitude $m_V = 10$), la stabilité du flux concentré dans le filtre spatial reste encore perfectible. La qualité du suivi des franges étant très dépendante de l'absence de passages à zéro du flux transmis par ce filtre, cet aspect de la correction revêt une grande importance, peut-être sous-estimée lors de la conception des systèmes d'optique adaptative. L'un des instruments envisagés actuellement pour la seconde

génération, GRAVITY, intègre d'ailleurs une optique adaptative dédiée.

Pour augmenter le pouvoir de résolution, la taille de la plate-forme de Paranal étant limitée physiquement, il n'est pas possible d'étendre la longueur maximale des bases du VLTI au delà des 200 m actuels. Il est envisagé de placer un télescope sur une des montagnes proches du Cerro Paranal pour augmenter la base au-delà du kilomètre. Il serait lié à la plate-forme du VLTI par fibre optique. L'autre possibilité pour augmenter la résolution angulaire est de diminuer la longueur d'onde. Ceci n'est pas identique à une augmentation de la longueur de base, car la morphologie des objets observés change avec la longueur d'onde. Passer par exemple de l'infrarouge au visible ne permet plus d'observer les enveloppes froides des étoiles évoluées. Cependant, le domaine visible reste extrêmement prometteur car il permet d'accéder à la spectro-interférométrie des raies photosphériques et chromosphériques. Plus généralement, il permet de sonder efficacement la structure atmosphérique des étoiles grâce à l'assombrissement centre-bord, plus important et donc plus facile à mesurer qu'en infrarouge.

5.6 L'interférométrie dans l'espace

Des projets d'interféromètres dans l'espace existent depuis plusieurs dizaines d'années, mais le seul interféromètre optique dans l'espace à ce jour reste le *Fine Guidance Sensor* du télescope spatial Hubble. Cet instrument, dont la courte base est limitée par la taille du miroir primaire du télescope, est utilisé pour assurer le suivi du télescope lors des longues poses. Bien qu'il ne s'agisse pas à proprement parler d'un instrument scientifique, sa grande précision astrométrique sur un petit champ a permis d'obtenir une remarquable mesure de la parallaxe trigonométrique de la Céphéide δ Cep (Benedict et al. 2002).

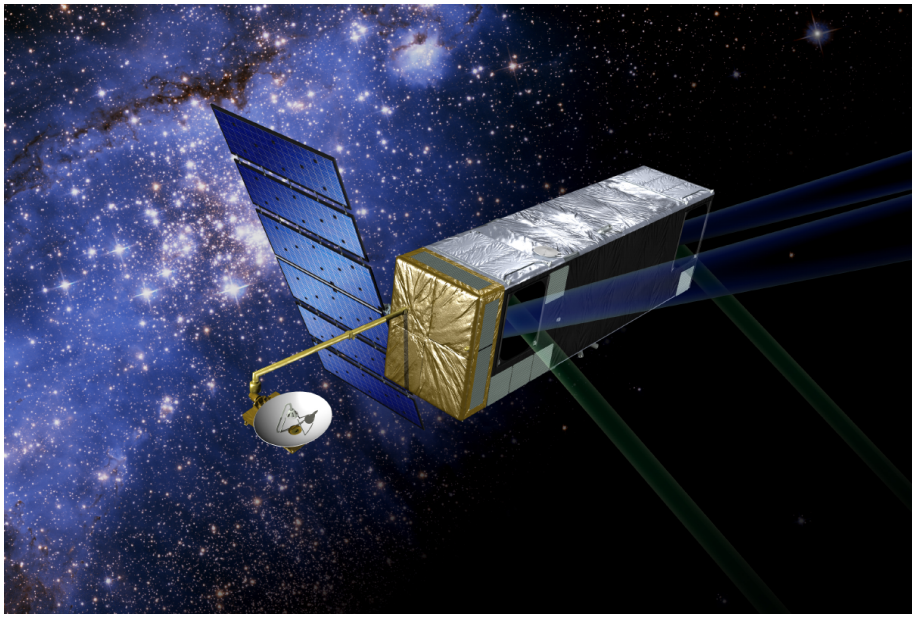

FIG. 5.5 – Vue d'artiste de la mission interférométrique SIM (illustration NASA/JPL).

Le projet spatial le plus avancé à ce jour est la mission d'astrométrie interférométrique SIM (Fig. 5.5). Ce satellite utilisera une base de 9 m de longueur pour mesurer avec une précision d'une microseconde d'angle (μas) l'écartement entre deux étoiles. Cette remarquable précision rendra possible la détection astrométrique de planètes terrestres dans la zone habitable des

étoiles proches (Catanzarite et al. 2006). En plus de cet objectif, SIM permettra de mesurer la parallaxe, le mouvement propre et la taille angulaire d'un grand nombre d'étoiles (y compris au voisinage du centre de notre Galaxie), ainsi que les orbites, et donc les masses, d'une grande variété d'étoiles multiples. Le lancement de la mission SIM était prévu pour 2015, mais le programme a été suspendu par la NASA en 2006.

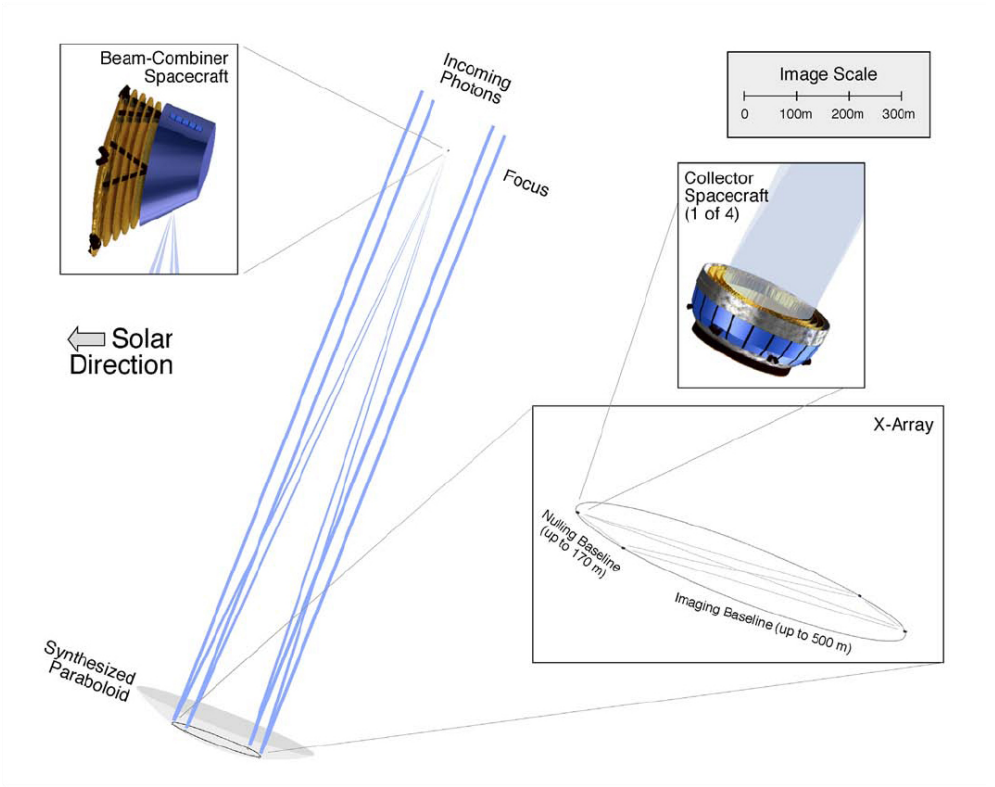

FIG. 5.6 – Configuration de la future mission Darwin de recherche de la vie extraterrestre (illustration tirée de Léger et al. 2007).

Darwin et sa contrepartie américaine TPF sont deux projets spatiaux de très grande envergure destinés à mesurer directement le spectre en lumière réfléchie de planètes semblables à la Terre orbitant autour d'autres étoiles. Le but ultime est d'y rechercher la signature de la vie extraterrestre.

Du côté européen, le projet Darwin (Fig. 5.6) est très actif et a été proposé officiellement en 2007 comme future mission spatiale majeure de l'agence spatiale européenne (Léger et al. 2003) pour la période 2015-2025. Il est soutenu par une large communauté internationale de chercheurs (PI : A. Léger), et comporte dans sa version actuelle quatre tèlescopes de 2 m de diamètre et une unité de recombinaison, les cinq vaisseaux volant en formation. La longueur des bases séparant les télescopes pourra varier de 7 à 500 m, pour une gamme de longueurs d'onde de 6 à 20 μm. L'infrarouge moyen est en effet le domaine de longueur d'onde où le contraste est le moins fort entre la planète et son étoile ($\approx 10^6$, au lieu de $\approx 10^9$ en visible). Darwin permettra de détecter la lumière provenant de la planète en éteignant la lumière de l'étoile par interférence destructive. Il est prévu d'observer 200 étoiles susceptibles de posséder des planètes de type terrestre pendant une période de 5 ans. Darwin sera également capable de fonctionner en mode constructif, pour permettre la synthèse d'images à très haute résolution angulaire.

Du côté américain, deux concepts pour TPF sont en cours d'étude : un interféromètre (TPF-

I) et un coronographe (TPF-C). Le concept interférométrique repose sur trois télescopes de 3 m de diamètre et une base centrale de recombinaison évoluant indépendemment dans l'espace. Malheureusement, comme pour SIM, la décision a été prise en 2006 par la NASA de suspendre le projet TPF *sine die*.

5.7 Un interféromètre sur la Lune ?

L'interférométrie présente cette particularité que les instruments sont naturellement très modulaires. Ceci permet d'imaginer d'immenses réseaux de télescopes pour l'imagerie à très haute résolution angulaire. Ce type d'instruments est cependant difficile à concevoir sur Terre, car la présence de l'atmosphère est une limitation critique à la sensibilité (du fait des poses très courtes nécessaires pour figer le piston), et au domaine de longueur d'onde accessible.

Plusieurs possibilités sont envisageables pour installer un futur réseau géant, par exemple pour l'imagerie des exoplanètes : dans l'espace interplanétaire, sur la Lune, ou sur une autre planète du système solaire ne possédant pas d'atmosphère dense. La première de ces possibilités est déjà prévue pour SIM et Darwin/TPF. Des projets d'interféromètres lunaires existent depuis déjà une vingtaine d'années (voir par exemple Arnold et al. 1996). La surface lunaire apparaît à plusieurs égards bien adaptée pour recevoir de grandes structures destinées à l'observation astronomique. La faible gravité permet d'alléger considérablement les édifices, alors que le sol reste suffisamment porteur et stable pour éviter l'enfoncement et les dérives des télescopes. Les sites les mieux adaptés sont ceux situés perpétuellement à l'ombre, en particulier près des pôles (Fig. 5.7). Ils permettent d'éviter les importantes contraintes thermiques imposées par les changements d'éclairement solaire. Plusieurs difficultés importantes existent cependant, et rendent la surface lunaire peu attractive par rapport à un instrument en vol libre spatial. En premier lieu, le déploiement des télescopes et l'installation des dispositifs de retardement des faisceaux nécessite un niveau de précision et d'automatisation peu compatible avec les aléas de la géographie lunaire. L'espace interplanétaire est à ce titre un milieu beaucoup plus prévisible et facile à maîtriser. D'autre part, la dépose d'équipement à la surface lunaire est un exercice difficile, qui demande en lui-même un système de contrôle complexe et surtout beaucoup d'énergie. Le bénefice de la présence du sol lunaire comme support des structures est compensé aujourd'hui par le progrès des techniques de contrôle de position des satellites en vol libre. Enfin, le sol lunaire étant constitué de poussière très fines, une contamination des optiques est pratiquement inévitable dès le déploiement de l'instrument. Ces problèmes se posent d'ailleurs de la même manière pour tous les satellites et les astéroïdes du système solaire. L'espace interplanétaire apparaît donc actuellement comme le meilleur endroit pour installer les futurs très grands réseaux interféromètriques, au-delà de SIM et Darwin.

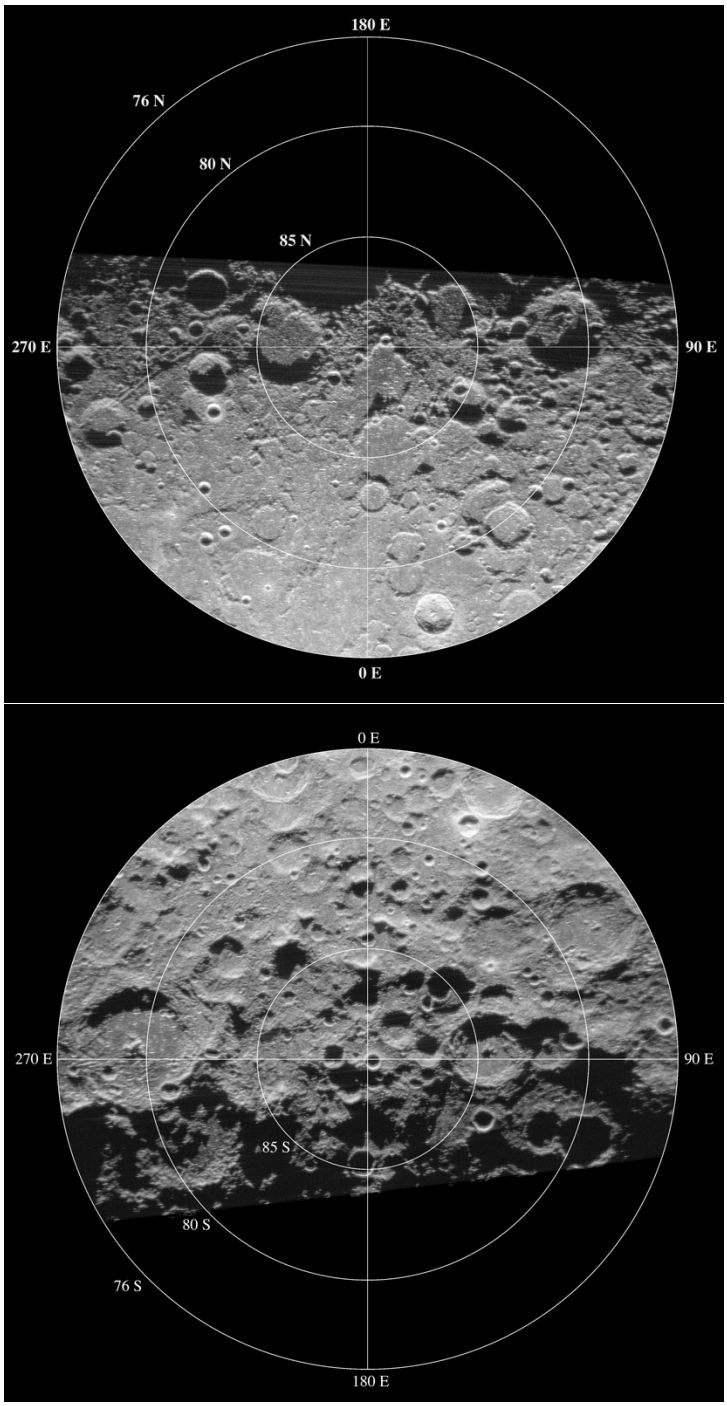

FIG. 5.7 – Les pôles Nord et Sud lunaires, cartographiés par le radiotélescope d'Arecibo : de bons sites pour un interféromètre optique géant ? (images Bruce Campbell/Arecibo Observatory).

Annexe A

Encadrement de jeunes chercheurs

A.1 Stage de Melle Jessica GALLY (2006)

Niveau : Stage de Master 1 de l'Université Paris 6.

Durée : 2 mois (du 1er Juin au 31 Juillet 2006).

Titre : Mesure de la vitesse de rotation d'Altaïr.

Contenu scientifique : On connaît de nombreuses étoiles, en particulier les plus chaudes, dont la période de rotation est de quelques heures seulement (contre 27 jours pour le Soleil). La vitesse des ces étoiles à l'équateur atteint plusieurs centaines de kilomètres par seconde, créant une force centrifuge énorme. Ceci provoque des déformations spectaculaires de leur surface. Une des plus brillantes étoiles en rotation rapide est Altaïr (α Aquilae). C'est une étoile naine plus chaude que le Soleil et la treizième étoile la plus brillante du ciel. Le stage a consisté en une mesure de la vitesse de rotation de l'étoile Altar par l'analyse d'un spectre de cette étoile obtenu par le spectrographe UVES du VLT. Cette mesure a été réalisée par la transformation de Fourier d'une raie spectrale du Mg II. Une extension à l'étoile en rotation lente Castor de même type spectral a permis de caractériser la modification du profil de la raie étudiée par la rotation.

A.2 Stage de Melle Lucile PUPIER (2006)

Niveau : Première année de l'ENSPS (Strasbourg).

Durée : 1 mois (du 1er au 31 Juillet 2006).

Titre : Mesure de la vitesse de rotation de Céphéides.

Contenu scientifique : Les Céphéides sont des étoiles supergéantes pulsantes. Du fait de leur très grande taille, leurs vitesses de rotation sont supposées faibles, mais elles échappent encore à la mesure directe. La largeur considérable de leurs raies spectrales rend en effet difficile la mesure du faible élargissement rotationnel qui lui est superposé. La pulsation des Céphéides introduit de plus une importante asymétrie des raies, variable au cours de la pulsation. Ce stage a permis de mesurer la vitesse de rotation de huit Céphéides brillantes, observées récemment avec le spectrographe à haute résolution HARPS ($R \approx 100000$). Les mesures ont été réalisées lors des phases de maximum et minimum de diamètre des étoiles, de manière à minimiser l'asymétrie due à la pulsation. Dans tous les cas, la position du premier minimum de la transformée de Fourier d'une raie spectrale sélectionnée (du Fe I) a pu être déterminée avec précision, donnant ainsi une mesure de la vitesse de rotation. Cette vitesse a également pu être retrouvée à d'autres phases de la pulsation même en présence d'asymétrie.

Annexe B

Résumé sur l'originalité des recherches

L'originalité de mon travail est d'avoir diffusé l'interférométrie optique dans des domaines de l'astrophysique où elle n'était pas encore utilisée, ou insuffisamment, en m'appuyant sur mon expérience instrumentale.

Je pense tout d'abord à la modélisation des étoiles naines de la séquence principale. Pour cette classe d'étoiles, la mesure du rayon fournit une contrainte majeure sur la masse, les autres observables classiques prenant une importance secondaire. En pratique, la mesure du rayon d'une étoile de type solaire avec une précision d'un pourcent nous permet d'estimer sa masse avec une précision comparable. Utilisée en conjonction avec l'astérosismologie, l'interférométrie stellaire nous permet d'estimer l'âge et la structure des étoiles avec une précision remarquable. Les fréquences sismiques nous renseignent sur la structure interne de l'étoile, et le rayon permet d'étalonner les paramètres d'ensemble comme la masse, la gravité de surface et la température effective. J'ai réalisé en 2003 la première association de ces deux techniques pour étudier l'étoile binaire α Centauri. A la suite de ce travail, j'ai participé à l'organisation scientifique d'un atelier de recherche intitulé "Workshop on Interferometry and Asteroseismology", qui s'est tenu fin 2005 à l'Université de Porto (Portugal), au cours duquel la complémentarité de ces techniques est apparue extrêmement prometteuse.

Les étoiles Céphéides sont des objets classiques de l'astronomie, au sens où beaucoup de recherches leur ont déjà été consacrées. On connaît le mécanisme physique de leur pulsation depuis 1941. Pourtant, alors que ce sujet paraissait "usé", j'ai établi grâce à des observations interférométriques que ces étoiles possédent des enveloppes circumstellaires, une découverte inattendue autour d'étoiles dont le fonctionnement paraissait simple et bien connu et qui sont une des références de l'échelle des distances extragalactiques. Au sein d'une collaboration internationale, je poursuis actuellement leur étude par différentes techniques d'observation, avec pour but de mieux comprendre les interactions entre la pulsation et les enveloppes.

Les étoiles en rotation rapide sont un autre exemple de l'apport de la haute résolution angulaire. J'ai démontré en 2003 que l'étoile Achernar, en rotation très rapide, présente un rapport d'aplatissement de plus de 1,5 (rapport de ses rayons polaire et équatorial). Les modèles de rotation interne utilisés actuellement ne permettent pas d'expliquer cette déformation. Cela signifie probablement que cette étoile possède une loi de rotation interne non uniforme. Cette découverte soulève des questions fascinantes sur le transport visqueux de moment cinétique et la turbulence, deux phénomènes clés en astrophysique. En 2006, j'ai mis en évidence le vent stellaire émis par les pôles de cette étoile, causé par leur température extrême.

L'interférométrie optique et infrarouge a ouvert ces dernières années un accès direct à des résolutions angulaires encore inexplorées en astronomie. J'ai contribué par mes travaux à rendre cette technique *utile* pour l'astrophysique. Autrefois réservée aux spécialistes, complexe et peu productive scientifiquement, l'interférométrie est devenue en quelques années un outil de premier plan pour la physique stellaire. Les collaborations que j'ai développées ont pris leur juste place dans cette renaissance, qui se manifeste par une augmentation rapide du nombre de publications référées (cf. Sect. 5). Avec la mise en service à leur plein potentiel de nouveaux instruments très performants (VLTI, CHARA), cet essor est appelé à s'amplifier encore dans les années à venir. Grâce à mon Habilitation à diriger les recherches, je souhaite accompagner ce développement par la formation de jeunes chercheurs maîtrisant à la fois les outils classiques de l'astronomie observationnelle et l'interférométrie optique, ainsi que leur application à la physique stellaire.

Bibliographie

Arnold, L., Labeyrie, A., & Mourard D. 1996, Adv. Space Res., 18, n°11, 49
Assus, P., Choplin, H., Corteggiani, J.-P. et al. 1979, Journal of Optics, 10(6), 345
Baade, W. 1926, Astron. Nachr., 228, 359
Baraffe, I., Chabrier, G., Allard, F., & Hauschildt, P. H. 1998, A&A, 337, 403
Benedict, G. F., McArthur, B. E., Fredrick, L. W., et al. 2002, AJ, 123, 473
Bester, M., Danchi, W. C., & Townes, C. H. 1990, Proc SPIE, 1237, 40
Böhm-Vitense, E., & Love, S. G. 1994, ApJ, 420, 201
Bouchy, F., Udry, S., Mayor, M., et al. 2005, A&A, sous presse
Burki, G., Mayor, M., & Benz, W. 1982, A&A, 109, 258
Catanzarite, J., Shao, M., Tanner, A., Unwin, S., & Yu, J. 2006, PASP, sous presse
Coudé du Foresto, V., & Ridgway, S. T. 1992, ESO Proc. "High Resolution Imaging by Interferometry II", vol. 39, 731
Coudé du Foresto, V., Ridgway, S., Mariotti, J.-M. 1997, A&A Suppl. Series, 121, 379
Deasy, H. P. 1988, MNRAS, 231, 673
Domiciano de Souza, A., Kervella, P., Jankov, S., et al 2003, A&A, 407, L47
Fouqué, P., & Gieren, W. P. 1997, A&A, 320, 799
Freedman, W., Madore, B. F., Gibson, B. K., et al. 2001, ApJ, 553, 47
Hanbury Brown, R., Davis, J., & Allen, L. R. 1974, MNRAS, 167, 121
Hanbury Brown, R., & Twiss, R. Q. 1956, Nature, 178, 1046
Havlen, R. J., 1972, A&A, 16, 257
Jackson, S., MacGregor, K. B., & Skumanich, A. 2004, ApJ, 606, 1196
Kervella, P. 2001, Thèse de Doctorat, Université Paris 7
Kervella, P., & Domiciano de Souza, A. 2006, A&A, 453, 1059
Kurucz, R. L. 1992, IAU Symp. 149 : The Stellar Populations of Galaxies, 149, 225
Labeyrie, A. 1974, ApJ, 196, L71
Lawson, P. R. éd. 1997, "Selected Papers on Long Baseline Interferometry", SPIE Milestone Series, volume MS 139
Léger, A., et al. 2007, "Darwin - A Proposal for the Cosmic Vision 2015-2025 ESA Plan", http ://arxiv.org/abs/0707.3385
Leinert, Ch., Graser, U., Richichi, A., et al. 2003, ESO Messenger, 112, 13
Mariotti, J.-M., Coudé du Foresto, V., Perrin, G., et al. 1996, A&A Suppl., 116, 381
McAlary, C. W. & Welch, D. L., 1986, AJ, 91, 1209
Mourard, D., Tallon-Bosc, I., Blazit, A., et al. 1994, A&A, 283, 705
Ohishi, N., Nordgren, T. E., & Hutter, D. J. 2004, ApJ, 612, 463
Perrin, G., Woillez, J., Lai, O. et al. 2006, Science, 311, 194
Perryman, M. A. C., Lindegren, L., Kovalevsky, J., et al., The Hipparcos Catalogue 1997, A&A, 323, 49
Peterson, D. M., Hummel, C. A., Pauls, T. A., et al. 2004, Proc. SPIE, 5491, 65

Petrov, R., Malbet, F., Richichi, A., et al. 2000, SPIE, 4006, 68
Pourbaix, D., Nidever, D., McCarthy, C., et al., 2002, A&A, 386, 280
Leavitt, H. S., & Pickering, E. C., Harvard Circulars, 173, 1
Michelson, A. A., & Pease, F. G. 1921, ApJ, 53, 249
Szabados, L. 2003, Comm. Konkoly Obs. 103, 115
Tassoul, J.-L. 1978, Theory of Rotating Stars, Princeton University Press
Tassoul, J.-L. 2000, Stellar Rotation, Cambridge University Press
Thévenin, F., Provost, J., Morel, P., Berthomieu, G., Bouchy, F., Carrier, F., 2002, A&A, 392, L9
Van Belle, G. T., Ciardi, D. R., Thompson, R. R., Akeson, R. L., & Lada, E. A. 2001, ApJ, 559, 1155
Von Zeipel, E. 1924, MNRAS, 84, 665
Wesselink, A. 1946, Bull. Astron. Inst. Netherlands, 10, 91
Wittkowski, M., Aufdenberg, J., & Kervella, P. 2004, A&A, 413, 711

Résumé

L'interférométrie est une technique puissante pour l'étude des étoiles, car elle permet de résoudre leur disque apparent. Je présente dans ce mémoire une application de l'interférométrie à trois types d'étoiles : les Céphéides, les étoiles de la séquence principale et les étoiles en rotation rapide. Les Céphéides sont une célèbre classe d'étoiles supergéantes pulsantes. Elles sont largement utilisées comme étalons de distance, grâce à leurs relations période-luminosité. L'interférométrie permet d'appliquer une version améliorée de la méthode Baade–Wesselink pour mesurer la distance des Céphéides, et ainsi d'étalonner les relations période-luminosité. Même si cette méthode est potentiellement très précise, plusieurs points sont critiques dans son application, en particulier le facteur de projection. Les étoiles de la séquence principale (SP) sont de loin la classe la plus nombreuse de l'Univers, toutes les étoiles passant la majorité de leur existence sous forme de naines. J'ai utilisé l'interférométrie sur une large gamme d'étoiles de la SP, depuis les étoiles de très faible masse (Proxima) jusqu'aux étoiles chaudes. En particulier, j'ai réalisé la première utilisation combinée de contraintes interférométriques et astérosismiques pour la modélisation des étoiles (α Centauri, etc...). Dans une troisième partie, je décris nos résultats récents sur les étoiles en rotation rapide. Du fait de l'importante force centrifuge à l'équateur, la photosphère de ces étoiles est déformée. L'interférométrie nous a permis d'observer directement ces déformations sur trois étoiles brillantes en rotation rapide : Altaïr (α Aql), Achernar (α Eri) et Véga (α Lyr).

Discipline : Astrophysique
Mots-clefs : interférométrie, étoiles, Céphéides, rotation stellaire, instrumentation, VLTI
Adresse : Observatoire de Paris, LESIA, 5 place Jules Janssen, 92195 Meudon Cedex

Abstract

Optical interferometry is a powerful technique for the study of stars in exquisite details, by enabling the spatial resolution of their disks. I present three applications of this technique to the study of different types of stars : Cepheids, main sequence stars, and fast rotators. Cepheids are a famous class of supergiants that are widely used as standard candles for distance measurements, through the period-luminosity (P–L) relations. Interferometry allows to apply a refined version of the Baade–Wesselink method to estimate the distance to nearby Cepheids, and therefore calibrate the P–L relations. While this method is promising and potentially very precise, several points in its application are critical, in particular the projection factor. Main sequence stars are by far the most numerous stellar class in the universe, as all stars spend the majority of their life as dwarfs. I have applied interferometry to a broad range of main sequence stars, from the very low mass Proxima to hot stars. In particular, I have realized the first combination of interferometric and asteroseismic constraints for the modeling of stars (the two components of α Centauri, as well as other stars). In a third part, I describe the recent results that we have obtained on fast rotating stars. Due to the very strong centrifugal force at the equator, the photosphere of these stars is strongly distorted. Interferometry allows to observe these deformations, and I describe our observations of three bright, fast rotating stars : Altair (α Aql), Achernar (α Eri) and Vega (α Lyr).